Contributions to Commercial Supersonic Aircraft Technology: Low-Speed Aerodynamic Design and Active Aeroelastic Control

Kuang-Ying Ting

A dissertation
submitted in partial fulfillment of the
requirements for the degree of

Doctor of Philosophy

University of Washington

2026

Reading Committee:

Eli Livne, Chair

Mehran Mesbahi, Chair

Chester P. Nelson

Behcet Açıkmeşe

Steven L. Brunton

Program Authorized to Offer Degree:
William E. Boeing Department of Aeronautics and Astronautics

©Copyright 2026
Kuang-Ying Ting

University of Washington

Abstract

Contributions to Commercial Supersonic Aircraft Technology: Low-Speed Aerodynamic Design and Active Aeroelastic Control

Kuang-Ying Ting

Co-Chairs of the Supervisory Committee:
Eli Livne
William E. Boeing Department of Aeronautics and Astronautics

Mehran Mesbahi
William E. Boeing Department of Aeronautics and Astronautics

This dissertation describes contributions to commercial supersonic technology in two areas: low-speed wind tunnel aerodynamic testing and analysis and active aeroelastic control with wind tunnel aeroservoelastic demonstrations and evaluation. The NASA Supersonic Configurations at Low Speeds (SCALOS) project addresses the research gap between the much needed work on low-speed characteristics that affect takeoff, approach, and landing of commercial supersonic aircraft and the high-speed cruise-optimized conditions on which existing designs and publications have focused for years. The SCALOS wind tunnel campaign spanned five years, with eight entries, 1415 runs, and 61.5 occupancy test days at the University of Washington's Kirsten Wind Tunnel, producing a low-speed aerodynamic database of supersonic configurations and their parametric variations, together with the dedicated tare-and-interference corrections developed for the slender geometries representative of what will drive commercial supersonic aircraft designs. The aerodynamic results, analysis, and findings of the SCALOS project have been published and submitted to NASA. In parallel, motivated by the aeroelastic challenges facing slender, thin-wing, supersonic configurations, the second part of the dissertation presents active aeroelastic control studies that include analysis, synthesis of control laws, and wind tunnel aeroservoelastic demonstrations using two flexible high-aspect-ratio wing testbeds developed at the University of Washington,

named MARGE and LARGE. The work covers gust load alleviation with preview $\mathcal{H}_2$ as well as $\mathcal{H}_\infty$ control for active flutter suppression. For the active flutter suppression analysis and tests different flutter mechanisms were created by a destabilize/stabilize approach. Mixed-sensitivity $\mathcal{H}_\infty$ robust control with modal damping was then used, focusing on closed-loop robustness, test/analysis correlation, and the experimental evaluation of readiness of the technology for implementation in actual flight vehicles. Together, these contributions add publicly accessible results and lessons that would contribute to the design and active aeroelastic control of the next generation of commercial supersonic aircraft.

TABLE OF CONTENTS

Page

List of Figures iv

List of Tables xix

Nomenclature xxi

Chapter 1: Introduction 1

Chapter 2: SCALOS 9
2.1 Project Background and Overview 9
2.1.1 Project Overview 9
2.2 Design Space Survey 29
2.2.1 Developed and Evolving Supersonic Airliner / SSBJ 31
2.2.2 University of Washington Models 36
2.2.3 Comparison and Discussion of Configuration Features 51
2.3 CFD Correlation and Simulation 65
2.3.1 Aerodynamic Simulation Software 66
2.3.2 Test / Simulation Correlation Discussion 71
2.4 SCALOS Configurations in the Wind Tunnel 75
2.4.1 Kirsten Wind Tunnel 75
2.4.2 Model Mounting System 76
2.4.3 Test Model and Test Letter Geometry 78
2.4.4 Test Conditions and Test Entries 82
2.4.5 Long-term and Short-term Test-to-Test Repeatability 83
2.4.6 Reynolds Number Effects 88
2.5 Aerodynamic Database 90
2.5.1 Data Structure 90
2.5.2 Part Designations and Part List 92
2.5.3 Model Geometry 95

2.5.4 Run Log . . . 95
2.5.5 Data Reduction and Standard UWAL Data Names . . . 96
2.6 Tare and Interference Correction . . . 100
2.6.1 Tested T&I Configurations . . . 102
2.6.2 Testing to Establish T&I Corrections . . . 103
2.6.3 Results and Discussion . . . 107
2.6.4 T&I Lessons Learned . . . 129
2.7 Aerodynamic Results and Analysis . . . 130
2.7.1 Wing Planforms . . . 136
2.7.2 Configuration Studies . . . 153
2.7.3 Fuselages . . . 164
2.7.4 Canards . . . 165
2.7.5 Horizontal Tails and Control Authority . . . 170
2.7.6 Vertical Tail . . . 185
2.7.7 Nacelles . . . 188
2.7.8 Leading Edges . . . 191
2.7.9 Trailing Edges . . . 208
2.7.10 Take-off and Landing Configuration . . . 248
2.8 Longitudinal Aerodynamics . . . 252
2.8.1 Wing Planform . . . 252
2.8.2 Detailed Longitudinal Database For Tail Deflections . . . 258
2.8.3 Canard Deflection Data Details . . . 274
2.8.4 Wing Control Surfaces - Incremental Effects Details . . . 277
2.9 Lateral-Directional Aerodynamics . . . 284
2.9.1 Configuration Lateral-directional Characteristics . . . 285
2.9.2 Flow Visualization Correlation . . . 290
2.9.3 Canard Deflection . . . 294
2.9.4 Directional Control Authority . . . 299
2.9.5 Nacelle locations and Engine-out conditions . . . 307
2.9.6 Aileron Deflections . . . 314
2.9.7 Take-off and Landing Conditions . . . 319
2.10 Lessons Learned . . . 324
2.10.1 Longitudinal Charateristics . . . 324

Chapter 3: Aeroservoelasticity . . . 335
3.1 Active Aeroelastic Control . . . 335
3.2 Experimental Setup . . . 341
3.2.1 Aeroelastic Model in 3'x3', MARGE . . . 341
3.2.2 Aeroelastic Model in Kirsten Wind Tunnel (KWT), LARGE . . . 344
3.3 Background Mathematics . . . 348
3.3.1 Robust Control . . . 348
3.3.2 The Destabilize/Stabilize Approach . . . 352
3.3.3 Chirp Z-Transform . . . 353
3.4 Wind Tunnel System Identification . . . 355
3.4.1 MARGE . . . 355
3.4.2 LARGE . . . 363
3.5 Control Design . . . 371
3.5.1 MARGE GLA . . . 371
3.5.2 MARGE AFS . . . 375
3.5.3 LARGE GLA . . . 379
3.6 Wind Tunnel Results . . . 380
3.6.1 MARGE GLA . . . 381
3.6.2 MARGE AFS . . . 394
3.6.3 LARGE GLA . . . 402

Chapter 4: Conclusion . . . 409

LIST OF FIGURES

Figure Number Page

1.1 American supersonic transport programs before N+ programs [1] 3
1.2 European supersonic transport programs before 2018 [1] 4
1.3 JAXA programs roadmap up to 2012 [2] 5
1.4 CFD challenges 6
1.5 YF-16 tested configuration [3] 7

2.1 The NASA SCALOS project team and areas of contribution [4] 10
2.2 SCALOS's information and tasks flow map [4] 11
2.3 UW capstone wind tunnel and RUAV models before SCALOS [4] 12
2.4 HSCT concept evolution: Ref-H, TCA, and TC configurations [5] 14
2.5 HISCAT advanced HSCT concept (1999) [5] 15
2.6 SSBJ 2003-2007 17
2.7 Boeing concepts [6–8] 18
2.8 Lockheed concepts [9, 10] 18
2.9 Boeing QEVC and Lockheed N+2 Phase II comparison 19
2.10 Boeing Elliptical Cowl Ramp Inlet [11] 19
2.11 Lockheed 1044 high-alpha pitch-up due to wing apex vortex formation [10] . 20
2.12 NASA-Lockheed Martin X-59 low-boom flight demonstrator [12] 21
2.13 NASA-Lockheed Martin X-59 low-boom flight demonstrator in flight (courtesy, NASA) 21
2.14 2013 UW AFRL-AFOSR model (SCALOS "core") [4] 23
2.15 Boeing's N+2 configurations vs. UW's UW-S-15A (schematic. not to precise scale) [4] 24
2.16 SCALOS 2015 model, and the UW-S-15A RUAV [4] 25
2.17 SCALOS 2016 model [4] 25
2.18 SCALOS 2017 model [4] 26
2.19 SCALOS 2021 model, UW-S-21A [4] 27
2.20 SCALOS notional configuration matrix [4] 28
2.21 SCALOS 2020 model, UW-S-20A [4] 28

2.22 Low-boom configuration with long fuselage, nacelle aft-deck, and T-tail, UW-S-20CL-3, in the KWT [4] . . . 29
2.23 Flow visualization [4] . . . 29
2.24 UW supersonic configurations polar chart . . . 38
2.25 Overall slenderness [13] . . . 52
2.26 Lifting slenderness [13] . . . 53
2.27 Forebody slenderness ratio [13] . . . 54
2.28 Aspect ratio (AR) [13] . . . 57
2.29 Inboard-wing sweep [13] . . . 57
2.30 Outboard-wing sweep [13] . . . 58
2.31 Number of engines [13] . . . 60
2.32 Horizontal tail sweep [13] . . . 62
2.33 Vertical tail sweep [13] . . . 63
2.34 Canard sweep [13] . . . 65
2.35 DATCOM model configurations [14] . . . 67
2.36 DATCOM ESDU model configurations [14] . . . 67
2.37 Mesh representations in OpenVSP [14] . . . 68
2.38 OpenVSP panel method difficulties [14] . . . 69
2.39 Meshed model for Star-CCM+ [14] . . . 71
2.40 DATCOM aerodynamic results [14] . . . 72
2.41 DATCOM (superpositioned) vs. KWT data [14] . . . 72
2.42 Various VLM methods result [15] . . . 73
2.43 VSPAERO pressure distribution solutions and trailing wakes at $\alpha = 6^\circ$ [14] . . . 74
2.44 Comparison of RANS CFD techniques to experimental data [16] . . . 74
2.45 Kirsten Wind Tunnel at the University of Washington [17] . . . 76
2.46 Kirsten Wind Tunnel test section [17] . . . 76
2.47 The fork 14H model mounting system [18] . . . 77
2.48 Configurations selected for tare and interference measurements [19] . . . 77
2.49 Wing and tail geometry variations . . . 80
2.50 Tested SCALOS configurations . . . 81
2.51 Wing-only and UW-S-21A without nacelles . . . 82
2.52 Test repeatability configurations . . . 84
2.53 2015 wing-only (W15) test-to-test repeatability across multiple dynamic pressures . . . 85
2.54 2015 wing+fuselage test-to-test repeatability across multiple dynamic pressures 86

2.55 UW-S-20A test-to-test repeatability across multiple dynamic pressures 87
2.56 Effects of dynamic pressure and Reynolds number for 2015 wing alone 89
2.57 Effects of dynamic pressure and Reynolds number for wing and aft-deck . . . 90
2.58 Effects of dynamic pressure and Reynolds number for wing and fuselage . . . 90
2.59 KWT Data Reduction Flow Chart [18] 97
2.60 Axis coordinate system [17] 98
2.61 Top view of tested configurations with selected dimensions [19] 102
2.62 Tare and interference configurations [17] 106
2.63 Tare and interference steps for wing only (W15) 107
2.64 Tare and interference steps for wing and aft-deck (W15+AD16) 107
2.65 Tare and interference steps for UW-S-21A without nacelles 107
2.66 KWT standard 14-H fork and pitch arm T&I corrections vs. sideslip ($\alpha = 0°$) [18] 110
2.67 KWT standard 14-H fork and pitch arm T&I corrections, lift-dependent with dynamic pressure [18] 111
2.68 Wing only (W15) KWT standard T&I dimensional corrections at $q = 32$ psf . 113
2.69 Wing only (W15) SCALOS-specific T&I dimensional corrections at $q = 32$ psf 113
2.70 Wing only (W15) SCALOS-specific T&I non-dimensional corrections at $q =$ 32 psf 114
2.71 Wing only (W15) T&I non-dimensional correction differences at $q = 32$ psf (SCALOS-KWT) 115
2.72 Wing and aft-deck (W15+AD16) KWT standard T&I dimensional corrections at $q = 32$ psf 117
2.73 Wing and aft-deck (W15+AD16) SCALOS-specific T&I dimensional corrections at $q = 32$ psf 118
2.74 Wing and aft-deck (W15+AD16) SCALOS-specific T&I non-dimensional corrections at $q = 32$ psf 119
2.75 Wing and aft-deck (W15+AD16) T&I non-dimensional correction differences at $q = 32$ psf (SCALOS-KWT) 120
2.76 Three surface configuration KWT standard T&I dimensional corrections at $q = 32$ psf 122
2.77 Three surface configuration SCALOS-specific T&I dimensional corrections at $q = 32$ psf 123
2.78 Three-surface configuration SCALOS-specific T&I non-dimensional corrections at $q = 32$ psf 124
2.79 Three-surface configration T&I non-dimensional correction differences at $q =$ 32 psf (SCALOS-KWT) 125

2.80 UW-S-21A on the support system w/ and w/o underwing nacelles 127
2.81 Upright and inverted nacelle force and moment increments at $q = 32$ psf [19] 127
2.82 Nacelle SCALOS-specific T&I dimensional correction at $q = 32$ psf 128
2.83 Nacelle SCALOS-specific T&I non-dimensional correction at $q = 32$ psf . . . 128
2.84 UW-S configurations 131
2.85 Tested configurations of the SCALOS program 132
2.86 Schematic of the vortices over a cranked delta wing [20] 137
2.87 Illustration of the vortices over a cranked delta wing [21] 138
2.88 Delta wing vortex flow stages as a function of angle of attack [22] 138
2.89 Flow visualization of 2015 wing only (W15) at $q = 32$ psf and $\beta = 0°$ [23] . . 141
2.90 2015 wing-only force and moment coefficients at $q = 32$ and $\beta = 0°$ 142
2.91 Flow visualization of UW-S-20A at $q = 32$ psf and $\beta = 0°$ [23] 142
2.92 Inboard wing only [24] 143
2.93 Simple cropped delta [24] 144
2.94 Longitudinal forces and moments of cranked-delta wing (W15) vs. inner cropped delta wing 145
2.95 Incremental longitudinal forces and moments of cranked-delta wing (W15) vs. inner cropped delta wing 145
2.96 Effects of leading edge shape and Reynolds number (q) for the cropped delta wing 147
2.97 Effects of leading edge on longitudinal forces and moments vs. α for inboard wing only with respect to tested wing inboard area 147
2.98 Effects of aft-deck on longitudinal forces and moments vs. α for wing only . . 148
2.99 Wing-fueslage-vertical-tail and three-surface, bottom mount nacelle, and conventional low-tail, outboard wing planform variations [24] 149
2.100Comparison of wing planform longitudinal trends for longitudinal forces and moments vs. α for wing-body-vertical-tail configuration 152
2.101Comparison of wing planform longitudinal trends for three-surface, low-nacelle, and conventional tail configuration (untrimmed, "clean" cruise wing) 153
2.102Design space configuration studies [13] 154
2.103Effects of β on force and moment coefficients vs. α for UW-S-20A 156
2.104Effects of α on force and moment coefficients vs. β for UW-S-20A 157
2.105Comparison of configuration general arrangement results for longitudinal forces and moments vs. α 159
2.106UW-S-23G configuration built-up [25] 161

2.107UW-S-23G configuration build-up, longitudinal force and moment vs. α at $\beta = 0°$ 161
2.108Comparison of configuration general arrangement characteristics for longitudinal forces and moments vs. α at $\beta = 0°$ 163
2.109Comparison of area-ruled and non-area-ruled fuselage with wing-body and three-surface configuration for longitudinal forces and moments vs. α at $\beta = 0°$ 165
2.110Canard on/off and location for UW-S-20A [23] 166
2.111Forward canard on/off and planform [23] 166
2.112Canard on/off and locations, UW-S-20A, force and moment coefficients at $\beta = 0°$ 167
2.113Comparison of canard planforms, C15 ($\Lambda = 50°$) vs. C17 ($\Lambda = 47.6°$) vs. C23 ($\Lambda = 55°$), on UW-S-21A for longitudinal forces and moments vs. α at $\beta = 0°$ 170
2.114UW-S-20E with different horizontal tail planforms [23] 171
2.115Horizontal tail mounting height locations [23] 172
2.116Horizontal tail planforms, UW-S-20E, force and moment coefficients at $\beta = 0°$ 172
2.117Horizontal tail positions, UW-S-20A, UW-S-20H, UW-S-20F, and UW-S-21A, force and moment coefficients at $\beta = 0°$ 173
2.118Effects of horizontal stabilizer deflections on the longitudinal force and moments vs. α at $\beta = 0°$ for UW-S-21A with 2015 horizontal tail, H15, and without nacelle and canard (basic wing-body-tail configuration) 174
2.119Effects of horizontal stabilizer deflections on the longitudinal force and moments vs. α at $\beta = 0°$ for UW-S-21A with 2015 RUAV horizontal tail, H15A, and without nacelle and canard (basic wing-body-tail configuration) 174
2.120Effect of horizontal stabilizer deflections on the longitudinal force and moments vs. α at $\beta = 0°$ for UW-S-21A with 2020 horizontal tail, H20, and without nacelle and canard (basic wing-body-tail configuration) 175
2.121Comparison of mid- and T-tail deflection on UW-S-20H and UW-S-20A [25] . 176
2.122Effects of horizontal stabilizer deflections on longitudinal force and moments vs. α at $\beta = 0°$ for UW-S-20H with mid-tail configuration 176
2.123Effects of horizontal stabilizer deflections on longitudinal force and moments vs. α at $\beta = 0°$ for UW-S-20A with T-tail configuration 177
2.124Comparison of tail height effects, H20L.2 vs. H20.M vs. H20.T, on UW-S-21A, UW-S-20H, and UW-S-20A for longitudinal forces and moments vs. α at $\beta = 0°$ 178
2.125UW-S-21A with H20L.2 and horizontal tail deflections [25] 179
2.126Comparison of tail deflection of UW-S-21A for longitudinal forces and moments vs. α at $\beta = 0°$ 180

2.127UW-S-21F with H15A and horizontal tail deflections [25] 181
2.128Comparison of tail planform effectiveness, H15A.2 vs. H20L.2, on UW-S-21A for longitudinal forces and moments vs. α at $\beta = 0°$ 181
2.129UW-S-23 with V-tail elevator deflection [24] 182
2.130V-tail arrangement elevator control effectiveness at $q = 10$ psf for UW-S-23E (Icon-II like configuration) 183
2.131V-tail arrangement elevator control *incremental* effectiveness at $q = 10$ psf for UW-S-23E (Icon-II like configuration) 183
2.132UW-S-23G with aft-deck elevator deflection [25] 184
2.133Comparison of aft-deck elevator and its effectiveness on UW-S-23H without nacelles for longitudinal force and moments vs. α at $\beta = 0°$ 184
2.1342015 wing-body-tail configurations [23] 185
2.135Vertical tail, ventral and dorsal fin, 2015 wing-body-tail, force and moment coefficients at $\beta = 0°$ 186
2.136UW-S-20E and UW-S-20F [23] 186
2.137Ventral and dorsal fins, UW-S-20E and UW-S-20F, force and moment coefficients at various α 187
2.138UW-S configurations [23] 188
2.139Nacelle locations, UW-S-20A and UW-S-20B, force and moment coefficients at $\beta = 0°$ 190
2.140Nacelle locations, UW-S-20A and UW-S-20B, force and moment coefficients with various α 191
2.141UW-S-20C with different "clean" (zero-deflection) leading edges, force and moment coefficients at $\beta = 0°$ 193
2.142UW-S-20A with leading edge device deflections [23] 195
2.143UW-S-20A with leading edge deflections force and moment coefficients at $\beta = 0°$ 195
2.144UW-S-21A with leading-edge inboard/outboard deflections [26] 197
2.145Effects of inboard leading edge deflection only, on longitudinal forces and moment at $\beta = 0°, 5°$ for UW-S-21A 198
2.146Effects of outboard leading edge deflection only, on longitudinal forces and moment at $\beta = 0°, 5°$ for UW-S-21A 198
2.147Effects of inboard and outboard leading edge deflection on longitudinal forces and moment at $\beta = 0°, 5°$ for UW-S-21A 198
2.148Effects of inboard-only leading-edge deflection on configuration UW-S-21A (untrimmed), BM $\equiv$ MVR 200

2.149Effects of outboard-only leading-edge deflection on configuration UW-S-21A (untrimmed) . . . 200
2.150Effects of combined leading-edge deflection on configuration UW-S-21A (untrimmed), BM ≡ MVR . . . 202
2.151Comparison of alternate inboard leading-edge with and without deflection on UW-S-21A for longitudinal forces and moments vs. α at $\beta = 0°$ (untrimmed) 204
2.152UW-S-20A, UW-S-21A, and UW-S-23A with LE deflections, $\delta_{\text{LE IB}} = 15°$ & $\delta_{\text{LE OB}} = 15°$ [23, 24, 26] . . . 205
2.153Cross-configuration LEIB/LEOB 0°/0° and 15°/15° sensitivity, UW-S-20A vs. UW-S-21A vs. UW-S-23A (different outboard LE sweeps), force and moment vs. α . . . 206
2.154UW-S-21A and UW-S-13A with LE inboard/outboard deflections, LEIB24.MVR/LEOB15 30°/30° [25] . . . 207
2.155Comparison of leading-edge deflection between UW-S-21A vs. UW-S-13A for longitudinal forces and moments vs. α at $\beta = 0°$ (untrimmed) . . . 208
2.156UW-S-21A with ailerons deflections with left and right of positive and negative deflection, respectively [26] . . . 209
2.157UW-S-20A with ailerons deflections with left and right of positive and negative deflection, respectively [26] . . . 210
2.158Effects of side-slip and aileron deflections on longitudinal forces and moment vs. α for UW-S-21A . . . 212
2.159Effects of side-slip and aileron deflections on lateral force and moments vs. α for UW-S-21A . . . 213
2.160Effects of side-slip and aileron deflections on longitudinal forces and moment vs. α for UW-S-20A . . . 215
2.161Effects of side-slip and aileron deflections on lateral force and moments vs. α for UW-S-20A . . . 216
2.162UW-S-20A outboard aileron deflection effects at various α, force and moment vs. β . . . 217
2.163UW-S-23A with TE deflections [24] . . . 218
2.164Effects of aileron deflection, δ_{TEOB}, on forces and moments vs. α for UW-S-21A vs. UW-S-23A (LEOB sweep $\Lambda = 41°$ vs. $\Lambda = 63°$) . . . 220
2.165Aileron control, δ_{TEOB}, lateral-directional effectiveness for UW-S-21A vs. UW-S-23A (LEOB sweep $\Lambda = 41°$ vs. $\Lambda = 63°$) . . . 220
2.166UW-S-21A with flap and aileron deflections [26] . . . 222
2.167Effects of side-slip and flaperon deflections on longitudinal forces and moment vs. α for UW-S-21A . . . 222

2.168Effects of side-slip and flaperon deflections on lateral force and moments vs. α for UW-S-21A . . . 223
2.169UW-S-20A with flap and aileron deflections [26] . . . 224
2.170Effects of side-slip and flaperon deflections on longitudinal forces and moment vs. α for UW-S-20A . . . 225
2.171Effects of side-slip and flaperon deflections on lateral force and moments vs. α for UW-S-20A . . . 226
2.172UW-S-20A flaperon deflection effects at various α, force and moment vs. β . 227
2.173Effects of flaperon deflection, $\delta_{\mathrm{IB/OB}}$, on longitudinal forces and moments vs. α for UW-S-20A vs. UW-S-21A vs. UW-S-23A (LEOB sweep $\Lambda = 53°$ vs. $\Lambda = 41°$ vs. $\Lambda = 63°$, untrimmed, legend displays TEIB deflection/TEOB deflection) . . . 228
2.174Flaperon control, $\delta_{\mathrm{IB/OB}}$, longitudinal effectiveness for UW-S-20A vs. UW-S-21A vs. UW-S-23A (LEOB sweep $\Lambda = 53°$ vs. $\Lambda = 41°$ vs. $\Lambda = 63°$, untrimmed, legend displays TEIB deflection/TEOB deflection) . . . 229
2.175UW-S-20A with alternate control devices [26] . . . 231
2.176UW-S-20A with aileron spoilers [26] . . . 231
2.177Exploratory spoiler-slot deflector (not to scale) [25, 26] . . . 232
2.178UW-S-20A with 2021 spoiler-slot deflector downward [26] . . . 232
2.179UW-S-20A with 2021 spoiler-slot deflector upward [26] . . . 232
2.180UW-S-20A with 2023 spoiler-slot deflector [25] . . . 233
2.181UW-S-20A with mid-chord spoilers [26] . . . 233
2.182UW-S-20A with after-body clam shell speed brakes [26] . . . 233
2.183Effects of side-slip and asymmetric control surface deflections on longitudinal forces and moment vs. α for UW-S-20A . . . 236
2.184Effects of side-slip and asymmetric control surface deflections on lateral force and moments vs. α for UW-S-20A . . . 237
2.185Effects of angles of attack and additional asymmetric control surface deflections on force and moments vs. β at $\alpha = 0°$ and $10°$ for UW-S-20A . . . 238
2.186Comparison of symmetric exploratory spoiler-slot deflectors with conventional reduced chord ailerons on UW-S-20A for longitudinal forces and moments vs. α at $\beta = 0°$ . . . 238
2.187Effects of side-slip and SSD/AU deflections on longitudinal forces and moment vs. α for UW-S-20A [26] . . . 240
2.188Effects of side-slip and SSD/AU deflections on lateral force and moments vs. α for UW-S-20A [26] . . . 241
2.189Effects of angles of attack and SSD/AU deflections on force and moments vs. β at $\alpha = 0°$ and $10°$ for UW-S-20A [26] . . . 242

2.190Effects of side-slip and symmetric drag-device deflections on longitudinal forces and moment vs. α for UW-S-20A 244

2.191Effects of side-slip and symmetric drag-device deflections on lateral force and moments vs. α for UW-S-20A 245

2.192Exploratory stability modification devices on UW-S-24A [25] 246

2.193Comparison of UW-S-24A with candidate stabilizing devices (NC24.F / NC24.B nose chines and WF24 wing fence) for longitudinal force and moments vs. α at $\beta = 0°$ 248

2.194Exploratory high-lift configuration at take-off and landing conditions [25] . . 249

2.195Comparison of incremental effect of high lift devices deployed for takeoff and landing, $\delta_C = +15°$, LEIB/LEOB $+30°/+30°$, TEIB15/TEOB15.R $+15°/+10°$, and landing gear (LG24), on UW-S-24A for longitudinal forces and moments vs. α at $\beta = 0°$ (untrimmed) 250

2.196Comparison of leading edge effect at takeoff and landing, $\delta_C = +15°$, TEIB15/TEOB15.R $+15°/+10°$, and landing gear (LG24), on UW-S-24A for longitudinal forces and moments vs. α at $\beta = 0°$ (untrimmed) 251

2.197Comparison of flaperon effect at takeoff and landing, $\delta_C = +15°$, LEIB/LEOB $+30°/+30°$, and landing gear (LG24), on UW-S-24A for longitudinal forces and moments vs. α at $\beta = 0°$ (untrimmed) 252

2.198Effects of wing planforms on longitudinal forces and moments vs. α for UW-S-21A without nacelle, canard, and horizontal tail 254

2.199Effects of wing planforms on pitching moments vs. lift with different CG locations for UW-S-21A without nacelle, canard, and horizontal tail 255

2.200Effects of wing planforms on pitching moments vs. α with different CG locations and linear fits for UW-S-21A without nacelle, canard, and horizontal tail 255

2.201Effects of wing planforms on static margins and neutral points at the lower range of angles of attack for UW-S-21A without nacelle, canard, and horizontal tail 256

2.202Effects of wing planforms on longitudinal forces and moments vs. α for conventional three-surface configuration 257

2.203Effects of wing planforms on pitching moments vs. lift with different CG locations for conventional three-surface configuration 257

2.204Effects of wing planforms on pitching moments vs. α with different CG locations and linear fits for conventional three-surface configuration 258

2.205Effects of wing planforms on static margins and neutral points for conventional three-surface configuration 258

2.206Effects of different horizontal stabilizers and their rotations on the longitudinal forces and moment vs. α for UW-S-21A without nacelle and canard at $\bar{c} = 25\%$ 260
2.207Effects of different horizontal stabilizers and rotations on pitching moments vs. lift with different CG locations for UW-S-15A without nacelle and canard 261
2.208Effects of different horizontal stabilizers and their rotations on static margins and neutral points for UW-S-15A without nacelle and canard 261
2.209Incremental effects of different horizontal stabilizers and rotations on the longitudinal forces and moment vs. α for UW-S-21A without nacelle and canard with respect to $\delta_{\mathrm{HT}} = 0^\circ$ 263
2.210Incremental effects of different horizontal stabilizers and rotations on the longitudinal forces and moment vs. α for UW-S-15A without nacelle and canard with respect to horizontal stabilizer off configuration 264
2.211Effects of different horizontal stabilizers and deflections on trimmed and untrimmed drag polar, lift-over-drag ratio, and tail deflection effectiveness on trimmed lift for UW-S-15A without nacelle and canard 265
2.212Effects of different horizontal stabilizers and deflections on lift and drag for UW-S-15A without nacelle and canard 266
2.213Effects of horizontal stabilizers locations and rotations on the longitudinal forces and moment vs. α for UW-S-20A and UW-S-20H 268
2.214Effects of horizontal stabilizers locations and rotations on pitch moments vs. lift with different CG locations for UW-S-20A and UW-S-20H 268
2.215Effects of horizontal stabilizers locations and rotations on static margins and neutral points for UW-S-20A and UW-S-20H 269
2.216Incremental effects of horizontal stabilizers locations and rotations on the longitudinal forces and moment vs. α for UW-S-20A and UW-S-20H with respect to $\delta_{\mathrm{HT}} = 0^\circ$ 270
2.217Incremental effects of horizontal stabilizers locations and rotations on the longitudinal forces and moment vs. α for UW-S-20A and UW-S-20H with respect to horizontal stabilizer off configuration 271
2.218Effects of horizontal stabilizers locations and rotations on trimmed and untrimmed drag polar, lift-over-drag ratio, and untrimmed tail deflection effectiveness on lift for UW-S-20A and UW-S-20H 272
2.219Effects of horizontal stabilizers locations and rotations on lift and drag for UW-S-20A and UW-S-20H 273
2.220UW-S-20A with canard deflections 274
2.221Effects of canard rotations on the longitudinal forces and moment vs. α for UW-S-20A 275

2.222Incremental effects of canard rotations on the longitudinal forces and moment vs. α for UW-S-20A with respect to $\delta_{HT} = 0°$ and canard off configuration . . 277
2.223Effects of canard rotations on trimmed and untrimmed drag polar, lift-over-drag ratio, and untrimmed tail deflection effectiveness on lift for UW-S-20A . 277
2.224Incremental effects of leading-edge deflections on forces and moments vs. α for UW-S-21A and UW-S-20A 280
2.225Effects of leading-edge deflections on forces and moments vs. α for UW-S-21A and UW-S-20A 280
2.226Incremental effects of flaperon deflections on longitudinal forces and moment vs. α for UW-S-21A 281
2.227Effects of flaperon deflections on longitudinal forces and moment vs. α for UW-S-21A 282
2.228Incremental effects of flaperon deflections on longitudinal forces and moment vs. α for UW-S-21A and UW-S-20A 284
2.229Effects of flaperon deflections on longitudinal forces and moment vs. α for UW-S-21A and UW-S-20A 284
2.230Configuration variation longitudinal forces and moments vs. α 287
2.231Configuration variations lateral directional forces and moments vs. α 288
2.232Configuration variations lateral directional forces and moments vs. β 290
2.233UW-S-21A without nacelle Flow Visualization at $\beta = 0°$ and $\beta = 5°$ [27] . . . 292
2.234UW-S-21A forces and moments vs. α 293
2.235UW-S-21A forces and moments vs. β 294
2.236UW-S-20A with canard deflections longitudinal forces and moments vs. α . . 296
2.237UW-S-20A with canard deflections lateral directional forces and moments vs. α 297
2.238UW-S-20A with canard deflections forces and moments vs. β 298
2.239UW-S-20A with vertical tail deflections 299
2.240UW-S-20A with rudder deflections forces and moments vs. α 301
2.241UW-S-20A with rudder deflections forces and moments vs. β 302
2.242UW-S-21A with rudder deflections 304
2.243UW-S-21A with vertical tail deflections forces and moments vs. α 305
2.244UW-S-21A with vertical deflections forces and moments vs. β 306
2.245UW-S-20 with nacelle location variation longitudinal forces and moments vs. α308
2.246UW-S-20 with nacelle location variation: lateral directional forces and moments vs. α 309
2.247UW-S-20 with nacelle location variation: lateral directional forces and moments vs. β 310

2.248UW-S-20A nacelle with reduced nozzle exit areas 311
2.249UW-S-20A with reduced nacelle exit area on the longitudinal forces and moments vs. α 312
2.250UW-S-20A with reduced nacelle exit area on the lateral directional forces and moments vs. α 313
2.251UW-S-20A with reduced chord ailerons deflections longitudinal forces and moments vs. α 315
2.252UW-S-20A with reduced ailerons deflections lateral directional forces and moments vs. α 316
2.253UW-S-20A with reduced ailerons deflections lateral directional forces and moments vs. β 317
2.254UW-S-21A with full and reduced ailerons deflections longitudinal forces and moments vs. α 317
2.255UW-S-21A with full and reduced ailerons deflections lateral directional forces and moments vs. α 318
2.256UW-S-24A with take-off and landing configuration built-up longitudinal forces and moments vs. α 320
2.257UW-S-24A LTO configuration with vertical tail deflections 321
2.258UW-S-24A with take-off and landing configuration built-up lateraial directional forces and moments vs. β 322
2.259UW-S-24A take-off and landing configuration with rudder deflections lateral directional forces and moments vs. β 323
2.260Wing planform effects 325
2.261Longitudinal control: canard, horizontail tail, and aft-deck options C_M vs. α 326
2.262Longitudinal control: canard, horizontail tail, and aft-deck options C_M vs. C_L 328
2.263Longitudinal control: effect of horizontal tail area 328
2.264Longitudinal control:canard effectiveness 329
2.265Longitudinal control: effect of vertical location of the horizontal tail 330
2.266Longitudinal control: clean vs. approach configurations - UW-S-24A 331
2.267Longituidnal aerodynamics comparison of RSAC type with low-boom configurations 332
2.268Lateral-directional stability comparison of RSAC type with low-boom concepts333
2.269Nacelle location: effect longitudinal stability 334
2.270Nacelle location: effect lateral-directional stability 334

3.1 Top view of University of Washington's 3ft by 3ft low-speed wind tunnel and gust generation system [28–30] 341
3.2 Model of aeroeslatic response to gust excitation [28] 342

3.3 MARGE-I hardware-in-the-loop and control block diagram setup 344
3.4 LARGE – bottom view of onboard actuators and sensors with accessing bays. 345
3.5 LARGE - finite element model modes shapes 347
3.6 Robust $\mathcal{H}_\infty$ control 348
3.7 Time history and frequency response of open-loop wing-root strain response to a 1-cos gust of 4° amplitude and a period equivalent to 1.4 Hz (*OL* stands for open loop and *R* stands for the run number) 357
3.8 Frequency response of wing-root strain response to control inputs (*Sim* stands for simulation and *Exp* stands for experiment) 358
3.9 Frequency and time response of elevator to wing-root strain and pitch rotation [31] 360
3.10 Control surfaces and sensors used for both the destabilizing and stabilizing control laws [31]. 361
3.11 State space model root locus, modal frequency, modal damping, and Bode plot for the destabilized system at 68 Pa $\leq q \leq$ 338 Pa with increment of 10 Pa [31] 362
3.12 Experimental time history of closed-loop hump-mode system at selected dynamic pressures (destabilizing controller is engaged after 10 s with pulses every 10 s) and modal frequency and damping ratio [31] 362
3.13 Multi-flap SISO plant. The outboard flap receives 100 % of the commanded signal, while the inboard flap receives 25 % of the commanded signal. 363
3.14 (a): Overlay of all four flaps performing a frequency sweep. (b): Close-in view of the flaps during the sweep highlighting the different amplitudes of each flap. 364
3.15 (a): Time response of the forward wing-tip accelerometer to the multi-flap sine-sweep input. (b): Frequency response and identified model for the multi-flap SISO plant. 365
3.16 Frequency response comparison between the numerical model of the multi-flap SISO plant and the experimental data. 366
3.17 Comparison of the gust-to-wing-tip accelerometer frequency response for the numerical model and the experimental data. 366
3.18 (a): Comparison of wing-tip acceleration between the Numerical model and the experimental data during a continuous gust excitation at 2.5 Hz. (b): Close-in view showing the decay at the end of the continuous gust. 367
3.19 Open loop strain response, measured in bay two, to a sinusoidal gust at 2.5 Hz. 368
3.20 Open loop response to a 1-cosine gust event at 2.5 Hz. 368
3.21 Frequency response to flap 6 frequency sweep inputs 369

3.22 Frequency response to flap 4 frequency sweep inputs 370
3.23 Frequency response to flap 4 input 370
3.24 Frequency response to gust vane inputs 371
3.25 Transfer function of weighted filters and weighted open-loop wing-root strain to gust excitation, and norms of $\mathcal{H}_2$ and $\mathcal{H}_\infty$ closed-loop transfer functions given preview information 374
3.26 Simulated transfer functions of $\mathcal{H}_2$ and $\mathcal{H}_\infty$ closed-loop wing-root strain response to gust excitation 376
3.27 Actuator dynamics and H_∞ weighting and scaling functions 377
3.28 Bode plots of controller and loop transfer function, and Nichols plot of loop transfer function at 68 Pa $\leq q \leq$ 338 Pa with increment of 10 Pa 378
3.29 Summary of simulation-results minimum gain and phase margin vs. dynamic pressure for the $\mathcal{H}_\infty$ AFS control. 379
3.30 Time history of $\mathcal{H}_2$ static weighted closed-loop response with a discrete gust disturbance 382
3.31 Time history of $\mathcal{H}_\infty$ static weighted closed-loop response with a discrete gust disturbance 383
3.32 Time history of $\mathcal{H}_2$ frequency weighted closed-loop response with a discrete gust disturbance 385
3.33 Time history of $\mathcal{H}_\infty$ frequency weighted closed-loop response with a discrete gust disturbance 386
3.34 Time history of 6th-order $\mathcal{H}_\infty$ frequency weighted closed-loop response with a discrete gust disturbance 387
3.35 Time history of 4th-order $\mathcal{H}_\infty$ frequency weighted closed-loop response with a discrete gust disturbance 388
3.36 Summary of static and frequency weighted normalized strain reduction and control actuation, on the y-axis, given preview information, on the x-axis, for variation of $\mathcal{H}_2$ and $\mathcal{H}_\infty$ in feedback and preview closed-loop control of simulation and experimental results 390
3.37 Summary of minimum gain margin, on the y-axis, given preview information, on the x-axis, for variation of $\mathcal{H}_2$ and $\mathcal{H}_\infty$ in feedback and preview closed-loop control results 393
3.38 Summary of minimum phase margin, on the y-axis, given preview information, on the x-axis, for variation of $\mathcal{H}_2$ and $\mathcal{H}_\infty$ in feedback and preview closed-loop control results 394
3.39 State space model root locus, modal frequency, modal damping, Bode plot for stabilized system by active flutter suppression at 68 Pa $\leq q \leq$ 338 Pa with increment of 10 Pa 395

3.40 Time history of simulated unstable and stabilized systems with disturbance and noise input at given dynamic pressure 397
3.41 Time history of the unstable hump-mode system stabilized by the AFS controller [31] 398
3.42 Experimental frequency sweep: time history of input and output 399
3.43 Experimental frequency sweep: loop transfer function frequency response . . 400
3.44 Experimental frequency sweep: loop transfer function coherence and error . . 400
3.45 Experimental frequency sweep: Nichols chart of uncertain system 402
3.46 Experimental frequency sweep: Nichols chart of uncertain system with bounds 402
3.47 Summary of minimum gain and phase margin vs. dynamic pressure for the $\mathcal{H}_\infty$ AFS control 402
3.48 Time history of system response to 1-cosine gust, simulation vs. experimental 403
3.49 Closed-loop feedback and feedforward mixed sensitivity $\mathcal{H}_\infty$ simulation vs. experiment. 405
3.50 Closed-loop feedback and preview mixed sensitivity $\mathcal{H}_\infty$ simulation vs. experiment. 406
3.51 Closed-loop feedback, feedforward, and preview mixed sensitivity $\mathcal{H}_\infty$ simulation vs. experiment. 407
3.52 Closed-loop feedback, feedforward, and preview mixed sensitivity $\mathcal{H}_\infty$ simulation vs. experiment 408

LIST OF TABLES

Table Number Page

2.1 SCALOS team charts . . . 11
2.2 Design space survey [13] . . . 32
2.3 Design space survey [13] . . . 33
2.4 Design space survey [13] . . . 34
2.5 Design space survey [13] . . . 35
2.6 UW low-speed wind tunnel models . . . 39
2.7 UW low-speed wind tunnel models . . . 40
2.8 2015 (UW2128) configuration build-up and variants . . . 41
2.9 2016 (UW2166) configuration build-up and variants . . . 42
2.10 2017 (UW2200) configuration build-up and variants . . . 43
2.11 2018 (UW2237) configuration build-up and variants . . . 44
2.12 SCALOS table of model configuration variations tested (2020-24) . . . 45
2.13 2017 low-tail configuration build-up and variants . . . 46
2.14 2020 low-tail configuration build-up and variants . . . 47
2.15 2020 T-tail configuration build-up and variants . . . 48
2.16 2021 low-tail configuration build-up and variants . . . 48
2.17 2023 configuration build-up and variants . . . 50
2.18 2024 configuration build-up and variants . . . 50
2.19 Aircraft icons and designations [13] . . . 51
2.20 Pitch control arrangement [13] . . . 54
2.21 Wing mount comparison [13] . . . 55
2.22 Wing aft-deck comparison [13] . . . 56
2.23 Nacelle location comparison [13] . . . 59
2.24 Inlet/nacelle type comparison [13] . . . 61
2.25 Tail configuration comparison [13] . . . 62
2.26 Canard location comparison [13] . . . 64
2.27 SCALOS model components specification . . . 79
2.28 Test letter geometry . . . 82

2.29 Dynamic pressure and Reynolds number at standard sea level 82
2.30 Kirsten Wind Tunnel test entries 83
2.32 SCALOS table of model configuration variations tested (2020-24) 92
2.31 SCALOS part designations 93
2.33 SCALOS control surfaces and deflections 94
2.34 SCALOS Run log variables 96
2.35 Configurations studied for T&I [19] 102
2.36 Cropped delta geometry [24] 144

3.1 Some aeroelastic testbeds 338
3.2 Some preview gust load alleviation works 339
3.3 Some active flutter suppression works 340
3.4 Overview of MARGE's key parameters [28, 29, 31, 32] 343
3.5 LARGE - finite element model mode characteristic 348
3.6 Generalized plant filters 373
3.7 $\mathcal{H}_2$ and $\mathcal{H}_\infty$ controllers examined in this work: $\odot$ designates designed and tested, $\otimes$ designates designed and tested yet unstable, and $\oslash$ designates designed but not tested 374
3.8 Experimental closed-loop frequency sweeps 398

Nomenclature

Abbreviations

AD	Aft Deck
AE	Aeroelastic
AFS	Active Flutter Suppression
ALT	Alternate
AOA	Angle of Attack
ASE	Aeroservoelastic
BA	Body Axis
BFF	Body Freedom Flutter
BMC	Balance Moment Center
BPR	ByPass Ratio
BR&T	Boeing Research & Technology
CAD	Computer-Aided Design
CCV	Control Configured Vehicle
CFD	Computational Fluid Dynamic
CG	Center of Gravity
CIFER	Comprehensive Identification from Frequency Responses
CST	Commercial Supersonic Technology
D-SEND	Drop test for Simplified Evaluation of Non-Symmetrically Distributed sonic boom
DAQ	Data Acquisition
DARPA	Defense Advanced Research Projects Agency

DATCOM Data Compendium

DERA Defence Evaluation and Research Agency

DLM Doublet Lattice Method

DLR The German Aerospace Center

DM Disk Margin

DOF Degree of Freedom

DR Data Reduction

DRAG Drag force

ECRI Elliptical Cowl Ramp Inlet

EDF Electrically Powered Ducted Fans

EPISTLE European Project for Improvement of Supersonic Transport Low Speed Efficiency

ESDU Engineering Sciences Data Unit

EU European Union

Exp Experimental results

FAA Federal Aviation Administration

FB Feedback control

FE Finite Elements

FF Feedforward control

FP Flex Panel Leading Edge

FRF Frequency Response Function

FVWT Flow Visualization Water Tunnel

FW Frequency Weight

GGS Gust Generation System

GLA Gust Load Alleviation

GM Gain Margin

GVT	Ground Vibration Tests
HISAC	environmentally friendly HIgh Speed AirCraft
HISCAT	Highly Integrated Supersonic Cruise Aircraft Technology
HLD	High Lift Devices
HSCT	High Speed Civil Transport
HSR	High Speed Research
HT	Horizontal Tail
IB	Inboard
ID	Identification
ILAF	Identically Located Accelerometer and Force
IP	Intellectual Property
IRAD	Independent Research And Development
JAXA	Japan Aerospace Exploration Agency
KWT	Kirsten Wind Tunnel
LAAT	Loop-at-a-time
LARGE	Large Model for Aeroelastic Response to Gust Excitation
LCO	Limit Cycle Oscillation
LE	Leading Edge
LFW	Large Flexible Wing
LIFT	Lift force
LOD	Lift-over-drag ratio
LPV	Linear Parameter-Varying
LQG	Linear Quadratic Gaussian
LQR	Linear Quadratic Regulator
LTI	Linear Time-Invariant

MAC Mean Aerodynamic Chord

MARGE Model for Aeroelastic Response to Gust Excitation

MDO Multidisciplinary Design Optimization

MFTF Mixed Flow Turbofan engines

MIMO Multi Input / Multi Output

MLA Maneuver Load Alleviation

MMC Model Moment Center

MORE&LESS (MDO and REgulations for Low boom Enviromentally Sustainable Supersonic aviation

MPC Model Predictive Control

MVR Morphing-Variable-Radius Leading Edge

NACA National Advisory Committee for Aeronautics

NASA National Aeronautics and Space Administration

NEXST National EXperimental Supersonic Transport

NLR Netherlands Aerospace Centre

NSRD Nozzle Shock-Reflecting Deck

OB Outboard

OL Open Loop

ONERA The French Aerospace Lab

PC Preview Control

PID Proportional-Integral-Derivative

PM Phase Margin

QEVC Quiet Experimental Validation Concept

R Run Number

RANS Reynolds-Averaged Navier-Stokes

RFA Rational Function Approximations (of unsteady aerodynamic forces)

RHP Right Half Plane

RM Rolling moment

RSAC Reference Supersonic Airliner Concept

RUAV Research Unmanned Air Vehicles

RUMBLE RegUlation and norM for Low sonic Boom LEvels

S&C Stability and Control

SA Stability Axis

SAI Supersonic Aerospace International

SBJ/SSBJ Supersonic Business Jet

SCALOS Supersonic Configurations at Low Speeds

SCAR Supersonic Cruise Aircraft Technology

SCT Supersonic Civil Transport

SENECA (LTO) noiSe and EmissioNs of supErsoniC Aicraft

SF Side force

Sim Simulated results

SISO Single Input / Single Output

SS Sealed-Slat panel Leading Edge

SSM State-Space Model

SST SuperSonic Transport

STEX Streamline-Traced External-Compression

SW Static Weight

T&I Tare and Interference

TC Technology Concept

TCA Technology Concept Airplane

TE Trailing Edge

TOL/LTO Take-off and Landing (used interchangeably)

UAV Unmanned Aerial Vehicle

UDP Uniform Distributed Panel

USAF United States Air Force

UW University of Washington

UWAL University of Washington Aeronautical Laboratory

VCCTEF Variable Camber Continuous Trailing Edge Flap

VLM Vortex Lattice Method

WA Wind Axis

WBV/WBT Wing-Body-Tail (used interchangeably)

YM Yawing moment

Variables

α Angle of attack

$\bar{c}$ Mean aerodynamic chord

β Sideslip angle

δ_C Canard deflection angle

δ_{ail} Aileron deflection angle

δ_{HT} Horizontal tail (all-moving) deflection angle

Γ Dihedral angle

Λ Sweep angle

Λ_{LE} Wing outboard leading edge sweep angle

ω Frequency

$\partial C_M/\partial C_L$ static margin (negative)

σ Singular values

A	State matrix
AR	Aspect Ratio
B	Control matrix
b	Wing span
BL	Force and moment with only balance interaction correction
C	Observed output matrix
C_D	Drag force coefficient
C_L	Lift force coefficient
C_L vs. C_D	Drag polar
C_L/C_D	Lift-over-drag ratio
C_M	Pitching moment coefficient
C_N	Yawing moment coefficient
C_R	Rolling moment coefficient
C_Y	Side force coefficient
C_{D_0}	Zero-lift drag coefficient
C_{D_A}	Axial drag force coefficient
C_{L_α}	Lift coefficient derivatives
$C_{L_{\max}}$	Maximum lift coefficient
$C_{L_{\text{uncorr}}}$	Uncorrected lift coefficient (balance interaction only)
C_{L_W}	Wing lift force coefficient
C_{M_0}	Zero-pitch moment coefficient
C_{M_α}	Pitching moment coefficient derivatives
$C_{M_{\alpha=0}}$	Zero-alpha pitching moment coefficient
C_{n_β}	Yawing moment coefficient derivative w.r.t. β
C_{R_β}	Rolling moment coefficient derivative w.r.t. β

C_{Y_β}	Side force coefficient derivative w.r.t. β
D	Feedthrough output matrix
d	Exogenous/disturbance input vector
d_f	Diameter of fuselage
e	Error Vector
F	Force and moment of the fork
F_l	Linear fractional transformation
$G(s)$	Transfer function
K	Controller gain
l_f	Length of fuselage
M	Force and moment of the model
n	Noise vector
q	Dynamic pressure
r	Reference vector
Re	Reynolds number
S	Sensitivity function
S_{ref}	Wing reference area
S_{wet}	Surface wetted area
T	Complementary sensitivity function
t/c	Thickness to chord ratio
u	Control input vector
w	Normalized exogenous/disturbance input vector
x	State vector
y	Observed output vector
z	Regulated output vector

ACKNOWLEDGMENTS

I would like to express my deepest gratitude to my advisor, Professor Eli Livne, for providing the sustainable funding, resources, and opportunities that made this commercial supersonic research possible. The breadth and depth of experiments and experience I gained under him, across two research areas and two wind tunnel programs, is what any PhD student could dream of. Through him, I had the opportunity to work with and learn from world-class researchers across academia and industry. His high standards, sharpened by a decade as Editor-in-Chief of the Journal of Aircraft, pushed every paper and every chapter of this dissertation to a higher level of rigor, which is both a blessing and a curse of having an advisor who knows this much; it is also a standard for academic work that I will always look up to. Beyond the research, I am grateful for his care: he made time to talk whenever I needed it, and he always listened, whether or not the problem at hand could be solved. I have deep respect for him as a researcher and as a professor, and I am proud to have been his student.

I am deeply grateful to my co-advisor, Professor Mehran Mesbahi, who advised my Master's research and agreed to continue guiding me when the GNC work of this dissertation grew out of that earlier foundation. Although I never sat in his lab, he treated me as one of his own, and he made time to talk whenever I wanted to discuss research. Conversations with him about control and research, and the chance to pick his brain, have been among the true joys of my graduate journey, and his career advice has been vital to my growth. He is also one of the most organized people I know, and someone I have always looked up to. I owe him a special debt for his advice at the very start of my doctoral journey. I did not fully grasp it at the time, but his encouragement to define my own research vision and stay the course became the compass that carried me through this process.

I would like to thank Chet Nelson for his mentorship and technical insight throughout

this project. As the lead aerodynamicist of the HSCT program and the chief engineer of the Sonic Cruiser, he holds a depth of knowledge in airplane design that I have not encountered anywhere else, and nearly everything I know about aircraft beyond what Eli taught me, I learned from him. He has been the center of this program from the beginning, and many of the ideas in this dissertation trace back to his insight and knowledge. His experience as a Boeing Technical Fellow brought a real-world perspective to our configuration designs and low-speed performance analysis, and kept the research grounded in practical aerodynamics, even when the sheer amount of information he shared in a single conversation made me feel my head might explode. What I admire most is his passion for aviation: through all the ups and downs of a long career in this industry, his love for airplanes never wavered, and that perspective taught me how small my own frustrations were by comparison. Having him as a mentor was a once-in-a-lifetime fortune, and I can only hope to one day be half the aerodynamicist he is.

My sincere thanks go to Reza Soltani, a true mentor to me throughout this project, and one of the kindest people I have ever known. A former department chair at Sharif University, he brought decades of experimental experience to our wind tunnel work, and he taught me the craft of testing down to the smallest details: the tape must lie flat without a single bubble, and the drag count has to be precise. He would sit down with me for data analysis and go through the code together, guiding me hand in hand through the aerodynamic analysis. I am grateful for the countless hours he spent standing by my side in the laboratory and through the long wind tunnel test campaigns, providing a reliable foundation when the workload was at its highest. His contributions reached well beyond the laboratory and into the writing of our publications, always with a generosity that asked for nothing in return. He has been, in everything but title, one of my advisors, and this dissertation owes him more than any official record will show. Much of the experimental discipline in this dissertation carries his fingerprints, and I am fortunate to have learned it from him.

I would like to thank the other members of my doctoral committee for their time,

their questions, and their feedback through my general exam and final defense. Professor Behçet Açıkmeşe's path to becoming a leading figure in trajectory optimization has been an inspiration for my own journey. I served as his teaching assistant and later took his class, and his lectures on robust control across both the time and frequency domains deepened my own grasp of the field. He once told our class not to hate the subject or the material, but to hate him instead if we did not like what he taught, and the care for students behind those words has stayed with me. Professor Steven Brunton, who served as the Graduate School Representative, offered his support and encouragement at my general exam, which meant a great deal to me, and I will never forget it. His lecture videos on YouTube are, to me, the best available online, and I returned to them many times over the course of this research.

I would also like to thank Professors Kristi Morgansen, Ed Habtour, Alvar Saenz-Otero, Amir Taghvaei, Dana Dabiri, and Karen Leung. Professor Morgansen first welcomed me into the aeroelastic group, which I had found through her webpage at the very beginning, and she has been a collaborator on the aeroelastic work ever since, serving on both my Master's committee and my qualifying exam along the way. Before I joined Professor Mesbahi's group, I spent my early days in the orbit of hers, bringing most of my questions to Jake, to the point that Professor Mesbahi mistook me for her student at the beginning. Jake came from her group, and she laid out the observer design for the project; her imprint on the aeroelastic effort runs through both. Professor Habtour's structural vibrations class was exactly the course I had hoped for at the start of my PhD; by the time I finally took it, the system identification work in §3 had already taught me the material the hard way, but I enjoyed it no less. With his students Bart Boom and Thijs Masmeijer, we explored computer-vision system identification on the LARGE wing, following their demonstration on a stingray-inspired structure; like too many good ideas in a finite PhD, it never came together on my end, but I am glad to see Barkın Sarıgöl carrying that direction forward. Professor Saenz-Otero, our teaching professor, led the capstone program where I served as the SCALOS capstone teaching assistant for three years. He once said that he is the last

line of defense before the students enter the real world, so he has to be tough and critical to prepare them, and I have admired that standard ever since. I did my best for the students, but I know he cut me some slack when research had me stretched thin, and I never took it for granted. Professor Taghvaei, smart and funny in equal measure, has always been fun to talk to; he organized a reading group that, true to form, my bandwidth made me drop halfway through, but I enjoyed every session I attended. Professor Dabiri was a collaborator in the early days of SCALOS; we never worked together directly, but he never failed to ask how I was doing and how the research was going, and I always enjoyed our chats. Professor Leung gave me practical advice on running events when I served as the student organizer for the controlX seminar, and it made the job far easier.

I am grateful to my manager at Meta, Nick Zacharov, for the internship opportunity and for the return offer that followed. A leading figure in perceptual audio evaluation, he holds high standards while running a reality check at every milestone to keep the project goals realistic, and it has been my fortune to work with him on a unique project. We came from different fields with different norms, and as our early alignment grew into mutual trust, he granted me the autonomy to operate as an independent researcher. He took his responsibility as a manager seriously, shielding me from unnecessary workload and making time to meet despite his schedule, and in many ways he is the industry version of my advisor. The internship also placed me in the front row of the current wave of artificial intelligence, and without learning there how to put modern AI tools to the right use, I do not think I could have pulled this dissertation together.

I would like to thank John Berg, my labmate and primary collaborator on the aeroelastic work in this dissertation. Most of what I know about circuits and hardware in the laboratory I learned from his hands-on skill, and he carries an in-depth command of SISO and classical control theory that few people of our generation take the time to learn anymore. The gust load alleviation and flutter suppression work in §3 was built alongside him, and discussing research and control theory with him has always been time well spent.

I owe special thanks to Daniel Calderone, for whom I served as a teaching assistant

during my Master's years. Dan has the passion and insight of a mathematician I could only dream of becoming, or at the very least, the one I look up to, and he is as easygoing as he is insightful (and a better dancer than either). One of my lasting regrets from graduate school is that we never collaborated on a paper.

I am thankful to the senior PhD peers who set the standard and offered invaluable guidance during the foundational years of my graduate journey: Jake Quenzer, Bijan Barzgaran, Kimber Hinson, Aditya Deole, Mengyuan Wang, Taewan Kim, and Shahriar Talebi. Jake, Bijan, and Kimber designed MARGE, the aeroelastic testbed at the heart of §3, and the work in this dissertation stands on the foundation they built. Jake and Bijan trained me hands-on in operating MARGE. My discussions with Kimber on Kalman filtering and observability were always insightful, and I respect her above all for completing her PhD while raising two kids and working full time at Boeing through COVID. Aditya, one year ahead of me, stepped up to lead the RAIN Lab and still actually listened to my troubles, and he always had good input for whatever hardship or struggle I brought to him. The happy hours with him were always something to look forward to. Mengyuan once wrote in her own acknowledgments that she would miss our casual conversations and small talk, and I will miss them just as much. I never found the bandwidth to join the optimal control work in her dissertation as I had hoped, but I am glad she made it through, and chatting with her was always a highlight. Taewan, from Professor Açıkmeşe's lab, welcomed me when I reached out hoping to apply his six-degree-of-freedom landing trajectory planning to our take-off and landing work; the collaboration never came together, entirely on my end, but the research meetings turned into coffee chats and breaks, and a good friendship grew out of them. In particular, I would like to thank Shahriar Talebi, who is smart and passionate about mathematics in a way I have aspired to since my early years in the program. I sought him out hoping to collaborate on his regularizability work, and although the publication never materialized, he always made time to meet with me, and I am grateful for every one of those discussions. Watching him go on to a postdoc at Harvard and now a professorship at UCLA has been a joy, and it is exactly the trajectory he deserves. Both he and Taewan

also generously shared their experience when I needed guidance well beyond research.

To Mohammad Al-Jarrah, who started his Master's at the same time I did and continued on to the PhD alongside me, thank you for your steadfast camaraderie through every academic pivot. You are one of the sharpest people I know; I kept signing up for classes with you even when research had me buried, and you ended up teaching me the homework and the intuition behind the math, every single time. I do not think I would have survived graduate school without you. And one of the best decisions I made was joining you at the gym; what started as a shared routine became a cornerstone of my daily life, my stress relief, and my mental therapy through the pressures of academia.

I would like to extend my thanks to the students who worked alongside me on the SCALOS project. In particular, I am grateful to Nicolas Mavriplis, who started on the commercial supersonic project at the same time I did. For the first two and a quarter years of my doctoral journey, Nick was an indispensable partner who stood by my side through every test campaign. Thank you for the camaraderie, for enduring the early and chaotic phases of this project, and for taking complete ownership of the CAD development that made our configurations possible, a skill I never managed to master myself. You also stepped up to TA the senior capstone while carrying your research, and the program owes you for both. Watching you navigate your own path and transition out of academia was a true point of inspiration, and I am glad our friendship has outlasted the lab; it meant a great deal to see you at my defense and graduation. And congratulations on your engagement to Nikki; I could not be happier for you both.

I am equally grateful to Kenneth Wiersema, whose exceptional ability I first recognized while teaching the senior capstone project, where he was already running OpenVSP and teaching himself CFD as an undergraduate. When the project needed a successor, Chet and I made the case to bring you on as a summer intern, and it remains one of the best calls we made. I have always trusted you as a fellow researcher rather than a student; you took over the CAD and CFD pipelines without missing a step, and the CAD in our final NASA submission is yours. Passing the torch to someone of your caliber has been one of the

most rewarding parts of my time in this lab, though I must officially apologize for handing you the curse of academia along with the project. I have no doubt you will carry your own Master's thesis with the same brilliance you have shown from the start, and I look forward to seeing your continued success.

A special thank you goes to Po Huang and Justin Chang, two exceptional Master's students who joined the project during the critical summer of 2024. Your contributions during that window were indispensable, and I simply could not have pulled off the final data correction framework without your hard work in the lab. I tried to mentor you both as well as my bandwidth allowed during that stretch, and I am proud of what you accomplished. It is a joy to see Justin, a sharp theorist, thriving as a first-year PhD student under Professor Mesbahi's guidance. Po went on to carry the μ-synthesis and LPV control directions from §3, the follow-on work I never had the chance to pursue, into a solid Master's thesis of his own, and I wish him the best in his next chapters beyond this funding cycle.

I would also like to thank the undergraduate students from the senior capstone design teams, whose dedication to CAD modeling and wind tunnel testing supported the broader goals of this supersonic effort. I am equally grateful to the SCALOS summer interns over the years, Danny Beeson, Colton Hill, Anwar Moustafa, Josh Ignacio, and Josie Wilson, who provided vital continuity between their academic milestones and the start of their careers.

I would also like to thank the current and former members of the Active Aeroelastic Control Laboratory (AACL), the Nonlinear Dynamics and Control Lab (NDCL), and the Robotics, Aerospace and Information Networks (RAIN) Lab: Alex Chin, Alex LaFranchi, and Barkın Sarıgöl of the AACL; Nick Andrews, Sofya M. Akhetova, and Alison Zongolowicz of the NDCL; and Siavash Alemzadeh, Niyousha Rahimi, Spencer Kaiser, Joseph Pinkston, Shiva Shakeri, and Ruiqi Li of the RAIN Lab. I am also grateful to Marat Mor, Professor Livne's former postdoc, who has continued to support our aeroelastic finite element modeling. I am glad to have shared the journey with friends from the neighboring labs as well: Bart Boom, Thijs Masmeijer, Xiaohai Hu, Danny Broyles, and Julius Baehrig. The time spent with all of you, discussing research questions and sharing the day-to-day life of these

laboratories, created an environment I will miss, and working alongside all of you has been a pleasure.

Beyond UW, I would like to thank the external collaborators I had the fortune to work with and learn from: Dr. Nhan Nguyen of NASA Ames Research Center, Professor Sergio Ricci of Politecnico di Milano, Dr. Todd Magee of Boeing Research & Technology, Professor Thiago Guimaraes, now at Princeton University, Professor Juan Alonso and Yiren Shen of Stanford University, and Professors Carlos Cesnik, Ilya Kolmanovsky, and Joaquim Martins, and Bernardo Bahia Monteiro of the University of Michigan. Dr. Nguyen's collaboration on the flexible-wing aeroelastic research, and his advice on the active control work, were invaluable. Professor Ricci hosted my controller on the X-DIA testbed during the FAA work; it did not work the first time, and the lessons from that failure became part of the foundation for the active flutter suppression journal work in §3. Dr. Magee was our SCALOS partner at Boeing Research & Technology on the water tunnel work. I would also like to thank Kioumars Najmabadi, Brian Rupnik, Alexander Ho, and Prachya Panyakeow of the Boeing Company for supporting the gust load alleviation research at the University of Washington and for many insightful discussions and suggestions. Professor Guimaraes, a postdoc at Michigan at the time, carried the aeroelastic work on the SCALOS side. Professor Alonso's group at Stanford and the groups of Professors Cesnik, Kolmanovsky, and Martins at Michigan held up their ends of the program, and working alongside their students, Yiren and Bernardo, was a pleasure throughout.

Support by NASA, Award/Contract #80NSSC19K1661, under the Commercial Supersonic Technology (CST) program, Supersonic Configurations at Low Speeds, with Sarah Langston as the NASA technical grant monitor, is gratefully acknowledged. I would also like to thank Sarah Langston, Sriram Rallabhandi, Melissa Carter, Lori Ozoroski, and Peter Coen of NASA for the opportunity to conduct this needed research for supersonic aircraft. Support by the Federal Aviation Administration (FAA) for the aeroservoelastic work, with contributions by Wael Nour and Sohrob Mottaghi of the FAA, is also gratefully acknowledged. I am also grateful for the Aerospace Career Enhancement (ACE) scholarship from

the Society of Professional Engineering Employees in Aerospace (SPEEA) from 2022 to 2024, and for the James L. Teslow Endowed Ph.D. Fellowship and the William E. Boeing Endowed Fellowship in Aeronautics and Astronautics at the University of Washington in my final year.

To my own worst critic and most dedicated supporter: myself. I want to thank me for doing all this hard work. I want to thank me for having no days off. I want to thank me for never quitting. I want to thank me for always being a giver and trying to give more than I receive. I want to thank me for trying to do more right than wrong. I want to thank me for just being me at all times. Your resilience, independence, and refusal to break under pressure across this eight-year marathon are the reasons this dissertation stands complete today.

I am grateful to my closest friends, who have been there for me through the different chapters of my engineering journey.

To the annual ski trip crew, who took me in when Amber first brought me along, Tristan Chen, Stefan Chen, Annie Hsu, Adrey Lin, Amanda Wu, Anderson Chang and Cynthia Yeh, Caroline Chuang and Jasper Zaporteza, Kevin Peng and Anny Hsu, and Yu-tsern Jou and Patty Liu: thank you for the mountains, the laughter, and a tradition I look forward to every winter.

I want to extend a special thanks to Jeffery Jow, Te-Li Wang, Jean Lee, Yung-Chia Yun, and Vivian Liang, the close friends who have shared countless hangouts with Amber and me through these years. The dinners, the trips, and the time spent together kept us sane through two doctorates, and I am grateful for every bit of it. I also want to thank Jeffery Lai and Ivy Hsu, my housemates during my second year of the Master's program, for the home we shared in those early years; congratulations on your marriage, and I am glad our friendship has lasted all this way.

To the Chang twins, Cindy and Ann, and to Daniel Lin: together with the two Kevins and Hong, you are the friendships I have kept since our undergraduate days, and your support through all these years has meant a great deal. Cindy and Ann, I truly wish you

both find the ones you deserve and the happiness that comes with them. Daniel, your luck in friendship has always run better than your luck elsewhere, and I am glad to be on the winning side; I have always enjoyed your company, on every trip back to Taiwan and through your visits out to Seattle. Friendships that survive this many years and this much distance are rare, and I do not take a single one of them for granted.

To Kevin Saddi, my closest friend from our undergraduate aerospace days and now here in Seattle, thank you for being there since the very beginning. We survived the endless undergraduate homework together, and you are one of the most genuine and generous people I know; you worked part-time all the way through undergraduate while struggling alongside me, who had no job at all. I failed the undergraduate control class, and you were the one who helped me through that homework; who would have known I would end up writing this dissertation on active aeroelastic control. I am sorry that the curse of academia kept us from hanging out as often as we should have, and that we have yet to make our trip to Vancouver. Now that this chapter is closing, I look forward to finally making that journey and reclaiming the time we lost to the grind.

I am also grateful to Kevin Su and Hong Lin, my closest friends from my undergraduate years, both with an exceptional eye for markets and investing. Kevin told me to buy Bitcoin as early as 2011, when I had no idea what it was, and to start a YouTube channel in 2014; had I listened to either call, I might be writing these acknowledgments from early retirement, and I hereby recognize him as the financial opportunity I never deserved. Hong carried weights through those undergraduate years that I never knew about until much later, weights that came from his own generosity toward others, and knowing that has only deepened my respect for him. Much of what I understand about Chinese culture and perspectives I learned from him, and I have always enjoyed his company and his insight; he is the kind of hardworking that comes home from a party and sits back down to study at midnight. Some people walked away from him in those years; to me he was simply my friend, and that is all our friendship has ever needed to be. I am not sure I deserve friends like you two, but I have no intention of letting you go.

My deepest gratitude belongs to my partner, Hsiao-Yang (Amber) Chou. We first met in our undergraduate years, found each other again on a ski trip in 2018, and have been together since early 2019, which means we have carried our graduate journeys side by side. I am not a person who knows how to relax, and you taught me how: work-life balance, reminders to close the laptop, breaks from the wind tunnel, and the planned trips I complained about every single time and loved by the end. You made coming home feel comfortable and safe, a place where I could simply be myself, whether that meant a night off binge-watching Netflix or sleeping in late on a weekend. More than anyone else, you helped me carry the emotional weight and burnout of this chapter, even when that meant telling me the hard truth about what the stress was doing to me. I also owe you a formal apology: when the wind tunnel campaigns had me at my most stressed, I vented on you more than you ever deserved, and you took it with a grace I will spend a long time repaying. I do not think I could have made it through this PhD without you. People often say that behind every PhD, the partner has done an equal share of the work; in your case it is literally true, as you finish your own doctorate and step into your postdoc, and I could not be prouder of you. I am glad we honored our pact to never let academia claim both of our futures, and I look forward to a lifetime of building our own passions, traveling the world, and protecting the life we create together.

Finally, to my family: thank you for your unconditional love and your truly unwavering support. We are a middle-class family in Taiwan, but I never once had to worry about money, because you always made me feel supported. You have carried me through studying abroad since high school, through my undergraduate years, and through graduate school, and I do not take a single year of it for granted. Thank you for never being the typical Asian parents; no one ever pressured me to chase a big paycheck or to have kids by thirty, and we are well past that now anyway. To my sister, Kuang-Ching Ting, thank you for your constant joy over the years. To my father, Jen-Chen Ting, thank you for carrying both my sister's and my education in the United States, and for every trip you made to visit me, with a suitcase full of food and snacks from Taiwan. To my mother, Ting-Hwa

Yu, thank you for never once losing faith in me. You stood by me at my lowest, when I was dismissed from my undergraduate university, and again when I chose to leave my first graduate program and start over in Seattle; you trusted my comeback every time, and this milestone is the proof of your faith. Now that my long academic journey finally comes to an end, it is my turn to support myself, and time for you both to finally retire.

DEDICATION

To my parents, Jen-Chen Ting and Ting-Hwa Yu (and my sister, Kuang-Ching Ting, as she insists).

Chapter 1

INTRODUCTION

Accurate aerodynamic data of flight vehicles and their configuration variations are indispensable for designers in the preliminary design stages. They are also invaluable in the research and development process, supporting design decisions, lessons learned, and solutions to unexpected aerodynamic problems. Airplane design technology in aerodynamics and stability and control (S&C) areas has benefited for many years from user-friendly databases that gather and organize information from large numbers of studies, computational and experimental, and from data for specific aircraft when it becomes available in the public domain. Examples include the rich selection of reports by the National Advisory Committee for Aeronautics (NACA) and later National Aeronautics and Space Administration (NASA) [12, 33, 34], by the British Reports & Memoranda [35] that led to the Engineering Sciences Data Unit (ESDU) information system [36], the United States Air Force (USAF) Data Compendium (DATCOM) [37], and other compendiums, such as [38, 39]. Selected data from [12, 33–39] can be found in many books on airplane design, applied aerodynamics, and flight stability and control [40–51]. The USAF DATCOM database is still the most commonly used public domain source for the quick estimation of the aerodynamic characteristics of aircraft in the preliminary design stage for configuration design space searches or configuration modifications in various research programs.

Regarding supersonic configurations, much has been studied and reported since the 1950s, with, except for the Concorde development years and later the SST and the NASA HSCT, a major interest in the development of fighter jet [52]. While a significant amount of fundamental research was dedicated to delta, double-delta, and other slender configuration variants, much of the configuration development work was either classified or kept as Intellectual Property (IP)-protected. NASA funded and published many works on the aerodynamics of slender configurations across the flight regimes [53–62]. The insights into

the physics of vortex lift, partial leading edge suction, vortex flaps, vortex generation and breakdown, the effects of vortex shedding by slender fuselages, and more [63–66], were key to the success of generations of advanced fighter jets. Examples include selected collections of information about fighter jets: The F-15 [67–74], YF-16 / F-16 [3, 75–89], YF-17/ F-18 [90–98], F-22 [99–107] F-35 [108–117] and experimental aircraft such as X-29 [118–128], X-31 [129–155], X-36 [156–159], X-62 [160–168]. Concorde [169], the B-58 [170–174], the XB-70 [174–188] and the American supersonic transport (SST) [189–192] were also described in the technical literature. The USAF DATCOM, with its last 1978 version, benefited from much of the work on the aerodynamics of supersonic aircraft done in the years before it was published.

Aerodynamic research and development (R&D) on slender configurations continued through the 1980s [193]. After the maturation of the Concorde and the end of work related to the American SST, work on commercial supersonic aerodynamics continued with the Supersonic Cruise Aircraft Research (SCAR) [194–200] and High Speed Research (HSR) [5, 201–209]. In the 1990s: conceptual aircraft design of High Speed Supersonic Transport (HSCT) [210–217] with specific area developments of MDO [218–225], S&C [226–234], aeroelastic [1, 235–251], pilot simulation [252–256], propulsion integration [257–263], noise predictions [264, 265], and more. Reference [266] collected more than 1200 papers/ documentations on only propulsion / aircraft integration for HSCT applications from 1980 to 1991. Figure 1.1 shows the developments of the SST from post-Concorde to the end of the HSR/ HSCT programs. After the end of the HSCT program, aerodynamic research work continued and focused on the environmental challenges of carbon emissions and sonic boom with NASA N+ programs [6, 8, 11, 267–278]. More recently, the NASA Commercial Supersonic Technology (CST) selected a demonstrator, the Quiet SuperSonic Technology (QUESST) X-59, to research and validate low-boom design and environmental impact, including perceptual evaluation [279–284].

The European Union (EU) also has its own development programs as shown in Fig. 1.2. The EUROSUP is a three-year EU project focusing on the drag reduction at Take-Off and Landing (TOL), cruise over land and over sea for the second generation of the Supersonic Civil Transport (SCT) from Concorde, with participants of Aerospatiale, DASA,

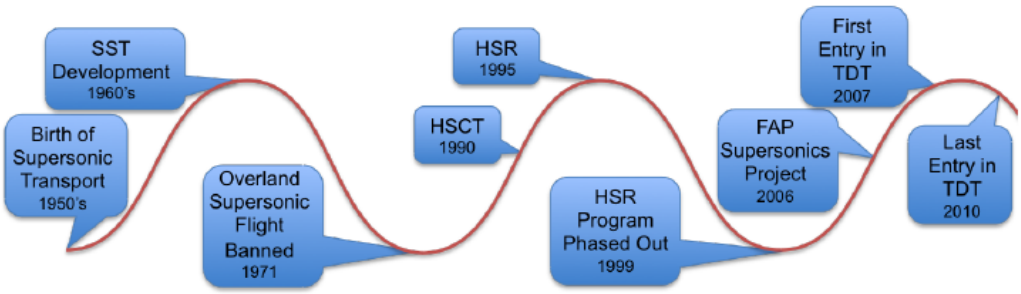


Figure 2. Supersonic passenger-transport aeroelastic research through the years.

Figure 1.1: American supersonic transport programs before N+ programs [1]

Alenia, Saab, The French Aerospace Lab (ONERA), The German Aerospace Center (DLR), Netherlands Aerospace Centre (NLR), and UK's Defence Evaluation and Research Agency (DERA) in 1996 [285, 286]. The follow-on European Project for Improvement of Supersonic Transport Low Speed Efficiency (EPISTLE) was to use CFD, specifically Navier-Stokes code, to validate low speed high lift design [287–296]. In 2005, the research direction shifted to Environmentally Friendly High Speed Aircraft (HISAC), and the focus was placed on future environmental regulation in noise, atmospheric emission, and sonic boom; technology maturation and road map to the future; general trade-off and Multidisciplinary Design Optimization (MDO) [297]. The project of RegUlation and norM for Low sonic Boom LEvels (RUMBLE) focused on the regulatory side of supersonic aviation, including noise and emissions at airport/local and global level, quantifying the efficiency of sonic boom, accepted and validated modeling tools that capture the physics of the generation and propagation of sonic booms, etc. The RUMBLE continues with two projects of (LTO) noiSe and EmissioNs of supErsoniC Aicraft (SENECA) [298] and MDO and REgulations for Low boom Environmentally Sustainable Supersonic aviation (MORE&LESS) [299] to further support Europe to shape global environmental regulations for future supersonic aviation, with publications of [300–316] and [317–322], respectively.

The Japanese Aerospace Exploration Agency (JAXA) has worked on SST closely with NASA and Boeing since the HSCT program [323]. After the end of the HSCT project, National Aerospace Laboratory (NAL, later became JAXA) initiated the National EXperimental Supersonic Transport (NEXST) program, which researched future supersonic

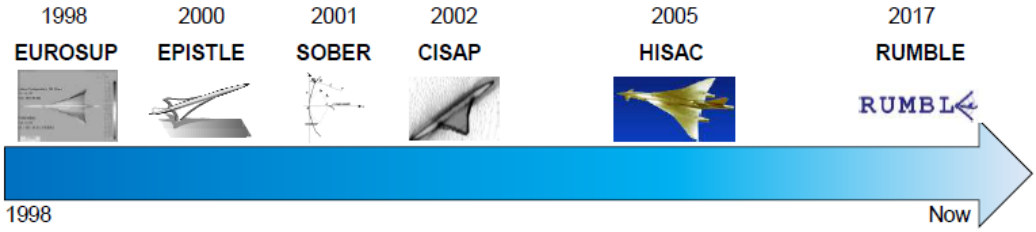


Figure 1.2: European supersonic transport programs before 2018 [1]

transport and development, flight tested of unmanned scaled airplanes, explored High Lift Devices (HLD), and validated CFD work [2, 324–339]. Figure 1.3 shows the roadmap of JAXA's NEXST program. In 2010, JAXA and DLR started collaborating in the field of supersonic aircraft research in flow prediction and optimization tools in terms of capabilities, accuracy, and speeds [340–342] based on JAXA-QSST model [328]. Meanwhile, the NEXST program shifted into Drop test for Simplified Evaluation of Non-Symmetrical Distributed sonic boom (D-SEND) where two axisymmetric bodies, D-SEND#1 and D-SEND#2, were dropped from balloons at 30 km altitudes for sonic boom studies [343–346]. The SST design evolved with studies from CFD, wind tunnel, and flight tests [347–349]. Lately, JAXA supported the wind tunnel testing for X-59 program [350–352].

In the last 20 years, supersonic designs have become more slender than the supersonic configurations designed, developed, and studied before 2000. The sonic boom and noise design considerations led to the slender designs for re-distributing the sonic boom signature. While significant works have been dedicated to the supersonic cruise phases with the quiet configurations, not enough study has been conducted on at low-speed region for the aerodynamic and S&C characteristics, where a publicly a accessible database with reference information and tradeoffs between supersonic and low-speed design would be available. The EU's EUROSUP and EPISTLE, and JAXA's NEXST objectives were to research low speed characteristic and develope CFD codes to validate low-speed predictions. But those projects plus a few others are exceptions [146, 226, 286–296, 326, 327, 329–342, 353].

The developments in hardware of computers with advanced CPUs and GPUs accelerates modeling and computational speed, have led to higher efficiency in simulation by Vortex Lattice Methods (VLM), panel codes, and Computational Fluid Dynamics (CFD) [354–

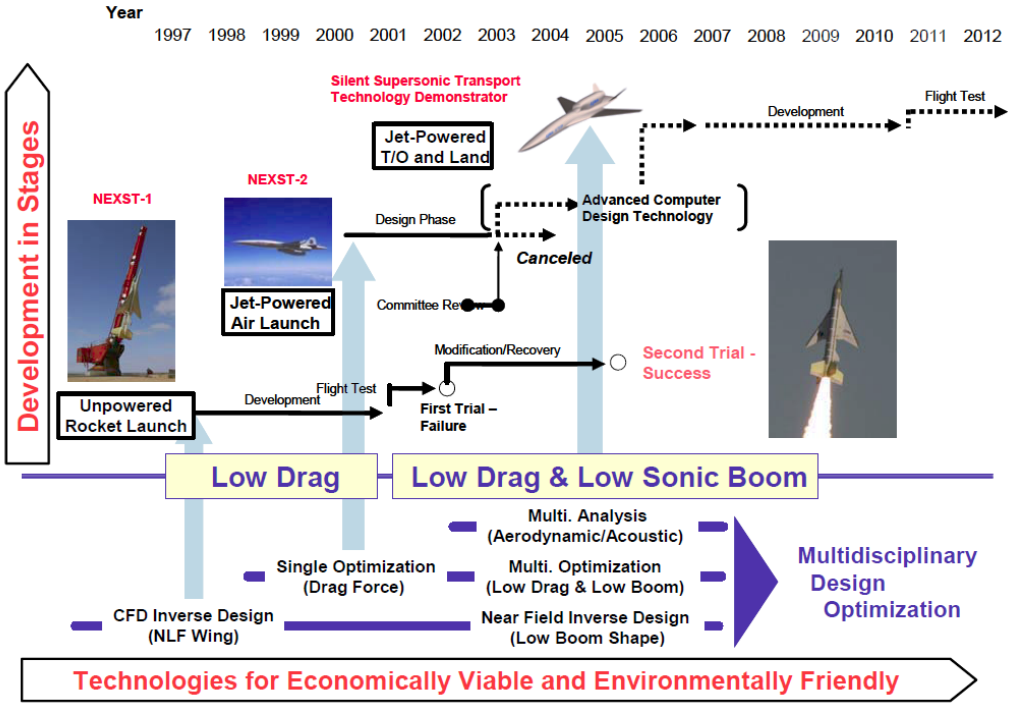
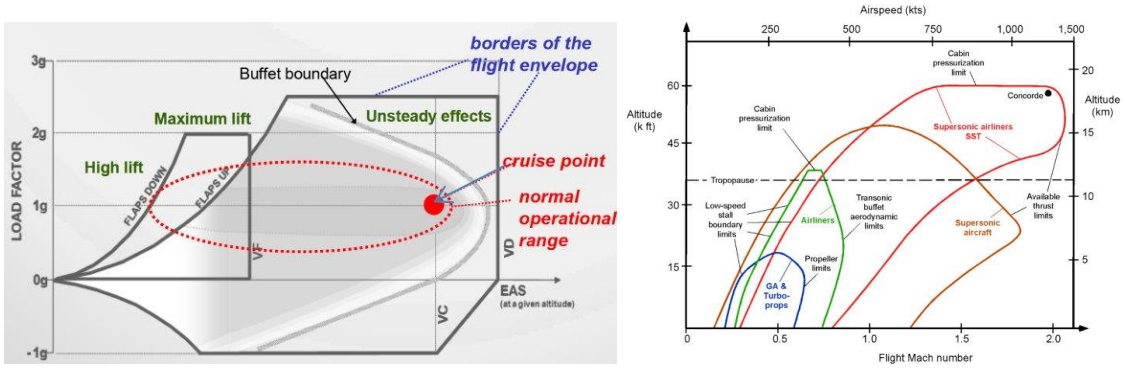


Figure 1.3: JAXA programs roadmap up to 2012 [2]

364]. Powerful and successful software developments over the last 30+ years may lead to the perception that wind tunnels would become obsolete. However, there are still major challenges in the numerical modeling of low-speed behavior of slender supersonic configurations, especially at high AOA [365–369] as reflected by the EU's EPISTLE and JAXA's NEXST programs. Figure 1.4a from the CFD vision 2030 study [367, 368] suggests that the corner or boundary of the flight envelope still remains an open challenge in CFD, especially for supersonic aircraft in Fig. 1.4b.

Now, there are few readily available public discussion of the quiet/efficient supersonic commercial transports (SCTs) and supersonic business jets (SBJs) and the key features of their low-speed characteristics. Reference [340] stated that *the experimental data obtained during EPISTLE project could not be shared with JAXA*, which likely led to the initiative of the NEXST and D-SEND projects of JAXA's own efforts. This demonstrates the need of widely accessible database for supersonic design. A major goal of the NASA Supersonic Configurations at Low Speeds (SCALOS) project was to generate data, build experience,



(a) Capability in flight envelope [368] (b) Capability in supersonic [370]

Figure 1.4: CFD challenges

and provide insights regarding the performance, handling qualities, and S&C low-speed behavior of variants of the emerging quiet supersonic configurations and of commercial supersonic configurations in general. The plan was to test and analyze a rich variety of alternative configurations to share with the aeronautics community, inspired by works such as in Fig. 1.5. The proposed plan included an evaluation of current CFD techniques and tools in their capacity to capture the aerodynamic behavior of the configurations of interest over the full range of relevant angles of attack at low speeds, to assess noise prediction methods, and to prepare the MDO foundation, including active control, for the design of such configurations.

But aerodynamic configuration shaping is one of the challenges of airplane design. The aeroelastic challenge is as significant, and slender, highly flexible supersonic configurations have to be designed so that undesirable aeroelastic behavior would be prevented at minimal weight penalties. Aeroelasticity is the interaction between a flexible airframe and the aerodynamic loads acting on it, where the loads deform the structure and the deformed structure changes the loads in a structure-aerodynamic feedback loop. Toward the end of the HSCT/HSR program, such aeroelastic coupling was identified as the major concern.

The S&C and handling qualities studies found that the Technology Concept Aircraft (TCA) was acceptable, from stability and control perspective, when modeled as a rigid body aircraft [221, 226, 229, 231, 232, 234]. The same configuration became difficult or impossible to fly when deformation and aeroelastic coupling materialized [233, 236]. Piloted

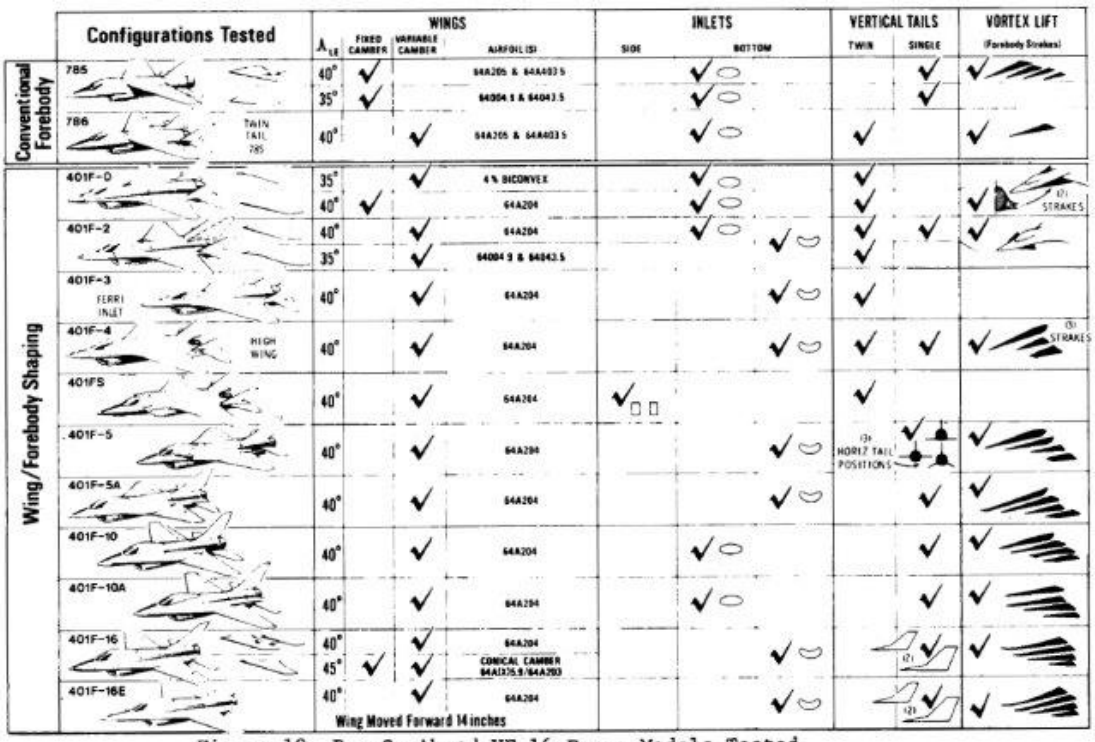


Figure 1.5: YF-16 tested configuration [3]

simulations confirmed these results, where the flexible-structural modes produced pilot-induced oscillations and biodynamic coupling that drove several configurations to handling qualities Cooper-Harper uncontrollable ratings [252–256].

At the time these effects could not be captured by rigid-body analysis or by computation alone, resulting in dedicated aeroelastic wind tunnel testing, initiated under the HSR program and completed under NASA's Supersonics Project. This effort led to in the Semi-Span Supersonic Transport (S4T), tested in four test entries in NASA Langley's Transonic Dynamics Tunnel (TDT) [1, 249]. On the S4T, active gust load alleviation (GLA), ride quality enhancement, and active flutter suppression (AFS) were demonstrated on a flexible supersonic configuration, supported by transonic limit-cycle characterization and system identification [245, 247, 250, 251]. The S4T was of much value as an aeroservoelastic wind tunnel testbed. But such programs, with large models in the TDT, are costly and limited to a single selected configuration.

This dissertation develops low-cost aeroservoelastic testbeds and demonstrates GLA and AFS on flexible high-aspect-ratio wing models, presented in §3, to establish the experimental evaluation quality and feasibility of active aeroelastic control toward flight safety, providing a transferable methodology for flexible configurations, including future commercial supersonic transports. To study active aeroelastic control that would be applicable to both flexible subsonic and supersonic aircraft, the work presented here combines analytical / numerical studies with low-cost active aeroelastic tests.

Overall, this dissertation makes contributions to commercial supersonic technology in two areas: low-speed wind tunnel aerodynamic testing and analysis, and active aeroelastic control supported by wind tunnel aeroservoelastic evaluation.

The rest of the dissertation is organized as follows. §2 presents the SCALOS project, including the project background and overview in §2.1, literature and design space survey in §2.2, test/simulation correlation in §2.3, experimental setup in §2.4, aerodynamic database in §2.5, dedicated tare and interference (T&I) correction in §2.6, aerodynamic results and analysis in §2.7, longitudinal aerodynamics in §2.8, lateral-directional aerodynamics in §2.9, and finally lessons learned in §2.10.

§3 presents the wind tunnel aeroservoelastic studies, including the literature review in §3.1, the experimental setup detailing wind tunnel models, MARGE and LARGE, in §3.2, the background mathematics on robust control in §3.3, wind tunnel system identification in §3.4, the control design for gust load alleviation and active flutter suppression in §3.5, and results and analysis of the wind tunnel evaluation in §3.6.

Lastly, §4 concludes the dissertation with a summary of contributions and calls for future work.

Chapter 2

SCALOS

The chapter describes the NASA SCALOS project and summarizes its resulting publications [4, 13, 14, 19, 23–27, 371–378]. The SCALOS project was concluded at the end of 2024, with the final report submitted to NASA. A part of the report is now accessible in [378]. This chapter is organized as follows. §2.1 describes the project background and overview, §2.2 presents the design space and existng designs, §2.3 studies the test/simulation correlations, §2.4 describes the experimental setup, §2.5 introduces the aerodynamic database, §2.7 shows aerodynamic results, §2.8 analyzes the longitudinal aerodynamics, §2.9 the lateral-directional aerodynamics, and finally §2.10 concludes the chapter with the lessons learned and insights from the project. Note that all the data in this chapter have been regenerated using the final SCALOS corrections and may slightly differ from earlier published versions.

2.1 Project Background and Overview

The historical material in this section is based on the overview of [4]. Some sections from Ref. [4] have been reorganized to fit the dissertation structure, including the tested SCALOS configuration variations tables to §2.2 and experimental setup, test model geometry, repeatability, and Reynolds number effects to §2.4.

2.1.1 Project Overview

The NASA SCALOS project team included groups at the University of Washington (UW), the University of Michigan (UM), Stanford University (SU), and Boeing Research and Technology (BR&T). The areas of contributions of each team are shown in Fig. 2.1. The plan called for substantial collaboration and integration, as wind tunnel tests at the UW and water tunnel tests by BR&T were compared and used for the evaluation of aerodynamic simulation tools of various levels of fidelity. The generated aerodynamic data were planned

to support S&C, handling qualities, and flight trajectory assessments. Work on the MDO and community noise aspects of the problem were included.

Figure 2.2 shows the planned flow of information and tasks in the SCALOS team. A strong emphasis was placed on aerodynamic analysis, supported by substantial wind tunnel testing, and on the validation of applied aerodynamic analysis capabilities for S&C work and for MDO.

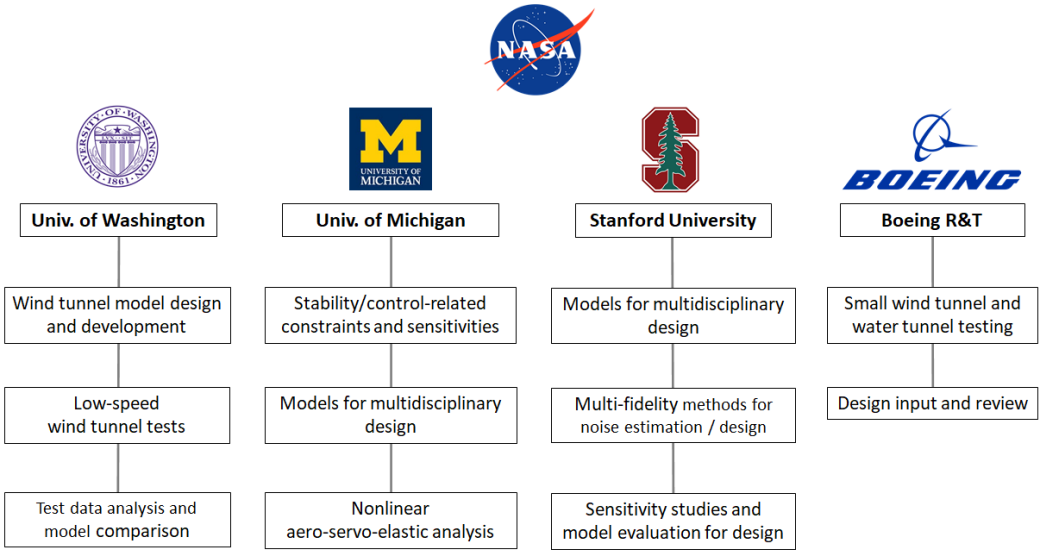


Figure 2.1: The NASA SCALOS project team and areas of contribution [4]

In addition to graduate-level research work, supersonic configurations have been used as a "future aircraft" design topic for undergraduate capstone courses over the last 20+ years at UW's William E. Boeing Department of Aeronautics and Astronautics (AA) (see Fig. 2.3). The UW AA capstone teams designed the small research UAVs (RUAVs) of supersonic configurations, tested them in the wind tunnel, and flew most of those large instrumented radio-controlled models in the years 2005-2019. Significant design, hands-on vehicle integration, and build/fly experience was gained by hundreds of University of Washington A&A (UWAA) seniors [379, 380]. Thus, hundreds of UWAA seniors were introduced to the challenges of commercial supersonic aircraft design.

The NASA SCALOS project was completed at the end of 2024. An overview of the SCALOS project's 2020-2024 effort in the applied aerodynamics area is presented in [4,

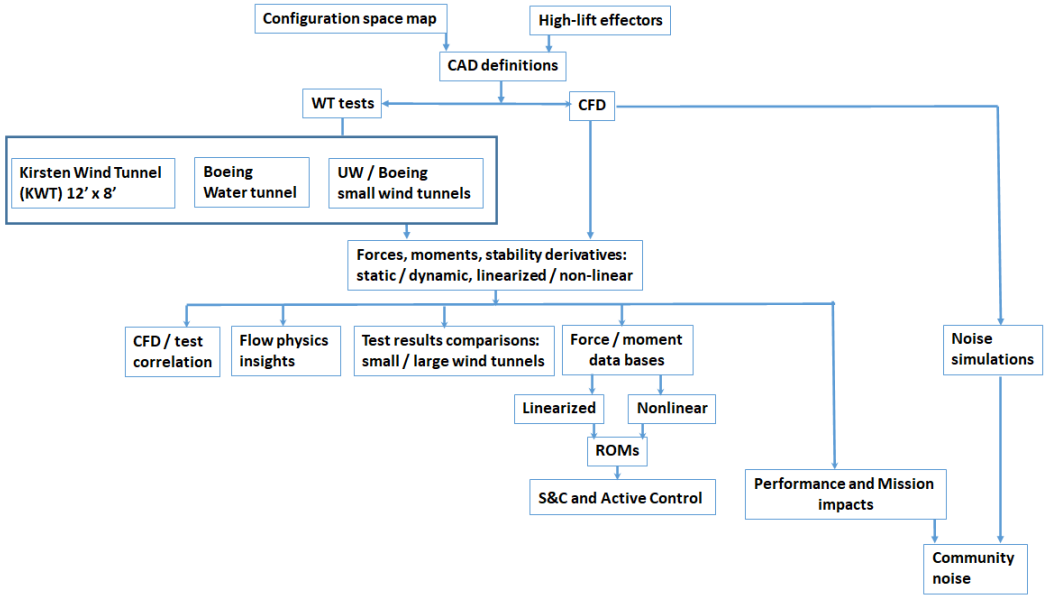
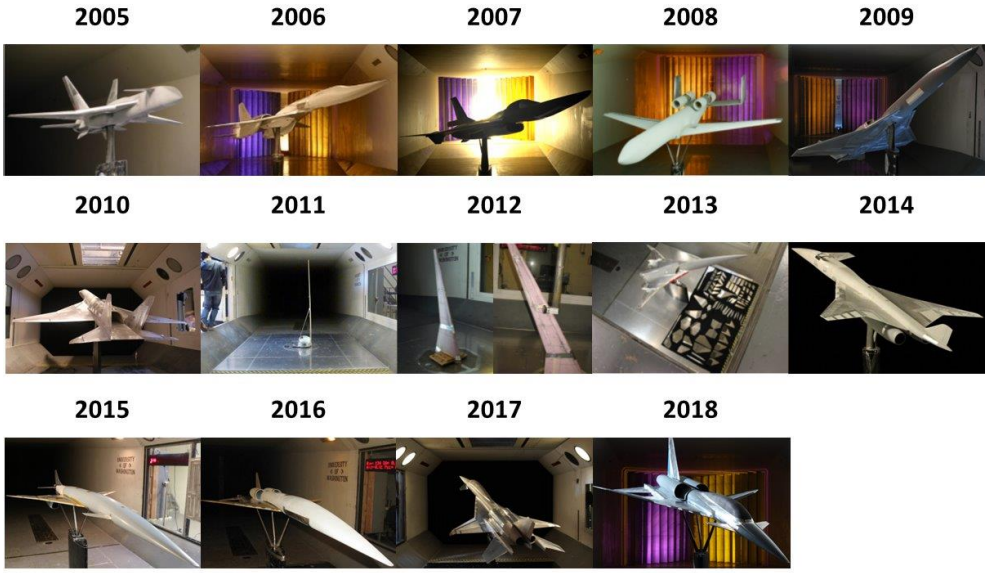


Figure 2.2: SCALOS's information and tasks flow map [4]

24, 25, 377], covering years of low-speed testing in the Kirsten Wind Tunnel (KWT) at the University of Washington Aeronautical Laboratory (UWAL). All publications from the project by the University of Washington include [4, 13, 14, 18, 19, 23–27, 371–377, 381–383]. Boeing Research & Technology contributions are described in [15, 384–386]. University of Michigan work is described in Refs. [16, 387–403]. Stanford University work is described in [404–408]. A summary chart of contribuotors in publications is shown in Table 2.1.

Table 2.1: SCALOS team charts

Organization	UW	UM	SU	BR&T
Prof./Dr.	Eli Livne	Carlos Cesnik	Juan J. Alonso	Todd Magee
Researcher/Dr.	Chester P. Nelson	Ilya Kolmanovsky	Ilan Kroo	Patrick J. Hayes
	Reza M. Soltani	Joaquim Martins		J. A. Dorgan
				Abdi Khodadoust
Post-doc/Dr.		Thiago Guimarães		
Research Fellow /Dr.		Torbjørn Cunis		
		Rafael Bertolin		
		Guilherme Barbosa		
Graduate Students	Kuang-Ying Ting	Sabet Seraj	Tejal Shanbhag	
	Nicolas Mavriplis	Bernado Monteiro	Yiren Shen	
	Kenneth Wieserma			
Undergraduate Students	SCALOS Capstone			
	2020-2024			
	60 students			
Publications	[4, 13, 14, 18, 19, 23–27, 371–377, 381–383]	[16, 387–402]	[404–408]	[15, 384–386]



(a) Wind tunnel models



(b) RUAV models

Figure 2.3: UW capstone wind tunnel and RUAV models before SCALOS [4]

Background: Post-Concorde Supersonic Airliner Development

From the perspective of investment and technical scope, the most significant effort to improve civil supersonic aircraft after Concorde's development, was the HSCT in the 1990s. In

the late 1980s emerging technologies and expanding demand for overseas travel prompted a decade-long U.S. commitment to R&D directed toward making supersonic airliners a feasible option for the next generation of commercial air transport. The goal was a 300 passenger, Mach 2.4 airplane with a 5000 nautical mile range capability with a fraction of Concorde's operating cost per seat. NASA harnessed the activities of its researchers and facilities and formed the joint NASA-industry High Speed Research (HSR) team comprised of about a dozen organizations and hundreds of engineers and scientists. Several of the industry partners also carried out significant internally funded development efforts - notably Boeing's early design and testing of airframe and propulsion concepts in 1989-1995. NASA contracted industry partners to support advances in basic propulsion, avionics, structural design, aerodynamics, and materials technologies. Boeing was "prime" on the airframe development team with partner McDonnell-Douglas. A Pratt & Whitney and General Electric consortium tackled the propulsion system. The HSR program continuously guided and measured the progress of the technology developments through the parallel evolution of a common baseline HSCT vehicle. Initially, configuration work and wind tunnel testing were conducted using Boeing's internally developed "Ref-H" configuration. Other studies were carried out on McDonnell-Douglas's "M2.4-7A" until a joint HSR Technology Concept Airplane (TCA) could be defined. Over roughly five years, the HSCT design concept evolved from the "Ref-H" to the "TCA", and finally to the "TC", HSR Technology Configuration (TC), as shown in Figure 2.4 [5].

The Technology Configuration (TC) incorporated all of the technical advances to date (at the time) into one example commercial airliner configuration, including structures, systems layout, and proposed certification solutions. The external aerodynamic design represented an "optimal compromise" across all mission flight regimes and expected operations. Relative to earlier conceptual designs, the TC featured added wingspan and aspect ratio, and significantly changed engine cycle, nozzle, inlet, materials and structural concepts. The large mixed-flow turbofans, bypass ratio (BPR) ≈ 0.8, achieved significant takeoff noise reduction through the use of advanced variable area ejector-suppressor nozzles. A third lifting surface was added - small canards on the forebody - both to reduce aeroelastic pitch control losses and to provide active structural mode control of the flexing of the long fuselage. The

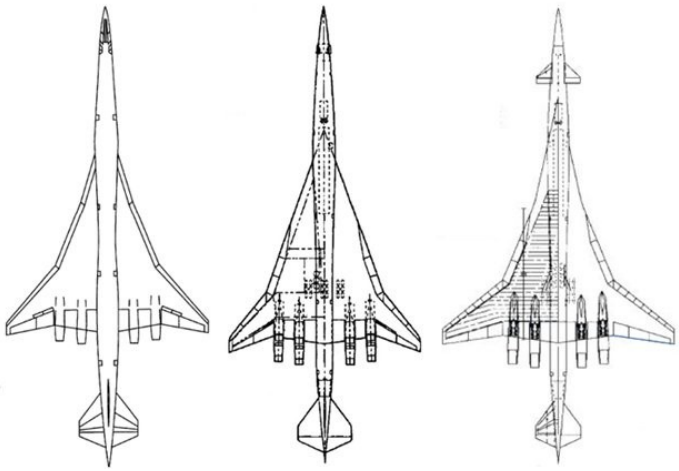


Figure 2.4: HSCT concept evolution: Ref-H, TCA, and TC configurations [5]

predicted characteristics of the TC were solidly based on ground testing and simulation. In spite of the HSR configuration's evolution, the TC baseline's general arrangement topology was held fixed; a slender tube-and-wing geometry with long aft body and fairly conventional aft tail and four slender nacelles mounted under the wing trailing edges.

HSR's Aerodynamics efforts included a massive amount of CFD work and wind tunnel testing involving multiple models of the Ref-H and TCA designs and their variants in different facilities at different scales. Multiple leading and trailing edge devices were explored, as well as several alternate canard arrangements and outboard wing panel geometries. Yet HSR was focused on tools and methods development, testing improvements, CFD validation, and experimenting with computer-driven detailed aero shape optimization. The objective was to develop the enabling technologies and examples, not to complete a production aircraft design or develop comprehensive DATCOM-like database [409, 410]. Boeing continued to independently design and test Proprietary HSCT concepts with their internal funding and to understand airline requirements, configuration integration and Federal Aviation Administration (FAA) certification.

Although HSR's advances in the individual disciplines were formidable by the late 1990s, critical assessments of the TC design indicated remaining viability shortfalls in light of ever-increasing noise restrictions and airline requirements. Additional technology advances and integrated configuration concepts would be needed. In the final year of HSR, the NASA-

industry HSR team mapped additional emerging technologies. NASA's industry partners brought forth some alternate configuration and propulsion concepts that were explored by internal research and development (IRAD). Selected technologies deemed achievable by 2013-2015 were used to evaluate a "2015-TC" design. Some of the alternate configurations indicated potential net benefits for more "fighter-like" general arrangements rather than retaining a "tube-and-wing" design. Promising features included integrated horizontal tails or "aft-deck" surfaces, minimally-spaced or "dual-podded" nacelles, 3-dimensional (3D) inward-compressing, "wave-rider"/streamline-traced external-compression (STEX), inlets, offset inlet diffusers, twin vertical tails, blended/lift-generating fore-bodies, and over-wing exhaust/nacelle locations for airframe noise-shielding. One study configuration, named Highly Integrated Supersonic Cruise Aircraft Technology (HISCAT) [5] showed potential for reduced landing and take-off (LTO) noise and transonic drag-rise, softened sonic boom, and improved aeroelastic stiffness with insignificant supersonic cruise lift-to-drag ratio (LOD) trade-offs, Figure 2.5.

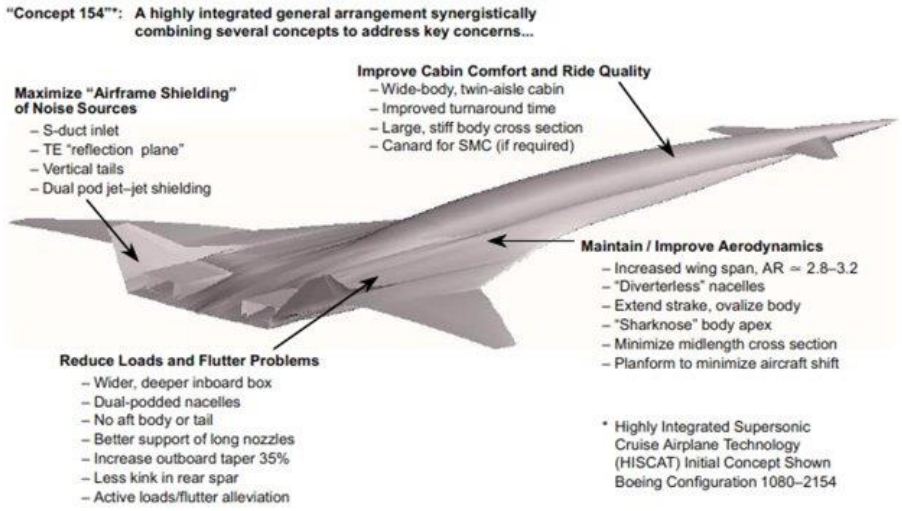


Figure 2.5: HISCAT advanced HSCT concept (1999) [5]

The combination of revised technology suites, new configurations, and application of improved MDO capabilities, indicated a path to eventually meeting most future HSCT requirements. However, budget pressures on both the NASA HSR and the industry IRAD side brought an end to the "HSCT decade" 1999, leaving a number of promising designs

untested. Those advances which were applicable to subsonic aircraft projects were further developed by industry and applied to several production engines and airframes between 2000-2010. Some of the final HSCT aerodynamic and configuration integration ideas were adapted to later high-speed aircraft studies, including Boeing's Sonic Cruiser and various supersonic business jet concepts. In the post-HSCT decade, Boeing, NASA, and others continued to work on civil supersonics at a reduced level of effort. NASA and the Defense Advanced Research Projects Agency (DARPA) sponsored renewed low-boom research in the early 2000's, including the first in-flight proof of low-boom shaping effects [271].

Background: Supersonic Business Jets

In the late 1990s and early 2000s, Gulfstream, Boeing, Supersonic Aerospace International (SAI)-Lockheed, Aerion, Tupolev, Sukhoi, Dassault, all began pursuing designs for smaller supersonic business jet (SBJ's, SSBJ's) - mainly corporate "bizjets" of 6-18 passengers. Corporate jets were seen by many as an emerging market and a "stepping stone" to civil supersonics, offering lower investment risk, lower environmental impact, and much greater ability of the customer to absorb higher direct operating costs. At the end of the HSR program, aeroelastic handling qualities, high altitude engine emissions, and sonic boom were still technical risk areas. Technical challenges in each of those areas would be more manageable with smaller aircraft. Performance vs cost trades showed SSBJ's flying somewhat lower and slower than HSCT. By the mid-2000s a range of configuration concepts were in the conceptual/early preliminary design stages. Some of these industry SSBJ concepts were wind-tunnel tested, but results have generally remained proprietary and unpublished. A European Union (EU) R&D effort called HISAC (Environmentally friendly high speed aircraft) brought a number of industry and academic organizations together to study small supersonic aircraft enablers and concepts for low-sonic boom designs.

Background: NASA N+ Studies

In 2008-2010 NASA kicked off a series of sponsored industry studies referred to as "N+2 and N+3". Multiple industry participants provided their visions of future civil aircraft,



(a) Boeing [411]



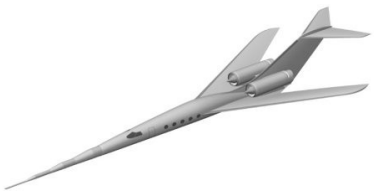
(b) SAI Lockheed [412]



(c) HISAC-Dassault [297]



(d) HISAC-Sukhoi[297]



(e) Gulfstream [413]



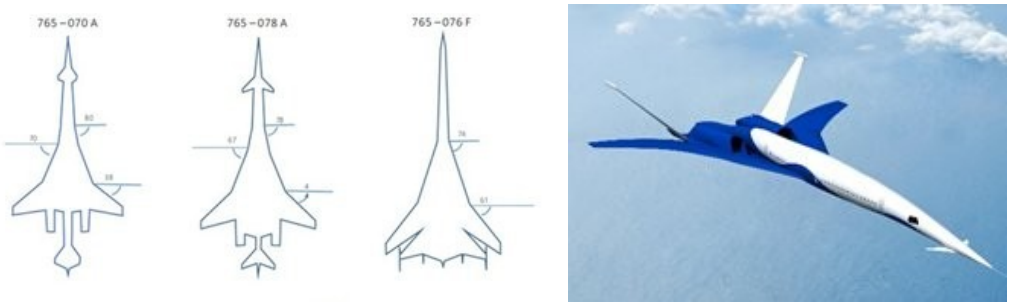
(f) Aerion [414]

Figure 2.6: SSBJ 2003-2007

subsonic and supersonic, and technology advances needed to make them happen within 2-decade and 3-decade time horizons (from a late 1990s technology reference point). Boeing and Lockheed conducted parallel studies for commercial supersonics.

Airplane requirement and market studies carried out by Boeing as part of their N+2 investigation [6–8] indicated a potentially viable market for several hundred SST's in the 50-150 seat category, even if full supersonic flight over land is not eventually approved. This prompted their study to include designs for over-water missions (high subsonic speed over land), and separate consideration of designs configured for low-boom operation, all using near-term technologies. Several candidate designs were shown, some emphasizing reduced emissions and fuel consumption (the Concorde-sized 070A and 072B), and a slightly smaller airliner designed specifically for low sonic boom (the 076 series). In the later years of HSR, the quest for large sonic boom reductions had reached a technical impasse due to mission sizing penalties and difficulties in reducing the aft shock signature to the levels predicted by theory. Follow-on work indicated however, some degree of "boom softening" could reduce the annoyance factor of "over-water" HSCT's, and this could be achieved with minimal performance impact. The N+2 configuration "078" was an example of an over-

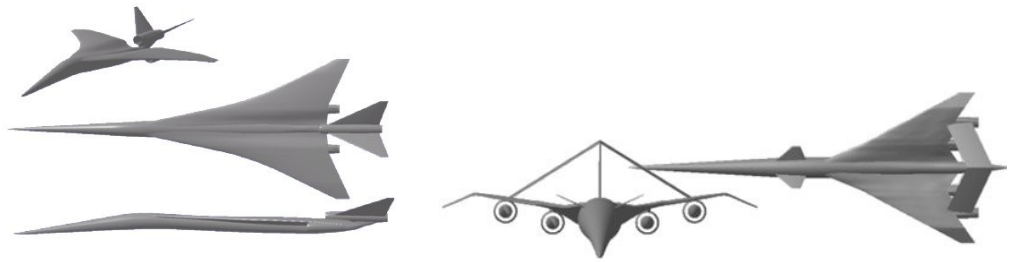
water airliner with some degree of sonic boom reduction (Figure 2.7). A scaled-up version of the 076 was used as the starting point for the more advanced "Icon-II" configuration used for the N+3 study to show what might be achievable in a larger aircraft given another 10 years of technology progress in key areas [6–8].



(a) N+2 (b) N+3 Icon-II

Figure 2.7: Boeing concepts [6–8]

Lockheed's initial N+2 concept and their N+3 concept (Figure 2.8) employed a joined-tail arrangement similar to the SAI-Lockheed business jet concepts of the early 2000s, but their preferred N+2 concept was a V-tailed tri-jet arrangement [9].

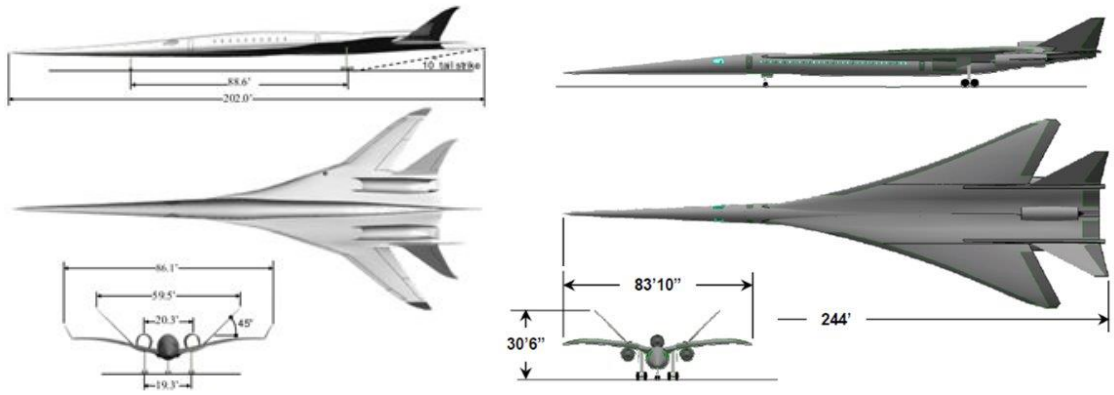


(a) N+2 1021 Tri-jet (b) N+3 4-engine joined-tail

Figure 2.8: Lockheed concepts [9, 10]

NASA saw the need to further promote and validate low-boom design and testing as long-lead technologies for future supersonic aircraft. The Boeing 076 and the Lockheed tri-jet concept were selected by NASA as points-of-departure for follow-on refinement, aero/boom shape optimization, and wind tunnel testing as shown in Figure 2.9.

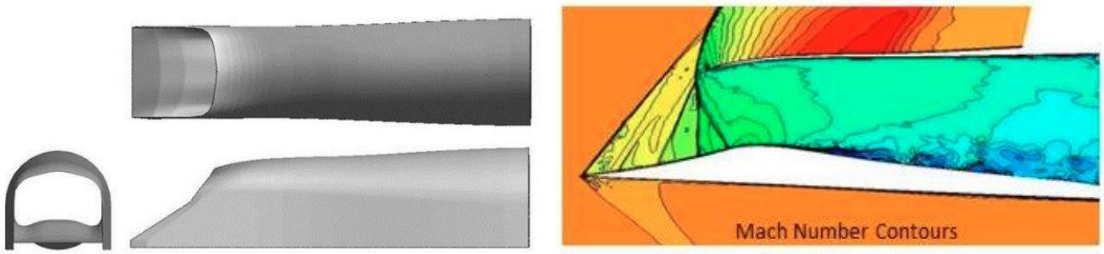
The re-designed, CFD-optimized 076 type was called the Quiet Experimental Validation



(a) Boeing QEVC [268] (b) Lockheed 1044 [10]

Figure 2.9: Boeing QEVC and Lockheed N+2 Phase II comparison

Concept (QEVC). It was used for sonic boom test instrumentation development, validation of CFD optimization and analysis tools, and for validation testing of a representative over-wing "3D" type supersonic inlet design, the Elliptical Cowl Ramp Inlet (ECRI) in Figure 2.10 [11]. After initial tests of their V-tailed concept Lockheed developed an improved configuration (L1004) incorporating an aft-deck, which was the subject of a second phase of testing.



(a) ECRI design (b) Ma number contours, $Re = 22 \times 10^6$

Figure 2.10: Boeing Elliptical Cowl Ramp Inlet [11]

Both Lockheed and Boeing published CFD, sonic boom pressures, and supersonic force and moment data in their final reports, shown in Figure 2.11 as an example. Lockheed also published selected low-speed test results on their concepts. The low-speed S&C results showed clear examples of the trade-off between low-speed characteristics and low boom; the lowest boom configuration from the later design iterations showed lower pitch stability.

"Pitch-Up" non-linearities started at a lower alpha and CL [10].

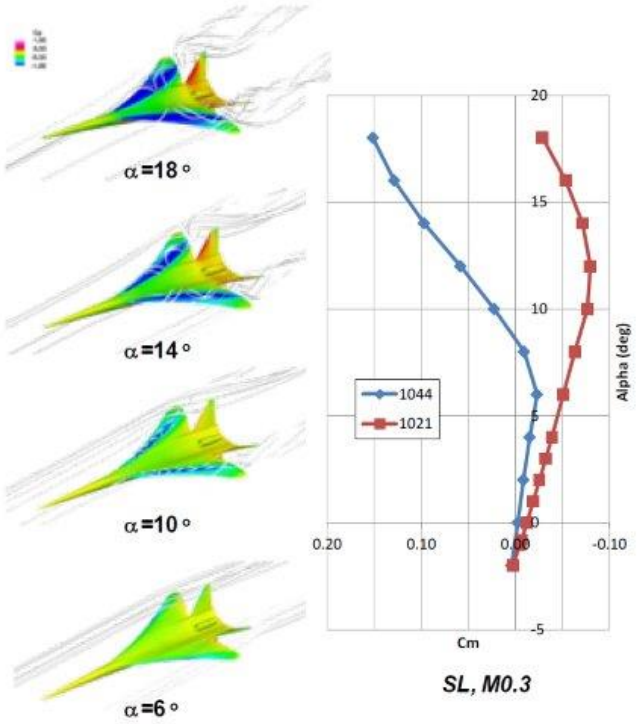


Figure 2.11: Lockheed 1044 high-alpha pitch-up due to wing apex vortex formation [10]

Background: NASA Low-Boom Flight Demonstrator, X-59

Encouraged by the success of the N+2 low-boom design and wind tunnel validation program, NASA awarded parallel study contracts to Lockheed and Boeing to propose designs for a purpose-built manned research aircraft (X-Plane) to finally demonstrate low sonic boom flight with fully shaped pressure signatures at both front and rear shocks. The aggressive goals set for boom reduction pushed the state of the art in low-boom design. After more than 2 years of independent design work, Boeing and Lockheed proposing roughly similar concepts; both employing inlets above the plane of the wing, both using F404/F414 series engines with exhaust-shielding fairings, low-mounted horizontal tails, highly swept wing planforms, electronic external vision systems in the cockpit, and extensive use of components and sub-systems from existing fighter and trainer aircraft. The Lockheed concept won-out and has proceeded through the detailed design development at build stages, with final

assembly completed and the aircraft already in flight tests currently (Figures 2.12 and 2.13). While it does not represent a sub-scale airliner prototype, the geometry features and proportions of the X-59 do give some idea of the configuration compromises and key features necessary for future designs that seek to drive sonic boom to minimal levels.

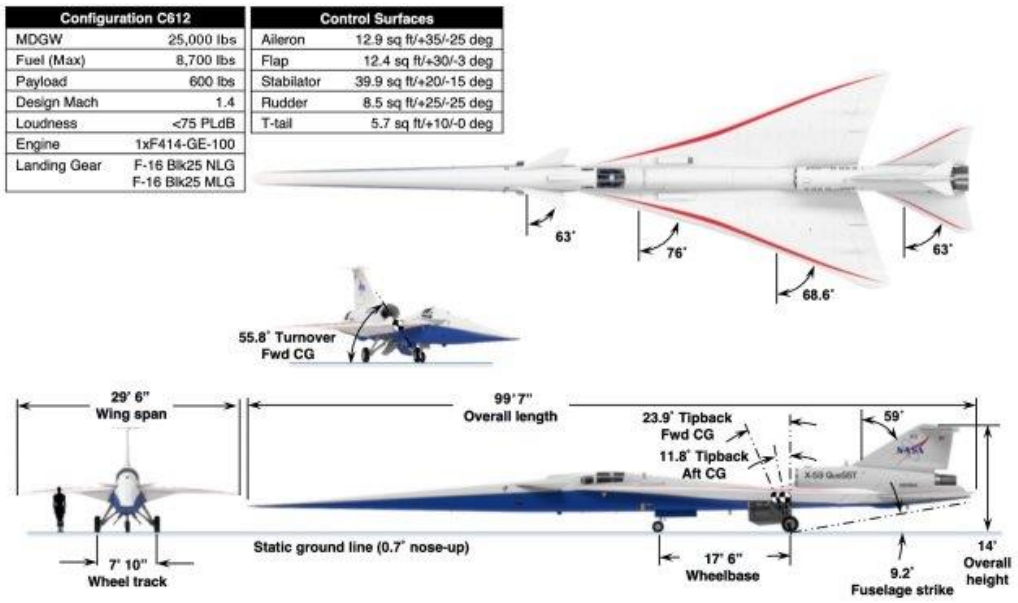


Figure 2.12: NASA-Lockheed Martin X-59 low-boom flight demonstrator [12]



Figure 2.13: NASA-Lockheed Martin X-59 low-boom flight demonstrator in flight (courtesy, NASA)

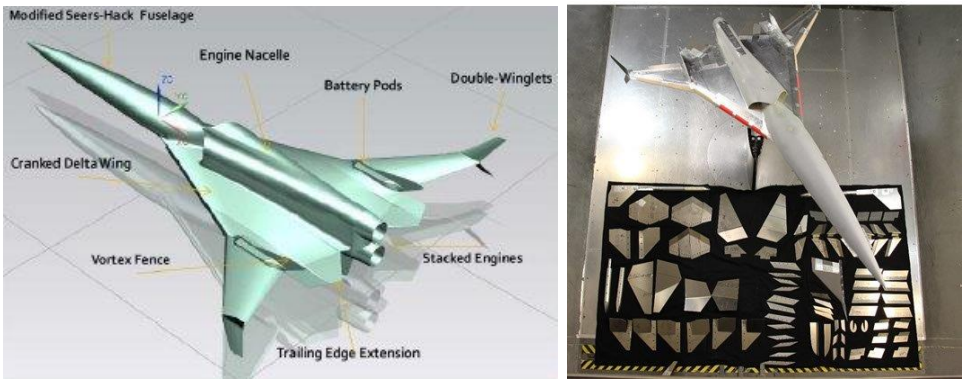
Progress at University of Washington: SCALOS Configurations

Post-HSCT designs for smaller supersonic airliners and SSBJ/SBJ types can be seen to incorporate some commonly recurring configuration features, depending on the degree of sonic boom reduction being attempted:

- Twin-engine or tri-jet configurations, higher engine BPR (lower FPR).
- Multi-stream propulsion flow-path /variable cycle engines.
- Engine sizing based on variable de-rate, PLR, or FADEC-modulated thrust lapse
- Non-axis-symmetric body cross-sections
- High efficiency axis-symmetric cone inlets or STEX 3D inlets
- Closely spaced or "dual podded" engine nacelles
- Flattened "shark nose" and/or body chines
- Increased body slenderness (or telescoping nose boom), more conic forebody area growth
- Increased wing LE sweep and "softened" planform breaks
- Lower wing aspect ratios (over-all length-to-wingspan ratios as high as 3.5)
- Joined tails, aft-decks, or widened aft fuselages or aft-body chines
- Twin vertical tails or V-tails
- Multi-surface pitch control, multi-use control surfaces
- Vertical and/or horizontal tails attached to aft-decks or engine nacelles

- Inlets shielded by the wing and/or aft-body
- Engine exhausts shielded by wings, aft-deck surfaces, or dedicated nozzle fairings
- Wing and tail tip fairings, anti-shock bodies
- Small auxiliary lifting surfaces (fixed canards, mini T-tail or cruciform stabilizers, aft-body chines)
- Dihedraled or "gulled" wings

SCALOS testing activities have studied and cataloged the effects of a number of these features. Testing in 2020-2021 at University of Washington Aeronautical Laboratory's (UWAL) Kirsten Wind Tunnel (KWT) facility employed a range of model components that attach to the common center-section of an existing semi-modular model. This chosen model "core" was originally built for a USAF-sponsored project in 2013-2015 under which UW graduate and undergraduate students explored novel control arrangements for "tailless" long-range supersonic cruise aircraft [380].

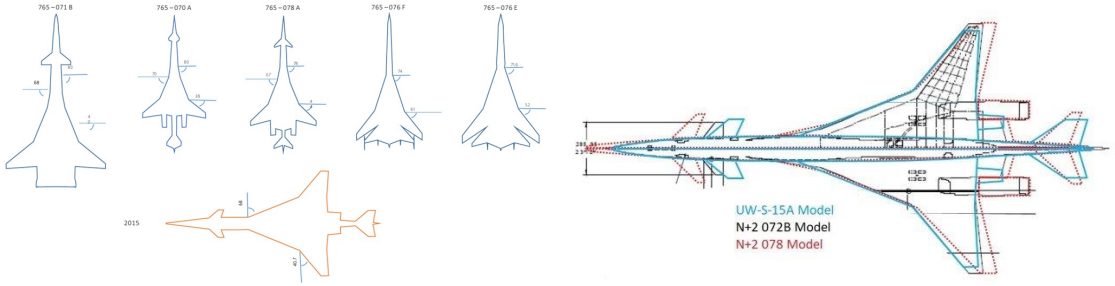


(a) Design (b) Wind tunnel model

Figure 2.14: 2013 UW AFRL-AFOSR model (SCALOS "core") [4]

In 2015, a more conventional general arrangement was chosen as reference test case for the USAF study. The 2015 model was designed to be geometrically similar to an industry supersonic airliner concept from NASA's "N+2" studies. The general arrangement chosen

was similar to Boeing's "070A" but with wing-body planform shapes closest to the "072B" concept as shown in Figure 2.15.



(a) Top-view side-by-side comparisons (b) Top-view overlay comparisons

Figure 2.15: Boeing's N+2 configurations vs. UW's UW-S-15A (schematic. not to precise scale) [4]

Wind tunnel model geometry for this generic 2015 supersonic airliner configuration, UW-S-15A, included several wing-body-nacelle lofting simplifications to accommodate the modular model core. It also incorporated nacelles sized to accommodate electrically powered ducted fans (EDF) propulsors. These EDF units could be operated in the wind tunnel and used on a flying RUAV version built to the same scale. The resulting model nacelles approximated one of the lower BPR (higher Vjet) type engine options from the N+2 studies. Horizontal spacing of the nacelles was minimal and accommodated a notional concept for main landing gears located on the outboard side of the nacelles. The wind tunnel model allows for testing canards at multiple fore-aft locations, various leading and trailing edge devices, and has removable horizontal and vertical tails and removable fore and aft fuselage sections.

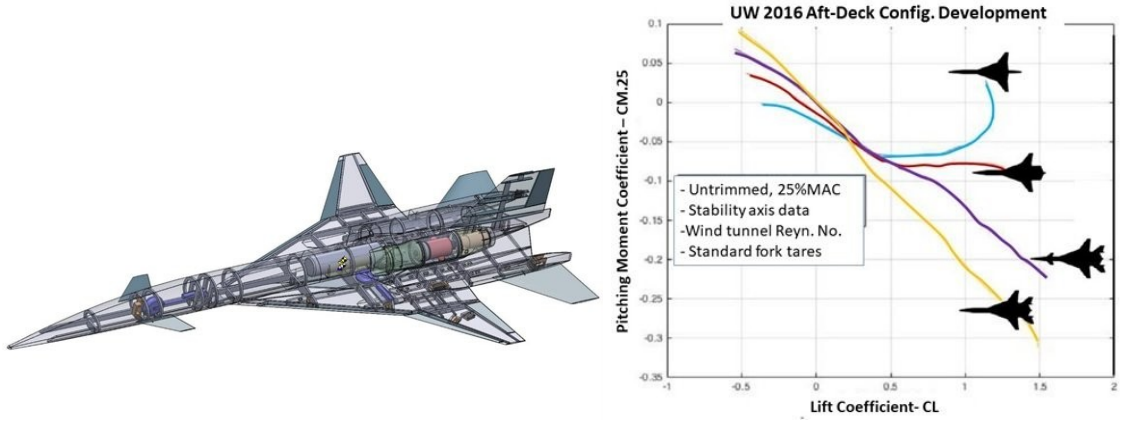
For the R-UAV version of the 2015 design, the aft-center of gravity limit was intentionally restricted. As a result, the main landing gear of the R-UAV was located farther forward and was somewhat longer than that of the full-scale aircraft to preserve LTO rotation angles, as shown in Figure 2.16. The thrust vectoring paddles that were investigated in the wind tunnel for the USAF project were removed from the R-UAV version which was successfully flown in 2017.



(a) Wind tunnel model (b) RUAV

Figure 2.16: SCALOS 2015 model, and the UW-S-15A RUAV [4]

The wind tunnel data from year 2015 tests of this configuration provided SCALOS with early configuration comparison data and a point of reference for long-term testing repeatability. The same wind tunnel model "core" was used by UW "Capstone" classes in 2016 to investigate non-linear aerodynamic characteristics of designs incorporating aft-decks and various pitch-control arrangements. The results were used to design a twin gas turbine powered RUAV as shown in Figure 2.17

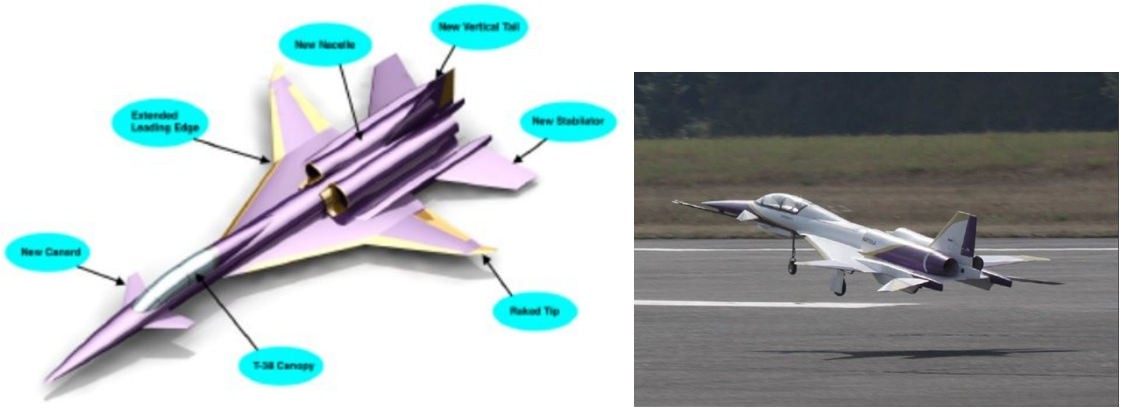


(a) Wind tunnel model (b) C_M vs α

Figure 2.17: SCALOS 2016 model [4]

A follow-on project in 2017-2018 covered the conceptual design and testing of a 2-seat supersonic cruise research aircraft. A 1/7th scale RUAV version, built by Capstone course seniors, based on the wind tunnel results, was test flown in 2017, as shown in Figure

2.18 Combinations of selected components from the 2015-2018 wind tunnel models were re-tested in 2020-2021 as part of the SCALOS effort to document incremental effects of specific features.



(a) Wind tunnel model (b) RUAV

Figure 2.18: SCALOS 2017 model [4]

Note again that this section is from [4], which was the first publication on the SCALOS project, detailing project background and initial directions. In terms of full configuration definitions, the testing to-date SCALOS work (as of 2020-2021) has focused on assessing the characteristics of three primary configuration types built using the 2015 wing-body as a point-of-departure core model:

1. An up-dated version of 2015's conventional "over-water" airliner concept

2. A T-tailed "boom-softened" variant with increased outboard wing sweep and the nacelles relocated to the upper surface of the wing

3. A "low-boom" variant with shielded nozzles, stretched fore-body, and ogee planform

The first of these, a "parent" geometry for the other two and designated UW-S-21A, features a more highly swept stabilator, aft-body ventral and dorsal fins, and nacelles more accurately representing the "low-Vjet" (higher BPR, lower FPR) end of the engine cycle spectrum that was studied during N+2. These larger diameter nacelles were re-positioned

farther outboard on the wing to improve engine-engine separation for rotor-burst certification and to provide room inboard of the nacelles for a diagonally retracting main gear (similar to the 072 design). The tail modifications were based on results of the 2015 wind tunnel tests and 2017 flight testing. The nacelles were sized based on N+2 published engine data, and the external lines of the inlet were based on the ECRI type that NASA tested on the QEVC model. This concept was further developed and documented in-depth by UW Capstone design students during 2021-2024 , as a Reference Supersonic Airliner Concept (RSAC) offered as a basis for future trade studies, as shown in Figure 2.19. This configuration defines the mid design space point in the notional SCALOS configuration matrix illustrating in Figure 2.20. The corresponding wind tunnel configuration represents a 1/22 scale (4.5%) model of the 75-100 seat airliner designed for Mach 1.8 cruise, with BPR $\approx$ 3.5 engines.

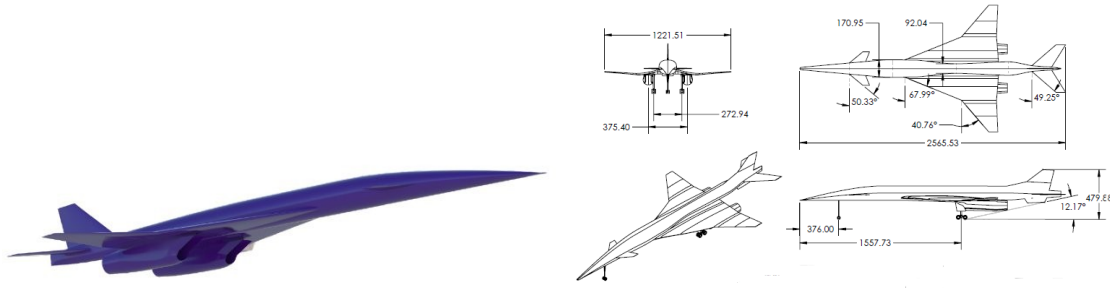


Figure 2.19: SCALOS 2021 model, UW-S-21A [4]

The second configuration concept, UW-S-20A, featured the same horizontal stabilator design as the first, but in a T-tail arrangement and the nacelles moved to the upper surface of the wing. This configuration was the baseline model configuration for 2020 tests in KWT and for dynamic stability testing in BR&T FVWT facility as shown in Figure 2.21

The third primary study configuration type is a low-boom variant of the second, incorporating a "stretched" fore-body, a small aft-deck with nozzle shielding, and an ogee-like planform with increased side-of-body leading edge sweep and softened planform breaks, in Figure 2.22. Configuration optimization for low-sonic boom was beyond the scope of the effort to date. While there are other more aggressive low-boom configurations that may be capable of quieter booms (e.g. X-59) this arrangement was deemed a reasonable place-holder

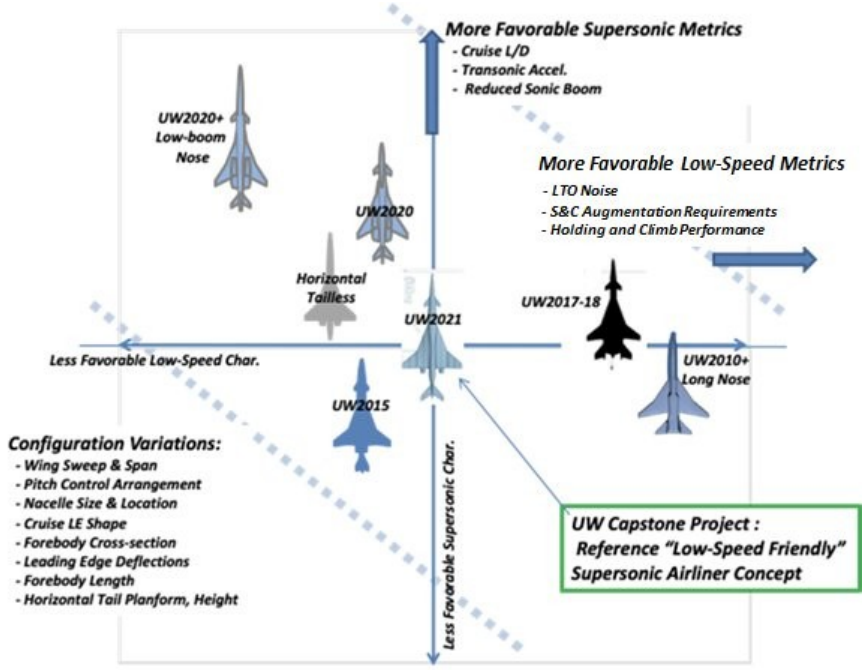
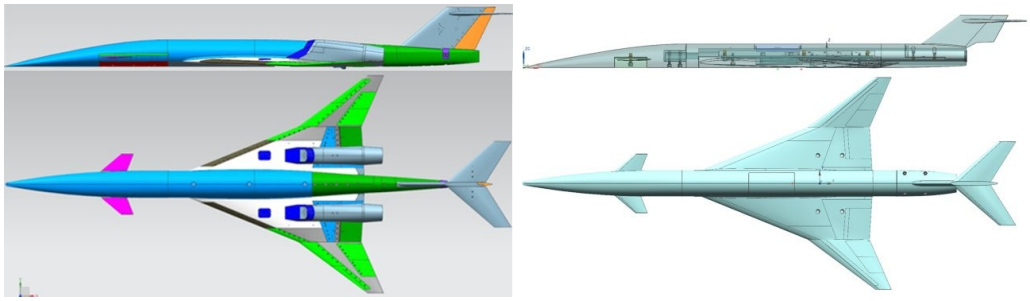


Figure 2.20: SCALOS notional configuration matrix [4]

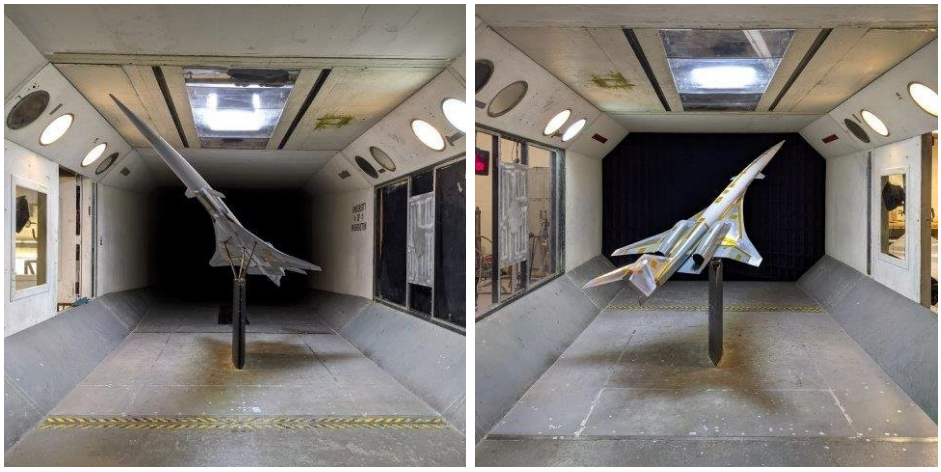


(a) Wind tunnel model (b) Water tunnel model

Figure 2.21: SCALOS 2020 model, UW-S-20A [4]

aircraft geometry that the present core wind tunnel model could parametrically represent.

Several types of flow visualization data were recorded for selected configurations to correlate observed flow physics with non-linearities in the force and moment data shown in Figure 2.23. Both florescent oil and mini-tuft surface flow visualization methods are shown as examples. Flow visualization observations are discussed in detail in 2.7.1 [23, 27].



(a) Downstream view (b) Upstream view

Figure 2.22: Low-boom configuration with long fuselage, nacelle aft-deck, and T-tail, UW-S-20CL-3, in the KWT [4]



(a) 2015 wing only (b) 2021 baseline model (c) 2020 baseline model

Figure 2.23: Flow visualization [4]

2.2 Design Space Survey

The literature and design space survey in this section are taken from [13], which studied the published supersonic airliner and business jet concepts of most interest to industry, NASA, and academia since the end of the HSR program in 1999. This section summarizes a "design

space" survey, tabulating configuration, general arrangements, and geometric parameters for a wide range of civil supersonic cruise airliner and corporate jet concepts.

Attention is given to those published airliner and business jet concepts of most interest to industry, NASA, and academia, since the early-2000's. General arrangements and design features tested as part of the NASA-funded SCALOS effort in 2020-2022 [4] are placed in the context of this design space. A fairly complete summary of the evolution of supersonic airliners (HSCT) under the HSCT, Highly Integrated Supersonic Cruise Aircraft Technology (HISCAT), and Independent Research And Development (IRAD) designs of "Ref-H", "TCA", "TC", Concept 154, etc. [4, 271, 409, 415], will be included [409, 410, 415]. SSBJ, corporate/private jets carrying 6-18 passengers were pursued in the late 1990's and early 2000's by Gulfstream, Boeing, Supersonic Aerospace International (SAI)-Lockheed, Aerion, Tupolev, Raytheon, Sukhoi, and Dassault. A European Union (EU) funded project, environmentally friendly High Speed Aircraft (HISAC), involving a collaboration between industry and academic organizations studied technologies and design concepts for low-sonic boom designs [297]. As has already been mentioned, in 2008-2010 NASA funded industry studies of future civil subsonic and supersonic aircraft referred as "N+2" and "N+3", which mean 2-decade and 3-decade time horizons from the late 1990's technology. Boeing and Lockheed conducted parallel studies for commercial supersonics [7–11, 268, 416, 417].

From the 2000s there have been independent agencies, companies, startups, and organizations working on supersonic airliner and SSBJ including the Japanese Aerospace Exploration Agency (JAXA) [418–421], Aerion [422–424], Gulfstream [425–427], Spike [428], Boom [429], Exosonic [430], HyperMach SonicStar [431], Tupolev [432], Cranfield University [414, 433, 434], etc. Recent research aircraft or technology demonstration programs include JAXA D-SEND [419], Boom XB-1 [429], and Lockheed X-59 [435, 436] (NASA funded X-plane). Note that it is unfortunate now that both Aerion and Exosonic went out of business, a sign of the technical and business challenges of supersonic aircraft programs.

2.2.1 Developed and Evolving Supersonic Airliner / SSBJ

In 2020 and 2021, University of Washington "Capstone" senior design project students began a literature search to identify civil supersonic configurations investigated since the early 2000s that would be of particular interest to NASA and academia. Students in the UW capstone design class of 2020–2022 assisted in using public domain information to estimate leading-edge sweep and other dimensional parameters of interest for these configurations. That compilation is tabulated in [13]. Note that all the tabulated values are from public domain information sources. The data and information were gathered from the beginning of 2020 to mid 2022. Some of the designs were still evolving and subject to change, i.e., Exosonic, Boom Overture, etc.

The compiled tables in [13] show various supersonic aircraft configurations along with some information about body shape, wing position, wing size, wing aspect ratio, horizontal and vertical stabilizers, canard, and nacelle from different research organizations, companies, and institutions. There exist a few similar design parameters common for all configurations in general from this table. Most configurations incorporate highly swept low aspect ratio wings, canards, slender bodies, and almost all these designs benefit from vortex lift by using strake or an inboard delta wing shape. The available data for the horizontal stabilizers for these configurations indicate that many of these designs have relatively high sweep mid to low mounted horizontal stabilizers. The vertical stabilizers are however of lower sweep angle in comparison to the horizontal stabilizer one and are of conventional mount type ones. The available information about canard types and locations is very limited, hence one cannot come up with a concrete conclusion about canard types and locations. The configurations are mostly accommodated with two or three nacelles which are either of 2-D or circular shapes. Most of these proposed configurations have been tested either in several wind tunnels, from low speed to high supersonic speeds, or have been analyzed using various CFD codes, and information about their aerodynamic criteria as well as the performance of these vehicles has been obtained. Still, the results for most cases are not available in the public domain.

Table 2.2: Design space survey [13]

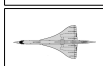
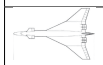
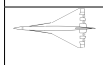
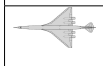
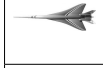
Figure	Aircraft	Body			Wing					Horizontal tail			Vertical tail			Canard			Nacelle	
	Company/ Model/ Class/ Program/ Year	Area–ruled Nose growth Side/Top	Fitness: Fore / Aft	Slenderness: Lifting/ Overall	Planform	Mount/ type	AR	Λ_w (°) IB/OB	Γ_w (°) IB/OB	Mount/ type	Λ_H (°)	Γ_H (°)	Mount/ Type	Λ_V (°)	Γ_V (°)	Mount/ Couple	Λ_C (°)	Γ_C (°)	# Mount	Type
	BAE Concorde Airliner Commercial 1962-2003 [437, 438]	No Conical/ Conical	6.26* 5.43*	1.87* 2.41*	Ogival delta	Mid gull	1.70	75.0 56.0	0.00* −9.00*	N/A	N/A	N/A	Conventional	50.0*	0.00	N/A	N/A	N/A	4 Under-wing Diverter	2D horizontal ramp
	North America Aviation NAC-60 Airliner FAA SST [439]	No Conical / Conical	5.15* 1.54*	1.52* 1.61*	Cranked delta	Low gull		66.8* 48.7*		N/A	N/A	N/A	Conventional	48.6*	0	High close-coupled	29.5*	0*	4 Under-wing Diverter	2D verical ramp
	Lockheed L-2000 Airliner FAA SST [9, 10, 440]	No Conical / Conical	3.92* 4.90*	2.10* 2.35*	Cranked delta	Low*	1.43	82* 62		N/A	N/A	N/A	Conventional		0	N/A	N/A	N/A	4 Under-wing	
	Boeing 2707 Airliner FAA SST [190]	No Conical/ Conical	7.11* 6.48*	1.49* 2.08*	Ogival delta	Low Polyhedral	2.67	75 50		Low	53*	0	Conventional	50*	0	N/A	N/A	N/A	4 Under-wing Diverter	Axis-symmetric
	Tupolev Tu-144 Airliner Commercial 1962-1999 [441–444]	No Conical/ Conical	6.5* 4.67*	1.90* 2.28*	Ogival delta	Low gull	1.66	76 57		N/A	N/A	N/A	Conventional	47.4	0	High anhedraled long-coupled folding	6	−18*	4 Under-wing Diverter	2D horizontal ramp
	Lockheed L–1021 Joint–wing Airliner N+2 [9, 10]	Yes Conical/ Conical	6.00* 2.11*	1.49* 1.82*	Cranked delta	High gull	2.61*	73* 63*	8.00* -23*	Joint-wing	-25*	-30.0*	Conventional	60.0*	0	N/A	N/A	N/A	4 Under-wing Empennage	Axis-symmetric
	Lockheed L–1021 Joint-wing + Airliner N+3 [9, 10]	Yes Conical/ Conical	8.2* 2.1*	2.51* 2.81*	Ogival delta	High gull	2.13*	63*	8.00* -23*	Joint-wing	-25*	-30.0*	Conventional	65.0*	0.00	High dihedral close-coupled	50.0*	25.0*	4 Under-wing	Axis-symmetric
	Lockheed L–1021 V–tail Airliner N+2 [9, 10]	Yes Conical/ Conical	8.80* 5.00*	2.45* 2.74*	Cranked delta	High Anhedral	2.14*	77.0* 65.0*		N/A	N/A	N/A	V-tail	60.6*	36.0*	N/A	N/A	N/A	3 Under-wing Empennage	Axis-symmetric
	Lockheed L–1044 Airliner N+2 [9, 10]	Yes Conical/ Ogive	9.78* 6.00*	2.57* 2.91*	Ogival delta	High	1.95	77.0* 67.0*	6.00* 0.00*	N/A	N/A	N/A	V-tail	60.3*	45.0*	N/A	N/A	N/A	3 Under-wing Empennage	Axis-symmetric
	Lockheed QSTA Airliner [9, 10, 445]	Yes Conical/ Ogive	9.3* 8.2*	2.67* 3.08*	Ogival delta	Mid Polyhedral	1.78*	76.9* 65.4*	9* 0*	N/A	N/A	N/A	V-tail	60.0*	45*	N/A	N/A	N/A	2 Empennage	Circular STEX
	Lockheed X-59 QueSST NASA X-plane 2016–present [435, 436, 446]	Yes Conical/ Parabolic	12.7* 4.44*	2.98* 3.38*	Ogival delta	Mid gull	1.41	76.0 68.6		Low T-strake	63	0*	Conventional	59.0	0	Mid Dihedraled close-coupled	63.0		1 Empennage	Circular STEX

Table 2.3: Design space survey [13]

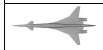
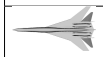
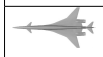
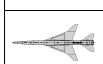
Figure	Aircraft	Body			Wing					Horizontal tail			Vertical tail			Canard			Nacelle	
	Company/ Model/ Class/ Program/ Year	Area–ruled Nose growth Side/Top	Fitness: Fore / Aft	Slenderness: Lifting/ Overall	Planform	Mount/ type	AR	Λ_w (°) IB/OB	Γ_w (°) IB/OB	Mount/ type	Λ_H (°)	Γ_H (°)	Mount/ Type	Λ_V (°)	Γ_V (°)	Mount/ Couple	Λ_C (°)	Γ_C (°)	# Mount	Type
	Boeing 765–070A Airliner N+2 [6, 8]	Yes Conical/ Ogive	6.22* 6.4*	1.65* 2.19*	Cranked delta	Low gull	3.43	78*/68* 40*		Low	54.2	0	Conven- tional	52.6	0	Long- coupled	54.2	0	2 Under-wing Diverter	Circular
	Boeing 765–071B Airliner N+2 [6, 8]	Yes Conical/ Ogive	6.69* 0.0*	1.66* 1.86*	Cranked delta	Low gull	3.43	78*/68* 40*		N/A	N/A	N/A	Conven- tional twin	45.5	14	Mid Long- coupled Dihedraled	48.0	0	2 Under-wing aft-deck Diverter	3D STEX
	Boeing 765–072B Airliner N+2 [6, 8]	Yes Conical/ Ogive	8.00* 5.14*	1.74* 2.04*	Cranked delta	Low gull	2.60	68.0 40.0		N/A	N/A	N/A	Conven- tional	39.4	0	Mid Long- coupled	40.0	0	2 Under-wing Diverter	2D horizontal ramp
	Boeing 765–076E Airliner N+2 [6, 8]	Yes Conical/ Ogive	6.29* 0.0*	1.65* 1.79*	Crescent	Low gull	2.94	72.0 50.0*		N/A	N/A	N/A	V-tail	48.0	45.0	N/A	N/A	N/A	2 Above-wing aft-deck	3D external compression
	Boeing 765–078A Airliner N+2 [6, 8]	Yes Conical/ Ogive	7.00* 5.85*	1.83* 2.09*	Cranked delta	Low gull	3.00	78.0 44.0	12 -4*	Low-mid	48.0	0	Conven- tional	58.0	0	Mid Long- coupled Dihedraled	48.0	10	2 Under-wing aft-deck	2D horizontal ramp
	Boeing QEVC Airliner N+2 [273]	Yes Conical/ Conical	9.6* 0.0*	2.09* 2.35*	Crescent	Low gull	2.86	80.0/71.0 52.0		N/A	N/A	N/A	V-tail	43.31*	45	N/A	N/A	N/A	2 Above-wing aft-deck	ECRI STEX
	Boeing Icon II Airliner N+3 [6, 8]	Yes Conical/ Ogive	9.75* 0.0*	1.75* 2.37*	Crescent	Low gull	2.90	72.0 52.0	12 0*/-4*	N/A	N/A	N/A	V-tail	38.14	45	Low Anhedraled Long- coupled	58.0	-20	2 Above-wing aft-deck	ECRI STEX
	JAXA V-tail Airliner 1997-2005 NEXST-1 [2]	Yes Ogive/ Conical	5.78* 7.63*	1.67* 1.98*	Cranked delta	Low dihedral	3.0	62.0* 51.0*		N/A	N/A	N/A	V-tail	55.0*	45.0*	N/A	N/A	N/A	2 Rear-fuselage	Semi- circular
	JAXA D-Send Demonstrator 2010-2015 S3CM [344, 447]	Yes Ogive/ Ogive	6.64* 5.50*	1.80* 2.25*	Crescent	Mid polyhedral	2.52*	68.0* 45.0*		Mid	55.0*	0	Conven- tional	55.0*	0	N/A	N/A	N/A	1 Rear-fuselage	N/A
	JAXA Mid-tail Airliner 2016- present S4 [421]	Yes Ogive/ Conical	7.15* 11.0*	1.73* 2.03*	Crescent	Low polyhedral	3.0	70.0* 57.0*		Mid-tail low strake	55.0*	0	Conven- tional	70.0*	0	Mid close- coupled	60.0*	0*	2 Rear-fuselage	Semi- circular

Table 2.4: Design space survey [13]

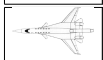
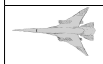
Figure	Aircraft	Body			Wing					Horizontal tail			Vertical tail			Canard			Nacelle	
	Company/ Model/ Class/ Program/ Year	Area–ruled Nose growth Side/Top	Fitness: Fore / Aft	Slenderness: Lifting/ Overall	Planform	Mount/ type	AR	Λ_w (°) IB/OB	Γ_w (°) IB/OB	Mount/ type	Λ_H (°)	Γ_H (°)	Mount/ Type	Λ_V (°)	Γ_V (°)	Mount/ Couple	Λ_C (°)	Γ_C (°)	# Mount	Type
	Sukhoi–Gulfstream S-21 SSBJ [427, 448]	Yes Ogive/ Conical	5.29* 6.07*	1.57* 1.90	Cranked delta	Low		68.0* 32.0*	0.0* 0.0*	Low	55.0*	0 0	Conventional		0	Low close-coupled	32.0 / 68.0	0 0	3 Under-wing Empennage	2D vertical ramp
	Gulfstream Quiet Spike SSBJ 1989-1991 [426]	Yes Conical/ Conical	11.17* 0*	1.55*/3.20* 1.86*/3.43*	Variable sweep	Mid Dihedral	7.43*/ 2.19*	68.0 68.0*/32.0*	6 6	T-tail	60.0*	0	Conventional	60.0*	0	N/A	N/A	N/A	2 Above-wing Empennage	Circular
	Gulfstream QSJ Low boom SSBJ [425]	Yes Ogive/ Ogive	5.33* 6.56*	2.11* 2.38*	Cranked delta	Low dihedral	1.80	75.0* 70.0*		T-tail	55.0*		Conventional		0	N/A	N/A	N/A	2 Above-wing Empennage	Circular
	Dassault HISAC–A: Low noise SSBJ 2005/05–2009/10 HISAC [297]	No Ogive/ Conical	5.31* 3.83*	1.64* 1.99*	Ogival delta	Mid	2.28	72.5 52.0	0 0	N/A	N/A	N/A	Conventional	57.0*	0	Mid close-coupled	45.0*	0	3 Under-wing Empennage	2D horizontal ramp
	Dassault HISAC–B1: Long range SSBJ 2005/05–2009/10 HISAC [297]	No Conical/ Ogive	9.14* 4.75*	1.32* 1.73	Trapezoid	Low	3.93	18	1.5	N/A	N/A	N/A	V-Tail	16.05*	37.69*	N/A	N/A	N/A	2 Mid-rear fuselage	2D Bifurcated Vertical Ramp
	ADSE HISAC–B2: Variable Geometry SSBJ 2005/05–2009/10 HISAC [297]	No Ogive/ Ogive	6.43* 4.67*	1.39*/2.05* 1.98/2.65	Variable sweep	Mid	5.66*/ 3.16*	70 35/60	0 0	Mid	45.0*		Conventional	58.0	0	N/A	N/A	N/A	2 Under-wing	Circular
	Sukhoi, TsAGI, CIAM HISAC–C: Low boom SSBJ 2005/05–2009/10 HISAC [297]	No Ogive/ Ogive	7.11* 6.00*	1.78* 2.14	Cranked delta	Mid Polyhedral	2.62*	79, 72.5 46	18.0 0	Low	50.0*		Conventional	50.0*	0	N/A	N/A	N/A	2 Empennage	2D horizontal ramp
	Dassault Additional–I: High Subsonic SSBJ 2005/05–2009/10 HISAC [297]	No Ogivel/ Conical	3.60* 2.88*	1.32* 1.59*	Ogival delta	Mid	4.17	65.0 40.0	0 0	N/A	N/A	N/A	Conventional	57.0*	0	Mid close-coupled	46.0*	0	3 Under-wing Empennage	2D horizontal ramp
	ADSE Additional–II: Low supersonic SSBJ 2005/05–2009/10 HISAC [297]	No Conical/ Ogive	7.77* 5.04*	1.49* 2.05	Crescent	Low	5.00	65.0 45.0	0 0	Mid	45.0*	0	Conventional	57.0*	0	N/A	N/A	N/A	3 Mid-rear fuselage	Circular

Table 2.5: Design space survey [13]

Figure	Aircraft	Body			Wing					Horizontal tail			Vertical tail			Canard			Nacelle	
	Company/ Model/ Class/ Program/ Year	Area–ruled Nose growth Side/Top	Fitness: Fore / Aft	Slenderness: Lifting/ Overall	Planform	Mount/ type	AR	Λ_w (°) IB/OB	Γ_w (°) IB/OB	Mount/ type	Λ_H (°)	Γ_H (°)	Mount/ Type	Λ_V (°)	Γ_V (°)	Mount/ Couple	Λ_C (°)	Γ_C (°)	# Mount	Type
	Aerion SBJ (AS-1) SSBJ 2004-2014 Startup [422]	Yes Conical/ Conical	7.67* 14.67*	1.67* 2.31	Trapezoid	Low	3.43	79.08, -75.0* 20.0*, 71.0*	0* 0*	Low dihedral	25.0		Conven-tional	31.0	0	N/A	N/A	N/A	2 Mid-rear fuselage	Ovoid
	Aerion AS-2 SSBJ 2014-2017 Startup [423]	Yes Conical/ Parabolic	7.90* 4.70*	1.52* 2.21*	Trapezoid	High	3.92	19.0*	0*	T-tail	21.0	0*	Conven-tional	36.0*	0*	N/A	N/A	N/A	3 Under-wing Empennage	Ovoid
	Aerion AS-3 SSBJ 2017-2020 Startup [424]	Yes Ogive/ Ogive	5.85* 5.18*	1.39* 1.69*	Ogive delta	Mid	3.00*	70.0* 53.0*		Mid	47.0*.0	0*	Conven-tional		0	N/A	N/A	N/A	3 Under-wing Empennage	Axis-symmetric
	Spike S-512 SSBJ 2014-present Startup [428]	No Conical/ Conical	5.18* 3.51*	1.91* 2.10*	Cranked delta	Low	2.01*	66.0* N/A		N/A	N/A	N/A	Conven-tional	50.0*	0	N/A	N/A	N/A	2 Rear-fuselage	Circular
	Boom Overture Airliner 2014-present Startup [429]	No Conical/ Ogive	5.00* 4.82*	1.92* 2.41*	ogival delta	Low	1.59*	80* 60*		N/A	N/A	N/A	Conven-tional	60*	0*	N/A	N/A	N/A	3 Under-wing	2D horizontal ramp
	Boom XB-1 Demonstrator 2014-Present Startup [429]	No Conical/ Ogive		1.92*	ogival delta	Mid				Low		N/A	Conven-tional		0	N/A	N/A	N/A	3 Under-wing Empennage	2D horizontal ramp
	Exosonic N/A SSBJ 2019-present Startup/Airforce [430]	No Conical/ Ogive	7.20* 2.20*	1.21* 1.54*	Crescent	High Polyhedral	3.89*	60* 50*		N/A	N/A	N/A	V-tail			N/A	N/A	N/A	2 Under-wing	STEX
	HyperMach SonicStar SSBJ 2011-present Startup [431]	No Conical/ Parabolic	8.30* 9.10*	2.66* 2.92*	Crescent	Mid	2.52	78.0* 59.0*		N/A	N/A	N/A	V-tail	65.0*		Long-coupled			2 Above-wing aft-deck	3D STEX
	Tupolev Tu-444 SSBJ [432]	Yes Conical/ Ogive	4.78* 9.11*	1.58* 2.22*	Cranked delta	Mid anhedral	1.93	75.0* 40.0*		N/A	N/A	N/A	Conven-tional	50.0*		N/A	N/A	N/A	2 Under-wing aft-deck	2D bifurcated vertical ramp
	Cranfield University E-5 SSBJ 2005 Research [414, 433]	No Conical/ Conical	4.26* 3.41*	2.22* 2.84*	Cranked delta	Low	1.58*	75.0* 60.0*	0.0* 0.0*	N/A	N/A	N/A	Conven-tional	47.0*		Mid dihedral close-coupled	57.0	15.0*	1 Empennage	

2.2.2 University of Washington Models

As mentioned in the introduction, using supersonic cruise aircraft technical challenges as a "platform" for studying aircraft design at the University of Washington goes back to more than 15 years. Various models with different configurations have been designed, manufactured, and tested in the subsonic wind tunnel. For a few configurations, large instrumented RC models (RUAV's) of proposed configurations were built and flown too (Fig. 2.3).

A lot of the information regarding dimensions, test data, analysis, etc. for these models is in the public domain. Hence various organizations can use these data sets to calibrate their CFD codes, compare the performance of the SCALOS with their proposed models, etc. Figure 2.24 shows the polar chart of the University of Washington supersonic transport vehicle development from 2005 till 2021. Various parts of the proposed models have been re-designed, tested and data for each variation is recorded and analyzed. Hence a rich set of accurate experimental data for these models is available[1].

In [13] detailed information and dimensions of various parts of each model such as body, wing, horizontal and vertical stabilizers, canard, and nacelle types are given. For all configurations presented, low speed wind tunnel data for various angles of attack, sideslip angles, configuration changes, high lift devices, etc. are available. Further tests and analysis along with configuration changes and the effect of each change on the performance criterion of the SCALOS model were conducted through the NASA CST SCALOS contract. Various SCALOS configurations tested in the Kirsten Wind Tunnel (KWT) at the University of Washington — aft-body configurations, wing shapes (with different inboard and outboard sweeps), canards, horizontal and vertical stabilizers, fins, and nacelles — were tested in the subsonic regime at various dynamic pressure/Reynolds number combinations, and for ranges of angles of attack and side slip angles. Tests for three different types of horizontal tail mounting (T-tail, mid-tail and conventional "low" tail) were performed. The components were added incrementally during tests (model build-up) to represent full configurations and variants of the post-2014 "baseline" models. Combinations of components tested have provided comparative data on tailless, aft-tail, canard, and 3-surface general arrangements,

[1]Pre-SCALOS data is available only in the form of UW capstone design reports and KWT test results.

effects of horizontal tail planform and low, mid, and T-tail mounting locations. Two different under-wing nacelle configurations and an over-wing nacelle installation have been tested. Three different outboard wing sweep angle/aspect ratio combinations have been tested, with representative LE and TE flaps. Three configuration variants with potential for reduced sonic boom have been tested, including one with an alternate "ogee" planform offering a continuously curved leading edge.

Pre-SCALOS component build-up to the low-boom concepts has provided data on the incremental subsonic effects of forebody slenderness (fineness) ratio and small "aft-deck" planform extensions (for shielding the local shockwaves and expansions produced by the engine nozzles and jet plume flows, similar to X-59's nozzle arrangement). For selected planforms, multiple leading edge and trailing edge device components have been tested to provide incremental comparisons of several leading and trailing edge flap shape options, at various deflection angles. Preliminary results from 2020–2021 SCALOS tests in KWT have been described in [4, 14, 18, 23, 26, 371] and updated with final corrected data in this dissertation.

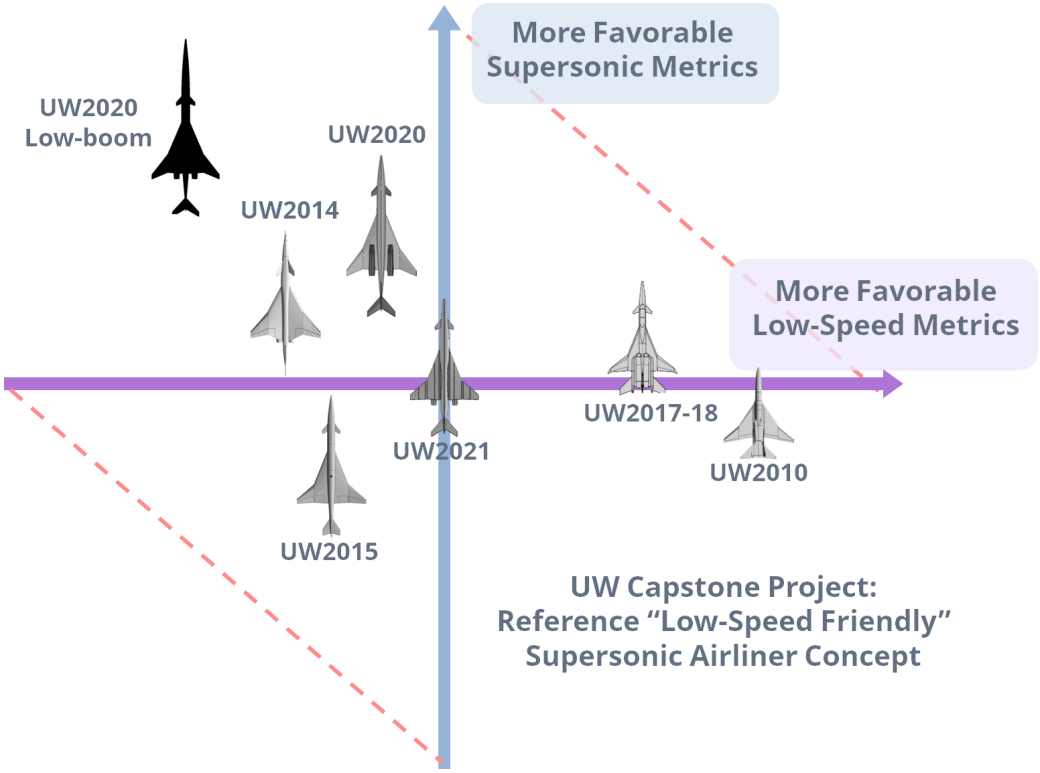


Figure 2.24: UW supersonic configurations polar chart

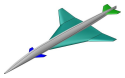
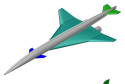
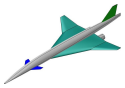
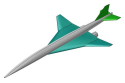
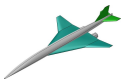
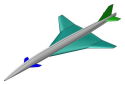
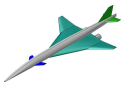
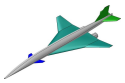
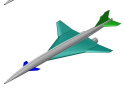
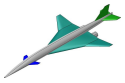
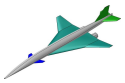
Table 2.6: UW low-speed wind tunnel models

Figure	Aircraft	Body			Wing					Horizontal tail			Vertical tail			Canard			Nacelle	
	Company/ Model/ Class/ Program/ Year	Area–ruled Nose growth Side/Top	Fitness: Fore / Aft	Slenderness: Lifting/ Overall	Planform	Mount/ type	AR	Λ_w (°) IB/OB	Γ_w (°) IB/OB	Mount/ type	Λ_H (°)	Γ_H (°)	Mount/ Type	Λ_V (°)	Γ_V (°)	Mount/ Couple	Λ_C (°)	Γ_C (°)	# Mount	Type
	UW UW-2005 SSBJ Capstone 2005 [379]	no Conical/ Parabolic	4.91 0	1.18 1.43	Cranked-delta	High none	3.25	69 40	0 0	Low	30	0	Conventional twin	45		close-coupled	33	0	2 Rear-fuselage	2D horizontal ramp
	UW UW-2006 SSBJ Capstone 2006 [379]	no Conical/ Parabolic	7.63 0	1.85 1.94	Cranked-delta	Low none	2.35	73 45	0 0	Low	41	0	Conventional	48	0	mid-coupled	60	0	1 empennage	2D horizontal ramp
	UW UW-S-2009A SSQR low-noise Capstone 2009 [379]	no Ogive/ Parabolic	4.76 1.33	1.19 1.42	Cranked-delta	Low dihedral	2.98	65 45		N/A	N/A	N/A	V-tail	56		N/A	N/A	N/A	2 empennage	2D bifurcated ramp
	UW UW-2010 NSRA noise-shield Capstone 2010 [379]	no Ogive/ Ogive	5.21 1.89	1.00 1.30	Cranked-delta	Low none	3.77	58 42		Low	47	0	Conventional twin	40		N/A	N/A	N/A	2 Empennage	Semi-circular
	UW UW-2014 USAF tailless Capstone 2014 [380]	no Conical/ Ogive	5.91 4.83	1.57 1.91	Cranked-delta	Low polyhedral	2.48	62 50		N/A	N/A	N/A	N/A	N/A	N/A	High dihedral close-coupled	62.4	30	2 Under-wing	2D horizontal ramp
	UW UW-S-2015A N+2/SSBJ Capstone 2015 [4, 14, 23]	no Conical/ Ogive	7.02 6.14	1.56 2.03	Cranked-delta	Low polyhedral	2.63	68 40.8	-4 4	Low	50	0	Conventional	53.1	0	Mid close-mid coupled	50	0	2 Under-wing	2D horizontal ramp
	UW UW-2016 SSBJ Capstone 2016 [4, 14, 18, 23, 26, 371]	no Ogive/ Ogive	7.02 0	1.83 1.92	Cranked-delta	Low polyhedral	2.63	68 40.8	-4 4	Low	50	0	Conventional	53.1	0	Mid close-mid coupled	50	0	2 On-fuselage	Body-mount D-inlet

Table 2.7: UW low-speed wind tunnel models

Figure	Aircraft	Body			Wing					Horizontal tail			Vertical tail			Canard			Nacelle	
	Company/ Model/ Class/ Program/ Year	Area–ruled Nose growth Side/Top	Fitness: Fore / Aft	Slenderness: Lifting/ Overall	Planform	Mount/ type	AR	Λ_w (°) IB/OB	Γ_w (°) IB/OB	Mount/ type	Λ_H (°)	Γ_H (°)	Mount/ Type	Λ_V (°)	Γ_V (°)	Mount/ Couple	Λ_C (°)	Γ_C (°)	# Mount	Type
	UW UW-2017/18 NASA X-plane Capstone 2017-2018 [4, 14, 23]	no Ogive/ Ogive	6.38 0	1.46 1.80	Cranked-delta	Low polyhedral	3.49	68 38	-4	Low	45	0	Conventional	49	0	Mid close-coupled	47.6	0	2 On-fuselage	Body-mount D-inlet
	UW UW-S-20A SSBJ Capstone 2020 SCALOS-I [4, 14, 23]	no Conical/ Ogive	7.02 6.14	1.74 2.23	Cranked-delta	Low polyhedral	2.40	68 53.5	-4 5	T-tail	49	0	Conventional	53.1	0	Mid close-mid coupled	50	0	2 Above-wing	2D horizontal ramp
	UW UW-S-20CL SSBJ Capstone 2020 SCALOS-I [4, 14, 23]	no Conical/ Ogive	10.72 6.14	2.24 2.68	Cranked-delta	Low polyhedral	2.40	68 53.5	-4 5	T-tail	49	0	Conventional	53.1	0	Mid Mid-coupled	50	0	2 Above-wing	2D horizontal ramp
	UW UW-S-21A SSBJ Capstone 2021 SCALOS-II [4, 14, 18, 23, 26, 371]	Yes Conical/ Ogive	7.02 6.14	1.56 2.03	Cranked-delta	Low polyhedral	2.63	68 40.8	-4 4	Low	50	0	Conventional	53.1	0	Mid close-mid coupled	50	0	2 Under-wing	2D horizontal ramp

Table 2.8: 2015 (UW2128) configuration build-up and variants

Figure	Designation	Forebody	Aft-body	Wing	Aft-deck	Nacelle	Vertical tail	Horizontal tail	Canard	Additional
				W15						
		F15	A15	W15						
		F15	A15	W15				H15		
		F15	A15	W15				H15	C15.M	
		F15	A15	W15.2		N15	V15			
		F15	A15	W15		N15		H15	C15.M	
		F15	A15	W15		N15	V15	H15A		
		F15	A15	W15.2		N15	V15		C15.F	
		F15	A15	W15.2		N15	V15	H15A		
		F15U	A15	W15		N15	V15	H15A		
		F15D	A15	W15		N15	V15	H15A		
		F15	A15	W15			V15	H15	C15.M	
		F15	A15	W15			V15	H15	C15.F	
	UW-S-15A	F15	A15	W15		N15	V15	H15	C15.M	
	UW-S-15B	F15	A15	W15		N15	V15	H15A	C15.M	
	UW-S-15C	F15	A15	W15		N15	V15	H15A	C15.F	
	UW-S-15D	F15	A15	W15		N15	V15	H15A	C15F.2	
	UW-S-15F	F15	A15	W15		N15	V15	H15A	C15M.2	

Continued on next page

Table 2.8 – continued from previous page

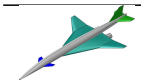
Figure	Designation	Forebody	Aft-body	Wing	Aft-deck	Nacelle	Vertical tail	Horizontal tail	Canard	Additional
	UW-S-15G	F15	A15	W15.2		N15	V15	H15A	C15F.2	

Table 2.9: 2016 (UW2166) configuration build-up and variants

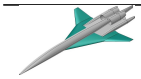
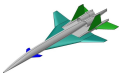
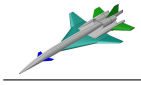
Figure	Designation	Forebody	Aft-body	Wing	Aft-deck	Nacelle	Vertical tail	Horizontal tail	Canard	Additional
		F15	A16	W15	AD16	N16				
		F15	A16	W15	AD16	N16		H16		
		F15	A16	W15	AD16	N16	V16T.2	H16		
		F15	A16	W15	AD16	N16	V16.F	H16		VF16.T
		F15	A16	W15	AD16	N16	V16.A	H16		VF16.T
		F15	A16	W15	AD16	N16	V16.F	H16		VF16T.2
		F15	A16	W15	AD16	N16	V16F.1	H16		VF16T.2
		F15	A16	W15	AD16	N16	V16T.2	H16		VF16.T
		F15	A16	W15	AD16	N16	V16T.3	H16		VF16.T
		F15	A16	W15	AD16	N16	V16T.3	H16	C15.F	VF16.T
		F15	A16	W15	AD16	N16	V16T.3	H16	C15.M	VF16.T
		F15	A16	W15	AD16	N16	V16T.3	H16	C15F.2	VF16.T
		F15	A16	W15	AD16	N16	V16T.3	H16	C15M.2	VF16.T
		F15	A16	W15	AD16	N16	V16F.1	H16	C15.F	VF16T.2

Table 2.10: 2017 (UW2200) configuration build-up and variants

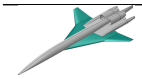
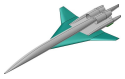
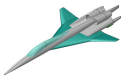
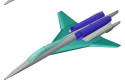
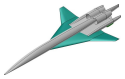
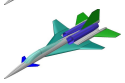
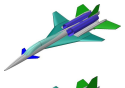
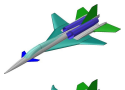
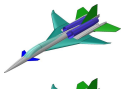
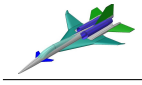
Figure	Designation	Forebody	Aft-body	Wing	Aft-deck	Nacelle	Vertical tail	Horizontal tail	Canard	Additional
		F15	A16	W15	AD16	N16				
		F15	A16	W15	AD16	N16				VF16T.2
		F15	A16	W15	AD16	N16				VF16T.2 +FD17
		F15	A16	W17	AD16	N17.1				VF16T.2 +FD17
		F15	A16	W17 +RT17	AD16	N17.1				VF16T.2 +FD17
		F15	A16	W15	AD16	N16	V16.F	H16	C15.F	VF16T.2
		F15	A16	W17 +RT17	AD16	N17.1	V17F.1	H17	C17.F	FD17
		F15	A16	W15	AD16	N16	V16.F	H16	C15.F	VF16T.2 +FD17
		F15	A16	W15	AD16	N16	V16.F	H16	C17.F	VF16T.2 +FD17
		F15	A16	W15	AD16	N16	V16.F	H17	C17.F	VF16T.2 +FD17
		F15	A16	W15	AD16	N17	V16.F	H17	C17.F	VF16T.2 +FD17
		F15	A16	W15	AD16	N17	V17.F	H17	C17.F	VF16T.2 +FD17
		F15	A16	W15	AD16	N17.1	V17.F	H17	C17.F	VF16T.2 +FD17
		F15	A16	W17	AD16	N17.1	V17.F	H17	C17.F	VF16T.2 +FD17
		F15	A16	W17 +RT17	AD16	N17.1	V17.F	H17	C17.F	VF16T.2 +FD17
		F15	A16	W17 +RT17	AD16	N17.1	V17.F	H17	C17F.D	VF16T.2 +FD17
		F15	A16	W17 +RT17	AD16	N17.1	V17F.1	H17	C17.F	VF16T.2 +FD17

Table 2.11: 2018 (UW2237) configuration build-up and variants

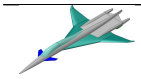
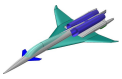
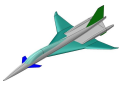
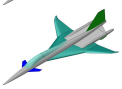
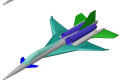
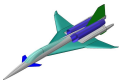
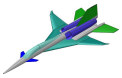
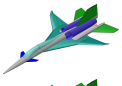
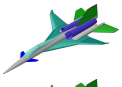
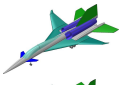
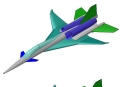
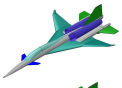
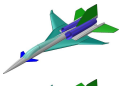
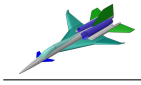
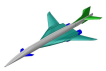
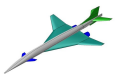
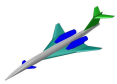
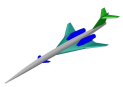
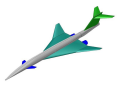
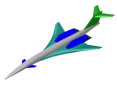
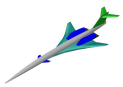
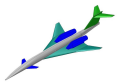
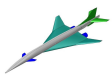
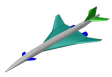
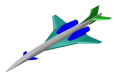
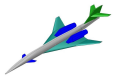
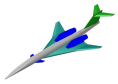
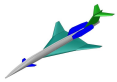
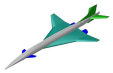
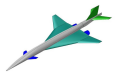
Figure	Designation	Forebody	Aft-body	Wing	Aft-deck	Nacelle	Vertical tail	Horizontal tail	Canard	Additional
		F15	A16	W17 +RT17	AD16					VF16T.2 +FD17
		F15	A16	W17 +RT17	AD16	N18				VF16T.2 +FD17
		F15	A16	W17 +RT17	AD16		V17.F			VF16T.2 +FD17
		F15	A16	W17 +RT17	AD16		V18.F			VF16T.2 +FD17
		F15	A16	W17 +RT17	AD16	N18	V17.F			VF16T.2 +FD17
		F15	A16	W17 +RT17	AD16	N18	V18.F			VF16T.2 +FD17
		F15	A16	W17 +RT17	AD16	N18	V18F.2	H17	C17.F	FD17
		F15	A16	W17 +RT18	AD16	N18	V18F.2	H17	C17.F	FD17
		F15	A16	W18	AD16	N18	V18F.2	H17	C17.F	FD17
		F15	A16	W18	AD16	N18	V18F.2	H17	C17.F	FD17 +LG18
		F15	A16	W17 +RT17	AD16	N18	V17.F	H17	C17.F	VF16T.2 +FD17
		F15	A16	W17 +RT17	AD16	N18	V17.F	H18	C17.F	VF16T.2 +FD17
		F15	A16	W18	AD16	N18	V18.F	H17	C17.F	VF16T.2 +FD17
		F15	A16	W18	AD16	N18	V18.F	H18	C17.F	VF16T.2 +FD17
		F15	A16	W18	AD16	N18	V18F.1	H17	C17.F	VF16T.2 +FD17
		F15	A16	W18	AD16	N18	V18F.2	H17	C17.F	VF16T.2 +FD17
		F15	A16	W18 +RT18	AD16	N18	V18F.2	H17	C17.F	VF16T.2 +FD17

Table 2.12: SCALOS table of model configuration variations tested (2020-24)

Figure	Designation	Forebody	Aft-body	Wing	Aft-deck	Nacelle	Vertical tail	Horizontal tail	Canard	Additional
	UW-S-13A	F15	A15	W13.5		N20.B	V15	H20.L	C15.F	DF.1 +VF.1
	UW-S-17A	F15	A15	W18		N20.B	V15	H20.L	C15.F	DF.1 +VF.1
	UW-S-20A	F15	A20	W20		N20.T	V20	H20.T	C15.F	
	UW-S-20AL	F15L	A20	W20		N20.T	V20	H20.T	C15.F	
	UW-S-20B	F15	A20	W20		N20.B	V20	H20.T	C15.F	
	UW-S-20C	F15	A20	W20	NSRD	N20.T	V20	H20.T	C15.F	OG +strake
	UW-S-20CL	F15.L	A20	W20	NSRD	N20.T	V20	H20.T	C15.F	OG +strake
	UW-S-20D	F15	A20	W20		N20.T	V20	H20.T	C17.F	
	UW-S-20E	F15	A15	W20		N20.B	V15	H20.L	C15.F	DF.1 +VF.1
	UW-S-20F	F15	A15	W20		N20.B	V15	H20.L	C15.F	
	UW-S-20G	F15	A15	W20		N20.T	V15	H20.L	C15.F	DF.1 +VF.1
	UW-S-20H	F15	A20	W20		N20.T	V20	H20.M	C15.F	
	UW-S-20I	F15	A20	W20		N20.T	V20	H20.T	C15.A	
	UW-S-20J	F15	A20	W20		N20.TR	V20	H20.T	C15.F	
	UW-S-21A	F15	A15	W15		N20.B	V15	H20.L	C15.F	DF.1 +VF.1
	UW-S-21B	F15	A15	W15		N20.B	V15	H20.L	C15.F	

Continued on next page

Table 2.12 – continued from previous page

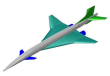
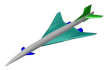
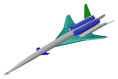
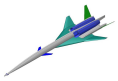
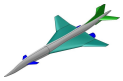
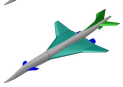
Figure	Designation	Forebody	Aft-body	Wing	Aft-deck	Nacelle	Vertical tail	Horizontal tail	Canard	Additional
	UW-S-21C	F15	A15	W15		N20.B	V15	H20.L	C17.F	DF.1 +VF.1
	UW-S-23A	F23	A23	W23		N20.B	V15	H20.L	C15.F	DF.1 +VF.1
	UW-S-23E	F15.L	A18	W20	AD16	N18	V23		C15.F	OG +strake
	UW-S-23F	F15.L	A18	W20	AD16	N18	V23		C23	OG +strake
	UW-S-23G	F15	A16	W15	AD16	N23.BR	V16T.2	H18	C15.F	
	UW-S-23H	F15	A16	W15	AD16	N23.BA	V16T.2		C15.F	
	UW-S-24A	F24	A24	W15		N20.B	V15	H24.L	C15.F	DF.1 +VF.1
	UW-S-24B	F24	A24	W15		N20.B	V15	H24.L	C15.F	DF.1 +VF.24

Table 2.13: 2017 low-tail configuration build-up and variants

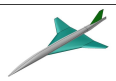
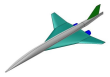
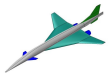
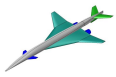
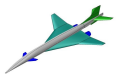
Figure	Designation	Forebody	Aft-body	Wing	Aft-deck	Nacelle	Vertical tail	Horizontal tail	Canard	Additional
		F15	A15	W17			V15			
		F15	A15	W17		N20.B	V15			
		F15	A15	W17		N20.B	V15		C15.F	DF.1 +VF.1
		F15	A15	W17		N20.B		H20.L	C15.F	VF.1
	UW-S-17A	F15	A15	W17		N20.B	V15	H20.L	C15.F	DF.1 +VF.1

Table 2.14: 2020 low-tail configuration build-up and variants

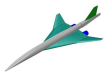
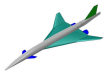
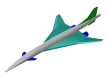
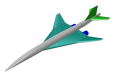
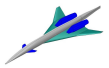
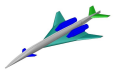
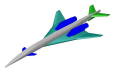
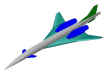
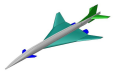
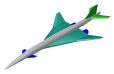
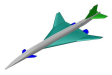
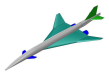
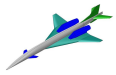
Figure	Designation	Forebody	Aft-body	Wing	Aft-deck	Nacelle	Vertical tail	Horizontal tail	Canard	Additional
		F15	A15	W20			V15			
		F15	A15	W20			V15			DF.1 +VF.1
		F15	A15	W20		N20.B	V15			
		F15	A15	W20		N20.B	V15		C15.F	
		F15	A15	W20		N20.B	V15		C15.F	DF.1 +VF.1
		F15	A15	W20		N20.B	V15	H20.L		
		F15	A15	W20		N20.B			C15.F	
		F15	A15	W20		N20.T		H20.L	C15.F	
		F15	A15	W20		N20.T		H20.L	C15.F	VF.1
		F15	A15	W20		N20.T	V15		C15.F	DF.1 +VF.1
	UW-S-20E	F15	A15	W20		N20.B	V15	H20.L	C15.F	DF.1 +VF.1
	UW-S-20F	F15	A15	W20		N20.B	V15	H20.L	C15.F	
	UW-S-20F-2	F15	A15	W20		N20.B	V15	H15.A	C15.F	
	UW-S-20F-3	F15	A15	W20		N20.B	V15	H15	C15.F	
	UW-S-20G	F15	A15	W20		N20.T	V15	H20.L	C15.F	DF.1 +VF.1
	UW-S-20G-2	F15	A15	W20		N20.T	V15	H20.L	C15.F	DF.1

Table 2.15: 2020 T-tail configuration build-up and variants

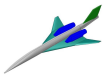
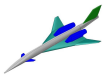
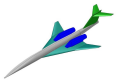
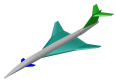
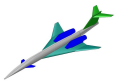
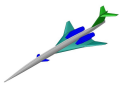
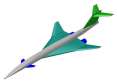
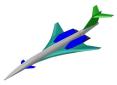
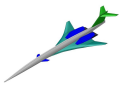
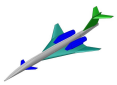
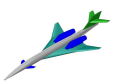
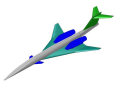
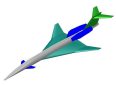
Figure	Designation	Forebody	Aft-body	Wing	Aft-deck	Nacelle	Vertical tail	Horizontal tail	Canard	Additional
		F15	A20	W20		N20.T	V20			
		F15	A20	W20		N20.T	V20		C15.F	
		F15	A15	W20		N20.B	V20	H20.T		
		F15	A20	W20			V20	H20.T	C15.F	
	UW-S-20A	F15	A20	W20		N20.T	V20	H20.T	C15.F	
	UW-S-20AL	F15.L	A20	W20		N20.T	V20	H20.T	C15.F	
	UW-S-20B	F15	A20	W20		N20.B	V20	H20.T	C15.F	
	UW-S-20C	F15	A20	W20	NSRD	N20.T	V20	H20.T	C15.F	OG +strake
	UW-S-20CL	F15.L	A20	W20	NSRD	N20.T	V20	H20.T	C15.F	OG +strake
	UW-S-20D	F15	A20	W20		N20.T	V20	H20.T	C17.F	
	UW-S-20H	F15	A20	W20		N20.T	V20	H20.M	C15.F	
	UW-S-20I	F15	A20	W20		N20.T	V20	H20.T	C15.A	
	UW-S-20J	F15	A20	W20		N20.TR	V20	H20.T	C15.F	

Table 2.16: 2021 low-tail configuration build-up and variants

Figure	Designation	Forebody	Aft-body	Wing	Aft-deck	Nacelle	Vertical tail	Horizontal tail	Canard	Additional
				W15						

Continued on next page

Table 2.16 – continued from previous page

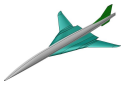
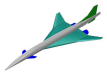
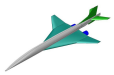
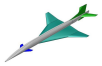
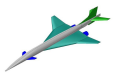
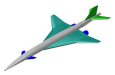
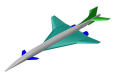
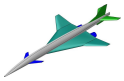
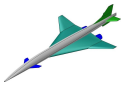
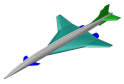
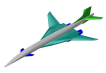
Figure	Designation	Forebody	Aft-body	Wing	Aft-deck	Nacelle	Vertical tail	Horizontal tail	Canard	Additional
		F15	A15	W15						
		F15	A15	W15			V15			DF.1 +VF.1
		F15	A15	W13.5			V15			DF.1 +VF.1
		F15	A15	W15			V15	H15		DF.1 +VF.1
		F15	A15	W15			V15	H15A		DF.1 +VF.1
		F15	A15	W15			V15	H20.L		DF.1 +VF.1
		F15	A15	W15		N20.B	V15		C15.F	DF.1 +VF.1
		F15	A15	W15		N20.B	V15	H20.L		DF.1 +VF.1
		F15	A15	W15			V15	H20.L	C15.F	DF.1 +VF.1
	UW-S-21A	F15	A15	W15		N20.B	V15	H20.L	C15.F	DF.1 +VF.1
	UW-S-21B	F15	A15	W15		N20.B	V15	H20.L	C15.F	
	UW-S-21C	F15	A15	W15		N20.B	V15	H20.L	C17.F	DF.1 +VF.1
	UW-S-21D	F15	A15	W15		N20.B	V15	H20L	C23.F	DF.1 +VF.1
	UW-S-21E	F15	A15	W15		N20.B	V15	H15	C15.F	DF.1 +VF.1
	UW-S-21F	F15	A15	W15		N20.B	V15	H15A	C15.F	DF.1 +VF.1
	UW-S-13A	F15	A15	W13.5		N20.B	V15	H20.L	C15.F	DF.1 +VF.1

Table 2.17: 2023 configuration build-up and variants

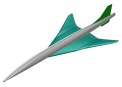
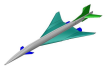
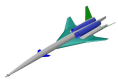
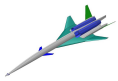
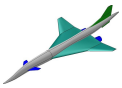
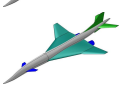
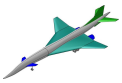
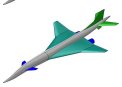
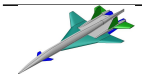
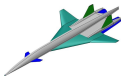
Figure	Designation	Forebody	Aft-body	Wing	Aft-deck	Nacelle	Vertical tail	Horizontal tail	Canard	Additional
				W (IB)						
				W15	AD16					
				W23						
		F15	A15	W23						
		F15	A15	W23			V15			
		F15	A15	W23			V15			DF.1 +VF.1
	UW-S-23A	F15	A15	W23		N20.B	V15	H20.L	C15.F	DF.1 +VF.1
	UW-S-23E	F15.L	A18	W20	AD16	N18	V23		C15.F	NC +OG +strake
	UW-S-23F	F15.L	A18	W20	AD16	N18	V23		C23	NC +OG +strake

Table 2.18: 2024 configuration build-up and variants

Figure	Designation	Forebody	Aft-body	Wing	Aft-deck	Nacelle	Vertical tail	Horizontal tail	Canard	Additional
		F24	A24	W15						
		F24	A24	W15		N20.B	V15		C15.F	DF.1 +VF.1
	UW-S-24A	F24	A24	W15		N20.B	V15	H24.L	C15.F	DF.1 +VF.1
		F24	A24	W15		N20.B	V15	H24.L	C15.F	DF.1 +VF.1 +LG24
	UW-S-24B	F24	A24	W15		N20.B	V15	H24.L	C15.F	DF.1 +VF.24
		F15	A16	W15	AD16		V16T.2		C15.F	

Continued on next page

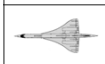
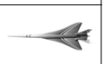
Table 2.18 – continued from previous page

Figure	Designation	Forebody	Aft-body	Wing	Aft-deck	Nacelle	Vertical tail	Horizontal tail	Canard	Additional
	UW-S-23G	F15	A16	W15	AD16	N23.BA	V16T.2	H18	C15.F	
	UW-S-23H	F15	A16	W15	AD16	N23.BA	V16T.2		C15.F	

2.2.3 Comparison and Discussion of Configuration Features

Table 2.19 summarizes Tables 2.2 through 2.7 with icons and designations used throughout the rest of this section. Comparison "icon tables" (Tabs. 2.20, 2.21, 2.22, 2.23, 2.24, 2.25, 2.26) accompany each component discussion. The following subsections compare quantitative geometric parameters of the SCALOS UW configurations with the design-space survey concepts, organized by airframe component, i.e. overall, wing, nacelle, tail, canard.

Table 2.19: Aircraft icons and designations [13]

Concorde	NAC-60	L-2000	B-2707	Tu-144	L-1021J	L-1021J+	L-1021V	L-1044	L-QSTA
									
X-59	**B-765-070A**	**B-765-071B**	**B-765-072B**	**B-765-076E**	**B-765-078A**	**B QEVC**	**B Icon II**	**JAXA V**	**JAXA D-Send**
									
JAXA M	**S-21**	**QuietSpike**	**Gulfstream QSJ**	**HISAC-A**	**HISAC-B1**	**HISAC-B2**	**HISAC-C**	**HISAC-I**	**HISAC-II**
									
AS1	**AS2**	**AS3**	**S-512**	**Overture**	**Boom XB1**	**Exosonic**	**SonicStar**	**Tu-444**	**CU-E5**
									
UW-2005	**UW-2006**	**UW-2009**	**UW-2010**	**UW-2014**	**UW-S-2015A**	**UW-2016**	**UW-2017/18**	**UW-S-2020A**	**UW-S-2021A**
									

Overall

A few key geometric descriptors can be used to help understand the basic geometry trends of the example supersonic configurations presented in the "design space" survey, summarized in Tables 2.2 to 2.5. Supersonic cruise configurations (as opposed to supersonic sprint fighters) typically require higher overall slenderness ("fineness") ratio. The overall slenderness ratio

of the configuration can be expressed as the ratio of the overall length to wingspan. To a first order, efficient supersonic cruise configurations will have highly swept, low aspect ratio (short span) wings and long fuselages. Figure 2.25 shows example overall slenderness trends of configurations examined in the design space survey, compared to the overall slenderness of UW's current and past supersonic conceptual designs tested in the KWT facility. The UW test configurations can be seen to be representative of industry and research configurations from the survey. The slightly less slender UW configurations from 2005, and 2009–2010 focused on applications for smaller (SSBJ-sized) aircraft and included general arrangement features for LTO noise-shielding, rather than supersonic L/D or low-boom. These show overall slenderness ratios closer to those of some commercial SSBJ concepts.

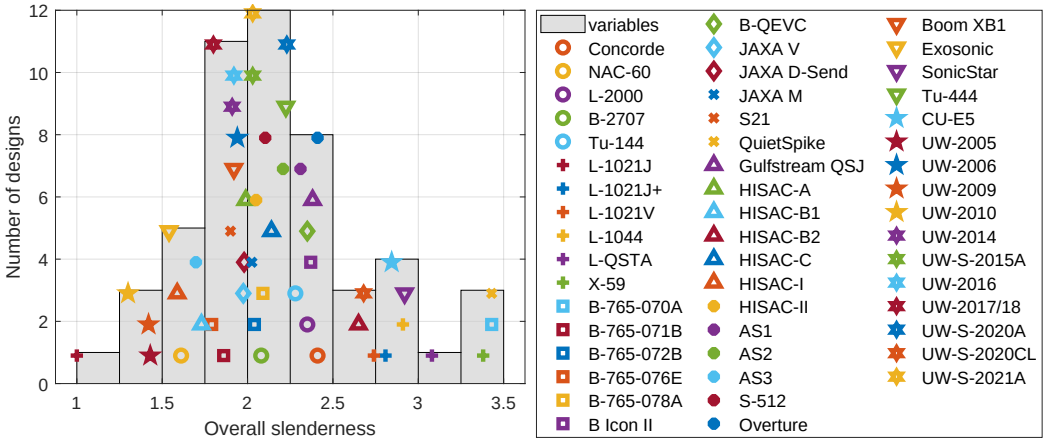


Figure 2.25: Overall slenderness [13]

The slenderness of the primary lift-generating portion of the configuration, typically from the apex of the nose to the rearmost cross-section station of the wing, relates to the steepness of the curve of cumulative lift versus stream-wise distance. The "equivalent area due to lift" is a key contributor to sonic boom [195]. To a first approximation, general arrangements that spread the lift of the configuration (including lift from the forebody ahead of the wing) over a longer streamwise distance have a better potential for sonic boom reduction. Figure 2.26 compares the lifting slenderness of configurations from the design space survey with UW conceptual designs. As with the design survey configurations, the UW concepts intended to represent configurations with increased boom reduction potential

show similar higher "lifting slenderness" ratios.

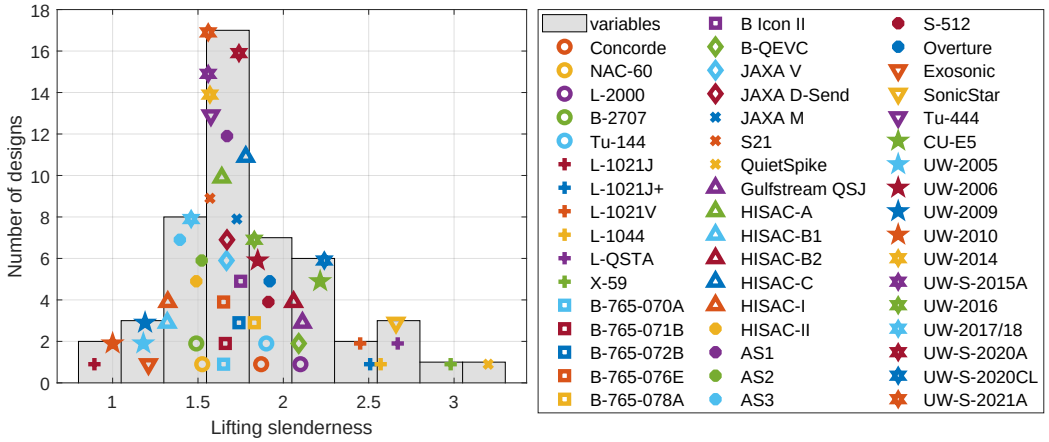


Figure 2.26: Lifting slenderness [13]

For most supersonic configurations, the body reaches maximum cross section near the wing leading edge intersection with the body. Therefore, the slenderness ratio of the fore-body (diameter to length of the body ahead of the wing) can be a rough indicator of the configuration's wave drag due to volume and potential for minimizing the forward sonic boom shock strength. As shown in Fig. 2.27, configurations from the design space survey tend to fall into three zones:

1. smaller aircraft (SSBJ's) whose design trade-offs for wing area, payload and balance would have shown a net weight and drag penalty for longer forebodies;

2. mixed-mission and medium boom configurations, optimized for weight, L/D and fuel consumption;

3. designs specifically biased toward sonic boom minimization, which benefit most from long forebodies.

The configuration concepts studied by UW are shown to have covered roughly the same range of forebody slenderness values.

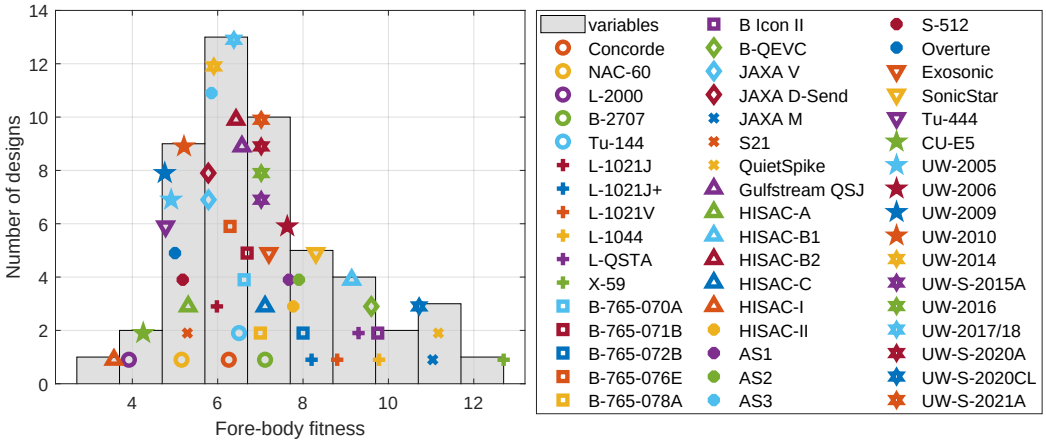
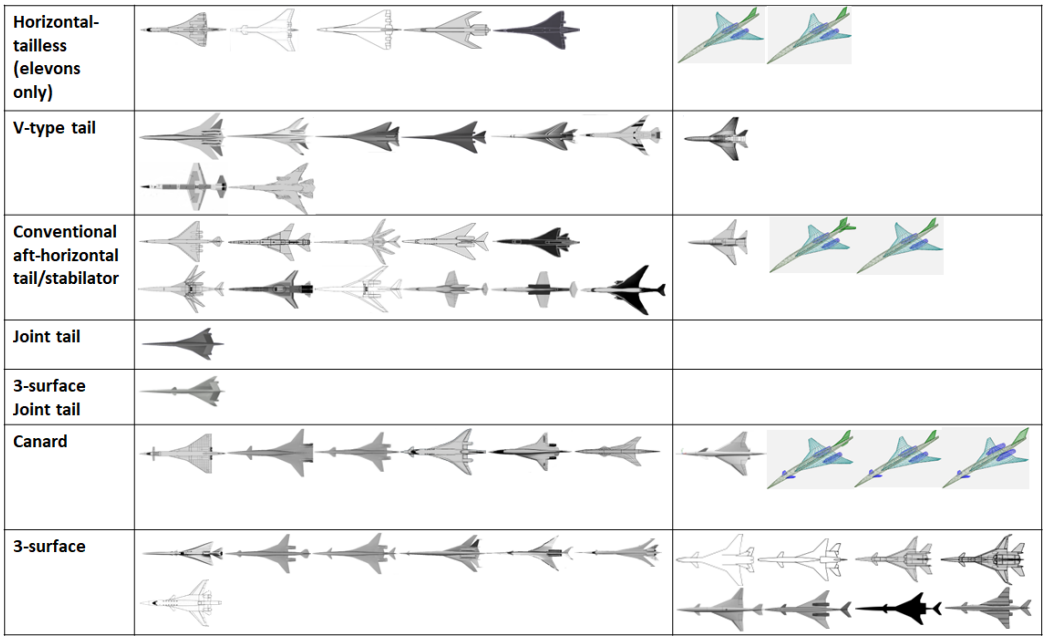


Figure 2.27: Forebody slenderness ratio [13]

Table 2.20: Pitch control arrangement [13]



Wing

Table 2.21 divides design space survey general arrangements into categories based on the wing location (mounting height) on the fuselage. While the terminology is in some cases subjective, nearly all of the configurations, including those investigated by UW, can be categorized as low-wing general arrangements. This is probably due to the fact that spatial

integration of payload, structures, and landing gear can be more problematic for mid-wing configurations and those considerations usually outweigh potential benefits such as reduced mid-body cross-section. The two horizontal-tailless low-boom x-plane concept models tested by UW in 2007 (see Fig. 2.3) were both mid-wing configurations with body-mounted landing gear. Although there can be potential advantages to the high wing option from the structural integration and low-boom shaping viewpoint, that general arrangement seriously constrains landing gear options and can present serious civil certification challenges for crashworthiness, ditching/floatation, emergency egress, and can create servicing challenges for operators.

Table 2.21: Wing mount comparison [13]

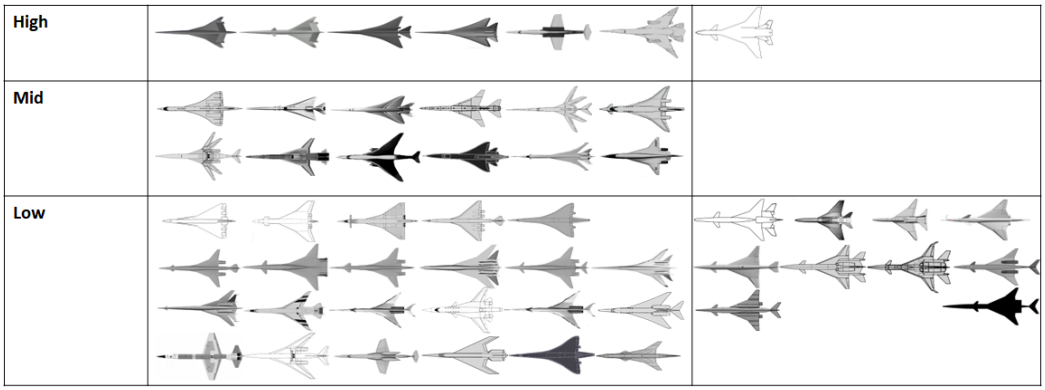
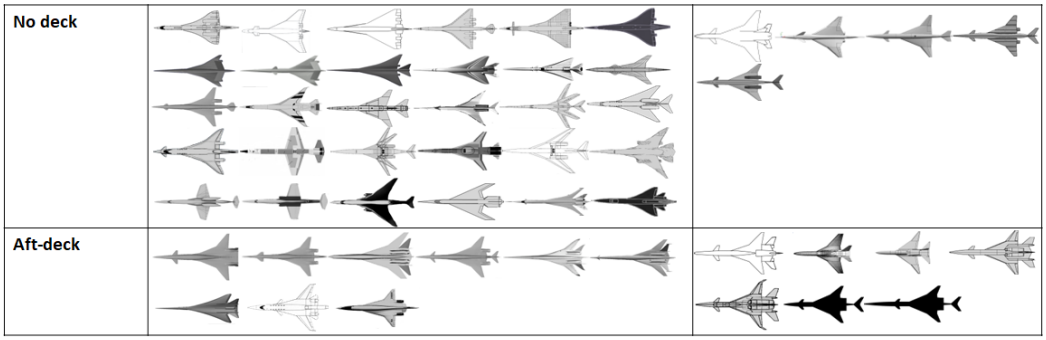


Table 2.22 identifies those configurations which include flattened aft fuselages behind the wing, or inboard wing trailing edge extensions, collectively referred to as “aft-decks”. Small aft-decks can be used as nozzle and jet plume shock shielding on low-boom concepts but have been more commonly used to structurally support nacelles (especially with long heavy suppressor nozzles), increase wing-body aeroelastic stiffness and/or to provide airframe shielding of inlet and nozzle noise sources during landing and takeoff. Aerodynamically, larger aft-decks can improve subsonic pitch stability, functioning as a conjoined horizontal tail. Aft decks can also provide lift at supersonic conditions, potentially extending the aircraft’s lift distribution farther aft which can provide increased options for low sonic boom shaping. Large aft decks also present a significant trade-off in that they can add wetted area drag and weight relative to a conventional aft-body. As indicated by the right hand of Tab. 2.22, UW-tested configurations have included conventional and aft-deck type general

arrangements, with both large aft-decks and nozzle shield decks.

Table 2.22: Wing aft-deck comparison [13]



Figures 2.28 to 2.30 categorize general arrangements by the basic wing geometry properties of aspect ratio, and inboard/outboard leading edge sweep angle. Figure 2.28 shows that virtually all of the configurations of interest fall between 1.7 and 5 in aspect ratio, consistent with supersonic cruise aerodynamic requirements. The lowest aspect ratios below ≈ 2.3 are generally the pre-1990's supersonic transports (SST) designed before LTO noise and subsonic performance considerations were more heavily weighted in design trades. The exceptions to this trend are some of the configurations proposed over the past 10 years that are focused on minimum sonic boom as the key performance metric (e.g., X-59). Figure 2.29 shows inboard wing sweep is on the order of $\approx 70°$ for most of the supersonic cruise designs. Some employ a side of body "strakelet" or small leading-edge extension of $75° \sim 80°$ sweep, but these generally cover only a small percentage of the wing semi-span, the main portion of the inboard wing being in the $65° \sim 70°$ sweep range regardless of whether the design cruise Mach number is 1.2 or 2.5. This trend is likely due to the fact that at low design cruise Mach numbers, distributing the wing's volume lengthwise helps reduce wave drag during transonic acceleration, while for low-boom designs or those intended for Mach 1.8-2.5 cruise speeds, distributing lift lengthwise reduces wave drag-due-to-lift and the "lift-equivalent area" contribution to sonic boom. Both of these factors would favor wings with inboard sweep in the $65° \sim 70°$ range. Most of the configurations tested by UW had similar inboard sweeps in part because of hardware limits on the wing center-body of the modular model used since 2013. Figure 2.30 shows a much larger variation in outboard wing sweeps, a parameter that

relates directly to trade-off in subsonic versus supersonic aerodynamic performance, stability and control characteristics as well as landing and takeoff noise and enroute sonic-boom. The focus of the SCALOS project was on characterizing which configuration features may provide the most favorable subsonic/supersonic compromises for performance and S&C so the majority of UW planforms shown on Fig. 2.30 fall in a somewhat smaller band than that spanned by the design space survey.

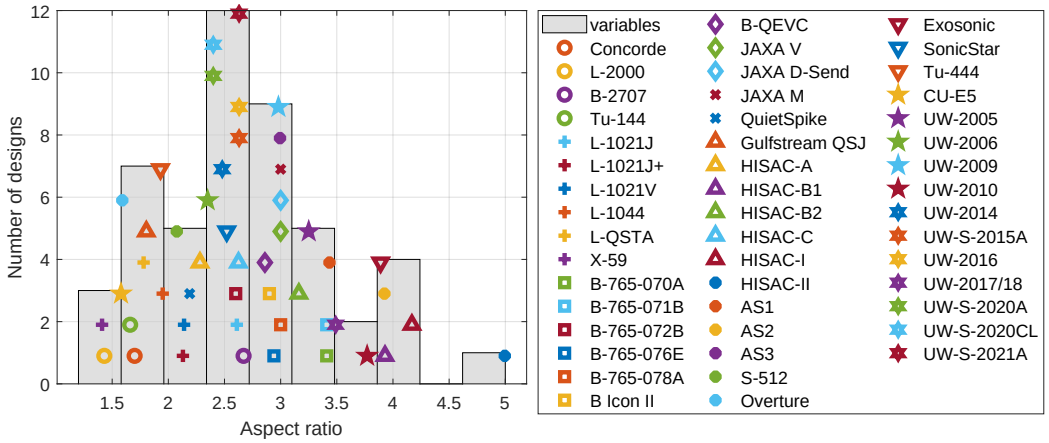


Figure 2.28: Aspect ratio (AR) [13]

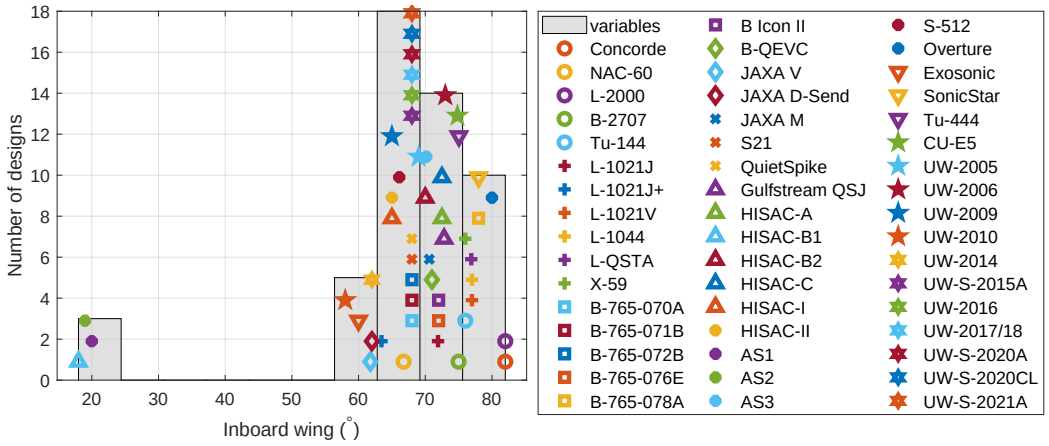


Figure 2.29: Inboard-wing sweep [13]

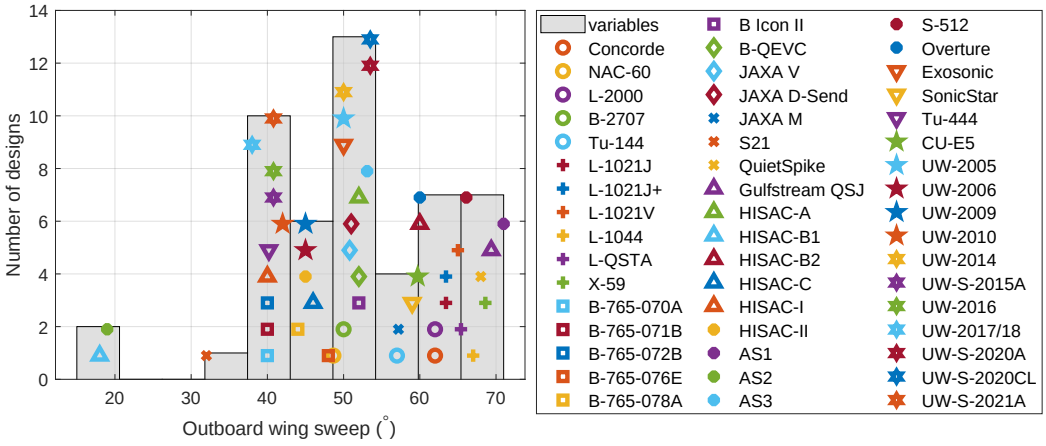


Figure 2.30: Outboard-wing sweep [13]

Nacelle

Table 2.23 attempts to categorize the wide variety of nacelle positions revealed by the design space survey. Many factors enter into the configurator's treatment of the propulsion system and the positioning and detailed orientation of the inlet, engine, and nozzle components. As shown on the right side of the table, the conceptual designs studied by the UW have covered the most common configuration options. The SCALOS effort focused on twin engines with over or under-wing nacelles located near the wing trailing edge, as these seem most promising for the next generation supersonic business jet or airliner. The majority of the nacelle data was gathered with model nacelles representing medium bypass turbofans from the NASA N+2 studies. While some of the variable cycle engines and tri-jet or quad-engine concepts may allow smaller nacelles, it was thought best to collect incremental nacelle subsonic aerodynamic effects using nacelles representing the larger end of the propulsion option spectrum exhibiting the maximum likely incremental effects as shown in Fig. 2.31.

Multiple configurations in the design space survey used side-by-side engine positioning, either "dual-podded" as on B-1 or Concorde, or close-mounted or semi-buried on the aft-body. These options show promise for reducing some structural weight elements, improving inlet flow quality for some flight conditions, improved propulsion noise shielding, and potentially helping to reduce sonic boom. However, current certification requirements for uncontained engine failures generally cannot be met with engines spaced closer than

roughly 1-1.5 maximum engine diameters apart (a rule-of-thumb that typically results from extensive analysis of major engine debris trajectories relative to adjacent engines and airframe components). Various schemes were proposed over the last 20 years, using shaped composite armor between adjacent engines to meaningfully decrease the statistical odds of engine-engine fratricide or catastrophic loss of structural integrity during an engine burst. However, each of these options would come at a considerable nacelle weight penalty and would require expensive comprehensive testing to ensure the civil certification safety requirements can be met. Furthermore, the size and weight of such barriers would go up as engine core or fan size increase, making it even more difficult for medium bypass engines versus turbojets. An exception to the ban on dual-podding nacelles (as on B-1 or Concorde) could be made in the case of a 4-engine airplane, provided that the total installed thrust is enough to continue safe flight assuming any uncontained engine failure or serious fire would disable the other engine in the same nacelle (i.e., the airplane would essentially follow twin-engine aircraft rules for performance certification).

Table 2.23: Nacelle location comparison [13]

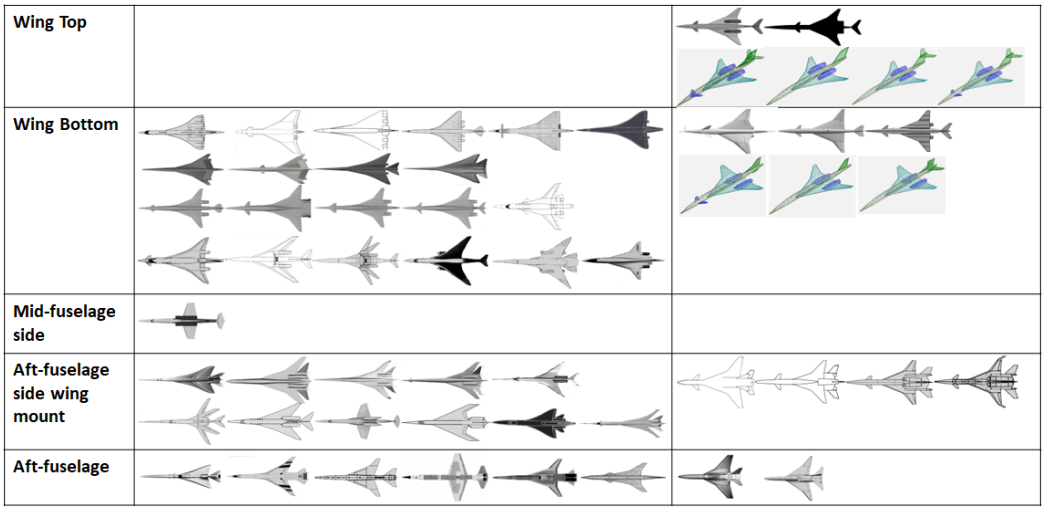


Table 2.24 shows the variety of nacelle/inlet types seen in the design space survey. As discussed in [4], concerns over engine durability cost, high altitude emissions, decompression certification and engine-airframe matching for community noise have pushed design cruise Mach numbers lower since Concorde was retired, and in the sub-Mach 2 regime relatively

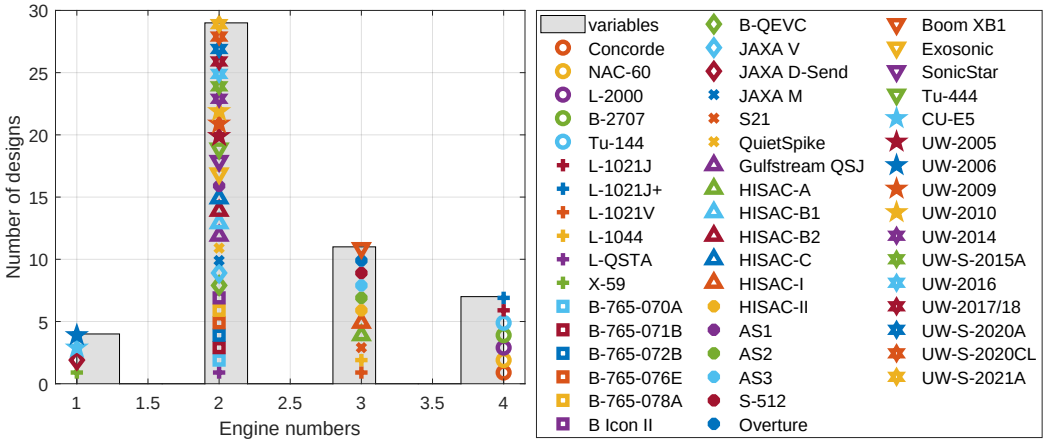
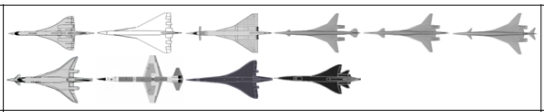
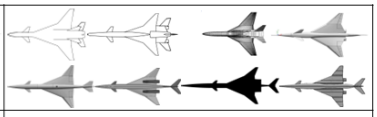
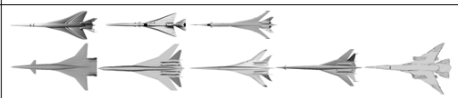


Figure 2.31: Number of engines [13]

simple external compression (EC) inlets can provide high pressure-recovery efficiency. A variety of inlet geometries were used, from traditional circular or rectangular external compression inlets, to fully "3D" STEX concepts and other custom-designed types. The inlet type used for a specific configuration concept is likely based more on off-design considerations of engine airflow schedule and spillage, nacelle weight, aircraft structural and spatial integration, and low sonic-boom considerations rather than absolute maximum supersonic inlet performance. While several inlet types were used on the UW supersonic concepts shown on the right side of the chart, in most cases the details of the inlet per-se are not expected to have a large effect on the airframe subsonic aerodynamic characteristics. For the SCALOS study the issue of inlet choice was more one of facilitating variations in general arrangement.

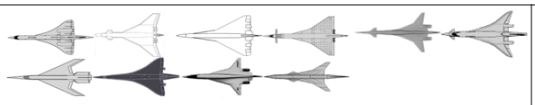
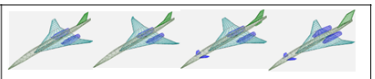
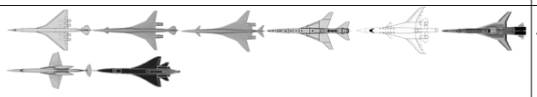
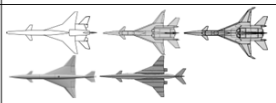
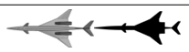
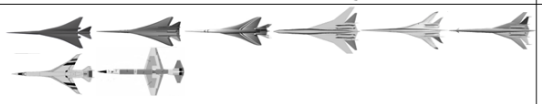
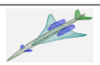
Table 2.24: Inlet/nacelle type comparison [13]

2D horizontal ramp		
Axis-symmetric		
Semi-circular		
Circular		
Elliptic / Ovid		
2D vertical ramp		
STEX (3D/ ECRI / circular)		

Tail

Table 2.25 (left side) shows the variety of tail configurations seen in the design space survey. As shown on the right side, configurations studied by the UW covered a number of these configuration options. Figure 2.32 compares the leading edge sweep angles of the various horizontal and vertical tails. For the configurations with horizontal tails, most tail sweep angles were between $50° \sim 60°$ with a few higher sweep examples attempted on configurations with minimum sonic boom as the leading performance metric. The prevalence of tail sweeps in the $50° \sim 60°$ range is likely due to this being a reasonable compromise between tail loads, aeroelastics, tail control authority, maximum lift, and drag. Horizontal tails on the UW configurations tested fall in roughly the same sweep range. The vertical tail leading edge sweep angles show much wider variability, indicating design choices that have as much to do with geometric constraints, weight trade-offs and integration issues as the straight aerodynamic properties in Fig. 2.33.

Table 2.25: Tail configuration comparison [13]

Vertical Tail Only		
Twin vertical tails only		
Conventional		
Conventional with twin vertical tail		
Mid-tail		
T-tail		
V-tail		
Joint Tail		
Horizontal tail only		
Tailless		

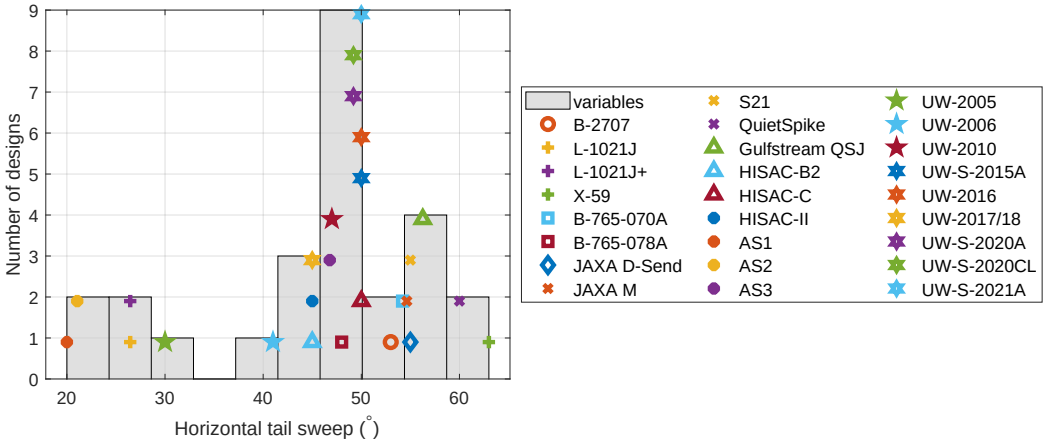


Figure 2.32: Horizontal tail sweep [13]

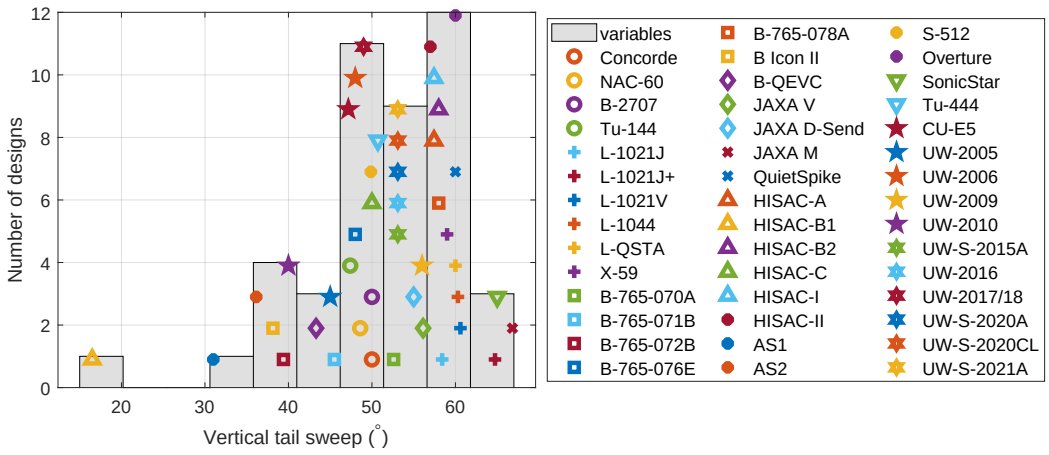
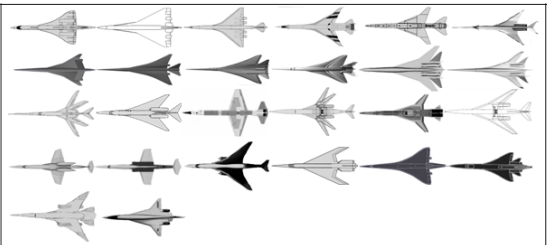
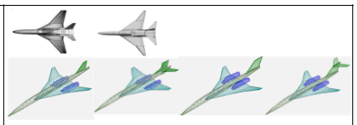
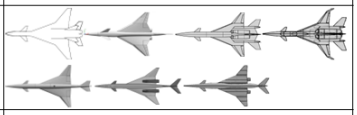
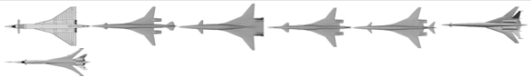


Figure 2.33: Vertical tail sweep [13]

Canard

Similar charts are shown for canard geometric parameters in Tables 2.26 and Fig. 2.34. Canard sweeps generally fall in the $45° \sim 55°$ range, for the same reasons as previously cited for horizontal stabilator surfaces. A few notable outliers are the Tu-144's high aspect straight canard which folds up for high speed flight, and the X-59 which has a highly swept fixed canard for trim and low-boom lift distribution. As shown in Fig. 2.34, the configurations tested by UW are consistent with and representative of designs from the design space survey.

Table 2.26: Canard location comparison [13]

No Canard		
Close-coupled		
Mid-coupled		
Long-coupled		

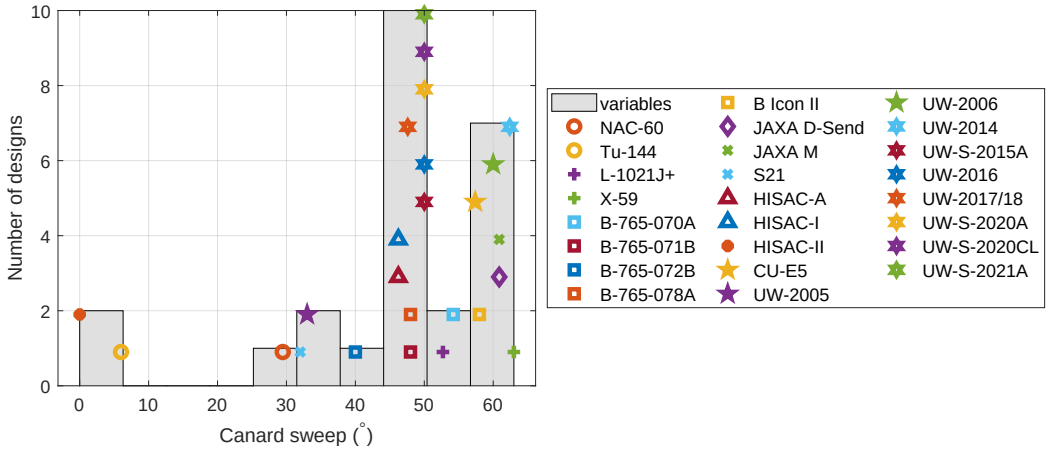


Figure 2.34: Canard sweep [13]

2.3 CFD Correlation and Simulation

The section summarizes the assessment of aerodynamic predictions at different levels of fidelity for a single pitch run of one configuration [14]. One of the goals of the SCALOS project was to evaluate the capability of current math modeling techniques and simulation tools to capture the physical behavior of the variety of configurations studied [14]. On the low modeling fidelity side, the United States Air Force (USAF) DATCOM was evaluated. The data used to create this capability were based on pre-1980s information, which already included information on many supersonic jets as well as low-speed, transonic, and supersonic wind tunnel tests. Of interest here was to study how well the aerodynamic properties of the new "quiet" and other emerging long-range supersonic configurations would be captured using DATCOM. In what may be categorized as a medium-fidelity modeling approach, panel methods, vortex lattice methods (VLM), and nonlinear panel codes capable of accounting for leading-edge thrust loss and vortex burst effects are attractive and of interest because of their high computational efficiency. As a representative of high-fidelity computational tools, the Star-CCM+ and OpenFOAM codes, which solve Reynolds-Averaged Navier–Stokes (RANS) equations and the Euler equations, were used. In an initial exploratory effort the simulations were all performed for and compared to a single pitch run done in the Kirsten Wind Tunnel (KWT) to assess basic, important, stability considerations for these long and slender configurations – covering longitudinal stability – in order to assess how

well the various codes could capture the vortex action and the resultant force and moment characteristics. All simulations modeled the wind tunnel model in freestream flight and were run at flow conditions equivalent to a dynamic pressure of 40 psf.

2.3.1 Aerodynamic Simulation Software

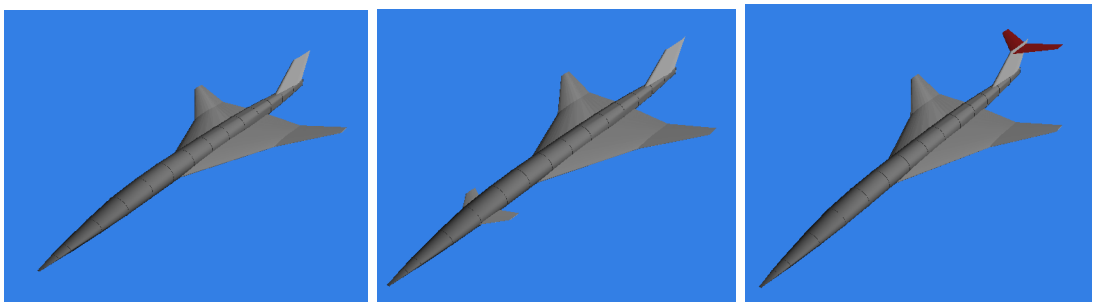
Digital DATCOM

The USAF DATCOM is a collection of equations and methods for configuration analysis of aircraft [37]. The equations and methods were assembled and published in the 1960's and updates were introduced in the 1970s. A digital version of DATCOM followed. A DATCOM+ Pro package [449], available today in the public domain, was used in this study. It includes more user friendly interfaces, improving the original digital DATCOM. It is important to note, however, that DATCOM+ Pro still uses the same methods and equations as the printed DATCOM. It is quite remarkable that DATCOM, created in the 1960s and 1970s, is still useful and quite widely used today. It represents the old but well proven engineering approach in which, because of the limitations on high-fidelity reliable and practical modeling and before automated machine learning, low fidelity methods combined with deep insights into the nature of aerodynamic flows around aircraft configurations and supported by many wind tunnel and flight tests served to create a data base and its structure that presented the geometries covered quite well. The modeling simplicity and computational efficiency of Digital DATCOM in its recent form can be very useful, especially in the early design stages, as long as the user works with configurations that are within the design space that was used to create DATCOM.

The question for the SCALOS project was how well DATCOM would capture the aerodynamic characteristics (for performance and S&C) of the emerging highly slender supersonic configurations of recent years. The recent supersonic configurations, including the ones investigated in the NASA SCALOS project, are outside of the range of configuration covered by DATCOM. The limitations regarding the SCALOS models using DATCOM include: i) maximum of two lifting-surfaces, ii) single airfoil definition, iii) single control surface deflection, iv) nacelle drag estimation, and v) no down-wash estimation for cranked-delta

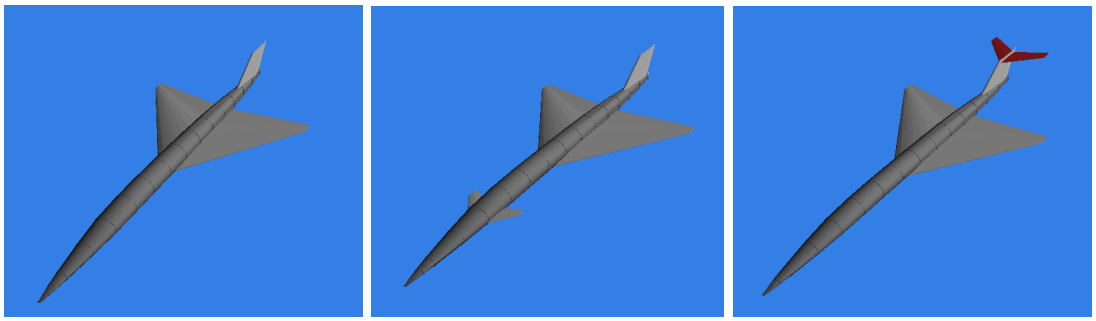
wings.

However, the argument was that if the canard of a quiet supersonic configuration is small and far ahead of the wing and if the tail and the canard are far away from each other, proper modeling in DATCOM of the configuration could be useful. Given that only two lifting-surfaces can be simulated at a time, wing-only, canard-wing, and wing-tail configurations were analyzed and their DATCOM predictions were added via superposition. For downwash estimation, the cranked-delta wing was replaced by an Engineering Sciences Data Unit (ESDU)-defined single trapezoid equivalent wing, shown in Figs. 2.35 and 2.36.



(a) Wing-only (b) Canard-wing-body (c) Wing-body-tail

Figure 2.35: DATCOM model configurations [14]

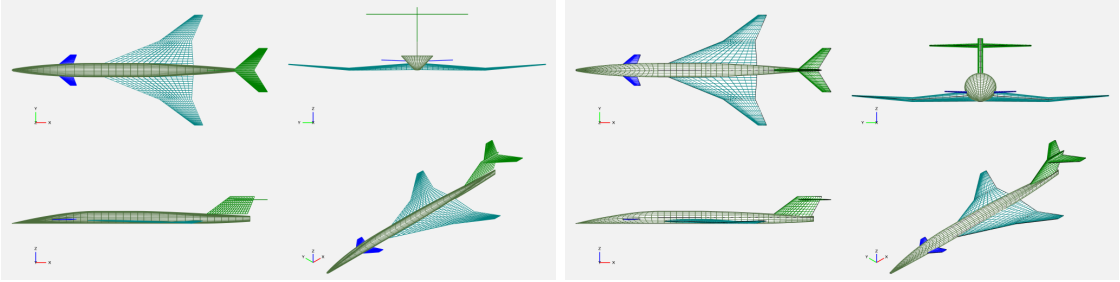


(a) Wing-only (b) Canard-wing-body (c) Wing-body-tail

Figure 2.36: DATCOM ESDU model configurations [14]

Vortex Lattice and Panel Method Codes

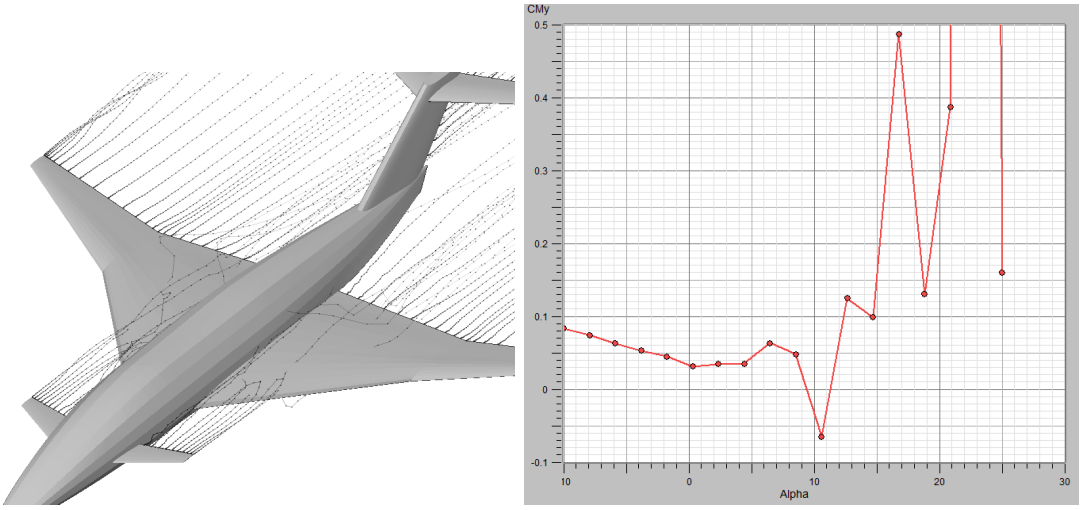
OpenVSP. OpenVSP is a particularly interesting software package because of its capability to quickly and accurately produce CAD models while also calling, in a user-friendly way, several valuable solvers. It contains several modules that are helpful in the conceptual design phase such as a parasitic drag build up calculator, interactive wave drag analysis, FEA structural modeling, and aerodynamic analysis. VSPAERO is the aerodynamic analysis module which provides either a vortex lattice solver or panel method solver, which also has features to estimate stability derivatives, something especially important in the conceptual design phase. As with any numerical simulation, the solutions depend heavily on the fidelity of the linearization of the model. The models shown in Fig. 2.37 were subjected to mesh refinement studies and were sufficient for solution convergence.



(a) VLM mesh representation (b) Panel method mesh representation

Figure 2.37: Mesh representations in OpenVSP [14]

A common problem in panel method solutions is the entanglement of the canard wake with the forming vortices on the wing, displayed in Fig. 2.38a. This leads to noisy data and inaccuracies that can be improved by increasing wake iteration along with making sure the mesh is as regular as possible at the intersections/corners. The solutions become much more unstable the more flow separation there is, making it difficult to rely on the data. On the other hand, this is indicative of vortex bursting which is helpful in its own regard. Furthermore, the panel method solver takes much longer to run than the VLM solver, yet is still very efficient in comparison to the time and memory requirements of CFD. These problems, along with some others, became limiters in producing more accurate results.



(a) Canard wake entanglement (b) Example pitching moment solution volatility

Figure 2.38: OpenVSP panel method difficulties [14]

Boeing UDP (Non-linear Panel Method). Of much interest in the context of the work reported here is the capability of nonlinear vortex lattice and panel methods to capture the aerodynamic characteristics of the new supersonic configurations in both the linear and nonlinear regimes. The computer code VORSTAB [450] was developed in the 1970s and 1980s to model slender configurations at high angles of attack. A more recent nonlinear unsteady vortex lattice code was modified to include effects such as leading edge suction loss and vortex burst [16].

Boeing Research & Technology (BR&T) recently used their nonlinear panel code to validate the results obtained in the Flow Visualization Wind Tunnel and so, it was important to also compare UDP results to KWT wind tunnel results. UDP is a panel method code that has optional non-linear "add-ons", such as leading edge thrust prediction [451], and vortex lift [452]. More information about recent work on UDP can be found in Reference [15].

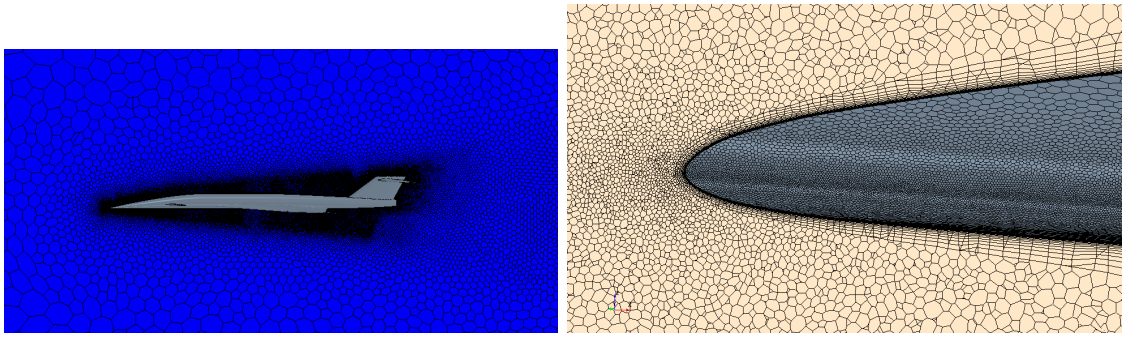
RANS CFD

Star-CCM+. The commercial CFD software Star-CCM+ has been used for CFD simulations at the UW for quite some time. The user-friendly integration in Star-CCM+ of CAD

mesh generation, the flow solvers, and post-processing capability makes it an attractive tool for CFD education and, for the project work presented here, an efficient research tool.

In order to build trust in the CFD results provided by Star-CCM+, a test case was run to validate mesher and solver methods using an M6 wing, comparing results to known values from the NASA Turbulence Modeling Resource [453]. The meshers used in Star-CCM+ include the surface remesher, polyhedral mesher (volume), and prism layer mesher (volume/surface interface to capture boundary layer). These meshers produce a robust, unstructured mesh. Half of the model was meshed with the use of a symmetry plane on the x-z plane. The flow region was a half sphere with radius equal to 50$\times$ the MAC. A velocity inlet constituted the front half of the half sphere and a pressure outlet for the rear half. The airplane surfaces have a no-slip condition so a prism layer mesh was applied with a first cell height of $y^+ = 1$, a total of 20 layers with 1.5 stretch ratio, for a total height of 1.65 cm (equivalent to the total height of the boundary layer at the end of the wing at MAC). The maximum cell surface size was 1 cm (roughly 1/100 the length of the root chord), the minimum size was 0.1 mm (for leading edge curvature refinement), and the surface growth rate was 1.1. The volume mesh growth rate was 1.1 and wake refinement was a combination of Star-CCM+'s built in wake refinement feature (cells limited to 5 cm in size, extended for 30 m downstream with a spread angle of 5°) and a manual, finer volume refinement (cells limited to 1 cm in size in a volume block around the airplane). The total size of the mesh was 40.1 million cells and images of the mesh are in Fig. 2.39.

The simulations were run using the steady, coupled-implicit solver in Star-CCM+ with turbulent incompressible flow using the Spalart-Allmaras turbulence model. Simulations were also run with inviscid incompressible flow and the mesh was scaled down accordingly (first cell in prism layer was roughly isotropic). Both cases were run at a dynamic pressure of 40 psf, equivalent to that tested in the KWT. (In later KWT tests, the dynamic pressure was reduced to 32 psf to prevent yaw buffeting of the model, for safety.) The model was simulated at various angles of attack ranging from $-10°$ to 25° at 0° sideslip and all solutions converged to a residual of 10^{-5} or lower.



(a) Mesh around configuration on the symmetry plane

(b) Prism layer mesh at the leading edge of the wing

Figure 2.39: Meshed model for Star-CCM+ [14]

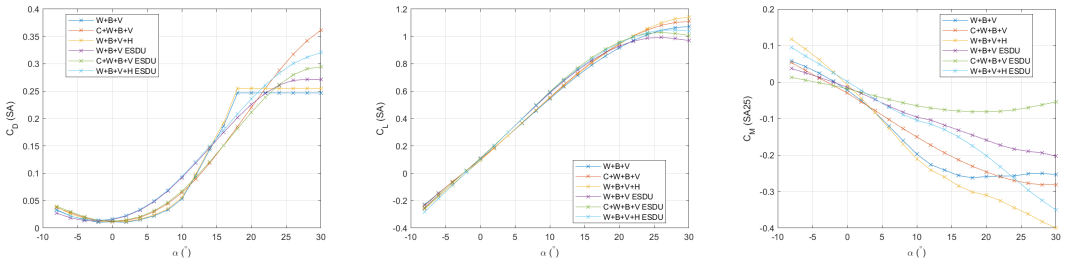
OpenFOAM. The University of Michigan ran the same configuration using ADflow in OpenFOAM with the Spalart-Allmaras turbulence model, with *compressible* flow, on a structured overset mesh with 11.1 million cells. All solutions were converged to a total residual of 10^{-7} or tighter relative to the freestream residual. More information about this work can be found in Reference [454].

2.3.2 Test / Simulation Correlation Discussion

DATCOM Predictions

As discussed previously, DATCOM does not allow modeling three lifting-surfaces nor nacelles. As a result some configuration superposition was necessary to obtain a 3-surface configuration data set. Obviously, the drawback is that this does not include the interaction and influences between all three lifting surfaces at once. The data presented below in Fig. 2.40 highlights the differences between the different 2-surface configurations. In Fig. 2.40, each letter stands for the part used, i.e., B for body, C for canard, H for horizontal tail, W for wing, V for vertical tail. Figure 2.41 shows the equivalent three-surface configuration force and moment coefficients, calculated by superposition of wing-body-canard plus wing-body-tail subtracting wing-body, i.e., $\big((C+W+B+V)+(W+B+V+H)\big)-(W+B+V)$.

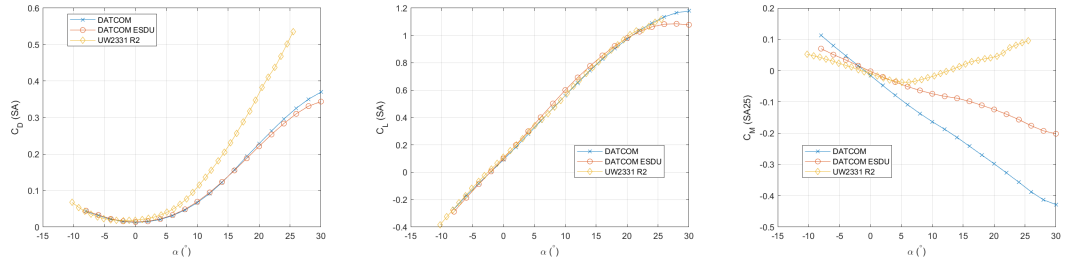
For both methods, drag is understandably under-predicted, lift was predicted surprisingly well, and the pitch stability was over-predicted. The single airfoil modeling in DAT-



(a) C_D vs. α (b) C_L vs. α (c) C_M vs. α

Figure 2.40: DATCOM aerodynamic results [14]

COM may contribute the lift differences between DATCOM and wind tunnel results. The replacement of the wing by its ESDU equivalent also explains differences between DATCOM results and wind tunnel tests since the single ESDU trapezoid cannot capture the complex interaction between the inner and outer vortices on a cranked-delta wing. It is not surprising, therefore, that DATCOM does not work well for such configurations in the nonlinear range. In the low angle of attack range its lift predictions seem useful. In both the drag and pitching moment cases, fuselage effects and actual pressure distributions over the wing are important and cannot, in the case of the configuration studied here, be not modeled by the semi-empirical method of DATCOM. An early lesson here may be that DATCOM can be useful for estimation of the effects of changes in configurations once the characteristics of the reference configuration are known.



(a) C_D vs. α (b) C_L vs. α (c) C_M vs. α

Figure 2.41: DATCOM (superpositioned) vs. KWT data [14]

VLM and Panel Method Predictions

Comparing all of the "medium-level" fidelity codes together, in Fig. 2.42, it becomes immediately evident that all methods only work well in the linear regime of flight. However, the VLM method in OpenVSP appears to best predict the point of change in the longitudinal stability derivative, albeit a few degrees later, and the panel method in OpenVSP is the only method that (somewhat) predicts the longitudinal stability being positive after the initial pitching moment derivative sign change. It is uncertain at this point in time if this is a trend that will carry over to other configurations or only applies to this specific configuration.

Figure 2.42 also shows that the nonlinear panel code also struggles with capturing the granular details of the force distribution needed to resolve the pitching moment curve. At this stage of the work, since modeling with the code is still under development, UDP is sufficient for predicting only the linear regime of flight. It is especially noteworthy to mention that the additional vortex lift added in UDP over-predicts lift above $\sim 5°$ angle of attack, which may be due to blunt inboard leading edges of the model.

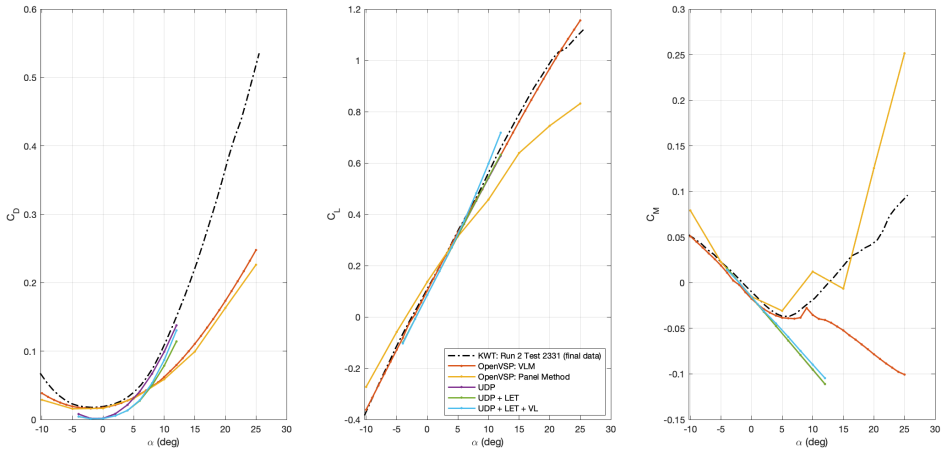
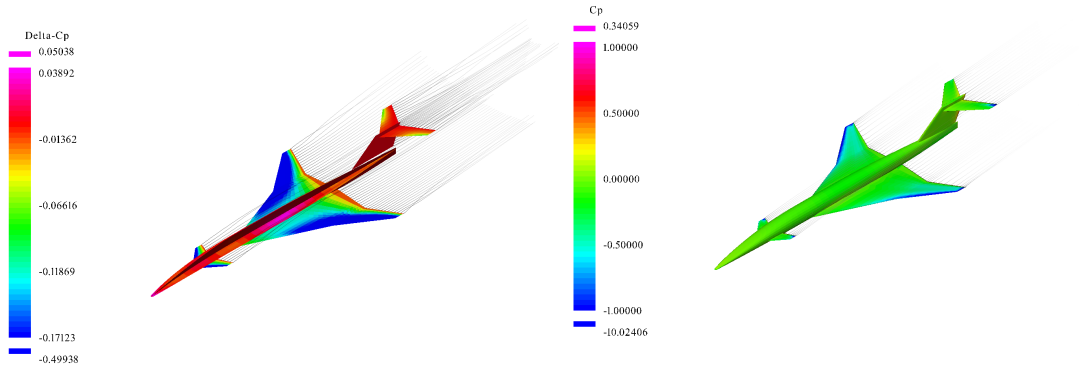


Figure 2.42: Various VLM methods result [15]

Figure 2.43 shows the similarities of the pressure distribution pattern between the two solver methods of VSPAERO, even though they are depicted using different scalars. Interestingly, the panel method solution is much more refined, despite having similar cell counts.



(a) VLM solution (b) Panel method solution

Figure 2.43: VSPAERO pressure distribution solutions and trailing wakes at $\alpha = 6°$ [14]

CFD Predictions

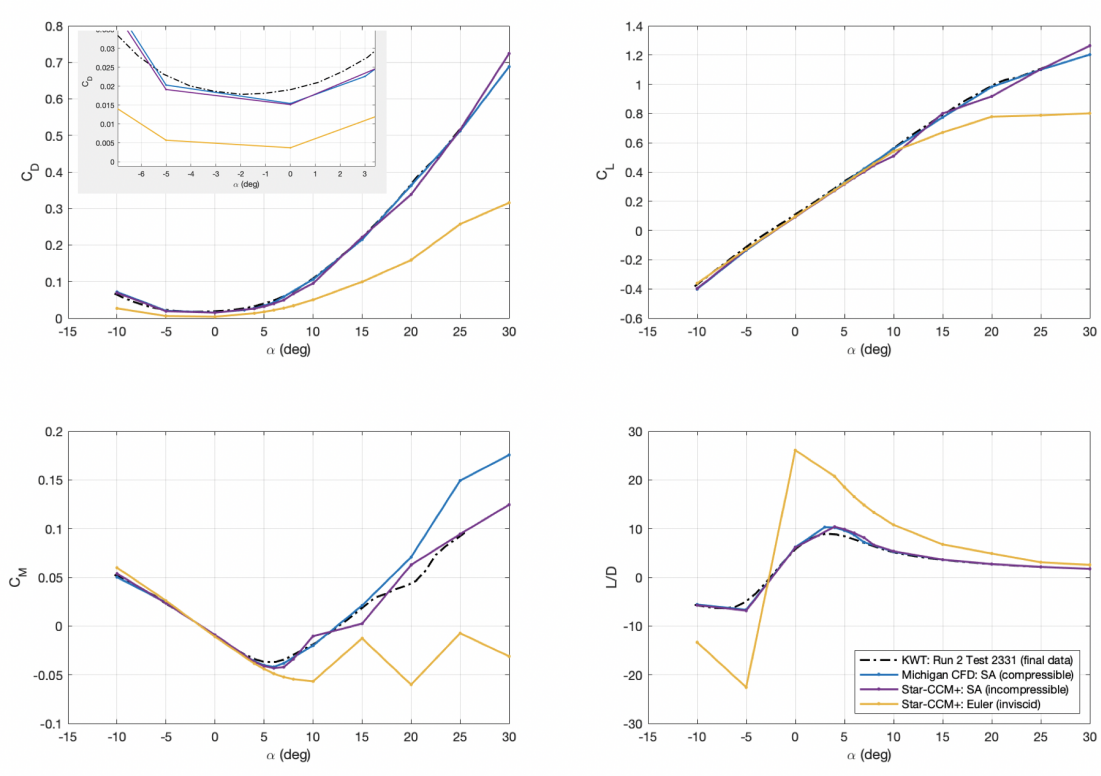


Figure 2.44: Comparison of RANS CFD techniques to experimental data [16]

As shown in Fig. 2.44, RANS CFD simulations using various meshing techniques and

solvers provide reasonably accurate results, even for the pitching moment curve which can be notoriously difficult to capture by analysis. The differences between Star-CCM+ and OpenFOAM results are likely a combination of different software packages, solvers, meshes, and compressibility assumptions. Using an inviscid flow assumption in Star-CCM+ did not capture the experimental data well. In the linear range lift and moment curves were captured acceptably well (with some difference in pitching moment angle of attack derivative). But the drag prediction is, as expected, too low, leading also to differences between test and analysis of the lift over drag ratio.

2.4 SCALOS Configurations in the Wind Tunnel

This section describes the wind tunnel experimental setup of the SCALOS project in the Kirsten Wind Tunnel (KWT) at the University of Washington including the model mounting system, the model and model reference geometry, the test conditions and test entries, long-term and short-term test-to-test repeatability, and Reynolds number effects. Most of the details of the experimental setup appeared in prior publicaitons [4, 13, 14, 18, 19, 23–27, 371–377, 381–383], and also in final report [378]. The long-term and short-term test-to-test repeatability, and Reynolds number effects sections are from [4] updated with final corrected data. The goal here is to make the presentation of the SCALOS wind tunnel test effort in this document self contained.

2.4.1 Kirsten Wind Tunnel

All wind tunnel tests were carried out in the Kirsten Wind Tunnel (KWT) at the University of Washington. The tunnel has a filleted rectangular test section of 12 ft in width by 8 ft in height and 10 ft in length. It is a low-speed, closed-circuit, atmospheric, dual-return wind tunnel as shown in Fig. 2.45 with dimensions in Fig. 2.46. The tunnel has two sets of 14’ 9” -diameter seven-bladed propellers that can move the air up to 200 miles per hour through the test section for a maximum dynamic pressure of 100 psf. The raw data from the external balance requires correction to obtain final force and moment values.

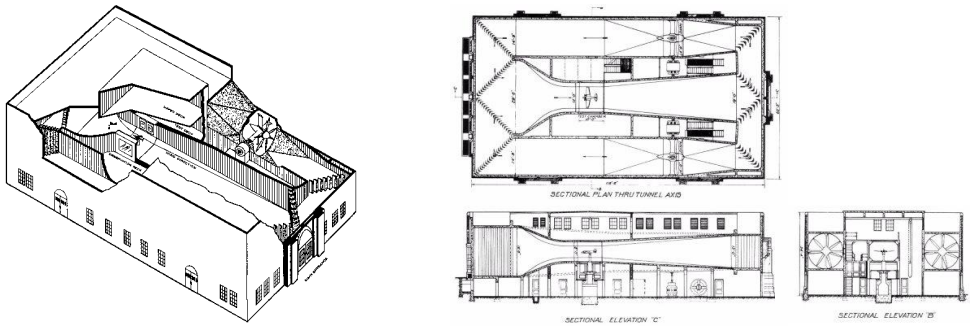
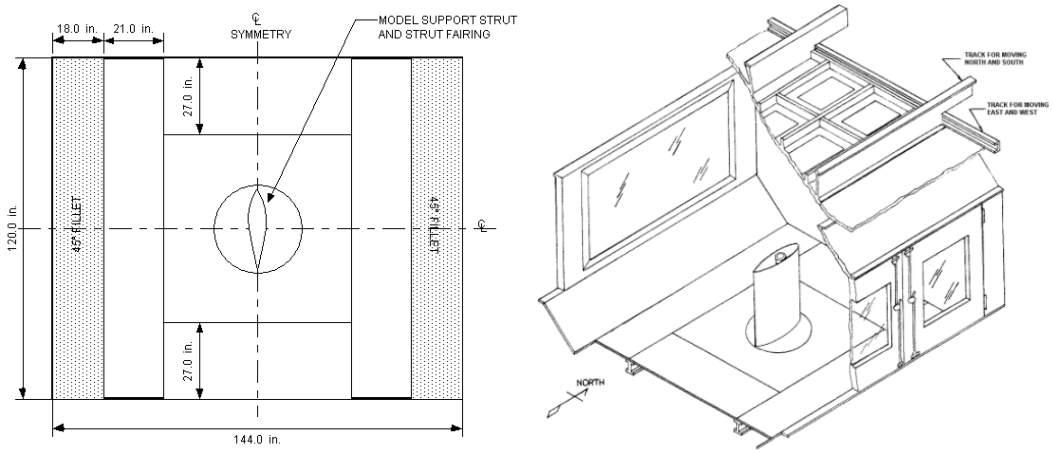


Figure 2.45: Kirsten Wind Tunnel at the University of Washington [17]



(a) Test section dimensions (b) Test section cutaway

Figure 2.46: Kirsten Wind Tunnel test section [17]

2.4.2 Model Mounting System

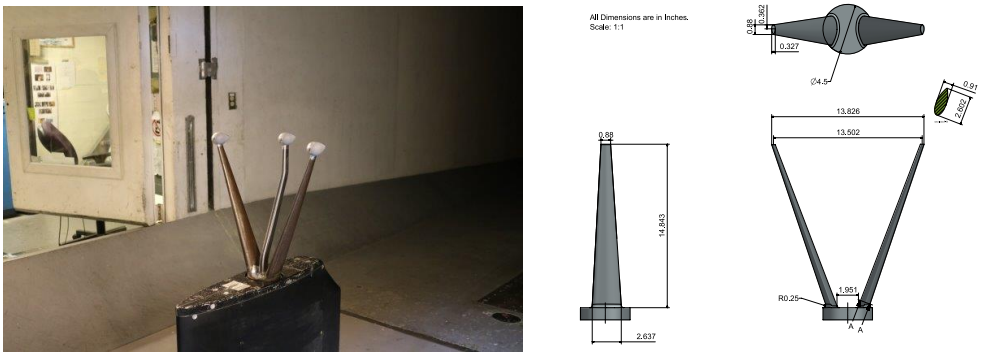
Over the years, about half of all KWT tests of capstone design supersonic configurations were conducted using one of the KWT's fork-styled model mounts as shown in Fig. 2.47. The reasons for selecting the fork-type mount/adaptor for the core model design were:

1. The thin struts of the mounting fork were expected to minimize flow interference on the surface of the model.

2. The fork mount allowed testing of wing-alone cases in the case of thin wings with no additional fairings or body components. Other adapter/mounts, because of the size of their areas of attachment to the model, would lead to protuberances on the model.

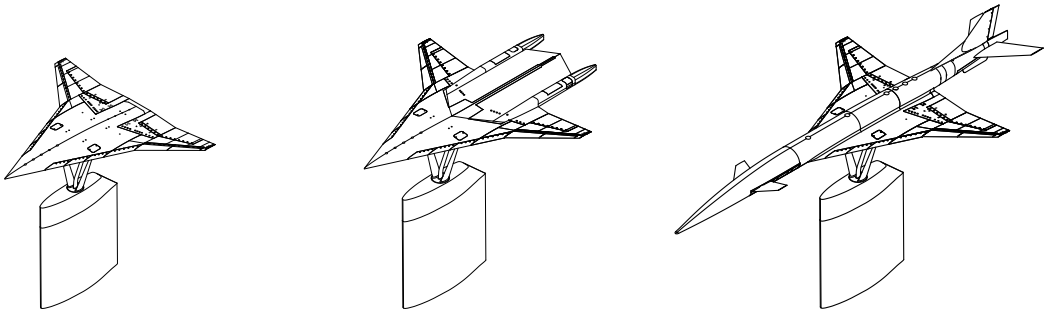
3. The KWT had an existing standard fork-mount correction (including model interference on the fork), that was based on substantial model testing over the years, including T&I tests.

The SCALOS test program discovered that the generic corrections were not sufficient for capturing the low-aspect-ratio / cranked delta wing required corrections [18, 381]. Experimental T&I corrections development work was conducted based on the standard T&I methodology dscribed in [455] with the selected configuration of Figure 2.61. More details can be found in Ref. [19, 374].



(a) Fork 14H in KWT (b) Fork 14H dimension

Figure 2.47: The fork 14H model mounting system [18]



(a) Wing only (W15) (b) Wing + aft-deck (W15+AD16) (c) UW-S-21A without nacelles

Figure 2.48: Configurations selected for tare and interference measurements [19]

2.4.3 Test Model and Test Letter Geometry

A core wind tunnel model for the tests was a 1/22 scale representation of a 75-100 seat, Mach 1.8 conceptual design airliner with twin mixed flow turbofan engines (MFTF). The test model was designed with an inboard wing section and support interface that could serve as a "backbone", allowing the creation of various configurations based on the same core model for semi-parametric studies.

The particular modular nature of the wind tunnel model made it possible to test wing-only configurations as well as wing plus aft deck configurations before proceeding to add a fuselage, tail surfaces, canard surfaces, engine nacelles, and landing gear. Figure 2.49 illustrates the major planform variations that were tested from 2015 and through 2024 with overlays of various shapes, e.g., different outboard wing shapes, different leading-edge shapes, canard shapes, nacelles, and their locations, etc. In addition, the effects of various high lift and roll control devices such as conventional ailerons, speed brakes/aileron spoilers, spoiler-slot deflectors (SSD), and mid-chord spoilers were studied too. Additional geometric variations such as area-ruled fuselage and landing gear effects were investigated.

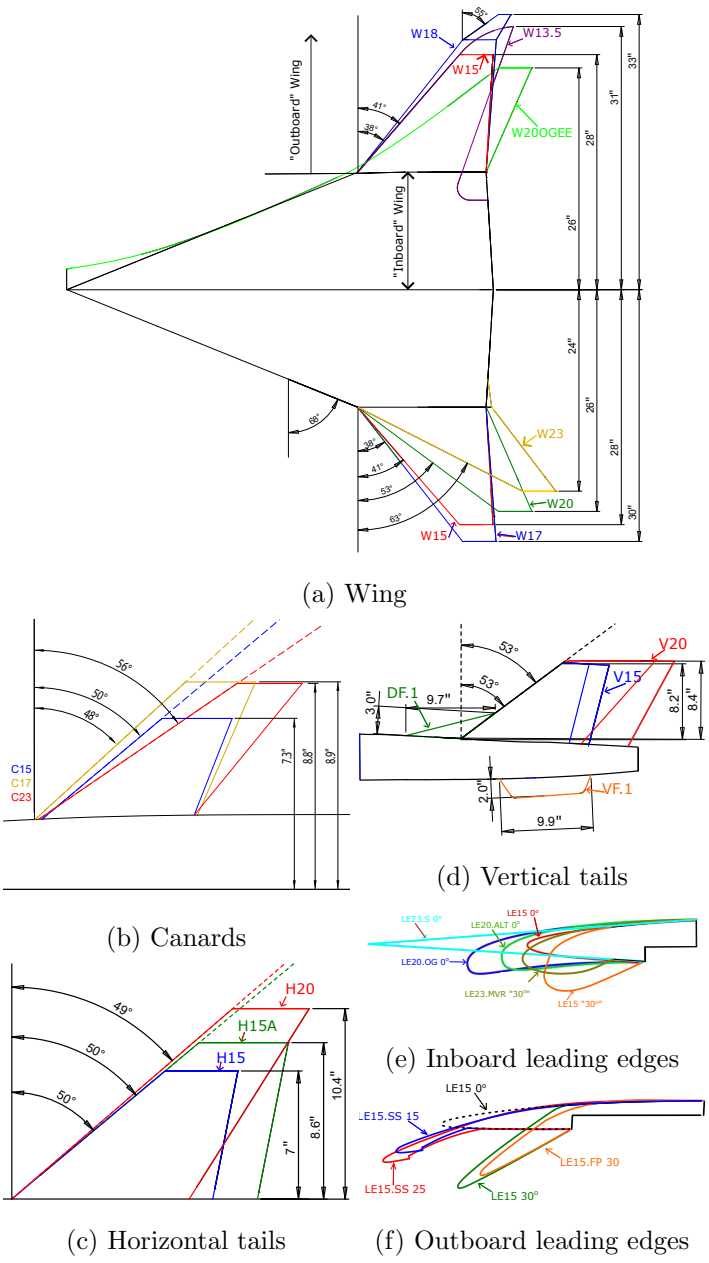
The key geometric information about the configurations tested in Fig. 2.49 is presented in Table 2.27. It should be noted that the span (b), mean aerodynamic chord ($\bar{c}$), wing reference area S_{ref}, and aspect ratio (AR) of the canard, horizontal, and vertical tails in Tab. 2.27 were based on their exposed area outside of the fuselage body. Interested readers can refer to Tabsles 2.8–2.18 in §2.2 for details of the various built-up models with their respective component parts designations in the §2.5 covering the designations of the modular components with corresponding control surfaces and deflection, the various model built-up, and model variations. Selected configurations from each year (Fig. 2.50) illustrate the modularity of the test model.

The core wind tunnel model plus 2015 outboard wing is shown in Fig. 2.51a. For comparison purposes, all the SCALOS data are referenced/normalized with respect to the 2015 wing (core + 2015 outboard wing) in Fig. 2.51a with tabulated test letter values in Tab. 2.28. The test letter values are computed based on the Engineering Science Data Unit (ESDU) method without the presence of the fuselage in Fig. 2.51a instead of Fig. 2.51b

with detailed geometry definitions in [375]. Note that each test entry in the data package had its own test letter but all the data are reprocessed with respect to values in Tab. 2.28. The subscript $_{\text{ref}}$ is the projected reference area without the fuselage. The center of gravity (CG) locations for the SCALOS program are defined at 15%, 20%, 25%, 33%, and 40% MAC according to Table 2.28. The acwx and acwz are the aerodynamic center of 25% MAC with respect to the balance moment center (BMC) which coincides with the trunnion ($x = z = 0$) for the SCALOS program. There are additional variables in the test letter. A brief discussion of the data correction processes can be found in §2.5.5 with details in [374]. The part designations are defined in §2.5.2 and the part geometries are shown in §2.5.3 with detailed part documentation in [375, 376].

Table 2.27: SCALOS model components specification

	Designation	$\Lambda_{\text{LE}}(^\circ)$	$\Gamma(^\circ)$	b (ft)	$\bar{c}$ (ft)	$S_{\text{ref}}(\text{ft}^2)$	t/c_{max}	AR
Canard	C15	50	0	1.22	0.400	0.277	0.04	5.37
	C17	47.6	0	1.48	0.535	0.380	0.04	5.76
	C23	55.6	0	1.42	0.399	0.350	0.04	5.76
Outboard Wing	W13.5	41.0	4.67	5.22	1.73	8.17	0.05	3.34
	W15	41.0	4.67	4.67	2.01	8.30	0.05	2.63
	W17	38.1	4.17	5.00	1.92	8.58	0.05	2.91
	W18	38.2	10.2	5.46	1.86	8.66	0.05	3.39
	W20	53.5	4.74	4.40	2.09	8.09	0.05	2.39
	W23	63.0	4.45	4.00	2.28	7.83	0.05	2.04
Horizontal Tail	H15	50.1	0	1.17	0.623	0.594	0.04	2.30
	H15A	50.2	0	1.43	0.777	0.939	0.04	2.18
	H18	50.2	10	1.97	0.828	1.54	0.05	2.51
	H20	49.2	0	1.74	0.585	0.882	0.08	3.43
	V23.H	37.6	50.3	1.41	0.617	0.804	0.05	2.47
	H24	49.25	0	1.81	0.581	0.865	0.08	3.78
Vertical Tail	V15	50.1	0	0.74	1.07	0.579	0.05	0.946
	V16T.2	51.1	0	0.610	0.706	0.409	0.05	0.910
	V20	53.3	0	0.777	1.36	0.934	0.05	0.646
	V23.V	37.6	50.3	1.77	0.659	1.00	0.025	3.13
Ventral Fin	VF.1	29.9	0	0.167	0.7334	0.0033	0.1	0.228
	VF.2	30.2	0	0.1775	0.7540	0.1329	0.0033	0.2370
	VF24T	16	30	0.1567	0.3501	0.1087	0.00714	0.4518
Dorsal Fin	DF.1	73.8	0	0.17	0.75	0.16	0.04	0.181
	Designation	d (ft)	l (ft)	$S_{\text{wet, ext}}$ (ft^2)	S_{f} (ft^2)	$S_{\text{wet, int}}$ (ft^2)		
Fuselage	F15	0.542	9.55	10.603	0.221			
	F15.L	0.542	11.57	12.927	0.211			
	F24	0.57	9.82	12.483	0.283			
	AD16	2.81	2.33	9.234	0.280			
Nacelle	N15	0.375	2.165	2.094	0.133	2.199		
	N16	0.398	1.990	1.623	0.082	1.822		
	N18	0.469	2.788	3.119	0.152	2.733		
	N20	0.389	1.952	2.284	0.138	1.708		
	N23	0.389	2.633	2.327	0.144	2.369		



(a) Wing

(b) Canards

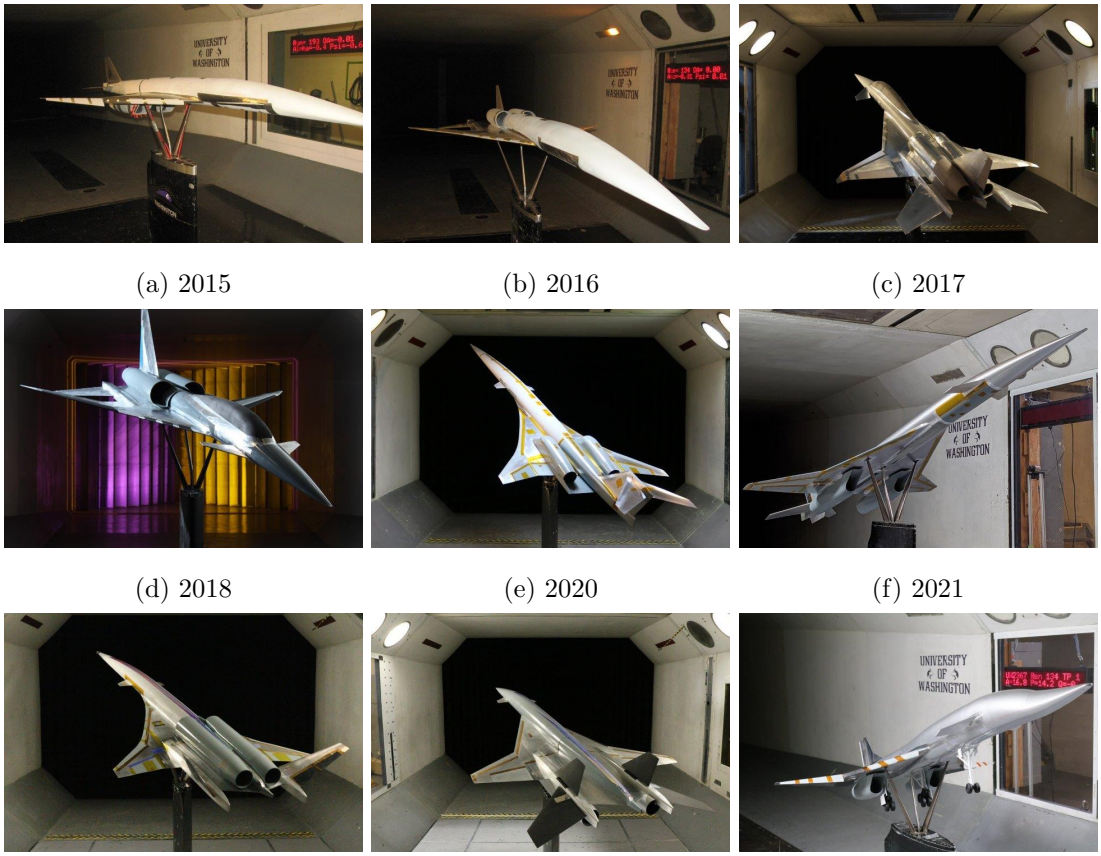
(d) Vertical tails

(c) Horizontal tails

(e) Inboard leading edges

(f) Outboard leading edges

Figure 2.49: Wing and tail geometry variations

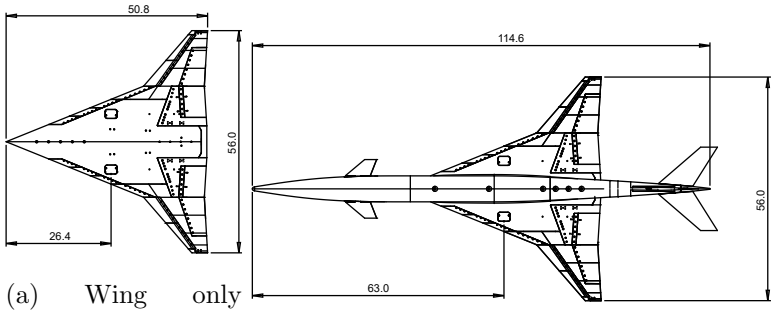


(a) 2015 (b) 2016 (c) 2017

(d) 2018 (e) 2020 (f) 2021

(g) 2023 (h) 2023 (i) 2024

Figure 2.50: Tested SCALOS configurations



(a) Wing only (W15)

(b) UW-S-21A without nacelles

Figure 2.51: Wing-only and UW-S-21A without nacelles

Table 2.28: Test letter geometry

S_{ref} (ft^2)	$\bar{c}$ (in)	b_{ref} (in)	AR (in)	c_{root} (in)	c_{tip} (in)	acwx (in)	acwz (in)	x (in)	z (in)
8.296	26.0656	55.925	2.618	44.7	4	-4.261	-0.12	0	0

2.4.4 Test Conditions and Test Entries

The wind tunnel test entries were conducted at several tunnel dynamic pressures. For each dynamic pressure, tests were carried out over a range of sideslip angles (β) and angles of attack (α). Table 2.29 presents the dynamic pressures (q) in psf with corresponding Reynolds numbers based on the length of the MAC in Tab. 2.28. The majority of tests were conducted at 40 psf and later at a lowered to 32 psf to prevent severe model dynamics at high angles of attack. Data between these two different dynamic pressures were shown to be fully repeatable, except for a slight skin friction drag change at low angles of attack as discussed in the subsequent sections in §2.4.5 and §2.4.6. All the SCALOS program test entries are in Table 2.30. The official SCALOS program started in 2020. All the test rfesults from 2015-2018 were add-on data, which were corrected and documented by the best of the author's experience and knowledge.

Table 2.29: Dynamic pressure and Reynolds number at standard sea level

q (psf)	3.5	6.25	10	14	20	30	32	40	60
Re	6.90×10^5	0.93×10^6	1.17×10^6	1.39×10^6	1.66×10^6	2.03×10^6	2.10×10^6	2.35×10^6	2.87×10^6

Table 2.30: Kirsten Wind Tunnel test entries

Entry number	Year	Month	Test period (days)	Total Runs (#)	Data collection
UW2128	2015	April	6	249	Force & moments and flow visualization
UW2166	2016	April	6	256	Force & moments and flow visualization
UW2200	2017	April	6	216	Force & moments and flow visualization
UW2237	2018	April	6	287	Force & moments and flow visualization
UW2292	2020	July	6	152	Force & moments (unresolved issues)
UW2295	2020	August	3	23	Force & moments
UW2298	2020	September	6	133	Force & moments
UW2320	2021	June	7.5	148	Force & moments
UW2324	2021	August	4	54	Flow visualization
UW2326	2021	September	6	225	Force & moments
UW2331	2021	November	5	150	Force & moments and flow visualization
UW2354	2023	May	20	456	Force & moments and tare & interference
UW2367	2024	Feb	10	226	Force & moments
12			85.5	2400	exclude UW2292

2.4.5 Long-term and Short-term Test-to-Test Repeatability

As previously mentioned in §2.1, the study of SCALOS-type configurations started over 15 years ago as a series of UWAA undergraduate capstone airplane design projects. Various model configurations were designed, manufactured, and tested in the KWT, a few of which were shown in Figure 2.3. From the year 2015 on, tests concentrated on wings, nacelles, tails, etc. that could be adapted semi-parametrically to the common "core" of the 2013 model hardware. These variations were tested in the KWT and the results were analyzed. Prior to testing each new configuration, the previous year's model configuration wwas tested to ensure short-term and long-term test-to-test repeatability. The data for three different configurations: 2015 wing only, 2015 wing and fuselage, and a representative full-configuration, UW-S-20A, shown in Figure 2.52, are presented here. Figure 2.53 shows the longitudinal force and moment data of 2015's wing alone (W15) at four dynamic pressures. The data show excellent long-term repeatability in lift and drag coefficients. The drag repeatability at a given dynamic pressure is within a 5 count (0.0005 ΔC_D) band expected for wing-alone. The difference in drag with q is as expected for difference in skin friction experienced between the two Reynolds numbers.

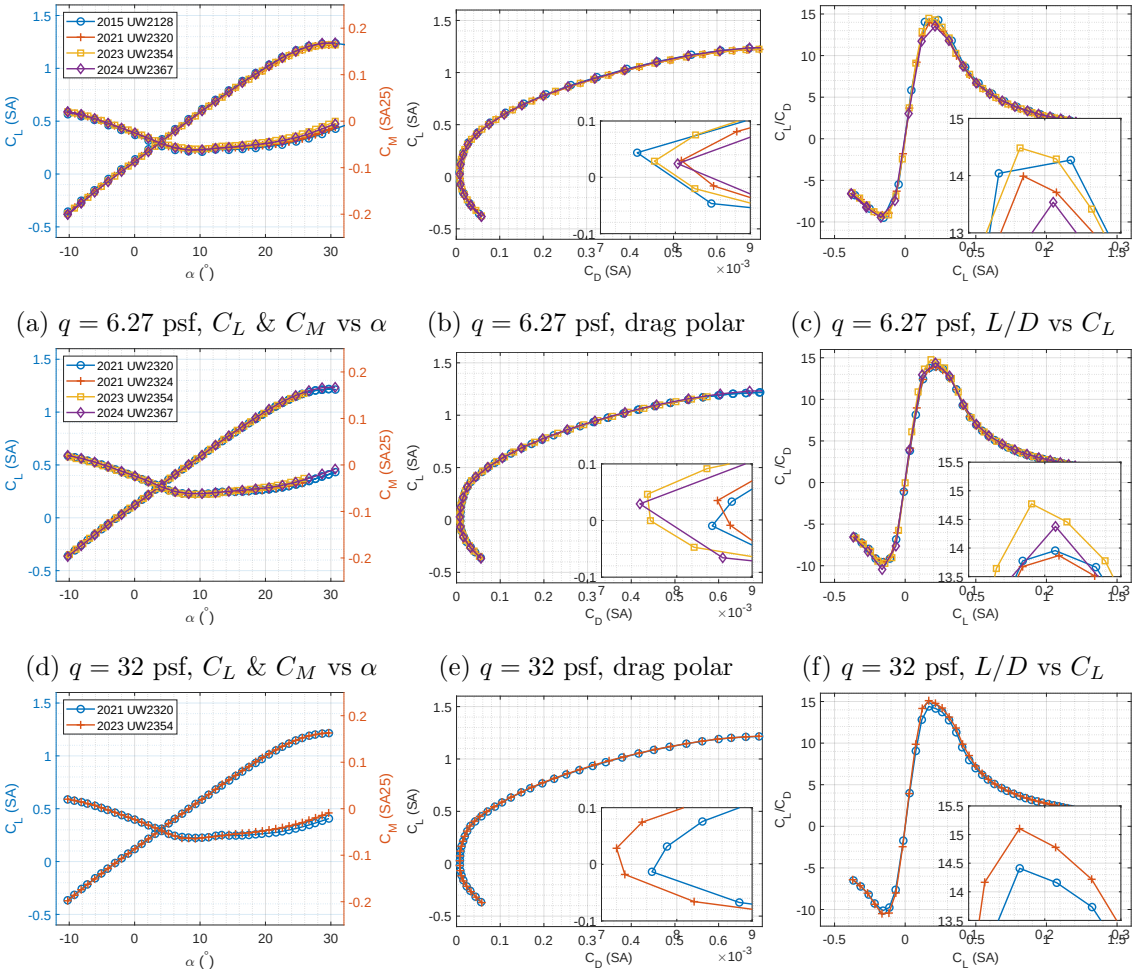
Some of the variations of drag and moment measurements from test to test (see Figure 2.54) may be explained by the slightly different taping that was used to cover screw holes and various joints over the model. Similar variations of the aerodynamic forces and moment

within different tests are seen from Figure 2.55 which shows the data for the UW-S-20A model across multiple tunnel entries. Again, the repeatability in the lift data is excellent for all tunnel entries. The drag force data shows slight variations which are within only a few counts of the drag coefficient.



(a) 2015 wing only (b) 2015 wing and fuselage (c) UW-S-20A

Figure 2.52: Test repeatability configurations

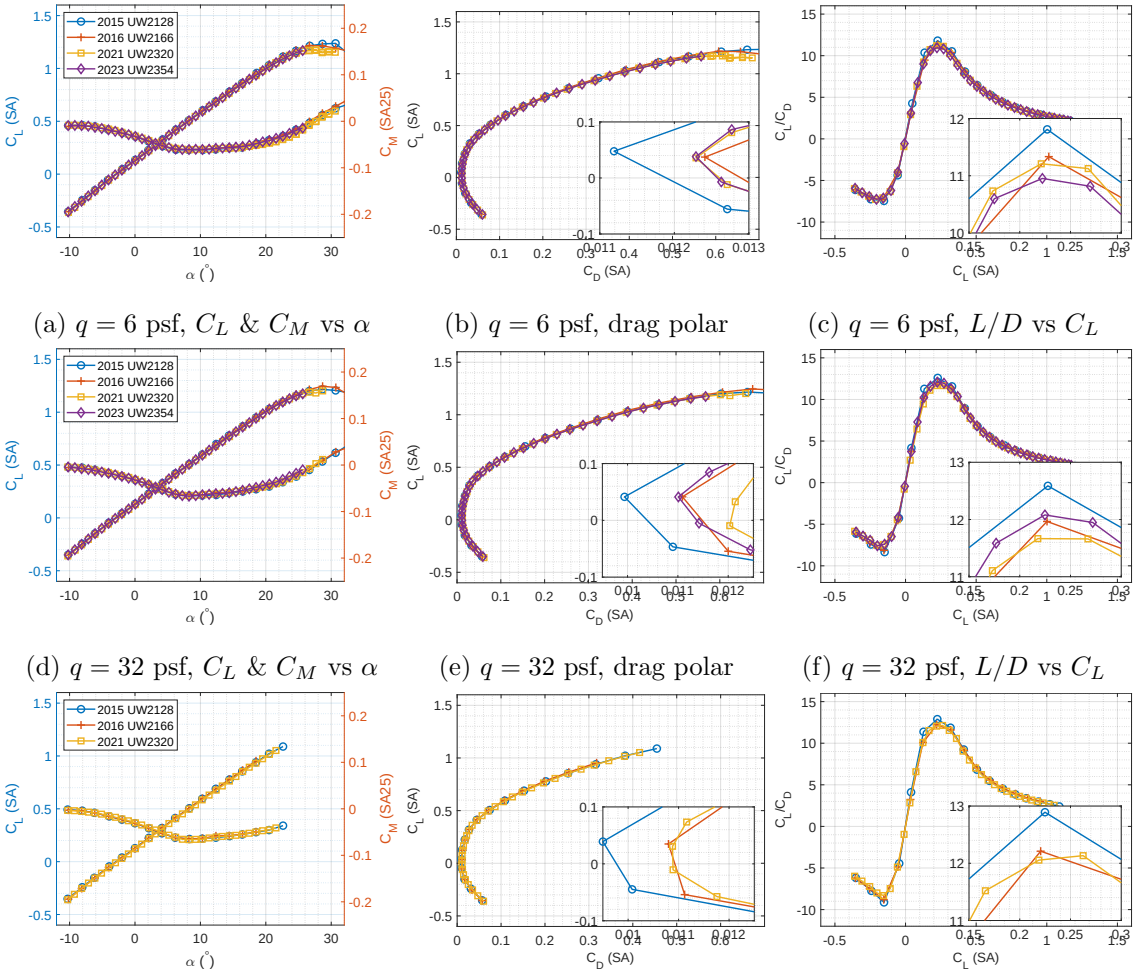


(a) $q = 6.27$ psf, C_L & C_M vs α (b) $q = 6.27$ psf, drag polar (c) $q = 6.27$ psf, L/D vs C_L

(d) $q = 32$ psf, C_L & C_M vs α (e) $q = 32$ psf, drag polar (f) $q = 32$ psf, L/D vs C_L

(g) $q = 40$ psf, C_L & C_M vs α (h) $q = 40$ psf, drag polar (i) $q = 40$ psf, L/D vs C_L

Figure 2.53: 2015 wing-only (W15) test-to-test repeatability across multiple dynamic pressures

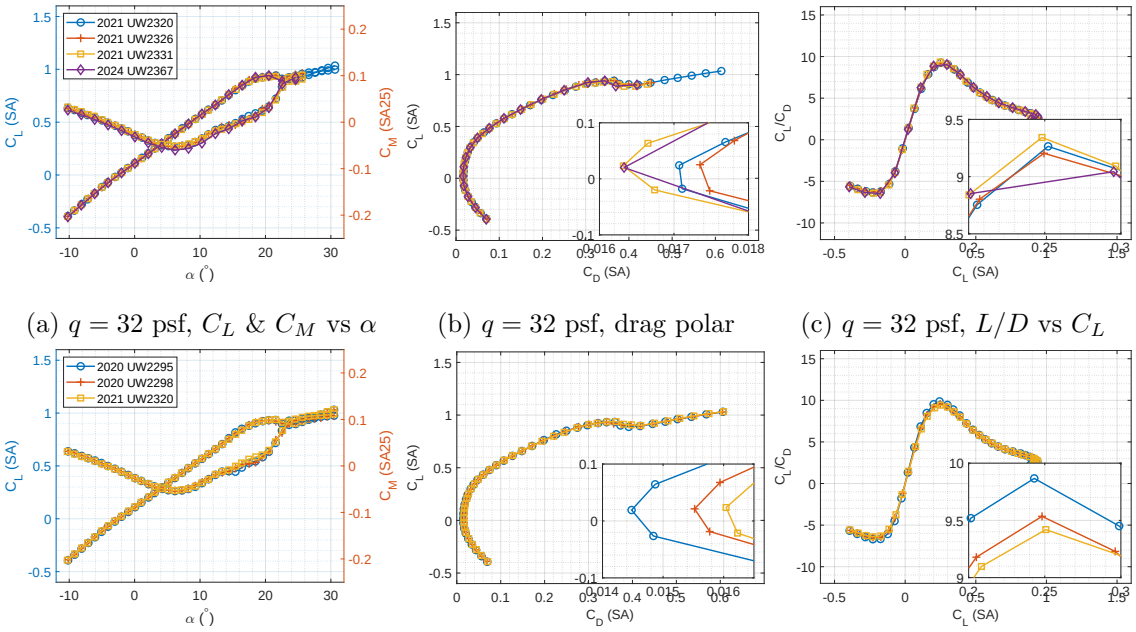


(a) $q = 6$ psf, C_L & C_M vs α (b) $q = 6$ psf, drag polar (c) $q = 6$ psf, L/D vs C_L

(d) $q = 32$ psf, C_L & C_M vs α (e) $q = 32$ psf, drag polar (f) $q = 32$ psf, L/D vs C_L

(g) $q = 60$ psf, C_L & C_M vs α (h) $q = 60$ psf, drag polar (i) $q = 60$ psf, L/D vs C_L

Figure 2.54: 2015 wing+fuselage test-to-test repeatability across multiple dynamic pressures



(a) $q = 32$ psf, C_L & C_M vs α (b) $q = 32$ psf, drag polar (c) $q = 32$ psf, L/D vs C_L

(d) $q = 40$ psf, C_L & C_M vs α (e) $q = 40$ psf, drag polar (f) $q = 40$ psf, L/D vs C_L

Figure 2.55: UW-S-20A test-to-test repeatability across multiple dynamic pressures

2.4.6 Reynolds Number Effects

The various tested dynamic pressures and their corresponding Reynolds numbers are shown in Table 2.29 in §2.4.4. Figures 2.56, 2.57, and 2.58 show the effects of dynamic pressure and Reynolds number on the 2015 wing-only model, wing and aft-deck, and wing-body configuration force and moment coefficient variations with angle of attack. Note that since the KWT is an atmospheric tunnel, Reynolds number variations cannot be studied independently of the Mach number. The curves, therefore, show the effects of both Reynolds number and Mach number, as well as model elastic deformation due to dynamic pressure. The pure Mach and dynamic pressure effects are likely small as the model is quite stiff for the test dynamic pressures, and the Mach numbers are well in the incompressible range. At low dynamic pressures and at small to moderate angles of attack, the flow over the entire surface of the model is practically incompressible, but it is possible that at higher dynamic pressures and at high angles of attacks compressibility effects should be considered, especially where the flow over the wing surface at moderate to high angles is dominated by vortices and the core speeds of the vortices can be relatively high. Potential Mach number sensitivity is an area to investigate further using CFD.

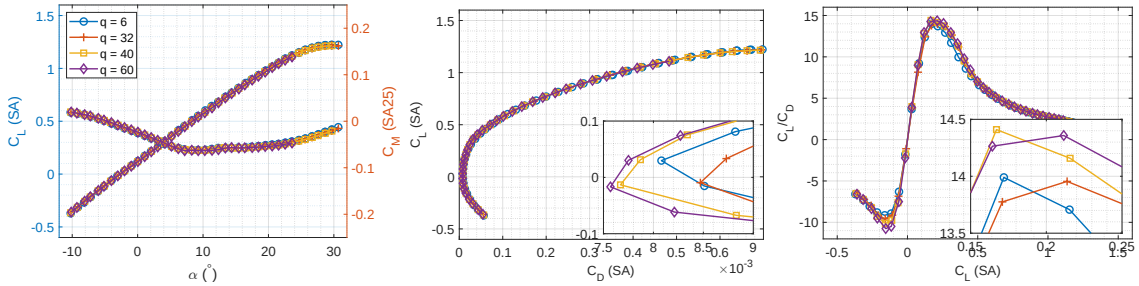
Analysis of and insights from the results of the many wind tunnel tests carried out so far are not within the scope of this test-effort overview chapter. A few general notes can be made, however, based on the sample test results shown here. Beyond relatively small angles of attack the lift and pitching moment are, not surprisingly, nonlinear - the results of leading edge vortices, vortex lift, vortex breakdown, and the sensitivity of pitching moments to even slight changes in pressure distributions due to the slenderness of the configuration and the large moment arms involved.

As has been presented already, the configurations developed, wind tunnel tested, and flown by the University of Washington, while representative of supersonic configuration planforms, were not always representative of airfoil shapes. In some cases moderate RUAV t/c increases were made to accommodate model construction, in what would be "razor-sharp" biconvex outboard supersonic leading edges on the full-scale aircraft that may have used thin NACA 64 series sections on the models (similar to fighters like F-15). LE vortices

created by the models tested so far, while generating the expected large scale vortex systems, may be more sensitive airfoil shape to effects that may slightly shift the LE vortices in the chordwise direction.

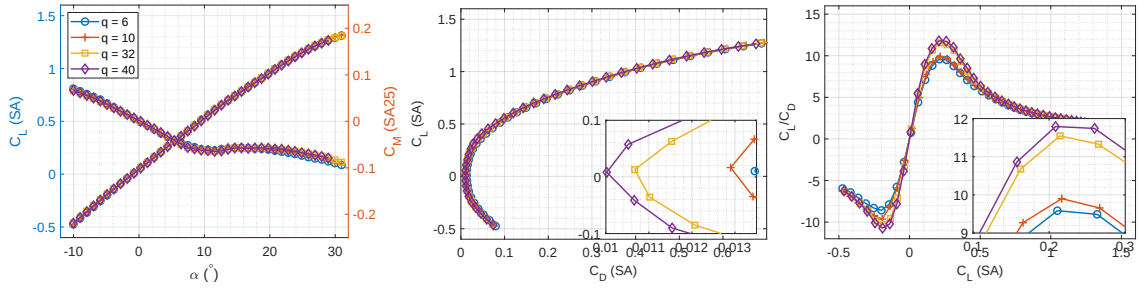
The models did capture the fundamental physics of the flow over cranked-delta wing configurations with long fuselages: the interaction of the vortices generated by the inner and outer wing sections, possible asymmetries created by the vortex system, the effects of the forward fuselage and the canard and tails. Coupling between longitudinal effects and lateral-directional effects was also captured, including rolling due to vortex system asymmetries as generated by the fuselage and the differences between right and left vortex systems.

For example, Figures 2.58 show that dynamic pressure variation does not have significant effects on the UW-S-20A aerodynamic behavior up to angles of attack of about $\alpha \approx 13°$. Beyond this angle of attack, although lift and drag do not vary significantly with varying the dynamic pressure, both pitching and rolling moments are seen to be affected, which could be attributed by the asymmetrical vortex breakdown/bursting and burst movement over various parts of the model. Figure 2.56 shows that dynamic pressure does not have effects on the lift and pitching moment of the 2015 wing alone (W15) model.



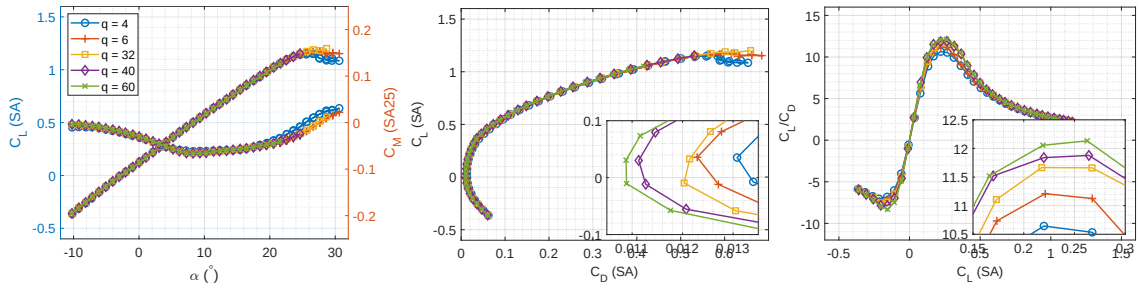
(a) C_L & C_M vs α (b) drag polar (c) L/D vs C_L

Figure 2.56: Effects of dynamic pressure and Reynolds number for 2015 wing alone



(a) C_L & C_M vs α (b) drag polar (c) L/D vs C_L

Figure 2.57: Effects of dynamic pressure and Reynolds number for wing and aft-deck



(a) C_L & C_M vs α (b) drag polar (c) L/D vs C_L

Figure 2.58: Effects of dynamic pressure and Reynolds number for wing and fuselage

2.5 Aerodynamic Database

This section briefly summarizes the SCALOS aerodynamic database, which is a collection of the wind tunnel test results from 2015 to 204 for the various SCALOS configurations and test conditions. It is provided for the self-containedness of this dissertation and to give the readers a high-level overview of the database, which is the basis for the aerodynamic analysis in the following sections and as part of the contribution of this dissertation. The detailed documentations of the database are available in [373–376], and the database itself is available by request to NASA

2.5.1 Data Structure

This section describes the SCALOS data package and guides the user regarding information look up. The data folder and data reduction information is omitted. Interested readers should refer to [373] for details. The following is the directory tree of the SCALOS data package.

```
SCALOS Data Package
├── DATA CSV
├── DATA REDUCTION
├── DOCUMENTATION
├── RUN LOG
├── UWXXXX
└── SCALOS_README.pdf
```

The SCALOS data package includes 17 subfolders with 13 test entries folders. For simplicity, `XXXX` in the directory refer to the test entry number in Tab. 2.30 in §2.4.4 where there should be 13 duplicates for `UWXXXX` folders and files in both `CSV` and `RUN LOG`. The rest of the section is divided into subsections corresponding to each subfolder of the directory tree. The order of folders is reorganized for "reader-friendliness" instead of alphabetically.

DOCUMENTATION

```
SCALOS Data Package
└── DOCUMENTATION
    ├── SCALOS_USERGUIDE.pdf[373]
    ├── SCALOS_DR.pdf[374]
    ├── SCALOS_GEOMETRY.pdf[375]
    ├── SCALOS_PARTS.pdf[376]
    └── CADP Geometry Definition
```

The `DOCUMENTATION` folder contains this user guide with additional detailed information on user guide, part list, geometry, and data reduction [373–376]. The part geometries are shown in §2.4.3 with additional different reference wing platforms and CG locations in [375]. The part list and designation are introduced in subsequent subsection in §2.5.2 with detailed compatibility and photo log in [376]. The standard UWAL data name in corresponding data reduction processes are shown in §2.5.5 with detailed assumptions and equation formulations in [374].

RUN LOG

```
SCALOS Data Package
└── RUN LOG
    ├── Autosort Run Log XXXX Update.xlsx
    └── Autosort Run Log SCALOS.xlsx
```

The `Autosort Run Log XXXX Update.xlsx` converts all the original test entry designa-

tions to SCALOS designation in §2.5.2. The `Autosort Run Log SCALOS.xlsx` concatenates all the `Autosort Run Log XXXX Updated.xlsx` into a single file such that all the run information from SCALOS program is in a single file.

DATA CSV

```
SCALOS Data Package
└── DATA CSV
    ├── finaldata_SCALOS.xlsx
    └── finaldata_uwXXXX.xlsx
```

The `finaldata_uwxxxx.xlsx` is the final data file in CSV format after data reduction processes, containing all the variables in §2.5.5. The `finaldata_SCALOS.xlsx` concatenates all the `finaldata_uwxxxx.xlsx` into a single file.

2.5.2 Part Designations and Part List

This section defines all the parts and corresponding designations that were used in the SCALOS program. This section contains the minimum part information for the users to read the run log in §2.5.4. Interested readers should refer to [376] for detailed part information and photolog. Table. 2.31 defines the part destinations which is consisted of the designation and the manufactured year. The designation after '.' is either the made version, the mount location, or the alternate version. Some examples of baseline models built up are shown in Tab. 2.32 here and Tab. 2.12 in §2.2.

Table 2.32: SCALOS table of model configuration variations tested (2020-24)

Designation	Forebody	Aft-body	Wing	Aft-deck	Nacelle	Vertical tail	Horizontal tail	Canard	Additional
UW-S-20A	F15	A20	W20		N20.T	V20	H20.T	C15.F	
UW-S-20CL	F15.L	A20	W20	NSRD	N20.T	V20	H20.T	C15.F	OG + strake
UW-S-21A	F15	A15	W15		N20.B	V15	H20.L	C15.F	DF.1 + VF.1
UW-S-23E	F15.L	A18	W20	AD16	N18	V23		C15.F	NC + OG + strake
UW-S-23G	F15	A16	W15	AD16	N23.BR	V16T.2	H18	C15.F	
UW-S-24A	F24	A24	W15		N20.B	VF.1	H24	C15.F	

All the control surface deflection capabilities are tabulated in Table 2.33.

Note for Table 2.33,

1. The inboard leading edges (LEIB) and inboard trailing edges (TEIB) are communi-

Table 2.31: SCALOS part designations

Designation	Description	Designation	Description
W	Wing	F	Forebody fuselage
AD	Aft-deck	A	Aft-body fuselage
IB	Inboard	U	Upper
OB	Outboard	D	Downward/lower
LE	Leading Edge	L	Long/extended
TE	Trailing Edge	N	Nacelles
LEIB	Leading Edge Inboard	P	Nacelle Paddles
ALT	Alternative concept leading edge	E	Nacelle Electric ducted fans
OG	Ogive	T	Top
S	Sharp leading edge	B	Bottom
MVR	Morphing-variable-radius leading edge	NSRD	Nacelle Shock Reflected Deck
LEOB	Leading Edge Outboard	TR	Top rear
SS	Sealed-Slate leading edge	BR	Bottom rear
FP	Flex-Panel leading edge	H	Horizontal tail
TEIB	Trailing Edge Inboard ≡ Flaps	V	Vertical tail
SF	Splitter Flap	DF	Dorsal Fin
FS	Mid-chord Flap spoilers	VF	Ventral Fin
TEAD	Trailing Edge Aft-Deck	WTD	Wing leading edge Trip Dots
TEOB	Trailing Edge Outboard ≡ Ailerons	NRTD	Nose Ring Trip Dots
AS	Aileron Spoiler	FTD	Forbody trip dots
SSD	Spoiler-Slot Deflector	FTDEX	Forebody Trip Dots Extended
CS	Clam-shell spoilers	FTDEX2	Forebody Trip Dots Extended from nose ring
WR	Wingtip Rudders	HTD	Horizontal stabilizer Trip Dots
WRD	Wingtip Rudders Deflection	NB	Fuselage Nose Boom
RT	Raked Wingtip	NC	Nose Chine
WF	Wing fence	NM	Nose Modification
ICE	Icing on wing leading edges	SM	Sheet Metal
C	Canard	LG	Landing Gears
CF	Canard Fairings	FD	Flight deck/cockpit
MS	Metal spine		

tative but not outboard (LEOB and TEOB). The exceptions are between W17 and W18 and between W15 and W13.5.

2. The flap and aileron are defined as inboard trailing edge (TEIB) and outboard trailing edge (TEOB), respectively.

3. All the sheet metal sleeves on parts have the deflection capability as the on parts including canard, vertical, and horizontal tails.

4. Note that a bias reference angle (Δ) was discovered toward the end of the SCALOS program. All the run logs are updated with the bias angle. The H15 and H15A.2 have a bias angle of $\Delta = +2^\circ$ and all the metal sleeves on H15 are assumed to be impacted

by the bias angle including H15A, H15A.1, H20.L, and H20L.2. The H20L.2, H20.M, H20.T, and H24 have a bias angle of $\Delta = +0.4°$.

Table 2.33: SCALOS control surfaces and deflections

	Designation	Deflections
Wing inboard leading edge	LEIB15	0°, +15°, +30°
(LEIB)	LEIB15.1	0°, +15°, +30°
	LEIB17	30°
	LEIB17.ALT	0°
	LEIB17.MVR	30°
	LEIB18	0°, +30°
	LEIB20.ALT	0°, +12°, +57°
	LEIB20.OG + Strake	0°
	LEIB23.S	0°
	LEIB23.MVR	30°
	LEIB24.MVR	30°
Wing inboard trailing edge	TEIB15.SM	0°, +32°
(flap ≡ TEIB)	TEIB15	0°, +15°, +30°
	TEIB13.5	0°
	TEAD24	0°, ±15°
Wing outboard leading edge	LEOB15	0°, +15°, +30°
(LEOB)	LEOB15.SS	+15°, +25°
	LEOB15.FP	+30°
	LEOB17	0°, +30°
	LEOB18	0°
	LEOB18.SM	+30°
	LEOB20	0°, +15°, +30°
	LEOB20.OG	0°
	LEOB23	0°, +15°, +30°
Wing outboard trailing edge	TEOB15.SM	±10°, +20°
(aileron ≡ TEOB)	TEOB15	0°, ±10°, ±25°
	TEOB15.R	±10°, ±25°
	TEOB13.5	0°
	TEOB17	0°, ±10°, ±20°
	TEOB20	0°, ±10°, ±25°
	TEOB20.R	±10°, ±25°
	TEOB20.AS21	−60°
	TEOB20.SSD21	±60°
	TEOB20.SSD23	±67°
	TEOB23	0°, ±10°, ±20°
Vertical tail (rudder)	V15	0°
	V15.1	0°, +10°, +25°
	V16/V16.1	0°, +20°, +30°
	V17/V17.1	0°, +10°, +20°
	V18/V18.1/V18.2	0°, +10°, +20°
	V20	0°, +10°, +20°
	V16T.2/V16T.3	0°
	V23	0°, ±10°, −20° , −30°
Horizontal tail (all-moving)	H15/H15A/H20.L/H15A.1/H20L.1	0°, ±5°, ±10°, ±15°, ±20°, ±25°, ±30° (+2.0°)
	H15A.2	0°, ±5°, ±10°, ±15°, ±20°, ±25°, ±30° (+2.0°)
	H20L.2	0°, ±5°, ±10°, ±15°, ±20°, ±25°, ±30° (+0.4°)
	H16/H17.1/H17.2	0°, −2.5°, ±5°, −10°, ±15°, −30°

Continued on next page

Table 2.33 – continued from previous page

	Designation	Deflections
	H18	$0°, -5°, \pm10°, \pm20°, -30°$ $0°, +10°, -20°, -30°$
	H20.M, H20.T	$0, \pm5, \pm10, \pm15$ $(+0.4°)$
	H24	0 $(+0.4°)$
Canard (all-moving)	C15/C15.2/C15.1/C17/C17D.1/C17D.2/C23/C23.1	$0°, \pm5°, \pm10°, \pm15°, \pm20°, \pm25°, \pm30°$
Additional	FS21	$\pm60°$
	CS21	$-60°$

2.5.3 Model Geometry

The model geometry and planform variations are presented in §2.4.3. This section provides additional information following the previous §2.5.2 part definitions and designations. The outboard wings, canards, vertical and horizontal tails, and inboard and outboard leading edges geometry are tabulated in Tab. 2.27 and shown in Fig. 2.49. The Λ is the sweep angle, the Γ is the dihedral angle with positive upward, and the t/c_{max} is the maximum thickness to chord ratio. The span, MAC, reference wing area, and aspect ratio of each planform and control surface are defined the same as in §2.4.3. The l and d are the length and diameter, respectively, for the fuselages and nacelles. The $S_{\text{wet, ext}}$, $S_{\text{wet, int}}$, and S_{f} are the exterior wetted area, interior wetted area, and maximum frontal body cross-section area defined for the fuselages and nacelles. It is important to note again that all the SCALOS data are referenced/normalized with respect to the W15 (Table 2.28) for comparison purposes. Interested readers should refer to [375] for additional reference geometry and C.G locations.

2.5.4 Run Log

This section details the run log information. Table. 2.34 tabulates all the information of the updated auto-sorted files for `Autosort Run Log XXXX Update.xlsx` and `Autosort Run Log SCALOS.xlsx` in §2.5.1. Note that the `Run Log XXXX.xlsx` in each test folder are in their original test entry documentation such that it may differ from Tab. 2.34. The configuration is the model composition of the part destinations in §2.5.2, i.e in Tab. 2.32. All the tested configurations are tabulated in Tab. 2.8–2.18 in §2.2.

Table 2.34: SCALOS Run log variables

Run log Variables	Units	Description	Reference and examples
TEST		Test number	Test entry designated by KWT as in Tab. 2.30
RUN		Run number	Run number in test entry
TARE		Weight tare run number	Wind-off three-point weight tare run
CONFIGURATION		Model configuration	Part destination from §2.5.2 and more in [373, 377]
TYPE OF RUN		Force and moment measurement or flow visualization	Run types include WT, P6, Y6, Q6, and Flow Viz
α	(°)	Angle of attack	$-12^\circ \leq \alpha \leq +32^\circ$
Ψ	(°)	Angle of yaw	$-22^\circ \leq \alpha \leq +22^\circ$
q_{nom}	(psf)	Dynamic pressure	The nominal dynamic pressure, QNOM in §2.5.5.
LE IB	(°)	Leading edge inboard deflection	Part deflections in Tab. 2.33 in §2.5.2
LE OB	(°)	Leading edge outboard deflection	Part deflections in Tab. 2.33 in §2.5.2
TE IB L	(°)	Trailing edge inboard left deflection (left flap)	Part deflections in Tab. 2.33 in §2.5.2
TE IB R	(°)	Trailing edge inboard right deflection (right flap)	Part deflections in Tab. 2.33 in §2.5.2
TE OB L	(°)	Trailing edge outboard left deflection (left aileron)	Part deflections in Tab. 2.33 in §2.5.2
TE OB R	(°)	Trailing edge outboard right deflection (right aileron)	Part deflections in Tab. 2.33 in §2.5.2
STAB L	(°)	All-movable horizontal tail left deflection	Part deflections in Tab. 2.33 in §2.5.2
STAB R	(°)	All-movable horizontal tail right deflection	Part deflections in Tab. 2.33 in §2.5.2
RUD	(°)	Vertical tail rudder deflection	Part deflections in Tab. 2.33 in §2.5.2
CAN	(°)	All-movable canard deflection	Part deflections in Tab. 2.33 in §2.5.2
MOD L	(°)	Modified parts left deflection	Part deflections in Tab. 2.33 in §2.5.2
MOD R	(°)	Modified parts right deflection	Part deflections in Tab. 2.33 in §2.5.2
N PADDLE	(°)	Nacelle exit paddles deflection	In UW2128 only only
N EDF POWER	(%)	Nacelle electric ducted fans power percentage	In UW2128 only only
N BLK L	(%)	Nacelle left exit area reduction percentage	In UW2166 and UW2331 only
N BLK R	(%)	Nacelle right exit area reduction percentage	In UW2166 and UW2331 only
TRIP DOTS		Trip dots definition	Trip dots types defined in [373, 377]
LE IB DEF		Leading edge inboard definition	Part definition in Tab. 2.33 in §2.5.2
LE OB DEF		Leading edge outboard definition	Part definition in Tab. 2.33 in §2.5.2
TE IB L DEF		Trailing edge inboard left definition	Part definition in Tab. 2.33 in §2.5.2
TE IB R DEF		Trailing edge inboard right definition	Part definition in Tab. 2.33 in §2.5.2
TE OB L DEF		Trailing edge outboard left definition	Part definition in Tab. 2.33 in §2.5.2
TE OB R DEF		Trailing edge outboard right definition	Part definition in Tab. 2.33 in §2.5.2
MOD L DEF		Modified parts left definition	Part definition in Tab. 2.33 in §2.5.2
MOD R DEF		Modified parts right definition	Part definition in Tab. 2.33 in §2.5.2
T&I STATUS		Model mounting position	Upright, inverted, or inverted with image strut.
FLOW VIS L		Flow visualization on the left of model	Flow visualization methods
FLOW VIS R		Flow visualization on the right of model	Flow visualization methods
NOTE		Additional notes	Comments in run log or run log notes files in §2.5.1
REC ALPHA	(°)	Recommended α adjustment	Adjustment are made for UW2354 in the EU files.
DATE		Date of data collection	MM/DD/YYYY

2.5.5 Data Reduction and Standard UWAL Data Names

Refs. [17–19, 374] describe the sequence of corrections used by the KWT. The full data reduction progress is shown, in the block diagram, in Fig. 2.59. It is based on well-known and widely used techniques [455] for correcting measured low-speed wind tunnel data and on decades of testing. The data correction processes are as follows:

1. The raw data is measured by the external balance and collected by the data acquisition

where the system, balance, alpha, and psi calibration are performed by the Kirsten Wind Tunnel and the wind off zero (WOZ) is subtracted from the balance data.

2. The mechanical interaction of forces and moments in the balance system is corrected based on balance calibration.

3. The corrections for all tare and inference (T&I) are applied, including strut, nacelles, and weight tares.

4. Moments are then transferred from the balance moment center (BMC) to the model moment center (MMC).

5. Corrections for blockage, flow angularity, and wall effects are computed and added to the initial coefficients.

6. The corrected coefficients are transferred from wind axes to stability and body axes.

The SCALOS program has additional nacelle interference correction in step 2 and nacelle interior drag, wing laminar flow, and horizontal laminar flow corrections in step 5. There are small physical area and MAC variations among different wing planforms. In the SCALOS data set, all data are non-dimensionalized for comparison purposes with respect to the test letter value of the 2015 wing (W15) in Tab. 2.28. Interested readers should refer to geometry documentation for specific planform values for conversions [375]. The corrections apply to all tests in Tab. 2.30. This document omits the lengthy data correction process and refers interested readers to [374].

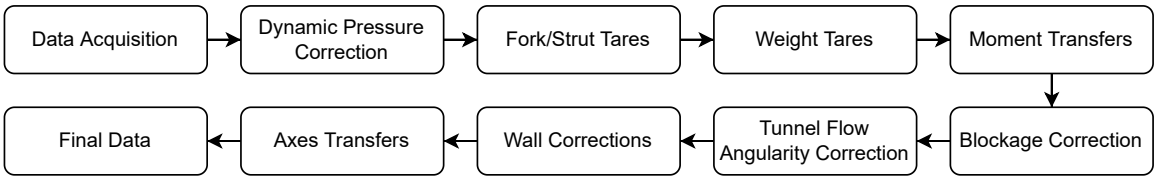
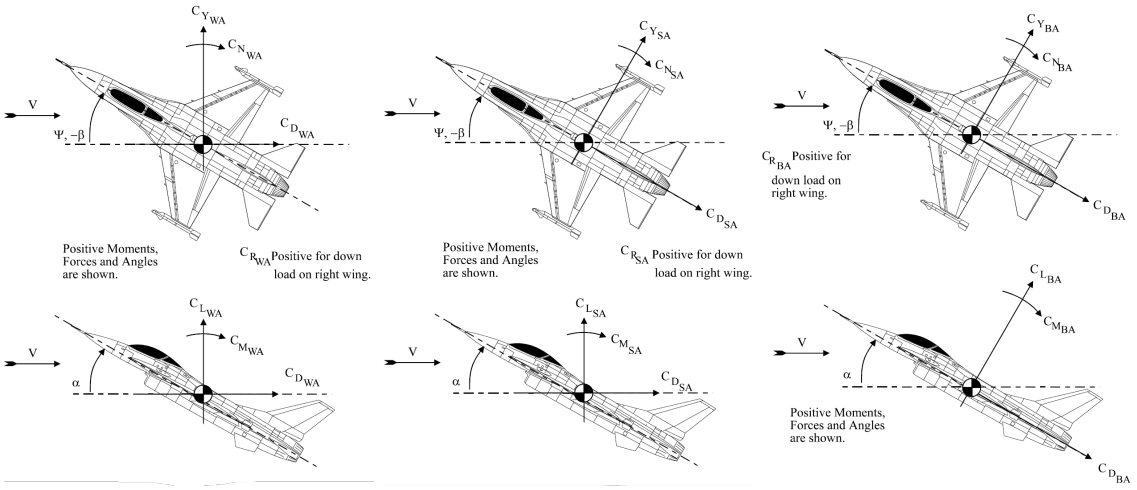


Figure 2.59: KWT Data Reduction Flow Chart [18]

The final corrected data are in coefficients form in three different systems of axes: wind, stability, and body. The wind axis coefficients are transferred to other axes based on α_C

and ψ in Fig. 2.60. Eqs. (2.1) and (2.2) transfer the wind axis coefficients to the stability axis. An additional variable of LOD is defined as the lift-over-drag ratio in the stability axes in Eq. (2.3). Eqs. (2.4) and (2.5) transfer wind and stability axis coefficients to the body axis. Note that the standard KWT correction uses the initial angle of attack without wall and upflow correction (α_I) in Eqs. (2.4) and (2.5), while the SCALOS program uses the corrected angle of attack (α_C) for axis transform in Eq. (2.6).



(a) Wind axis (b) Stability axis (c) Body axis

Figure 2.60: Axis coordinate system [17]

$$\begin{bmatrix} \text{CLSA} \\ \text{CDSA} \\ \text{CYSA} \end{bmatrix} = \begin{bmatrix} \text{CLWA} \\ \cos(\psi)\text{CDWA} - \sin(\psi)\text{CYWA} \\ \sin(\psi)\text{CDWA} + \cos(\psi)\text{CYWA} \end{bmatrix} = \begin{bmatrix} 1 & 0 & 0 \\ 0 & \cos(\psi) & -\sin(\psi) \\ 0 & \sin(\psi) & \cos(\psi) \end{bmatrix} \begin{bmatrix} \text{CLWA} \\ \text{CDWA} \\ \text{CYWA} \end{bmatrix} \tag{2.1}$$

$$\begin{aligned} \begin{bmatrix} \text{CNSAXX} \\ \text{CRSAXX} \\ \text{CMSAXX} \end{bmatrix} &= \begin{bmatrix} \text{CNWAXX} \\ \cos(\psi)\text{CRWAXX} + \frac{\bar{c}}{b_{\text{ref}}}\sin(\psi)\text{CMWAXX} \\ -\frac{b_{\text{ref}}}{\bar{c}}\sin(\psi)\text{CRWAXX} + \cos(\psi)\text{CMWAXX} \end{bmatrix} \\ &= \begin{bmatrix} 1 & 0 & 0 \\ 0 & \cos(\psi) & \frac{\bar{c}}{b_{\text{ref}}}\sin(\psi) \\ 0 & -\frac{b_{\text{ref}}}{\bar{c}}\sin(\psi) & \cos(\psi) \end{bmatrix} \begin{bmatrix} \text{CNWAXX} \\ \text{CRWAXX} \\ \text{CMWAXX} \end{bmatrix} \end{aligned} \tag{2.2}$$

$$\mathrm{LOD} = \frac{\mathrm{CLSA}}{\mathrm{CDSA}} \tag{2.3}$$

$$\begin{aligned}
\begin{bmatrix} \mathrm{CLBA} \\ \mathrm{CDBA} \\ \mathrm{CYBA} \end{bmatrix} &= \begin{bmatrix} \cos(\psi)\sin(\alpha_C)\mathrm{CDWA} - \sin(\psi)\sin(\alpha_C)\mathrm{CYWA} + \cos(\alpha_C)\mathrm{CLWA} \\ \cos(\psi)\cos(\alpha_C)\mathrm{CDWA} - \sin(\psi)\cos(\alpha_C)\mathrm{CYWA} - \sin(\alpha_C)\mathrm{CLWA} \\ \sin(\psi)\mathrm{CDWA} + \cos(\psi)\mathrm{CYWA} \end{bmatrix} \\
&= \begin{bmatrix} \cos(\alpha_C) & \sin(\alpha_C) & 0 \\ -\sin(\alpha_C) & \cos(\alpha_C) & 0 \\ 0 & 0 & 1 \end{bmatrix} \begin{bmatrix} \mathrm{CLSA} \\ \mathrm{CDSA} \\ \mathrm{CYSA} \end{bmatrix} \\
&= \begin{bmatrix} \cos(\alpha_C) & \sin(\alpha_C) & 0 \\ -\sin(\alpha_C) & \cos(\alpha_C) & 0 \\ 0 & 0 & 1 \end{bmatrix} \begin{bmatrix} \mathrm{CLWA} \\ \cos(\psi)\mathrm{CDWA} - \sin(\psi)\mathrm{CYWA} \\ \sin(\psi)\mathrm{CDWA} + \cos(\psi)\mathrm{CYWA} \end{bmatrix} \\
&= \begin{bmatrix} \cos(\alpha_C) & \sin(\alpha_C) & 0 \\ -\sin(\alpha_C) & \cos(\alpha_C) & 0 \\ 0 & 0 & 1 \end{bmatrix} \begin{bmatrix} 1 & 0 & 0 \\ 0 & \cos(\psi) & -\sin(\psi) \\ 0 & \sin(\psi) & \cos(\psi) \end{bmatrix} \begin{bmatrix} \mathrm{CLWA} \\ \mathrm{CDWA} \\ \mathrm{CYWA} \end{bmatrix}
\end{aligned} \tag{2.4}$$

$$\begin{aligned}
\begin{bmatrix} \mathrm{CNBAXX} \\ \mathrm{CRBAXX} \\ \mathrm{CMBAXX} \end{bmatrix} &= \begin{bmatrix} \cos(\psi)\sin(\alpha_C)\mathrm{CRWAXX} + \frac{\bar{c}}{b_{\mathrm{ref}}}\sin(\psi)\sin(\alpha_C)\mathrm{CMWAXX} + \cos(\alpha_C)\mathrm{CNWAXX} \\ \cos(\psi)\cos(\alpha_C)\mathrm{CRWAXX} + \frac{\bar{c}}{b_{\mathrm{ref}}}\sin(\psi)\cos(\alpha_C)\mathrm{CMWAXX} - \sin(\alpha_C)\mathrm{CNWAXX} \\ -\frac{b_{\mathrm{ref}}}{\bar{c}}\sin(\psi)\mathrm{CRWAXX} + \cos(\psi)\mathrm{CMWAXX} \end{bmatrix} \\
&= \begin{bmatrix} \cos(\alpha_C) & \sin(\alpha_C) & 0 \\ -\sin(\alpha_C) & \cos(\alpha_C) & 0 \\ 0 & 0 & 1 \end{bmatrix} \begin{bmatrix} \mathrm{CNSAXX} \\ \mathrm{CRSAXX} \\ \mathrm{CMSAXX} \end{bmatrix} \\
&= \begin{bmatrix} \cos(\alpha_C) & \sin(\alpha_C) & 0 \\ -\sin(\alpha_C) & \cos(\alpha_C) & 0 \\ 0 & 0 & 1 \end{bmatrix} \begin{bmatrix} \mathrm{CNWAXX} \\ \cos(\psi)\mathrm{CRWAXX} + \frac{\bar{c}}{b_{\mathrm{ref}}}\sin(\psi)\mathrm{CMWAXX} \\ -\frac{b_{\mathrm{ref}}}{\bar{c}}\sin(\psi)\mathrm{CRWAXX} + \cos(\psi)\mathrm{CMWAXX} \end{bmatrix} \\
&= \begin{bmatrix} \cos(\alpha_C) & \sin(\alpha_C) & 0 \\ -\sin(\alpha_C) & \cos(\alpha_C) & 0 \\ 0 & 0 & 1 \end{bmatrix} \begin{bmatrix} 1 & 0 & 0 \\ 0 & \cos(\psi) & \frac{\bar{c}}{b_{\mathrm{ref}}}\sin(\psi) \\ 0 & -\frac{b_{\mathrm{ref}}}{\bar{c}}\sin(\psi) & \cos(\psi) \end{bmatrix} \begin{bmatrix} \mathrm{CNWAXX} \\ \mathrm{CRWAXX} \\ \mathrm{CMWAXX} \end{bmatrix}
\end{aligned} \tag{2.5}$$

$$\alpha_C = \alpha_I + \Delta\alpha_{wc} + \Delta\alpha_{\text{UPFLOW}} \tag{2.6}$$

2.6 Tare and Interference Correction

This section describes the T&I tests that were carried out and presents comparisons of newly established test-based T&I corrections for the different configurations tested and the standard KWT corrections from [19]. The results presented in this section are updated with the latest data reduction and analysis, which may differ from the results presented in [19]. A note to the reader: The present section completes the presentation of the testing effort and the data extraction techniques that were used. To get directly to the test results and the insights and lessons they lead to, the reader may skip this section and go directly to 2.7.

Models can be supported in the test section of the KWT in two ways. The most often used is the main KWT balance, located under the floor of the test section. A vertical strut from the balance into the test section supports the models [456]. The models are mounted on an adaptor that connects the model to the strut. A two-point connector and a three-point "fork" connector can be used. A pylon (an aerodynamic fairing shell) covers the strut up to quite close to the model/adapter attachment. The strut and pylon assembly can be removed to allow the use of a floor-mounted turntable for half-model testing on the main under-floor balance. The wind tunnel also has a sidewall balance [457].

As with any wind tunnel test, certain "corrections" have to be applied to the measured data in order to produce estimates of the aerodynamic characteristics of the model in free flight. In the low-speed cases, such corrections include corrections for test section blockage, the effects of the test section walls, test section flow angularity, buoyancy, and various corrections that are specific to the balance and its mechanics of converting loads on the model to balance measurements. Weight tares must be accounted for. Another important correction that must be applied to the measurements, a correction for the effects of the model support system, known as the tare & interference (T&I) correction.

The support system affects the measurements in two ways. It changes the flow field by the presence of its geometry. Because a part of it is supported by the balance, balance

measurements also include aerodynamic forces on the support system itself. In the case of the KWT support system, the strut and adapter in the flow field transfer to the balance aerodynamic loads due to their own geometry. These aero forces on the support can also be altered by flow field changes induced by the presence of the model.

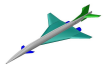
Reference [455] is a classic book on low-speed wind tunnel testing detailing wind tunnel corrections. Traditionally, the corrections are applied sequentially, one by one, to allow insight into the process and evaluations of the sensitivity of the results to the different corrections. Each wind tunnel has its own "standard corrections", developed, usually, over years of dedicated tests and aerodynamic simulations. While, ideally, dedicated corrections may be desired for each new particular configuration and test conditions, this would make wind tunnel tests of aircraft configurations extremely expensive, and so the "standard" corrections a wind tunnel has would usually be used for scoping and developmental testing, until a final design needs exact quantitative evaluation. Desirably, of course, the tunnel would develop such "standard" corrections over time to apply to a wide range of configuration shapes on commonly used model supports that would cover the range of configurations that the tunnel would test for customers.

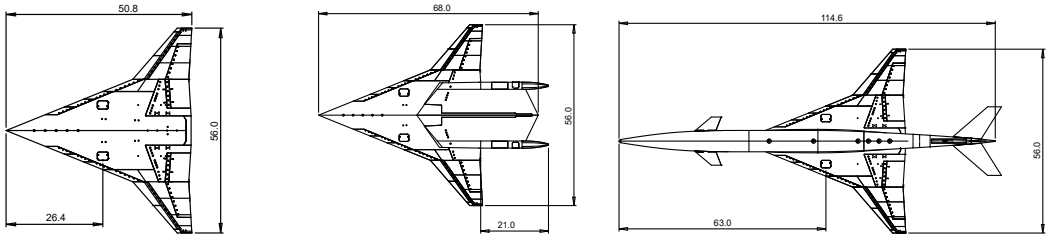
For quite some time, based on KWT test results for various supersonic commercial configurations at the UW over the years, a concern grew that the "standard" T&I KWT corrections did not apply in an accurate enough way to the geometries that were tested. Studying the history of how the "standard" KWT T&I corrections were developed for the three-point "fork" adapter that was used to support the models in all SCALOS tests (details in subsequent sections), it was found that a combination of dedicated T&I tests for the fork type support system were carried out years ago using a medium aspect ratio rectangular wing and a specially designed disk – both mounted on the fork adapter and tested in the KWT. The SCALOS configurations, with their large center-wing area over the fork, strut, pylon, and long fuselages, are much different, especially in terms of the model lifting surface geometry relative to the supports.

2.6.1 Tested T&I Configurations

Following the work of [18], it was deemed desirable to test a full configuration that included a wing-body-tail-canard configuration and one representative of an alternate concept presenting different lift distribution and total area, which included a large aft-deck extension to the main wing platform. The three model configurations chosen for T&I measurements are shown in Tab. 2.35. Table 2.27 presents key geometric information about the configurations and their year of fabrication and component designations are defined in §2.5.2. The tested models in Tab. 2.35 are shown in the top view in Fig. 2.61 with key dimensions.

Table 2.35: Configurations studied for T&I [19]

Figure	Designation	Forebody	Aft-body	Wing	Aft-deck	Nacelle	Vertical tail	Horizontal tail	Canard	Additional
				W15						
				W15	AD16					
		F15	A15	W15			V15	H20.L	C15.F	DF.1 + VF.1
	UW-S-21A	F15	A15	W15		N20.B	V15	H20.L	C15.F	DF.1 + VF.1



(a) Wing only (W15) (b) Wing and aft-deck (W15+AD16) (c) UW-S-21A without nacelles

Figure 2.61: Top view of tested configurations with selected dimensions [19]

2.6.2 Testing to Establish T&I Corrections

The primary balance below the floor of the test section measures loads on both the wind tunnel model and the part of the support strut in the test section that is exposed to the flow. It does not measure any forces on the floor pylon that functions as an aerodynamic fairing that is not connected to the model or strut. The balance also measures forces on the model and the support structure in the test section that include aerodynamic interference between the model and the strut and pylon: the aerodynamic effect of the support structure on the model and the effect of the model on the aerodynamics of the support structure. The T&I correction depends on the wind tunnel used, the type of the support structure used, the geometry of the tested model, and the type of balance (whether it is external or internal to the model).

Methodology

The sequence of steps is illustrated in Fig. 2.62 and are described as follows:

(a) Test the model in its upright position on the fork. The fork is attached to the model from below (a "low" fork). Measured forces and moments are only those transferred to the primary KWT balance below the test section. In this step the balance measures the forces on the model plus the forces on the exposed part of the fork. The forces on the model include the "pure" model-only forces (M_M, no support effects), the forces on the model due to interference by the fork (M_F), and the forces on the model due to interference by the pylon (M_P). Similarly, the forces on the fork are by the "pure" fork (F_F, no model effects), the forces on the fork due to interference by the model (F_M), and the forces on the fork due to interference by the pylon (F_P). Then:

$$BL_{\text{step-a}} = M_M + M_{LF} + M_{LP} + F_{LF} + F_{LM} + F_{LP} \tag{2.7}$$

where $BL_{\text{step-a}}$ is the load measured by the balance with balance interaction correction in T&I test step a; M_{LF} and M_{LP} are the balance loads due to the aerodynamic effect of the lower fork and pylon on the model; F_{LF} is the load on the lower fork by itself

(no model), and F_{LM} and F_{LP} are the balance loads due to the interference effects of the model and pylon on the lower fork, respectively.

(b) Test the same configuration upside down (inverted) on the "lower" fork.

In the second step, the model is upside down on the floor fork and pylon. This is the same as mounting the model from above and measuring the loads on the model supported by pylon and fork from above. The loads measured by the balance now are:

$$BL_{\text{step-b}} = M_M + M_{UF} + M_{UP} + F_{UF} + F_{UM} + F_{UP} \tag{2.8}$$

where $BL_{\text{step-b}}$ is the load measured by the balance in T&I configuration b; M_{UF} and M_{UP} are the loads on the model due to the aerodynamic interference by fork and pylon from above; and F_{UM}, and F_{UP} are the loads on the upper fork due to the aerodynamic effects of the model and upper pylon. The aerodynamic effects of the upper pylon on the upper fork loads in step b is approximated to be the same as the effects of the lower pylon on the lower fork loads in step a. That is,

$$F_{LP} = F_{UP} = F_P. \tag{2.9}$$

Thus, Eqs. (2.7) and (2.8) become

$$BL_{\text{step-a}} = M_M + M_{LF} + M_{LP} + F_{LF} + F_{LM} + F_P \tag{2.10}$$

$$BL_{\text{step-b}} = M_M + M_{UF} + M_{UP} + F_{UF} + F_{UM} + F_P \tag{2.11}$$

(c) Test the same configuration upside down (inverted) on the "lower" fork with the addition of a dummy pylon and support system from above.

In the third step, the configuration is mounted in the inverted position on the lower fork with in addition of a dummy pylon and support system from above mirrored the support system above and below, without the actual support from the floor of the inverted model would simulate, by hanging from the ceiling, the support on the floor fork and pylon of the model in the upright position of step a. The dummy fork from

above is connected to the model transferring the loads acting on it to the below-the-floor pylon. Note that it is **not** structurally connected to the pylon above. The top fork is free to move inside the dummy pylon so it does not transfer any force from the top fork to the top pylon. The balance now measures the forces acting on the model and the two forks that are attached to it. The loads measured by balance are now due to the model, lower fork, upper fork, and the interference effects among these three components plus the interference effects due to both pylons. The loads on the pylons are not transferred to the balance.

$$\begin{aligned} BL_{\text{step-c}} =& M_M + M_{LF} + M_{LP} + M_{UF} + M_{UP} + F_{LF} + F_{LM} \\ &+ F_{LP} + F_{LUFP} + F_{UF} + F_{UM} + F_{UP} + F_{ULFP} \\ =& M_M + M_{LF} + M_{LP} + M_{UF} + M_{UP} + F_{LF} + F_{LM} \\ &+ F_P + F_{LUFP} + F_{UF} + F_{UM} + F_P + F_{ULFP} \end{aligned} \tag{2.12}$$

where F_{ULFP} and F_{LUFP} are the balance loads due to the upper fork as affected by interference by the lower fork and pylon, and the loads due to the lower fork as affected by interference by the upper fork and pylon, respectively. The aerodynamic interference effects of the lower pylon and fork on the upper pylon and fork and vice versa are assumed to be negligible.

$$F_{ULFP} = F_{LUFP} = 0 \tag{2.13}$$

By adding Eqs. (2.10) and (2.11) and subtracting Eq. (2.12), given Eq. (2.13) leads to:

$$M_M = BL_{\text{step-a}} + BL_{\text{step-b}} - BL_{\text{step-c}} \tag{2.14}$$

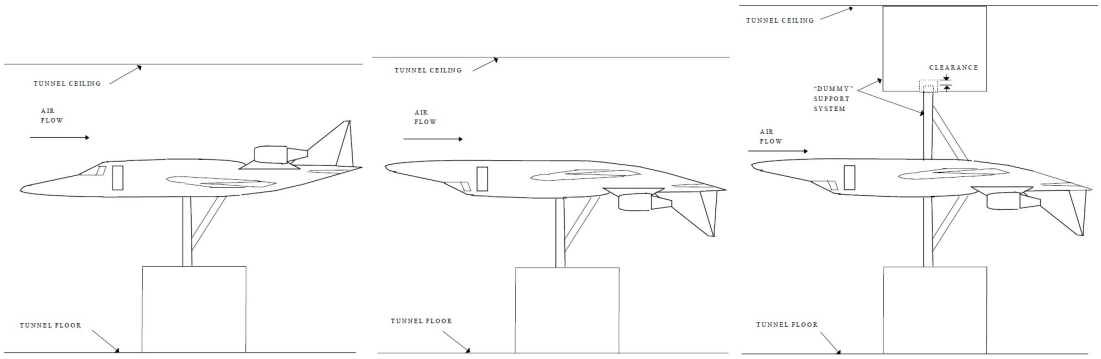
which is equivalent to

$$BL_{\text{step-a}} = M_M + S_{\text{below}} \tag{2.15}$$

$$BL_{\text{step-b}} = M_M + S_{\text{above}} \tag{2.16}$$

$$BL_{\text{step-c}} = M_M + S_{\text{above}} + S_{\text{below}} \tag{2.17}$$

where S_{above} and S_{below} are the balance loads due to the model support systems plus all interference effects and loads on and due to these systems, but neglecting the interference effects of the real and "dummy" support systems on each other. The estimated T&I of the support system by the sequence of tests described above assumes linearity in the way that such effects and interactions add up.



(a) Step. a (b) Step. b (c) Step. c

Figure 2.62: Tare and interference configurations [17]

Tested Configurations and Support System

The three configurations in Fig 2.61 for the 2023 T&I tests were tested in the step a-b-c sequence, also presented in Fig. 2.61 from §2.4.2. Figures 2.63, 2.64, and 2.65 show the configurations in their step a-b-c stages of testing in the KWT test section. It should be noted that the T&I tests are time consuming and that special attention had to be paid throughout the test to making sure that no loads were transferred from the pylons (especially the upper "dummy" pylon) to the strut and forks, and, thus, to the balance. This can prove to be quite challenging in the case of the upper pylon and the freedom of the "dummy" upper fork to move inside it without touching it, especially when angles of attack became high. An electric circuit was used to identify cases in which the upper "dummy" fork touched the upper pylon, and in such cases adjustments were made as necessary to eliminate such contact.



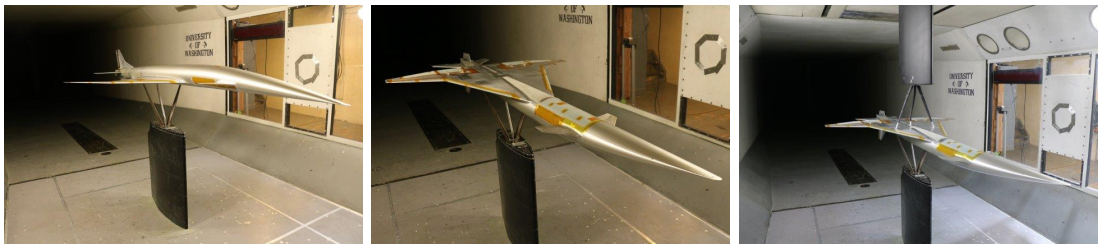
(a) Step. a (b) Step. b (c) Step. c

Figure 2.63: Tare and interference steps for wing only (W15)



(a) Step. a (b) Step. b (c) Step. c

Figure 2.64: Tare and interference steps for wing and aft-deck (W15+AD16)



(a) Step. a (b) Step. b (c) Step. c

Figure 2.65: Tare and interference steps for UW-S-21A without nacelles

2.6.3 Results and Discussion

While wind tunnel tests were conducted at several tunnel dynamic pressures for the T&I tests. These measurements are designated as follows; lift force (LIFT), drag force (DRAG), side force (SF), pitching moment (PM), rolling moment (RM), yawing moment (YM), lift force coefficient (C_L), drag force coefficient (C_D), side force coefficient (C_Y), pitching moment coefficient (C_M), rolling moment coefficient (C_R), and yawing moment coefficient

(C_N). The effects of various model configuration variations on the aerodynamic parameters of the UW-SCALOS model are presented and discussed at the nominal dynamic pressure of 32 psf, $Re = 2.23 \times 10^6$. There are small physical area and MAC variations among different wing planforms. In this section, all data are non-dimensionalized with respect to the W15 model in S_{ref}, mean aerodynamic chord (MAC), and moment centers for comparison purposes as in Tab. 2.28. The moments presented here are at 25%$\bar{c}$ for center of gravity (CG).

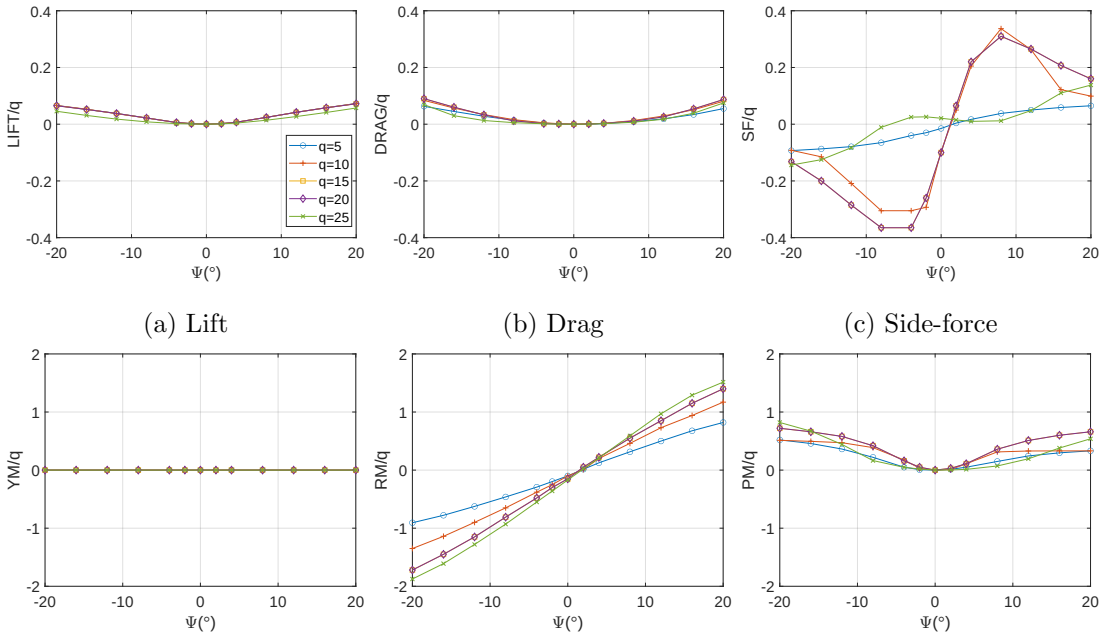
To make general wind tunnel corrections useful for various configurations, it is common to present them as force or moment per dynamic pressure corrections to "free" them from the dependence on the particular reference areas and reference chords or spans of particular models. If the development of T&I corrections is part of a particular wind tunnel test and would be applied only to the model tested, then, of course, the correction can be presented in the form of non-dimensional lift, drag, side force, and moment coefficient deltas using the reference geometry of the particular model.

Full T&I tests with wing only, wing plus aft deck, and a three surface configuration without engine nacelles

Figure 2.66 shows the KWT standard T&I correction versus support yaw angle, plotted in terms of balance force and moment measurements normalized by the dynamic pressure q. Reference [18] described previous efforts to test the support fork and pitch arm by themselves to understand the true "tare" part of the T&I. As can be seen from Fig. 2.47, the geometry of the airfoil-shaped cross-sections of the support fork struts, when in free air, acted like very high aspect ratio wings with extreme dihedral, and likewise the pitch strut acted like a thick-airfoiled very tall vertical tail. As the assembly is yawed as needed to position a model at a non-zero sideslip angle, the support elements develop a side-ward angle of attack, producing lift, induced drag, and some moment components.

At even modest yaw angles, the relatively thick thickness-to-chord ratio of the support element airfoils also created significant "form" drag, especially at the lowest test Reynolds numbers (KWT lowest dynamic pressure, $q = 3.5$ psf). The non-linearities and data asym-

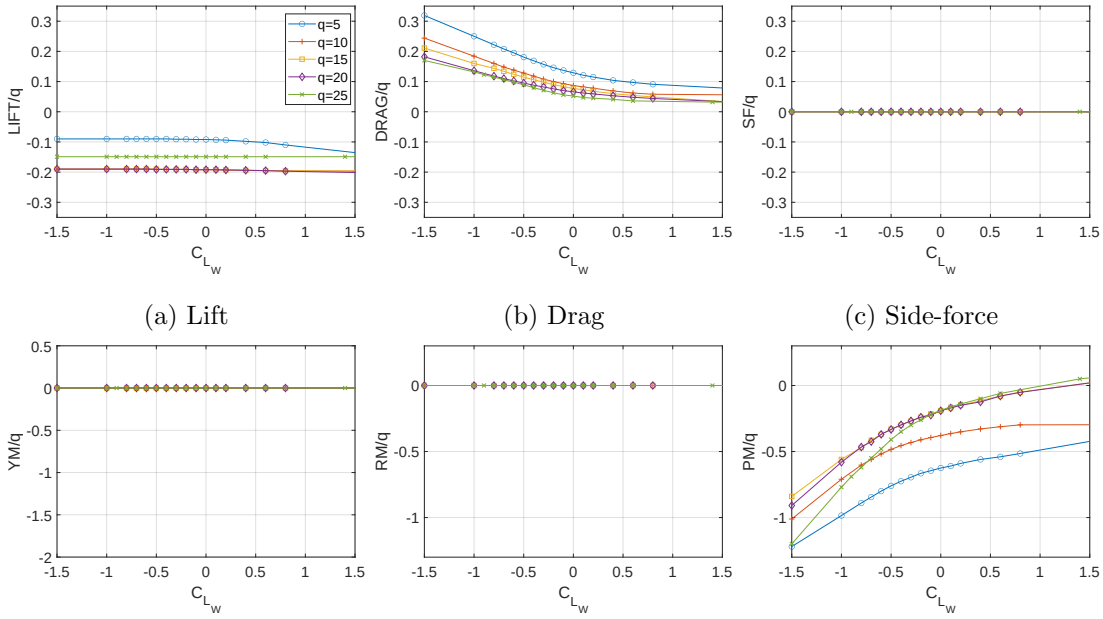
metries in the T&I measurements, which are believed to be caused by flow separation on the yawed support airfoils, diminish with increasing tunnel dynamic pressure and the data become much more well-behaved at $q \geq 25$ psf. When the supports are attached to a model wing, including the NACA rectangular calibration wing used by the KWT in the past for T&I corrections, the model's lower surface has an end-plating effect on the fork elements which can cause some change to the fork-alone aerodynamic tares. At the same time, as long as the wing is thin and generating no lift, the influence of the supports on the wing's forces and moments should be negligible, i.e. this "end-plate" effect is primarily model interference on the airflow over the support elements. Reference [18] also described previous CFD simulations and testing to separate out and quantify this interference effect by end-plating the mount with a simple, thin circular plate at zero angle of attack. The circular planform made the test article nearly insensitive to yaw angles such that the force variations measured were mainly due to the "tare" of the aero forces on the fork and pitch-arm assembly. While these efforts did show that the largest effects of the support T&I were seen in drag and side-force support tares, previous NACA wing measurements on which KWT's standard correction was based showed that the pressure field around the wing at lifting alphas would create added interference on the supports. Accordingly, as the model's angle of attack is changed, the measured changes to T&I were shown to correlate well with how much force and moments the wing is generating to turn the flow (i.e. C_L). Thus, the standard T&I corrections are applied as a function of yaw angle, and separate correction as a function of uncorrected lift ($C_{L_{\text{uncorr}}}$). Note that $C_{L_{\text{uncorr}}}$ is the total lift only corrected for balance interaction. Figure 2.67 shows the C_{L_W}-dependent portion of the standard T&I correction. On this basis, it could be expected that the lift generated by a large cranked delta planform with several times the chord of the original rectangular NACA calibration wing, flying to higher alphas, could have a much larger mutual interference with the support system versus angle of attack (or at least a different correlation versus C_{L_W}).



(a) Lift (b) Drag (c) Side-force

(d) Yawing moment (e) Rolling moment (f) Pitching moment

Figure 2.66: KWT standard 14-H fork and pitch arm T&I corrections vs. sideslip ($\alpha = 0°$) [18]



(a) Lift (b) Drag (c) Side-force

(d) Yawing moment (e) Rolling moment (f) Pitching moment

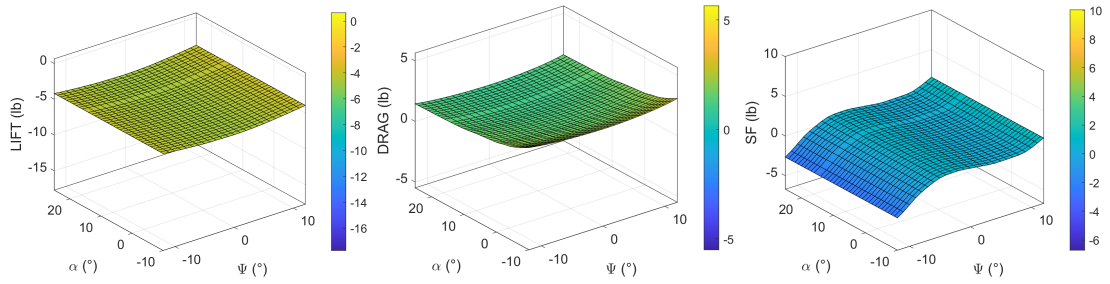
Figure 2.67: KWT standard 14-H fork and pitch arm T&I corrections, lift-dependent with dynamic pressure [18]

Wing only (W15) For the SCALOS wing W15 alone, Figure 2.68 illustrates the magnitude of the KWT standard correction in terms of dimensional balance forces and moments at the SCALOS nominal test at $q = 32$ psf. The data used for the standard T&I correction has been smoothed and interpolated for generic application to multiple types of configurations and the trends appear to give reasonable results for conventional, higher aspect ratio planforms with limited sweep.

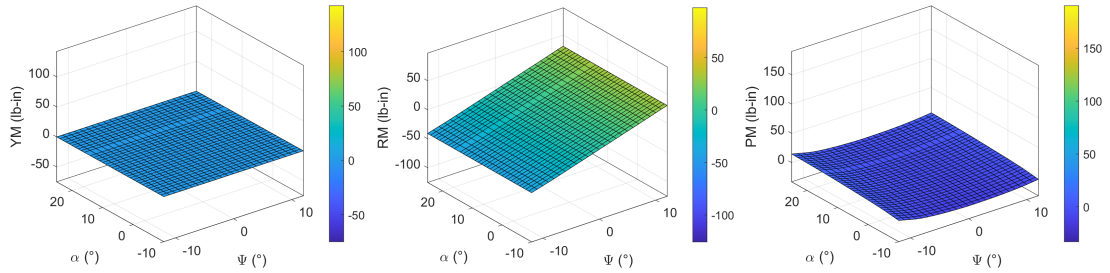
Figure 2.69 shows the comparable plots for the T&I corrections on the SCALOS type cranked-delta class planform as measured with the test apparatus on SCALOS baseline wing W15. While the data appear very similar in level to that of the NACA calibration wing (standard T&I) for zero psi and moderate alphas, the data is much more non-linear, especially near the edges for the pitch/sideslip test envelope. When the data is re-plotted in terms of non-dimensional coefficients in stability axes, as shown in Fig. 2.70, the differences between the two corrections are not as dramatic in Fig.2.71.

Figure 2.70 updates from the original plots in [19] to surface plot showing both variation with alpha and beta. Certainly, the use of the SCALOS-specific T&I corrections measured using a representative wing planform is different enough that it should be applied. It does not appear here to be so dramatically different, however, as to negate any previous conclusions drawn Fig. 2.71. The corrections are different, but the application of the standard T&I corrections seems to have captured the first-order effects well, at least for wing-alone cases.

Note that the new analysis and results presented here for the wing-only configuration are different from those previously published in [19]. The previous previous plots were only shown at either pitch or yaw runs, while the updated plots here show the full variation with both alpha and beta. The updated plots show that standard T&I correction only capture first order behavior of the side force and yawing moment, but misses the lift, drag, rolling moment, and pitching moment first order behavior and absolute level of variation, especially at higher angles of attack and sideslip.

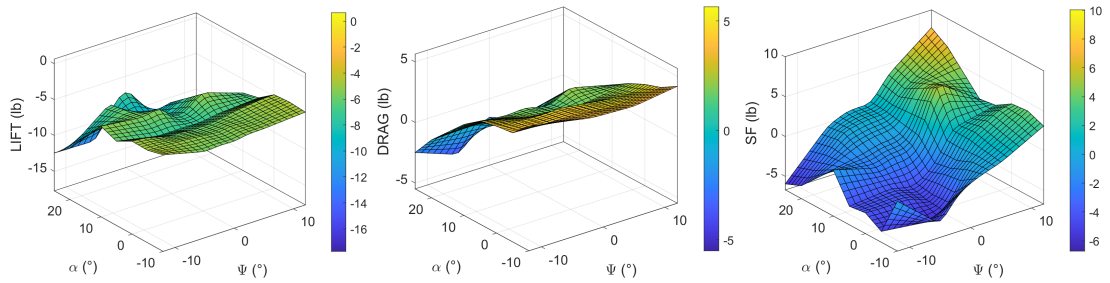


(a) Lift (b) Drag (c) Side-force

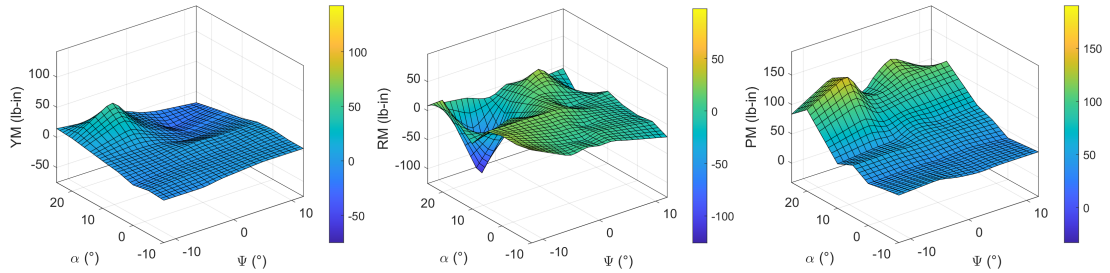


(d) Yawing moment (e) Rolling moment (f) Pitching moment

Figure 2.68: Wing only (W15) KWT standard T&I dimensional corrections at $q = 32$ psf

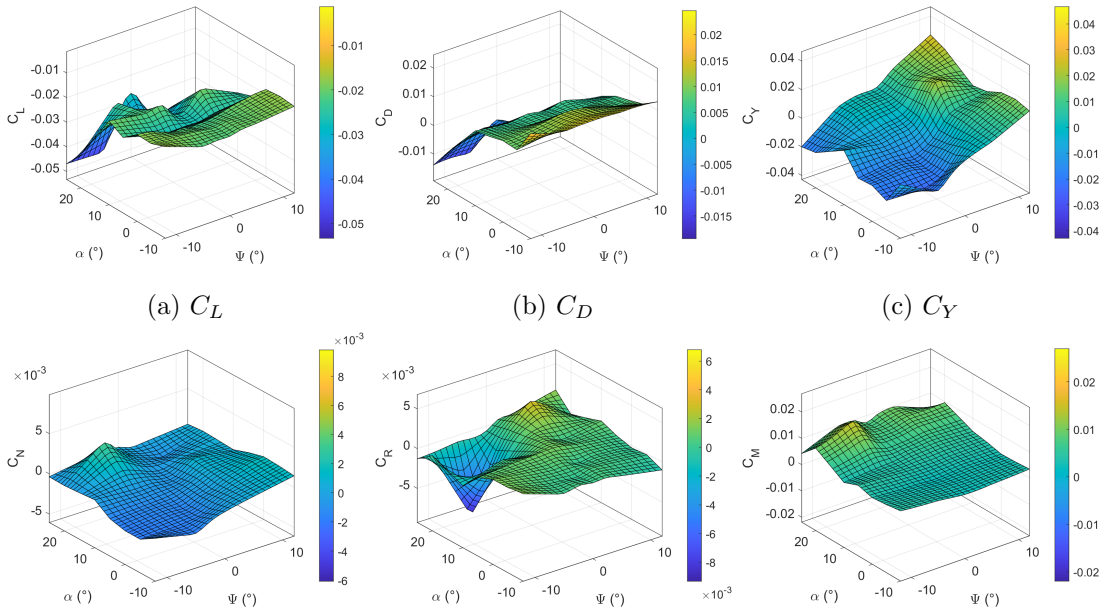


(a) Lift (b) Drag (c) Side-force



(d) Yawing moment (e) Rolling moment (f) Pitching moment

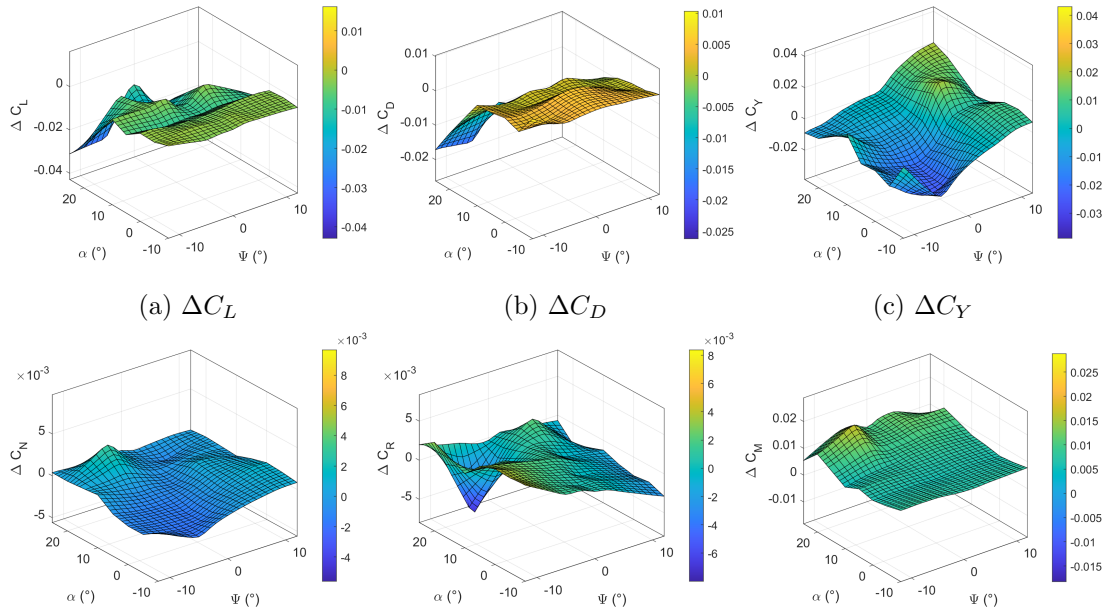
Figure 2.69: Wing only (W15) SCALOS-specific T&I dimensional corrections at $q = 32$ psf



(a) C_L (b) C_D (c) C_Y

(d) C_N (e) C_R (f) C_M

Figure 2.70: Wing only (W15) SCALOS-specific T&I non-dimensional corrections at $q = 32$ psf



(a) ΔC_L (b) ΔC_D (c) ΔC_Y

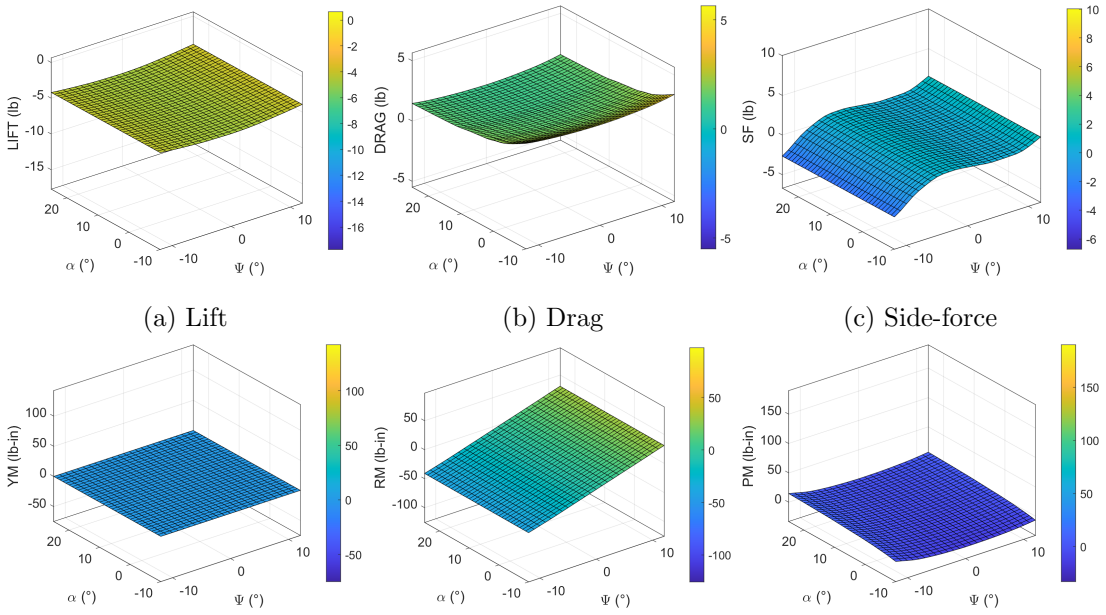
(d) ΔC_N (e) ΔC_R (f) ΔC_M

Figure 2.71: Wing only (W15) T&I non-dimensional correction differences at $q = 32$ psf (SCALOS-KWT)

Wing and aft-deck (W15+AD16) Figure 2.72 shows what the standard correction would predict for the T&I of the wing plus aft-deck lifting arrangement. The main difference between the surface plots shown in this set from those in Fig. 2.68 for the wing-alone case is due to the added ± lift generated by the aft deck as it is swept through the range of test alphas. The reference area is held constant for this planform arrangement as the aft-deck is treated as an add-on fairing, a kind of integrated horizontal tail. As shown in Fig. 2.73, the measured T&I specific to this configuration was very similar to that of the cranked-delta tested alone (W15 in Fig. 2.69) with the differences occurring mainly at the corner cases, the extremes of the α/β test matrix.

A comparison of non-dimensional aero coefficients for this configuration, reduced using the standard T&I correction versus that reduced using the SCALOS-specific/configuration-specific are shown in Fig. 2.74 and 2.75, also at the nominal test condition of $q = 32$ psf. Again the results show that although there are absolute level differences between the two sets of lines that are worth accounting for, the generic "standard" KWT correction captured the first-order trends such that SCALOS data that was previously published based on the standard KWT T&I corrections should still be generally valid for the wing plus aft-deck type lifting surface arrangements.

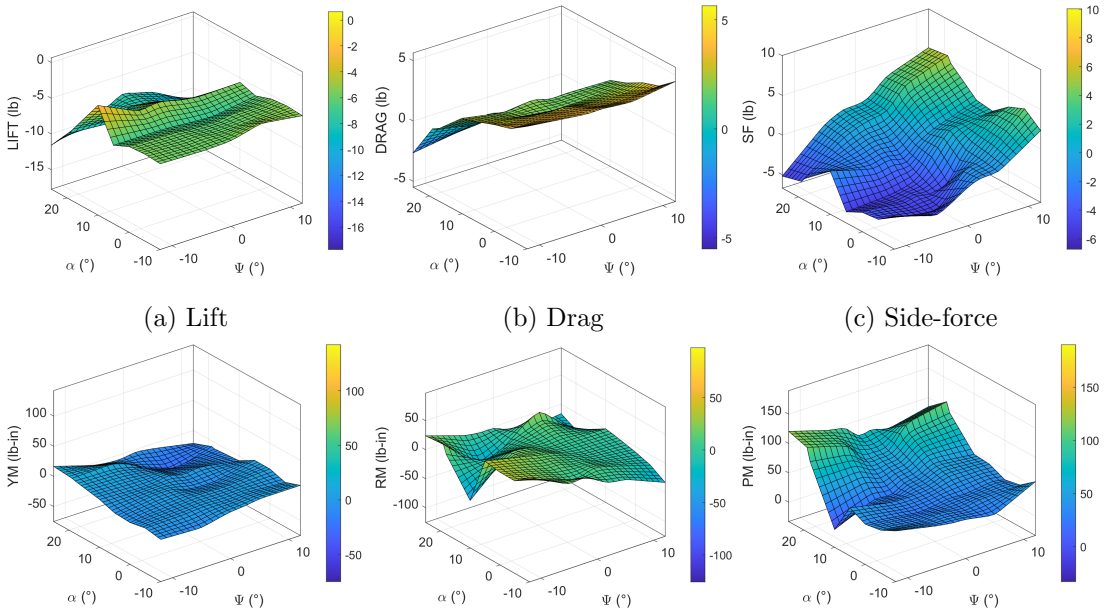
Again, note that the new analysis and results presented here for the wing and aft-deck configuration are different from those previously published in [19]. The result here is similar to that of the wing-alone case where the standard T&I correction ony capture first order behavior of the side force and yawing moment, but misses the lift, drag, rolling moment, and pitching moment first order behavior and absolute level of variation, especially at higher angles of attack and sideslip.



(a) Lift (b) Drag (c) Side-force

(d) Yawing moment (e) Rolling moment (f) Pitching moment

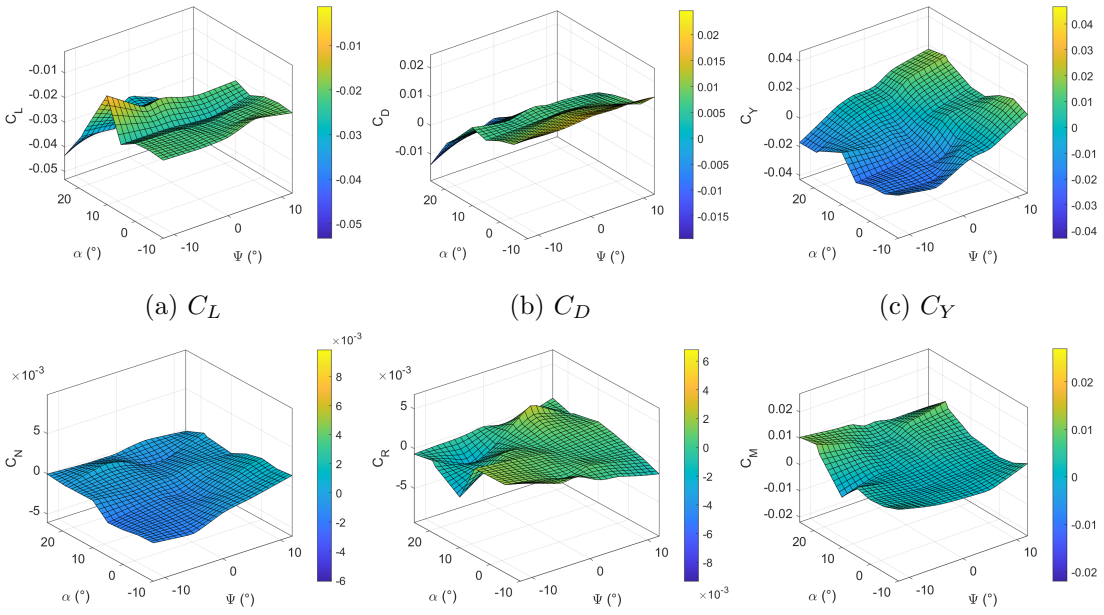
Figure 2.72: Wing and aft-deck (W15+AD16) KWT standard T&I dimensional corrections at $q = 32$ psf



(a) Lift (b) Drag (c) Side-force

(d) Yawing moment (e) Rolling moment (f) Pitching moment

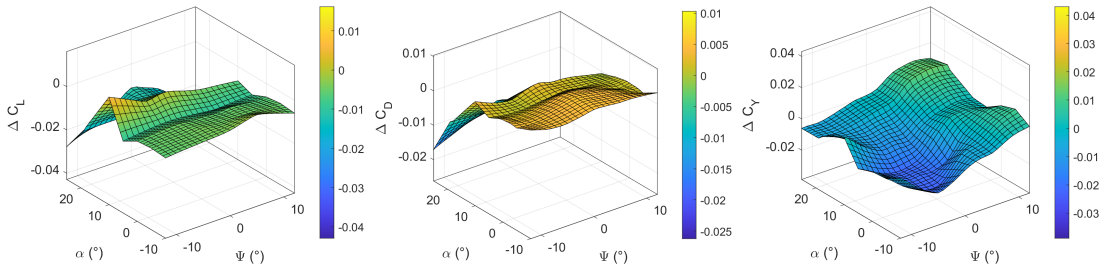
Figure 2.73: Wing and aft-deck (W15+AD16) SCALOS-specific T&I dimensional corrections at $q = 32$ psf



(a) C_L (b) C_D (c) C_Y

(d) C_N (e) C_R (f) C_M

Figure 2.74: Wing and aft-deck (W15+AD16) SCALOS-specific T&I non-dimensional corrections at $q = 32$ psf



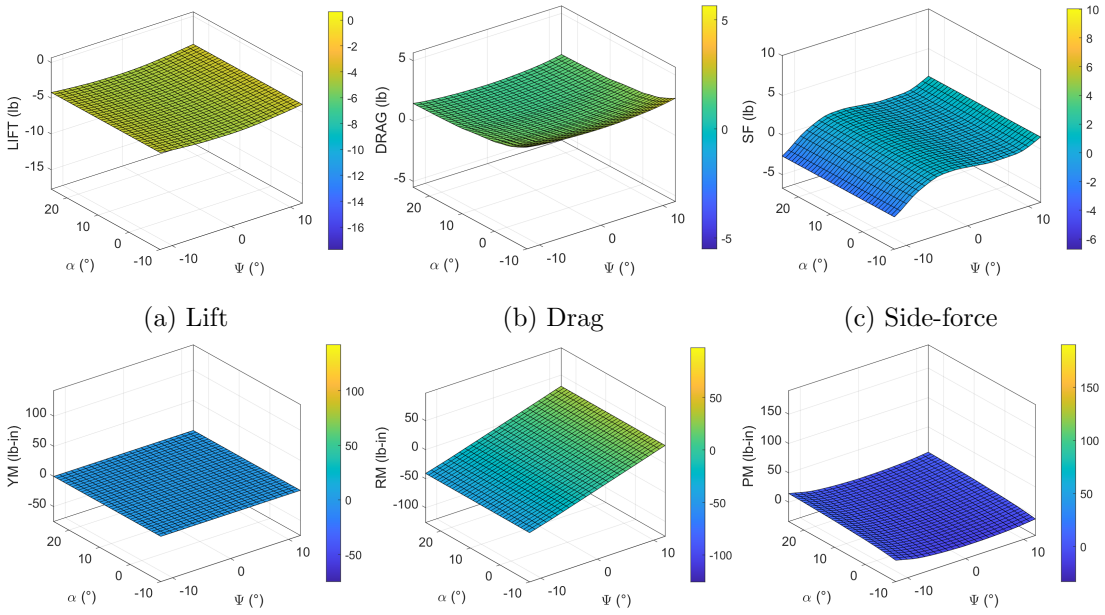
(a) ΔC_L (b) ΔC_D (c) ΔC_Y

(d) ΔC_N (e) ΔC_R (f) ΔC_M

Figure 2.75: Wing and aft-deck (W15+AD16) T&I non-dimensional correction differences at $q = 32$ psf (SCALOS-KWT)

Three-surface configration The third general arrangement chosen for the evaluation of T&I effects was a full configuration with three lifting surfaces and a slender fuselage (wing-body-horizontal-vertical-tail-canard). The UW-S-21A configuration without nacelles was chosen as shown previously in Fig. 2.61, and Tab. 2.28 in §2.4.3. Figure 2.76 shows a surface plot of the KWT standard T&I correction corresponding to this general arrangement. Figure 2.77 shows the measured T&I corrections from the SCALOS three-surface configuration. While the results in the region corresponding to small alpha and side-slip angles are qualitatively similar to the KWT generic "standard" correction, the measured data shows some offset in levels and significant non-linearities, including a few distinct "hills" and "valleys" that did not show up to that extent in the wing-alone or wing plus aft-deck cases. It is hoped that CFD studies will help resolve whether these effects are related to the effect of the support system wakes interfering with the horizontal and vertical tails or the wake of the fuselage forebody and canard interfering with the local flow over the support forks [382, 383].

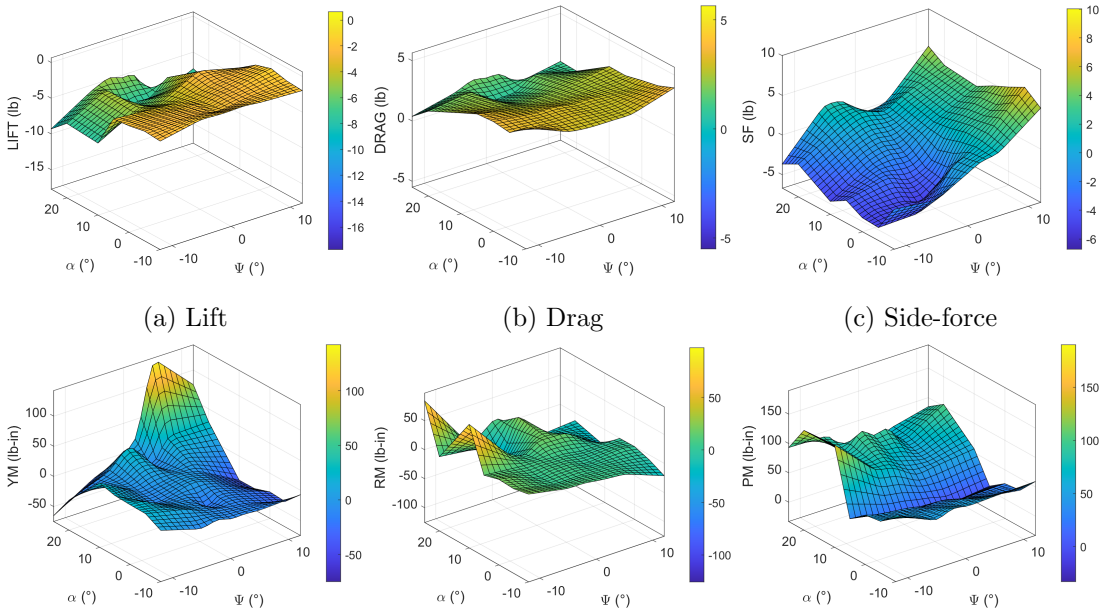
As shown in Figs. 2.78 and 2.79, the effects of applying the KWT generic "standard" T&I correction versus using the SCALOS configuration-specific T&I as measured on the full configuration, show some significant differences at the level of the aero coefficient, especially offsets in pitching moment. Unlike with the wing-alone and wing and aft-deck geometries, these offsets seem to be occurring even at zero yaw angle and small angle of attack. This shows that not only were the SCALOS-specific T&I measurements valuable, but tailed configurations and wing-alone cases probably need to be corrected separately with their own corresponding measured T&I corrections. This finding is illustrated in Figs. 2.71, 2.75, and 2.79, which clearly indicate that the T&I corrections in terms of direct balance forces for the three general arrangement types do not collapse onto each other for a given alpha.



(a) Lift (b) Drag (c) Side-force

(d) Yawing moment (e) Rolling moment (f) Pitching moment

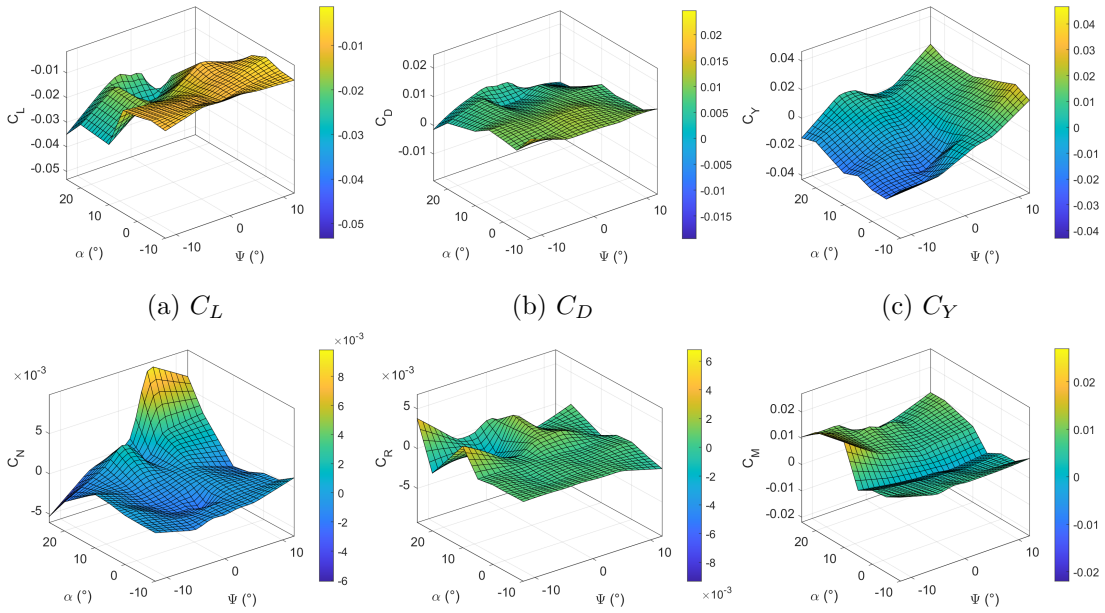
Figure 2.76: Three surface configuration KWT standard T&I dimensional corrections at $q = 32$ psf



(a) Lift (b) Drag (c) Side-force

(d) Yawing moment (e) Rolling moment (f) Pitching moment

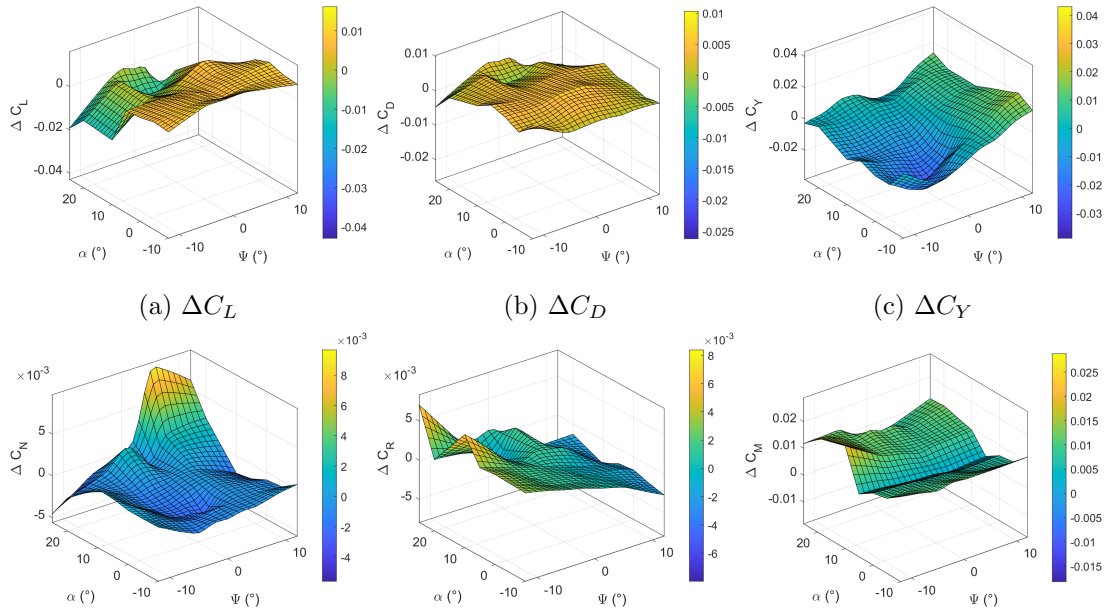
Figure 2.77: Three surface configuration SCALOS-specific T&I dimensional corrections at $q = 32$ psf



(a) C_L (b) C_D (c) C_Y

(d) C_N (e) C_R (f) C_M

Figure 2.78: Three-surface configuration SCALOS-specific T&I non-dimensional corrections at $q = 32$ psf



(a) ΔC_L (b) ΔC_D (c) ΔC_Y

(d) ΔC_N (e) ΔC_R (f) ΔC_M

Figure 2.79: Three-surface configration T&I non-dimensional correction differences at $q =$ 32 psf (SCALOS-KWT)

Engine Nacelles' Interference

The SCALOS configurations with the nacelles mounted on the wing lower surface presented a concern for the SCALOS' UW team as the wake of the support forks obviously would impinge on the nacelles. This interference of the support on the nacelles has been recognized as a source of experimental uncertainty for all of the nacelle-under-wing increments and nacelle location comparisons reported to date. Modification of the core SCALOS model with inverted testing capability for supporting the T&I measurements allowed, for the first time, the incremental effect of under-wing nacelles to be obtained free from the mounting fork's wake interference. As shown in Fig. 2.80, a complete UW-S-21A configuration was tested in the inverted position with and without the "N20" nacelles. The model was also re-tested in the upright position with and without nacelles to provide a repeatability tie-in to previous test entries and to provide back-to-back comparisons of the nacelle increments obtained with and without the fork wake interference. Figure 2.81 compares the nacelle increments obtained from the upright and inverted test cases. The results show similar trends but the upright and inverted aero coefficients do not collapse on each other, showing that the support wake interference was having a measurable effect on the inferred nacelle characteristics. The differences between the wake-free and wake interference cases provided a nacelle "T&I" correction that can be used to remove the support wake effects from previously acquired data on configurations with under-wing nacelles. This "nacelle T&I" adjustment, directly plotted in Fig. 2.82 indicates that the "delta-delta" taken to construct this plot is a "lumpy" dataset, but it nevertheless shows some clear trends. While the wake interference effect was measurable, in Fig.2.83, the net effect of applying the nacelle T&I adjustment was not dramatic in terms of the airplane level coefficient data, meaning that nacelle comparisons published previously were probably unaffected by the presence of the support wake interference on the under-wing nacelle configurations.

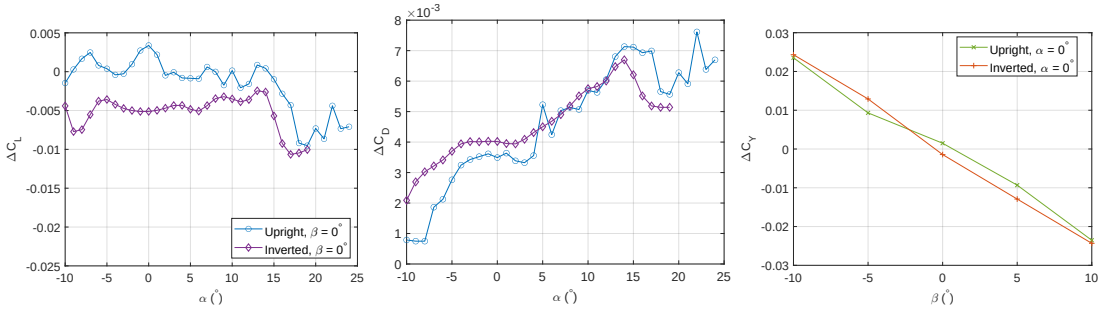


(a) Upright, no nacelles (b) Upright, bottom nacelles



(c) Inverted, no nacelles (d) Inverted, bottom nacelles

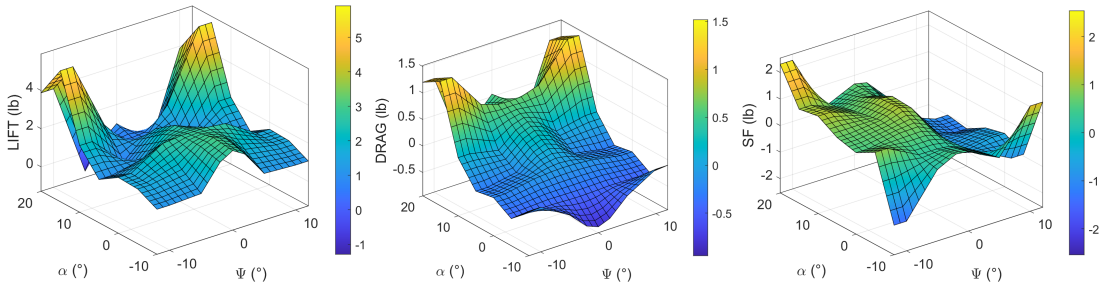
Figure 2.80: UW-S-21A on the support system w/ and w/o underwing nacelles



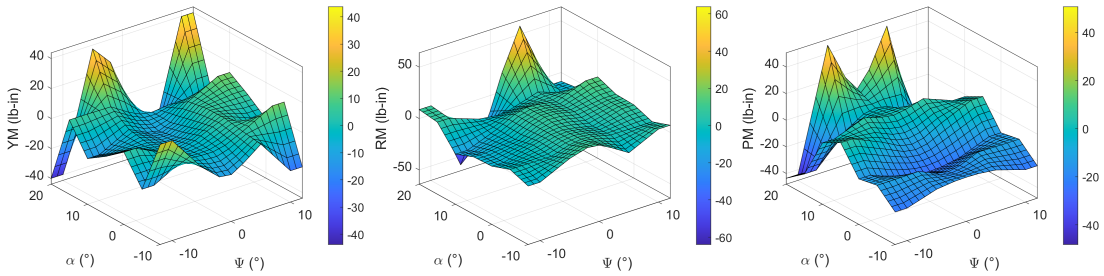
(a) ΔC_L vs. α (b) ΔC_D vs. α (c) ΔC_Y vs. β

(d) ΔC_N vs. β (e) ΔC_R vs. β (f) ΔC_M vs. α

Figure 2.81: Upright and inverted nacelle force and moment increments at $q = 32$ psf [19]

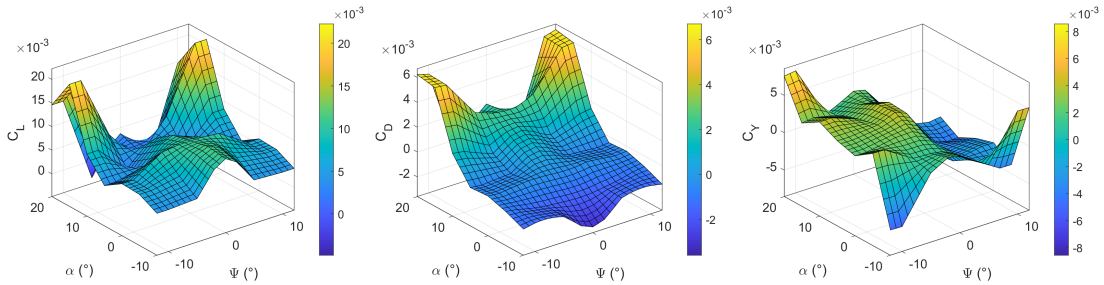


(a) Lift (b) Drag (c) Side-force

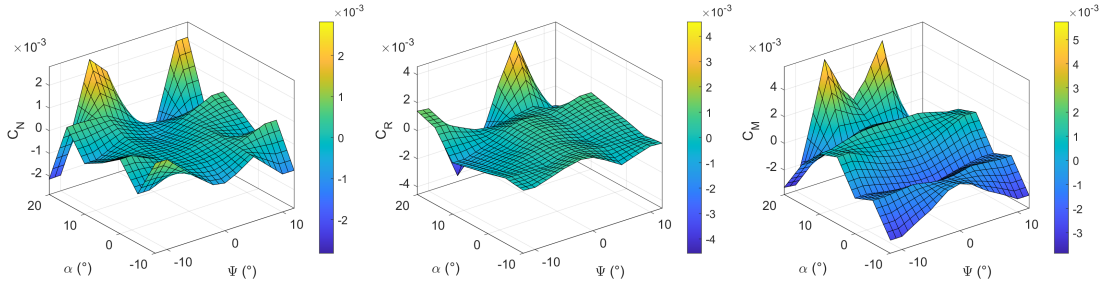


(d) Yawing moment (e) Rolling moment (f) Pitching moment

Figure 2.82: Nacelle SCALOS-specific T&I dimensional correction at $q = 32$ psf



(a) C_L (b) C_D (c) C_Y



(d) C_N (e) C_R (f) C_M

Figure 2.83: Nacelle SCALOS-specific T&I non-dimensional correction at $q = 32$ psf

2.6.4 T&I Lessons Learned

The section presents the experimental work that was aimed at developing T&I corrections for the University of Washington's Kirsten Wind Tunnel (KWT) for tests that involve supersonic commercial aircraft configurations tested as part of the NASA SCALOS project. The questions that motivated the tests were: (a) how adequate were "standard" KWT T&I corrections for the SCALOS configurations? and (b) how sensitive KWT T&I corrections were to variations among SCALOS configurations. If a single set (or a very small number of sets) of T&I corrections for the SCALOS configurations can be used for tests of all SCALOS tests, this will lead to major savings in test times and costs, which, in the case of "mapping" the design space of configuration variations by wind tunnel tests, is highly desirable. Three configurations were tested for T&I corrections: a wing only configuration (W15), a wing plus aft-deck configuration, and a full three-surface configuration without engine nacelles. The effects of engine nacelles on T&I corrections were studied by tests of the three-surface configuration with underwing nacelles in the upside up and upside down positions and comparing the results to those of the three-surface configuration without nacelles in those positions.

Previous conclusions in [19] suggested that the generic "standard KWT correction" captured the first-order trends similarly to the wing-only and wing plus aft deck cases, except for some differences in the corner cases of angle of attack and sideslip angle. However, the new results and their analysis presented here for the wing and aft-deck configuration show that the results are similar to the three-surface configuration in the region corresponding to small alpha and side-slip angles in which they are qualitatively similar to the KWT generic "standard" corrections. The measured data show some offset in levels and significant non-linearities, including a few distinct "hills" and "valleys" that did not show up to that extent in the wing-alone or wing plus aft-deck cases. The effects of applying the KWT generic "standard" T&I correction versus using the SCALOS configuration-specific T&I as measured on the full configuration, show some significant differences at the level of the aero coefficient, especially offsets in pitching moment. These offsets seem to be occurring even at zero yaw angle and small angle of attack. This shows that not only were the SCALOS-

specific T&I measurements important, but that all configurations need to be corrected with the closest corresponding configuration for which which there are measured T&I correction.

Regarding the effects of engine nacelles on T&I corrections: The differences between the nacelles in the wake of the support system (nacelles under the wing in the upside up test) and wake-free (under the wings in the upside-down position) provided a nacelle T&I correction that can be used to remove the support wake effects from previously acquired data on configurations with under-wing nacelles. While the wake interference effect was measurable, the net effect of applying the nacelle T&I adjustment was not dramatic in terms of the airplane level coefficient data. The nacelle configuration comparisons published previously were, therefore, probably unaffected by the presence of the support wake interference on the under-wing nacelle configurations.

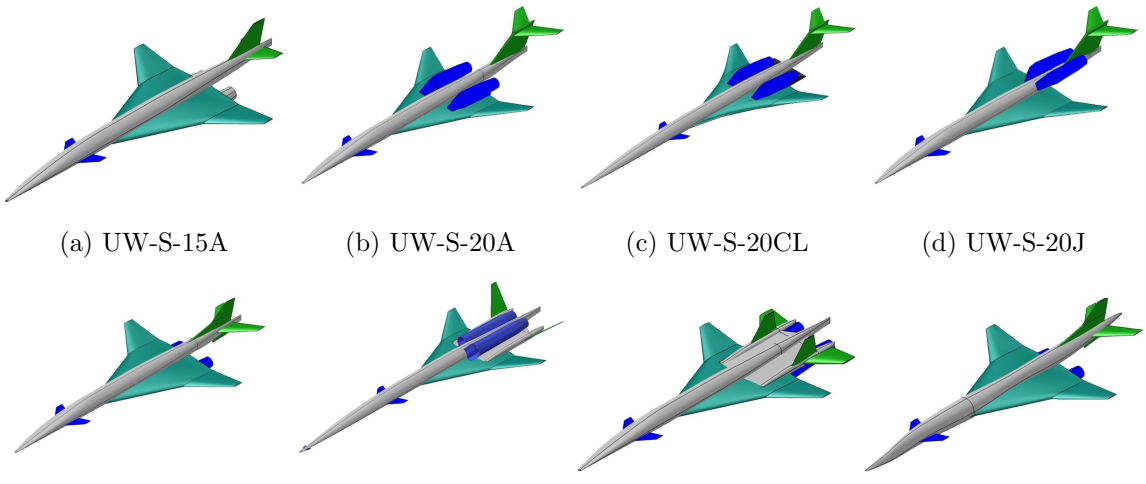
2.7 Aerodynamic Results and Analysis

Progress of the SCALOS aerodynamic results and analysis has been published every year since 2022. §2.4.5 discussed the long-term and short-term test-to-test repeatability, where the wing alone, wing-body, and a baseline model were used for repeatability examination at the beginning of every test entry [4]. The dynamic pressure and Reynolds' number effects were also studied in §2.4.6. The nominal dynamic pressure was $q = 40$ psf but later lowered to $q = 32$ psf due to severe fuselage oscillation. This section presents all the aerodynamic results based on: [23–26]. It is important to note that all the earlier published papers [4, 19, 23, 24, 26, 371, 377] present results with KWT's standard corrections, except for [25, 27] which are with the SCALOS final correction as the final deliverable data set.

All the data presented in this dissertation are updated with the final corrections. The published papers presented the aerodynamic results in parametric comparisons on configuration, wing planform, nacelle effects, horizontal tail platforms deflections, leading and trailing edge effects, canard planform and deflections, and additional high lift devices. Based on the standard KWT corrections, they still provide useful information regarding trends and variations. References [27, 371] took a deeper dive into the longitudinal and lateral-directional aerodynamic analysis which are presented in later sections in §2.8 and §2.9, respectively.

In the tested configurations, the UW-S-20A and UW-S-21A were the baseline models in

2020 and 2021 [23]. The UW-S-20CL is the low-boom variation of the UW-S-20A with a longer forebody fuselage, ogive leading edges, and nozzle-shock reflection deck (NSRD) [26] The design space survey [13] studied existing designed aircraft and was used as a guide to expand the tested configurations. The UW-S-20J, UW-S-23E, and UW-S-23G were added to the test matrix representing the SBJ/SSBJ, Boeing Icon-II, and Boeing 765-071B or Sonic Cruiser-like configurations. The UW-S-20J and UW-S-23E were tested in 2023 and reported in [24]. The UW-S-23G was pushed back to be tested in 2024 along with the area-rule fuselage and the result was presented at SciTech 2026 [25]. The area-ruled fuselage was tested with simple wing-body and three-surface configurations for body increments and effects. The lateral-directional aerodynamics of angle of attack at different sideslip angles and sideslip angles given different angle of attacks were presented in [27]. The force and moment were also correlated with flow visualization for UW-S-21A. At the end of 2024, UW-S-24A was selected to be the ideal candidate for preliminary SST design and was tested with control surfaces and landing gears deployed for take-off and landing configurations. All the tested SCALOS configurations are shown in Fig. 2.85, not including the configurations from 2015-2018. Detail built-ups with component specification could be found in Table 2.8–2.18 in §2.2.



(a) UW-S-15A (b) UW-S-20A (c) UW-S-20CL (d) UW-S-20J

(e) UW-S-21A (f) UW-S-23E (g) UW-S-23G (h) UW-S-24A

Figure 2.84: UW-S configurations

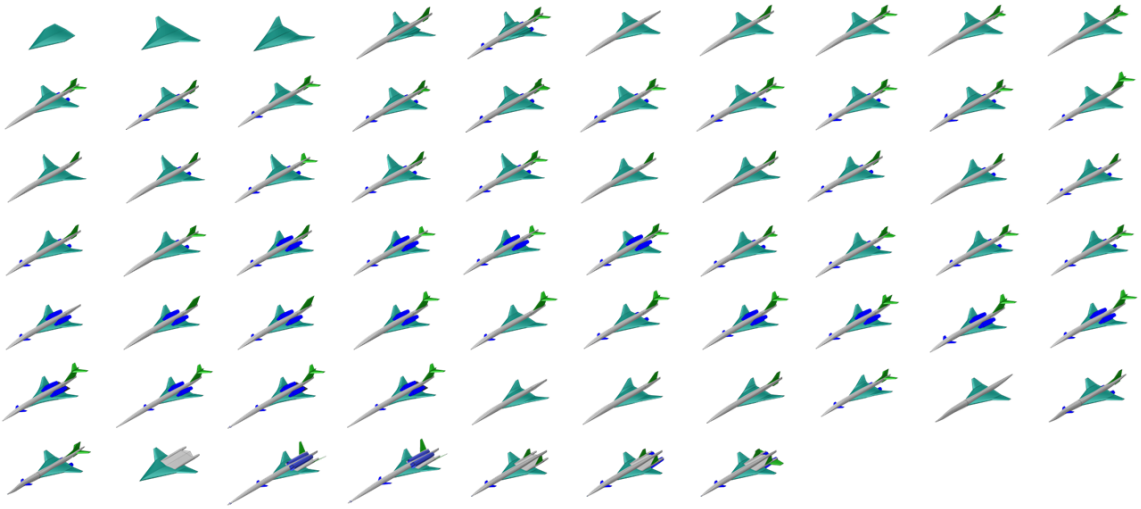


Figure 2.85: Tested configurations of the SCALOS program

On the wing planform, §2.7.1 starts with the leading edge vortex and flow visualization because vortex lift was exploited heavily for SCALOS designs. A dedicated test, UW2324, was for flow visualization after a proof-of-concept test in the 3"x3" low-speed wind tunnel for wing alone (W15), UW-S-20A, and UW-S-21A in §2.7.1 and §2.9. The flow visualization was used to accompany force and moment data for flow physics and insight. The wing planform studies further compared wing-body-vertical-tail and three-surface low-tail configurations with planform variation as in Fig. 2.49a in §2.4.3. The crank-delta wing was the core model of the SCALOS program. However, most of the existing published experimental and computational results have sharp leading edges and thin delta or cranked-delta wing models with almost zero-thickness airfoils. Most of the SCALOS models do not have sharp leading edges, such that wing thickness and leading edge shape effects are presented in 2.7.1 [24]. The additional higher sweep outboard wing and aft-deck increment are in §2.7.1 [24], guided by the design space survey. The wing-body-vertical-tail with wing planform variations were tested back-to-back in a day to ensure data collection and eliminate different test entries and setup concerns in [25] and in §2.7.1. The longitudinal analysis was published in [371] on CG and static margin for both simple wing-body-vertical-tail and three surface configurations in the next section in §2.8.

Canards, mounted in forward and aft positions on the UW-S-20A configuration and the

canard increment and planforms in Fig. 2.49 on the UW-S-21A configuration are presented in §2.7.4 [23]. The higher sweep canard was added in [24]; however, the very thin part was initially 3D-printed and suffered from aeroelastic deformation at higher dynamic pressure. A new pair of aluminum canards were machined and tested with deflections in [25]. Three sets of canards from low to high sweeps with deflections were tested for parametric studies. The full range of canard deflection with longitudinal analysis were published in [371] with deflected incremental effect, trimmed drag polar, and tail deflection effectiveness. The lateral-directional aerodynamics of angle of attack at different sideslip angles and sideslip angles given different angle of attacks is presented in §2.9 [27].

§2.7.5 reports horizontal tail resutls. The horizontal tail increment and planform in Fig. 2.49 comparisons were tested on UW-S-20E, like UW-S-21A but with the 2020 outboard wing. The horizontal tail increment for mid- and T-tail configuration, UW-S-20H and UW-S-20A, were presented in [23]. The UW-S-20H and UW-S-20A in [23] were tested with all-moving stabilator deflection for tail authorities studies in [26]. The additional horizontal tail increment and planform comparison from [23] were tested on the simple wing-body-tail configuration for built-up and clean airfoil purpose, without canard and nacelle effect. The all-moving stabilators were tested for full ranges from $-25^\circ \leq \delta_{HT} \leq +25^\circ$ to investigate the tail authorities and limits [25], Three sets of different tail planforms were tested at low-tail configuration with deflection to study planform and deflection effectiveness. The same tail planform, H20, at different tail height with deflections were compared to study the tail height effect and deflection effectiveness. The horizontal tail planform and deflection on the simple wing-body-vertical-tail and three-surface mid- and T-tail configurations, UW-S-20H and UW-S-20A, from [26] were analyzed in [371] on longitudinal aerodynamics, including incremental effect, trimmed polar, tail lift curve, and downwash in §2.8.

§2.7.6 reports vertical tail results. The vertical tail with ventral and dorsal fin increments on wing-body-tail and three surface configurations at side slip angles was presented in [23]. The UW-S-23E, Boeing Icon-II like with V-tail configuration, was tested with differential and symmetric V-tail for yaw and pitch control in 2023 and reported in [24]. The rudder deflections of UW-S-20A and UW-S-21A with angle of attack at different sideslip angles and sideslip angles given different angle of attacks is presented in §2.9 [27]. The UW-S-20A

exhibits some roll and yaw reversal at $\alpha \approx 20°$.

§2.7.7 studies the effect of nacelles locations. The nacelle increment and location studies were conducted on the UW-S-20A configuration with nacelle off, nacelle on top of the wing, and nacelle on the bottom of the wing in [23]. The design space studies [13] explored the SBJ/SSBJ concept and added the nacelle on the afterbody fuselage to represent business jet-like supersonic aircraft in [24]. Further studies were also conducted on the model support system interference effect on the nacelle due to the low-mount nacelle sitting in the wake of the model mounting system, such that a T&I for nacelle was done and added to the final correction presented in previous §2.6 The influence of part-throttle or engine-out conditions were also investigated on UW-S-20A by partially or fully closing one or both nacelle exits in [27] and presented in §2.9.

§2.7.8 reports leading edge results. The baseline leading edges are shown in Fig. 2.49 in §2.4.3. Note that the inboard leading edge is shared (commutative) but not outboard, refer to [373, 376] for details. The UW-S-20A with baseline leading edges and deflections was published in [23]. The UW-S-21A with baseline leading edges and deflections was tested inboard-only, outboard-only, and all leading edge deflections to study the inboard and outboard contributions for UW-S-21A and compared with results of UW-S-20A from [23] in [26]. The UW-S-23A and UW-S-13A, which are UW-S-21A with outboard wing variations, with leading edge deflections were tested and compared with UW-S-21A in 2023 and 2024, reported in [24] and [25], respectively. As mentioned earlier, the wing core was tested to study the leading edge effect, where the sharp leading edges were compared with round leading edges for vortex lift. The morphing-variable-radius (MVR), sealed-slat, and flax panel leading edges are shown in Fig. 2.49. The morphing-variable-radius (MVR) inboard leading edges were designed to bulge out of the lower surface of the leading edge to increase airfoil nose thickness and camber allowing smooth flow attachment and preventing separation while keeping the upper surface cruise LE shape fixed. The sealed-slat (SS) outboard leading edges were designed with smooth upper wing surfaces and increasing leading edge areas when deployed. The flex panel outboard leading edges were designed with a smooth upper surface transition at the hinge line and bending to conform with a straight lower surface. Those alternative leading edges were tested on UW-S-21A and

published in [24]. The second version of morphing-variable-radius and alternate leading edges were designed and tested in 2024 [25]. The deflected incremental effects subject to the planform were compared in [371].

§2.7.9 reports trailing edge results. The trailing edge were studied in [26]. The baseline ailerons and reduced chord length ailerons were tested on UW-S-21A to compare the roll effectiveness given aileron mechanical design constraints and compared with the effectiveness of UW-S-20A. The combined inboard and outboard trailing edge devices, flap and aileron, were tested as flaperon for high lift devices for both UW-S-20A and UW-S-21A. The UW-S-23A was added to the databases with aileron and flaperon deflections and compared with UW-S-21A in [24]. Note the inboard tailing edges, flaps, have the same area with different outboard wings; however, the ailerons of different outboard wing have different span, chord length, and area due to physical constraints. Interested reader should refer to [375, 376] for details. The aft-deck pitch control were evaluated in [25]. The trailing edges deflected incremental effects subject to the planform were compared in [371]. The additional test results at different sideslip angles and yaw runs were reported in [27] and in §2.9.

A few exploratory control and drag-producing devices were also tested, including aileron spoiler, spoiler-slot deflector (SSD), mid-chord spoiler, and clamshell brakes [26]. The SSDs are typically used as roll controller effectors at all Mach numbers to avoid large aeroelastic losses or aileron reversal due to wing twisting, e.g.. North American Vigilante. They could also be used as a drag device for flight path control, like regular spoilers. A second version of SSDs was designed in 2023 but postponed to be tested in 2024. A few other stability enhancement devices were explored, such as nose chines, body strakes, and wing fences. Most importantly, the landing gear parts were 3D-printed and tested to represent take-off and landing configuration as a major effort in 2024 [25].

The take-off and landing configuration with canard, leading and trailing edges, landing gear deployed on UW-S-24A was tested with vertical tail deflection, examining the rudder's authority in [25] and in §2.7.10.

2.7.1 Wing Planforms

A prime motivation for investigating the low-speed characteristics of slender supersonic configurations in the wind tunnel is their inherently non-linear aerodynamic behavior, commonly beginning at moderate to high angles of attack and continuing to angles well beyond classical "stall". This is due to the influence of complex interacting vortex flows that originate from slender fuselages, canards, and thin highly-swept wing and tail leading edges. Recognizing and understanding these dominant off-body flow-fields is important to understanding the measured performance and stability characteristics of slender configurations, especially at subsonic maneuver and takeoff / approach / landing flight conditions.

Figure 2.86 shows a sketch of the vortices formed over a classical simple sharp-edged flat double delta wing model at zero sideslip angle [20]. At low angles of attack, the flow over these wings is similar to that of the swept wing attached flow and the lift increases linearly with angles of attack.

At moderate to high angles of attack, the flow field over cranked-delta wings is dominated by two strong vortices and the lift force increases nonlinearly, while the axial force, C_{D_A}, remains relatively constant for low angles of attack and increases with further increases of alpha. As shown in Figure 2.86, the inner vortex is shed from the wing apex while the outer vortex is shed from the kink portion of the leading-edge, denoted as inner and outer vortices, respectively. The two vortices rotate in the same direction, hence they tend to move around each other.

The interaction causes attraction between the two vortices as illustrated in Figure 2.86. These vortices remain stable for some angles of attack. At certain angles of attack, depending on the wing leading-edge sweep, the vortices breakdown/burst causing decrease in the slope of the lift force and significant increase in the drag force. Much has been published on the aerodynamics of cranked-delta wings, however, almost all of the existing published experimental and computational results have sharp leading-edge thin-delta or cranked-delta wing models with an almost zero-thickness (beveled flat-plate) airfoils. The present model does not have sharp leading edges and so wing thickness and leading edge shape effects cannot be ignored. The vortex formation, vortex behavior, and vortex breakdown/burst-

ing for the present SCALOS study wings may be different than those of the simple sharp leading edge flat plate examples, mainly due to differences in LE vortex initiation location and the behavior of the LE suction force. Some references for wings with flat plate and sharp leading-edge are presented below. Figure 2.87 from [21] illustrates vortex formation, vortex merging, and vortex breakdown over a cranked delta wing at three different angles of attack, while Figure 2.88 from [22] shows stages of vortex formation and breakdown as a function of angles of attack and wing sweep angle. Figure 2.88 correlates the extent of laminar flow and the transition to turbulent flow over the surface of the wing as a function of both angles of attack and wing sweep angle.

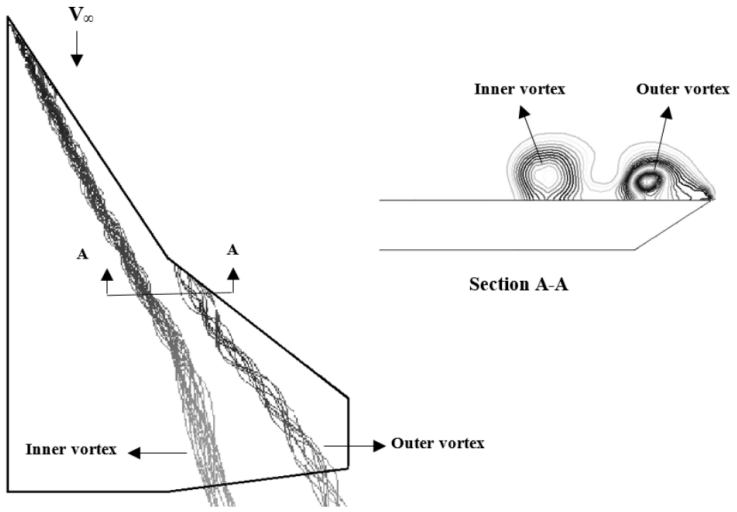
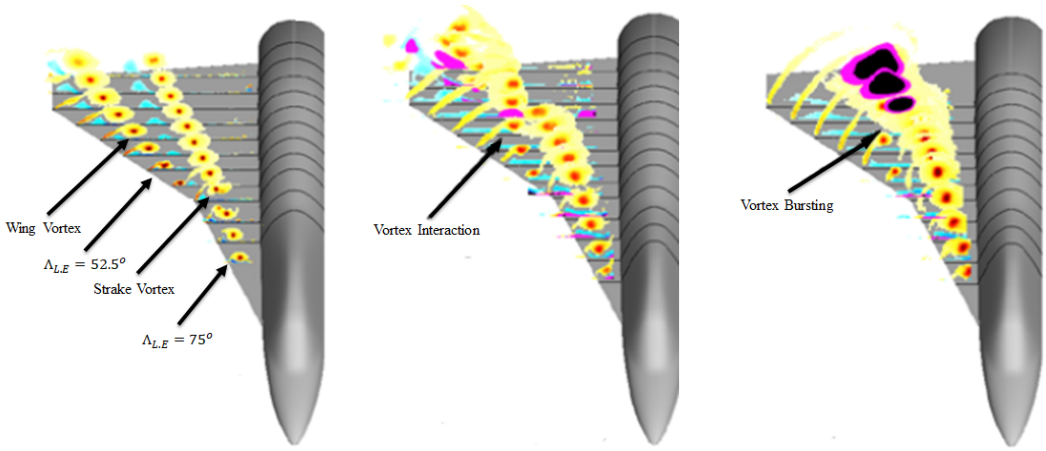


Figure 2.86: Schematic of the vortices over a cranked delta wing [20]



(a) $\alpha = 8°$ (b) $\alpha = 16°$ (c) $\alpha = 24°$

Figure 2.87: Illustration of the vortices over a cranked delta wing [21]

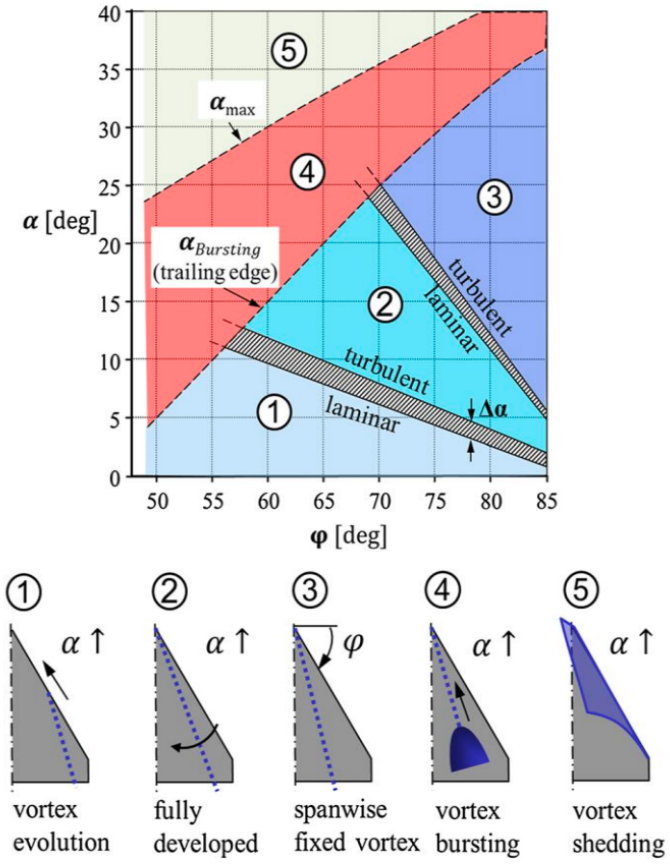


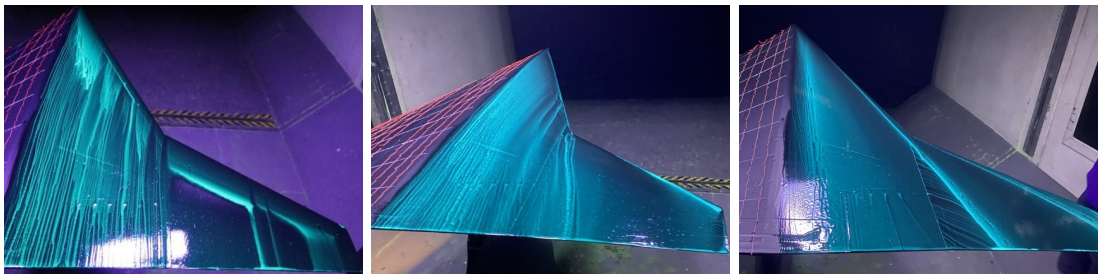
Figure 2.88: Delta wing vortex flow stages as a function of angle of attack [22]

Flow Visualization

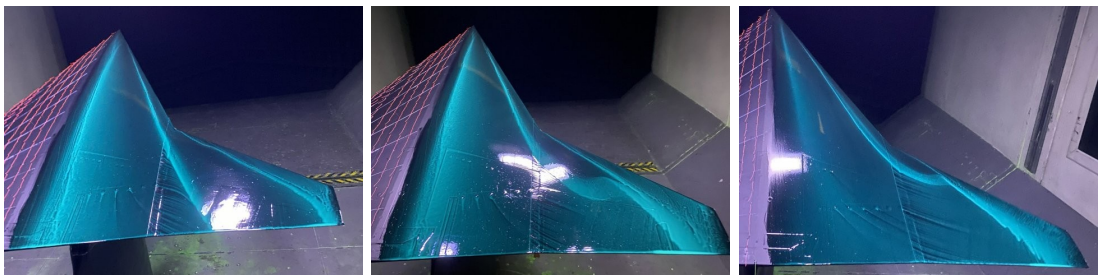
It was expected that the family of planforms to be used for the first set of tests in the NASA SCALOS project would feature generically similar phenomena, but with performance and S&C quantitative behaviors that are more complex and are highly influenced by the rest of the configuration such as canards, nacelles, and tails as well as wing camber, twist, leading edge shaping, and leading edge and trailing edge flap deflections. Therefore, flow visualization tests were conducted to augment force and moment tests by studying the vortices "in action".

The tested configurations of 2015 wing (W15) and UW-S-20A are shown in Figures 2.89 and 2.91. Both are shown for the "clean wing" case, i.e. no LE or TE deflections. Figure 2.89 shows flow visualization photos for the 2015 wing at several angles of attack and at zero sideslip angle. The right half of the model is covered with fluorescent oil, a mixture of mineral oil and fluorescent dye, and the left side is covered with fluorescent tufts illuminated with UV lamps. The flow visualization tests were performed at the nominal dynamic pressure, $q = 32$ psf, and were run for a few minutes to take photos and movies of both sides of the wing. The tunnel was then turned off to take several close-up images of the right side of the wing for further analysis. The tuft photos and snapshots from the movies clearly show attached flow, cross flow over the wing surface, and the flow separation developments with respect to angles of attack, while the oil flow visualization photos show signatures of vortex formation, emergence, and breakdown with respect to angles of attack. Figure 2.90 shows variations of the longitudinal force and moment coefficients of the 2015 wing with angles of attack. The abbreviations in the legends indicate the axis of the force or moment coefficients are in. Body, wind, and stability axis are abbreviated as BA, WA, and SA respectively. Figure 2.90 shows that pitching moment coefficient derivative (C_{M_α}) for the 2015 wing is constant up to $\alpha \approx 5^\circ$ and then starts to decrease, in absolute value, when $\alpha \geq 5^\circ$. For these angles of attack, the lift force ($C_{L,\mathrm{BA}}$) is increasing, while the axial drag force ($C_{D,\mathrm{BA}}$) decreases. The reduction of axial force coefficient is typically due to the leading-edge suction force. For $5^\circ \leq \alpha \leq 10^\circ$, the pitching moment coefficient decreases, while the axial force coefficient remains almost constant and the lift force coefficient continues to increase.

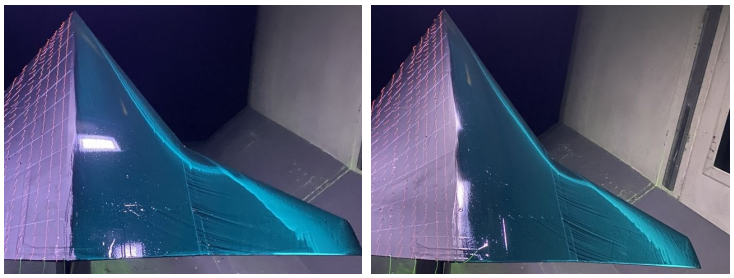
The reduction of pitching moment coefficient is attributed to the flow separation at the outboard section of the wing which has a relatively large moment arm with respect to the wing moment center ($C_{M_{25\%}}$). The increase in drag caused by this flow separation seems to almost cancel the leading-edge suction force such that axial drag force remains almost constant. With further increase of alpha, the inner and outer vortices start to merge, the outer vortex starts to move inboard while the inboard one moves outboard, and the wing tip separation becomes severe. The increase in the axial force coefficient, $\alpha \geq 10^{\circ}$ in Figure 2.90, is due to the extent of flow separation at the wing tip and vortex breakdown/bursting phenomenon which happens at higher angles of attack. The vortex breakdown/bursting is when the vortex abruptly "explodes" causing chaotic flow from that point downstream. Further flow visualization tests were conducted for the 2020-2021 configuration, UW-S-20A, at several angles of attack and at nominal dynamic pressure of $q = 32$ psf in Figure 2.91. The oil flow visualization results are very similar to those of the 2015 wing ones with the exception of the flow behavior in the vicinity of the nacelle and the boundary layer development at the wing body junction.



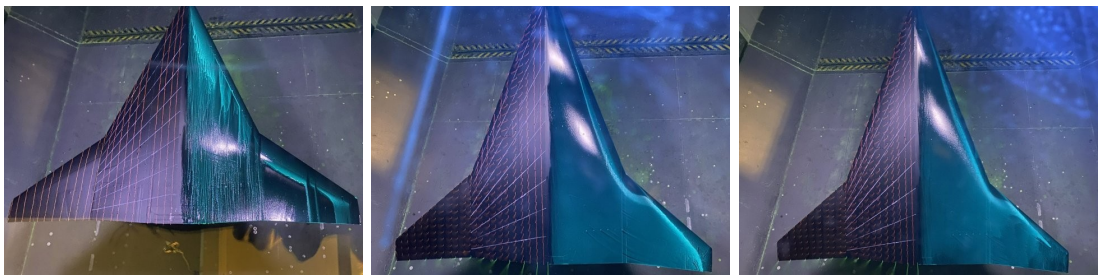
(a) $\alpha = 0°$, wind off (b) $\alpha = 5°$, wind off (c) $\alpha = 10°$, wind off



(d) $\alpha = 12°$, wind off (e) $\alpha = 15°$, wind off (f) $\alpha = 20°$, wind off

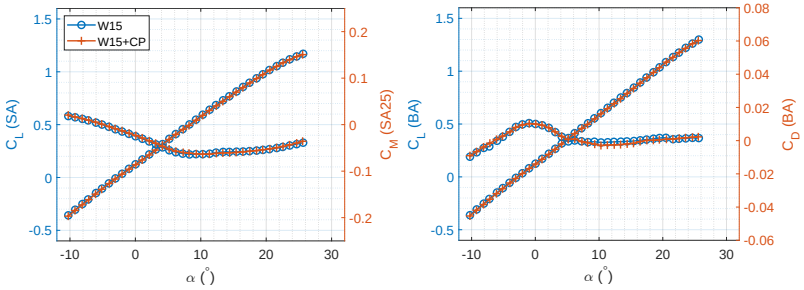


(g) $\alpha = 25°$, wind off (h) $\alpha = 30°$, wind off



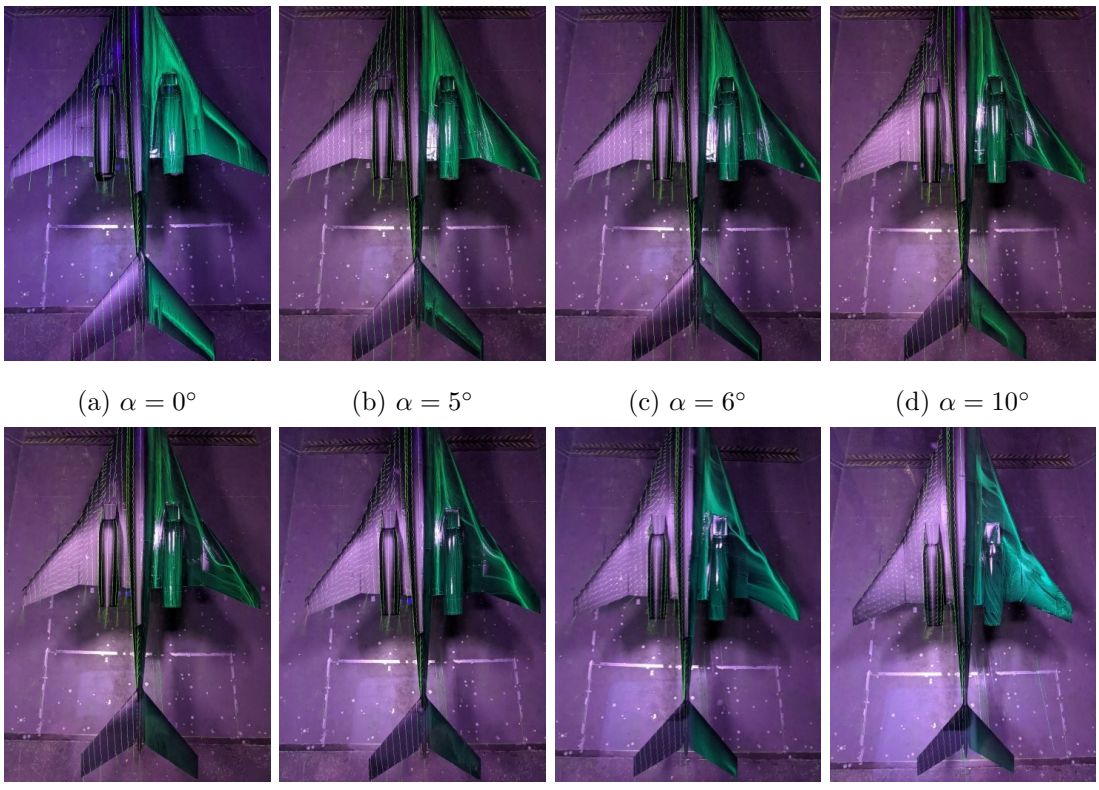
(i) $\alpha = 0°$, wind on (j) $\alpha = 25°$, wind on (k) $\alpha = 30°$, wind on

Figure 2.89: Flow visualization of 2015 wing only (W15) at $q = 32$ psf and $\beta = 0°$ [23]



(a) C_L and C_M vs α (b) C_L and C_D vs α, body axis

Figure 2.90: 2015 wing-only force and moment coefficients at $q = 32$ and $\beta = 0°$



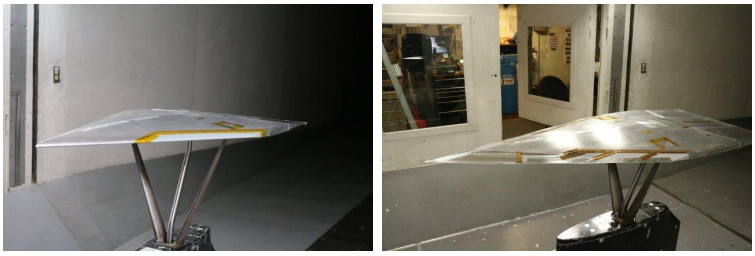
(a) $\alpha = 0°$ (b) $\alpha = 5°$ (c) $\alpha = 6°$ (d) $\alpha = 10°$

(e) $\alpha = 12°$ (f) $\alpha = 15°$ (g) $\alpha = 20°$ (h) $\alpha = 25°$

Figure 2.91: Flow visualization of UW-S-20A at $q = 32$ psf and $\beta = 0°$ [23]

Wing Only

Inboard Contribution and Leading Edge Study Previous sections reviewed vortex theory and formation of vortex systems on the cranked-delta wing [23]. Wind tunnel flow visualization test results were presented. Most of the existing published experimental and computational results have sharp leading-edge and thin delta or cranked-delta wing models with almost zero-thickness airfoils. Most of the SCALOS models do not have sharp leading edges. Therefore wing thickness and leading edge shape effects are essential to study. The vortex formation, vortex behavior, and vortex breakdown/bursting for the present SCALOS study wings are, accordingly, different than those of the sharp leading edge flat plate examples, mainly due to differences in LE vortex initiation location and the behavior of the LE suction force. Recognizing that it can be informative and useful to collect some data using a simplified geometry, the 2023 effort included the study of the inboard wing's contribution and corresponding leading edge shape effects by testing a simple "cropped delta" shape created from available parts of the core 2015 model. Figure 2.92 shows the cropped delta wing-only wind tunnel configuration with round and sharp leading edges, respectively. The cross-section of the leading edges geometries are shown in Fig. 2.93.



(a) Round leading edge (b) Sharp leading edge

Figure 2.92: Inboard wing only [24]

Figure 2.96 presents the effects of the shapes of leading edges on the longitudinal forces and moments. The test results presented in Fig. 2.96 are normalized with respect to the W15 aero reference quantities and the test results presented in Fig. 2.97 are normalized with respect to the cropped delta's projected planform areas (see Fig. 2.93 and Table 2.36).

Table 2.36: Cropped delta geometry [24]

Leading edge	Round	Sharp
S_{ref} (ft^2)	6.42	7.02
frontal delta of S_{ref} (ft^2)	3.34	3.95
b (ft)	2.33	2.33
tested S_{ref} (ft^2)	5.52	6.00
tested frontal delta of S_{ref} (ft^2)	1.95	2.43
tested b (ft)	1.78	1.78

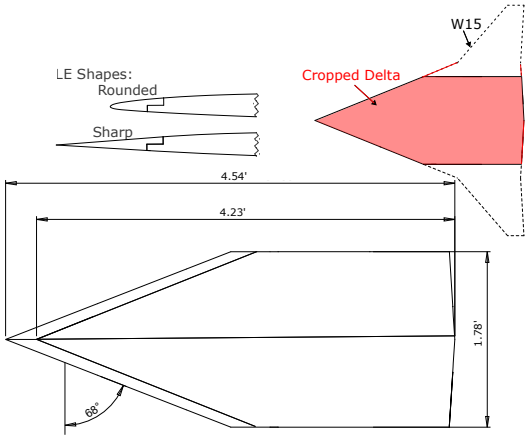
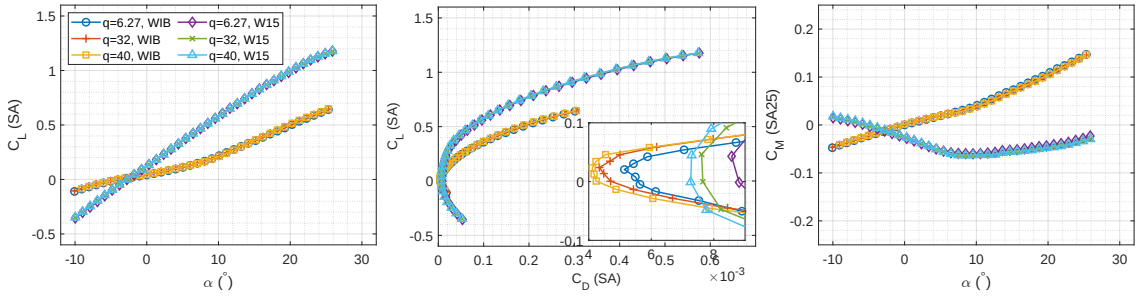
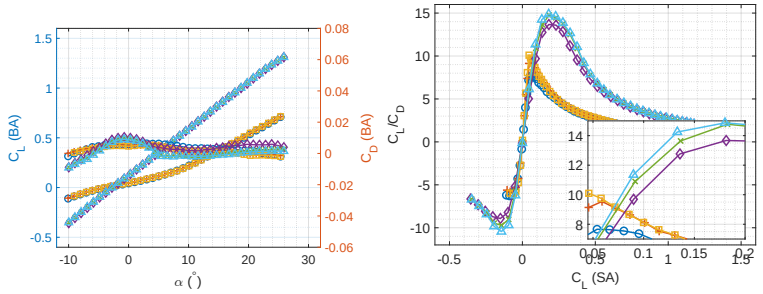


Figure 2.93: Simple cropped delta [24]

Figures 2.94 and 2.95 compare the W15 wing-alone longitudinal aero characteristics to those of the inner "cropped delta" portion of the wing at the nominal dynamic pressure of q=32 psf. The coefficients in Figs. 2.94 and 2.95 are normalized with respect to the W15 wing reference area and moment center. These data give some indication of the relative force and moment contributions of the inner portion of the W15 planform, which uses rounded leading edges selected based on the inboard LE sweep, providing a subsonic Mach number at supersonic cruise conditions (the outboard wing panel, outboard of the LE sweep break, is sharp edged). Thus, the incremental forces and moments in Fig. 2.95 include the effects of the inboard section, outboard section, and mutual interference of both inboard and outboard. The incremental lift curve slopes (Fig. 2.95) indicate a loss in the lift after $\alpha \geq 10°$, suggesting outboard wing flow separation for the "clean wing" case correlating with flow visualization results in the previous section [23]. The optimized wing design would require an outboard wing twist (and/or LE flap deflections) to ensure moderate to high angle of attack performance without flow separation and loss in lift. The incremental pitching moment change in slopes correlates to the vortex lift change in slope in lift at $\alpha \approx 5°$.

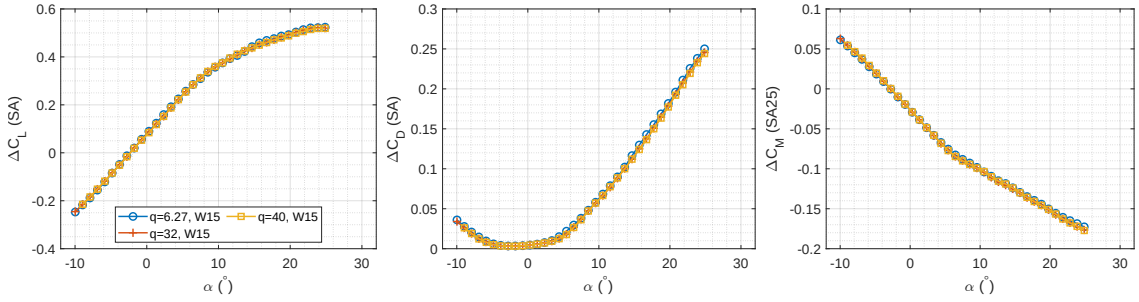


(a) C_L vs. α (b) C_L vs. C_D (c) C_M vs. α



(d) C_L & C_D vs. α (body axis) (e) C_L/C_D vs. C_L

Figure 2.94: Longitudinal forces and moments of cranked-delta wing (W15) vs. inner cropped delta wing



(a) ΔC_L vs. α (b) ΔC_D vs. α (c) ΔC_M vs. α

Figure 2.95: Incremental longitudinal forces and moments of cranked-delta wing (W15) vs. inner cropped delta wing

The lack of variation with dynamic pressure in the deltas shown in Fig. 2.96 would indicate that for the W15 leading edge case (rounded) the increments are only a function of planform, not Reynolds number. Figure 2.96 shows the longitudinal forces and moments of the sharp and round tested on the "cropped delta" planform with respect to angles of

attack and dynamics pressures. The lift and pitching moment coefficients appear to be independent of dynamic pressure. The drag has some variation due to Reynolds number both in skin friction and attainable LE suction levels at the lowest dynamic pressure tested of 6.25 psf. The sharp leading edge, as expected, has more lift than the round leading edge, with corresponding higher induced drag and pitching moment instability. The drag coefficients at the body axis confirm the flow detachment and vortex lift of the sharp leading edge. Examples of the leading edge studies can be found in [64–66].

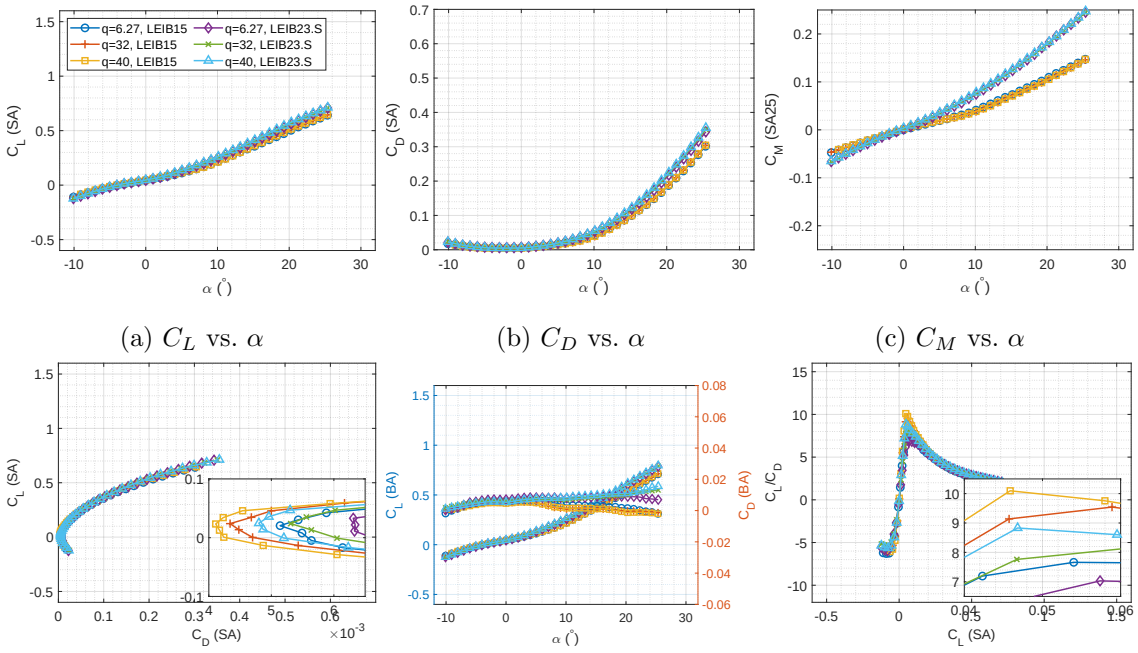
Figures 2.96 and 2.97 have coefficients normalized using the projected planform areas of the cropped delta cases as in Figure 2.93 and Table 2.36. Figure 2.97 rescaled the forces at stability and body axis based on the values in Table 2.36. By the Polhamus vortex lift math model [458], the total lift is a combination of potential lift and vortex lift

$$C_L = C_{L_p} + C_{L_v} = K_p \sin\alpha \cos^2\alpha + K_v \sin^2\alpha \cos\alpha \tag{2.18}$$

where C_{L_p} and C_{L_v} are denoted as the potential lift and vortex lift, respectively. The K_p and K_v are potential and vortex lift factors depending on the wing aspect ratio.

The Polhamus vortex lift assumes a sharp leading edge and thin airfoil. However, the SCALOS inboard wing is cambered, and the thickness of the wing and leading edges cannot be ignored even for a sharp LE geometry. The data in Fig. 2.97 is adjusted for wing incidence angle of $i = 1.45°$. The lift of the inner cropped delta section at a low angle of attack of $-3° \leq \alpha \leq 3°$ is higher than the potential lift and the vortex lift. The zero-alpha lift coefficient shows the cambered airfoil providing lift at zero angle of attack. The vortex lift starts dominating after $\alpha \geq 4°$ where the lift curve changes in slope. That the theoretical vortex lift is less than experimental results may result from the thickness of the airfoil. The drag used the Eq. (2.19) is from [66].

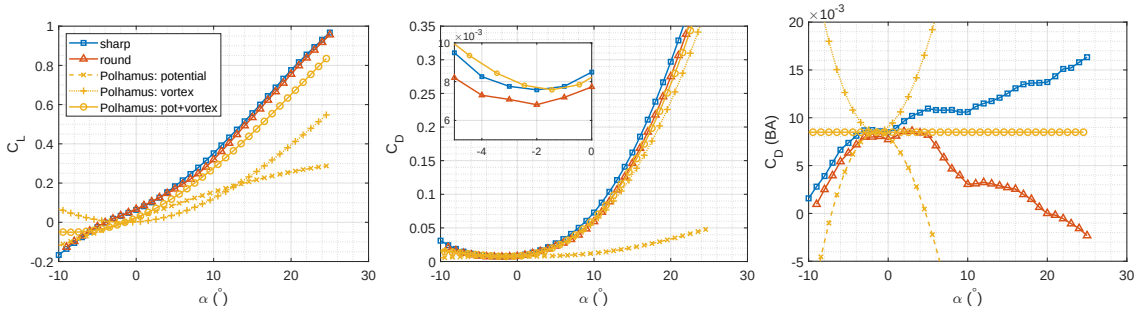
$$C_{D_i} = (C_{L_p} + C_{L_v}) \tan\alpha \tag{2.19}$$



(a) C_L vs. α (b) C_D vs. α (c) C_M vs. α

(d) C_L vs. C_D (e) C_D vs. α (body axis) (f) C_L/C_D vs. C_L

Figure 2.96: Effects of leading edge shape and Reynolds number (q) for the cropped delta wing



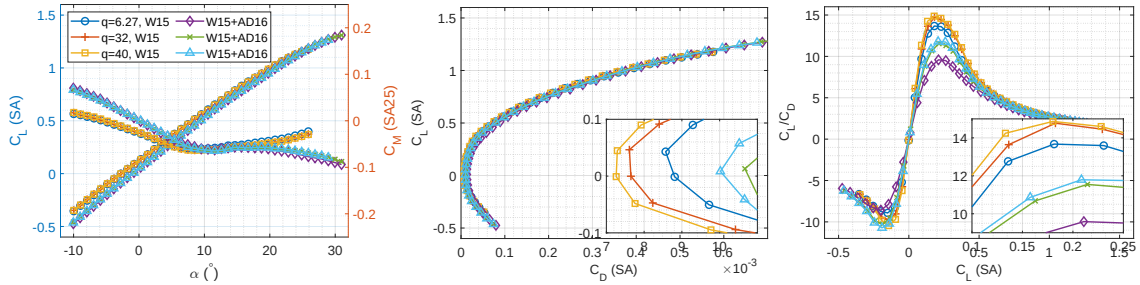
(a) C_L vs. α (b) C_D vs. α (c) C_D vs. α at body axis

Figure 2.97: Effects of leading edge on longitudinal forces and moments vs. α for inboard wing only with respect to tested wing inboard area

Wing + Aft-deck

The wing and aft-deck configuration is shown in Fig. 2.64 in §2.6. Figure 2.98 shows an example of results obtained over a range of dynamic pressures for the wing and wing-aftdeck

longitudinal force and moments. The lift curve and lift coefficient derivative (C_{L_α}) appear independent of Reynold's number. The wing-aftdeck has less lift at $\alpha \leq 20°$ and almost the same lift at the high angle of attack because of the local negative angle of attack for aftdeck at the low angle of attack due to wing downwash. The aftdeck is not producing any lift until $\alpha \geq 10°$. The addition of aft-deck provides a positive zero pitch moment (C_{M_0}) and increases pitch moment stability derivatives (C_{M_α}). The pitch break point is extended from $\alpha \approx 8°$ to $\alpha \approx 11°$. After pitch break point ($C_{M_\alpha} = 0$), the wing alone becomes unstable, and the wing-aftdeck configuration is unstable beyond pitch break point at $11° \leq \alpha \leq 16°$ and stable after another break point at $\alpha \approx 16°$. This suggests natural recovery from pitch-up with addition of aftdeck. The addition of aft-deck increases zero-lift drag (C_{D_0}) which is dominated by skin friction at low speeds. At dynamic pressure of $q = 32$ psf, the difference of zero-lift drag (C_{D_0}) is around 0.0025 (≈ 25 counts). Although the skin friction dominates drag at low speeds, the wave drag dominates at supersonic speed, and the added skin friction of aftdeck becomes less at flight Reynolds numbers.



(a) C_L & C_M vs. α (b) C_L vs. C_D (c) C_L/C_D vs. C_L

Figure 2.98: Effects of aft-deck on longitudinal forces and moments vs. α for wing only

Wing Planform

The effects of OB wing shape, illustrated in Figure 2.49 and specified in Table 2.27, on the longitudinal force and moment coefficients are shown in Figures 2.100 and 2.101. The data presented in Figure 2.100 are for the model without canard, nacelles, and horizontal tail as shown in Figure 2.99, while Figure 2.101 shows similar effects but for the a complete model with forward canard, bottom mounted nacelles, and low horizontal tail as shown in Figure

2.99.

A new 2023 OB wing,(W23), was manufactured to fill "gaps" in configuration design space guided by the design space survey, [13]. The goal was to extend the database for higher OB wing sweep angle as shown in Figs. 2.49. A second alternate planform, designed to "push" the outboard panel aspect ratio and LE sweep lower bound is designated as W13.5. The modifications include a decreased trailing edge and raked wingtip to increase the aspect ratio and decrease chord wetted area while maintaining the same wing reference area as shown in Tab. 2.27 and Figs. 2.49.



(a) Wing-fueslage-vertical-tail model

(b) Three-surface complete model

Figure 2.99: Wing-fueslage-vertical-tail and three-surface, bottom mount nacelle, and conventional low-tail, outboard wing planform variations [24]

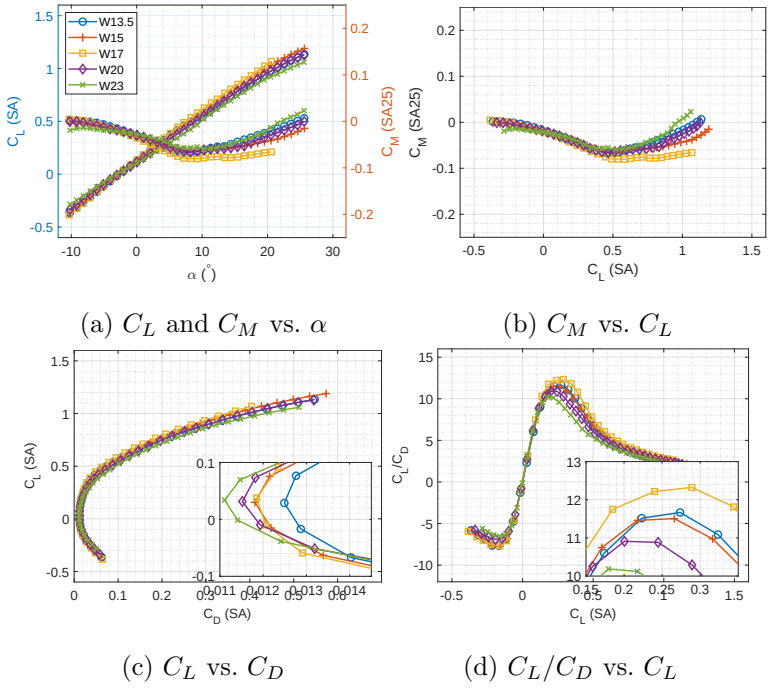
The analysis from [26] is presented in this paragraph without the W13.5 and W23 planforms, which were added in 2023 and are not included in the original paper's analysis. Figures 2.100 and 2.101 show that the W17 shape shows better lift over drag ($L/D \equiv$ LOD $\equiv C_L/C_D$), characteristics for $C_L > 0.2$. For low lift force coefficients, all three shapes show similar behavior. All data currently shown is at wind tunnel Reynolds number and are untrimmed. Figure 2.100 and 2.101 show that the 2020 planform has larger pitch moment derivatives for $\alpha \leq 8°$. The pitching moment derivatives for all shapes become positive almost at the same angles of attack. The pitching moment derivatives of the model with the 2017 planform shape seems to change at large angles of attack, $\alpha \geq 23°$, indicating that the aircraft may become stable again. It could be concluded that the 2017 planform might have better performance characteristics. Figure 2.100 shows that CG location has significant effects on the pitch moment characteristics for all three shapes tested here and

the CG location at 25% of $\bar{c}$ gives a much better pitching moment behavior for all angles of attack. These variations are due to the fact that at low speeds, the leading edge sweep angles and the associated shifts of areas forward and to the rear (together with airfoil shapes and any leading edge and trailing edge flaps) determine the nature of the leading-edge vortex generated by the outer wing, its interactions with the inner leading-edge vortices from the inboard wing, strake, and canard, and the capacity of the wing at higher angles of attack to "hold" its flow and lift without separation. The effects of various CG locations on the static stability of the model with different outboard wing shapes are further shown in Figures 2.100 and 2.101.

The analysis from [24] is presented in this paragraph without simple wing-fuselage-vertical-tail planforms with W13.5 wing, which were tested back-to-back in 2024 and are not included in the original paper's analysis. Figure 2.100 shows the measured variation of longitudinal aero parameters for a simple wing-fuselage-vertical tail configuration. The effects of the outboard wing on the lift curve slope are shown in Fig. 2.100a. The W23 outboard wing has the smallest semi-span ($b/2 = 2.00$ ft), planform-specific wing reference area, $S_{\text{ref}} = 7.83$ ft^2, and the highest sweep angle, $\Lambda = 62°$, from Table 2.27. Note that all the data is normalized with respect to W15 aero reference quantities. This planform leads to the smallest lift coefficient derivatives, pitching moment derivative, static stability, and lift-over-drag ratio as indicated in Fig. 2.100. Note that as the wing sweep angle increases, its low-speed lift decreases and the lift coefficient derivatives are inversely proportional to the sweep angle [23, 371]. The W23 outboard wing has the least stability and lowest angle of attack for the pitching moment break point compared to all other tested planforms. Moreover, the W23 outboard wing has an abrupt slope change behavior at $C_L \approx 0.43$ or $\alpha \approx 9°$ where the pitch moment derivatives change from unstable to stable condition and then become unstable again at $C_L \approx 0.57$ or $\alpha \approx 11.5°$ in Fig. 2.100b. The test results presented to date suggest that the W17 planform has the best untrimmed low-speed aerodynamic characteristics, including lift performance, static stability, and lift over drag compared to the other tested planforms. This is an indicator of the design tradeoffs that must be faced when trying to balance LTO field performance and community noise against supersonic L/D and low boom goals.

The analysis from [25] is presented in this paragraph with all tested simple wing-fuselage-vertical-tail planforms in back-to-back same day testing with final corrected data. The W13.5 was modified from W15 with respect to the same wing reference area but with a higher wing span and aspect ratio, but shorter MAC. The W13.5 three-surface model was tested and presented in [24] but not the simple wing-body-fueslage-vertical-tail in Fig. 2.99, which is tested and presented in Fig. 2.100. The W13.5 lift performance is similar to W15 at $\alpha \leq 8°$, and the W13.5 has a reduction in lift and comparable lift performance to W20 at a high angle of attack. It is likely due to the wing outboard flow separation, which appears to be due to the low sweep causing early leading edge vortex break-down into disorganized unsteady flow, has been observed in the flow visualization in [23]. The loss of vortex lift and organized steady flow over the lower-swept outboard panel degrades the drag polar shape, hence some of the expected benefit of increased span on induced drag is lost. Although the W13.5 outboard wing decreases in lift coefficient at $\alpha \geq 8°$ and pitch moment break point by a degree, it increases in pitching moment derivative, static stability, and lift-over-drag ratio compared to the original W15 wing, like the three-surface configurations. The performance and C_{M_0} would likely be improved with likely at a small loss in C_L at alpha if a wing twist (wash-out) is added to the design (left as future work).

The analysis from [24] is presented in this paragraph with all wing planforms on three-surface configurations, which were across test entires and all the skin frictions are adjusted with respect to Reynolds number. Figure 2.101 shows the effects of the wing planforms on the longitudinal forces and moment versus angles of attack (at zero sideslip angle) for the complete three-surface configuration. The effects are similar to the case of the wing-fuselage-vertical-tail configuration discussed in the previous paragraph. There are differences, however, when comparing the wing-fuselage-vertical-tail configuration to the complete configuration in Figs. 2.100 and 2.101. The three-surface models, as expected, produce more lift as a function of the angle of attack compared to the wing-fuselage-vertical-tail models. The additional lift, generated by the canard and horizontal tail, multiplied by the moment arms, results in additional pitching moments. The contributions of the canard and tail can be positive or negative depending on their own angles of attack, including wing and body downwash and upwash fields. From static stability perspective, the pitching moment break



(a) C_L and C_M vs. α

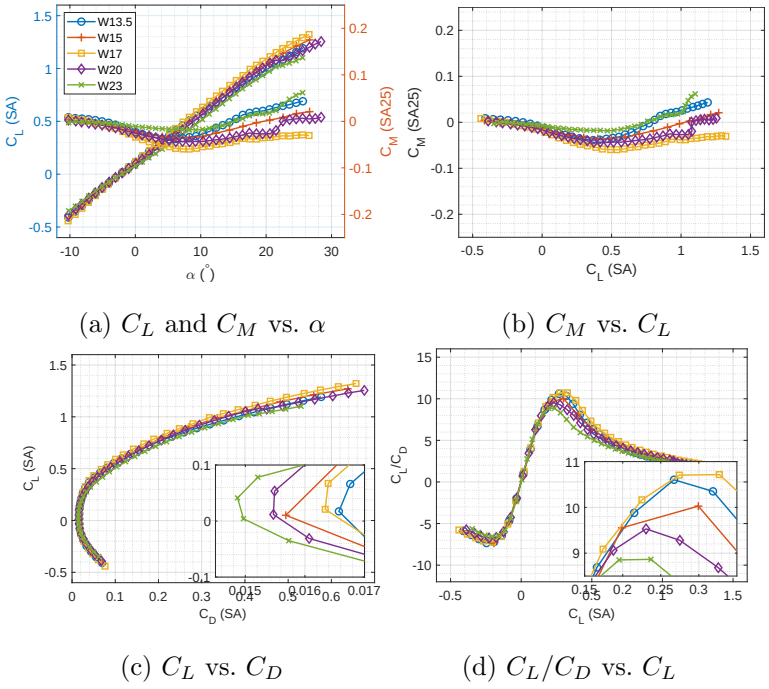
(b) C_M vs. C_L

(c) C_L vs. C_D

(d) C_L/C_D vs. C_L

Figure 2.100: Comparison of wing planform longitudinal trends for longitudinal forces and moments vs. α for wing-body-vertical-tail configuration

points of the W15, W17, and W20 wing planforms for the complete model are the same (clean configuration, untrimmed) at $\alpha \approx 6°$ (Fig. 2.101a) and are lower compared to the simple wing-fuselage-vertical-tail model, Fig. 2.100a. The additional wing planforms, W23 and W13.5, marking the extremes of sweep and aspect ratio, have a lower pitch moment break point at $\alpha \approx 5°$. The W23 wing planform behaves similarly to the wing-fuselage-vertical-tail configuration, showing the smallest lift coefficient derivatives, pitching moment derivatives, stability level, and untrimmed lift-over-drag ratio of all wing planforms. Although W13.5 outboard wing decreases in lift coefficient at $\alpha \geq 13°$ and pitch moment break point by a degree, it increases in pitching moment derivative, static stability, and lift-over-drag ratio compared to the original W15 wing.



(a) C_L and C_M vs. α

(b) C_M vs. C_L

(c) C_L vs. C_D

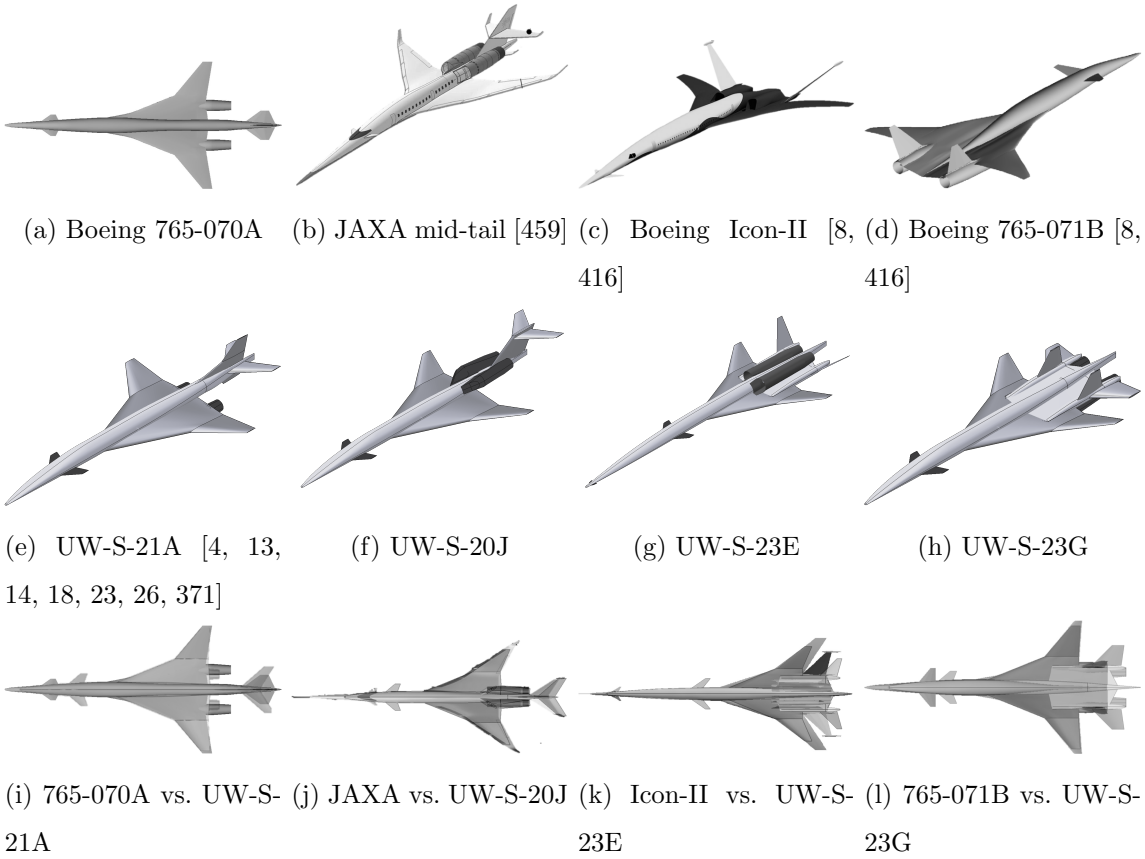
(d) C_L/C_D vs. C_L

Figure 2.101: Comparison of wing planform longitudinal trends for three-surface, low-nacelle, and conventional tail configuration (untrimmed, "clean" cruise wing)

2.7.2 Configuration Studies

Figure 2.102 shows some major general arrangements/aircraft designs from the design space survey in §2.2 [13] and how the selected SCALOS configurations at UW resemble them. A key part of the SCALOS research is the characteristics of general arrangements of candidate designs. The following section presents the corresponding 2023 test effort. Figure 2.102a presents the Boeing 765-070A (N+2 study) configuration derived from the "Ref H" and "2015TC" concepts of the HSCT program. The UW baseline 2015 model was designed to be geometrically similar to Boeing 765-070A. The further evolved 2021 model, designated as UW-S-21A, incorporated the SCALOS study-specific N20 nacelles and improved the horizontal tail authority and lateral stability by enlarging the horizontal tail area and adding ventral and dorsal fins as in Fig. 2.102e. This wind tunnel configuration is the basis for the "RSAC" UW's Reference Supersonic Airliner Concept, a detailed integrated concept aircraft design intended as a point of departure for further technology trades, optimization

problems, or performance and S&C simulations. The second column of Fig. 2.102 shows a typical aft-body nacelle configuration from the Japan Aerospace Exploration Agency (JAXA) design. Figure 2.102c is the Boeing "Icon-II" concept airplane from NASA's N+3 studies emphasizing low-boom and environmental "friendliness". The Icon-II conceptual plane was developed from the earlier Boeing 765-076E and QEVC. The UW-S-23E in Fig. 2.102g was designed to approximate such a configuration and was tested in April 2023. Figure 2.102d is the Boeing 765-071B configuration from the N+2 studies (like the Boeing 765-070A configuration). This general arrangement includes the canard, cranked delta wing, area-ruled fuselage, twin-vertical tail, and under-aft-deck-mounted nacelles. The Boeing Sonic Cruiser design is similar to this general arrangement. The UW-S-23G in Fig. 2.102h was designed to represent a published Boeing SSBJ conceptual design's general arrangement, tested in 2024.



(a) Boeing 765-070A (b) JAXA mid-tail [459] (c) Boeing Icon-II [8, 416] (d) Boeing 765-071B [8, 416]

(e) UW-S-21A [4, 13, 14, 18, 23, 26, 371] (f) UW-S-20J (g) UW-S-23E (h) UW-S-23G

(i) 765-070A vs. UW-S-21A (j) JAXA vs. UW-S-20J (k) Icon-II vs. UW-S-23E (l) 765-071B vs. UW-S-23G

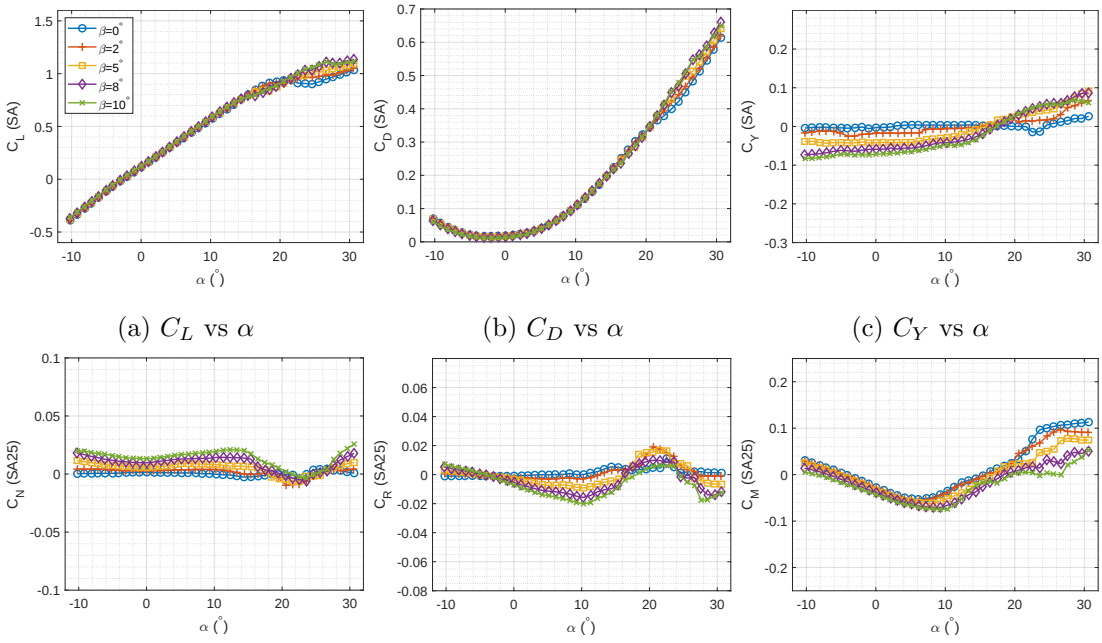
Figure 2.102: Design space configuration studies [13]

UW-S-20A Baseline (2020–2021 Model)

All comparisons here are for "clean" cruise wing geometry (no leading or trailing edge flap deflections). Figure 2.104 shows the effect of yaw angles on the variations of the aerodynamic forces and moments of the SCALOS model with angles of attack for a dynamic pressure at 32 psf. For these tests, the model was first set to a specific yaw angle, $\beta = 0°, 2°, 5°, 8°, 10°$, and the angles of attack were varied from $\alpha = -10°$ to $30°$ for each yaw angle. From this figure one can see that the variations are linear for low sideslip angles and low angles of attack. At higher sideslip and angles of attack the variations are nonlinear because of the asymmetry, emergence, and breakdown/bursting of the vortices. It is important to note that when the model is set at a sideslip angle, the side of the wing into the wind has less effective sweep angle, $\Lambda_{\text{effective}} = \Lambda_{\text{LE}} - \beta$, and the other side of the wing has more effective sweep angle, $\Lambda_{\text{effective}} = \Lambda_{\text{LE}} + \beta$. Therefore, the vortices over the left and right wing are asymmetric resulting in asymmetric forces and moments over the left and right wings. The lift force coefficient does not vary with sideslip angle up to $\alpha \approx 15°$. Beyond $\alpha \approx 15°$, stall occurs at higher angles of attack as the sideslip angle increases because of the delay in vortex breakdown/burst over the side of the wing with larger effective sweep angle. The pitching moment coefficient derivative is almost independent of the sideslip angle. The pitching moment coefficient at zero angle of attack ($C_{M_{\alpha=0°}}$) varies as the yaw angle is varied in Figure 2.103. The figure further shows that UW-S-20A becomes longitudinally unstable for $\alpha \geq 8°$ for all sideslip angles examined here and the pitching moment coefficient varies nonlinearly with an erratic behavior as $\alpha \geq 18°$ for all yaw angles.

The lateral directional moment coefficients behave stably and linearly for low angles of attack at all sideslip angles. Roll and yaw moment coefficients (C_R and C_N) change sign and become nonlinear for $\alpha > 10°$ because of the asymmetric vortex breakdown/burst over the wing surface. For $\alpha > 15°$, the lateral directional moments show erratic behavior with angles of attack at all sideslip angles from $\beta = 0°$ to $10°$ examined here. As a consequence, the control surfaces of the elevator, rudder, and ailerons must be designed so that the moments created by their deflections would be able to overcome the configuration moment variations without large penalties. The current results do not cover the effect of re-sizing tails or

control surface areas, or what limits might be placed on the operating center of gravity (CG) range of the aircraft as a function of fly-by-wire stability augmentation scenarios. More wind tunnel tests and validated CFD simulations should be used for that.



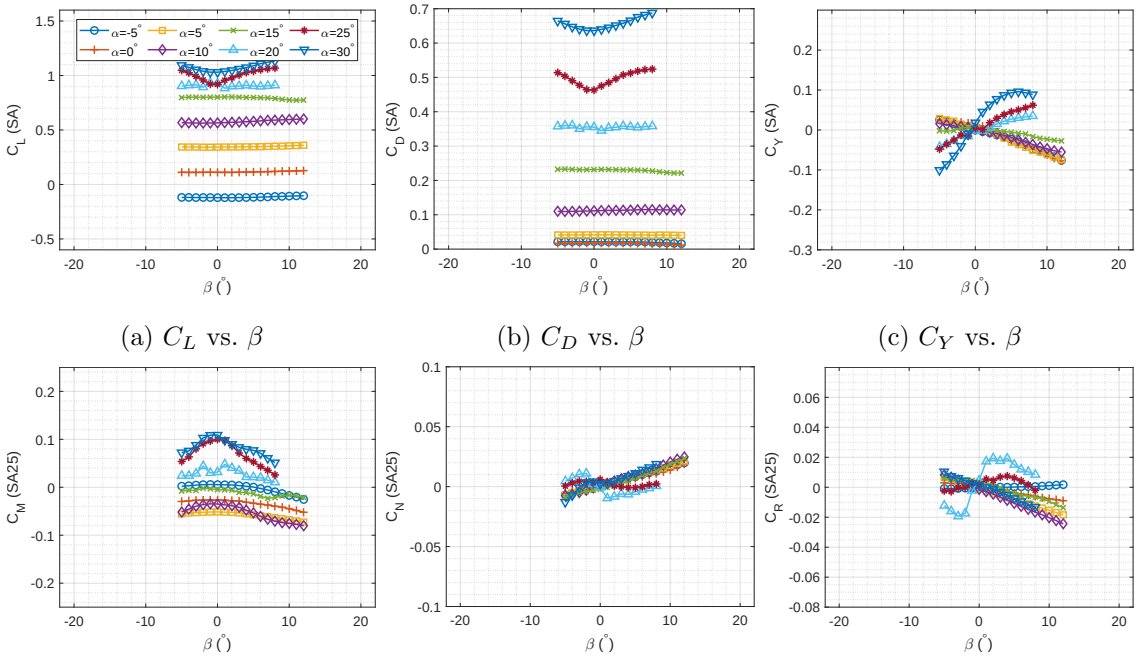
(a) C_L vs α (b) C_D vs α (c) C_Y vs α

(d) C_N vs α (e) C_R vs α (f) C_M vs α

Figure 2.103: Effects of β on force and moment coefficients vs. α for UW-S-20A

Figure 2.104 shows variations of the aerodynamic force and moment coefficients with sideslip angles at angles of attack of $\alpha = -5°$ to $30°$. For these tests, the model was set to a specific angle of attack and the sideslip was varied to record all aerodynamic forces and moments. This figure shows that for all sideslip angles, the lift force coefficient increases as $\alpha = -5°$ to $30°$; however, the increase in lift force coefficient decreases beyond $\alpha > 15°$ significantly. Moreover, the variations of lift force coefficient with sideslip angles are almost constant for $-5° < \alpha < 15°$, but are nonlinear for lift force coefficient at $\alpha > 15°$ caused by the vortex breakdown and flow separation over the wing surface. These variations are evident from drag force coefficients as plotted in Figure 2.104. For $-5° < \alpha < 0°$, drag force coefficients are independent of both angles of attack and sideslip angles because of the potential flow nature of the flow. As the angle of attack increases, the drag force coefficient

increases from the flow separation at the outboard sections of the wing and the vortex breakdown over the side of the wing away from the wind, and the drag force coefficient variations with the sideslip angles are constant for $-5° < \alpha < 20°$ as shown in Figure 2.104. For $\alpha > 20°$, the drag force coefficient varies nonlinearly with sideslip angles. The figure further shows both roll and yaw moment coefficients varying linearly at $-5° \leq \beta \leq 5°$ and $-5° \leq \alpha \leq 10°$ and becoming nonlinear at $\beta > 5°$ and $\alpha \geq 10°$. Both roll and yaw moment coefficients vary erratically with sideslip angles due to the flow separation over various portions of UW-S-20A. Note that the longitudinal force and moment coefficients do not show significant sensitivity to β as the lateral directional ones do. Not surprisingly, the longitudinal force and moment coefficients are very sensitive to the changes of angle of attack, while the lateral directional ones are sensitive to the sideslip angles.



(a) C_L vs. β (b) C_D vs. β (c) C_Y vs. β

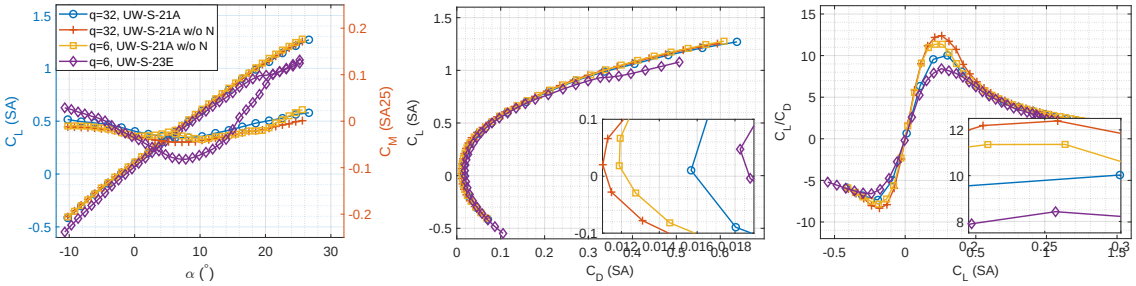
(d) C_M vs. β (e) C_N vs. β (f) C_R vs. β

Figure 2.104: Effects of α on force and moment coefficients vs. β for UW-S-20A

UW-S-23E (Icon-II-like Configuration)

Figure 2.84 shows the wind tunnel models that correspond to the configurations, UW-S-21A and UW-S-23E, presented in Fig. 2.102. Figure 2.105 shows the aircraft design / general arrangement effects on the longitudinal forces and moments with respect to the angle of attack between UW-S-21A and UW-S-23E, omitting UW-S-20J. The UW-S-23E was tested at lower dynamic pressures of $q = 6$ and $q = 10$ psf to avoid severe model dynamics at $\alpha \geq 20°$; however, the C_{D_0} is adjusted to the $q = 32$ psf level for comparison with UW-S-21A. The UW-S-21A has been previously presented in [4, 23, 26, 371] and appears to provide the best low-speed friendly candidate so far in this program. The UW-S-21A was used to study the T&I as previously mentioned in §2.6 and was tested at a lower dynamic pressure which is used to compare with UW-S-23E. The Icon-II like UW-S-23E is a three-surface canard-wing-aftdeck-V-tail model, which is comprised of the 2015 extended "low boom" fuselage, W20 outboard wing with ogive leading edges and strake blending into the fuselage, a large aft-deck (AD16), nacelles integrated with aft-body fuselage (N18), canards (C15), and new V-tails (V23). The details of the model build-up are in §2.5 with part designations in Tab. 2.31 and the corresponding dimensions in Tab. 2.27. Note again that the preliminary trends presented in earlier papers are replaced with final corrected data in this dissertation. Since the lift curve is independent of dynamic pressure, the UW-S-23E should have the same lift performance at $q = 32$ psf. The aft-deck has lift reduction previously shown in Fig. 2.98 with a simple wing-aftdeck configuration. Although UW-S-23E uses the W20 outboard wing ($\Lambda_{\text{LE}} = 53.5°$) instead of the W15 outboard wing ($\Lambda_{\text{LE}} = 41.0°$), similar performance and lift reduction could be expected from Fig. 2.98. The same lift reduction is observed in UW-S-23E, except the lift reduction is extended to a higher angle of attack. The dip in lift near $\alpha = 20°$ seems to be the combination effect of the higher sweep W20 wing and top-mounted nacelles. The aftdeck increases the pitching moment derivatives as previously observed in Fig. 2.98, except the complete model does not seem to exhibit the natural pitching moment recovery but becomes completely unstable after the pitch break point. Ref [23] discussed the effect of canard effeteness, which flattens maximum lift coefficient ($C_{L_{\max}}$) and improves stall characteristics; however, the canard

reduces pitching moment coefficient derivatives and losses longitudinal stability after pitch break. Further work on the comparative results and flow visualization may help understand the physics of the flow interaction between the canards, the wing, and the nacelles better on the UW-S-23E type configuration. Both UW-S-21A and UW-S-23E reduce the angle of attack of the pitch break point (undersizable), and the zero-alpha pitching moments (C_{M_0}) are negative in both online and final data. It should be noted that the aftdeck geometries are only representative of the general arrangement class and were in no way optimized for the SCALOS studies. The untrimmed flaps-up clean wing drag polar shows UW-S-21A at both $q = 6.27$ and $q = 32$ psf with and without nacelle compared with UW-S-23E. The reduction in lift and increases in drag cause lower lift-over-drag for the UW-S-23E configuration compared to UW-S-21A in both preliminary and final comparison.



(a) C_L & C_M vs. α (b) C_L vs. C_D (c) C_L/C_D vs. C_L

Figure 2.105: Comparison of configuration general arrangement results for longitudinal forces and moments vs. α

UW-S-23G (Boeing 765-071B / "Sonic Cruiser"-like)

Figure 2.106 shows the UW-S-23G and UW-S-23H configuration with incremental build-up starting with no nacelles (N23.BR). The wing and aft-deck were tested and presented in previous sections [24]. A quick summary of the addition of aft-deck onto the wing: the addition of aft-deck onto the wing has less lift at $\alpha \leq 20°$ and almost the same at $\alpha > 20°$; the aft-deck provides a positive zero pitch moment (C_{M_0}) and increase pitching moment stability derivatives (C_{M_α}); pitch break ($C_{M_\alpha} = 0$) is extended, and negative pitching moment at $\alpha > 0°$. It is also important to note that the aft-deck geometries are only representative of

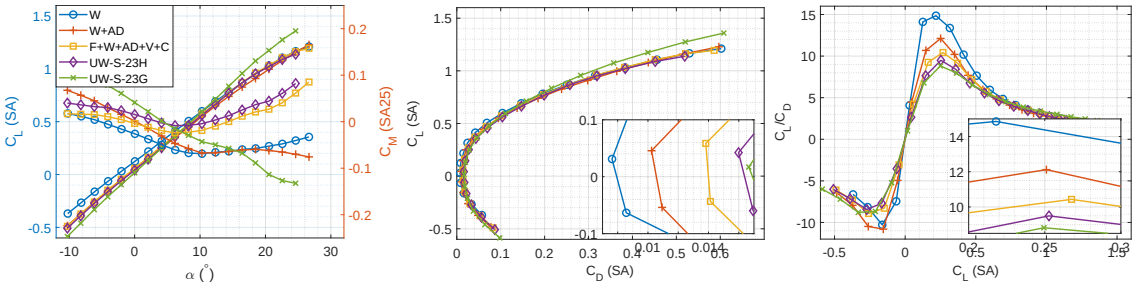
the general arrangement class and were in no way optimized for the SCALOS studies. The UW-S-23G is a three-surface canard-wing-aft-deck-vertical-horizontal-tail model, which is comprised of the 2015 fuselage, W15 outboard wing with normal leading edges, a large aft-deck (AD16), under aft-deck nacelles (N23.BR), forward canards (C15), twin vertical tails (V16T.2), and aft-deck horizontal tails (H18) in Tab. 2.12.

Representative aero measurements are plotted in Fig. 2.107 for the UW-S-23G built-up with the respective configurations shown in Fig. 2.106. Figure 2.107 shows the longitudinal aerodynamics at zero sideslip angle. The buildup from wing-aft-deck to UW-S-23H without nacelles increased C_L at $-4^\circ \leq \alpha \leq 24^\circ$ and the addition of the nacelles decreased C_L at $\alpha \leq 16^\circ$, while the pitching moment break point was reduced from $\alpha \approx 10^\circ$ to $\alpha \approx 6^\circ$. Reference [23, 24] and later in §2.7.4 discuss the effect of canard, which flattens the maximum lift coefficient ($C_{L_{\max}}$) and improves stall characteristics; however, the canard reduces pitching moment coefficient derivatives, losing longitudinal stability after pitch break. The canard has a destabilizing effect causing pitch up at $\alpha > 6^\circ$ and the addition of the nacelles results in an almost constant pitching moment shift (ΔC_{M_0}), like the result in UW-S-20 nacelles location studies in [24]. The UW-S-23G is UW-S-23H with aft-deck horizontal stabilizer. The horizontal stabilizer increased the C_{L_α} with some nonlinear lift increase at $\alpha \approx 16^\circ$ where the C_{M_α} changed. The UW-S-23G is the most longitudinally statically stable SCALOS aircraft tested so far, as might be expected for less slender, more "fighter-like" general arrangements. From the drag polar (C_L vs. C_D), the buildup increased zero-lift drag (C_{D_0}). The fuselage, canard, and twin vertical tails are roughly 35 counts (1 count = 0.0001). The additions of under-deck nacelles are roughly 20 counts, and horizontal tails are roughly 8 counts. The penalty of the horizontal stabilizer is roughly 8 counts of C_{D_0} and decreases the lift-over-drag ratio (LOD, C_L/C_D) from 9.5 to 8.8, but with negative C_{M_α} throughout angles of attack. The increased zero-lift drag due to higher wetted area would be smaller for the full-scale aircraft operating at higher Reynolds number, but would need to be traded against stability and trim drag benefits. Note that the test configuration is only representative of a class of general arrangement, and the aero loft shapes and tail sizes have not been optimized for any particular flight condition or weight-drag trade.



(a) UW-S-23H without nacelles (b) UW-S-23H (c) UW-S-23G

Figure 2.106: UW-S-23G configuration built-up [25]



(a) C_L & C_M vs. α (b) C_L vs. C_D (c) C_L/C_D vs. C_L

Figure 2.107: UW-S-23G configuration build-up, longitudinal force and moment vs. α at $\beta = 0°$

Overall Comparison

The comparisons between three-surface, bottom-mounted nacelles, low-tail empennage system and three-surface, top-mounted nacelles, T-tail empennage system were previously presented in [23, 24, 26, 371]. The UW-S-21A has been a target of interest for its low-speed characteristics. The area-ruled fuselage was designed with linear supersonic tools, targeting a smooth net configuration area distribution that approximates a Sears-Haack equivalent body, and integrated with the UW-S-21A to become the UW-S-24A. The only differences are the fuselage definition and horizontal tail-to-aft-body intersection shape (H24, essentially the same as H20). The aerodynamic test results are presented in Fig. 2.108, but more detailed analyses are presented in §2.7.3. The model configurations are tabulated in Tab. 2.12 and shown in Figs. 2.84. The UW-S-23E was tested at lower dynamic pressures of $q = 6$ and $q = 10$ psf to avoid severe model dynamics at $\alpha \geq 20°$ (likely related to the

model's mass distribution and flexing of the fork mount); however, Ref [24] showed that the dynamic pressure affected the C_{D_0} (due to skin friction differences) and shifting the corresponding drag polar, but not lift or pitching moments.

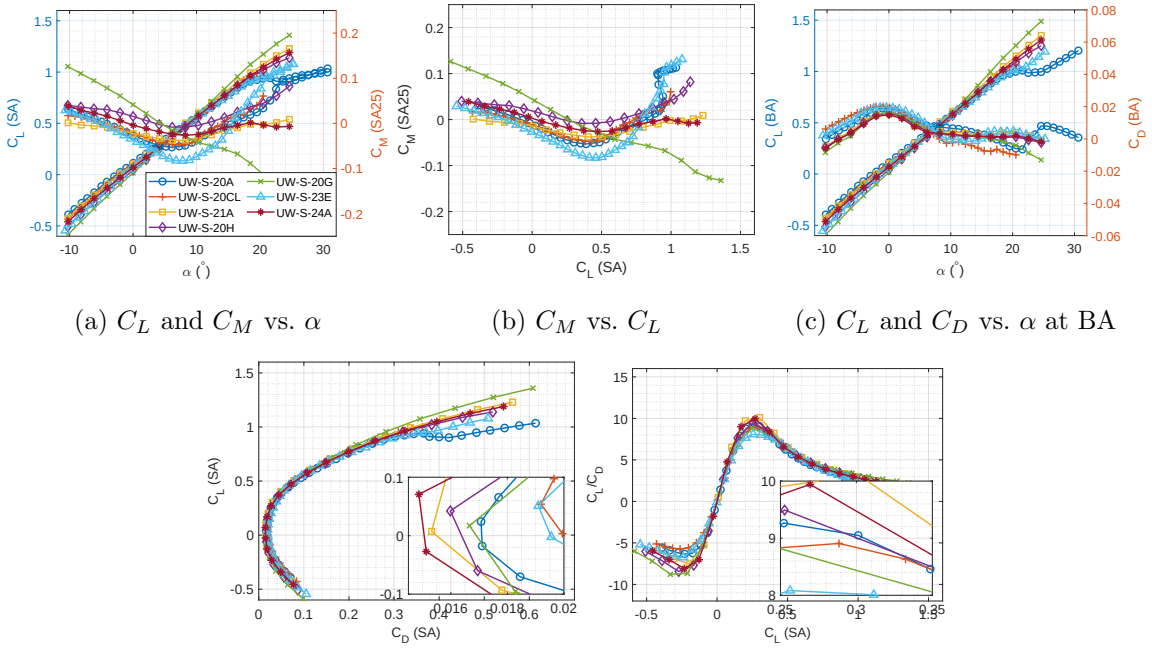
The aft-deck addition results in a lift reduction in both UW-S-23E, shown in the previous section [24], and UW-S-23H in Fig. 2.107. Although UW-S-23H uses the W15 outboard wing ($\Lambda_{\text{LE}} = 41.0°$), unlike the UW-S-23E configuration which uses the W20 outboard wing ($\Lambda_{\text{LE}} = 53.5°$), similar performance and lift reduction are shown in Fig. 2.108. Unlike the UW-S-23E, the UW-S-23H doesn't have lift reduction at $\alpha \approx 20°$, which is likely due to the top-mounted nacelles flow-field interference effect.

Given the same general configuration, the pitching moment derivatives are dominated by the outboard wing. The UW-S-21A, UW-S-23H, and UW-S-24A have the same W15 outboard wing with similar pitching break points and C_{M_α} before pitch break. Although UW-S-20A and UW-S-20CL have similar configurations, the long forward fuselage, nozzle shock reflection deck (NSRD), and ogee leading edge planform shifted the aerodynamic center and rotated C_{M_α}. The UW-S-23E has the most negative C_{M_α}; however, it also has the most severe pitch up after the pitching break point. The pitching moment behavior resulted from the combination of the long forward fuselage, large aft-deck, top-mounted nacelles, and V-tail arrangements.

The long forward fuselage, canard, and top-mounted nacelles interaction have a destabilizing effect, while the aft-deck has a stabilizing effect. The drag polar and LOD figures in Fig. 2.108 show that the UW-S-21A and UW-S-24A have the lowest C_{D_0} and highest LOD. The UW-S-20A, UW-S-23G, and UW-S-23H have similar C_{D_0} and LOD, but UW-S-23G, with additional horizontal stabilizers, has a bit more drag and lower LOD. Lastly, the UW-S-20CL has the highest drag due to the long forward fuselage and NSRD. This gives some indication of the drag penalties that must be trades-off, even at subsonic conditions, when biasing the configuration toward the lowest potential cruise sonic boom levels. The UW-S-23E requires additional analysis for Reynolds number effect on C_{D_0}, but similar performance is expected like UW-S-20CL on C_{D_0} and LOD. The lift and drag coefficient in body axis (BA) is also plotted in Fig. 2.108.

At lower alphas, the inverted parabola shape of the C_D BA indicates the flow attachment

on the aircraft, and the abrupt departure of the curve from parabolic behavior usually suggests flow detachment initially resulting in increased lift (Polhamus Suction Analogy), and then indications of vortex breakdown at the higher alphas. As mentioned above that the UW-S-21A, UW-S-23H, and UW-S-24A have the same W15 outboard wing with similar C_D BA. Although UW-S-20A and UW-S-20CL have similar configurations and the same W20 outboard wing, the flow is more attached for UW-S-20CL due to the ogee leading edge design as shown in Fig. 2.49. The abrupt behavior of UW-S-20A and UW-S-23E seem to be correlated with the outboard wing stall at $\alpha \approx 20°$ (LE vortex break-down) and at pitching moment derivative change at $\alpha \approx 16°$, respectively.



(a) C_L and C_M vs. α (b) C_M vs. C_L (c) C_L and C_D vs. α at BA

(d) C_L vs. C_D (e) C_L/C_D vs. α

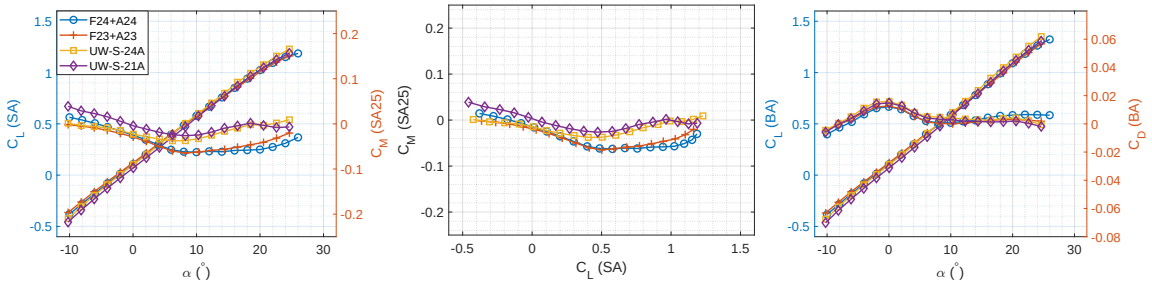
Figure 2.108: Comparison of configuration general arrangement characteristics for longitudinal forces and moments vs. α at $\beta = 0°$

2.7.3 Fuselages

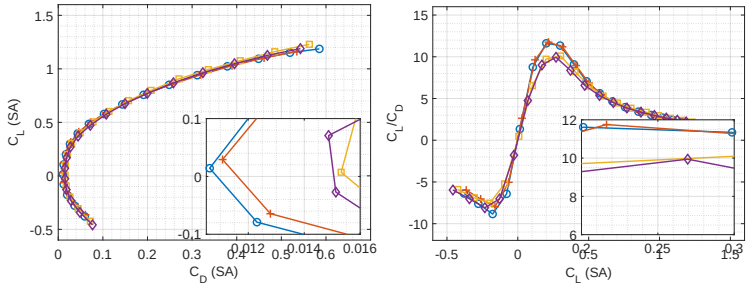
F23+A23 vs. F24+A24 Wing Body

The UW-S-21A has been the selected configuration concept for RSAC for the SCALOS project. However, it used the generic SCALOS model un-cambered, non-area-ruled fuselage. An area-ruled fuselage was proposed in [24] and left as future work. A major effort of in 2024 was studying the area-ruled fuselage effect at low speeds. The area-ruled fuselage (forward and aft components, F24 and A24) was designed with a total area distribution closely approximating a Sears-Haack body and incorporated centerline camber and nose shaping more representative of a full-scale configuration with adequate pilot visibility, reduced trim drag (more positive C_{M_0}), and improved high alpha directional stability. The area-ruled fuselage is shown in Fig. 2.84 and has the same smooth paint as the 2023 fuselage (2015 definition with T&I testing capability) in [24]. Aforementioned in §2.7.2, the UW-S-24A has the same configuration as UW-S-21A except with an area-ruled fuselage, different horizontal tail hardware (H24), and small adjustments to the stream-wise and vertical mounting locations versus H20. The basic wing-body and three-surface configurations' aerodynamic force and moments are presented in Fig. 2.109.

The area-ruled fuselage has less lift at $\alpha \leq 10^\circ$ and more lift at $\alpha \geq 10^\circ$. The area-ruled fuselage increases in C_{M_0}, C_{M_α}, and pitching break point for both simple wing-body and three-surface configurations. Both changes in lift and pitching moments suggest the area-ruled fuselage is generating some forward lift, as intended. The C_{M_0} difference for three surface configuration is likely resulted from the combination effect of the area-ruled fuselage, the slight difference in H24, and its mounting location. The UW-S-24A has a softer pitch-up behavior ($C_{M_\alpha} > 0$) and almost the same pitch-up moment ($C_M \approx 0$) as the UW-S-21A. Furthermore, the UW-S-24A has another pitch break at $\alpha \approx 18.5^\circ$, becomes stable again $18.5^\circ \leq \alpha \leq 22.5^\circ$, a break point at $\alpha \approx 22.5^\circ$, and then unstable beyond. The area-ruled fuselage has lower C_{D_0} (roughly 5 counts) and almost the same LOD for simple configuration, and the difference for three surface might be a bit more due to the combined horizontal tail difference,



(a) C_L and C_M vs. α (b) C_M vs. C_L (c) C_L and C_D vs. α at BA



(d) C_L vs. C_D (e) C_L/C_D vs. α

Figure 2.109: Comparison of area-ruled and non-area-ruled fuselage with wing-body and three-surface configuration for longitudinal forces and moments vs. α at $\beta = 0°$

2.7.4 Canards

The SCALOS model could be equipped with canards on the fuselage ahead of the main wing. The canard option has three different longitudinal mount locations. The C15, C17, and C23 canards' geometric details are listed in Table 2.27 and illustrated in Figure 2.49. Both 2015 and 2017 canards have the same sweep angles, but with different chord length and wingspan were as shown in Table 2.27 and in Figure 2.49. The C23 canards were designed to be of higher sweep and span, guided by the design space survey in §2.2 [13]. In the interest of getting an early exploratory test, the C23 canards were 3D printed using carbon-filled plastic in 2023. These proved to have excessive aeroelastic deflections which limited them to test at q=6.25 psf. The comparison between the C15 and C23 canards was conducted at $q = 6.25$ psf on the UW-S-23E configuration as shown in Fig. 2.84. Note that the UW-S-23E was tested at a lower dynamic pressure due to severe model dynamics, as previously mentioned in §2.7.2. Figure 2.110 shows the UW-S-20A with canard increments and mount locations

and Figure 2.111 shows UW-S-21A with canard increments and planform difference.



(a) No canard (b) Forward position (C15.F) (c) Aft position (C15.A)

Figure 2.110: Canard on/off and location for UW-S-20A [23]



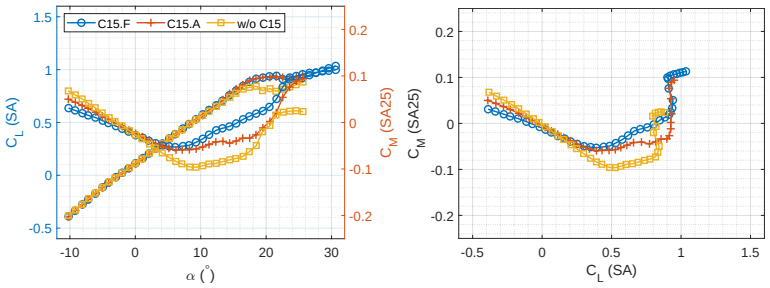
(a) UW-S-21A/C no canard (b) UW-S-21A (C15.F) (c) UW-S-21C (C17.F)

Figure 2.111: Forward canard on/off and planform [23]

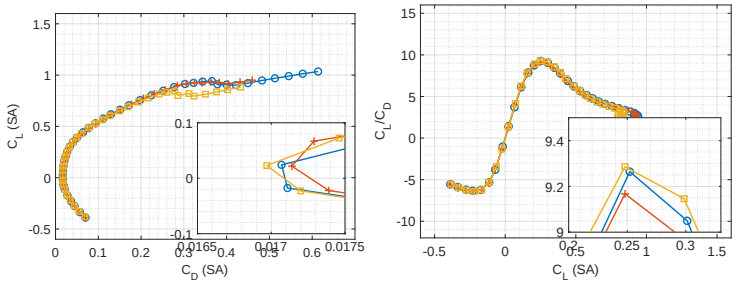
Canard Longitudinal Location – UW-S-20A

Figure 2.112 shows that the canard does not influence the lift coefficient until up to $\alpha \approx 18°$ and it flattens the $C_{L_{\max}}$ for better stall characteristics. The effects of the canard on the pitching moment variation are significant leading to pitch up at lower angles of attack and reduced C_{M_α} resulting in loss of longitudinal stability. Similar results are seen when the CG is changed in Figures 2.112 and 2.113. The small canards, which are installed at a distance ahead of the main part of the wing, studied here would have the lifting surface contribution to shifting the neutral point of the configuration forward, but they would also affect the configuration by the flow associated with their lift (and corresponding canard downwash) and tip vortices. Those canard vortices interact with the strakes (i.e. more highly swept inboard wing panels) and the leading edges' vortices of the wing to delay the separation on the wing when the canards are effective and lose this effect when the canards

are no longer effective. Additional studies, will, hopefully, add insight into the physics of supersonic canard/wing configurations when the forward fuselage is long and the canard is small at a distance from the wing. Note that both tail and nacelle location effects need be considered for potential coupling with the canard effects. The data gathered in the tests can shed light on such coupling effects.



(a) C_L and C_M vs. α (b) C_M vs. C_L



(c) C_L vs. C_D (d) C_L/C_D vs. C_L

Figure 2.112: Canard on/off and locations, UW-S-20A, force and moment coefficients at $\beta = 0°$

Canard Planform Sizes

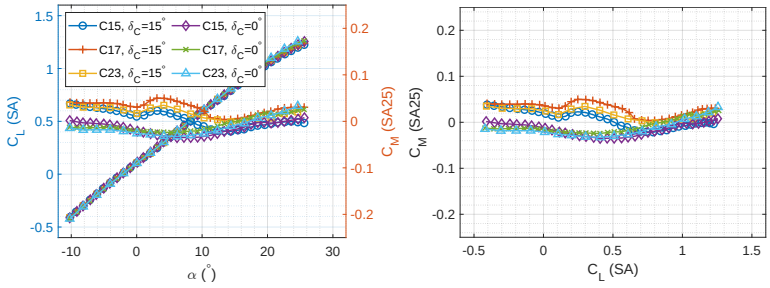
The analysis from [23] is presented in this section without the C23 canard planforms, which were added in 2023 with 3D printed and fabricated in solid aluminum in 2024, and are not included in the original paper analysis. Figure 2.113 compares SCALOS models with two different canards, the 2015 and 2017 canard models. The lift curves do not vary significantly with canard sizes and angles of attack as well as C_L/C_D shown in Figure 2.113. Canard sizes significantly affect the pitching moment coefficient variations. The pitching moment coefficient derivatives, the pitching moment coefficient at $\alpha = 0°$, the angle of attack when

pitch up condition occurs, and the pitch moment variations after the pitch up conditions are all affected by the size of the canard. Of course, some of these variations are caused by the lift of the canard surfaces multiplied by the moment arm, creating a large nose-up pitching moment. Therefore, the position of the canard plays a significant role in these variations. The interaction of the wake of the canard as well as its vortices and their interactions with the wing and horizontal tail flow field might have caused some of these variations. Future work of flow visualization and CFD simulations help understand the physics of the flow interactions between the canard, the wing, and the horizontal tail better.

The analysis from [24] is presented in this paragraph with the 3D-printed C23 canard planforms, which was suffered from aeroelastic deformation and fabricated in solid aluminum in 2024. The comparison between C15 and C17 canards was presented in [23], and the C15 canards control authority was presented in [371]. Figure 2.113 compares SCALOS models with two different canards, the C15 and C17. Figure 2.113 shows the C23 canards do not influence the lift coefficient until up to $\alpha \approx 13^{\circ}$ and then show a slight offset compared to the C15 canards. The sizes of the lifting surfaces resulted in the difference in lifts as discussed in [23]. The resulting lift difference multiplied by the moment arm translates the lift force to the pitch moment coefficient deltas. As opposed to the horizontal tails, the canards act in the opposite direction and cause the aircraft to pitch up, resulting in a slight loss in longitudinal stability as shown in Figure 2.113. The loss in longitudinal stability between the C15 and C23 canards is not as great as between C15 and C17. From the untrimmed drag polar, Fig. 2.113 suggests that the zero-lift drag of the C15 canards are lower than the C23 canards which is as expected due to reduced wetted area. The interaction of the wake of the canard as well as its vortices and their interactions with the wing and horizontal tail flow field, might have caused some of these variations. Future work using flow visualization and CFD simulations may help understand the physics of the flow interactions of the components on UW-S-23E.

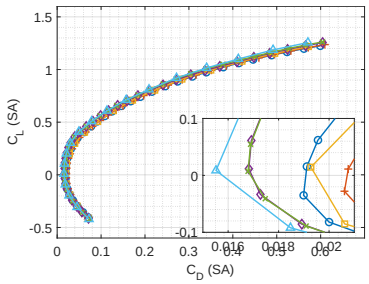
The analysis from [25] is presented in this paragraph with the alumimun-made C23 canard planforms in 2024. The solid aluminum C23 was manufactured and tested at the nominal dynamic pressure, $q = 32$ psf. It is important to note that during the final phase of the SCALOS project, a bias was discovered in the tail incidence block. The bias is

documented in the final report and the run logs are updated in the final data package. A $+2^\circ$ tail incidence off-set had been was built-in resulting in H15 tail fitted with metal sleeves to do initial tail planform explorations (H15A, H15A.1, H20.L, and H20L.1) having a $\Delta\delta_{HT} = +2^\circ$. The C17F.1 $\delta = 0^\circ$, C15F.1 $\delta = +15^\circ$, and C17F.1 $\delta = +15^\circ$ has a positive tail deflection at $\delta_{HT} = +2^\circ$. The comparison between the C15, C17, and C23 canards was conducted at $q = 32$ psf on the UW-S-21A configuration with ($\delta_C = +15^\circ$) and without ($\delta_C = 0^\circ$) canard deflection as shown in Fig. 2.113. Alike in last paragraph, the C23 increased the lift at $\delta_C = 0^\circ$ compared to C15 and C17, which had the same performance [24]. The C23 deflection at $\delta_C = +15^\circ$ reduced the lift like C15 and C23 but with less incremental changes. The C23 has 2 counts differences from C15 and the larger difference with C17 is likely attributed to the $\delta_{HT} = +2^\circ$. The last two paragraphs discussed the sizes of the lifting surfaces affecting the deltas of the lifts and pitch moments [23, 24, 27]. The C23 and C17 generated more lift than C15 creating a destabilizing effect and reducing C_{M_α}. The absolute level in C_M of the C17 should be the same as C23 due to the horizontal tail bias of $\delta_{HT} = +2^\circ$. The positive canard deflection on UW-S-21A did not behave the same as UW-S-20A in [27, 371] where the UW-S-20A with canard deflection shifted the C_M up and down like horizontal tail deflection, except at $\delta_C = \pm 30^\circ$ where the C_{M_α} changes. The pitch break reduced to $\alpha \approx 0^\circ$ for all three planform and destabilized at $0^\circ \leq \alpha \leq 4^\circ$ with another pitch break at $\alpha \approx 14.5^\circ$. The absolute level of C_M for C15F.1 $\delta = +15^\circ$ and C17F.1 $\delta = +15^\circ$ should be lower due to $\delta_{HT} = +2^\circ$ but the general C_M behaviors are still valid. Future work using flow visualization and CFD simulations may help understand the physics of the flow interactions of the deflected canard on UW-S-21A.

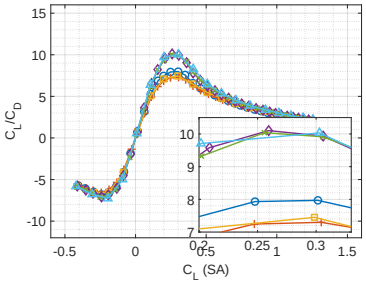


(a) C_L and C_M vs. α

(b) C_M vs. C_L



(c) C_L vs. C_D



(d) C_L/C_D vs. C_L

Figure 2.113: Comparison of canard planforms, C15 ($\Lambda = 50°$) vs. C17 ($\Lambda = 47.6°$) vs. C23 ($\Lambda = 55°$), on UW-S-21A for longitudinal forces and moments vs. α at $\beta = 0°$

2.7.5 Horizontal Tails and Control Authority

Three different horizontal stabilizers - the 2015 horizontal tail, 2015 RUAV horizontal tail and the 2020 horizontal tail - were designated H15, H15A, and H20, respectively. As shown in Fig. 2.49, H15A maintained the basic trapezoidal planform shape of H15 but had a greater exposed area for larger control authority. H20 maintained the same leading edge sweep but had a higher span and aspect ratio, slightly increasing the tail arm and tail lift curve slope, and attempting to reduce trim drag when deflected by improving the tail's induced drag. It was recognized that these potential benefits could require trade-offs for increased tail aeroelastics (or weight to increase structural stiffness). The tails could be attached in three different ways: conventional, mid-tail, and T-tail. The naming convention for the tail locations of conventional (low), mid-tail, and T-tail uses L, M, and T, respectively, followed by the tail designation. The overlay of horizontal planforms is shown in Fig. 2.49 and the geometric properties are specified in Tab. 2.27. The designations and descriptions are listed

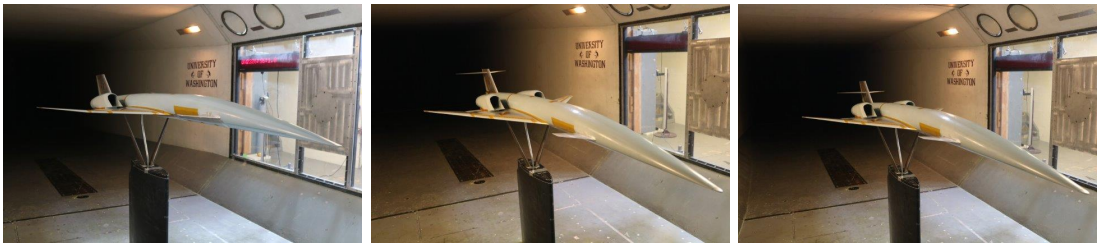
in Tab. 2.31. 3D images of the various configurations tested are shown at the beginning of Fig. 2.84. Test results with different tail planforms and tail locations at various angles of attack and side slip angles were acquired. The horizontal stabilizer in all cases is an all-moving control surface and its rotation angles tested are $\delta_{HT} = 0, \pm 10, \pm 15$. All three tail mounting heights are compatible with both top and bottom mount nacelles; however, the low-tail is not feasible to pair with top mounted nacelles due to hot engine exhaust impingement as shown in Figs. 2.114 and 2.115.

As mentioned in §2.7.4 that there is a incidence off-set for the tail incidence blocks that H15A.2 and H15 with sleeves (H15A, H15A.1, H20.L, and H20L.1) would have a $\Delta\delta_{HT} = +2°$. Note that the "sleeves" are the aluminium-bent airfoils installed on the H15 for rapid proof-of-concept and in-test modification. There is a $+0.4°$ difference between the tail reference and the aircraft water line such H20L.2, H20.M, and H20.T has a $\Delta\delta_{HT} = +0.4°$. The mid- and T-tail deflections were constrained by the hardware within $-15° \leq \delta_{HT} \leq +15°$. The low-tail configuration geometry allowed the use of incidence blocks instead of pin fixtures for tail deflections, allowing a wider range of horizontal tail deflection, $-30° \leq \delta_{HT} \leq +30°$.



(a) 2015 HT (H15) (b) 2015 RUAV HT (H15.A) (c) 2020 HT (H20)

Figure 2.114: UW-S-20E with different horizontal tail planforms [23]

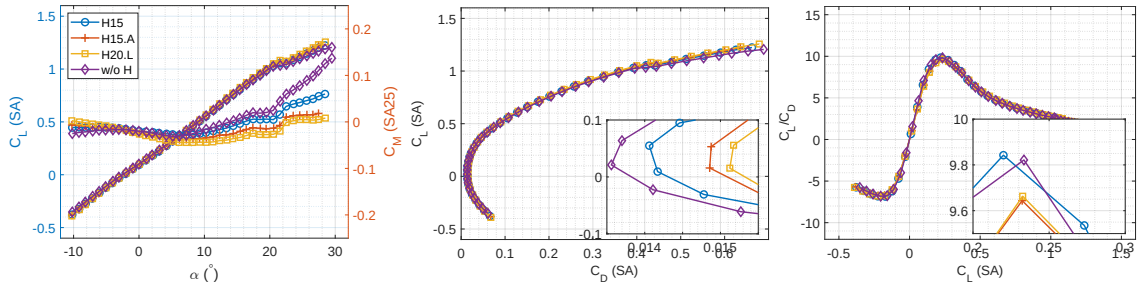


(a) UW-S-20A/H without HT (b) UW-S-20A (H20.T) (c) UW-S-20H (H20.M)

Figure 2.115: Horizontal tail mounting height locations [23]

Horizontal Tail Planform Size – UW-S-20E

The effects of the shapes on the longitudinal forces and moment are shown in Figure 2.116 while those of the mounting locations are shown in Figure 2.117. Both geometric shapes and locations of the horizontal stabilizers do not have appreciably different effects on the lift and drag characteristics but have significant effects on the pitching moment behavior. Figure 2.116 shows that the 2020 stabilizer (H20 planform) has a better C_{M_α} behavior at low angles of attack for stable conditions and the instability characteristics at higher alpha seems to be moderate.



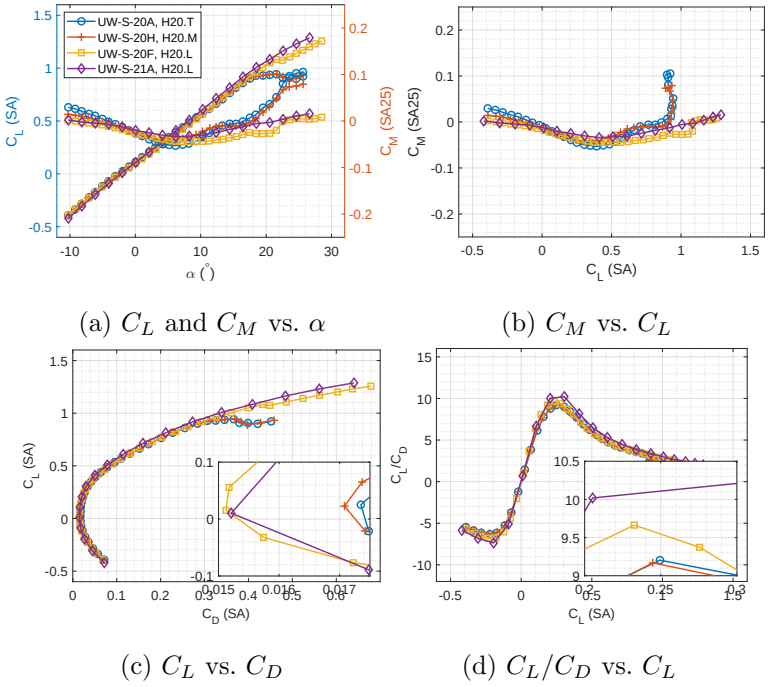
(a) C_L and C_M vs. α (b) C_L vs. C_D (c) C_L/C_D vs. C_L

Figure 2.116: Horizontal tail planforms, UW-S-20E, force and moment coefficients at $\beta = 0°$

Horizontal Tail Mounting Location – T-Tail, Mid-Tail, Low-Tail

The effects of location of the horizontal stabilizer at zero-sideslip angle with angles of attack are shown in Figure 2.117. This figure shows that the low-tail configuration has better pitch moment characteristics for both stable, low alpha, and unstable, moderate to high alpha,

conditions.



(a) C_L and C_M vs. α (b) C_M vs. C_L

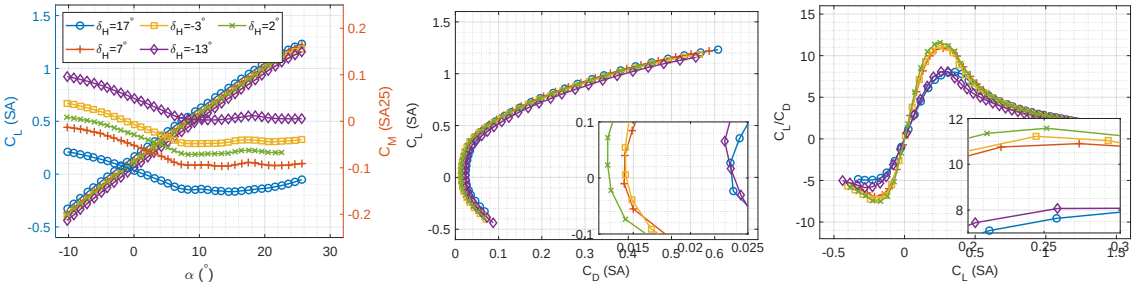
(c) C_L vs. C_D (d) C_L/C_D vs. C_L

Figure 2.117: Horizontal tail positions, UW-S-20A, UW-S-20H, UW-S-20F, and UW-S-21A, force and moment coefficients at $\beta = 0°$

All-Moving Tail Deflection (Pitch Control Effectiveness)

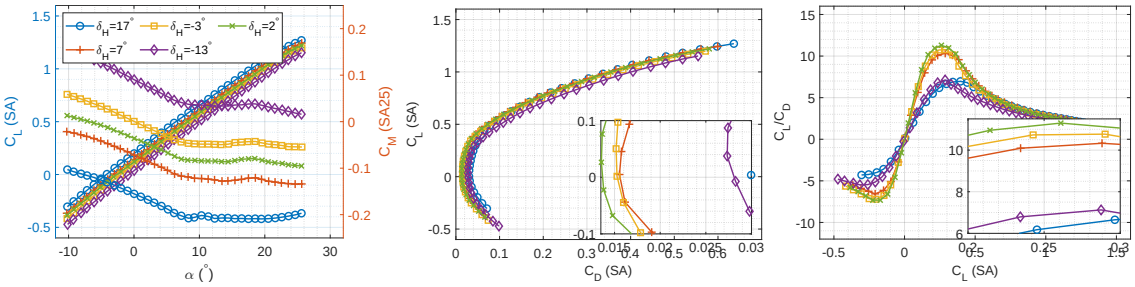
Wing-Body-Tail (UW-S-21A without nacelle and canard) Figures 2.118 to 2.120 shows the corresponding longitudinal forces and moment at various angles of attack for various tail deflection angles. Note that the model shown in Fig. 2.114 has canards and nacelles, whereas the data presented in this section is for the configuration without them. Not surprisingly, the size of the horizontal stabilizer has some effects on the pitching moment variations as seen from Figs. 2.118 to 2.120. The generated moment is proportional to the size of the tail planforms and the tail moment arm which is distance to the aerodynamic center of the swept tail , and the values of zero pitch moment (C_{M_0}) and pitch moment derivative (C_{M_α}) are affected. The pitching moment break point where the pitch moment derivative changes signs, however, is seen to be independent of the size of the horizontal stabilizer. The main contributor to this behavior seems to be flow separation on the wing,

i.e., dominated by the wing planform and leading edge geometry. The tail deflection (δ_{HT}) has significant effects on lift-over-drag ratio (C_L/C_D), drag polar (C_L vs. C_D) reflecting the relative trim drag vs. the pitch moment change. The effects of the tail deflection on the pitching moment variations become more pronounced as the size of the horizontal tail is varied, as shown in Figs. 2.118 to 2.120.



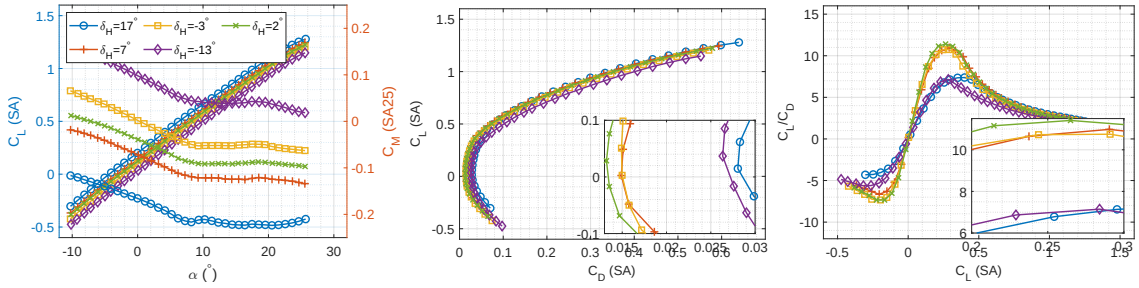
(a) C_L and C_M vs. α (b) C_L vs. C_D (c) C_L/C_D vs. C_L

Figure 2.118: Effects of horizontal stabilizer deflections on the longitudinal force and moments vs. α at $\beta = 0°$ for UW-S-21A with 2015 horizontal tail, H15, and without nacelle and canard (basic wing-body-tail configuration)



(a) C_L and C_M vs. α (b) C_L vs. C_D (c) C_L/C_D vs. C_L

Figure 2.119: Effects of horizontal stabilizer deflections on the longitudinal force and moments vs. α at $\beta = 0°$ for UW-S-21A with 2015 RUAV horizontal tail, H15A, and without nacelle and canard (basic wing-body-tail configuration)



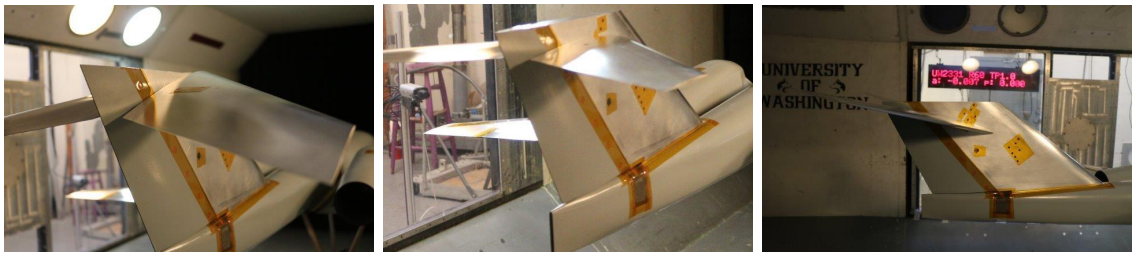
(a) C_L and C_M vs. α (b) C_L vs. C_D (c) C_L/C_D vs. C_L

Figure 2.120: Effect of horizontal stabilizer deflections on the longitudinal force and moments vs. α at $\beta = 0°$ for UW-S-21A with 2020 horizontal tail, H20, and without nacelle and canard (basic wing-body-tail configuration)

UW-S-20 - tail location difference Figure 2.115 shows two alternate horizontal stabilizer locations on the UW-S-20 models and Figs. 2.122 and 2.123 show the effects of tail locations on the longitudinal forces and moment. The UW-S-20A and UW-S-20H models are equipped with nacelle and canards as shown in Fig. 2.115. The location of the horizontal stabilizer does not seem to have significant effects on the untrimmed drag and lift over drag. The effects on the pitching moment variations are noticeable in Figs. 2.122 and 2.123. Both zero pitching moment and the pitching moment derivatives are affected by the horizontal tail locations. The pitching moment break point is independent of the tail locations, but the magnitude of the pitching moment at the pitching moment break point and beyond are affected by the horizontal tail locations. Over the range of tail deflection angles tested, the total moment change generated indicates the T-tail model appears to produce about 11% greater control authority than the mid-tail model and 13% greater than the low-tail model. This may be party due to variation in local dynamic pressure at the tail, and/or a slightly longer effective tail arm for the stabilizers that are mounted of the vertical. For these equal horizontal tail planforms, un-trimmed, the low tail model exhibits the most stable pitch moment derivatives below the clean-wing pitch break, followed by the T-tail model. Beyond the pitch-up break at $\alpha \geq 5°$, the T-tail arrangement is the most unstable, followed by the mid-tail arrangement. For both the mid and T-tail configurations, the change in static stability level at pitch-up appears larger than that of the low-tail arrangement.

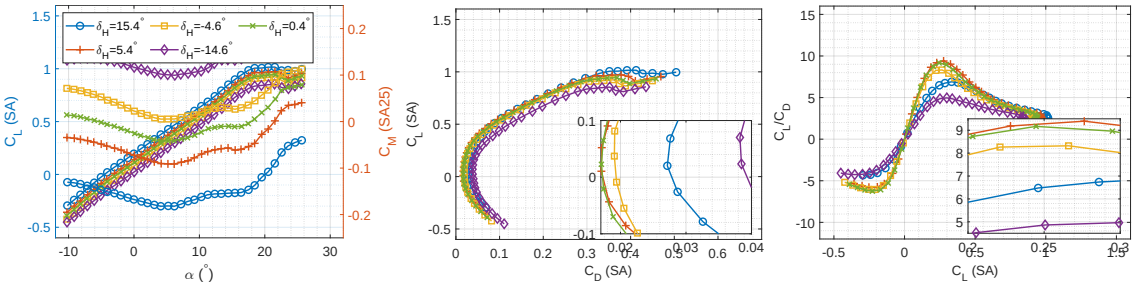


(a) UW-S-20H, $\delta = +15,4°$ (b) UW-S-20H, $\delta = +0.4°$ (c) UW-S-20H¡ $\delta = -14.6°$



(d) UW-S-20A, $\delta = +15.4°$ (e) UW-S-20A, $\delta = +0.4°$ (f) UW-S-20A, $\delta = -14.6°$

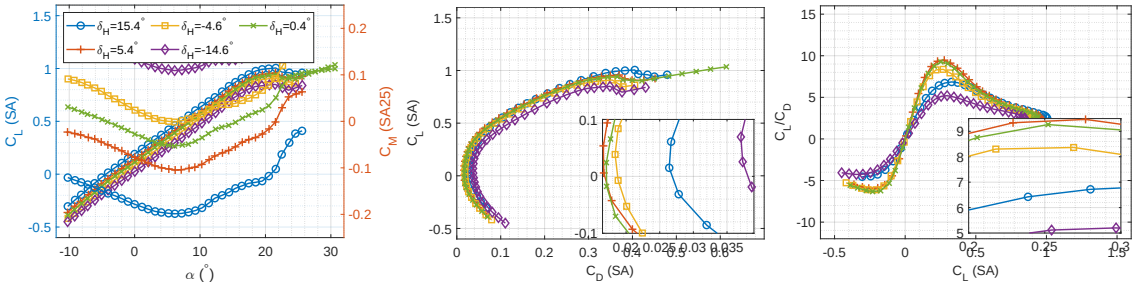
Figure 2.121: Comparison of mid- and T-tail deflection on UW-S-20H and UW-S-20A [25]



(a) C_L and C_M vs α (b) C_L vs C_D (c) C_L/C_D vs C_L

Figure 2.122: Effects of horizontal stabilizer deflections on longitudinal force and moments vs. α at $\beta = 0°$ for UW-S-20H with mid-tail configuration

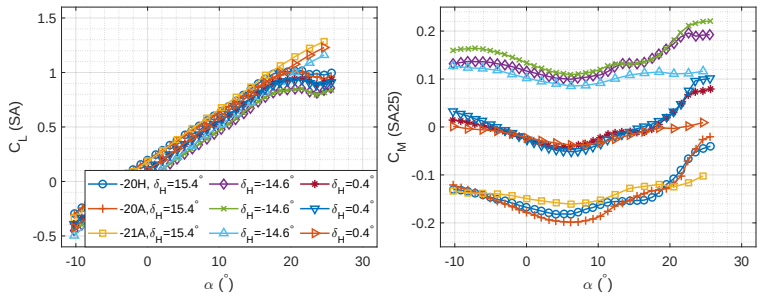
Figure 2.124 shows the experimental results of the UW-S-20A and UW-S-20H, T- and mid-tail, with tail deflections from $-14.6° \leq \delta_{HT} \leq +15.4°$ and compared with the UW-S-21A from Fig. 2.125 in Fig. 2.124. Past references presented on the aerodynamics performance of the UW-S-20A and UW-S-21A are in last paragraph [23, 24, 26, 371]. The UW-S-20A, UW-S-20H, and UW-S-21A has the same lift at $\alpha = 0°$ but UW-S-21A has slight higher lift curve slope, C_{L_α}. The UW-S-20A and UW-S-20H has almost identical lift and stall performance at $\alpha \approx 20°$, while UW-S-21A does not stall up to the tested



(a) C_L and C_M vs α (b) C_L vs C_D (c) C_L/C_D vs C_L

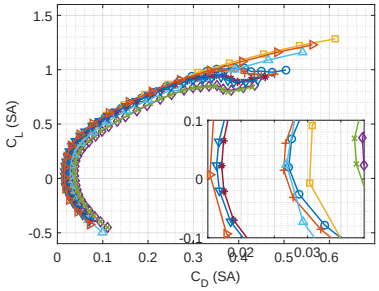
Figure 2.123: Effects of horizontal stabilizer deflections on longitudinal force and moments vs. α at $\beta = 0°$ for UW-S-20A with T-tail configuration

angles of attack range, $\alpha \leq 24°$. The stall is majorly influenced by the configuration with top-mounted nacelles and its flow interaction. The slight pitching moment derivative and pitch up behaviors are results of the mount difference in longitudinal and height. The pitch moment suggests a linear relationship for tail deflections for all tail locations; however, tail locations/ heights affect the authority of the all-movable horizontal stabilizers.

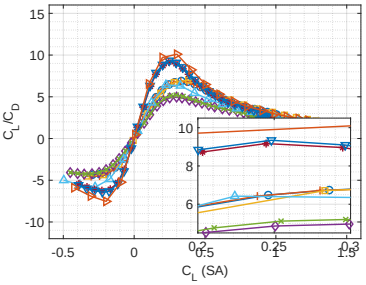


(a) C_L vs. α

(b) C_M vs. α



(c) C_L vs. C_D

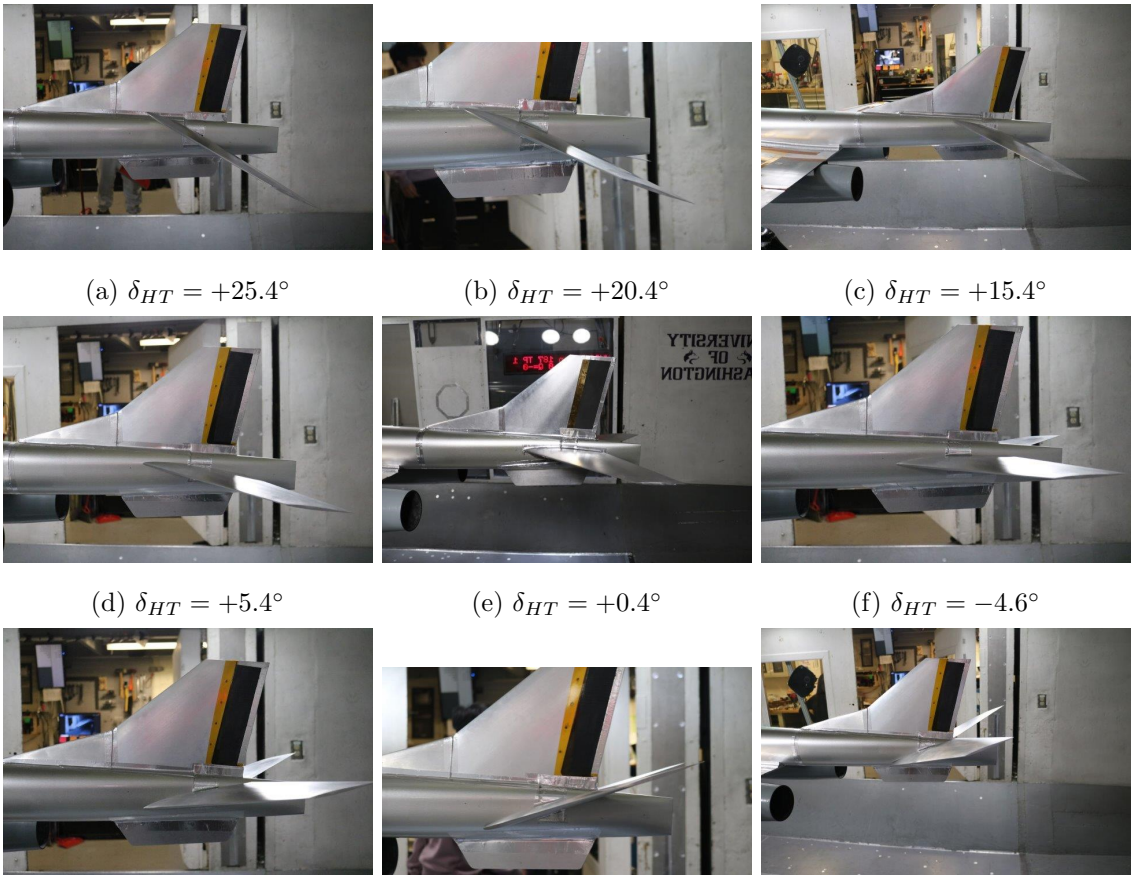


(d) C_L/C_D vs. α

Figure 2.124: Comparison of tail height effects, H20L.2 vs. H20.M vs. H20.T, on UW-S-21A, UW-S-20H, and UW-S-20A for longitudinal forces and moments vs. α at $\beta = 0°$

Low-tail planform difference – UW-S-21A Figure 2.125 shows the UW-S-21A with tail deflections from $-25° \leq \delta_{HT} \leq +25°$ and the corresponding longitudinal aerodynamic force and moments are plotted in Fig. 2.126. The lift increments, ΔC_L, is proportional to tail deflections except $\delta_{HT} \geq 15°$ at $\alpha \geq 14°$ and $-15° \leq \delta_{HT}$ at $\alpha \leq -4°$. The lift increments multiplied by the moment arm translate the lift force to the pitch moment coefficient deltas. The pitch moment of the tail deflection suggests the H20L.2 losing its effectiveness at $|\delta_{HT}| \geq 15°$ and the ΔC_M is no longer linear. The analysis method was presented [371] with preliminary data and in §2.8 with final data.

Figure 2.127 shows the experimental results of the UW-S-21F with H15A.2 and tail deflections from $-13° \leq \delta_{HT} \leq +17°$ and compared with the UW-S-21A with H20L.2 in Fig. 2.125. The $\Delta\delta_{HT} = 2°$ shifted the lift curve of H15A.2 apart from H20L.2 and the same increments translate to the offset in lift to the pitch moment coefficient deltas. The pitch moment of H15A.2 at $\delta_{HT} = +17°$ in Fig. 2.128 confirms the tail losing effectiveness at $\alpha \geq 20°$ similar to Fig. 2.126. The loss in maximum lift-to-drag ratio versus tail deflection

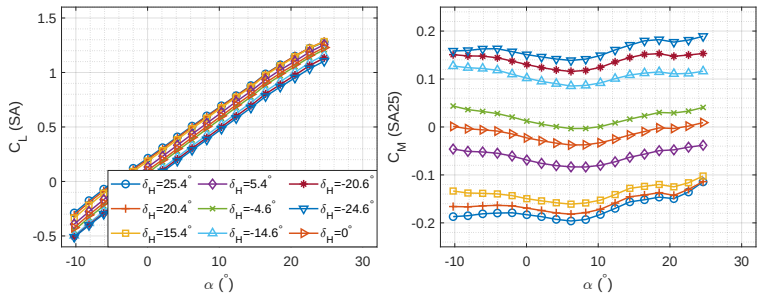


(a) $\delta_{HT} = +25.4°$ (b) $\delta_{HT} = +20.4°$ (c) $\delta_{HT} = +15.4°$

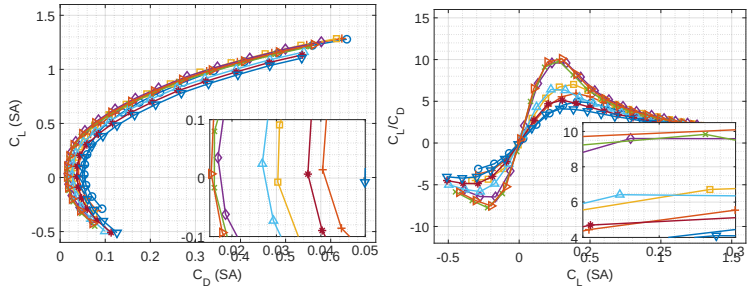
(d) $\delta_{HT} = +5.4°$ (e) $\delta_{HT} = +0.4°$ (f) $\delta_{HT} = -4.6°$

(g) $\delta_{HT} = -14.6°$ (h) $\delta_{HT} = -19.6°$ (i) $\delta_{HT} = -24.6°$

Figure 2.125: UW-S-21A with H20L.2 and horizontal tail deflections [25]



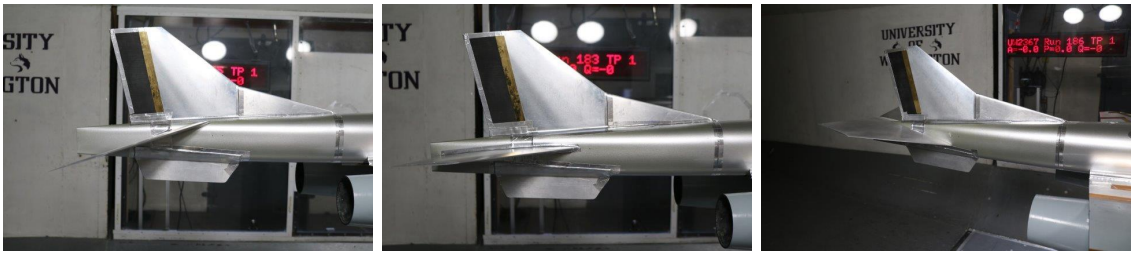
(a) C_L vs α (b) C_M vs α



(c) C_L vs. C_D (d) C_L/C_D vs α

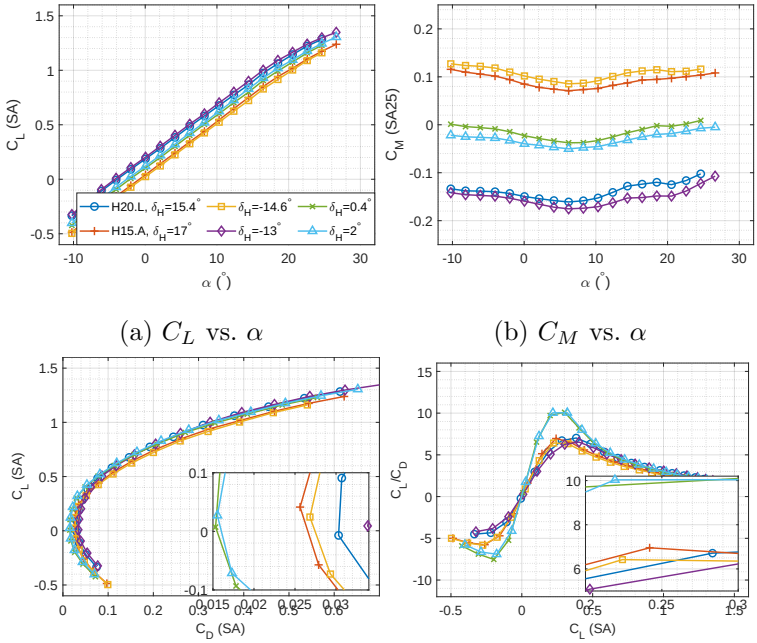
Figure 2.126: Comparison of tail deflection of UW-S-21A for longitudinal forces and moments vs. α at $\beta = 0°$

is an indicator of potentially large trim drag penalties should it be necessary to restrict the CG to the forward range to avoid negative static margins beyond pitch-up.



(a) $\delta_{HT} = +17°$ (b) $\delta_{HT} = +2°$ (c) $\delta_{HT} = -13°$

Figure 2.127: UW-S-21F with H15A and horizontal tail deflections [25]



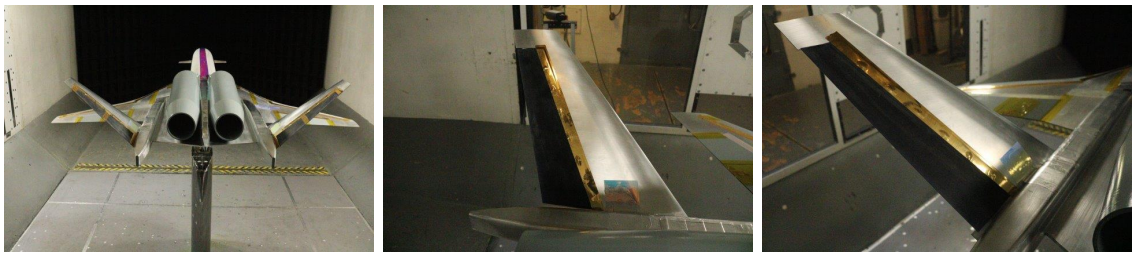
(a) C_L vs. α (b) C_M vs. α

(c) C_L vs. C_D (d) C_L/C_D vs. α

Figure 2.128: Comparison of tail planform effectiveness, H15A.2 vs. H20L.2, on UW-S-21A for longitudinal forces and moments vs. α at $\beta = 0°$

V-tail integrated pitch-yaw control–UW-S-23E Figure 2.129 shows the Icon-II like SCALOS model, UW-S-23E, with V-tail deflections as previously shown in Section §2.7.2. The configuration represents a proposed "low boom" design with a longer forebody, nacelles on top of the long aft-deck, shielded exhaust, and V-tail control arrangement as shown in Figure 2.102. The V-tail's trailing edge device deflects symmetrically, working like an elevator, and deflects asymmetrically to provide rudder (yaw) control. The deflection was

set, and the angle of attack was varied from -10 to 25 degrees in small increments. Note that this configuration limited to runs at $q = 10$ psf due to severe model dynamics at a high angle of attack ($\alpha \geq 20°$), believed to be due to the high mass/inertia combination of the long body and aft deck.



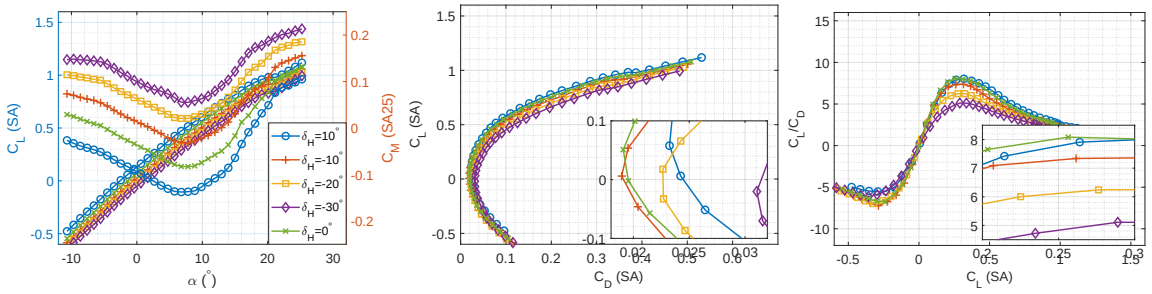
(a) $\delta_{HT} = 0°$ (b) $\delta_{HT} = +10°$ (c) $\delta_{HT} = -10°$



(d) $\delta_{HT} = -20°$ (e) $\delta_{HT} = -30°$

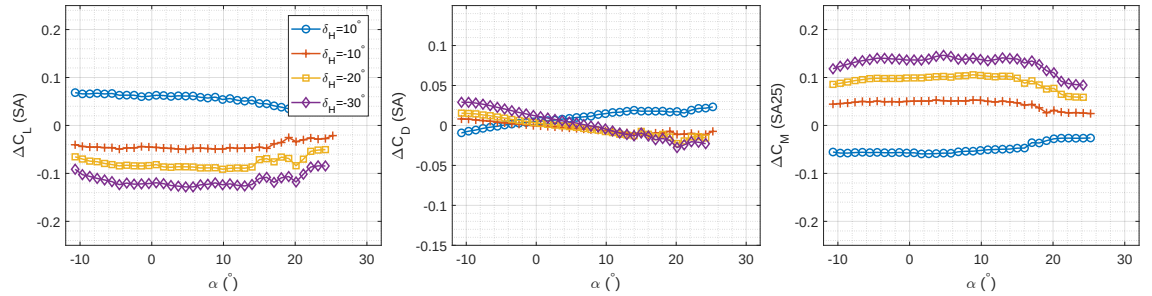
Figure 2.129: UW-S-23 with V-tail elevator deflection [24]

The effects of symmetrical V-tail (elevator) deflection on the longitudinal forces and moment and their increments with respect to angles of attack for the UW-S-23 are shown in Figs. 2.130 and 2.131. The differences in lift and drag are proportional to symmetrical V-tail deflection. The lift generated by the symmetrical V-tail deflection multiplied by a moment arm results in overall moment variations with some contribution from the drag term, i.e. observed control effects are conventional and monotonic. The pitching moment break point in the cases presented here is independent of symmetrical V-tail deflection in Figure 2.130. "Absolute level" characteristics of this representative "low boom" concept await final corrections, including T&I for the arrangements having long aft decks.



(a) C_L and C_M vs. α (b) C_L vs. C_D (c) C_L/C_D vs. C_L

Figure 2.130: V-tail arrangement elevator control effectiveness at $q = 10$ psf for UW-S-23E (Icon-II like configuration)

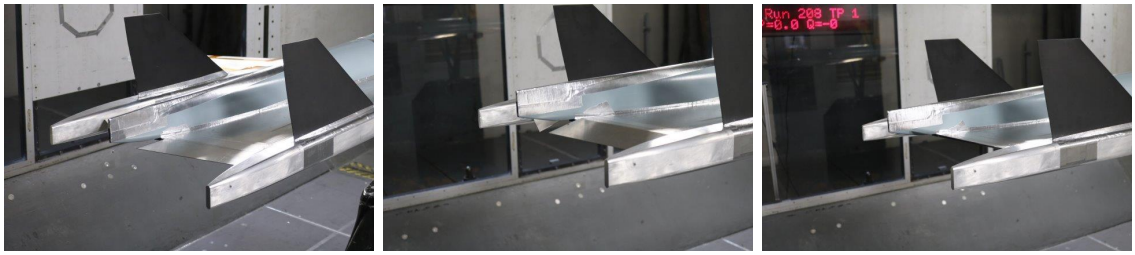


(a) ΔC_L vs. α (b) ΔC_D vs. α (c) ΔC_M vs. α

Figure 2.131: V-tail arrangement elevator control *incremental* effectiveness at $q = 10$ psf for UW-S-23E (Icon-II like configuration)

Aft-deck elevator pitch control – UW-S-23G Figure 2.106 shows the N+2 study Boeing 765-071B concept [416] general arrangement SCALOS model, UW-S-23H, without nacelles as previously shown in §2.7.2. The configuration represents an alternate design from the N+ studies with a wing-aft-deck, nacelles on the bottom of the long aft-deck, canards, and twin V-tail control arrangement as shown in Fig. 2.106. The aft-deck trailing edge was added with aft-deck elevator or pitch-control device working like an elevator in Fig. 2.132. The deflection was set at $\delta = \pm 15°$, and the angle of attack was varied from -10 to 25 degrees in small increments.

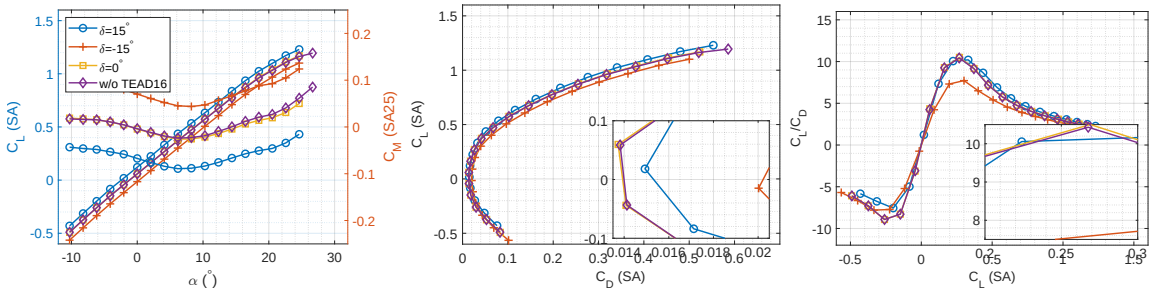
The effects of aft-deck elevator deflection on the longitudinal forces and moment with respect to angles of attack for the UW-S-23H without nacelles are shown in Figs. 2.133.



(a) $\delta = 0°$ (b) $\delta = +15°$ (c) $\delta = -15°$

Figure 2.132: UW-S-23G with aft-deck elevator deflection [25]

The nacelles are removed due to the hardware conflict between the aft-deck elevator and nacelles. The addition of deck area added by the aft-deck elevator has minimal effect on all the data except the pitch moment break, and pitch up becomes softer compared to the case without the aft-deck elevator. The differences in the lift are almost constant throughout the tested AOA, and the pitching moment is inversely proportional to the direction of deflection. The drag polar and LOD show no differences at C_{D_0} and the highest LOD. The elevator deflection improved the drag polar at $C_L > 0.3$, which is a desired characteristic for a high lift device candidate. The aft-deck elevator becomes the aft-deck extension and the end-plate effect results in the pitch down when the aircraft is at moderate to high AOA. The pitching moment break point presented here is independent of deflections.



(a) C_L and C_M vs. α (b) C_L vs. C_D (c) C_L/C_D vs. α

Figure 2.133: Comparison of aft-deck elevator and its effectiveness on UW-S-23H without nacelles for longitudinal force and moments vs. α at $\beta = 0°$

2.7.6 Vertical Tail

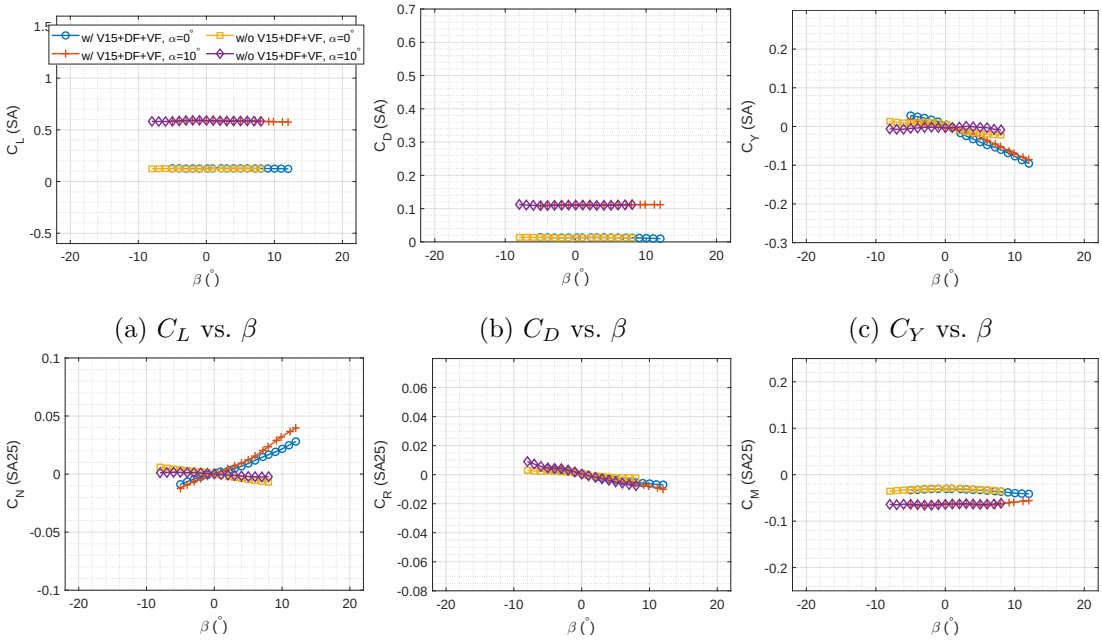
Vertical Tail, Ventral and Dorsal Fin Effectiveness

Two vertical stabilizers were designed and manufactured for the model. They are specified in Table 2.27 and shown in Figure 2.49. To improve the yaw stability behavior of the smaller vertical tail, dorsal and ventral fins were manufactured (permitted by the low-mount horizontal tail, or Concorde-style horizontal-tailless arrangement). Figures 2.134 and 2.136 show the mentioned configurations. Figure 2.135 shows the effect of tail and no-tail on the aerodynamics of the wing-body configuration and Figure 2.137 shows the effect of dorsal and ventral fins on the aerodynamics of the UW-S-20E. The dorsal and ventral fins do not affect longitudinal forces and moment. The effects on the yawing moment at moderate to high sideslip angles are clearly shown in in both figures. Dorsal and ventral fins increase yawing moment coefficient derivative, C_{n_β}, for $\beta \geq 5°$ and for $\alpha \neq 0$. For $\beta < 5°$, dorsal and ventral fins do not have significant influence on the yawing moment coefficient derivative. For all sideslip angles tested, dorsal and ventral fins do not affect the rolling moment characteristics of the UW-S-20E, as seen from Figure 2.137.



(a) Without V15, DF, VF (b) With V15, DF, VF

Figure 2.134: 2015 wing-body-tail configurations [23]



(a) C_L vs. β (b) C_D vs. β (c) C_Y vs. β

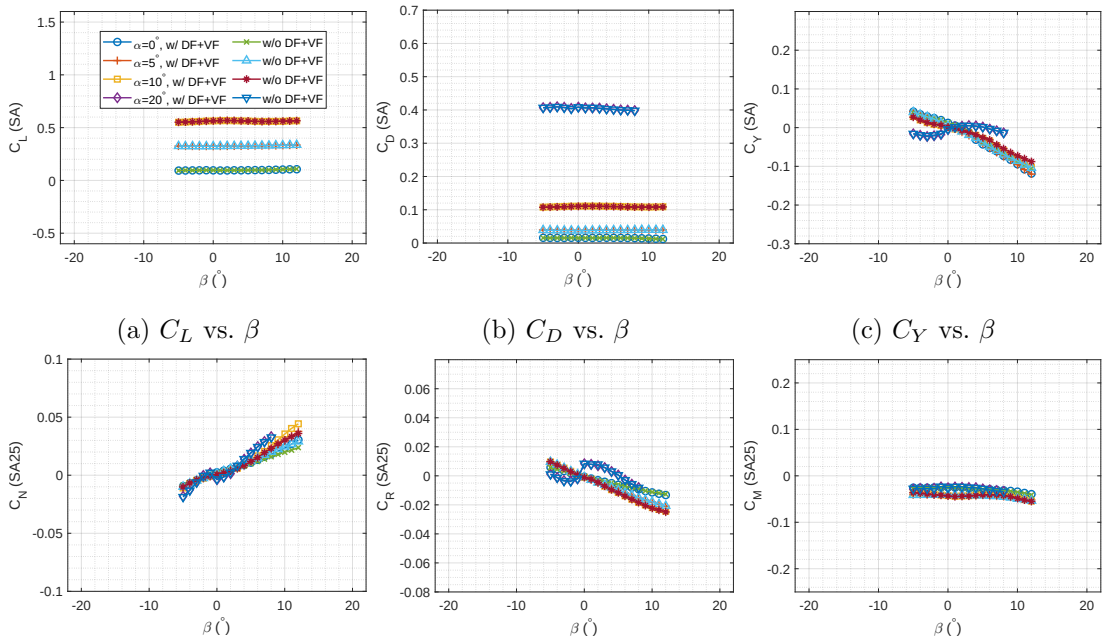
(d) C_N vs. β (e) C_R vs. β (f) C_M vs. β

Figure 2.135: Vertical tail, ventral and dorsal fin, 2015 wing-body-tail, force and moment coefficients at $\beta = 0°$



(a) UW-S-20E, with VF and DF (b) UW-S-20F, no VF and DF

Figure 2.136: UW-S-20E and UW-S-20F [23]



(a) C_L vs. β (b) C_D vs. β (c) C_Y vs. β

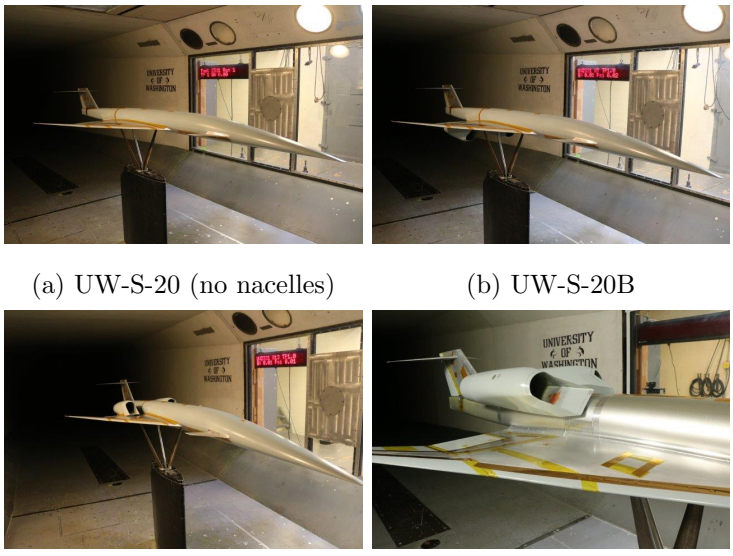
(d) C_N vs. β (e) C_R vs. β (f) C_M vs. β

Figure 2.137: Ventral and dorsal fins, UW-S-20E and UW-S-20F, force and moment coefficients at various α

2.7.7 Nacelles

Nacelle Location Effects (Top vs Bottom Mount)

The nacelles could be mounted on the top or on the bottom surface of the wing with an addition of installation point along the wingspan to study the effects of nacelle separation. In this section, the nacelles mounting location on the surface with respect to wingspan is fixed (the distance between the nacelles). The effects of top or bottom mounts are presented here. Figure 2.138 shows the models without nacelles and with nacelles on the top and bottom of the wing surface. Tests were conducted to study the incremental difference due to nacelles and their locations. The aft body-mounted nacelle arrangement was added in 2023. Figure 2.138d displays the "subsonic business jet type" of aft body-mounted nacelle arrangement from §2.2 [13]. The nacelles are mounted to the upper side of the fuselage, above the wing level, and toward the rear of the aircraft. N20 nacelles represent the aft body configuration configuration as in Fig. 2.138.



(a) UW-S-20 (no nacelles) (b) UW-S-20B

(c) UW-S-20A (d) UW-S-20J

Figure 2.138: UW-S configurations [23]

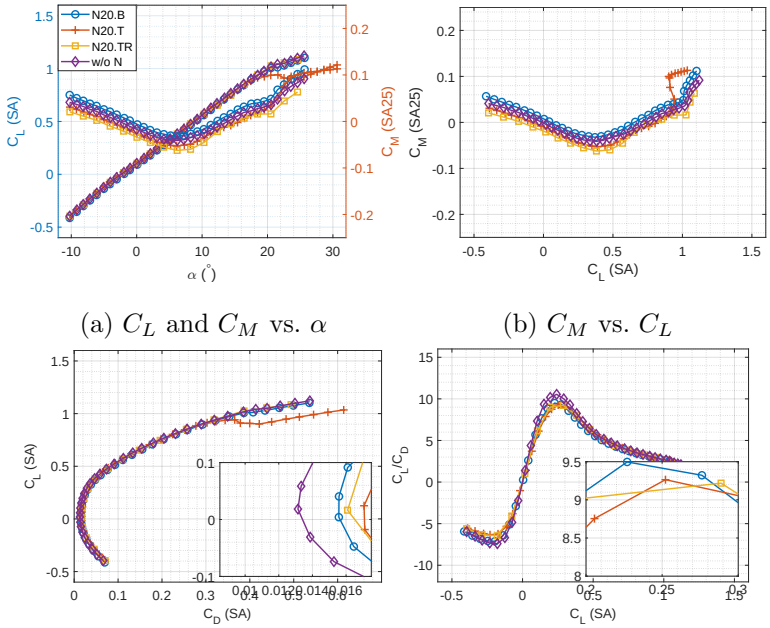
The analysis from [23] is presented in this paragraph without the aft body-mounted nacelle arrangement, which were added in 2023 and are not included in the original paper

analysis. Figure 2.139 indicates the "nacelles on the bottom" configuration has a higher C_L/C_D and also has a higher trimmable angle of attack. The pitching moment coefficient derivatives for top, bottom mounts, and no nacelles cases are the same for both stable, $C_L \leq 0.37$, and unstable, $C_L > 0.37$, flight conditions. The model with the nacelle installed on the top surface of its wing has $C_{M_{\alpha=0}} < 0$, while the nacelle installed on the bottom surface of the wing has $C_{M_{\alpha=0}} > 0$. The effects of nacelle locations at various sideslip angles and angles of attack on both longitudinal and lateral directional characteristics are shown in Figure 2.140. The effects of sideslip angles on both lift and pitching moment coefficient variations for both nacelle location cases are not significant. For $\alpha > 10^\circ$ the pitching moment coefficient variations with sideslip angles become nonlinear due to the asymmetrical vortex formation and vortex breakdown/bursting over the wing surface, as discussed earlier. Similar behaviors are observed for the rolling and yawing moment coefficients. The model has a positive yaw stiffness and nacelle location does not have a significant effect on the yaw stability. The rolling moment indicates that the nacelle location has some effects on the dihedral stability of the model. The model is stable for all angles of sideslip and angles of attack but the variations with sideslip angle become nonlinear for $\beta \leq -5^\circ$ and $\beta \geq 5^\circ$ where there are asymmetric flow over the wing surface.

A new pair of strut-diverter-type mounts were designed and manufactured for the existing 2020 nacelles in 2023. Representative aero measurements are plotted in Fig. 2.138, comparing longitudinal forces and moments. The upper-rear-fuselage-mounted nacelles configuration (N20.TR) has nearly the same lift curve and slope as the rest of the configurations. At high angle of attack ($\alpha \geq 20^\circ$), there is a reduction in lift compared to no nacelle configuration, N20 off, and comparable to bottom-mounted nacelle configuration, N20.B, but does not stall like the top-mounted nacelle configuration, N20.T. The pitching moment break point is observed to be independent of the nacelle mount locations even with upper-rear-fuselage mount (at least for this interim untrimmed comparison without T&I corrections). The magnitude is almost the same as the top-mounted nacelles configuration with less pitching moment coefficient derivatives at low angle of attacked $\alpha \leq 5^\circ$. Without removing nacelle internal duct forces, both online and final comparisons indicate that the models with nacelles installed on the top surface of its wing and upper-rear fuselage decrease in C_{M_0},

while the nacelle installed on the bottom surface of the wing increases C_{M_0} with respect to no nacelle configuration.

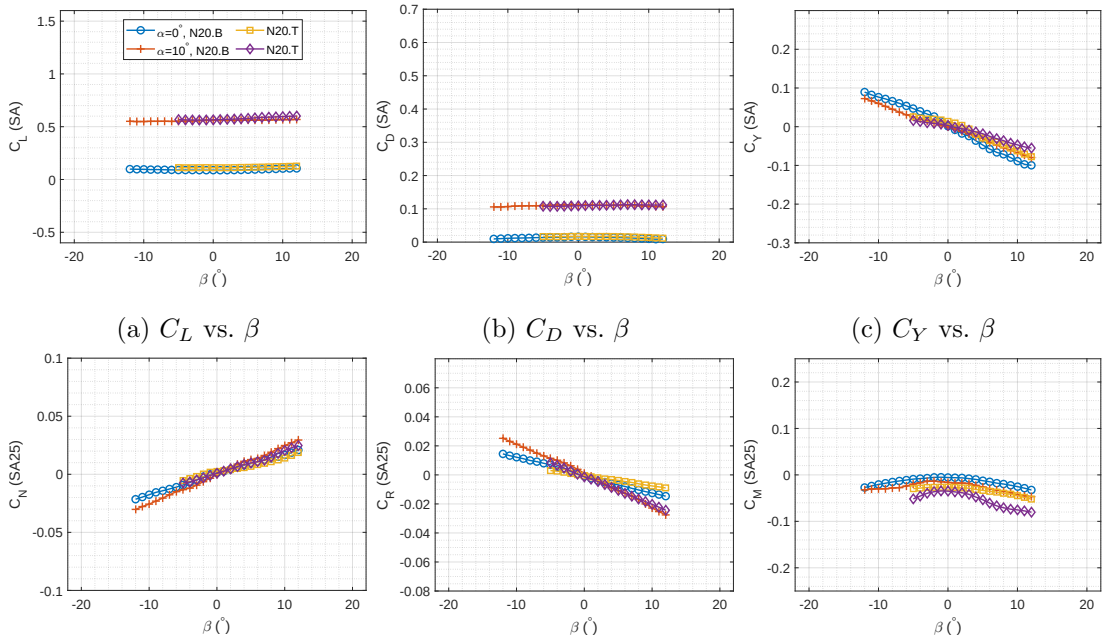
The drag polar (C_L vs. C_D) suggests that the bottom-mounted nacelle configuration has the least zero-lift drag, followed by upper-rear-fuselage mount and top-mounted nacelle configurations. With almost the same lift curve slope, the lift-over-drag ratio reflects the performance dominated by the drag, except at a higher angle of attack, the stall affects the top-mounted nacelles configuration. It is important to note that the test result presented here only studied the aerodynamic effect of the nacelle's arrangement, including flow-through duct forces (corrected by nacelle-duct-drag reduction in final data), without considering the mass of the engines and how that might impact the moment center or dynamic stability.



(a) C_L and C_M vs. α (b) C_M vs. C_L

(c) C_L vs. C_D (d) C_L/C_D vs. C_L

Figure 2.139: Nacelle locations, UW-S-20A and UW-S-20B, force and moment coefficients at $\beta = 0°$



(a) C_L vs. β (b) C_D vs. β (c) C_Y vs. β

(d) C_N vs. β (e) C_R vs. β (f) C_M vs. β

Figure 2.140: Nacelle locations, UW-S-20A and UW-S-20B, force and moment coefficients with various α

2.7.8 Leading Edges

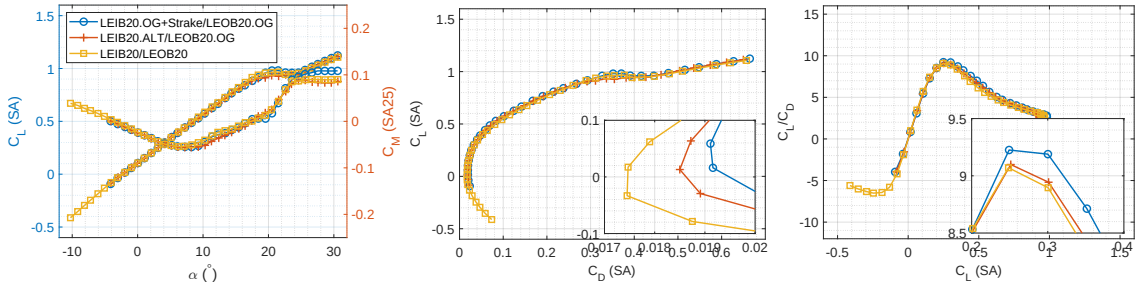
The SCALOS models have movable leading and trailing edge devices (drooping ailerons, flaperons, or elevons). The very thin airfoils needed for this class of aircraft have a very narrow alpha/Mach regime in which the clean cruise wing's camber shape is aerodynamically efficient and maintains fully attached flow. For this reason, it is likely that small leading and trailing edge deflections would be needed at all speeds below low-supersonic conditions to keep the wing from operating too far "off-design". These small deflections, in conjunction with fuel CG management and trim with tails and/or canards, would enable the best LOD to be attained at each C_L/Mach combination. The term "high-lift" is used to refer to larger deflections of leading and trailing needed for landing, takeoff, or near-stall conditions, where the operating CL point can be 4-8x times greater than at subsonic or supersonic "cruise" conditions. This section discusses the leading-edge effects on two different three-surface configurations, UW-S-20A and UW-S-21A. The UW-S-20A, three-surface T-tail model, and

UW-S-21A, three-surface conventional low-tail model, are shown in Fig. 2.84. The UW-S-20A has a pair of canards, two nacelles located on top of the wing and a T-tail empennage configuration without the dorsal or ventral fins as shown in Fig. 2.142, while the UW-S-21A model has a pair of canards, two nacelles located under the wing, and conventional low-tail empennage configuration with dorsal and ventral fins as shown in Fig. 2.144. The UW-S-20A and UW-S-21A are different in their nacelle locations, outboard wing planforms, and empennage configuration which include horizontal tail locations, vertical tail size and thickness, dorsal and ventral fins. The detailed configuration built-up and difference are summarized in Tab. 2.12 in §2.2.

UW-S-20A Leading-Edge Planforms and Devices

Tests were conducted using three different leading edges; a baseline cruise leading edge shape, an alternate cruise leading edge shape, and Ogee planform leading edges, as shown in Figure 2.49 with the configuration of UW-S-20C, as shown in Tab. 2.12 in §2.2. The test results are plotted in Figure 2.141. It is seen that all leading edges behave similarly, except the Ogee planform has a slightly larger LOD value. The "alternate cruise LE" shape was intended to better approximate the local camber/twist and inboard bluntness of a typical CFD-optimized supersonic cruise shape. The "Ogee" leading edge used the same basic leading edge airfoil shapes as the "alternate cruise" geometry but stretched onto an Ogee-type planform, blending into the side-of-body with increased sweep, and having a "soft" planform sweep break. The curved gothic tip shape of the Concorde's Ogee planform was omitted. Figure 2.141 shows that, as expected, the model moment center (CG location of the aircraft) has significant effects on the pitching moment coefficient variations. As the CG moves backward, the pitching moment coefficient derivative increases, indicating the aircraft is less "pitch stiff" and eventually unstable, $C_{M_\alpha} > 0$. In addition, the CG has a strong influence on the variations of pitch moment coefficient derivatives for $C_L \geq 0.5$. At a higher angle of attack where $C_L \geq 0.95$, the SCALOS models become highly unstable for all leading edges, but without much change to the C_M curve shape at the highest alphas.

The analysis from [23] is presented in the following two paragraphs. Leading-edge flap



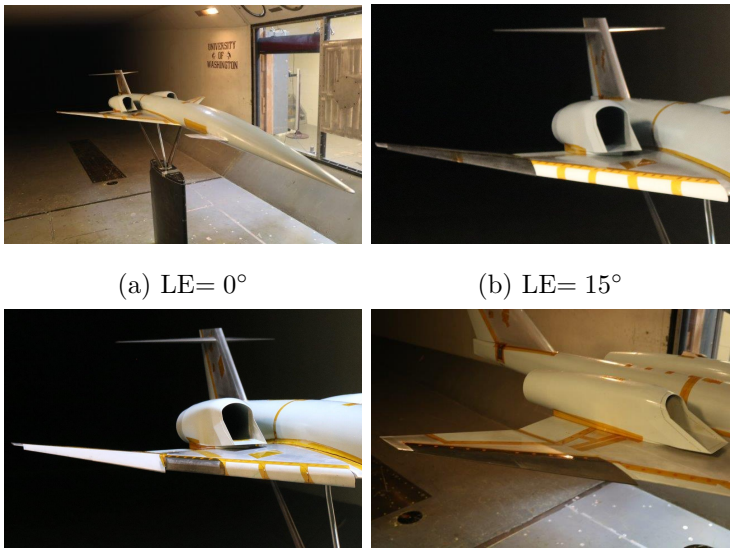
(a) C_L and C_M vs. α (b) C_L vs. C_D (c) C_L/C_D vs. C_L

Figure 2.141: UW-S-20C with different "clean" (zero-deflection) leading edges, force and moment coefficients at $\beta = 0°$

deflections were also tested with the UW-S-20A configuration and the test results are plotted in Figure 2.143. It is evident that the leading-edge deflection causes the lift force coefficient reduction because of the delay in vortices forming and rotation of the leading-edge suction force, and the leading-edge angles increase the alpha for zero lift in the attached flow regime. It is interesting to note that deflection of the OB leading edge only has different characteristics than deflection of all leading edges. The leading edge device deflections are shown to produce the desired net effect of sliding the drag polars up in C_L and to the right in C_{D_0}, thereby shifting the LOD curve right and increasing the LOD noticeably in the C_L region of interest for landing approach and takeoff climb-out ($C_L \approx 0.5 - 0.6$).

The roll and yaw moment coefficients indicate no vortex breakdown/bursting for OB leading-edge deflections, while full leading-edge deflections at 15° has similar breakdown/burst effect as 0° and full leading-edge deflections at 30° has less than the magnitude in breakdown/burst effect compared to 0° and 15°. The possibility is that OB leading-edge deflections have no vortices emergence between IB and OB because of delayed formation of OB vortices. While 15° deflection has similar intensity and breakdown/bursting effect of vortices as 0°, the 30° deflection has delayed vortex formation and significant less intensity with less vortex breakdown/burst effects at same angle of attack. The OB leading-edge deflection has the lowest instability in pitching moment coefficient, $C_M > 0$. With full leading-edge deflections, the reduction in lift is proportional to deflections, but it improves LOD and instability for pitch moment coefficients.

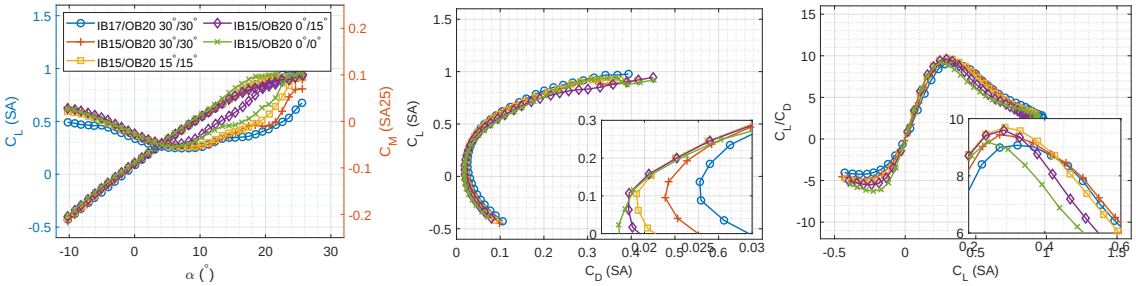
The analysis from [26] is presented in the following paragraph. The untrimmed results suggest the lift over drag in the performance regime at $3° \leq \alpha \leq 12°$ is higher for the UW-S-21A configuration due to lower outboard wing sweep and slightly more span. Figure 2.147 indicates the UW-S-20A model captures less benefit from LE deflection than the UW-S-21A model. Figure 2.143 shows the effects of all leading-edge deflections on the longitudinal forces and pitching moment of the UW-S-20A model similar to Figs. 2.145–2.147. The pitching moment variations, however, are notably different. The pitching moment break points for this model are seen to be independent of the leading-edge deflections in Fig. 2.143. There are some effects observed at higher angles of attack where the maximum lift over drag and the corresponding angles of attack which it occur are increased, as shown in Fig. 2.147. Note that the conventional tail model, UW-S-21A model, with slightly larger span and less outboard wing leading-edge sweep, did not stall at $\alpha = 25°$ in Figs. 2.145–2.147, while the T-tail configuration, UW-S-20A model, stalled at $\alpha \approx 20°$ in Fig. 2.143. Beyond $\alpha > 20°$, the lift is decreased until $\alpha \approx 24°$ and then it is increased after that. The pitching moment variations for UW-S-20A with leading-edge deflections show a change in the slope of the pitching moment curve data for tested ranges of angles of attack in Fig. 2.143, These variations may indicate that the flow is fully separated over the entire wing surface at $\alpha \approx 25°$ for this model The stall difference and the differences in the longitudinal forces and moment variations of these two models are due to configuration differences in nacelle locations, outboard wing planform, and empennage configuration which includes horizontal tail locations, vertical tail size and thickness.



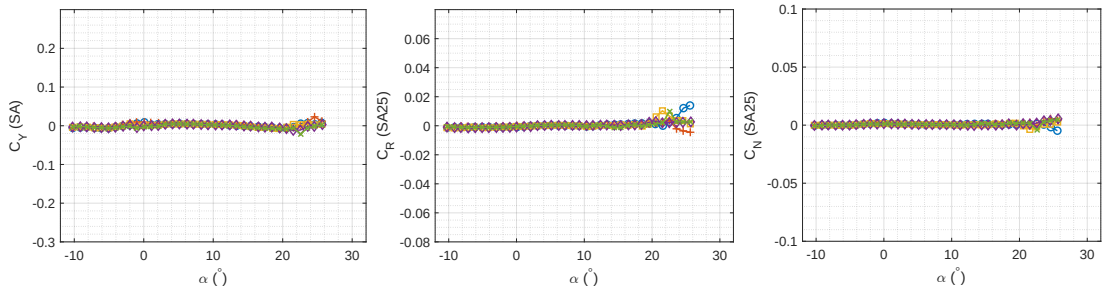
(a) LE= 0° (b) LE= 15°

(c) LE= 30° (d) OB LE= 15°

Figure 2.142: UW-S-20A with leading edge device deflections [23]



(a) C_L and C_M vs. α (b) C_L vs. C_D (c) C_L/C_D vs. C_L



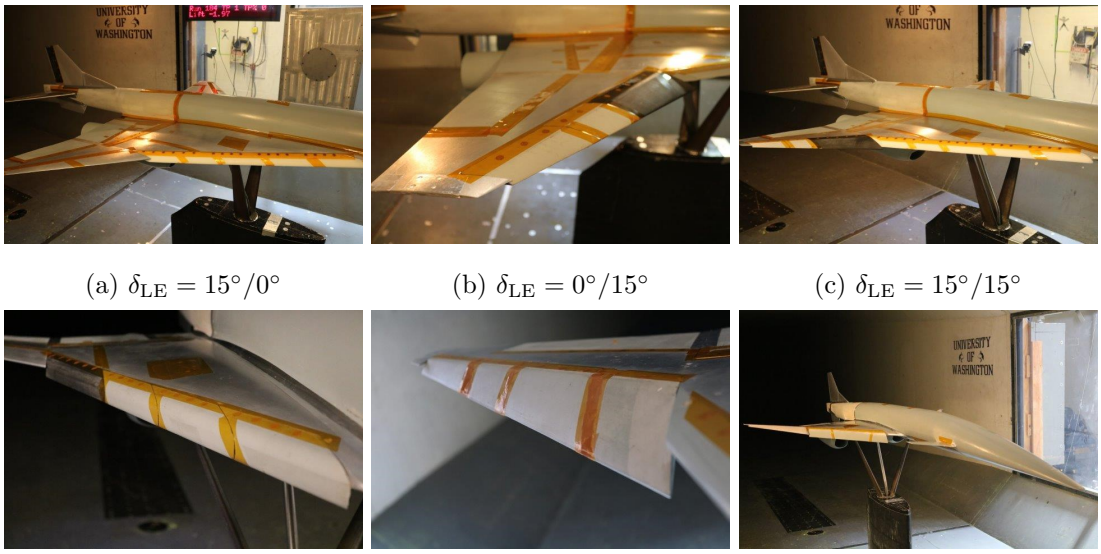
(d) C_Y vs. α (e) C_R vs. α (f) C_N vs. α

Figure 2.143: UW-S-20A with leading edge deflections force and moment coefficients at $\beta = 0°$

UW-S-21A Leading-Edge Studies

The analysis from [26] is presented in the following two paragraphs. Figure 2.144 shows the UW-S-21A model with inboard (IB), outboard (OB), and all leading-edge (LE) segments deflections. Figures 2.145–2.147 shows the corresponding longitudinal forces and moment with respect to angles of attack at zero side slip angle. Both inboard and outboard LE deflections have some effect on the lift curve at moderate to high angles of attack, $\alpha > 10°$, with minimal effects at low alphas, $\alpha < 10°$. Figures 2.145 and 2.146 shows that the leading-edge deflection, either inboard or outboard, reduces the lift coefficient for angles of attack above 10°. This likely reflects that the leading-edge deflections intend to delay of vortex lift, and vortex drag, versus angle of attack. The drag values are also affected by these deflections. The pronounced effects of the leading edges, however, are on the variations of the pitching moment, pitching moment break angles, trimmed angles of attack ($C_M = 0$,), pitching moment at high angles of attack , etc. For the several deflection cases shown here, the test results show that the inboard leading-edge deflection has a higher effect on the pitching moment break point than those of the outboard ones, Figs, 2.145 and 2.146. For the inboard leading-edge deflection, Fig. 2.145 shows a second pitching stability change at high angles of attack, $\alpha \approx 17°$. The effects of simultaneous inboard and outboard deflections on the lift-over-drag ratio and on the pitching moment are also shown in Fig. 2.147. It is interesting to note that the inboard leading-edge deflection reduces lift more than the outboard and all-leading-edge deflection cases. While outboard deflection at $\delta = 30°$ reduces lift less than an inboard deflection at $\delta = 15°$, the drag reduction of the outboard deflection is higher than the inboard deflection in Figs. 2.145 and 2.146. The inboard deflection maintains the lift-over-drag curve as that of the undeflected LE case, while outboard and all leading-edge deflections slightly increase the angle of attack where maximum lift over drag occurs and the maximum lift over drag is maintained or increased comparing to the undeflected LE case in Fig. 2.147. This is desirable to reduce thrust required at low-speed flight/ LTO conditions where the operating speeds are generally on the slower (higher C_L) side of $(C_L/C_D)_{\max} \approx 0.5 - 0.6$. The effects on the pitching moment variations are more pronounced with pitching moment break occurring at much higher

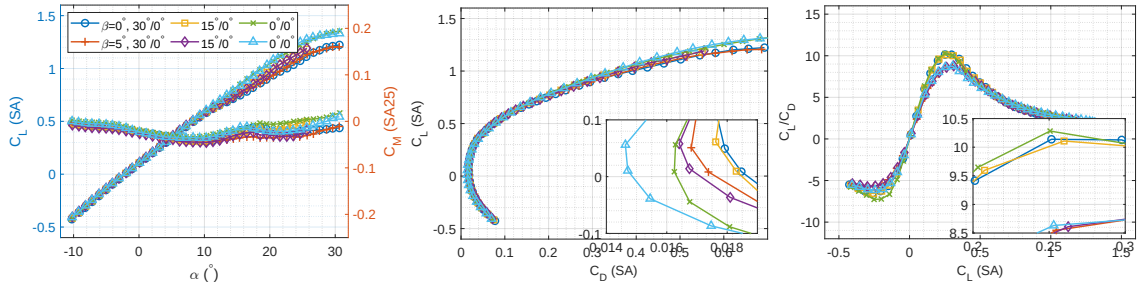
alphas as well as the much larger absolute value of the pitch moment in Fig. 2.145–2.147. The influence of the LE flaps on the forces and pitching moment in the longitudinal plane is linked, of course, to their effect on the flow field over the wing. The shape and location of the LE flaps together with their angles of deflection, determine, as a function of angle of attack, separation patterns as well as leading edge vortex locations and intensity. CFD simulations and flow visualization are tools that add insight. Work that links flow field characteristics to the behavior of force and moment curves will be future work/direction.



(a) $\delta_{\mathrm{LE}} = 15°/0°$ (b) $\delta_{\mathrm{LE}} = 0°/15°$ (c) $\delta_{\mathrm{LE}} = 15°/15°$

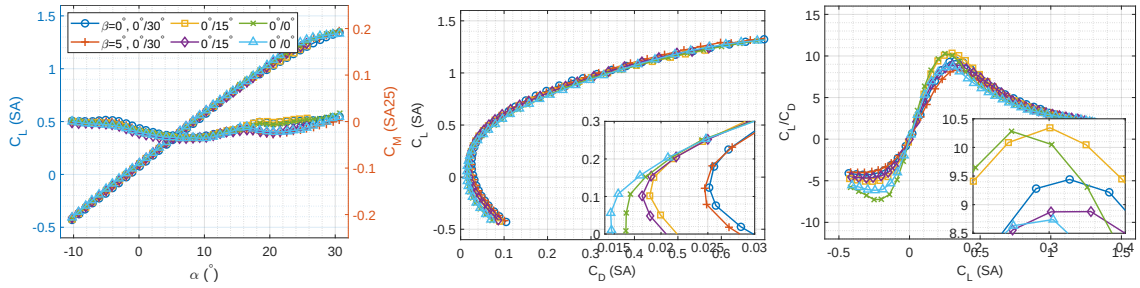
(d) $\delta_{\mathrm{LE}} = 30°/0°$ (e) $\delta_{\mathrm{LE}} = 0°/30°$ (f) $\delta_{\mathrm{LE}} = 30°/30°$

Figure 2.144: UW-S-21A with leading-edge inboard/outboard deflections [26]



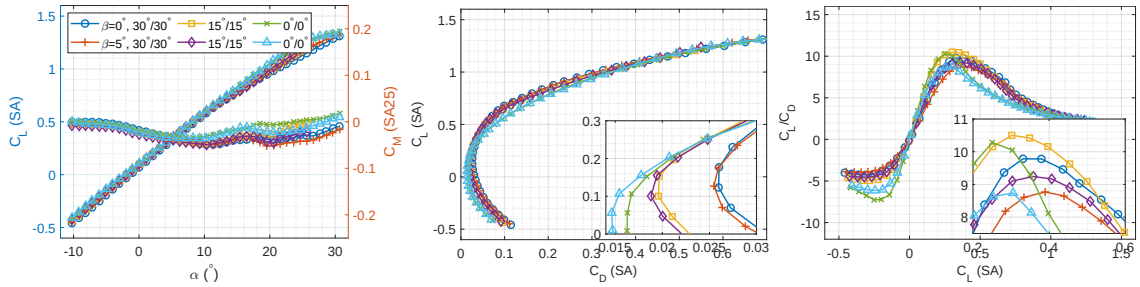
(a) C_L & C_M vs. α (b) C_L vs. C_D (c) C_L/C_D vs. C_L

Figure 2.145: Effects of inboard leading edge deflection only, on longitudinal forces and moment at $\beta = 0°, 5°$ for UW-S-21A



(a) C_L & C_M vs. α (b) C_L vs. C_D (c) C_L/C_D vs. C_L

Figure 2.146: Effects of outboard leading edge deflection only, on longitudinal forces and moment at $\beta = 0°, 5°$ for UW-S-21A



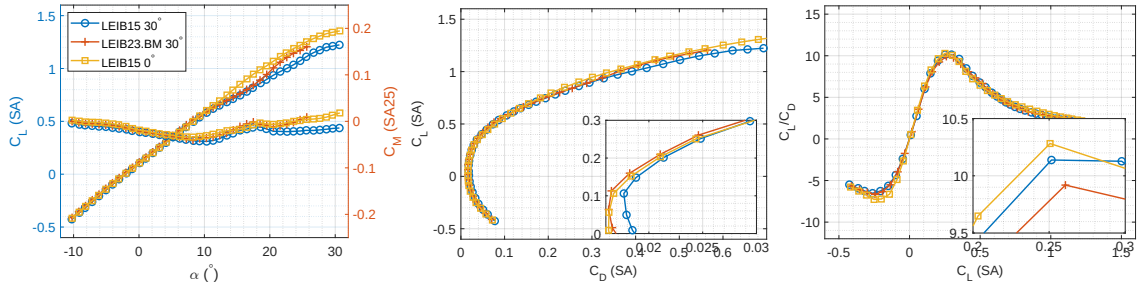
(a) C_L & C_M vs. α (b) C_L vs. C_D (c) C_L/C_D vs. C_L

Figure 2.147: Effects of inboard and outboard leading edge deflection on longitudinal forces and moment at $\beta = 0°, 5°$ for UW-S-21A

UW-S-21A Alternate Leading Edge Devices The analysis from [24] is presented in the following two paragraphs. The exploratory alternate leading edges consisting of morphing-variable-radius, sealed-slat panel, and flex panel type leading edges are shown in Fig. 2.49. The exploratory leading edges are in addition to the baseline concept lower-surface-hinged simple leading edges presented in last section [26, 371]. All the leading edges in Fig. 2.49 were designed to improve subsonic characteristics. The morphing-variable-radius (MVR) inboard leading edges were designed to bulge the lower surface of the leading edge to increase airfoil nose thickness and camber allowing smooth flow attachment and preventing separation while keeping the upper surface cruise LE shape fixed. The sealed-slat outboard leading edges were designed with smooth upper wing surfaces and increasing leading edge areas when deployed. Due to the geometry constraints, the sealed-slat leading edges were designed at the highest deflection of $\delta_{\text{LE SS}} = 25°$ instead of 30°. The flex panel outboard leading edges were designed at deflection of $\delta_{\text{LE FP}} = 30°$ with a smooth upper surface transition at the hinge line and bending to conform with a straight lower surface.

Wind tunnel test results are plotted in Figs. 2.148 to 2.150 examining the effects of the leading edges on longitudinal forces and moments. Figure 2.148 compares the effect of varying the inboard leading edge types. The morphing-variable-radius leading edge shows similar reduction in lift as the baseline W15 30° inboard leading edges but not as much in magnitude. The 30° baseline inboard leading edges have minimal lift reduction at $\alpha \geq 5°$, and the effect becomes moderate after $\alpha \geq 10°$. The morphing-variable-radius edge only reduces in lift after $\alpha \geq 10°$, and the reduction decreases as the angle of attack increases to $\alpha \approx 23°$. As intended, both of the alternate leading edges increase the angle of attack of the pitch break point. However, the pitch break of the morphing-variable-radius leading edge is more abrupt compared to the baseline 30° inboard leading edges suggesting abrupt separation at $\alpha \approx 8°$. The zero-lift drag of the morphing-variable-radius inboard leading is lower than the baseline 30° LE flaps. Untrimmed lift-over-drag ratio indicates no loss for the morphing-variable-radius inboard leading edges. The lift-over-drag ratio improved slightly at the region of $0.3 \leq C_L \leq 0.5$.

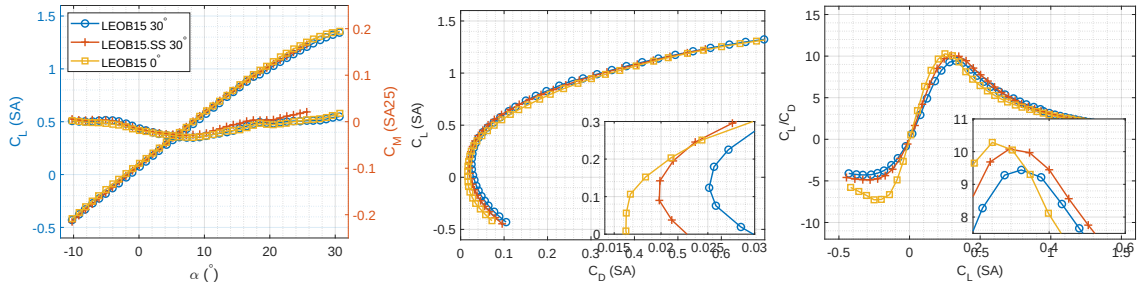
Figure 2.149 compares the effect of varying outboard leading edge types. The sealed-slat leading edges show relative lift reduction at $\alpha \leq 3°$ and $\alpha \geq 15°$, less than the baseline



(a) C_L and C_M vs. α (b) C_L vs. C_D (c) C_L/C_D vs. C_L

Figure 2.148: Effects of inboard-only leading-edge deflection on configuration UW-S-21A (untrimmed), BM $\equiv$ MVR

30° outboard leading edges (except at $\alpha \leq -5°$). This may be due to the fact that the sealed-slat panel leading edges have an 80% increase in area when deployed, increasing the local wing chord. The deflections for these exploratory LE devices were not optimized. The sealed-slat shows almost the same pitch moment behavior as the undeflected LE with the same pitch break point and pitch-up moment derivatives. The drag polar suggests less drag increase compared to the 2015 30° outboard leading edges. The effect on lift and drag is further reflected in the lift-over-drag ratio. The sealed-slat increases the maximum lift-over-drag ratio as opposed to a reduction in the maximum lift-over-drag ratio of the 2015 30° outboard leading edges. The lift-over-drag ratio increases at the region of $0.3 \leq C_L \leq 1$.



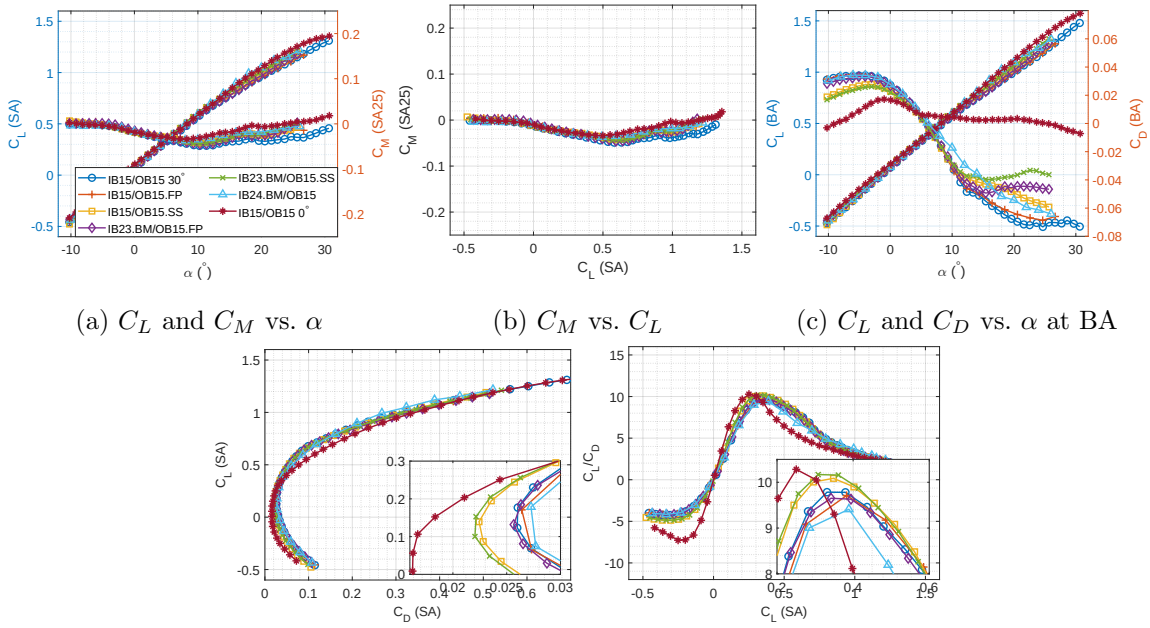
(a) C_L and C_M vs. α (b) C_L vs. C_D (c) C_L/C_D vs. C_L

Figure 2.149: Effects of outboard-only leading-edge deflection on configuration UW-S-21A (untrimmed)

Finally, Figure 2.150 presents the combined effect of deflecting both inboard and outboard leading edge flaps. The lift curves show that 30° deflection of both inboard and

outboard simple-hinged leading edges (2015 baseline concept, LE15/LE15 30°/30°) results in the most suppression of vortex lift (lower C_L vs. α), and lower peak L/D, but have the largest delay in alpha for the pitch-up break. The morphing-variable-radius inboard and sealed-slat outboard leading edges have the highest lift, lowest drag, and highest lift-to-drag ratio. The flex panel leading edges were not tested alone, and combined inboard and outboard leading edge studies were conducted. The same 2015 30° inboard leading edges and the morphing-variable-radius inboard leading edges are paired with both outboard sealed-slat and flex panel leading edges. The flex panel leading edges produce less lift compared with sealed-slat panel leading edges. The pitching moment derivatives are similar with a degree angle of attack increase in pitching moment break point. The drag polar suggests that the sealed-slat panel leading edge has lower drag when paired with either the 2015 30° inboard or the morphing-variable-radius inboard leading edges. The lift-over-drag ratio shows a slight reduction in the maximum lift-over-drag ratio and lift region compared with sealed-slatpanel leading edges. Based on this test data, the alternative leading edges of the morphing-variable-radius inboard, sealed-slat outboard, and the outboard flex panel leading edges seem to provide better low-speed characteristics than the nominal deflected leading edges. Further CFD simulations and wind tunnel flow visualization are tools that may add insight to the study the physics and the effects of geometry on the angle of attack pitch moment break point of the morphing-variable-radius inboard leading edges in Fig. 2.148 and the coupling effect between inboard and outboard leading edges in Fig. 2.150. For CFD much care has to be taken to capture, by math modeling, the behavior of the flow as affected by the fine details of the geometry of the wing in the very small area of the leading edge.

The analysis from [25] is presented in the following two paragraphs. In addition to the baseline concept, lower-surface-hinged simple leading edges in the previous section [26, 371], exploratory alternate leading edge concepts including morphing-variable-radius (MVR, originally designated as bulge-morphing BM), sealed-slat panel (SS), and flex panel (FP) type leading edges were explored in last few paragraphs [24]. The 2023 morphing-variable-radius inboard leading edges (LEIB23.MVR) were designed to bulge the lower surface of the leading edge to increase airfoil nose thickness and camber, allowing smooth flow attachment



(a) C_L and C_M vs. α (b) C_M vs. C_L (c) C_L and C_D vs. α at BA

(d) C_L vs. C_D (e) C_L/C_D vs. α

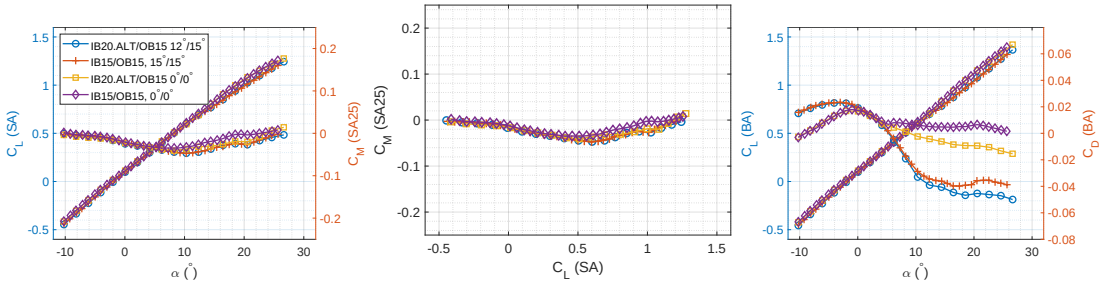
Figure 2.150: Effects of combined leading-edge deflection on configuration UW-S-21A (untrimmed), BM $\equiv$ MVR

and delaying separation while keeping the upper surface cruise LE shape fixed. The 2024 morphing-variable-radius inboard leading edges (LEIB24.MVR) were designed based on the 2023 design, improving the upper surface contour accuracy and reduce flow separation on the lower surface. The morphing leading edge shapes were to investigate the aerodynamic potential and constrained to a particular kinematic concept. Figure 2.150 shows the longitudinal forces and moments of the effects of the combined deflection of both inboard and outboard leading edge flaps. Note that the tested morphing-variable-radius leading edges employed on the inboard wing were combined with the baseline outboard leading edge (LEOB15) deflected at $\delta = +30°$. Last section [26] presents the effects of the inboard, outboard, and combined inboard outboard deflections. The results presented here show the combined effect, and further analysis is required to isolate the effectiveness of the inboard and outboard. Last section [24] showes that the baseline outboard leading edge deflection alone does not change pitch break location and the LEIB23.MVR extends the pitching moment break from $\alpha \approx 5°$ to $\alpha \approx 8°$ alone and to $\alpha \approx 10°$ with combined in-

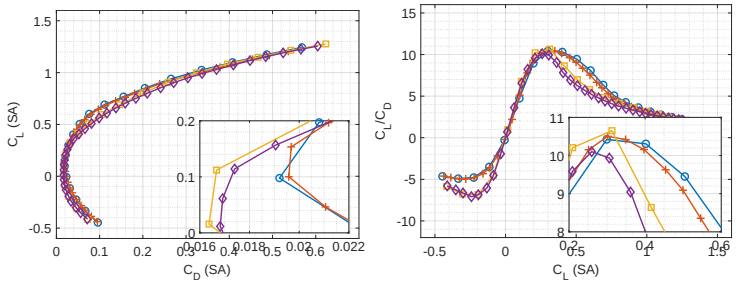
board and outboard in the data, aligning with the results in Fig. 2.150. The LEIB24.MVR maintained the same lift up to $\alpha \approx 18^\circ$ and lost slightly beyond. The C_D in body axis provides more insight into LEIB24.MVR/LEOB15 started separating at $\alpha \approx 8^\circ$ where the pitch break happens. The LEIB23.MVR/LEOB15.SS and LEIB23.MVR/LEOB15.FP have break points at $\alpha \approx 10^\circ$ where the flows start to separate as shown in Fig. 2.150.

The drag polar and LOD suggest that the combination of LEIB23.MVR/LEOB15.SS has the best deflection performance, improving LOD and drag polar at $0.3 \leq C_L \leq 0.8$. Further parametric test or extended CFD analysis on LEIB23.MVR and LEIB24.MVR would help to determine the final selection of the LE geometry.

The alternate inboard cruise leading edge with deflections is studied and tested based on the 2020 alternate cruise leading edge (LEIB20.ALT) in Fig. 2.49. The 2020 alternate cruise inboard leading edge (LEIB20.ALT) geometry is designed to blend with the 2015 outboard wing (LEOB15), and the deflection is rotated at the hinge location on the wing's lower surface, maximizing the radius of the transition from fixed leading edge to the deflected portion to delay flow separation at the flap hinge-line. The LEIB20.ALT at $\delta = 12^\circ$ was supposed to be $\delta = 15^\circ$ for parametric comparison with the baseline leading edge, LEIB15; however, the as-tested geometry came out to be less deflected due to fabrication issues. The longitudinal force and moment of the baseline and alternate leading edges with and without deflections are shown in Fig. 2.151. Note that LEIB15/LEOB15 at $0^\circ/0^\circ$ and $+15^\circ/+15^\circ$ have tail bias $\delta = +2^\circ$ such that the general trend of C_M is still valid but shifted. The alternate leading edge type, undeflected, showed the highest LOD relative to the others at C_L below 0.18 and showed a generally "softened" pitch break. The pitch break point without deflection are roughly the same with and without deflections. The C_D in body axis further confirms the flow separation (loss of leading edge forward suction) aligning with pitch break points. The drag polars are almost identical with 5 counts difference at C_{D_0}, and the deflected alternate leading edge has less drag at a $0.4 \leq C_L \leq 0.8$ compared to baseline, which corresponds to the higher LOD with and without deflection. The alternate leading edge geometry is extended in length from the normal leading edge and with little droop, delaying the flow separation and pitch break point to higher angles of attack.



(a) C_L and C_M vs. α (b) C_M vs. C_L (c) C_L and C_D vs. α at BA



(d) C_L vs. C_D (e) C_L/C_D vs. α

Figure 2.151: Comparison of alternate inboard leading-edge with and without deflection on UW-S-21A for longitudinal forces and moments vs. α at $\beta = 0°$ (untrimmed)

Leading Edge Effectiveness Sensitivity to Wing Planform

UW-S-20A vs. UW-S-21A vs. UW-S-23A The analysis from [24] is presented in the following two paragraphs. This section discusses the leading edge effectiveness on two different wing planforms with the same three-surface configurations, UW-S-21A and UW-S-23A, as previously shown in Fig. 2.84. Both the UW-S-21A and UW-S-23A are three-surface, bottom-mounted nacelles, and conventional low-tail configuration models with buildup information in Tab. 2.12and geometry specifications in Tab. 2.27 in §2.4. The only difference is the outboard wing sweep. The leading-edge effectiveness on two different configurations, UW-S-21A and UW-S-20A, has been presented in last few sections [23, 26, 371]. The UW-S-21A and UW-S-23A with cruise and $\delta = 15°$ deflected leading edge are shown in Fig. 2.152. Both configurations use the same (baseline) inboard leading edge for the LE15 0°, and the $\delta = 15°$ deflected leading edges, LE15 15°.

The UW-S-21A and UW-S-23A wing planforms are presented in §2.4. Lift is reduced for the UW-S-21A with both $\delta = 15°$ leading edge deflection and $\delta = 30°$ less in the first case.

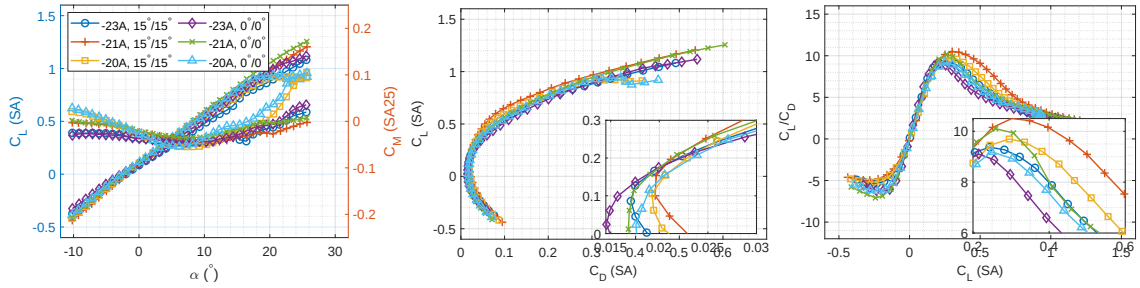


(a) UW-S-20A ($\Lambda = 53°$) (b) UW-S-21A ($\Lambda = 41°$) (c) UW-S-23A ($\Lambda = 63°$)

Figure 2.152: UW-S-20A, UW-S-21A, and UW-S-23A with LE deflections, $\delta_{\text{LE IB}} = 15°$ & $\delta_{\text{LE OB}} = 15°$ [23, 24, 26]

The UW-S-21A also has less drag (untrimmed), as shown by the drag polar, leading to higher lift-over-drag compared to the $\delta = 30°$ case in Fig. 2.150. The UW-S-23A has interesting behavior in which the reduction in lift happens at $\alpha \approx 4°$ and has a sudden change in lift coefficient derivatives at $\alpha \approx 15°$ corresponding to the abrupt change in the pitching moment coefficient curve. It is also interesting to note that all of the combined inboard and outboard leading edge deflection cases increased the pitching moment derivatives before the pitch curve break point and "pushed" the pitching moment curve break point further [23, 26]. However, the UW-S-23 has a non-smooth pitch break at $3° \leq \alpha \leq 10°$ (likely indicating more abrupt vortex formation and interactions between inboard and outboard leading edge vortices) and has an abrupt increase in lift and decrease in pitching moment at $\alpha \approx 15°$. Leading edge deflections on the wing with 41° outboard sweep (W15) appear highly effective in providing better drag "polar shape" and higher untrimmed L/D over the entire takeoff/landing C_L regime ($C_L \approx 0.4 - 0.8$) while maintaining a softer pitch-up break at a delayed pitch-up C_L.

The UW-S-23A leading edge deflection increases in drag as the UW-S-21A case, but less in magnitude. The lift-over-drag ratio is also increased and extended in the lift coefficient region of $0.2 \leq C_L \leq 0.8$, and the deflected leading edge UW-S-23A model has almost the same lift-over-drag ratio as that of the UW-S-21A cruise configuration.

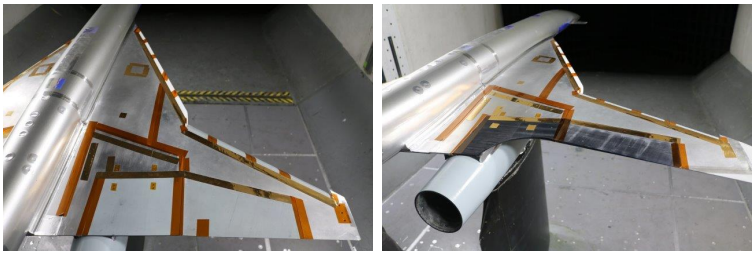


(a) C_L and C_M vs. α (b) C_L vs. C_D (c) C_L/C_D vs. C_L

Figure 2.153: Cross-configuration LEIB/LEOB 0°/0° and 15°/15° sensitivity, UW-S-20A vs. UW-S-21A vs. UW-S-23A (different outboard LE sweeps), force and moment vs. α

UW-S-21A vs. UW-S-13A (W13.5) The analysis from [25] is presented in the following paragraphs. Last section [23, 26, 371] presented the leading edge effectiveness sensitivity between UW-S-20A and UW-S-21A where both configurations have three surfaces but differ in outboard wing geometry, nacelles locations, and empennage system arrangement (T-tail vs. low-tail) with details in Tab. 2.12 and geometry specifications in Tab. 2.27 in §2.4. Ref [24] added the comparison between UW-S-21A and UW-S-23A where both configurations have three-surface, bottom-mounted nacelles, and conventional low-tail configuration models except the outboard wing reference area, sweep, span, MAC, and leading edges differed in Fig. 2.49. For the 2024 wind tunnel entry, a parametric test was conducted comparing the UW-S-21A and UW-S-13A. The UW-S-13A outboard wing uses modified W15 such that the overall outboard wing reference area, sweep, and leading-edge geometry are the same except for the MAC and span thereby providing a higher effective aspect ratio (see Fig. 2.49 and Tab. 2.27 in §2.4). Both UW-S-21A and UW-S-13A use the same baseline leading edges for cruise and the 2024 morphing-variable-radius inboard leading edges and baseline outboard deflected leading edge for $\delta = +30°$ as in §2.7.8.

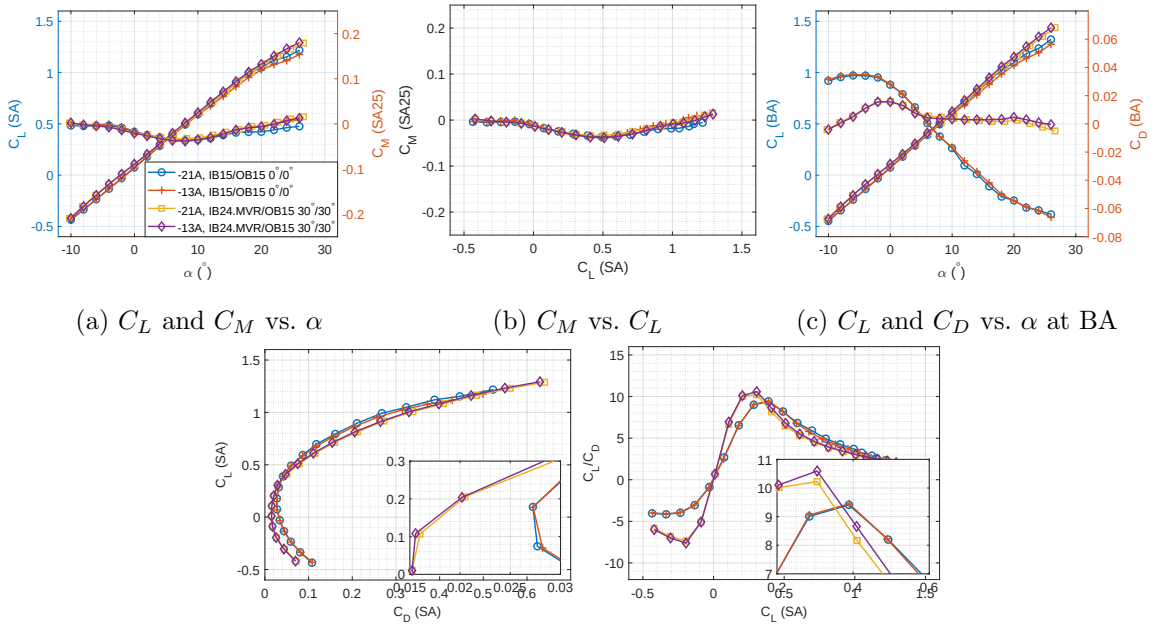
The lift is increased for the UW-S-13A at $-3° \leq \alpha \leq 10°$ and reduced at $\alpha \geq 10°$ for $\delta = 0°$ in Fig. 2.155. The increase in lift is favored by the high aspect ratio design at $-3° \leq \alpha \leq 10°$, and the reduction in lift is due to the outboard wing separation starting at $\alpha \approx 10°$ [23, 24]. The increase in lift at $-3° \leq \alpha \leq 10°$ is diminished when the leading edge is deflected. Both deflection cases show a reduction in C_{L_α} at $\alpha \approx 19°$. The pitching



(a) UW-S-21A (b) UW-S-13A

Figure 2.154: UW-S-21A and UW-S-13A with LE inboard/outboard deflections, LEIB24.MVR/LEOB15 30°/30° [25]

moment coefficient suggests increases in C_{M_α} for high aspect ratio design but also higher instability past the pitch break and lower angle of attack for $C_M > 0$. The leading edge deflection decreases C_{M_α} for both before and after the pitch break and extends the pitch break point and angle of attack $C_M > 0$, which is discussed in §2.7.8 [24, 26]. The drag polar and LOD show similar behaviors except that UW-S-21A has better performance. The wing twist would likely yield different results, and is left as future work to delay outboard wing flow separation. Similarly, add-on flow control devices such as discontinuous "dog-tooth" leading edges, flow fences, or vortilons were not investigated here and might help capture the advantages of the higher aspect ratio outboard panel without the premature disorganized flow separation.



(a) C_L and C_M vs. α (b) C_M vs. C_L (c) C_L and C_D vs. α at BA

(d) C_L vs. C_D (e) C_L/C_D vs. α

Figure 2.155: Comparison of leading-edge deflection between UW-S-21A vs. UW-S-13A for longitudinal forces and moments vs. α at $\beta = 0°$ (untrimmed)

2.7.9 Trailing Edges

The SCALOS models accommodated a range of deflectable "high-lift" leading-edge devices as well as trailing-edge devices (drooping ailerons, flaperons, or elevons). For each device, the model was tested at various angles of attack and side slip angles, and aerodynamic forces and moments were measured and analyzed. The alternate trailing edge control devices were presented in [26], and the alternate leading-edge devices, including a morphing-variable-radius (MVR) leading edge, sealed-slat (SS) leading edge, and flex panel (FP) leading edge were covered in the last leading-edge section. The planform comparison for trailing edge effectiveness is discussed in this section.

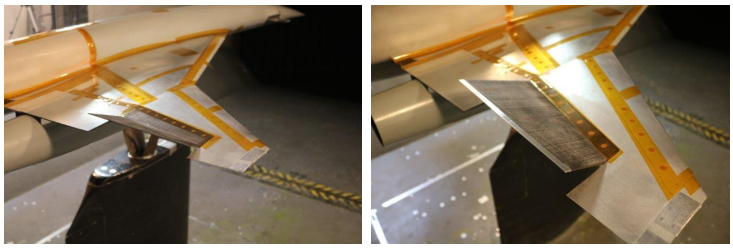
Aileron Deflection/Roll Control Effectiveness

This section discusses the aileron effectiveness on two different three-surface configurations, UW-S-20A and UW-S-21A in Fig. 2.84. The UW-S-21A is the three-surface conventional

low-tail model and the UW-S-20A is three-surface T-tail model. The configurations are different in nacelle locations, outboard wing planform, and empennage, which includes horizontal tail locations, vertical tail size and thickness, dorsal and ventral fins. The detailed configuration built-up and difference are summarized in Tab. 2.12 in §2.2. The UW-S-21A and UW-S-20A with aileron deflections are shown in Figs. 2.156 and 2.157, respectively. The *R* stands for *Reduced* in Figs. 2.156 where the aileron chords are reduced by one-third, $\bar{c}_{\text{ail R}} = \frac{2}{3}\bar{c}_{\text{ail}}$, and so is the area, $S_{\text{ail R}} = \frac{2}{3}S_{\text{ail}}$. These two different TE device chords were tested to generate some basic sensitivity trends that could help size TE devices early in conceptual design. The ailerons are deflected differentially on both sides of the wing where negative deflection, upward, on right wing and positive deflection, downward, on left wing. In longitudinal cases, the ailerons are deflected differentially on both sides of the wing such that lateral-directional aerodynamic effects are also studied due to the expected asymmetric behavior of lift and drag. It should be noted that the thin wings of this class of configurations are very susceptible to aeroelastic losses, reducing roll control authority. The SCALOS model wings were essentially rigid for all dynamic pressures tested.

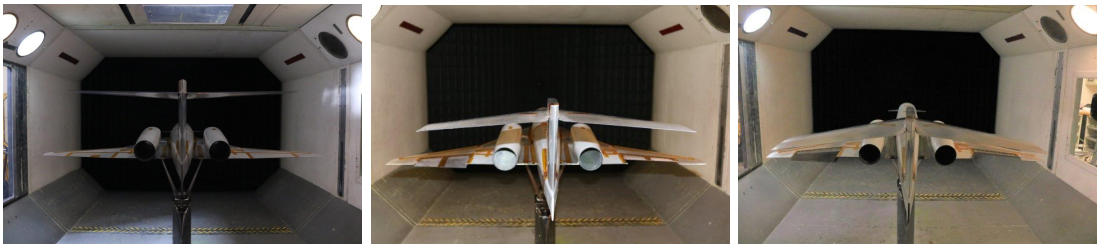


(a) $\delta_{\text{ail}} = \pm 10°\text{R}$ (b) $\delta_{\text{ail}} = \pm 10°$



(c) $\delta_{\text{ail}} = \pm 25°\text{R}$ (d) $\delta_{\text{ail}} = \pm 25°$

Figure 2.156: UW-S-21A with ailerons deflections with left and right of positive and negative deflection, respectively [26]



(a) TEOB20, $\delta = 0°$ (clean) (b) $\delta_{\text{ail}} = \pm 10°\text{R}$ (c) $\delta_{\text{ail}} = \pm 25°\text{R}$

Figure 2.157: UW-S-20A with ailerons deflections with left and right of positive and negative deflection, respectively [26]

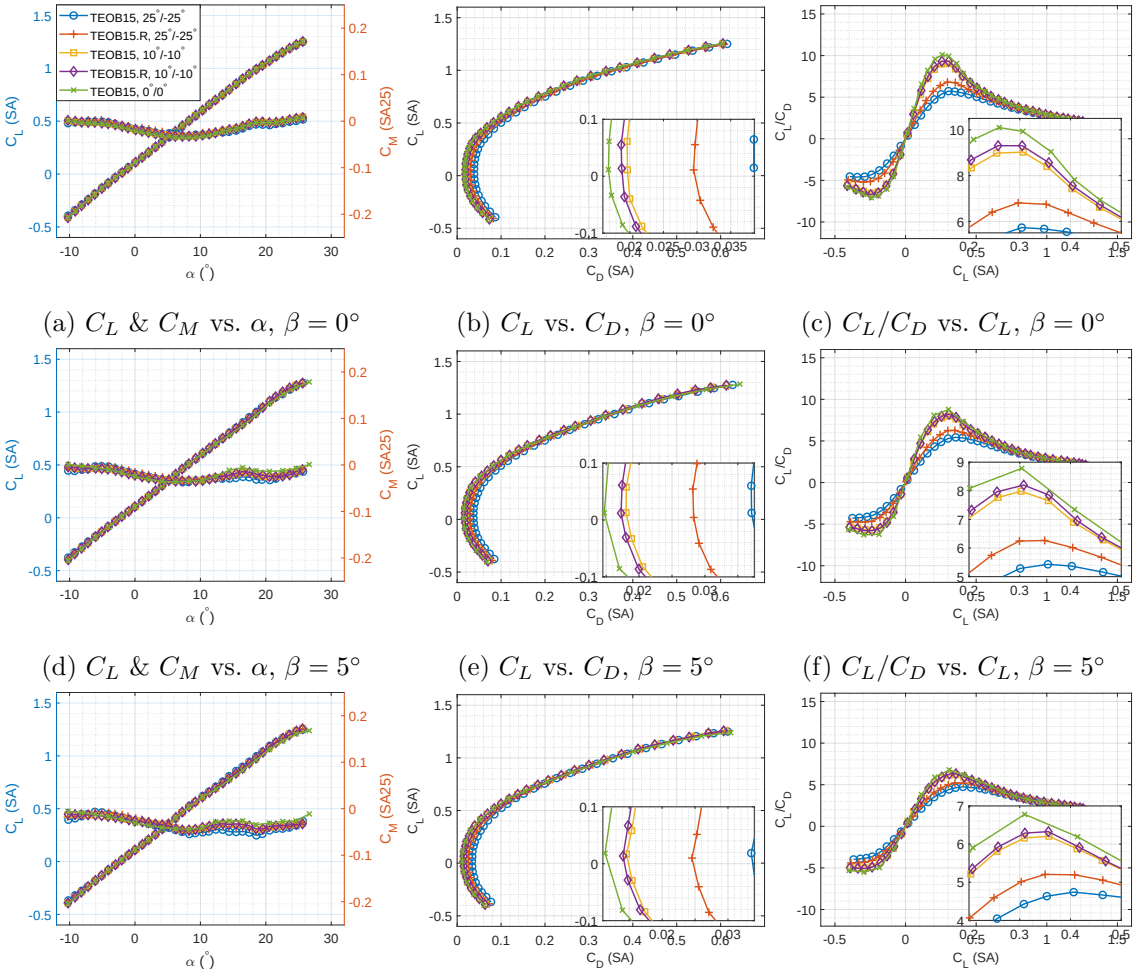
UW-S-21A Figure 2.156 shows the UW-S-21A model with the outboard aileron deflection angles of $\delta_{\text{ail}} = \pm 0°$, $\pm 10°$, $\pm 10°\text{R}$, $\pm 25°$, $\pm 25°\text{R}$. The effects of aileron deflections on both longitudinal and lateral forces and moments for various angles of attack at zero-side slip angle and various sideslip angles are shown in Figs. 2.158 and 2.159. The figure shows that aileron deflections do not have a significant effect on the longitudinal forces and moment. There is a slight increase in drag, however, at low to moderate alphas corresponding to reduction in the lift-to-drag ratio. The aileron deflections increase the pitching moment. Although the pitching moment break is independent of the aileron deflections (influenced, mainly, by the wing planform and its leading edges), the magnitude of the pitching moment at the pitching moment break point is affected by the aileron deflections and the reduced-chord ailerons case is the most effective. Figure 2.159 shows that aileron deflections has significant effects on the lateral moments of the model with some effects on the lateral force at high angles of attack. Both yaw and roll moments for the zero-angle deflection ($\delta = 0°$) remain almost constant (C_N, $C_R \approx 0$) up to $\alpha \approx 18°$. Beyond $\alpha \approx 18°$, both yaw and roll moments are observed to vary with angle of attack and become non-zero, typically resulting from asymmetric flow separation on the slender forebody/canards, and potentially asymmetric vortex breakdown on the wings, plus interaction of these flows with the tail surfaces.

The $\alpha \approx 18°$ point where both yaw and roll moments begin to vary matches almost exactly the point where the pitching moment curves change slope for the zero-angle deflection case. C_{N_α} is proportional to the aileron deflection angles, while the yaw break angle

is independent of the aileron angles. The aileron deflection effectiveness is proportional to the aileron areas and the reduced-chord ailerons are, as expected, less effective compared to full-chord ailerons. The difference between full-chord and reduced chord ailerons is minimal for $\delta = \pm 10^\circ$ at $-5^\circ \leq \alpha \leq 5^\circ$ and for $\delta = \pm 25^\circ$ at $-3^\circ \leq \alpha \leq 0^\circ$ and significant elsewhere. Similar results are observed for rolling moment variations. The rolling moment is proportional to aileron deflections and aileron areas where the rolling moment is almost constant at $-5^\circ \leq \alpha \leq 5^\circ$ and nonlinear elsewhere. The differences between reduced- and full-chord ailerons are minimal ($< 10\%$) for $\delta = \pm 10^\circ$ and significant ($\approx 20\%$) for $\delta = \pm 25^\circ$. The rolling moment breaks, like the yaw moments, are independent of aileron deflections but happen at lower angles of attack, $\alpha \approx 5^\circ$. The aileron effectiveness decreases beyond $\alpha \approx 5^\circ$ and the rolling moment decreases in a way that is inversely proportional to the angle of attack.

Figure 2.159 shows effects of side-slip, $\beta = 0^\circ, 5^\circ, 10^\circ$, on the UW-S-21A model yaw and rolling moments with respect to angles of attack. Both roll and yaw moments are nearly zero for $\alpha \approx 18^\circ$ at $\beta = 0^\circ$. For $\beta \neq 0^\circ$, the windward side has larger effective sweep angle with an opposite effect on the other side. Flow asymmetry increases proportionally with angle of attack over the wings and canards and creates rolling and yawing moments as shown in Figure 2.159.

The rolling moment is almost constant at $5^\circ \leq \alpha \leq 13^\circ$ for $\delta = 0^\circ$. However, the none-zero rolling moment ($C_R \neq 0$) at other angles of attack is due to the side force generated by the vertical tail. These constant values of the rolling moment with angles of attack indicate that the flow field over both sides of the wing are still relatively symmetric. Yet, the asymmetry of the flow, $\alpha \leq 5^\circ$ and $13^\circ \leq \alpha$, over the right and left wing and canard creates rolling moments and yawing moments due to differences in lift and drag on the two sides of the model. The effectiveness of aileron area is similar at different sideslip cases, as shown in Fig. 2.159.

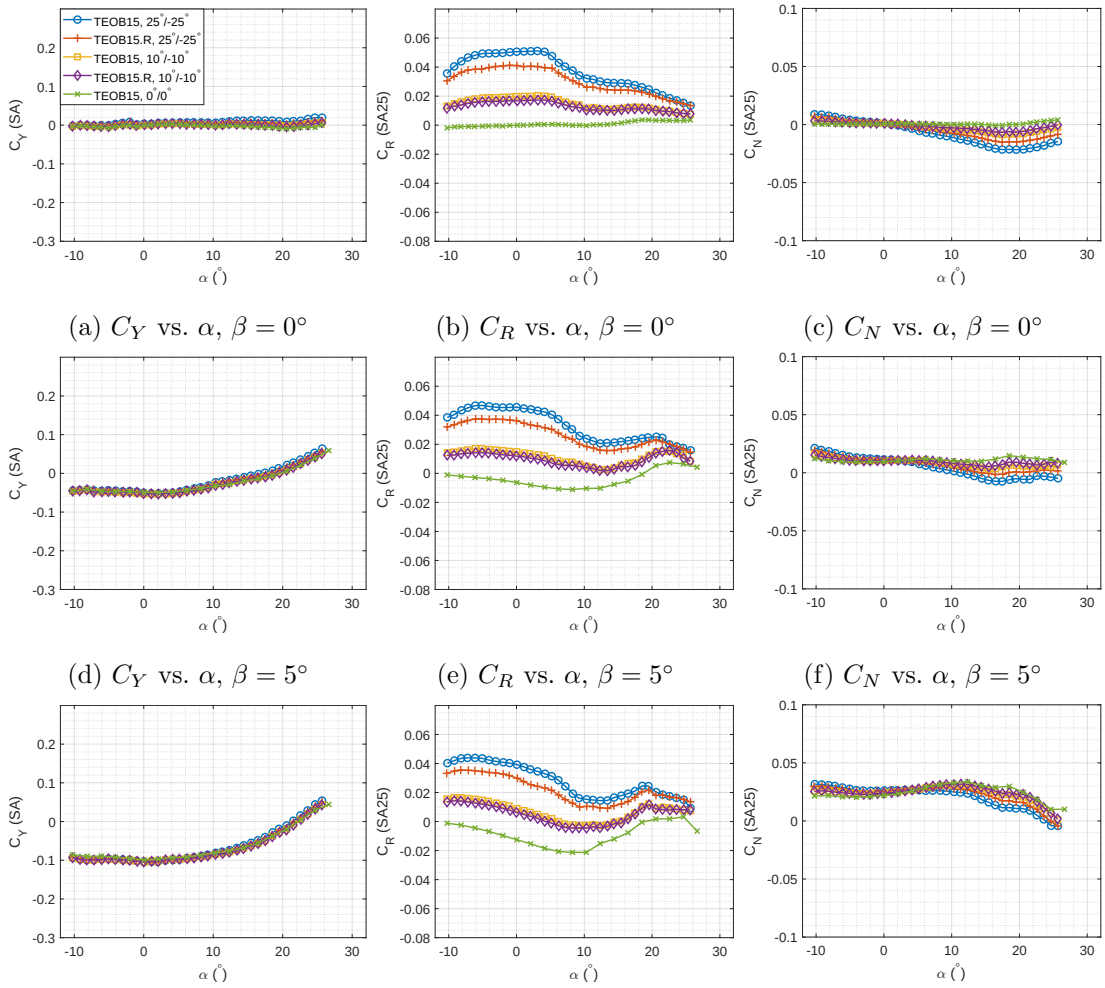


(a) C_L & C_M vs. α, $\beta = 0°$ (b) C_L vs. C_D, $\beta = 0°$ (c) C_L/C_D vs. C_L, $\beta = 0°$

(d) C_L & C_M vs. α, $\beta = 5°$ (e) C_L vs. C_D, $\beta = 5°$ (f) C_L/C_D vs. C_L, $\beta = 5°$

(g) C_L & C_M vs. α, $\beta = 10°$ (h) C_L vs. C_D, $\beta = 10°$ (i) C_L/C_D vs. C_L, $\beta = 10°$

Figure 2.158: Effects of side-slip and aileron deflections on longitudinal forces and moment vs. α for UW-S-21A



(a) C_Y vs. α, $\beta = 0°$ (b) C_R vs. α, $\beta = 0°$ (c) C_N vs. α, $\beta = 0°$

(d) C_Y vs. α, $\beta = 5°$ (e) C_R vs. α, $\beta = 5°$ (f) C_N vs. α, $\beta = 5°$

(g) C_Y vs. α, $\beta = 10°$ (h) C_R vs. α, $\beta = 10°$ (i) C_N vs. α, $\beta = 10°$

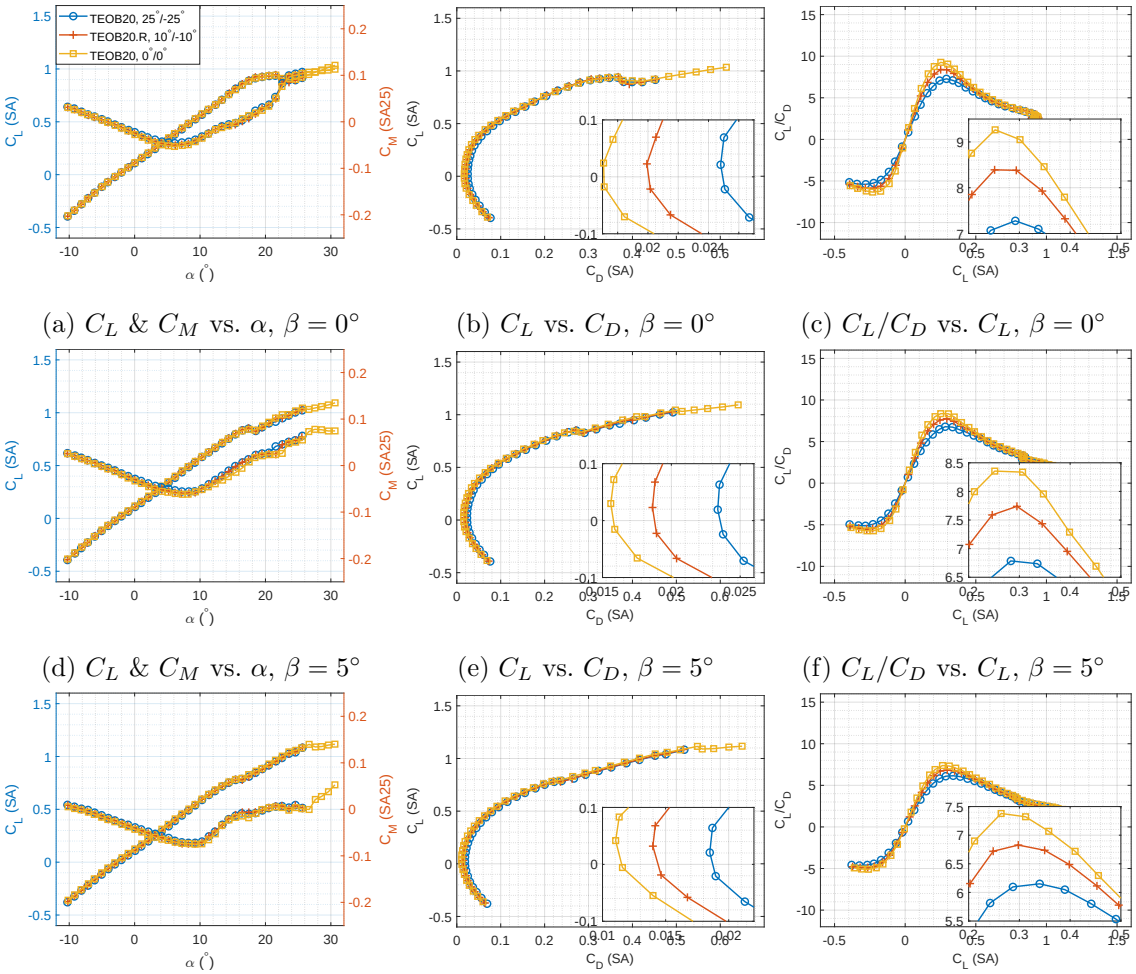
Figure 2.159: Effects of side-slip and aileron deflections on lateral force and moments vs. α for UW-S-21A

UW-S-20A Figure 2.157 shows the UW-S-20A model with the reduced-chord aileron deflection angles of $\delta_R = \pm 10°, \pm 25°$. Figs. 2.160 and 2.161 show the variation of longitudinal and lateral forces and moments of this model with angles of attack for several aileron deflection angles and for the zero sideslip angle case. As discussed in §2.7.8, there are notable differences in both longitudinal and lateral forces and moment variations between the two models, UW-S-21A and UW-S-20A, at $\alpha \geq 22°$. As mentioned in §2.7.8, there is a reduction in lift at $\alpha \approx 22°$ where $\beta = 0°$ corresponding with sharp reduction in the side force and yaw moment along with a sharp rise in the roll moment. The non-linear variations of the lateral force and moments, at $\alpha \approx 22°$ where $\beta = 0°$, could be caused, partly, by the force generated on the vertical tail resulting from asymmetrical flow separations of the canard, fuselage, nacelles, and wing surfaces.

Note that the two models are different in nacelle locations, outboard wing planform, and empennage configuration which includes horizontal tail locations, vertical tail size and thickness, dorsal and ventral fins. It appears that these configuration differences play a significant role in both longitudinal and lateral forces and moment at high angles of attack, near stall and beyond. At zero-side slip angle, a dramatic change in lateral-directional moments at an angle of attack of approximately 22°, the asymmetrically burst vortices are not expected to create such severe variations in lateral force and moments just at this $\alpha \approx 22°$. The lack of an abrupt increase in yawing moment at a specific high alpha for zero beta indicates that forebody vortex asymmetry is not causing the observed trends (no "nose-slice" behavior). The interaction of the support system fork with the flow field does not create such a drastic change in the lateral force and moments at this angle of attack as shown in Fig. 2.159. The sudden variations of the lateral forces and moment of the UW-S-20A at $\alpha \approx 22°$ is most likely due to the asymmetric flow with the combined effects of nacelles and outboard wing planforms in §2.7.1 [23, 26].

Figures 2.160 and 2.161 show the effect of during side-slip and aileron deflections on configuration UW-S-20A forces and moment with respect to angle of attack. The ailerons are deflected upward on right-wing and downward on left-wing. For zero side-slip, the aileron roll control authority goes to zero above about 14 degrees angle of attack. The lift curve reaches a plateau at $\alpha \approx 17°$ for all aileron deflection angles for $\beta = 5°$ and is smoothed at

$\beta = 10°$. This plateau is suspected to be due to the asymmetrical vortex bursting over the wing and canard surfaces. For $\beta \neq 0°$, the windward effective sweep angles increases while leeward effective sweep angles decreases for the canards and wings, causing asymmetrical vortex formation and burst over these surfaces. The effects of aileron deflection angles on the lateral forces and moment of are similar for the two models as shown in Figs. 2.159 and 2.161.

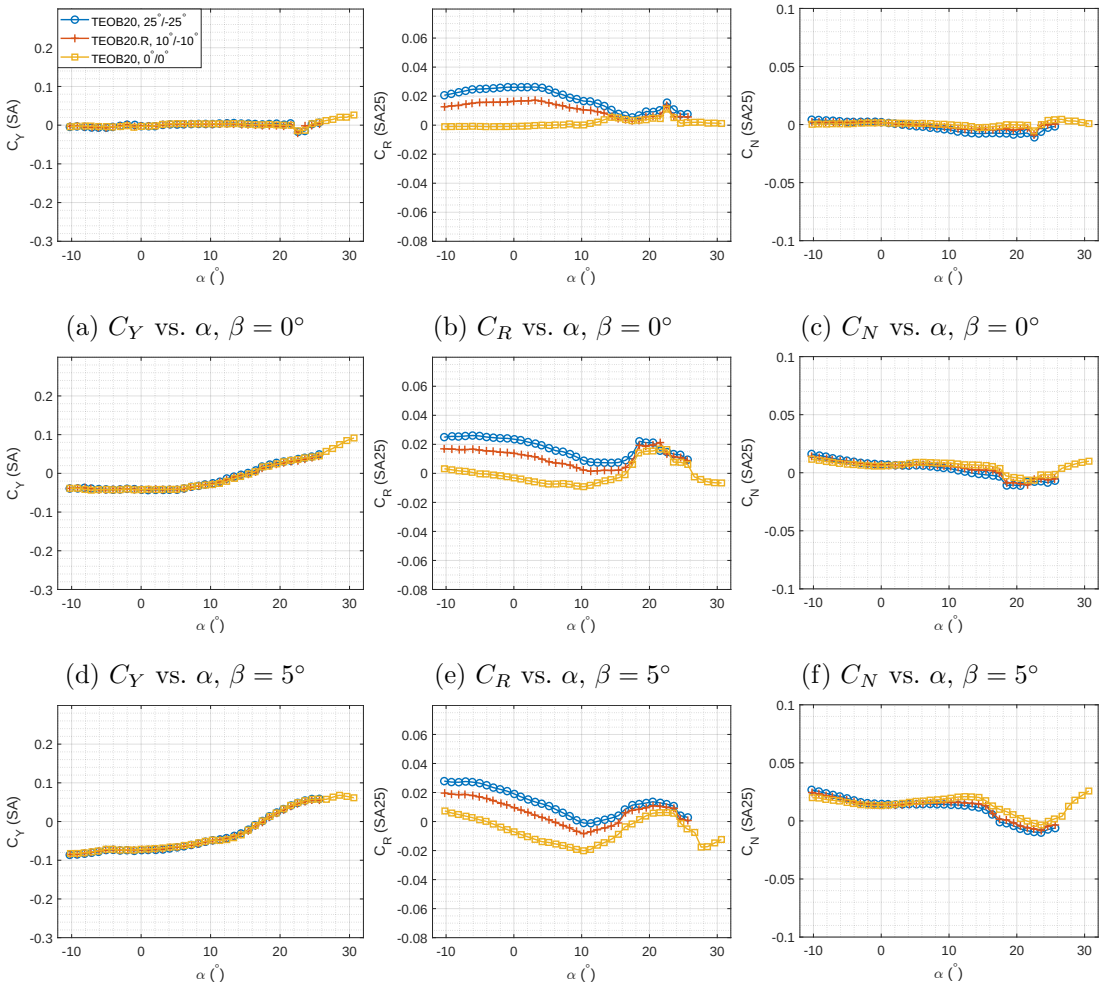


(a) C_L & C_M vs. α, $\beta = 0°$ (b) C_L vs. C_D, $\beta = 0°$ (c) C_L/C_D vs. C_L, $\beta = 0°$

(d) C_L & C_M vs. α, $\beta = 5°$ (e) C_L vs. C_D, $\beta = 5°$ (f) C_L/C_D vs. C_L, $\beta = 5°$

(g) C_L & C_M vs. α, $\beta = 10°$ (h) C_L vs. C_D, $\beta = 10°$ (i) C_L/C_D vs. C_L, $\beta = 10°$

Figure 2.160: Effects of side-slip and aileron deflections on longitudinal forces and moment vs. α for UW-S-20A

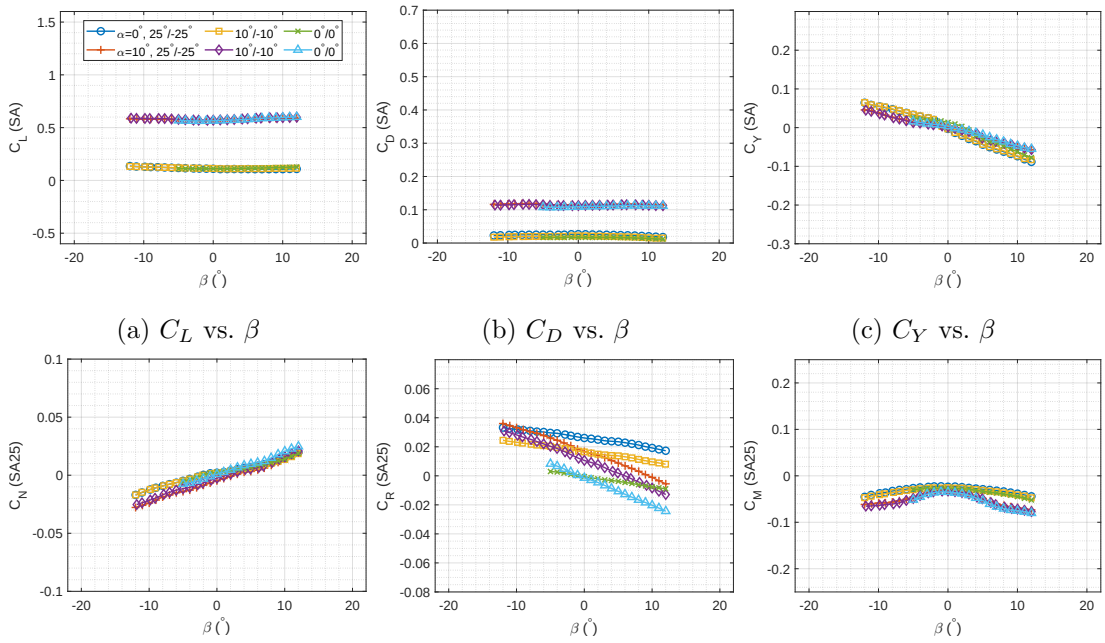


(a) C_Y vs. α, $\beta = 0°$ (b) C_R vs. α, $\beta = 0°$ (c) C_N vs. α, $\beta = 0°$

(d) C_Y vs. α, $\beta = 5°$ (e) C_R vs. α, $\beta = 5°$ (f) C_N vs. α, $\beta = 5°$

(g) C_Y vs. α, $\beta = 10°$ (h) C_R vs. α, $\beta = 10°$ (i) C_N vs. α, $\beta = 10°$

Figure 2.161: Effects of side-slip and aileron deflections on lateral force and moments vs. α for UW-S-20A

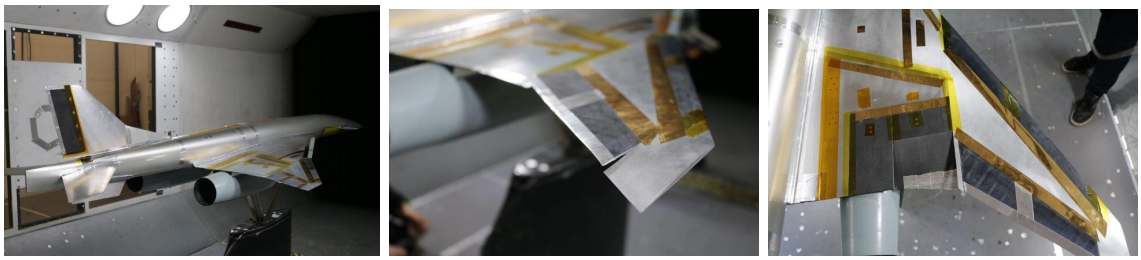


(a) C_L vs. β (b) C_D vs. β (c) C_Y vs. β

(d) C_N vs. β (e) C_R vs. β (f) C_M vs. β

Figure 2.162: UW-S-20A outboard aileron deflection effects at various α, force and moment vs. β

Aileron-Droop/Flaperon Deflection Effectiveness vs. Wing Planform This section shows selected results for the aileron and flaperon effectiveness of two different three-surface configurations, UW-S-21A and UW-S-23A, providing a variation of outboard wing LE sweep (see Fig. 2.84). Both the UW-S-21A and UW-S-23A are three-surface, underwing-mounted nacelles, and conventional low-tail arrangements: buildup information in Tab. 2.12 in §2.2 and geometry specifications in Tab. 2.27 in §2.4. Both aileron and flaperon aerodynamic comparisons and incremental effectiveness were presented in [26, 371] and here. The additional 2023 wing aileron and flaperon deflections augment the database of trailing edge effectiveness. Figures 2.156 and 2.163 show the trailing edge deflections of UW-S-21A and UW-S-23A, planforms respectively.

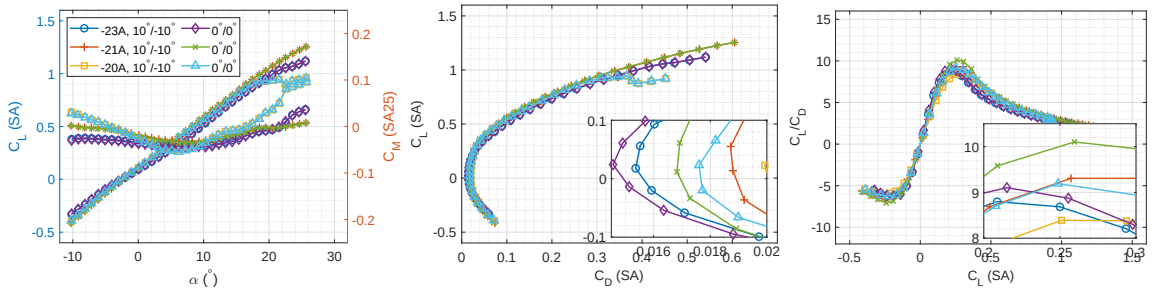


(a) $\delta_{\text{flap}} = 0°$ & $\delta_{\text{ail}} = 0°$ (b) $\delta_{\text{flap}} = 0°$ & $\delta_{\text{ail}} = \pm 10°$ (c) $\delta_{\text{flap}} = 15°$ & $\delta_{\text{ail}} = 10°$

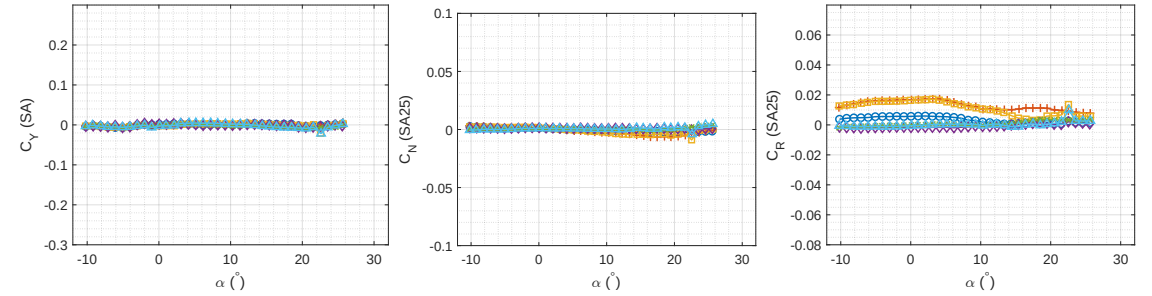
Figure 2.163: UW-S-23A with TE deflections [24]

Figure 2.163 shows the UW-S-23A model with the outboard aileron deflection angles of $\delta_{\text{ail}} = 0°$ and $\pm 10°$. The results for aileron deflections on both longitudinal and lateral forces and moments for various angles of attack at zero-side slip angle are shown in Figs. 2.164. The figure shows that aileron deflections do not have a significant effect on the longitudinal forces and moment. The aileron deflections slightly increase the nose-up pitching moment and drag and decrease the untrimmed lift-over-drag ratio as shown in Fig. 2.164. Although the pitching moment break is independent of the aileron deflections (influenced, mainly, by the wing planform and its leading edges), the magnitude of the pitching moment at the pitching moment break point is affected by the aileron deflections. Figure 2.164 further shows that aileron deflections have significant effects on the lateral moments of the model (as intended for roll control), with some effects on the lateral force at high angles of attack,

$\alpha \geq 10^{\circ}$. Both yaw and roll moments for the zero-angle deflection ($\delta = 0^{\circ}$) remain almost constant (C_N, $C_R \approx 0$) up to $\alpha \approx 18^{\circ}$. Beyond $\alpha \approx 18^{\circ}$, both yaw and roll moments are observed to vary with the angle of attack and become non-zero, typically resulting from asymmetric flow separation on the slender forebody/canards, and potentially asymmetric vortex breakdown on the wings, plus the interaction of these flows with the tail surfaces. The $\alpha \approx 18^{\circ}$ point where both yaw and roll moments begin to vary matches almost exactly the point where the pitching moment curves change slope for the zero-angle deflection case. The yawing moment derivatives with respect to the angle of attack (C_{N_α}) are proportional to the aileron deflection angles, while the yaw break angle is independent of the aileron angles. The aileron deflection effectiveness is proportional to the aileron areas and the W23 wing ailerons are less effective compared to the W15 wing ailerons (as W15 has lower outboard wing sweep and less swept aileron hinge-lines). Similar results are observed for rolling moment variations. The rolling moment is proportional to aileron deflections and aileron areas where the rolling moment is almost constant at $-5^{\circ} \leq \alpha \leq 5^{\circ}$ and nonlinear elsewhere. The differences between W15 and W23 ailerons are in magnitude. The rolling moment breaks, like the yaw moments, are independent of aileron deflections but happen at lower angles of attack, $\alpha \approx 5^{\circ}$. At least for the zero-deflection LE case ($\delta_{\mathrm{LE}} = 0^{\circ}$), the aileron effectiveness decreases beyond $\alpha \approx 5^{\circ}$ and the rolling moment decreases in a way that is inversely proportional to the angle of attack. The roll control effectiveness of the ailerons is generally greater on the less-swept outboard panels (likely due to the lower sweep of the ailerons themselves).

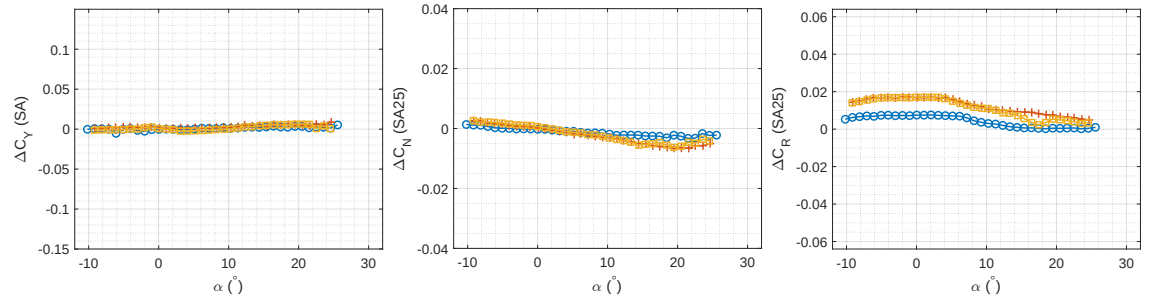


(a) C_L and C_M vs. α (b) C_L vs. C_D (c) C_L/C_D vs. C_L



(d) C_Y vs. α (e) C_N vs. α (f) C_R vs. α

Figure 2.164: Effects of aileron deflection, δ_{TEOB}, on forces and moments vs. α for UW-S-21A vs. UW-S-23A (LEOB sweep $\Lambda = 41°$ vs. $\Lambda = 63°$)



(a) ΔC_Y vs. α (b) ΔC_N vs. α (c) ΔC_R vs. α

Figure 2.165: Aileron control, δ_{TEOB}, lateral-directional effectiveness for UW-S-21A vs. UW-S-23A (LEOB sweep $\Lambda = 41°$ vs. $\Lambda = 63°$)

Flaperon Deflection

This section discusses the trailing-edge effectiveness on two different three-surface configurations, which are UW-S-20A and UW-S-21A, shown in Fig. 2.84. The UW-S-21A is three-surface conventional low-tail model with pair of canards, two nacelles located under

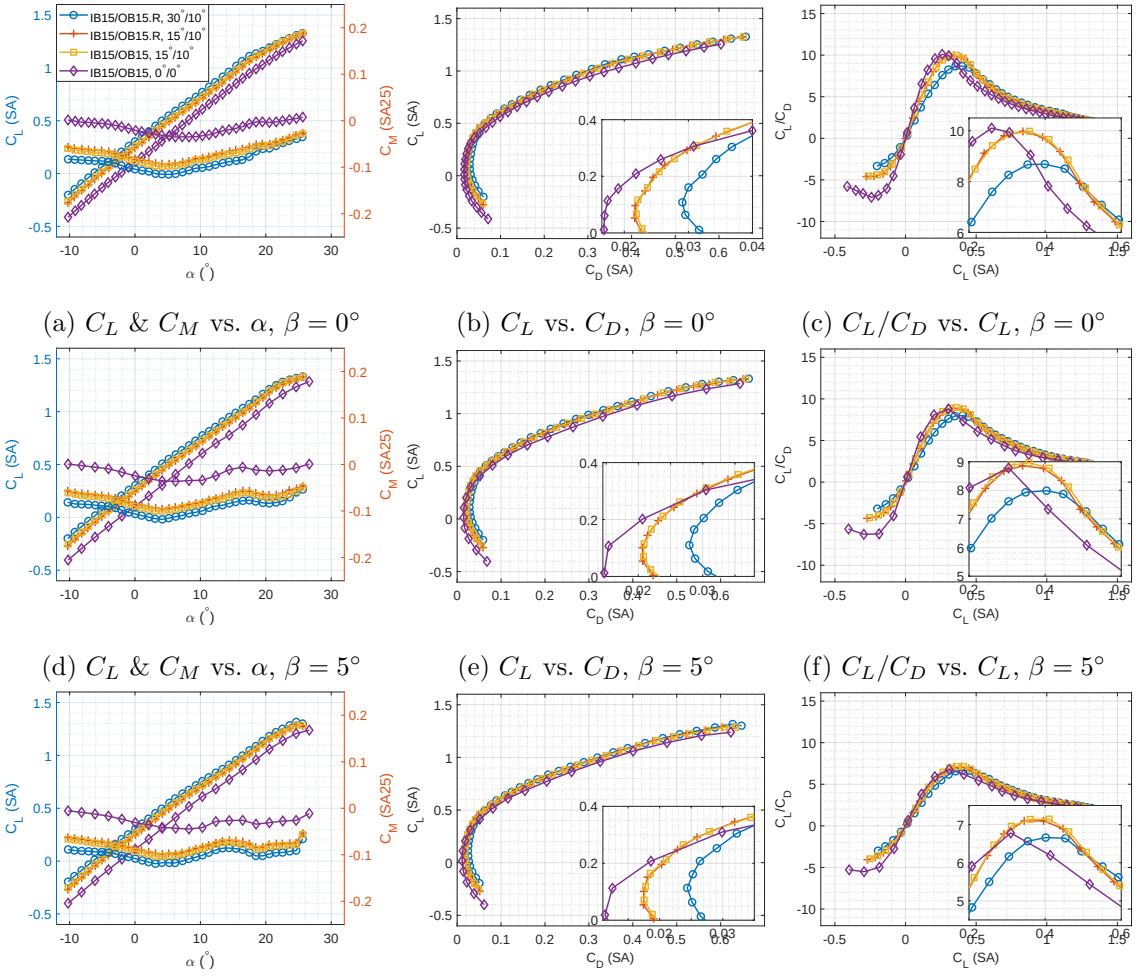
the wing, and conventional empennage configuration with dorsal and ventral fins and the UW-S-20A is three-surface T-tail model with pair of canards, two nacelles located on top of the wing and a T-tail empennage configuration without dorsal or ventral fins. They are different in nacelle locations, outboard wing planform, and empennage configuration which includes horizontal tail locations, vertical tail size and thickness, dorsal and ventral fins. The detailed configuration build-up and difference are summarized in Tab. 2.12 in the §2.2. The UW-S-21A and UW-S-20A with trailing-edge deflections are shown in Figs. 2.166 and 2.169, respectively. The TE deflection is a simultaneous deflection of flaps and ailerons acting as high-lift device in the role of *flaperons*. The ailerons are deflected downward ("drooped") on both left- and right-side of the wing instead of differentially. The R followed by the deflection angles stands for Redued-chord ailerons which was presented in §2.7.9.

UW-S-21A The three deflected flaperon configurations are shown in Fig. 2.166. The UW-S-21A longitudinal forces and moment with respect to angles of attack at different sideslip angles are shown in Fig. 2.167. The present plots show the effects of TE deflections for the cruise, zero-LE deflection. The effect of the aileron droop and flap deflection, is seen to be an increase in lift at a given angle of attack which is desirable for reduced body attitude on approach and increased lift at takeoff rotation. At low angles of attack, the lift increase on both configurations makes a significant improvement in lift over drag. This improves the performance during the takeoff ground-roll and around liftoff, but poses a potential problem when slowing the aircraft down at low angle of attack flight condition. The benefits in lift also come at a significant nose-down zero-pitch moment penalty which would need to be trimmed out by a combination of canard and horizontal stabilator deflection. At takeoff-climb conditions where $\alpha \approx 7^\circ \sim 10^\circ$, the TE flap deflections also produce a slight loss in untrimmed lift over drag. At least up to the initial zero-LE pitch-up break, the TE deflections have little effect on the basic pitch moment curve shapes, and at operating angles of attack, there is little variation of the TE increments with sideslip angles. For all combinations of TE deflections, the UW-S-21A model did not stall in the range of angles of attack tested, shown in Fig. 2.167.



(a) $\delta_{\text{flap/ail}} = 15°/20°$ (b) $\delta_{\text{flap/ail}} = 15°/10°\text{R}$ (c) $\delta_{\text{flap/ail}} = 30°/10°\text{R}$

Figure 2.166: UW-S-21A with flap and aileron deflections [26]

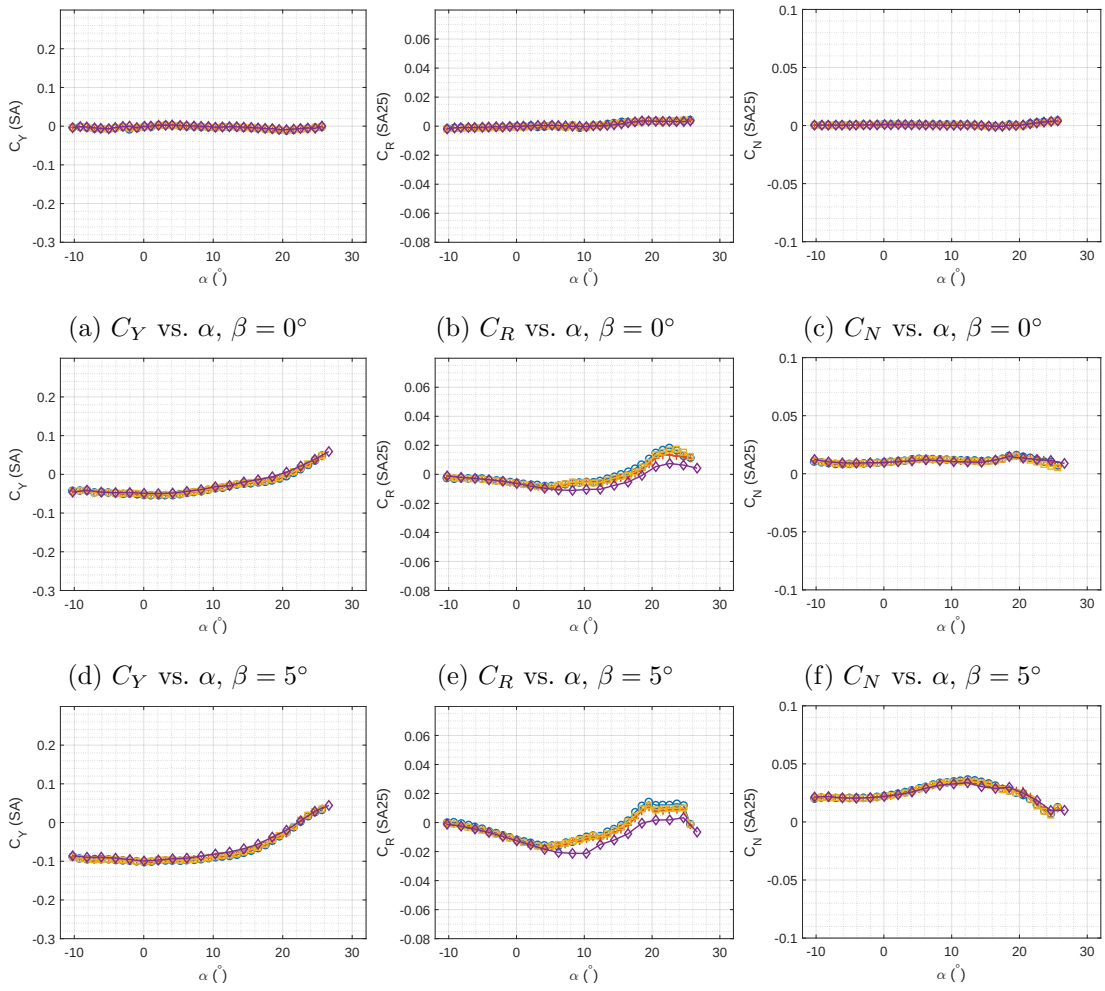


(a) C_L & C_M vs. α, $\beta = 0°$ (b) C_L vs. C_D, $\beta = 0°$ (c) C_L/C_D vs. C_L, $\beta = 0°$

(d) C_L & C_M vs. α, $\beta = 5°$ (e) C_L vs. C_D, $\beta = 5°$ (f) C_L/C_D vs. C_L, $\beta = 5°$

(g) C_L & C_M vs. α, $\beta = 10°$ (h) C_L vs. C_D, $\beta = 10°$ (i) C_L/C_D vs. C_L, $\beta = 10°$

Figure 2.167: Effects of side-slip and flaperon deflections on longitudinal forces and moment vs. α for UW-S-21A



(a) C_Y vs. α, $\beta = 0°$ (b) C_R vs. α, $\beta = 0°$ (c) C_N vs. α, $\beta = 0°$

(d) C_Y vs. α, $\beta = 5°$ (e) C_R vs. α, $\beta = 5°$ (f) C_N vs. α, $\beta = 5°$

(g) C_Y vs. α, $\beta = 10°$ (h) C_R vs. α, $\beta = 10°$ (i) C_N vs. α, $\beta = 10°$

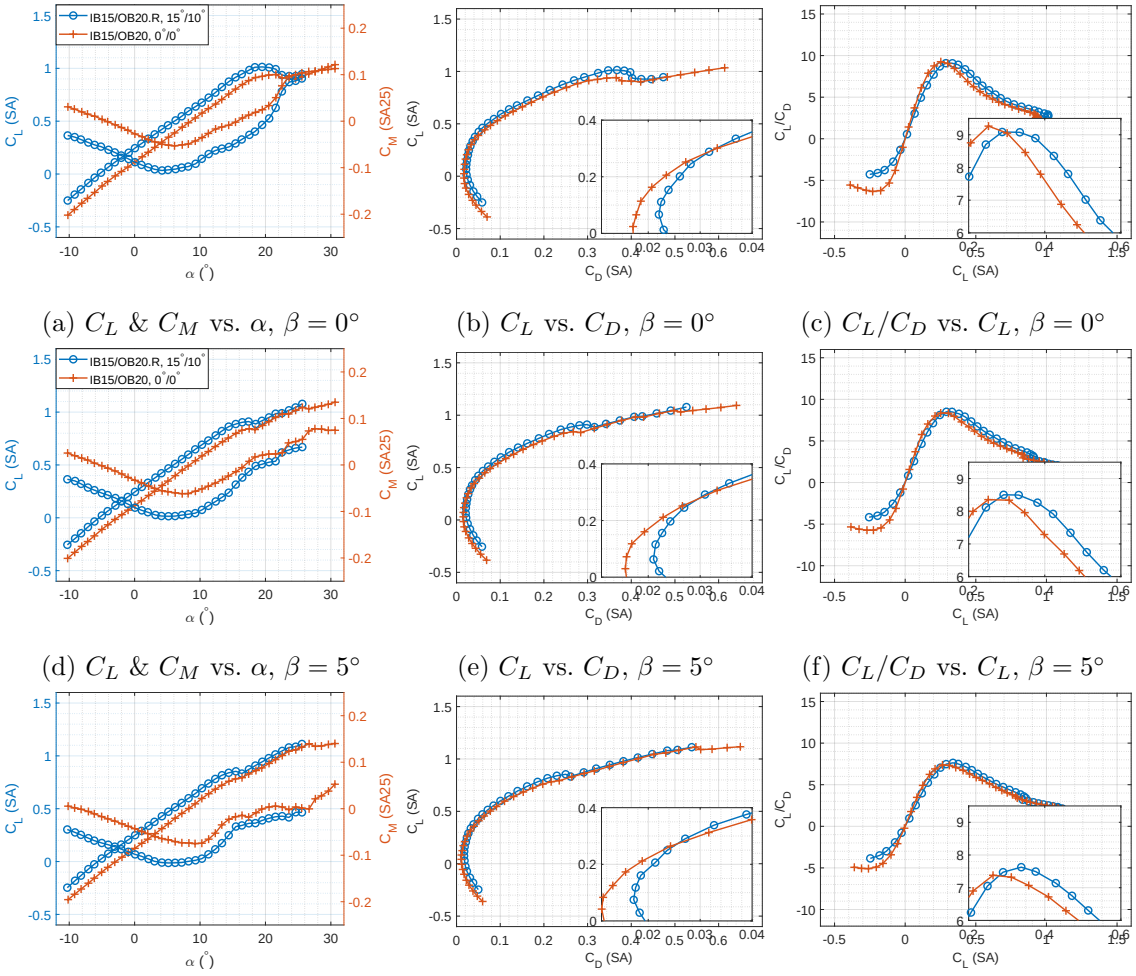
Figure 2.168: Effects of side-slip and flaperon deflections on lateral force and moments vs. α for UW-S-21A

UW-S-20A The two flaperon configurations tested on UW-S-20A are shown in Fig. 2.169. Similar trends are observed for the UW-S-20A model in Fig. 2.167 except that the model stalls at $\alpha \approx 22^\circ$ as discussed in §2.7.8. The TE deflections increase the max lift ($C_{L_{\max}}$) value but reduce the angle of attack of stall. It is interesting to note that the pitching moment break angles, $\alpha \approx 4^\circ$, are the same for both models and they vary slightly with respect to sideslip angles.



(a) $\delta_{\text{flap/ail}} = 0^\circ/0^\circ$ (b) $\delta_{\text{flap/ail}} = 15^\circ/10^\circ\text{R}$

Figure 2.169: UW-S-20A with flap and aileron deflections [26]

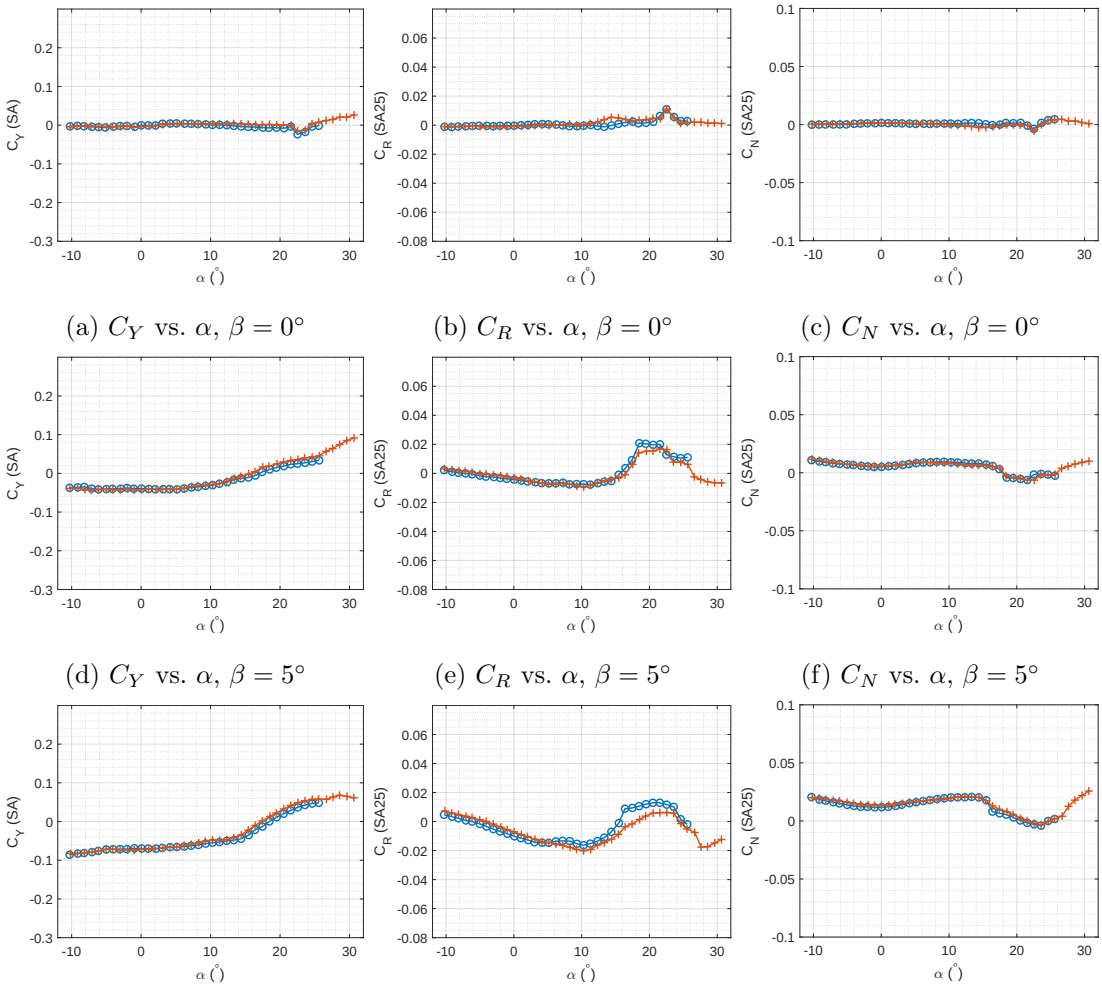


(a) C_L & C_M vs. α, $\beta = 0°$ (b) C_L vs. C_D, $\beta = 0°$ (c) C_L/C_D vs. C_L, $\beta = 0°$

(d) C_L & C_M vs. α, $\beta = 5°$ (e) C_L vs. C_D, $\beta = 5°$ (f) C_L/C_D vs. C_L, $\beta = 5°$

(g) C_L & C_M vs. α, $\beta = 10°$ (h) C_L vs. C_D, $\beta = 10°$ (i) C_L/C_D vs. C_L, $\beta = 10°$

Figure 2.170: Effects of side-slip and flaperon deflections on longitudinal forces and moment vs. α for UW-S-20A

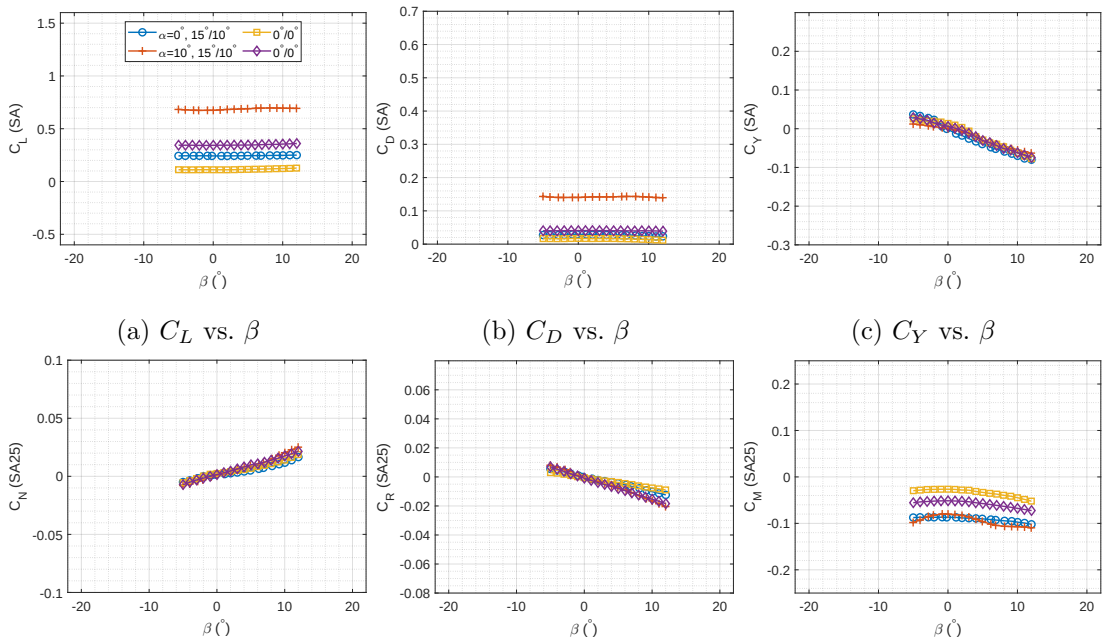


(a) C_Y vs. α, $\beta = 0°$ (b) C_R vs. α, $\beta = 0°$ (c) C_N vs. α, $\beta = 0°$

(d) C_Y vs. α, $\beta = 5°$ (e) C_R vs. α, $\beta = 5°$ (f) C_N vs. α, $\beta = 5°$

(g) C_Y vs. α, $\beta = 10°$ (h) C_R vs. α, $\beta = 10°$ (i) C_N vs. α, $\beta = 10°$

Figure 2.171: Effects of side-slip and flaperon deflections on lateral force and moments vs. α for UW-S-20A

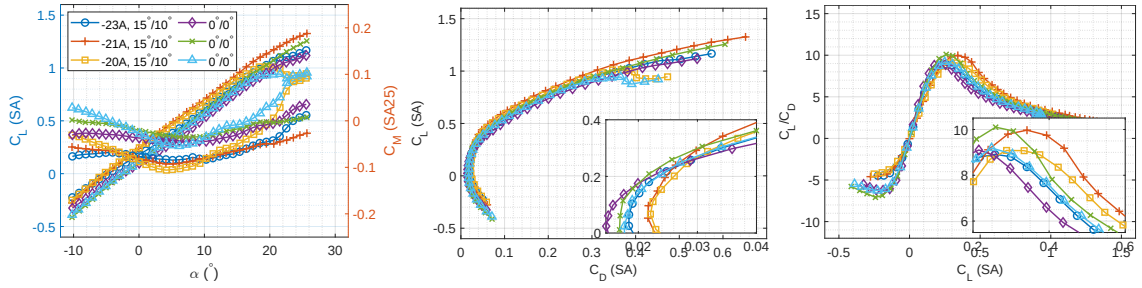


(a) C_L vs. β (b) C_D vs. β (c) C_Y vs. β

(d) C_N vs. β (e) C_R vs. β (f) C_M vs. β

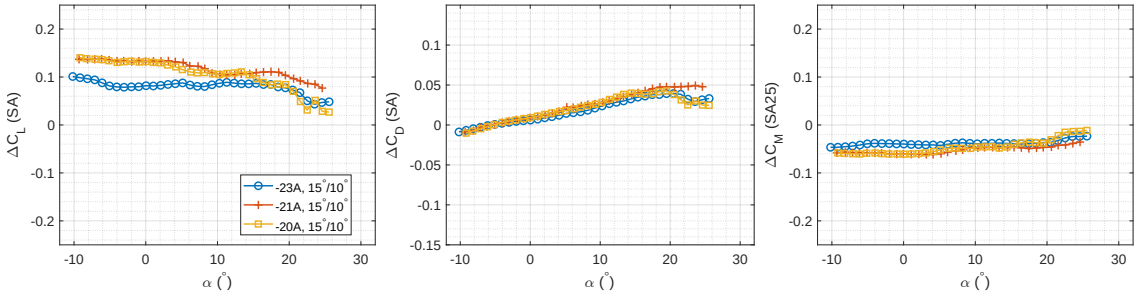
Figure 2.172: UW-S-20A flaperon deflection effects at various α, force and moment vs. β

Full-Span Trailing Edge Deflection Effectiveness vs. Wing Planform The UW-S-21A and UW-S-23A longitudinal characteristics are shown in Fig. 2.173. Deflection of the trailing edges simultaneously deflects both flaps and "drooping" ailerons, acting as the high-lift device. That is, in the role of flaperons. The ailerons are deflected downward on both the left and right sides of the wing instead of differentially, as done for roll control. The effect of the aileron droop and flap deflection is seen to be an increase in lift at a given angle of attack, which is desirable for reducing body attitude on approach and increasing lift at takeoff rotation. For all combinations of TE deflections, the UW-S-21A model did not stall in the range of angles of attack tested; similar trends are observed for the UW-S-23A model except that the model stalls at $\alpha \approx 21^\circ$ in Fig. 2.173 and in §2.7.2 [26]. The flaperon deflections increase the max lift value but reduce the angle of attack of the stall for the UW-S-23A. The incremental effects of flaperon deflections on forces and moments of both models as functions of the angle of attack are compared in Fig. 2.174. The incremental lift is inversely proportional to angles of attack at $\alpha \geq -5^\circ$ for UW-S-21A but almost constant for UW-S-23A from $-5^\circ \leq \alpha \leq 15^\circ$. The UW-S-23A has less aileron effectiveness/authority than the UW-S-21A configuration in ΔC_L and ΔC_M. The slopes of ΔC_D are different for both UW-S-21A and UW-S-23A. This suggests that flaperons are more effective on the UW-S-21A model because of the lower outboard wing sweep and better subsonic characteristics.



(a) C_L and C_M vs. α (b) C_L vs. C_D (c) C_L/C_D vs. C_L

Figure 2.173: Effects of flaperon deflection, $\delta_{\text{IB/OB}}$, on longitudinal forces and moments vs. α for UW-S-20A vs. UW-S-21A vs. UW-S-23A (LEOB sweep $\Lambda = 53^\circ$ vs. $\Lambda = 41^\circ$ vs. $\Lambda = 63^\circ$, untrimmed, legend displays TEIB deflection/TEOB deflection)



(a) ΔC_L vs. α (b) ΔC_D vs. α (c) ΔC_M vs. α

Figure 2.174: Flaperon control, $\delta_{\text{IB/OB}}$, longitudinal effectiveness for UW-S-20A vs. UW-S-21A vs. UW-S-23A (LEOB sweep $\Lambda = 53°$ vs. $\Lambda = 41°$ vs. $\Lambda = 63°$, untrimmed, legend displays TEIB deflection/TEOB deflection)

Exploratory Roll Control And Drag Device Effectiveness

The SCALOS models were equipped with other effectors for varying and controlling aerodynamic forces and moments particularly for speed/path control and aeroelastic roll control in the cruise and LTO configuration. Those include: conventional roll-control speed brakes/aileron spoilers (A.U), spoiler-slot deflectors (SSD), mid-chord spoilers (FS), and clam shell speed brakes (CS). Photos of these devices are shown in Fig. 2.175 with detail views in Figs. 2.176 to 2.182.

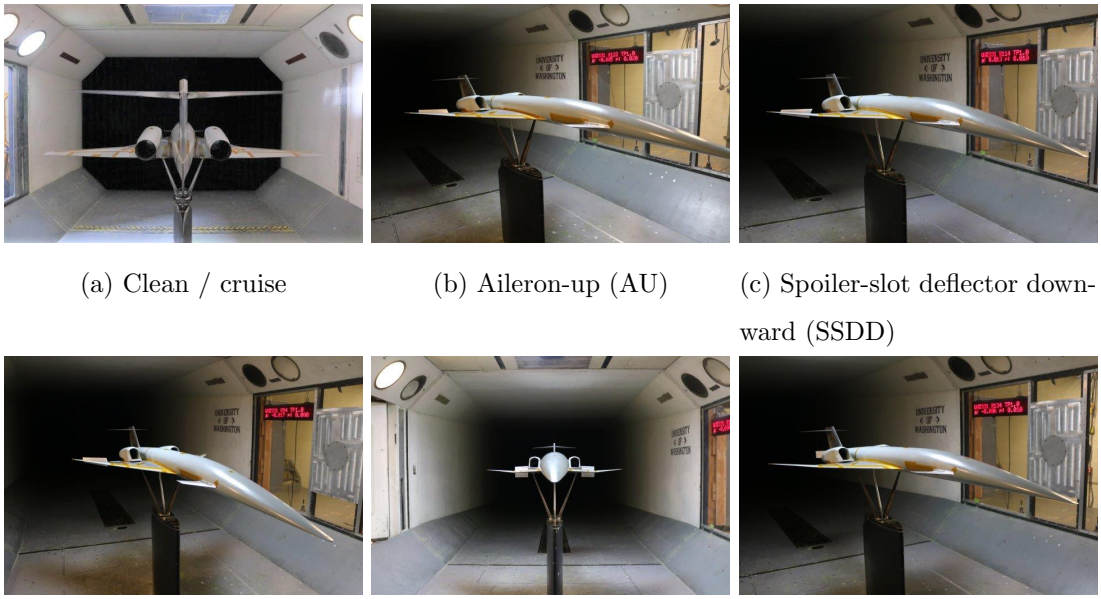
The aileron spoilers are deflected upward at $\delta = 60°$ with the same hinge line as the reduced-chord aileron and the same spanwise location on the wing. The aileron spoiler has the same span as the original aileron and reduced-chord aileron, but with half of the chord length as the reduced-chord aileron and equivalent to one-third of the full-chord aileron, $\bar{c}_{\text{A.U}} = \frac{1}{2}\bar{c}_{\text{ail R}} = \frac{1}{3}\bar{c}_{\text{ail}}$, and so are the area, $S_{\text{A.U}} = \frac{1}{2}S_{\text{ail R}} = \frac{1}{3}S_{\text{ail}}$ as shown in Fig. 2.176.

The exploratory spoiler-slot deflectors are studied and illustrated not to scale in Fig. 2.177. Figure 2.177a shows side view of the downward and upward SSD deflections and Fig. 2.177b further displays the implementation of SSD on the wing. The left wing is full-scale aircraft implementation which consists of inboard and outboard, Type 1 and Type 2, SSDs, respectively. The roll control deflects the SSDs differentially with type 1 upward on one wing and type 2 downward one other and the speed control deflects the SSDs symmetrically with either or both types in same directions. These can be used as drag devices for flight

path control like conventional subsonic airliner spoilers, but are mainly intended to provide roll controls at all Mach numbers without large aeroelastic losses or aileron reversal due to wing-twisting. These devices have been used successfully including on the supersonic North American Vigilante, a carrier-based Vietnam era supersonic recon-bomber [460]. For the purposes of this exploratory test, the SSDs were made in single up or down devices as shown on the right side of the wing in Fig. 2.177b and were set at maximum deflection of $\delta = 60^\circ$ in Figs. 2.178 and 2.179. The slotted-slat deflector chord length and area are the same as those of the aileron spoiler and with the same hinge line and spanwise location on the wing.

The mid-chord spoilers are deployed at $\delta = 60^\circ$ on both sides of the wing, and on both top and bottom of the wing, in Fig. 2.181. The mid-chord spoilers have the same span length but with half of the chord length as the flaps, $\bar{c}_{\text{FS}} = \frac{1}{2}\bar{c}_{\text{flap}}$, with the area: $S_{\text{FS}} = \frac{1}{2}S_{\text{flap}}$. The hinge line of the mid-chord spoilers is one chord length of ahead of the flap hinge line with the same spanwise location on the wing.

The after-body clam shell speed brakes are deflected at $\delta = 60^\circ$ and placed at the end of the fuselage in Fig. 2.182. A similar concept of "air brakes" has been successfully used on aircraft, like the Fokker F100 airliner and the F-106 delta-winged supersonic fighter. The clamshell speed brakes have the same chord length as the root-chord length of the rudder of 2020 vertical tail, V20, and span of the fuselage. The hinge line of the clamshell speed brakes is the same as the hinge line of the root chord of the rudder.



(a) Clean / cruise

(b) Aileron-up (AU)

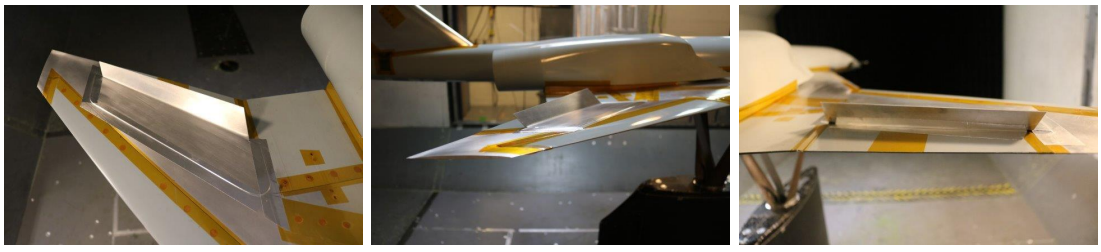
(c) Spoiler-slot deflector downward (SSDD)

(d) Spoiler-slot deflector upward (SSDU)

(e) Mid-chord spoiler (FS)

(f) Clamshell speed brake (CS)

Figure 2.175: UW-S-20A with alternate control devices [26]

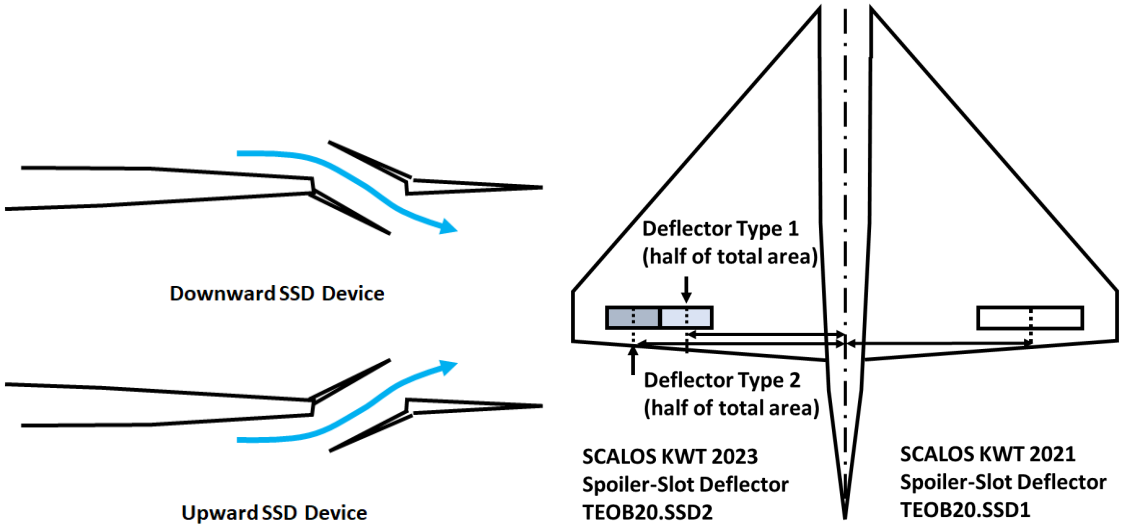


(a) Front view

(b) Side view

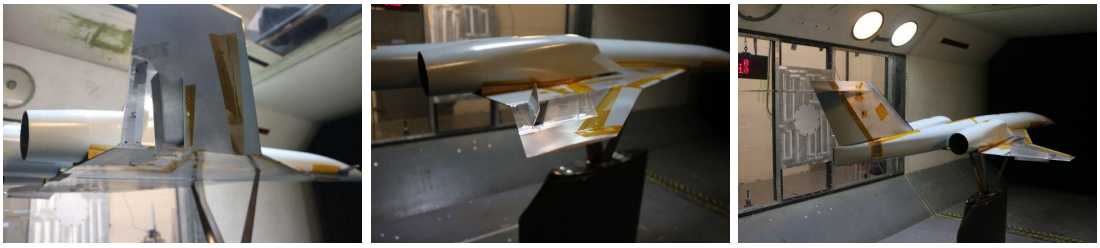
(c) Rear view

Figure 2.176: UW-S-20A with aileron spoilers [26]



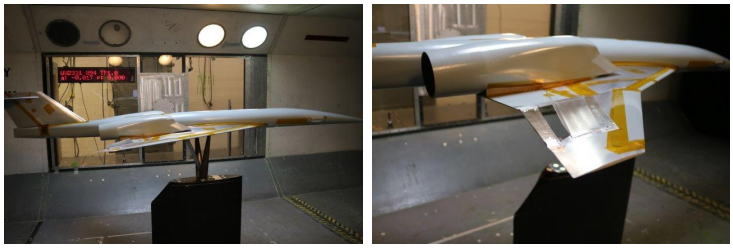
(a) Side view (b) Top view

Figure 2.177: Exploratory spoiler-slot deflector (not to scale) [25, 26]



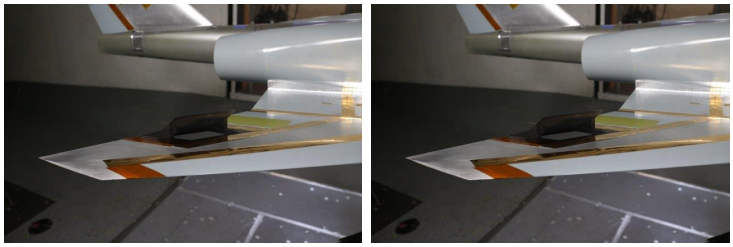
(a) Bottom view (b) Side view (c) Rear view

Figure 2.178: UW-S-20A with 2021 spoiler-slot deflector downward [26]



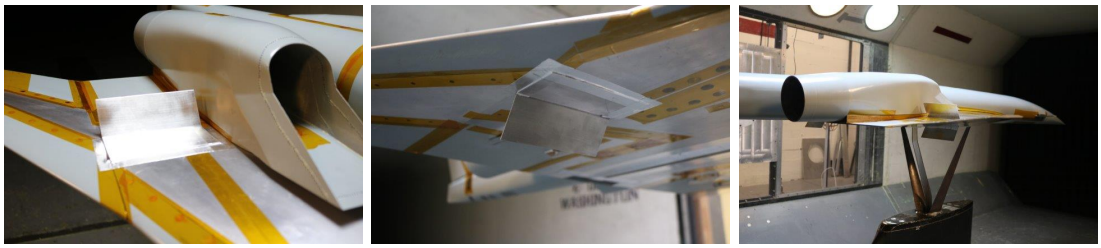
(a) Side view (b) Side view 2

Figure 2.179: UW-S-20A with 2021 spoiler-slot deflector upward [26]



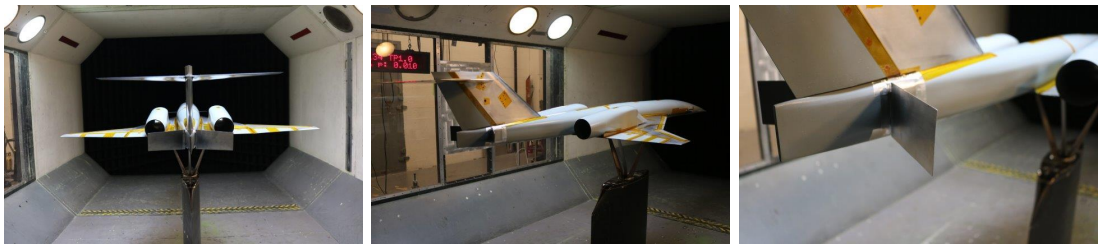
(a) TEOB20.SSD23 $\delta = +66°$ (b) TEOB20.SSD23 $\delta = \pm 66°$

Figure 2.180: UW-S-20A with 2023 spoiler-slot deflector [25]



(a) Top view (b) Bottom view (c) Side view

Figure 2.181: UW-S-20A with mid-chord spoilers [26]



(a) Rear view (b) Side view (c) Side view 2

Figure 2.182: UW-S-20A with after-body clam shell speed brakes [26]

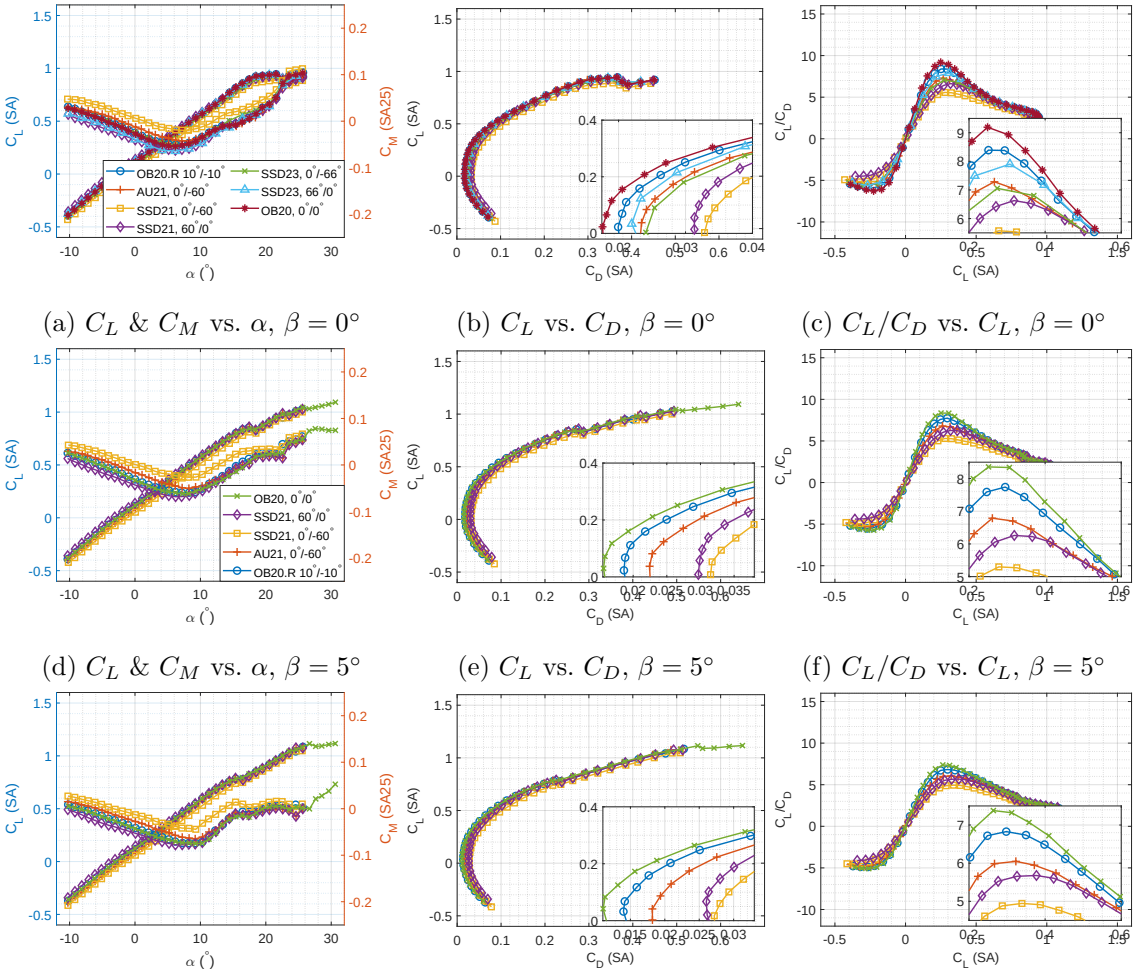
Asymmetric (Single-Side) Roll Control Results The analysis from [26] is presented in the following paragraphs. This section studies the asymmetric deflection of the devices described and shown in Figs. 2.176 to 2.182. All devices are deployed on the right side of the wing and the left-side surface is left clean. The corresponding effects of the devices on both longitudinal and lateral forces and moments on UW-S-20A are shown in Figs. 2.183, 2.184, and 2.185. Figure 2.183 shows that these control surfaces have effects on the lift-over-drag ratio and zero-pitch moment but that the pitching moment break point is independent of the deflection of the devices, §2.7.9. The same effect on lift is present at $\alpha \approx 22^\circ$ discussed earlier in §2.7.8 and §2.7.9. The more pronounced effects are in the lateral force and moments variations and the same effect at $\alpha \approx 22^\circ$ is shown in Fig. 2.184 discussed in §2.7.8 and §2.7.9.

Similar behaviors are observed for the non-zero sideslip angles. However, the effects of these additional control surfaces on lift-over-drag values for the zero-sideslip case are seen to be larger than those of the nonzero-sideslip ones in Fig. 2.183. The slope and variations of the rolling moment are seen to be affected significantly due to the asymmetric vortex formation and bursting over the wing surface. The effects of varying side slip angles while the angle of attack is kept constant, $\alpha = 10^\circ$, on both longitudinal and lateral forces and moments of the UW-S-20A are shown in Fig. 2.185. The variations are similar to the previous cases examined in §2.7.9, with the exception of the slotted-slat deflector-upward case where the values of lift, roll and pitching moments for this configuration are affected significantly, Fig. 2.185.

The analysis from [25] is presented in the following paragraphs. Figure 2.180 shows the asymmetric deflection of the devices described in Fig. 2.177, which are deployed on the right side of the wing, and the left-side surface is left clean. Note that a $\delta = -66^\circ$ was tested instead of $\delta = +66^\circ$ such that the lateral directional force and moments are flipped in Fig. 2.178 for better visualization. The 2023 SSD deflection is $\delta = 66^\circ$ and the 2021 SSD deflection is $\delta = 60^\circ$. The 2023 SSD area is 1/2 of the 2021 SSD area. The yawing moment, C_N, is almost half as of the area reduction with the same C_{N_α} at $-10^\circ \leq \alpha \leq 10^\circ$. The rolling moment, C_R, has almost constant value at $-4^\circ \leq \alpha \leq 4^\circ$ while the TEOB20.SSD21 has varying but higher C_R at the same range of angles of attack. It is important to note

that the TEOB20.SSD23 $\delta = +66$ is outboard and $\delta = -66^\circ$ is inboard such that the result shown here is flipped $\delta = -66^\circ$. It would seem like the TEOB20.SSD23 be more effective; however, it is likely that large deflection and outboard separation causing the nonlinearity of the rolling authority. The current results focused on scoping the maximum authority provided and future work would need to include combinations of intermediate deflections to determine the degree of non-linearity between small and larger deflections.

Figure 2.186 shows the differential deflection of the devices described in Fig. 2.177, which are deployed differentially on both sides of the wing. The 2023 SSDs are deflected at $\delta = \pm 66^\circ$ and compared with the conventional reduced area aileron (TEOB20.R) effectiveness at $\delta = \pm 10^\circ$. The 2023 SSDs area are 1/4 of the conventional reduced area aileron on W20. The 2023 SSDs were deflected asymmetrically, resulting in positive rolling moments in Fig. 2.186. The details is in §2.9 [27] on the conventional aileron control authorities on UW-S-20A and UW-S-21A. One of the result is that the aileron lost effectiveness beyond $\delta = +10^\circ$ where the ΔC_R is not linear even for the aeroelastically rigid wing of the wind tunnel model; however, more experimental results are required to validate the effectiveness. The 2023 SSDS rolling moment has an almost constant value at $-5^\circ \leq \alpha \leq 4^\circ$ and is halved of the effectiveness of the reduced aileron at $\delta = 10^\circ$. However, the drag polar suggests a higher drag than for the ailerons across all lift regions.

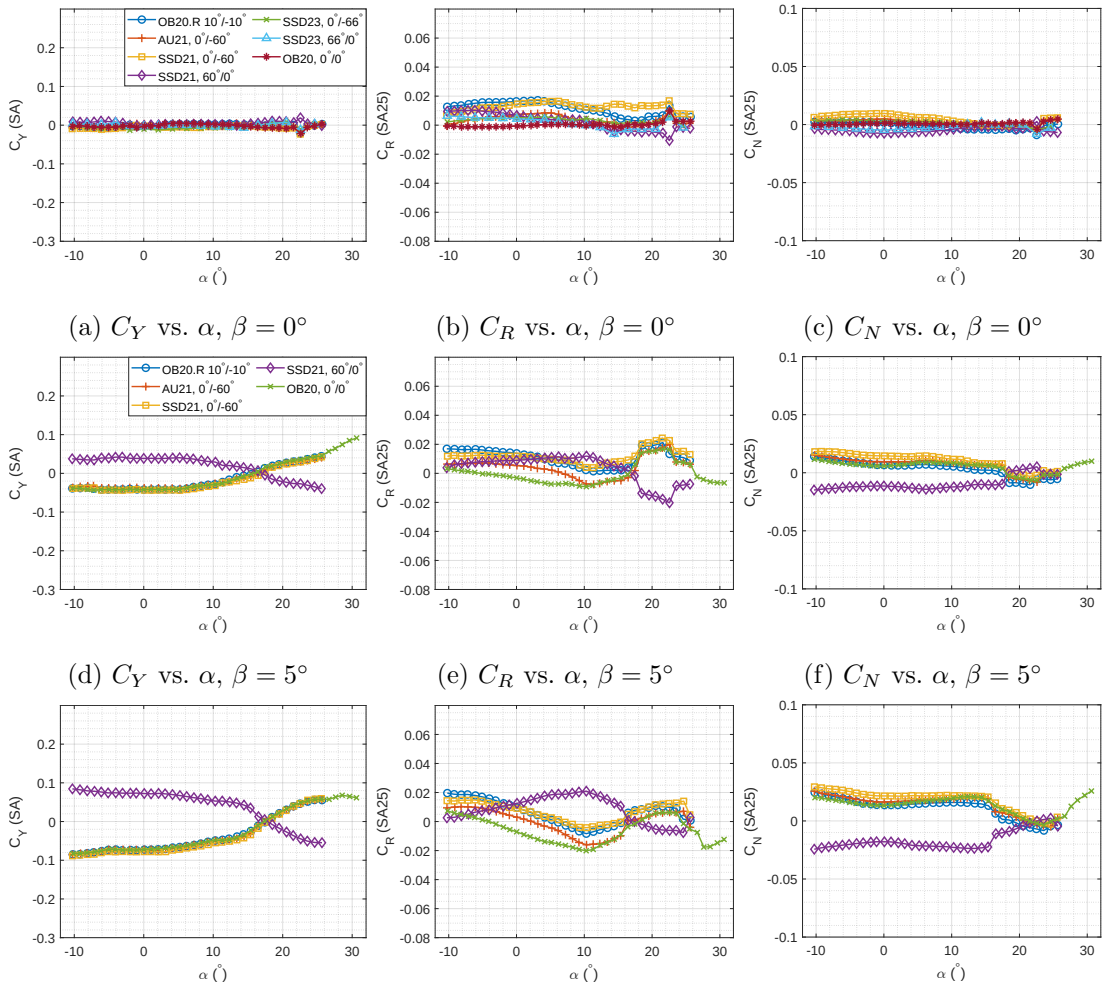


(a) C_L & C_M vs. α, $\beta = 0°$ (b) C_L vs. C_D, $\beta = 0°$ (c) C_L/C_D vs. C_L, $\beta = 0°$

(d) C_L & C_M vs. α, $\beta = 5°$ (e) C_L vs. C_D, $\beta = 5°$ (f) C_L/C_D vs. C_L, $\beta = 5°$

(g) C_L & C_M vs. α, $\beta = 10°$ (h) C_L vs. C_D, $\beta = 10°$ (i) C_L/C_D vs. C_L, $\beta = 10°$

Figure 2.183: Effects of side-slip and asymmetric control surface deflections on longitudinal forces and moment vs. α for UW-S-20A

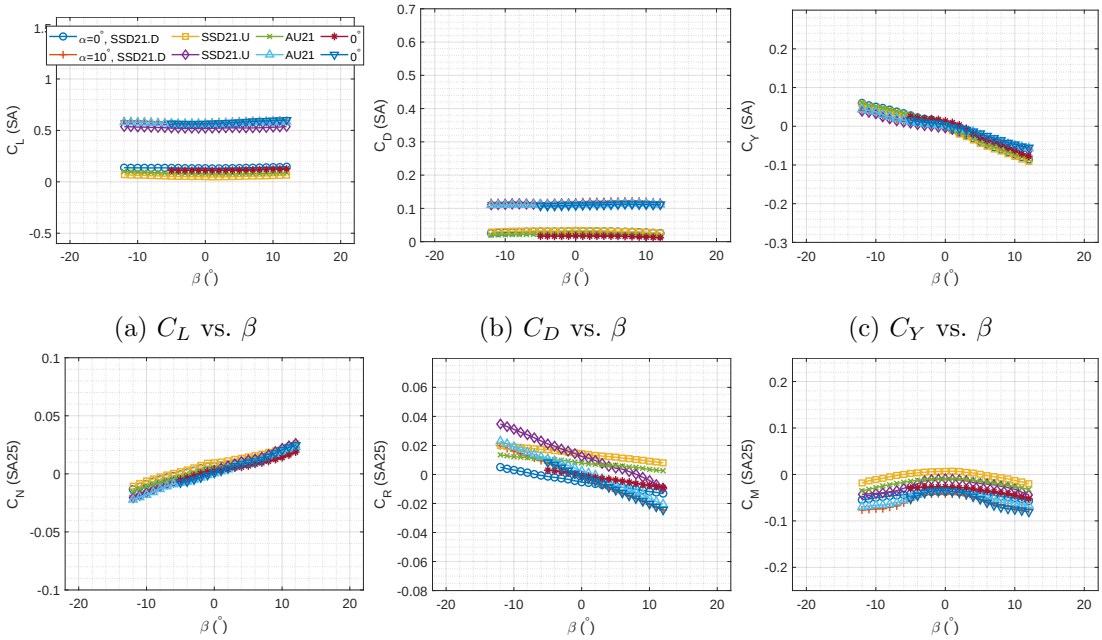


(a) C_Y vs. α, $\beta = 0°$ (b) C_R vs. α, $\beta = 0°$ (c) C_N vs. α, $\beta = 0°$

(d) C_Y vs. α, $\beta = 5°$ (e) C_R vs. α, $\beta = 5°$ (f) C_N vs. α, $\beta = 5°$

(g) C_Y vs. α, $\beta = 10°$ (h) C_R vs. α, $\beta = 10°$ (i) C_N vs. α, $\beta = 10°$

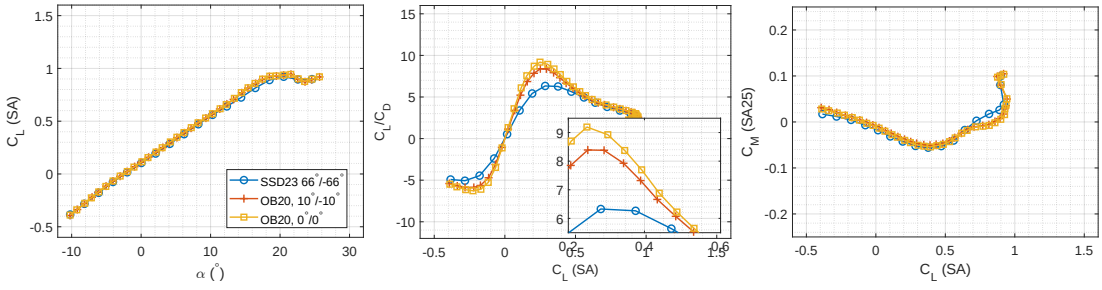
Figure 2.184: Effects of side-slip and asymmetric control surface deflections on lateral force and moments vs. α for UW-S-20A



(a) C_L vs. β (b) C_D vs. β (c) C_Y vs. β

(d) C_N vs. β (e) C_R vs. β (f) C_M vs. β

Figure 2.185: Effects of angles of attack and additional asymmetric control surface deflections on force and moments vs. β at $\alpha = 0°$ and $10°$ for UW-S-20A

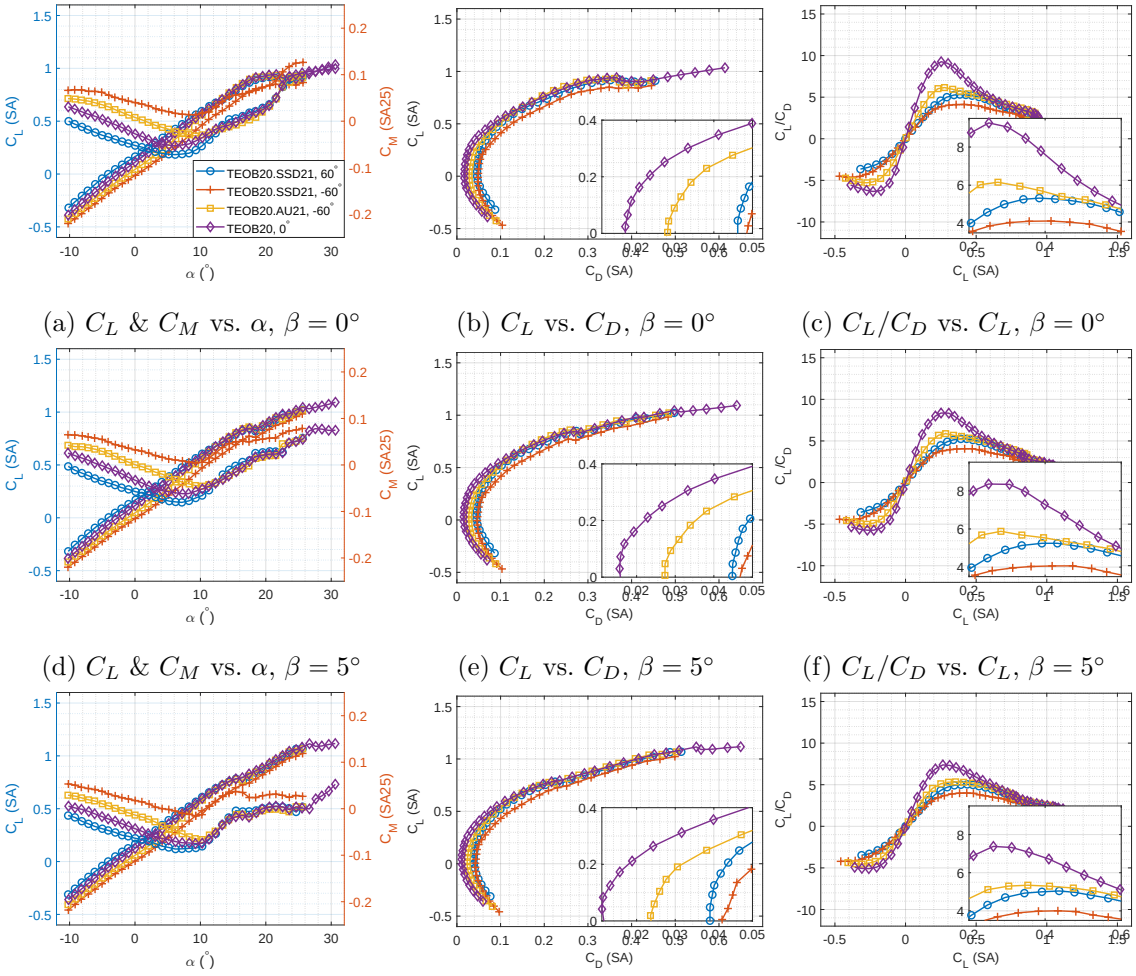


(a) C_L vs. α (b) C_L/C_D vs. C_L (c) C_M vs. C_L

Figure 2.186: Comparison of symmetric exploratory spoiler-slot deflectors with conventional reduced chord ailerons on UW-S-20A for longitudinal forces and moments vs. α at $\beta = 0°$

Symmetric (Both-Side) Roll Control Results This section studies the symmetric deflection of the devices described and shown in Figs. 2.176 to 2.182. All the devices are deployed symmetrically on both sides of the wing. Figures 2.187 and 2.188 show effects of variations of the added symmetric control surfaces, aileron spoiler, spoiler-slot deflectors on the aerodynamic forces and moments of the UW-S-20A model. The longitudinal variations are similar to those of the asymmetric conditions in Figs. 2.183 to 2.185, but differences in yaw and roll moments variations. For the zero sideslip angles of attack, the pitching moment break points are independent of sideslip angles as discussed in §2.7.9 and §2.7.9. The break point varies slightly with deployment of aileron spoilers in Fig. 2.190. The pitching moment break points shown in Fig. 2.190 match the roll moment break point in Fig. 2.191. However, the yawing moment break points happen at much lower angles of attack of $\alpha \approx 0^\circ$ in Fig. 2.191.

The effects of the side slip angle variations are shown in Fig. 2.189 at $\alpha = 10^\circ$. The variations are similar to those of Figs. 2.162 and 2.162 with the exception of the symmetrical deflection, where the values of lift and pitch moment for this configuration have been affected significantly.

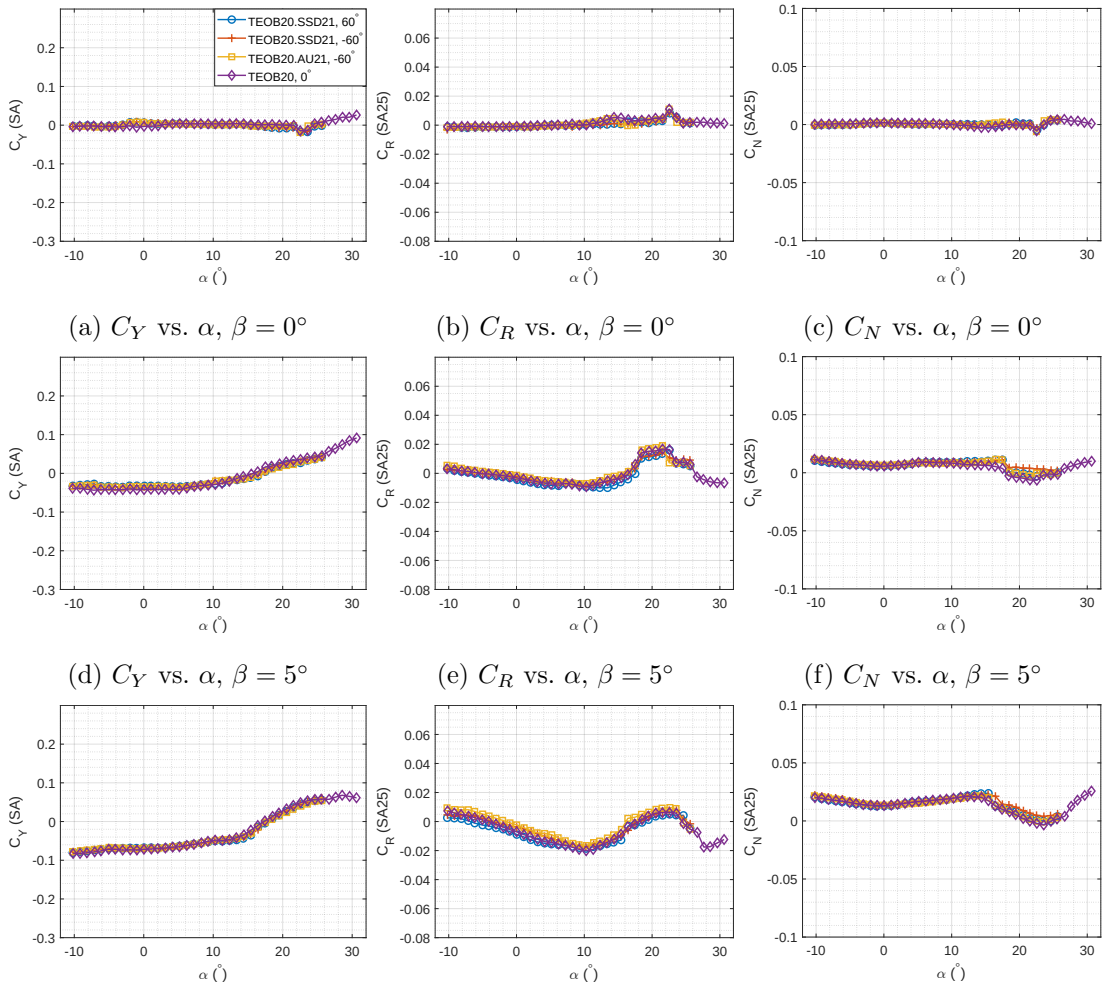


(a) C_L & C_M vs. α, $\beta = 0°$ (b) C_L vs. C_D, $\beta = 0°$ (c) C_L/C_D vs. C_L, $\beta = 0°$

(d) C_L & C_M vs. α, $\beta = 5°$ (e) C_L vs. C_D, $\beta = 5°$ (f) C_L/C_D vs. C_L, $\beta = 5°$

(g) C_L & C_M vs. α, $\beta = 10°$ (h) C_L vs. C_D, $\beta = 10°$ (i) C_L/C_D vs. C_L, $\beta = 10°$

Figure 2.187: Effects of side-slip and SSD/AU deflections on longitudinal forces and moment vs. α for UW-S-20A [26]

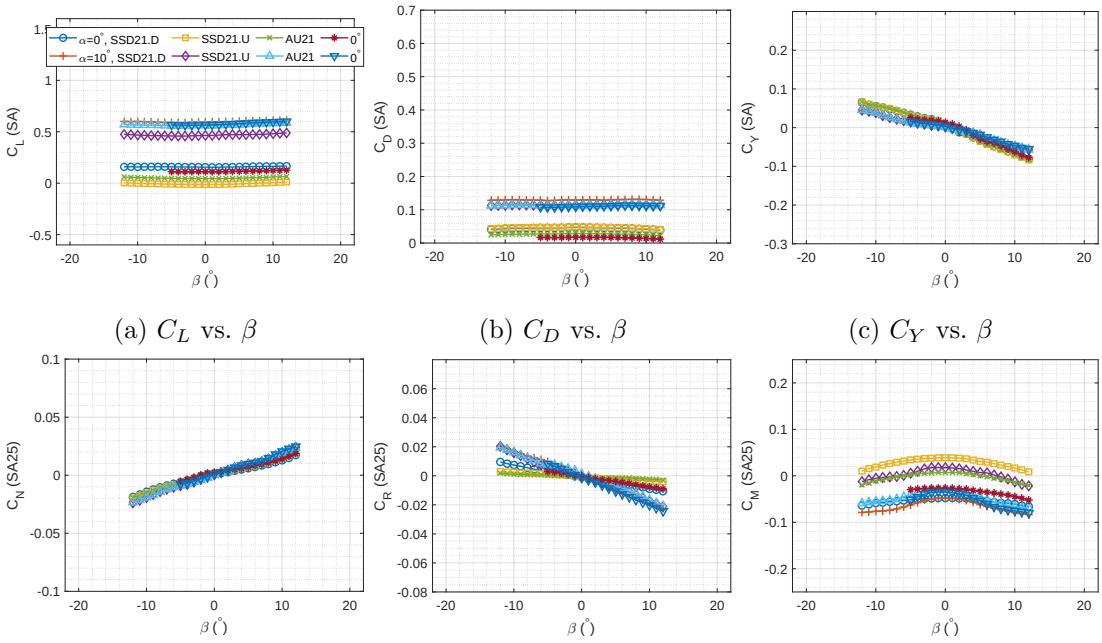


(a) C_Y vs. α, $\beta = 0°$ (b) C_R vs. α, $\beta = 0°$ (c) C_N vs. α, $\beta = 0°$

(d) C_Y vs. α, $\beta = 5°$ (e) C_R vs. α, $\beta = 5°$ (f) C_N vs. α, $\beta = 5°$

(g) C_Y vs. α, $\beta = 10°$ (h) C_R vs. α, $\beta = 10°$ (i) C_N vs. α, $\beta = 10°$

Figure 2.188: Effects of side-slip and SSD/AU deflections on lateral force and moments vs. α for UW-S-20A [26]



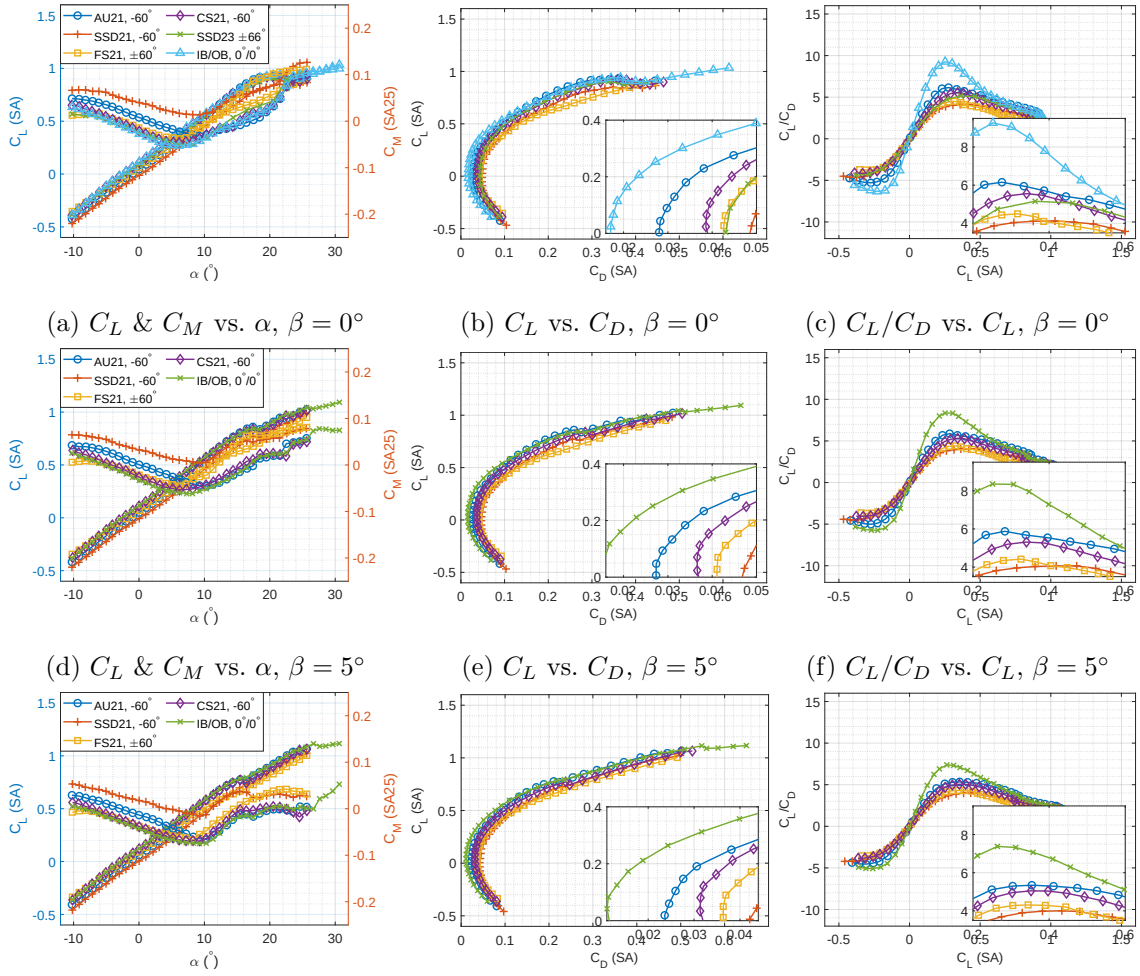
(a) C_L vs. β (b) C_D vs. β (c) C_Y vs. β

(d) C_N vs. β (e) C_R vs. β (f) C_M vs. β

Figure 2.189: Effects of angles of attack and SSD/AU deflections on force and moments vs. β at $\alpha = 0°$ and $10°$ for UW-S-20A [26]

Spoiler/Speed Brakes The results previously published in [26] are re-presented here. All devices are deployed symmetrically. Figures 2.190 and 2.191 show the effects of candidate drag producing devices (used for ground braking, descent path control, and emergency descent) on the aerodynamic forces and moments of the UW-S-20A model. The clam shells have lower drag, higher lift-over-drag ratio, and better pitching moment derivative characteristics. Of interest are the effects of mid-chord spoilers on both longitudinal and lateral forces and moments. The lift curve shows no stall when mid-chord spoilers are installed for the data presented in Fig. 2.190 as well as in the lateral lateral force and moments in Fig. 2.191 at $\alpha \approx 22^\circ$. As mentioned in previous cases for UW-S-20A model, the lateral force and moments behave erratically at $\alpha \approx 22^\circ$ and so are the cases in Figure 2.191 except for the flap spoiler case, where the sharp change is seen to be diminished. Further tests are needed to explore this "erratic" behavior with the associated configuration at this angle of attack, $\alpha \approx 23^\circ$.

As discussed in [25], Figures 2.190 and 2.191 show the forces and moments of the exploratory devices shown in Fig. 2.177, particularly the 2023 SSD deflects both type 1 and type 2 deflections symmetrically in the opposite direction in Fig. 2.177. The 2023 SSD deflection is deflected at $\delta = \pm 66^\circ$ on both left and right wings and compared with the high lift device in [26]. The lift curve indicates a loss of lift at $\alpha \leq -6^\circ$ comparing to the clear configuration, TEOB20 0°. The pitching moments slope changed slightly due to both type 1 and type 2 deflection, and the pitching moment break was extend by a degree. The drag polar suggests a comparable drag increase to the more conventional flap spoilers and is only lower than the 2021 SSD deflected at $\delta = -60^\circ$, but with the highest drag at higher C_L resulting in the lowest LOW at $C_L = 0.4$. The 2023 SSD's drag, lift-over-drag ratio, and pitching moment derivatives are comparable to those of clamshell speed brakes, making it a good candidate for speed brake control devices. Further experimental studies or CFD would be required to validate the results and enrich deflection points in order to finalize the sizing and deflection angles of the SSDs.

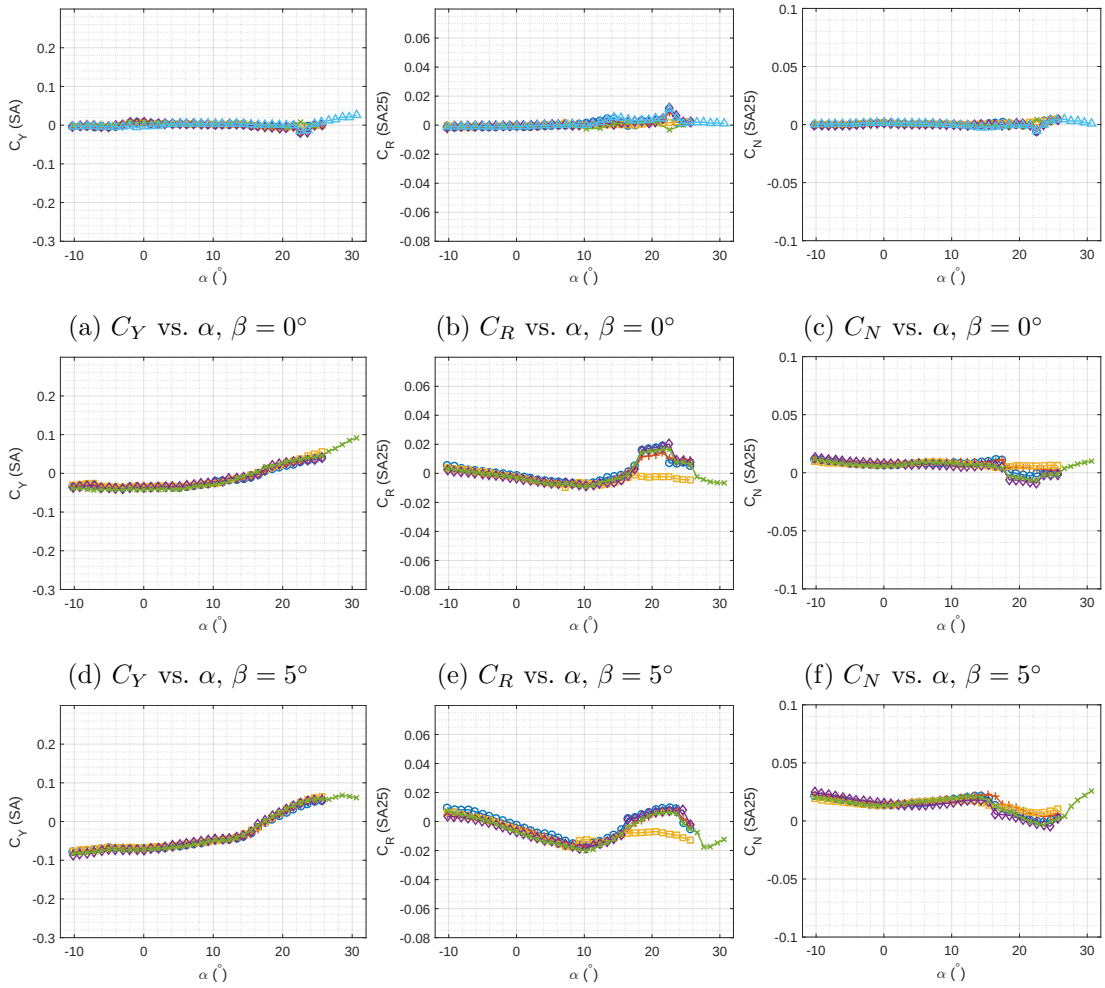


(a) C_L & C_M vs. α, $\beta = 0°$ (b) C_L vs. C_D, $\beta = 0°$ (c) C_L/C_D vs. C_L, $\beta = 0°$

(d) C_L & C_M vs. α, $\beta = 5°$ (e) C_L vs. C_D, $\beta = 5°$ (f) C_L/C_D vs. C_L, $\beta = 5°$

(g) C_L & C_M vs. α, $\beta = 10°$ (h) C_L vs. C_D, $\beta = 10°$ (i) C_L/C_D vs. C_L, $\beta = 10°$

Figure 2.190: Effects of side-slip and symmetric drag-device deflections on longitudinal forces and moment vs. α for UW-S-20A



(a) C_Y vs. α, $\beta = 0°$ (b) C_R vs. α, $\beta = 0°$ (c) C_N vs. α, $\beta = 0°$

(d) C_Y vs. α, $\beta = 5°$ (e) C_R vs. α, $\beta = 5°$ (f) C_N vs. α, $\beta = 5°$

(g) C_Y vs. α, $\beta = 10°$ (h) C_R vs. α, $\beta = 10°$ (i) C_N vs. α, $\beta = 10°$

Figure 2.191: Effects of side-slip and symmetric drag-device deflections on lateral force and moments vs. α for UW-S-20A

Subsonic/transonic cruise configuration and exploratory devices

Figure 2.192 shows the new RSAC model, UW-S-24A, three-surface, area-ruled fuselage, bottom-mounted nacelles, single vertical tail, and low horizontal tails previously shown in §2.7.2 and §2.7.3. The configuration represents the baseline general arrangement with refinements simulating full-scale airliner concept. The alternate cruise configuration deflected baseline outboard leading edges (LEOB15) at $\delta_{LEOB} = +15°$ and reduced-chord outboard trailing edges (TEOB15.R) at $\delta_{TEOB} = +10°$, changing the camber of the outboard wing to shift the LOD curve toward the operating C_L range. This alternate cruise configuration is intended to be representative of improved camber for subsonic/transonic cruise conditions, i.e., subsonic climb, descent, overland cruise, transonic acceleration phase. Two exploratory devices, a nose chine (NC) and a wing fence (WC), were also tested with the alternate cruise configuration in Fig. 2.192 to assess the influence of representative flow-control devices. The nose chines were placed in front and level with canards, NC24.F, and aligned with the wing apex on top of the wing, NC24.B. The wing fences were placed at the wing break between the inboard and outboard wings at half-inch in height from the reduced aileron hinge line and around the leading edge.

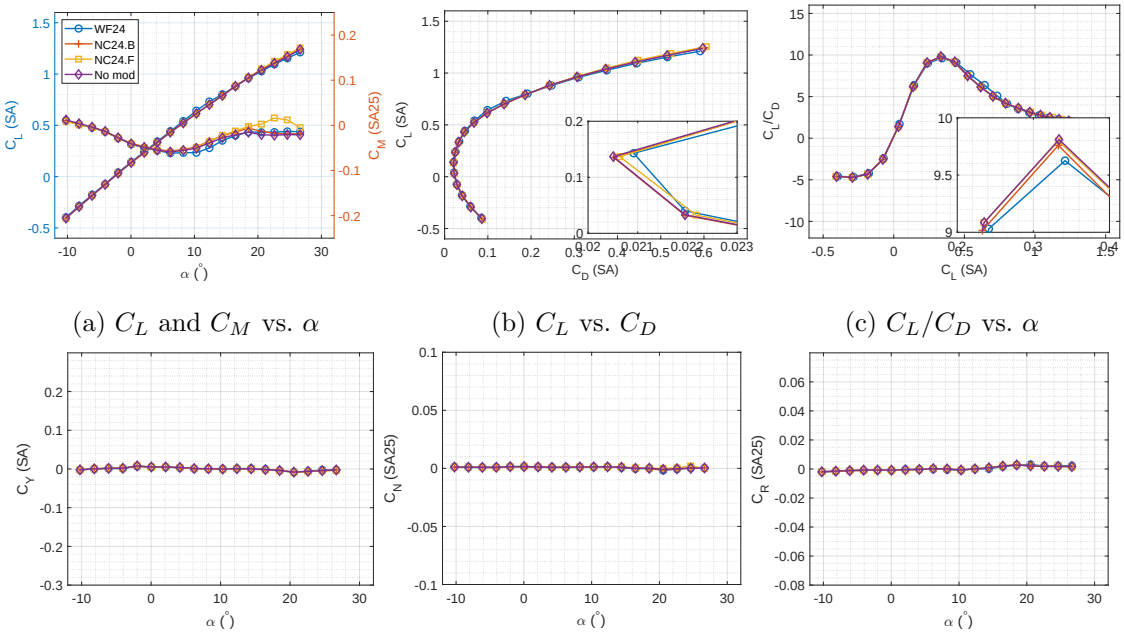


(a) Nose chine – forward (b) Nose chine – body (wing top) (c) Wing fence

Figure 2.192: Exploratory stability modification devices on UW-S-24A [25]

Figure 2.193 shows the forces and moments of the exploratory devices with alternate cruise configuration (for subsonic/transonic operations beyond LTO flight phases). The outboard leading and trailing edges deflections changed the camber of the outboard wing and provided additional lift at $-10° \leq \alpha \leq 14°$. The corresponding drag is increased and

shifted upward in the drag polar and the lift-over-drag ratio curve is shifted toward a C_L range of interest for subsonic operations between 0.3 Mach and transonic climb conditions, LOD is increased at maximum and at the region of $0.3 < C_L < 0.8$. The C_{M_0} was decreased due to the lift multiplied the moment arm behind the CG. The C_{M_α} was increased slightly compared to no deflection (clean) and the pitch up C_{M_α} after pitch break was increased. Note that the data shown represents fully corrected wind tunnel results, but the data is presented at the test Reynolds number such that the full-scale aircraft $\mathrm{L/D_{max}}$ and drag polars would be more favorable at full-scale. The nose chine at both locations had minimal to no effect on lift, drag, and lift-over-drag ratio; however, both locations had impacts on pitching moments, especially the forward nose chine worsen the pitch-up instability at $\alpha \geq 18°$. The wing fence seemed to stop the cross-flow from the inboard wing to the outboard wing and delayed the outboard flow separation by 4° in the lift and pitch moment break point, but the lift at $\alpha \geq 18°$ is reduced. The drag polar shape and lift-over-drag ratio are improved slightly from the alternate cruise condition. The nose chines were designed to improve lateral direction aerodynamics of the asymmetric vortex of the fuselage at higher angles of attack; however, nothing was observed (an indication that the body camber and cross-section modifications incorporated in the area-ruled fuselage were in themselves mitigating high alpha yaw instabilities).



(a) C_L and C_M vs. α (b) C_L vs. C_D (c) C_L/C_D vs. α

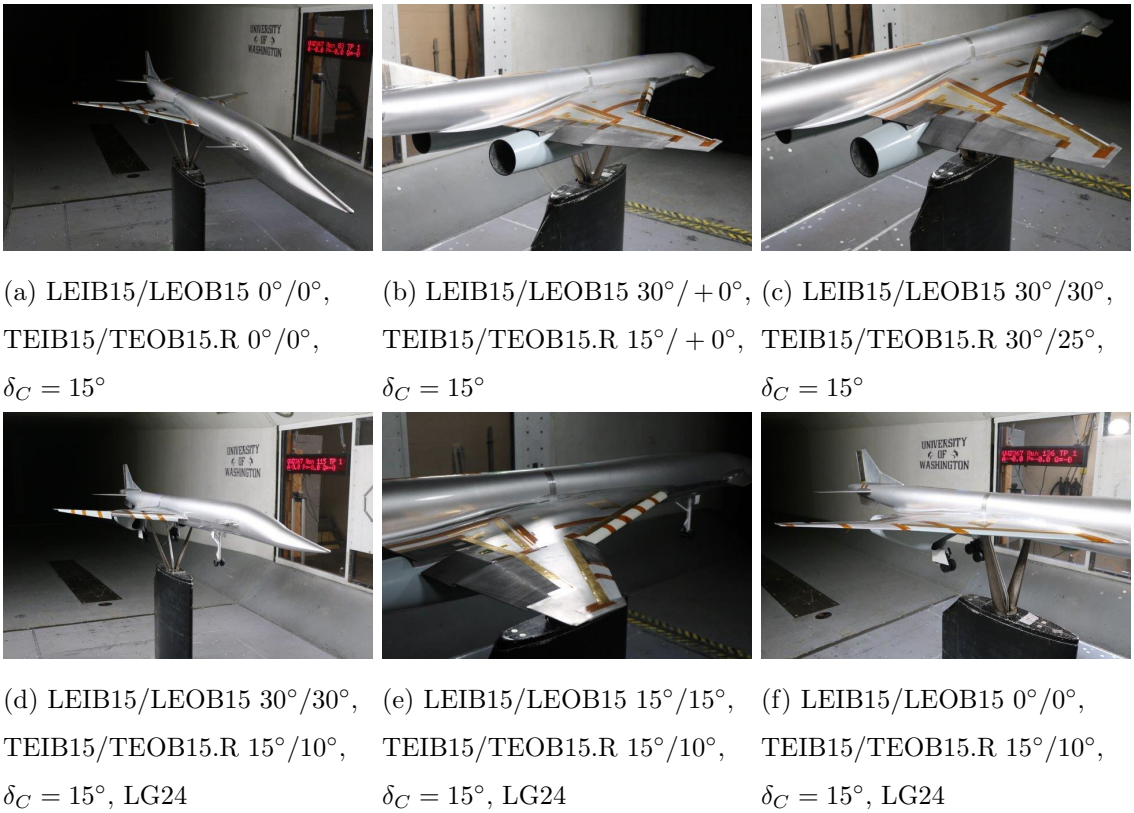
(d) C_Y vs. α (e) C_N vs. α (f) C_R vs. α

Figure 2.193: Comparison of UW-S-24A with candidate stabilizing devices (NC24.F / NC24.B nose chines and WF24 wing fence) for longitudinal force and moments vs. α at $\beta = 0°$

2.7.10 Take-off and Landing Configuration

As mentioned in all previous references [23, 24, 26, 371], the SCALOS project focused on the low-speed characteristics of aircraft configurations and high-lift effectors, particularly the take-off and landing phases of the flight. The nose and main gears with realistic geometry and sizing were paired to the UW-S-24A model to represent the RSAC model at take-off and landing conditions. Figure 2.195 shows the incremental build-up with the presence of landing gear. The take-off and landing employed high lift effectors of canard, leading edges, and flaperons. The 2024 horizontal tail (H24) was manufactured together with the 2024 area-ruled fuselage because of the aft-body loft contouring discussed in §2.7.2 and §2.7.3. Only the zero-degree incidence block was made, and the data in §2.7.5 should be sufficient enough for a linear combination since the difference is only the fuselage, a slight difference tail, and its mounting location. The incremental effect of the tail deflection authority is

still valid. Some results have been presented in [27], but with details on lateral-directional static stability at the TOL condition.



(a) LEIB15/LEOB15 0°/0°, TEIB15/TEOB15.R 0°/0°, $\delta_C = 15°$

(b) LEIB15/LEOB15 30°/+0°, TEIB15/TEOB15.R 15°/+0°, $\delta_C = 15°$

(c) LEIB15/LEOB15 30°/30°, TEIB15/TEOB15.R 30°/25°, $\delta_C = 15°$

(d) LEIB15/LEOB15 30°/30°, TEIB15/TEOB15.R 15°/10°, $\delta_C = 15°$, LG24

(e) LEIB15/LEOB15 15°/15°, TEIB15/TEOB15.R 15°/10°, $\delta_C = 15°$, LG24

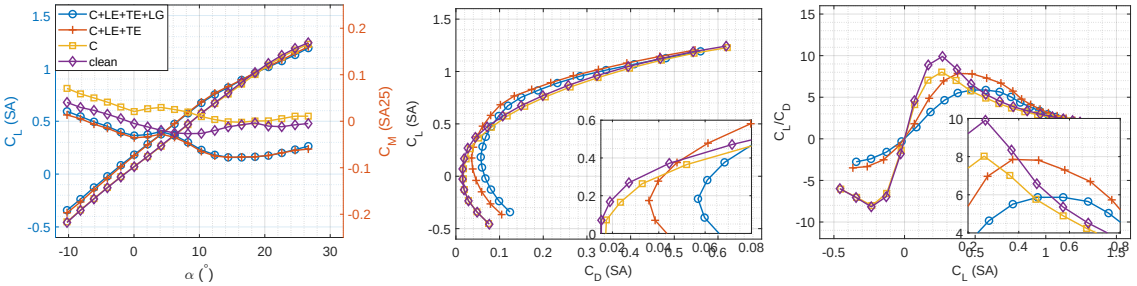
(f) LEIB15/LEOB15 0°/0°, TEIB15/TEOB15.R 15°/10°, $\delta_C = 15°$, LG24

Figure 2.194: Exploratory high-lift configuration at take-off and landing conditions [25]

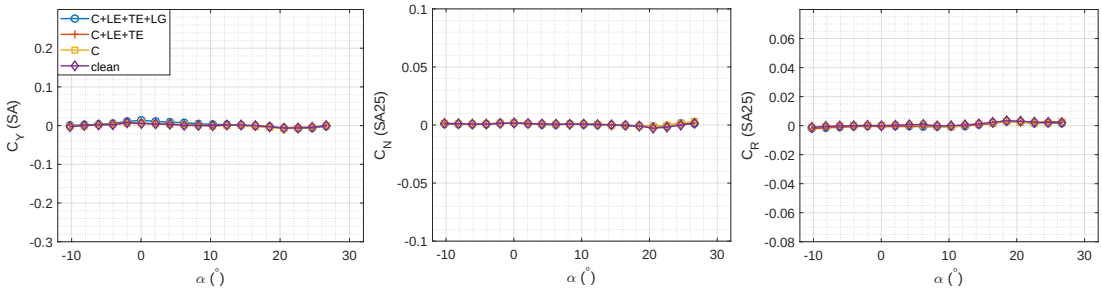
Figure 2.195 shows the longitudinal force and moment aerodynamics incremental changes to the fully deployed canard, leading edges, trailing edges, and landing gear at TOL conditions. The canard rotation has been previously discussed in §2.7.4 [27, 371]. The individual effects of leading edges and trailing edges have been presented in §2.7.8 and §2.7.9 [24, 26, 27, 371].

The canard caused the destabilizing effect, and the combined leading and trailing edge changed the camber of the wing and created pitching down moment. The deployment of the leading and trailing edges also generated additional lift at $\alpha \leq 16°$ and improved the drag polar and LOD at $0.3 < C_L < 1$. The deployment of the landing gear only added drag, roughly 200 counts ($\Delta C_D \approx 0.02$), and shifted drag polar right and LOD down (an indication

of the higher thrust required levels and noise in the gear-down TOL configuration). The TOL configurations show no sign of instability in lateral directional aerodynamics at $\beta = 0°$ in Fig. 2.195. The lateral-directional aerodynamics results are presented in §2.9.



(a) C_L and C_M vs. α (b) C_L vs. C_D (c) C_L/C_D vs. α



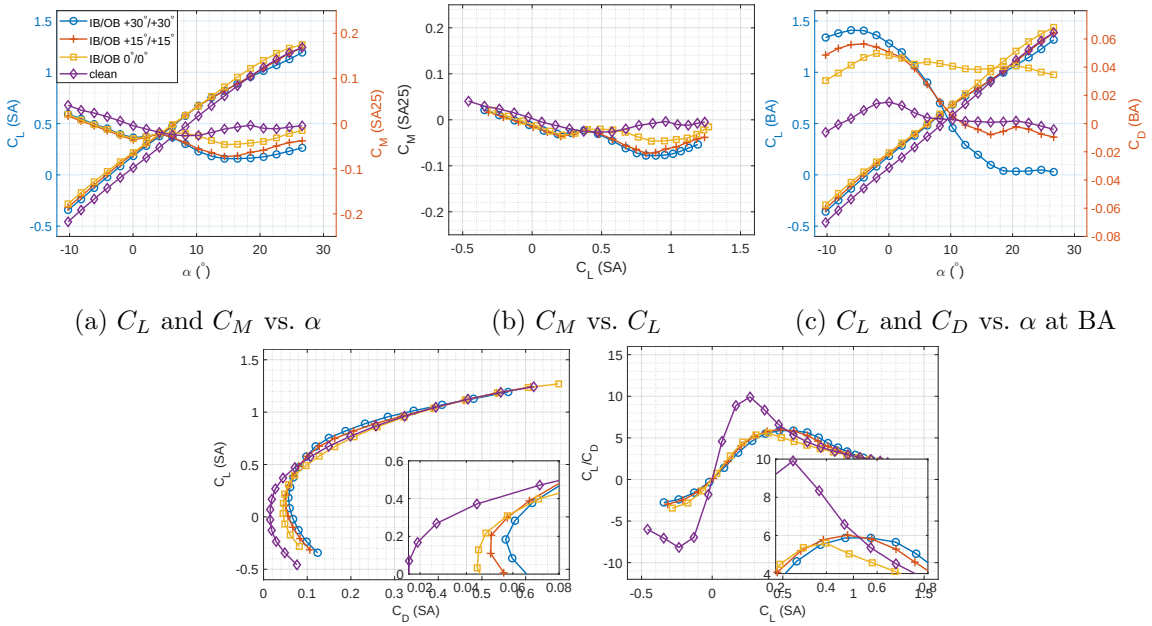
(d) C_Y vs. α (e) C_N vs. α (f) C_R vs. α

Figure 2.195: Comparison of incremental effect of high lift devices deployed for takeoff and landing, $\delta_C = +15°$, LEIB/LEOB $+30°/+30°$, TEIB15/TEOB15.R $+15°/+10°$, and landing gear (LG24), on UW-S-24A for longitudinal forces and moments vs. α at $\beta = 0°$ (untrimmed)

Figures 2.196 and 2.197 show the leading edge and trailing edge effectiveness, respectively, on the longitudinal force and moment at the TOL condition. Figure 2.196 shows the leading edge deflections subject to the same canard, trailing edges, and landing gear setting, while Fig. 2.197 shows the trailing edge deflections subject to the same canard, leading edges, and landing gear setting. The leading edge deflection reduced lift, but improved the pitching moment, drag polar, and LOD as previously presented in §2.7.8 [24, 26, 371]. The drag polar and LOD show that at $C_L \approx 0.4$, the $\delta = +15°$ performed better than $\delta = +30°$ for leading edge deflection. As discussed previously, the SCALOS tests were intended to provide the effects of representative features, and the performance levels shown do not reflect

an optimal leading edge deflection schedule.

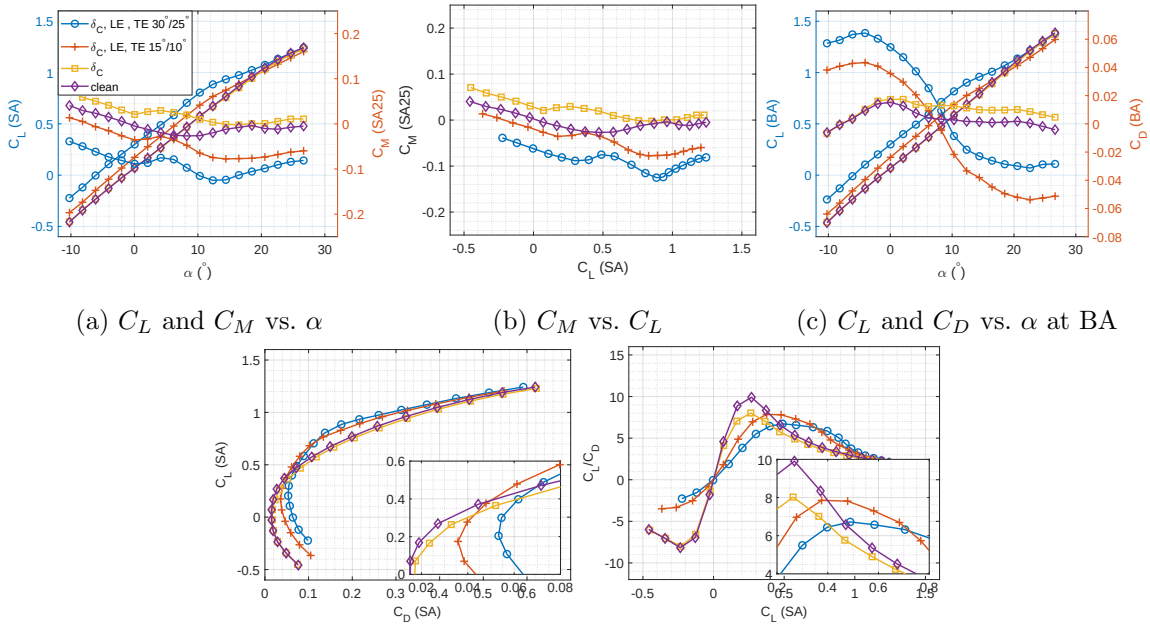
The combined inboard and outboard trailing edge deflection represents the flaperon effect and has been presented in §2.7.8 and §2.7.9 [24, 26, 371]. The trailing edge deflection increased lift, reduced pitching moment, and improved the drag polar and LOD, similar to the leading edge deflection by changing the camber of the wing. The increase in lift is constant at $\alpha \leq 12°$ and diminished beyond likely due to flow separation on the deflected devices. The flaperon has more impact on the drag polar and LOD than the leading edge, where the flaperon deflection continuously improved drag polar and LOD at $0.3 < C_L < 1$. It is also interesting to note that the trailing edge has a constant change on C_D in body axis, while the leading edge has a major impact on the flow and determines the leading edge flow separation and point of leading edge vortex initiation. Additional analysis are needed to present trimmed results and finalize the linked LE and TE for gain schedule and optimal take-off and landing configurations.



(a) C_L and C_M vs. α (b) C_M vs. C_L (c) C_L and C_D vs. α at BA

(d) C_L vs. C_D (e) C_L/C_D vs. α

Figure 2.196: Comparison of leading edge effect at takeoff and landing, $\delta_C = +15°$, TEIB15/TEOB15.R $+15°/+10°$, and landing gear (LG24), on UW-S-24A for longitudinal forces and moments vs. α at $\beta = 0°$ (untrimmed)



(a) C_L and C_M vs. α (b) C_M vs. C_L (c) C_L and C_D vs. α at BA

(d) C_L vs. C_D (e) C_L/C_D vs. α

Figure 2.197: Comparison of flaperon effect at takeoff and landing, $\delta_C = +15°$, LEIB/LEOB $+30°/+30°$, and landing gear (LG24), on UW-S-24A for longitudinal forces and moments vs. α at $\beta = 0°$ (untrimmed)

2.8 Longitudinal Aerodynamics

This section presents the wind tunnel results from the test years 2020-2021 of several selected configurations, focusing on the incremental effects of planform variations and control surfaces on longitudinal aerodynamics. The results identify a few configuration shape parameters that have pronounced effects on the performance and stability characteristics of the SCALOS models at low-speeds [371]. Note that the results presented here are udpated with final wind tunnel corrections described in §2.5.

2.8.1 Wing Planform

The outboard (OB) wing planforms investigated here are shown in Figs. 2.99a and 2.99b. The wing-body-vertical tail model is corresponding to the model in Figure2.198; the three-surface canard-wing-tail with bottom-mounted nacelles and conventional low-tail empen-

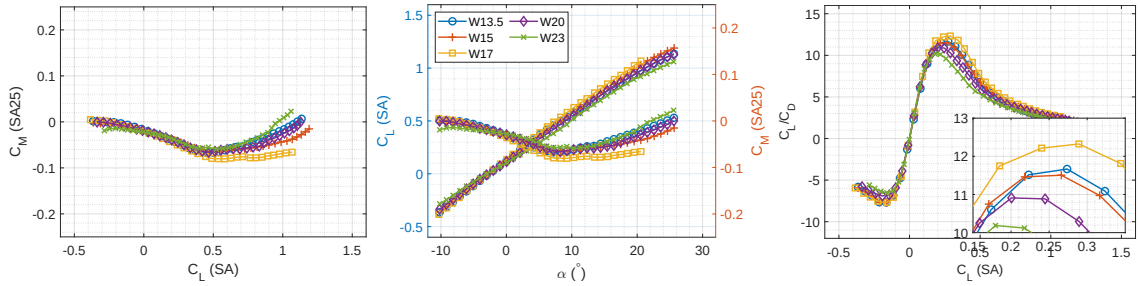
nage system model is corresponding to the model in Fig. 2.202. Three different outboard wing planforms: The 2015 wing, 2017 wing, and 2020 wing are designated W15, W17, and W20, respectively. The overlay of wing planforms is shown in Figure 2.49 and the geometric properties are specified in Table 2.27 in §2.4. The designations and descriptions are tabulated in Table 2.12. 3D images of the various configurations tested are shown in Tabs. 2.8 to 2.18 in §2.2. The simple wing-fuselage-vertical-tail configuration, UW-S-21A without nacelles, canard, and horizontal stabilizer, is detailed in §2.7.1; the complete three-surface configuration including canard, nacelles, and conventional low-tail empennage system is detailed in §2.7.2. Test data with different tail planforms and tail locations at various angles of attacks and sideslip angles was collected.

UW-S-21A without nacelle, canard, and horizontal tail

Figure 2.198 shows the effects of outboard wing planforms on the longitudinal forces and moment at various angles of attack for a simple wing-fuselage-vertical-tail configuration. The effects of outboard wing on the lift curve slope are illustrated in Fig. 2.198b. The W17 outboard wing has the largest semi-span, $b/2 = 2.75$ ft, and the lowest sweep angle, $\Lambda = 38^\circ$, from Table 2.27. This outboard wing geometry leads to the largest static margin (dC_M/dC_L), lift curve slope (C_{L_α}), pitching moment α derivative (C_{M_α}) and lift-over-drag ratio (C_M/C_L) in Figures 2.198a, 2.198b, and 2.198c, respectively. Note that as the wing sweep angle increases, its low-speed lift decreases. However, the stall angle increases. The more slender wings in our case have lower C_{L_α}. The pitching moment break points (where pitch moment α derivatives change signs) for the W17 and W20 outer wings occur almost at the same lift, but W17 has an abrupt slope change behavior at $C_L \approx 0.7$ or $\alpha \approx 12^\circ$ where the pitch moment derivatives changes from unstable to stable condition and then becomes unstable again at $C_L \approx 0.8$ or $\alpha \approx 14^\circ$. See Figures 2.198a and 2.198b.

Figure 2.198b shows that the W17 outboard wing has the highest angle of attack at zero pitching moment ($C_M = 0$) and the largest pitching moment derivatives. The W20 outboard wing has a smaller semi-span and wing area, than the W15 outboard wing but the pitching moment derivatives are the same with a slightly higher angle of attack at zero

pitching moment. The test results presented here suggest that the W17 outboard wing has the best low-speed aerodynamic characteristics including lift performance, static margin, and lift over drag than the other two outboard wing planforms. This is not surprising because of its lower LE sweep and higher aspect ratio.

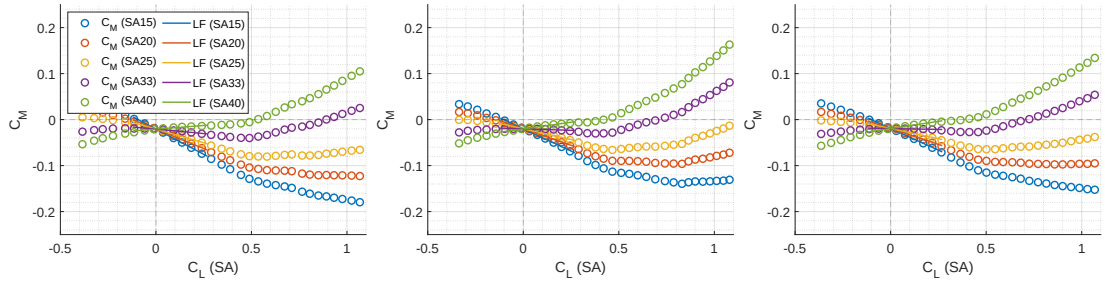


(a) C_M vs. C_L (b) C_L and C_M vs. α (c) C_L/C_D vs. C_L

Figure 2.198: Effects of wing planforms on longitudinal forces and moments vs. α for UW-S-21A without nacelle, canard, and horizontal tail

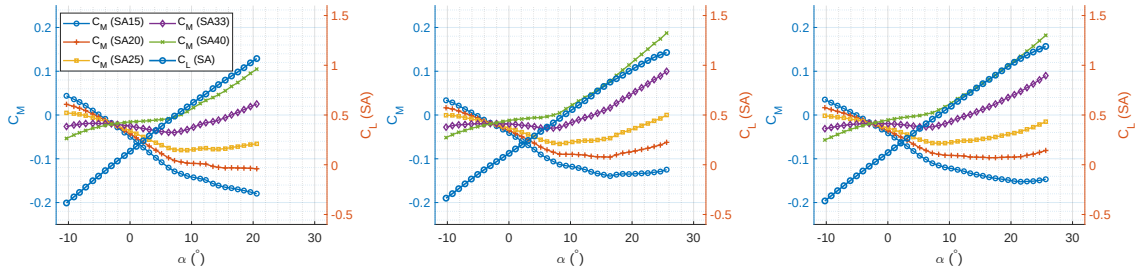
Figure 2.199 shows the effects of CG locations on the C_M vs. C_L curve for the three different outboard wing planforms. The acronym LF stands for linear fit of the data. The static margin and zero pitching moment vary with respect to CG locations, of course. As the CG moves backward along the MAC, both the angle of attack for zero pitching moment and the static margin are reduced. All of the outboard wings studied here with the simple wing-fuselage-vertical-tail configuration remain stable for a wide range of CG locations (CG $< 35\%$). They are not trimmable ($C_{M_0} < 0$) for positive angle of attack for all CG locations in Fig. 2.199. Note that the wings have no twists. It should be noted that the SCALOS effort was focused on characteristics heavily dependent on planform and leading edge shape rather than wing twist optimization. Supersonic optimization, beyond the scope of the SCALOS effort, would result in varying degrees of wash-out depending on the planform and design Mach/CL point, but all would generally shift the C_{M_0} to positive values for the clean wing. The collected data for the three outboard wing planforms are fitted with linear regression and compared in Fig. 2.200. The pitching moments are fitted linearly at $-5^\circ \leq \alpha \leq 5^\circ$ and $8^\circ \leq \alpha \leq 20^\circ$. The linear regression captured the pitch moment characteristic except for the case of the W20 outboard planform which has the

largest sweep angle of $\Lambda = 63.5°$. Differences can be seen at $8° \leq \alpha \leq 20°$ in Figure 2.200. The essential nonlinearity of the data for this wing at higher angles of attack is not surprising, given its higher sweep angle.



(a) 2017 OB wing, W17 (b) 2020 OB wing, W20 (c) 2015 OB wing, W15

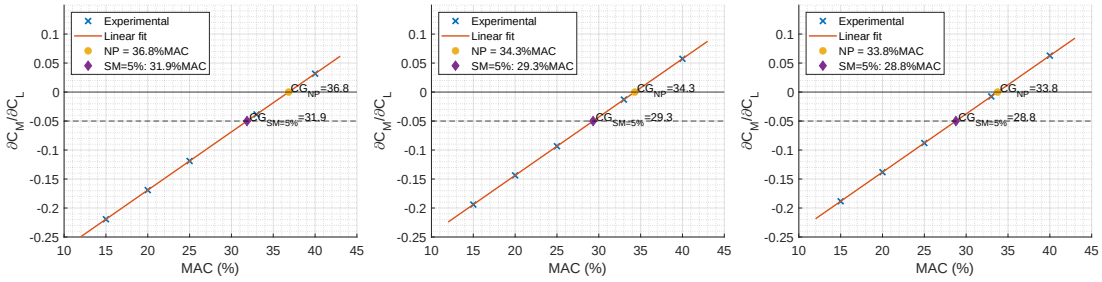
Figure 2.199: Effects of wing planforms on pitching moments vs. lift with different CG locations for UW-S-21A without nacelle, canard, and horizontal tail



(a) C_M vs. α, W17 (b) C_M vs. α, W20 (c) C_M vs. α, W15

Figure 2.200: Effects of wing planforms on pitching moments vs. α with different CG locations and linear fits for UW-S-21A without nacelle, canard, and horizontal tail

The static margin variations, dC_M/dC_L vs. the location of the CG along the MAC, are computed from the low angle of attack (low lift coefficient) linear fit in Figure 2.199 and are plotted in Fig. 2.201. The results show the higher static stability of the W17 outboard wing compared to the other two wings.



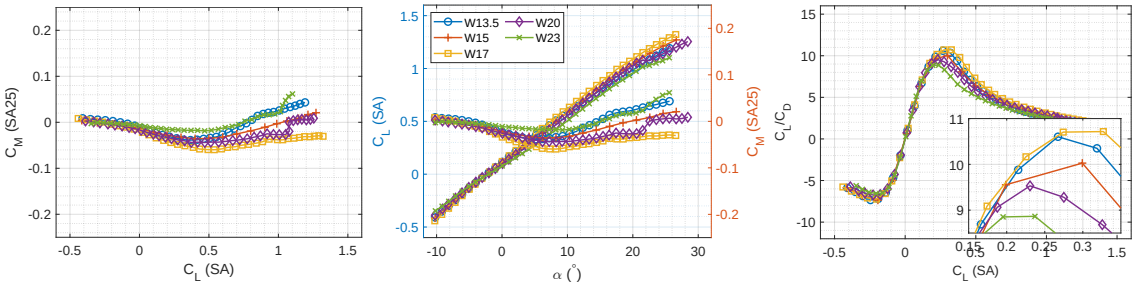
(a) 2017 OB wing, W17 (b) 2020 OB wing, W20 (c) 2015 OB wing, W15

Figure 2.201: Effects of wing planforms on static margins and neutral points at the lower range of angles of attack for UW-S-21A without nacelle, canard, and horizontal tail

Conventional Three-Surface Configuration - Low Mounted Nacelle and Conventional Empennage System

Figure 2.202 shows the effects of the outboard wing planform on the longitudinal forces and moment with respect to various angles of attack (at zero sideslip angle) for the complete three-surface configuration. The effects are similar to the case of the wing-fuselage-vertical-tail configuration discussed in the previous section §2.8.1. There are difference, however, when comparing wing-fuselage-vertical tail configuration to the complete configuration in Figures 2.198 and 2.202. As expected, the complete model produces more lift as function of angle of attack comparing to the no-canard-and-tail model. The additional lift, generated by the canard and horizontal tail, multiplied by the moment arms, results in additional pitching moments. To be clear: the emphasis here is on variations of forces and moment with angle of attack. The contributions of the canard and tail can be positive or negative depending on their own angles of attack. From static stability perspective the pitching moment break points of all outboard wing planforms for the complete model are the same at $\alpha \approx 6°$, Figure 2.202b, and are lower comparing with the simple wing-fuselage-vertical-tail model, Fig. 2.198b. Moreover, the static margin, pitching moment derivatives, and zero pitching moment of the different outboard wing planforms for the complete model become more distinct in comparison, for example, W15 and W20.

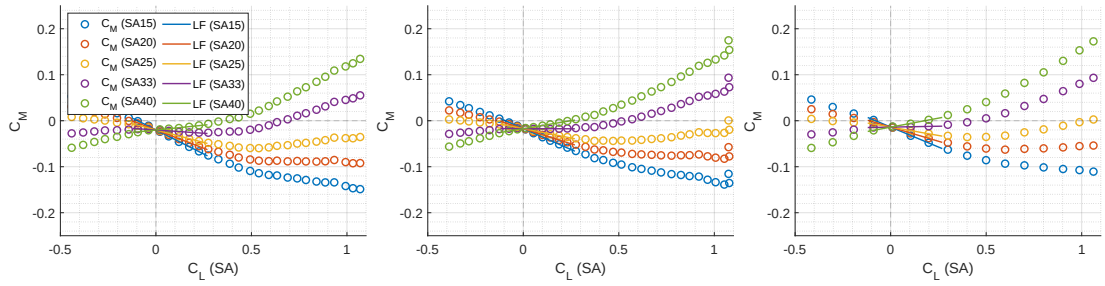
Figure 2.203 shows the effect of CG locations on the C_M vs. C_L curves for the three outboard wing planforms on the complete model (with canard, h.tail, and nacelles). The



(a) C_M vs. C_L (b) C_L and C_M vs. α (c) C_L/C_D vs. C_L

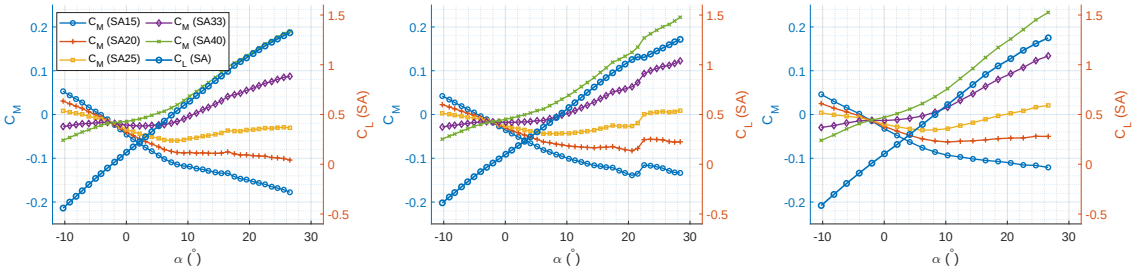
Figure 2.202: Effects of wing planforms on longitudinal forces and moments vs. α for conventional three-surface configuration

static margin variations are computed from Figure 2.203 and plotted in Figure 2.205. The three-surface model shares similar characteristics with the fuselage-wing-vertical tail model, but there is a shift in values. The neutral point for the complete model is located at a lower MAC location of the CG, as shown in Figure 2.205. The differences in the neutral points between the wing-fuselage-vertical tail and the three-surface models with W17 outboard wings are about $\approx$ 1% in MAC, while the same differences between the wing-fuselage-vertical tail and the three-surface models with W20 and W15 outboard wings are about $\approx$ 1.5% and $\approx$ 3% of in MAC, respectively. These differences are caused by additions of the canard, nacelle, and horizontal stabilizer in lift and moments.



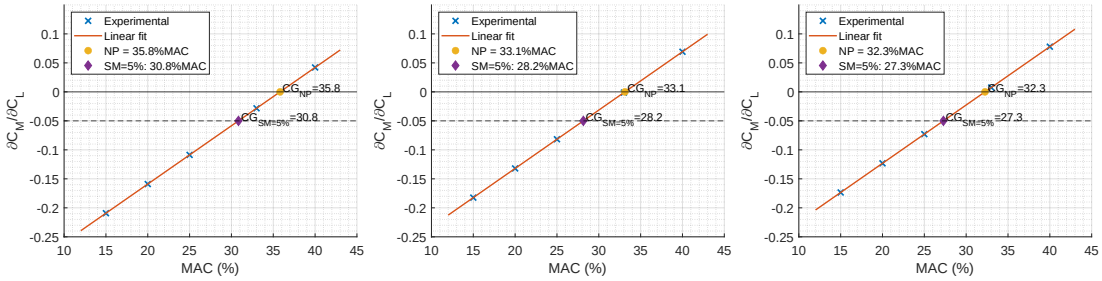
(a) UW-S-17A, W17 (b) UW-S-20F, W20 (c) UW-S-21A, W15

Figure 2.203: Effects of wing planforms on pitching moments vs. lift with different CG locations for conventional three-surface configuration



(a) C_M vs. α, W17 (b) C_M vs. α, W20 (c) C_M vs. α, W15

Figure 2.204: Effects of wing planforms on pitching moments vs. α with different CG locations and linear fits for conventional three-surface configuration



(a) UW-S-17A, W17 (b) UW-S-20F, W20 (c) UW-S-21A, W15

Figure 2.205: Effects of wing planforms on static margins and neutral points for conventional three-surface configuration

2.8.2 Detailed Longitudinal Database For Tail Deflections

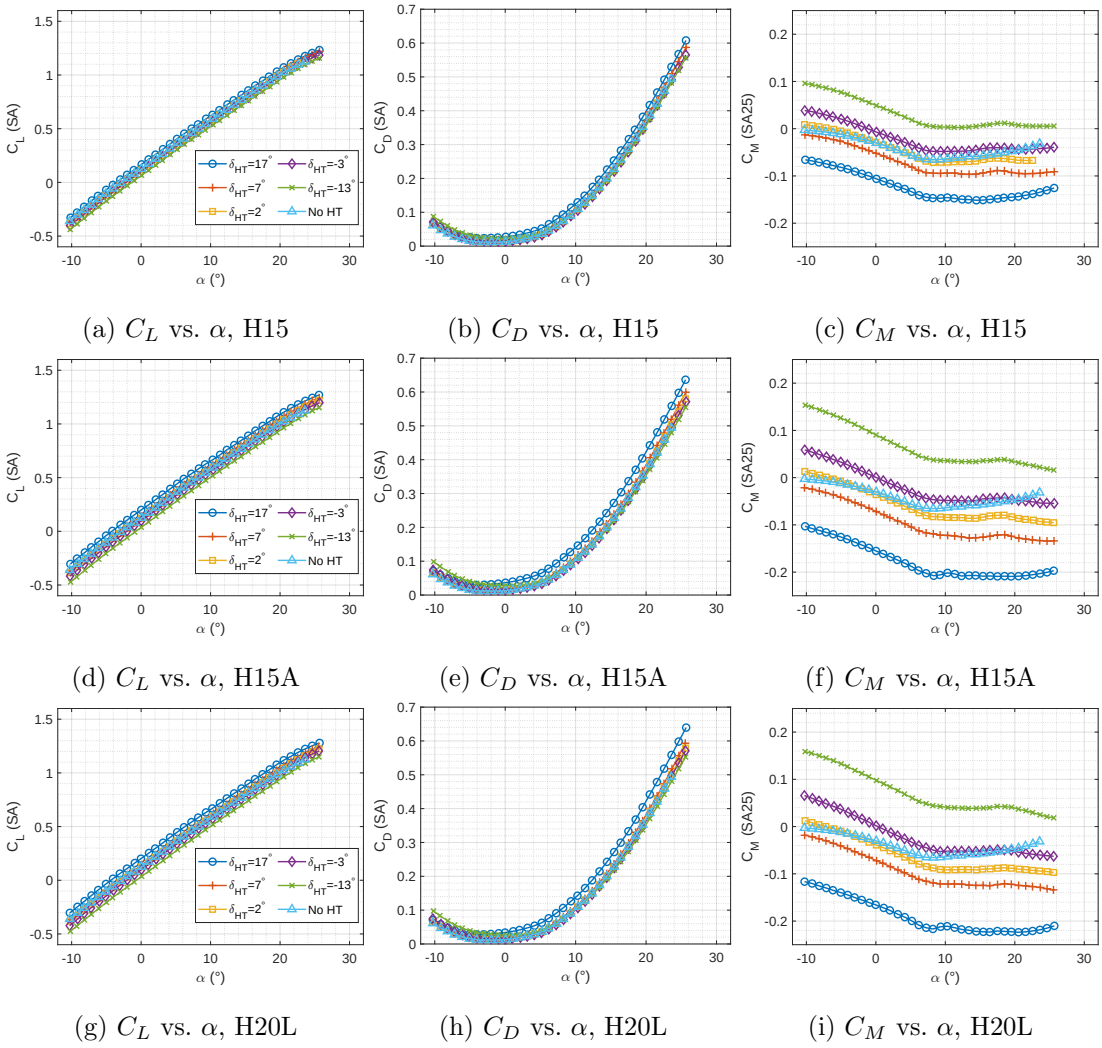
Different horizontal tail planforms and tail locations are shown in Figs. 2.125 and 2.121 of §2.7.5. Three different horizontal stabilizers - the 2015 horizontal tail, 2015 RUAV horizontal tail, and the 2020 horizontal tail - are designated H15, H15A, and H20, respectively. The tails could be attached in three different ways: conventional, mid tail, and T-tail. The naming convention for the tail locations of conventional (low), mid tail, and T-tail uses L, M, and T, respectively, followed by the tail designation. The overlay of wing planforms is shown in Fig. 2.49 and the geometric properties are specified in Table 2.27. The designations and descriptions are tabulated in Tab. 2.32. 3D images of the various configurations tested are shown in Tab. 2.12 at the beginning of §2.2. Test results with different tail planforms and tail locations at various angles of attack and side slip angles were acquired. This section,

however, presents the data at zero sideslip angles only. The horizontal stabilizer in all cases is an all-moving control surface and its rotation angles are $\delta_{HT} = 0°, \pm 10°, \pm 15°$.

UW-S-21A Without Nacelle and Canard: Tail Planform Differences

The effects of horizontal stabilizer planforms and rotations on the longitudinal forces and moment with respect to angles of attack for the UW-S-21A without nacelle and canard are shown in Figure 2.206. The configuration is the same as in Figure 2.202 but with horizontal tail planform variations and without nacelle and canard. Figure 2.206 shows no significant trend variations in both lift and drag among different horizontal tail planforms except the difference in magnitude. The differences in lift and drag are proportional to tail rotation. The difference in magnitude of lift and drag are, not surprisingly, proportional to the tail area. The lift generated by the horizontal stabilizers, multiplying by a moment arm results in overall moment variations with some contribution from the drag term. The pitching moment break point in the cases presented here is independent of the size of the horizontal stabilizer and its rotations and the pitching moment variations for the zero-degree deflection angle are the almost same for all three planforms in Fig. 2.206.

Figure 2.207 shows the reduction in static margin of C_M vs. C_L curve as the CG location moves backwards along the MAC. The static margin is almost zero at CG $\approx$ 37% and becomes positive, unstable condition, at CG $\geq$ 37% for all three planforms. Figure 2.207 further shows that the configuration cannot be trimmed at $C_L > 0$ for all tails (at least with the model's flat, untwisted wing). The static margin, dC_M/dC_L, is constant at $0 \leq C_L \leq 0.4$ and change in value, constant, at $0.4 \leq C_L \leq 0.9$ for all tails and for all CG locations; however, the values of the static margin change as the CG are changed and become positive for a few CG locations in Fig. 2.207. The static margin, for all CG locations in Fig. 2.207, variations are computed from Fig. 2.207 and plotted in Fig. 2.208. The static margin and neutral point location on the on MAC are proportional to horizontal tail area, as shown in Figs. 2.208a and 2.208b, and proportional to the aspect ratio of the horizontal tail in Figs. 2.208b and 2.208c. Note that the difference between configurations presented in this section and §2.8.1 are the canard and nacelles. The static margin and neutral points are reduced



(a) C_L vs. α, H15 (b) C_D vs. α, H15 (c) C_M vs. α, H15

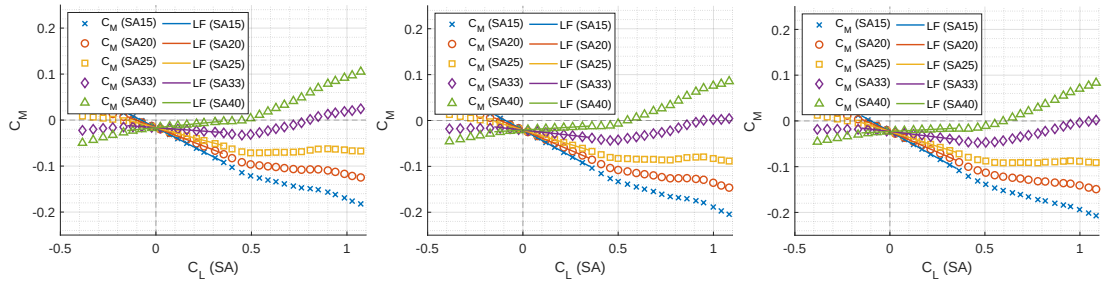
(d) C_L vs. α, H15A (e) C_D vs. α, H15A (f) C_M vs. α, H15A

(g) C_L vs. α, H20L (h) C_D vs. α, H20L (i) C_M vs. α, H20L

Figure 2.206: Effects of different horizontal stabilizers and their rotations on the longitudinal forces and moment vs. α for UW-S-21A without nacelle and canard at $\bar{c} = 25\%$

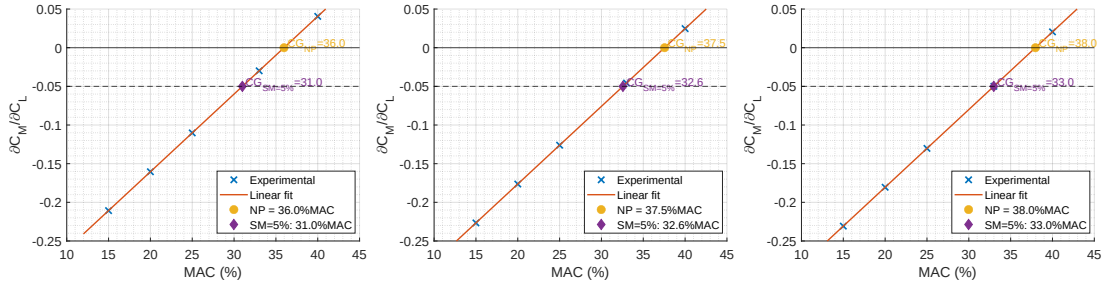
significantly in Figure 2.205c compared to Figure 2.208c. The additional pitch moment due to the angle of attack (canard lift multiplying the moment arm to the CG) destabilizes the configuration such that the operating CG would need to be farther forward to retain the equivalent static stability of the canard-off case.

To better clarify the effects of horizontal stabilizer profile and angle of attack on the longitudinal forces and moment, their incremental effects on the lift, drag and pitching moment, ΔC_L, ΔC_D, and ΔC_L vs. α, are shown in Figs. 2.209 and 2.210 for the cases of



(a) H15 (b) H15A (c) H20L

Figure 2.207: Effects of different horizontal stabilizers and rotations on pitching moments vs. lift with different CG locations for UW-S-15A without nacelle and canard



(a) H15 (b) H15A (c) H20L

Figure 2.208: Effects of different horizontal stabilizers and their rotations on static margins and neutral points for UW-S-15A without nacelle and canard

zero horizontal tail rotation, $\delta_{\text{HT}} = 0°$. The incremental values in lift (ΔC_L), drag (ΔC_D), and pitching moment (ΔC_M) adds insights regarding the effects of the horizontal stabilizer on the longitudinal forces and moment with respect to angle of attack as shown in Figures 2.209 and 2.210. The increments with respect to zero-degree tail rotation, $\delta_{\text{HT}=0°}$, are defined as

$$\Delta C_L = C_{L_{\delta_{\text{HT}\neq 0°}}} - C_{L_{\delta_{\text{HT}=0°}}}, \quad \Delta C_D = C_{D_{\delta_{\text{HT}\neq 0°}}} - C_{D_{\delta_{\text{HT}=0°}}}, \quad \Delta C_M = C_{M_{\delta_{\text{HT}\neq 0°}}} - C_{M_{\delta_{\text{HT}=0°}}}, \tag{2.20}$$

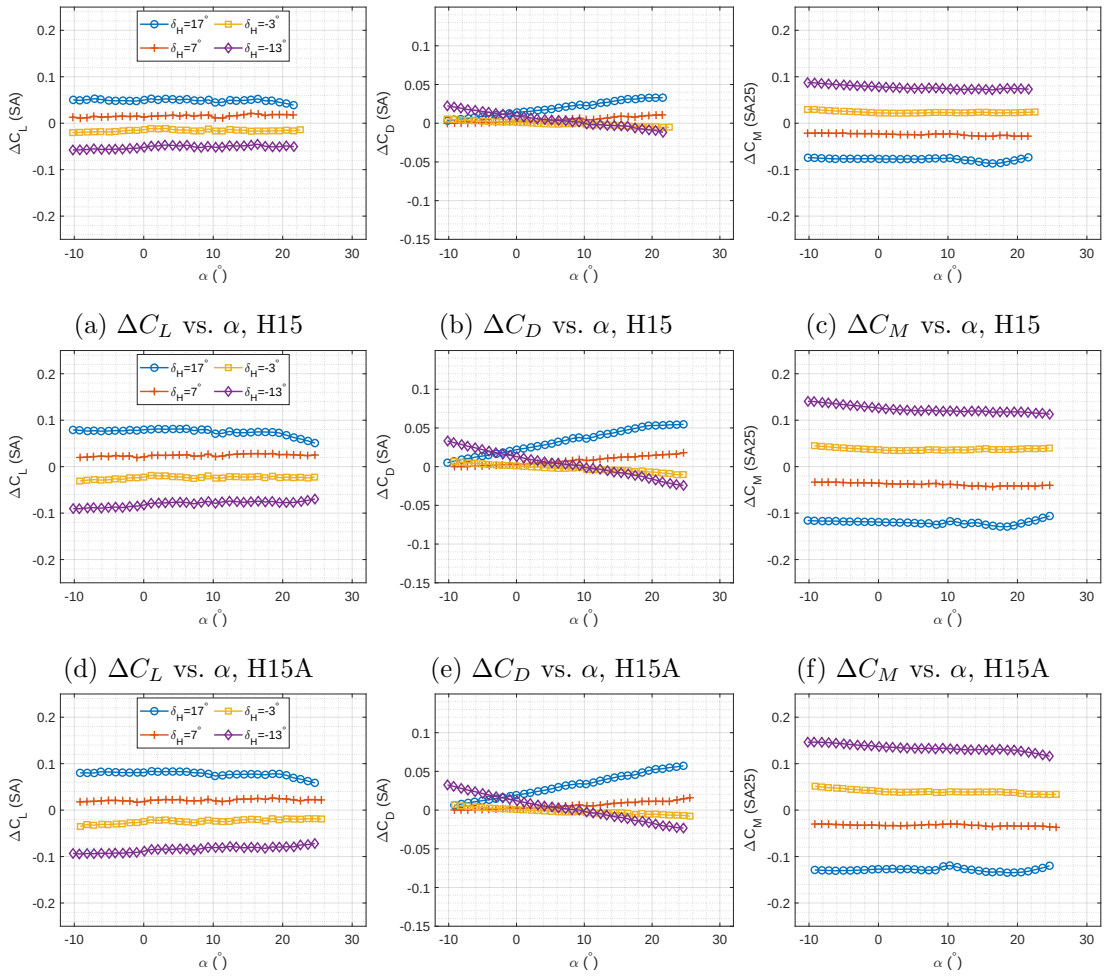
and shown in Fig. 2.209; and the increments with respect to the no the horizontal stabilizer

configuration are defined as

$$\Delta C_L = C_{L_{\delta_{\text{HT}\neq 0^\circ}}} - C_{L_{\text{No HT}}}, \quad \Delta C_D = C_{D_{\delta_{\text{HT}\neq 0^\circ}}} - C_{D_{\text{No HT}}}, \quad \Delta C_M = C_{M_{\delta_{\text{HT}\neq 0^\circ}}} - C_{M_{\text{No HT}}}, \tag{2.21}$$

and shown in Fig. 2.210. The non-dimensional forces and moment for incremental differences are all normalized by the same dimensional variables, i.e., dynamic pressure, wing reference area (W15), and MAC. Figure 2.210 indicates that as the horizontal tail angles increase the magnitudes of ΔC_L and ΔC_M increase, but their variations with angles of attack are constant. That is, no α variation. Figure 2.209 shows that the rotation angle is proportional to magnitudes of ΔC_L and ΔC_M and the variations with angles of attack are constant with respect to $\delta_{\text{HT}=0^\circ}$. On the other hand, ΔC_D has linear relationship, not constant, with angles of attack and same sign of derivatives as the sign of rotation angle, δ_{HT}. Similar variations are observed in Figure 2.210 for the increments with respect to no horizontal tail configuration in Eq. (2.21). The ΔC_L and ΔC_M have positive and negative linear relationship, respectively, at $-10^\circ \leq \alpha \leq -7^\circ$, almost zero derivatives at $\alpha \approx 9^\circ$, and new derivatives value at $10^\circ \leq \alpha \leq 19^\circ$ for all deflection angles and for all three tail planforms with respect to the no tail configuration. Outboard wing flow separations and inboard wing vortex formation (with their downwash effect on the tail affect this behavior).

Figure 2.211 shows the trimmed and untrimmed drag polars, and lift-over-drag curves, as well as trimmed tail rotations as functions of lift at different CG locations for the three tail planforms. For each horizontal tail planform the tail is rotated at $-10^\circ \leq \delta_{\text{HT}} \leq 10^\circ$ with $-10^\circ \leq \alpha \leq 25^\circ$. The CG location is selected at $25\%\bar{c}$, $dC_M/dC_L \approx -10\%$, from Fig. 2.208 where the trimmed lift and drag are obtained from the corresponding zero pitching moment for drag polar and lift over drag. Figure 2.211 shows that the smallest horizontal tail, H15, has slightly larger drag penalty and lower lift-over-drag values than the other two tail planforms. For a constant drag, the trimmed lifts are less than the untrimmed ones and the differences between trimmed and not-trimmmed increase proportional to the angle of attack. However, trimmed lift-over-drag values at $-0.1 \leq C_L \leq 0.1$ remain the same as untrimmed ones for all tail planforms. Furthermore, Figure 2.211 shows the horizontal tail rotation effectiveness, δ_{HT}, vs. C_L at trim conditions for various CG locations. All three



(a) ΔC_L vs. α, H15 (b) ΔC_D vs. α, H15 (c) ΔC_M vs. α, H15

(d) ΔC_L vs. α, H15A (e) ΔC_D vs. α, H15A (f) ΔC_M vs. α, H15A

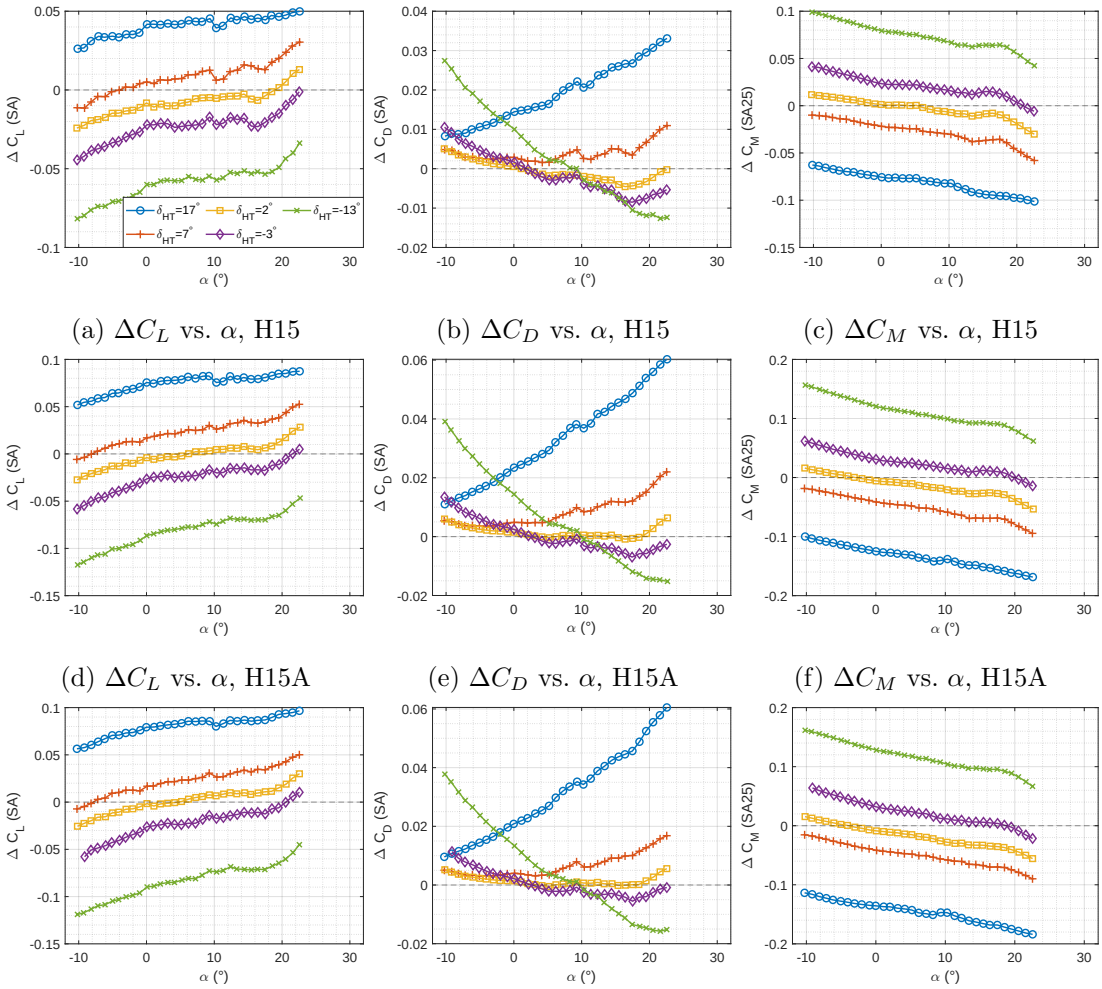
(g) ΔC_L vs. α, H20L (h) ΔC_D vs. α, H20L (i) ΔC_M vs. α, H20L

Figure 2.209: Incremental effects of different horizontal stabilizers and rotations on the longitudinal forces and moment vs. α for UW-S-21A without nacelle and canard with respect to $\delta_{\text{HT}} = 0°$

horizontal stabilizers are trimmable at CG $= 15\% - 33\%\bar{c}$ for $-0.4 \leq C_L \leq 0.4$.

The incremental difference due to the horizontal stabilizer lift with respect to the no tail configuration at $\alpha = 0°$ is in Eq. (2.21) and is nondimensionalized by the wing reference area in Fig. 2.212a. The horizontal tail lift, nondimensionalized by the area of the tail planfrom, is defined as

$$C_{L_{\text{tail}}} = \Delta C_L \frac{S_{\text{wing}}}{S_{\text{tail}}} \tag{2.22}$$



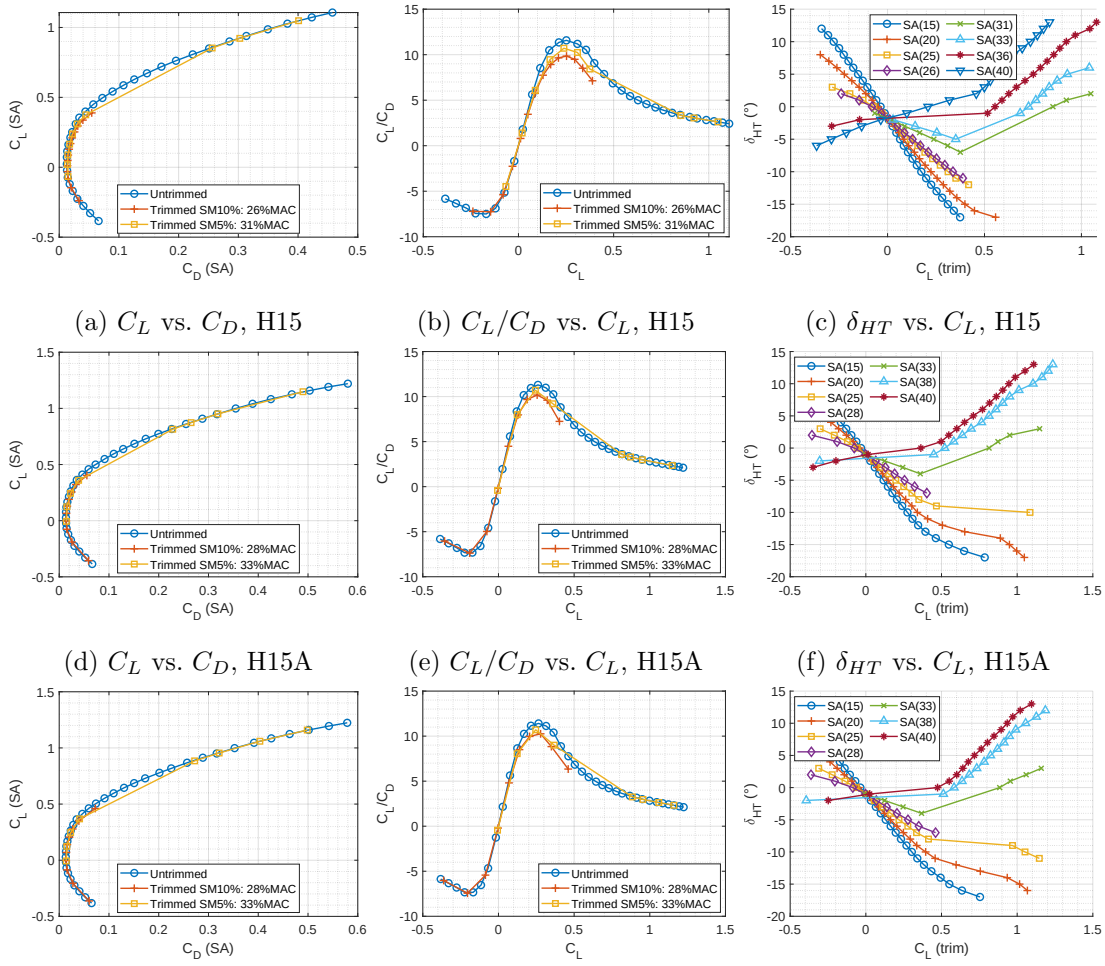
(a) ΔC_L vs. α, H15 (b) ΔC_D vs. α, H15 (c) ΔC_M vs. α, H15

(d) ΔC_L vs. α, H15A (e) ΔC_D vs. α, H15A (f) ΔC_M vs. α, H15A

(g) ΔC_L vs. α, H20L (h) ΔC_D vs. α, H20L (i) ΔC_M vs. α, H20L

Figure 2.210: Incremental effects of different horizontal stabilizers and rotations on the longitudinal forces and moment vs. α for UW-S-15A without nacelle and canard with respect to horizontal stabilizer off configuration

and the lift curves with respect to tail rotations are shown in Fig. 2.212b. The difference between H15 and others are due to the planform areas and the differences between H15A and H20L are minimal. Note that the incremental difference at $\alpha = 0°$ in Figs. 2.212a and 2.212b are essentially the lift curves normalized by the wing reference area and tail planform area, respectively. Thus, the incremental drag polar and lift over drag in Figures 2.212c and 2.212d are the horizontal tails drag polar and lift over drag normalized by the wing reference



(a) C_L vs. C_D, H15 (b) C_L/C_D vs. C_L, H15 (c) δ_{HT} vs. C_L, H15

(d) C_L vs. C_D, H15A (e) C_L/C_D vs. C_L, H15A (f) δ_{HT} vs. C_L, H15A

(g) C_L vs. C_D, H20L (h) C_L/C_D vs. C_L, H20L (i) δ_{HT} vs. C_L, H20L

Figure 2.211: Effects of different horizontal stabilizers and deflections on trimmed and untrimmed drag polar, lift-over-drag ratio, and tail deflection effectiveness on trimmed lift for UW-S-15A without nacelle and canard

area. The incremental drag polar, ΔC_L vs. ΔC_D, and the incremental lift-over-drag value, $\Delta C_L/\Delta C_D$, are shown in Figs. 2.212c and 2.212d, respectively. The H15 produces the least incremental drag proportional to the tail area and thickness at $|C_L| \leq 0.2$, while vice versa at $|C_L| \geq 0.2$ due to tail authority and aspect ratio in Fig. 2.212c. The downwash angle on the horizontal stabilizers is defined as

$$\epsilon = \alpha + \delta_{\mathrm{HT}} - \alpha_{\mathrm{HT}} \tag{2.23}$$

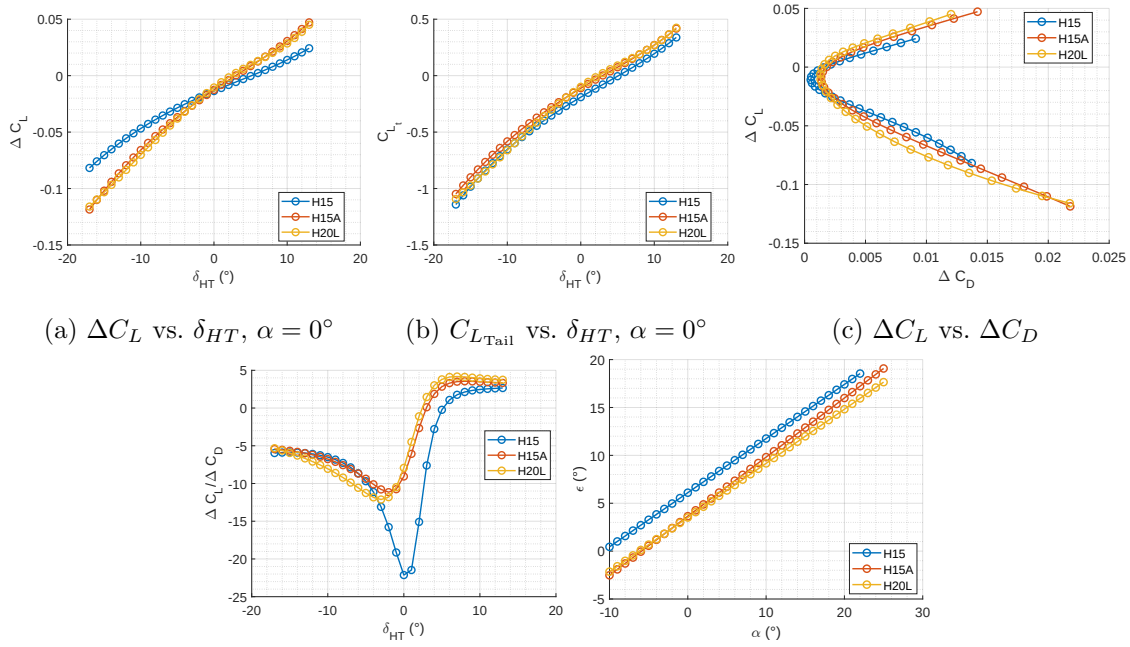
where ϵ is downwash angle, α is angle of attack, δ_{HT} is the tail rotation angle relative to the line that defines the zero angle of attack for the airplane, and α_{HT} is tail angle of attack with respect to local flow field. When the local angle of attack of a symmetric untwisted tail is zero, there is no lift on the tail. In such a case Equation (2.23) becomes

$$\epsilon = \alpha + \delta_{\mathrm{HT}}, \tag{2.24}$$

when $\alpha_{\mathrm{HT}} = 0^\circ$ and the local flow field is align with tail,

$$\Delta C_L = C_{L_{\mathrm{HT}\neq 0^\circ}} - C_{L_{\mathrm{No\ HT}}} = 0. \tag{2.25}$$

For a known tail angle relative to the model, the angles of attack could be used at which the incremental lift contribution from the tail is zero (comparing tail-on and tail-off cases) to find the downwash on the tail. The computed downwash angles with respect to angles of attack for each tail planform are plotted in Fig. 2.212e.



(a) ΔC_L vs. δ_{HT}, $\alpha = 0^\circ$ (b) $C_{L_{\mathrm{Tail}}}$ vs. δ_{HT}, $\alpha = 0^\circ$ (c) ΔC_L vs. ΔC_D

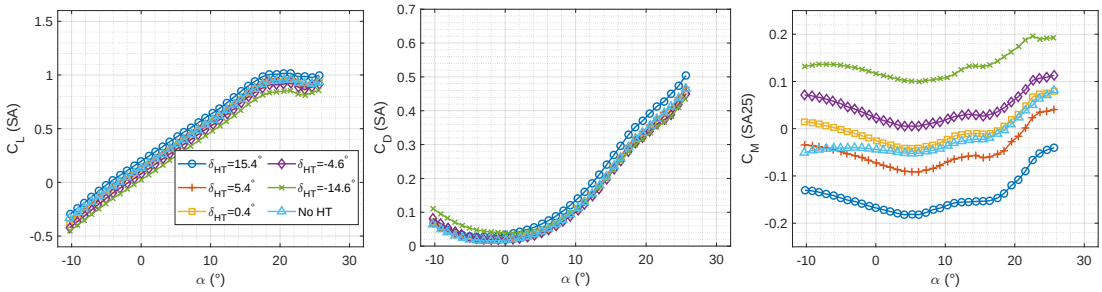
(d) $\Delta C_L/\Delta C_D$ vs. δ_{HT}, $\alpha = 0^\circ$ (e) ϵ vs. δ_{HT}

Figure 2.212: Effects of different horizontal stabilizers and deflections on lift and drag for UW-S-15A without nacelle and canard

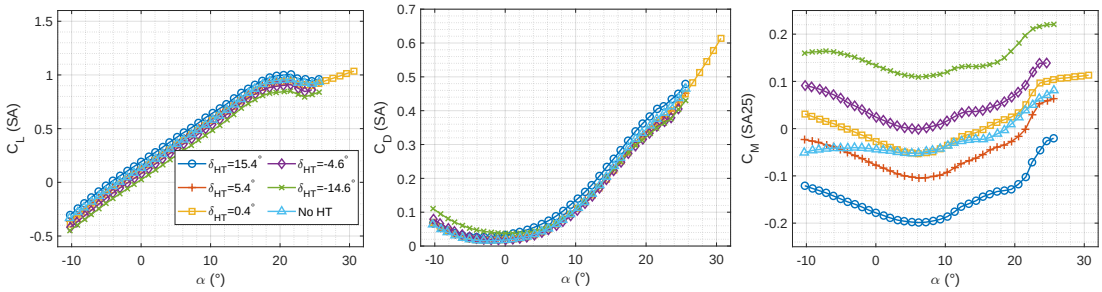
UW-S-20 - mount location difference

Two configurations of three-surface model with commons in outboard wing, canards, and top mounted nacelle with only differences in the horizontal tail mounts, T-tail and mid-tail, are shown in Fig. 2.213 in §2.7.5. Figure 2.213 shows the effects of horizontal stabilizer locations and rotations on the longitudinal forces and moment with respect to the angles of attack for UW-S-20A and UW-S-20H. Figure 2.213 shows no significant variations in both lift and drag trends among the different tail mounts except for a difference in magnitude. The stall of the mid-tail configuration is gradual, $18^\circ \leq \alpha \leq 21^\circ$, comparing to T-tail configuration, $\alpha \approx 21^\circ$. This gradual stall of the mid-tail model is preferred over the sharp stall of the T-tail model from an S&C and stall recovery perspective. Both tail positions, mid- and T-tail, stall at $\alpha \approx 21^\circ$, but not for the three-surface conventional low-tail configuration in Fig. 2.202b from previous §2.8.1 or the conventional two-surface configuration without canard and nacelles in Fig. 2.206 from previous §2.8.2. The effect of tail rotations on the pitch moment in Figs. 2.213c and 2.213f are similar to Figs. 2.206c, 2.206f, and 2.206i. The tail planform geometry, H20, is the same for both tail locations, mid- and T-tail, such that the differences in pitch moment are due to differences in the moment arm, in Figs. 2.213c and 2.213f.

Figure 2.214 shows the reduction in static margin of C_M vs. C_L curve as the CG location moves rearwards along MAC. The static margin is almost zero at $\text{CG}_{\text{NP}} \approx 35\%$ and $\text{CG}_{\text{NP}} \approx 40\%$ for mid- and T-tail, respectively, and becomes negative, unstable, beyond that neutral point. Figure 2.214 further shows that the configuration cannot be trimmed at $C_L > 0$, $C_M < 0$ at all CG locations, for all tails like the conventional low-tail three-surface configuration in Fig. 2.202a from §2.8.1 and the conventional low-tail two-surface configuration without canard and nacelles in Fig. 2.207 from §2.8.2. The static margins, dC_M/dC_L, are constant at $C_L \leq 0.35$ and become nonlinear at $C_L \geq 0.35$ for both tail positions, mid- and T-tail, in contrast to the conventional low-tail configurations. The static margin variations are computed from Fig. 2.214 and plotted in Fig. 2.215. The static margin and neutral point on the MAC are proportional to moment arm - the longitudinal distance from CG to tail aerodynamic center - in Fig. 2.215. Furthermore, the three-surface Mid-



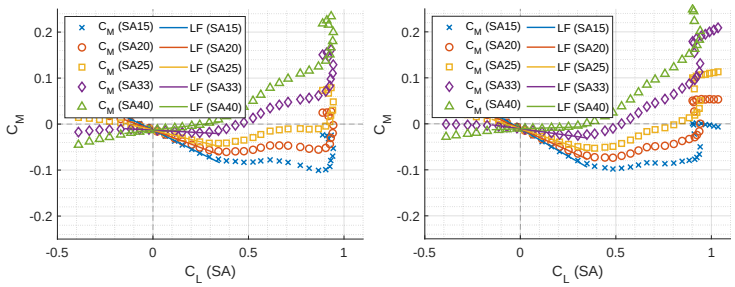
(a) C_L vs. α, H20M (b) C_D vs. α, H20M (c) C_M vs. α, H20M



(d) C_L vs. α, H20T (e) C_D vs. α, H20T (f) C_M vs. α, H20T

Figure 2.213: Effects of horizontal stabilizers locations and rotations on the longitudinal forces and moment vs. α for UW-S-20A and UW-S-20H

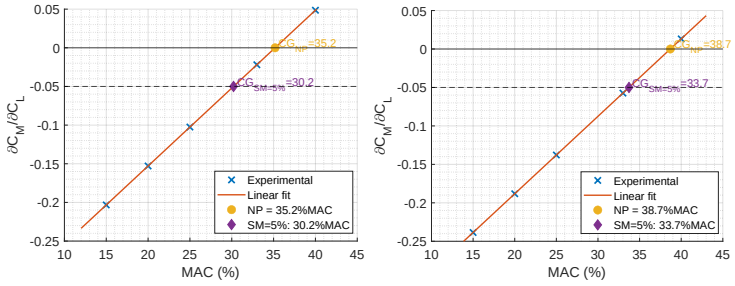
and T-tail configurations have larger static margins and neutral points than the two- and three-surface conventional low-tail configurations in Figs. 2.205 and 2.208, respectively.



(a) UW-S-20H, mid-tail, H20M (b) UW-S-20A, T-tail, H20T

Figure 2.214: Effects of horizontal stabilizers locations and rotations on pitch moments vs. lift with different CG locations for UW-S-20A and UW-S-20H

The incremental effects of horizontal stabilizer locations and rotations on the longitudinal forces and moment with respect to $\delta_{\mathrm{HT}=0^\circ}$ and no tail configuration are computed as in Eqs.

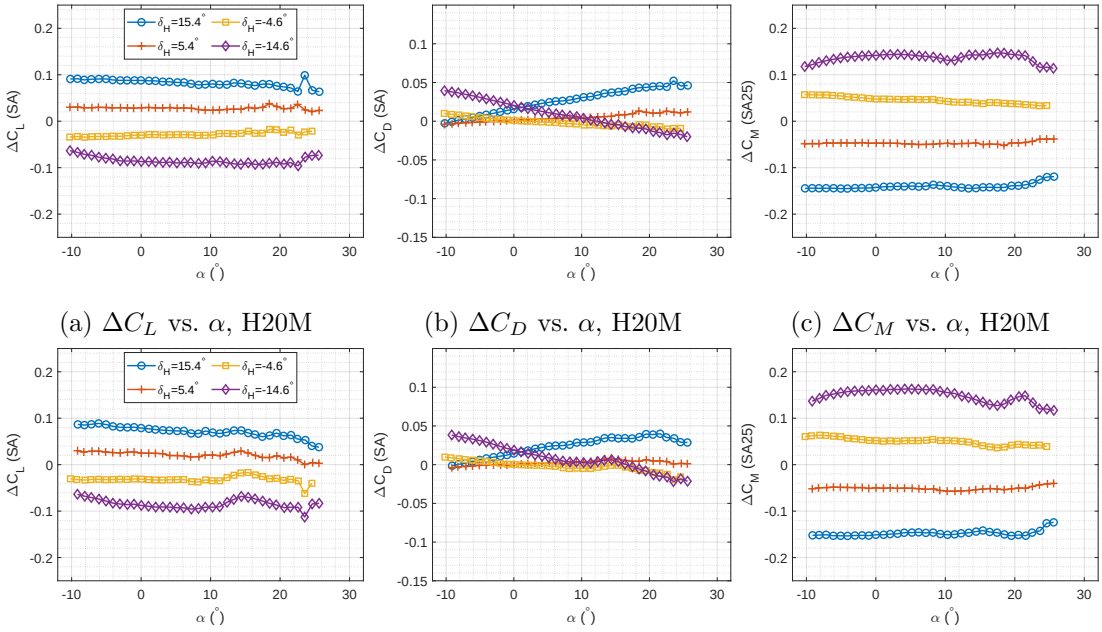


(a) UW-S-20H, mid-tail, H20M (b) UW-S-20A, T-tail, H20T

Figure 2.215: Effects of horizontal stabilizers locations and rotations on static margins and neutral points for UW-S-20A and UW-S-20H

(2.20) and (2.21), respectively, from §2.8.2. The results are shown in Figs. 2.216 and 2.217 and are similar to Figs. 2.209 and 2.210 in §2.8.2. The incremental ΔC_L with respect to $\delta_{\text{HT}=0^\circ}$ in Fig. 2.216 are similar to Fig. 2.209, except for the abrupt variations at $\alpha \approx 22^\circ$ and constant offsets in pitch moments due to differences in moment arm. The incremental ΔC_L with respect to the no tail configuration is shown in Fig. 2.217. See Fig. 2.210 for comparison.

Figure 2.218 shows the trimmed and untrimmed drag polar, and lift-over-drag curves, and trimmed tail rotation effect on lift at different CG locations for two tail locations. For each tail locations, the horizontal stabilizer is rotated over $-10^\circ \leq \delta_{\text{HT}} \leq 10^\circ$ with $-10^\circ \leq \alpha \leq 25^\circ$. The CG location is selected at $25\%\bar{c}$, $dC_M/dC_L \approx -10\%$, from Fig. 2.215 and the trimmed lift and drag are obtained from the corresponding zero-pitch moment for drag polar and lift over drag. The difference between trimmed and untrimmed drag polar suggest small drag penalties for both Mid- and T-tail mounts compared to the conventional low-tail two-surface configuration without nacelle and canard in Fig. 2.211 from §2.8.2. Figure 2.218 shows the horizontal tail rotation effectiveness, δ_{HT} vs. C_L, at trim conditions for various CG locations. Mid-and T-tail locations are trimmable at $CG = 15\% - 30\%\bar{c}$ and $CG = 15\% - 33\%\bar{c}$, respectively, at $C_L \leq 0.35$, in Figures 2.218c and 2.218f. The absolute values of trimmed C_L and δ_{HT} decrease as CG moves to the rear along MAC. For the mid-tail configuration at CG = 20%, the maximum absolute tail deflection angle is $|\delta_{\text{HT}}| \leq 5^\circ$ with corresponding maximum absolute trimmed lift coefficient at $|C_{L_{\text{trim}}}| \leq 0.3$,



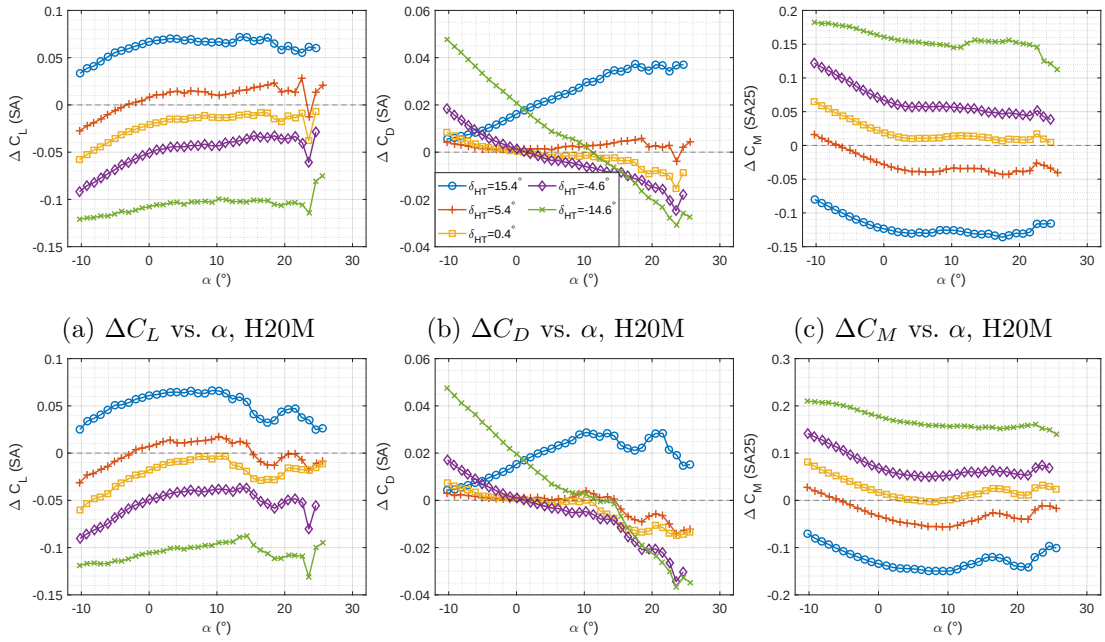
(a) ΔC_L vs. α, H20M (b) ΔC_D vs. α, H20M (c) ΔC_M vs. α, H20M

(d) ΔC_L vs. α, H20T (e) ΔC_D vs. α, H20T (f) ΔC_M vs. α, H20T

Figure 2.216: Incremental effects of horizontal stabilizers locations and rotations on the longitudinal forces and moment vs. α for UW-S-20A and UW-S-20H with respect to $\delta_{\text{HT}} = 0°$

while at CG = 30%, the maximum absolute tail deflection angle decreases $|\delta_{\text{HT}}| \leq 2°$ with corresponding maximum absolute trimmed lift coefficient at $|C_{L_{\text{trim}}}| \leq 0.2$ in Fig. 2.218c.

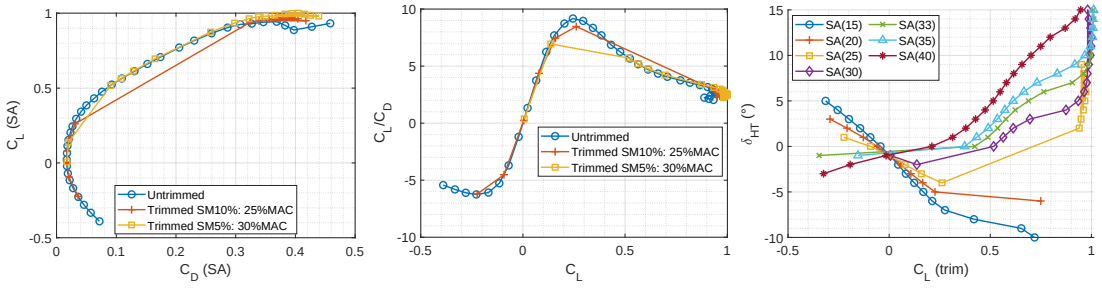
The incremental effects of horizontal stabilizer lift with respect to the no tail configuration at $\alpha = 0$ are shown in Eq. (2.21) and are nondimensionalized by the wing reference area in Fig. 2.219a. The horizontal tail lift, nondimensionalized by the area of tail planfrom, is defined in Eq. (2.22) and shown in Fig. 2.219b. As mentioned earlier in §2.8.2, the incremental difference in Fig. 2.219, except for Fig. 2.219b, are the horizontal tail lift, drag polar and lift over drag normalized by the wing reference area. The tail locations have minimal effects on tail drag polar and lift over drag. The mid-tail has better characteristics in drag polar and lift over drag shown in Figs. 2.219c and 2.219d where the T-tail configuration has higher ΔC_D at most $\Delta C_L < 0$ and higher $\Delta C_L/\Delta C_D$ at $\delta_{\text{HT}} < 2°$ compared to mid-tail configuration.



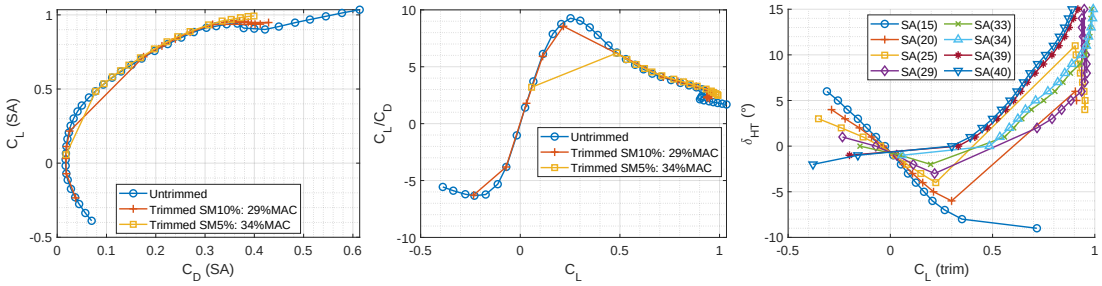
(a) ΔC_L vs. α, H20M (b) ΔC_D vs. α, H20M (c) ΔC_M vs. α, H20M

(d) ΔC_L vs. α, H20T (e) ΔC_D vs. α, H20T (f) ΔC_M vs. α, H20T

Figure 2.217: Incremental effects of horizontal stabilizers locations and rotations on the longitudinal forces and moment vs. α for UW-S-20A and UW-S-20H with respect to horizontal stabilizer off configuration

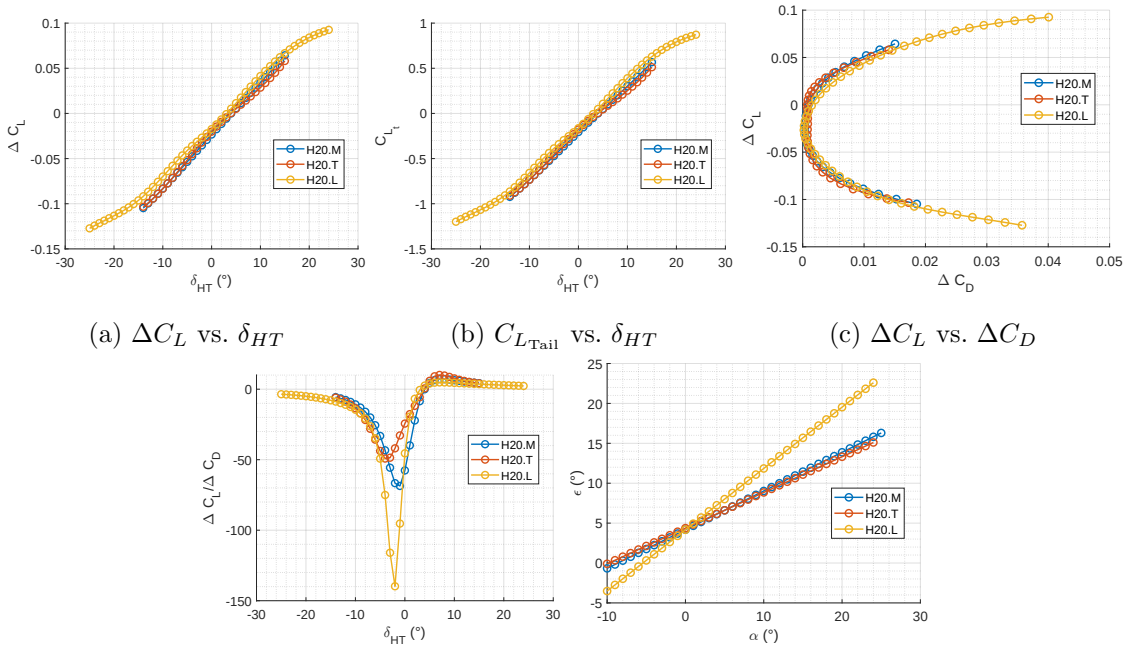


(a) C_L vs. C_D, H20M (b) C_L/C_D vs. C_L, H20M (c) δ_{HT} vs. C_L, H20M



(d) C_L vs. C_D, H20T (e) C_L/C_D vs. C_L, H20T (f) δ_{HT} vs. C_L, H20T

Figure 2.218: Effects of horizontal stabilizers locations and rotations on trimmed and untrimmed drag polar, lift-over-drag ratio, and untrimmed tail deflection effectiveness on lift for UW-S-20A and UW-S-20H



(a) ΔC_L vs. δ_{HT} (b) $C_{L_{\text{Tail}}}$ vs. δ_{HT} (c) ΔC_L vs. ΔC_D

(d) $\Delta C_L/\Delta C_D$ vs. δ_{HT} (e) ϵ vs. δ_{HT}

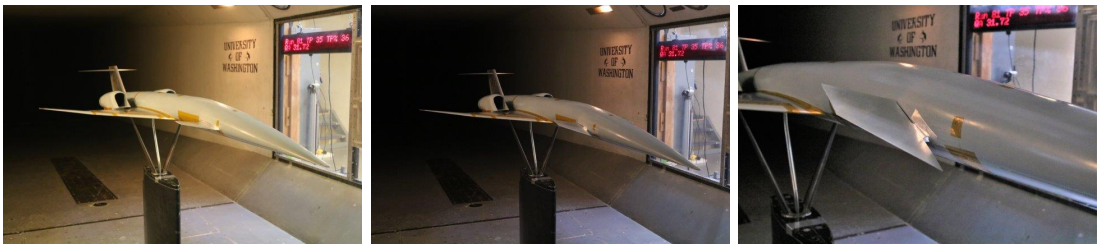
Figure 2.219: Effects of horizontal stabilizers locations and rotations on lift and drag for UW-S-20A and UW-S-20H

2.8.3 Canard Deflection Data Details

The SCALOS model could be equipped with canards on the fuselage ahead of the main wing. There are two different canard planforms. The 2015 canard and the 2018 canard are designated C15 and C18, respectively. The canard has three different longitudinal mounting locations. The naming convention for the canard locations - forward, mid, and aft - is *F*, *M*, and *A*, respectively, followed by the canard designation. Canard locations and sizes are tabulated in Tab. 2.27 and are shown in Fig. 2.49. Prior studies of the influence of canard locations and sizes have were presented in §2.7.4. This section discusses the canard rotation effectiveness on the UW-S-20A configuration, which has the 2015 canard at the forward position, C15.F, as shown in Fig. 2.110 of §2.7.4. The UW-S-20A three-surface T-tail model and the UW-S-20A without canard two-surface wing-T-tail model are shown in Fig. 2.84 at the beginning of §2.7.2. The designations and descriptions are tabulated in Tab. 2.32. The CG location is selected at 25%$\bar{c}$ with a static margin of 10% - Figures 2.214 and 2.215. Figure 2.221 shows canard rotation at $-30° \leq \delta_C \leq 30°$.



(a) $\delta_C = +30°$ (b) $\delta_C = +15°$ (c) $\delta_C = +5°$

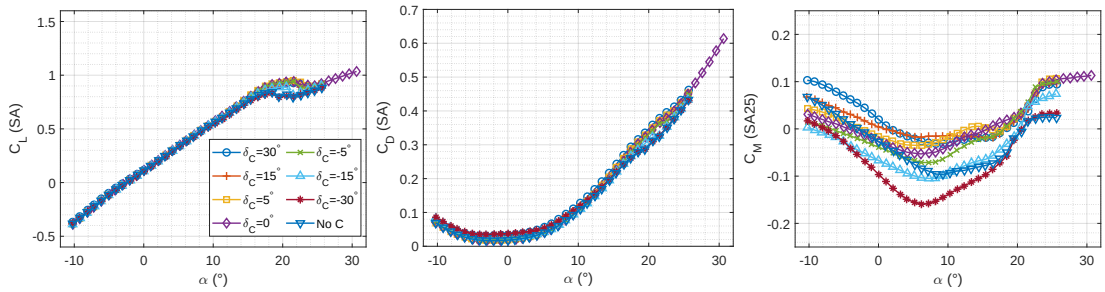


(d) $\delta_C = -5°$ (e) $\delta_C = -15°$ (f) $\delta_C = -30°$

Figure 2.220: UW-S-20A with canard deflections

The effect of canard rotation on the longitudinal forces and moment as a function of angle of attack for UW-S-20A are shown in Fig. 2.221. The figure shows that the lift forces

are practically the same at $-10^\circ \leq \alpha \leq 10^\circ$ for all canard rotations but are affected by the canard rotations at $\alpha > 10^\circ$. For the largest negative rotation at $\delta_C = -30^\circ$ the canard does not have any effect on lift, maximum lift, and stall angle of attack compared to the no canard case in Fig. 2.221a. For other rotations at $-15^\circ \leq \delta_C \leq 30^\circ$, the maximum lift and stall angled of attack are significantly affected by canard rotations. Furthermore, as the canard rotation angle increases, the stall becomes smoother. That is, the maximum lift plateaus for a short range of angles of attack, $19^\circ \leq \alpha \leq 22^\circ$. The addition of canard to the model extends the stall angle from $\alpha \approx 18^\circ$ to $\alpha \approx 21^\circ$ and the maximum lift from $C_{L_{\max}} \approx 0.8 \rightarrow 0.92$. The canard is located ahead of the CG of the model. Hence, the additional pitching moment, generated by canard lift multiplied by the corresponding moment arm, is proportional to the canard rotation angles, and the positive canard rotations create positive lift and destabilize the aircraft. The pitching moment break point at $\alpha \approx 5.5^\circ$ is almost independent of canard rotation, except for the no-canard case and $\delta_C = -30^\circ$ at $\alpha \approx 8^\circ$ and $\alpha \approx 7^\circ$, respectively, in Fig. 2.221a. The pitching moments vary with the canard rotations between $\alpha = -10^\circ$ and the pitching moment break point. The pitching moment derivative is linear for the no-canard configuration for $|\delta_C| \leq 15^\circ$, and becomes very nonlinear for $|\delta_C| \geq 15^\circ$ between $\alpha = -10^\circ$ and the pitching moment break point.



(a) C_L vs. α (b) C_D vs. α (c) C_M vs. α

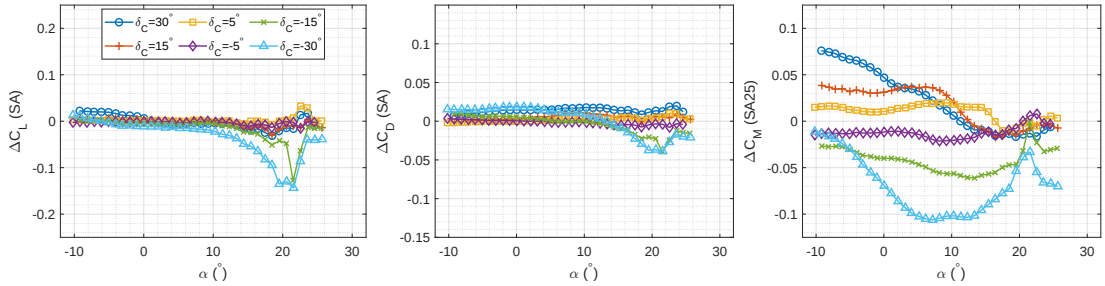
Figure 2.221: Effects of canard rotations on the longitudinal forces and moment vs. α for UW-S-20A

The incremental effects of canard deflections on the longitudinal forces and moment for the zero rotation, $\delta_C = 0^\circ$, and for the no-canard configuration are shown in Figs. 2.222d - 2.222f and Figs. 2.222b - 2.222c, respectively. The data is processed according to Eqs. (2.20)

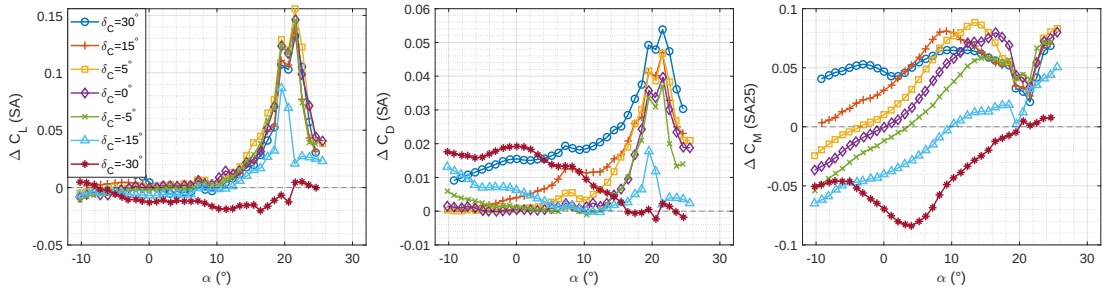
and (2.21) in §2.8.2. The incremental lift, ΔC_L, with respect to $\delta_C = 0^\circ$ is shown in Fig. 2.222d. Compared to the horizontal stabilizer in §2.8.2, where the incremental lift generated by the horizontal stabilizer is almost constant with angles of attack and proportional to the tail deflections, the effect of the canard is much different. For $\delta_C > 0^\circ$, as is well known, the canards deflect the local flow field onto the wing down, similar to the effect of the wing on the horizontal tail. Thus, even though the canard generates additional lift, its downwash reduces the effective angle of attack of the wing and the lift of the wing behind the spanwise locations of the canard. Furthermore, the canard downwash on the wing would propagate a downwash effect on the horizontal tail. These combined effects make the incremental lift and drag very nonlinearly in contrast to the horizontal stabilizer case.

The large negative canard rotations, at $\delta_C = 15^\circ, 30^\circ$, cause early flow separation and reduce the stall angle of attack, lift, and drag as shown in Figs. 2.222d and 2.222e. The pitching moment variations are different than those of the horizontal stabilizers that were previously discussed. The constant offsets in pitching moments with respect to $\delta_C = 0^\circ$ are for $|\delta_C| \leq 15^\circ$ at $|\alpha| \leq 5^\circ$ in Fig. 2.222f. Similar variations are observed with respect to the no-canard configurations in Figs. 2.222a, 2.222b, and 2.222c. The canard extends the stall angles and maximum lift from $\alpha \approx 18^\circ \rightarrow 21^\circ$ in Fig. 2.222a with proportional incremental drag as shown in Fig. 2.222b. For $\delta_C > 0^\circ$, the pitching moment relationships are not constant because of the flowfield and downwash induced by canard on the inboard portion of the wing and horizontal stabilizers and the mutual interface effects among all lifting surfaces present.

Figure 2.223 shows the trimmed and untrimmed drag polars, lift-over-drag curves, and trimmed tail rotation effectiveness on lift at different CG locations for canard rotations. Figure 2.223 shows that the UW-S-20A model is not trimmable at $C_L > 0$ for $\bar{c} = 34\%$ because of $C_M < 0$ at all CG locations. The differences in the lift for the trimmed and untrimmed drag polars are minimal as shown in Fig. 2.223a. However the differences in the drag for the trimmed and untrimmed drag polar cannot be ignored.

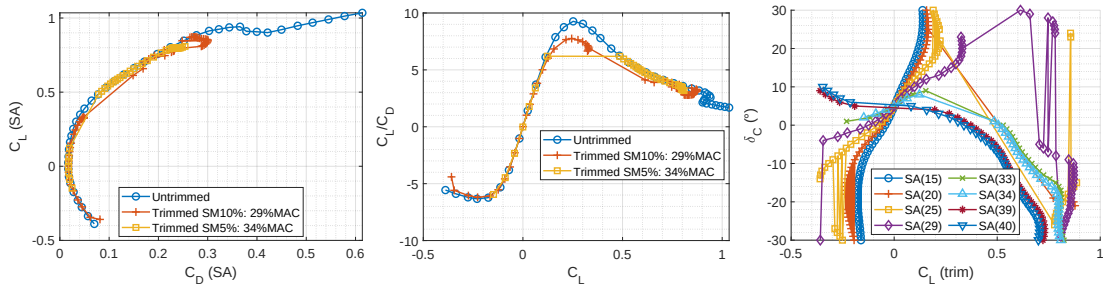


(a) ΔC_L vs. α, no C (b) ΔC_D vs. α, no C (c) ΔC_M vs. α, no C



(d) ΔC_L vs. α, $\delta_C = 0°$ (e) ΔC_D vs. α, $\delta_C = 0°$ (f) ΔC_M vs. α, $\delta_C = 0°$

Figure 2.222: Incremental effects of canard rotations on the longitudinal forces and moment vs. α for UW-S-20A with respect to $\delta_{HT} = 0°$ and canard off configuration



(a) C_L vs. C_D (b) C_L/C_D vs. C_L (c) δ_C vs. C_L

Figure 2.223: Effects of canard rotations on trimmed and untrimmed drag polar, lift-over-drag ratio, and untrimmed tail deflection effectiveness on lift for UW-S-20A

2.8.4 Wing Control Surfaces - Incremental Effects Details

This section discusses the effects of wing control surfaces - leading-edge and trailing-edge deflections - on the aerodynamic forces and moments in the case of two three-surface configurations: UW-S-20A and UW-S-21A. The UW-S-21A model, from §2.8.1, has canards,

nacelles located under the wing, and conventional low-tail empennage configuration with dorsal and ventral fins. The UW-S-20A, from §2.8.2, has canards, nacelles located on the top of the wing, and a T-tail empennage configuration without dorsal or ventral fins. Both configurations have the same inboard wing, fuselage. canard geometry and canard mounting locations but differ in nacelle locations, outboard wing planforms, and empennage configurations which include horizontal tail locations, vertical tail size and thickness, as well as dorsal and ventral fins. The UW-S-21A three-surface conventional low-tail model and the UW-S-20A three-surface T-tail model are shown in Fig. 2.84 of §2.7.2. The geometric properties are specified in Tab. 2.27 and the designations and descriptions are listed in Tab. 2.32. 3D images of the various configurations tested are shown in Fig. 2.84 at the beginning of §2.7.2. The detailed configuration build-up and differences are summarized in Tab. 2.32.

The effects of CG locations on the C_M vs. C_L curves for both UW-S-20A and UW-S-21A models are shown in Figs. 2.203 and 2.214. The static margins and neutral points of both models are computed and plotted in Figs. 2.205 and 2.215. Discussion of the models can be found in §2.8.1 and §2.8.2. Both three-surface configuration models have a linear relationship in C_M vs. C_L at $|C_L| < 0.35$ and the static margins, dC_M/dC_L, are different with respect to CG locations. For $0.4 \leq C_L \leq 1$, the relationships in C_M vs. C_L remain linear but change in static margins and the configuration becomes unstable for CG $\geq 20\%$ for UW-S-21A. The static margins change again at $C_L \geq 1$ and become unstable for CG $\geq 25\%$ for UW-S-21A. The UW-S-20A model has negative static margins and neutral point at CG $\approx 40\%$ for $|C_L| < 0.35$. For $C_L > 0.35$, the static margins become nonlinear and highly unstable, especially $dC_M/dC_L \to \infty$ for $C_L \approx 0.92$ in Fig. 2.214. The static margins are summarized in Figs. 2.205 and 2.215 where the UW-S-21A model has $\mathrm{CG_{NP}} = 31.9\%$ and $\mathrm{CG_{SM}} = 22.0\%$, while the UW-S-20A model has $\mathrm{CG_{NP}} = 39.6\%$ and $\mathrm{CG_{SM}} = 29.7\%$.

Figures 2.144 and 2.142 in §2.7.8 show the UW-S-21A and UW-S-20A models, respectively, with leading-edge (LE) deflection of both inboard (IB) and outboard (OB) leading edges. The leading-edge deflection is a simple hinge deflection with the crank delta shape preserved. Figures 2.166 and 2.169 in §2.7.9 show the UW-S-21A and UW-S-20A model, respectively, with trailing-edge (TE) deflections of both flaps and ailerons. The trailing-edge deflection is a simultaneous deflection of flaps and ailerons acting as high-lift devices in the

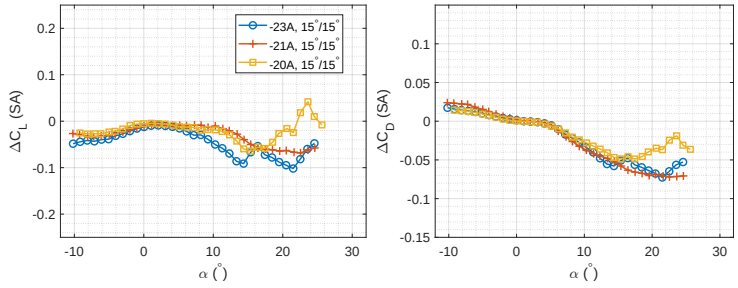
role of *flaperons*. The ailerons are rotated downward on both left-and right-side of the wing instead of differentially, which would be used for lateral-directional control. The R stands for *Reduced* in Figs. 2.166 and 2.169 where the aileron chords are reduced by one-third, $\bar{c}_{\text{ail R}} = \frac{2}{3}\bar{c}_{\text{ail}}$, and so is the area, $S_{\text{ail R}} = \frac{2}{3}S_{\text{ail}}$.

Leading-Edge Deflection Effects

This section discusses the leading-edge deflection effects on two different three-surface configurations, which are UW-S-20A and UW-S-21A. The incremental effects of leading-edge deflections on forces and moments of both models with respect to $\delta_{\text{LE}} = 0^\circ$ are compared in Figure 2.224 according to Eq. (2.20). The incremental pitching moment variations are shown at two different CG locations of 25% and 30%. The incremental lift curve trends for both leading-edge deflections of $\delta_{\text{LE}} = 15^\circ, 30^\circ$ are very similar, with some constant offsets. The UW-S-21A has constant lift increments at $3^\circ \leq \alpha \leq 9^\circ$ for both deflection angles while UW-S-20A has a slight negative slope in lift increments at $3^\circ \leq \alpha \leq 9^\circ$. The magnitudes in the case of both models are similar up to $\alpha \approx 15^\circ$ where ΔC_L and start to vary drastically in Fig. 2.224a. The differences are likely due to the flow separation caused by the nacelles locations and empennage systems.

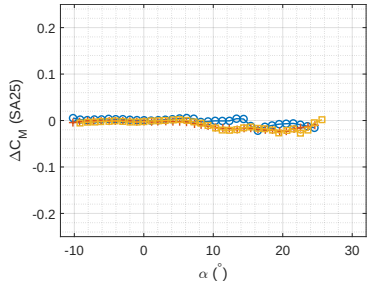
The incremental pitching moment shows similar variations up to $\alpha \approx 15^\circ$ in Fig. 2.224c. The pitching moment derivatives, $dC_M/d\alpha$, for both models at CG locations of 25% is shown in Figure 2.225. The data for the $\delta_{\text{LE}} = 0^\circ$ are also shown in the same figure for comparison.

The pitching moment derivatives for both models at $\delta_{\text{LE}} = 0^\circ$ are different significantly, especially when $\alpha \geq 5^\circ$. However, for $\delta_{\text{LE}} \neq 0^\circ$, they are similar to $\delta_{\text{LE}} = 0^\circ$ for the same configuration, but different in magnitudes at $\alpha \leq 15^\circ$. The lift-over-drag ratio variations with angles of attack are shown in Figure 2.225b where UW-S-21A has higher maximum lift-over-drag ratios than UW-S-20A. The flap deflections increase maximum lift-over-drag ratios and increase the angle of attack at maximum lift-over-drag value.

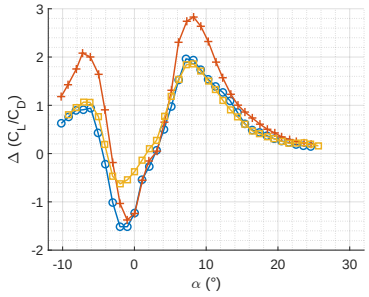


(a) ΔC_L vs. α

(b) ΔC_D vs. α

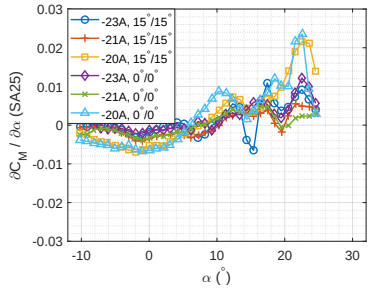


(c) ΔC_M vs. α

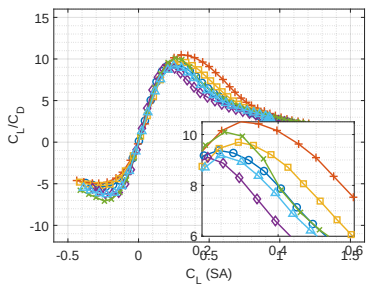


(d) $\Delta(C_L/C_D)$ vs. α

Figure 2.224: Incremental effects of leading-edge deflections on forces and moments vs. α for UW-S-21A and UW-S-20A



(a) $dC_M/d\alpha$ vs. α



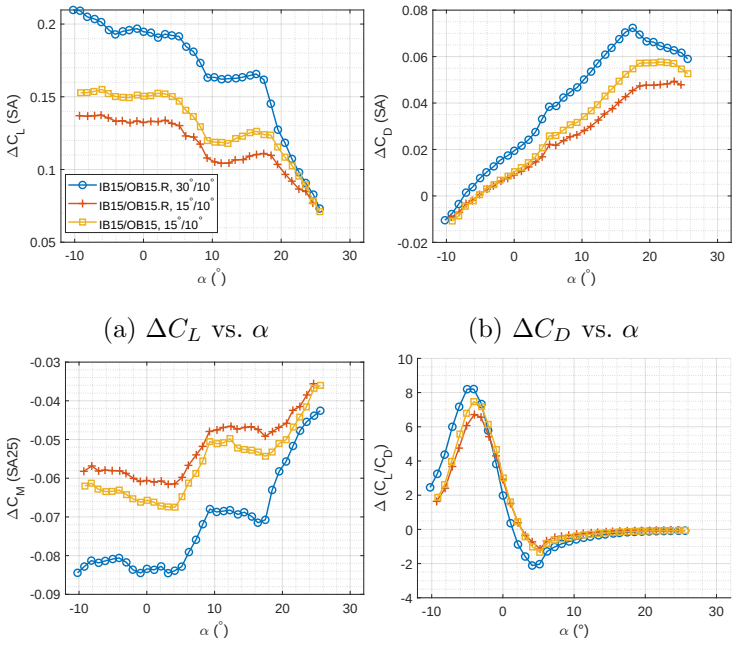
(b) C_L/C_D vs. C_L

Figure 2.225: Effects of leading-edge deflections on forces and moments vs. α for UW-S-21A and UW-S-20A

The Effects of Flap and Aileron (Flaperon) Deflections - The Deflections Effectiveness

This section discusses the effects of wing trailing-edge devices on UW-S-21A (see Fig. 2.166 of §2.7.9). Figure 2.166 shows the UW-S-21A model with the TE device deflections which combine flap and aileron deflections of $\delta_{\text{flap}} = \pm 15°, \pm 30°$ and $\delta_{\text{ail}} = \pm 10°, \pm 10°$R, re-

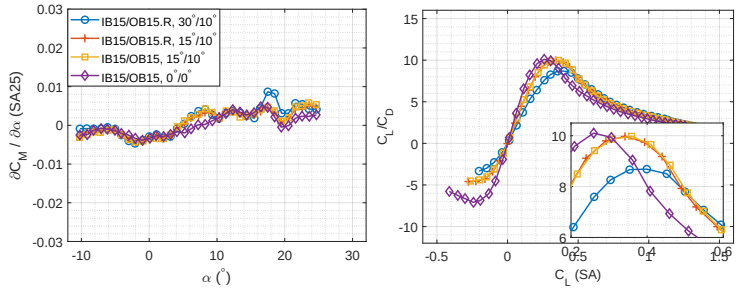
spectively. The incremental effects of flaperon deflections on the longitudinal forces and moment for the UW-S-21A model are shown in Fig. 2.226. The reduced-chord aileron reduces the forces and moment compared to the full-chord aileron at $-7° \leq \alpha \leq 17°$. The increments between all deflections are constant at $-7° \leq \alpha \leq 17°$ and are the same for pitching moments. The lift-over-drag ratio and its increments do not change for $\alpha \geq 10°$, as shown in Figures 2.227b, and 2.226d, respectively. For the largest flaperon deflection angle, $\delta_{\text{flap}} = 30°$ and $\delta_{ail} = 10°\text{R}$, the incremental pitching moment variations do not vary at $-3° \leq \alpha \leq 5°$, while the other two have negative slopes (see Fig. 2.226c) indicating that for the combined effects of flaperons on the pitching moment variations are zero. Further note that the incremental lift-over-drag ratio becomes zero at $\alpha \geq 15°$ in Fig. 2.227b.



(a) ΔC_L vs. α (b) ΔC_D vs. α

(c) ΔC_M vs. α (d) $\Delta(C_L/C_D)$ vs. α

Figure 2.226: Incremental effects of flaperon deflections on longitudinal forces and moment vs. α for UW-S-21A



(a) $dC_M/d\alpha$ vs. α (b) C_L/C_D vs. C_L

Figure 2.227: Effects of flaperon deflections on longitudinal forces and moment vs. α for UW-S-21A

Flap and Aileron (Flaperon) Deflections - The Effect of the Configuration

This section discusses the trailing-edge, flaperon, effectiveness on two different three-surface configurations, which are UW-S-20A and UW-S-21A, shown in Figs. 2.166 and 2.169 of §2.7.9, respectively. The incremental effects of flaperon deflections on forces and moments of both models as functions of angle of attack with $\delta_{\text{LE}} = 0°$ are compared in Fig. 2.228 according to Eq. (2.20). The incremental pitching moment variations are shown at CG locations of 25% in Fig. 2.229. The incremental lift is inversely proportional to angles of attack at $\alpha \geq -5°$ with the same trends for both models suggesting the flaperon is losing effectiveness in lift at higher angle of attack.

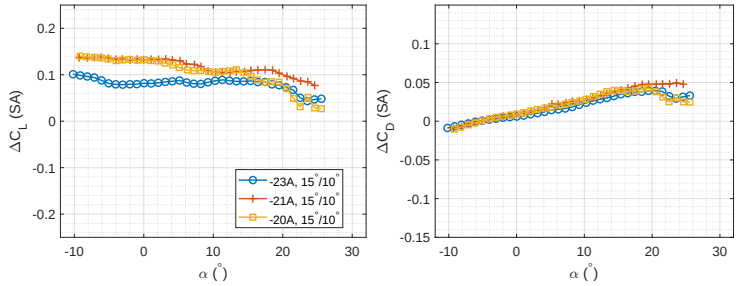
The UW-S-20A configuration decreases in ΔC_L more than UW-S-21A configuration. Note that there is an increase in ΔC_L at $\alpha \approx 11°$ and $\alpha \approx 15°$ for the UW-S-20A and UW-S-21A models, respectively, shown in Fig. 2.228a. The ΔC_L continues to decrease, beyond point of sudden increase in ΔC_L, at higher angle of attack with particular sharper reduction for the UW-S-20A model. The differences are due to the configuration differences, as mentioned in §2.8.4, in nacelle and empennage geometries.

The ΔC_D varies differently at $\alpha \geq 5°$ corresponding to the ΔC_L variations for both models in Fig. 2.228b. Both models show the same behavior in the incremental lift-over-drag, except that the UW-S-21A model has higher differences in ratios, shown in Fig. 2.228d. This suggests that flaperons are more effective on the UW-S-21A model because of less interaction with upper wing surface flowflied by the presence of nacelles. The UW-S-

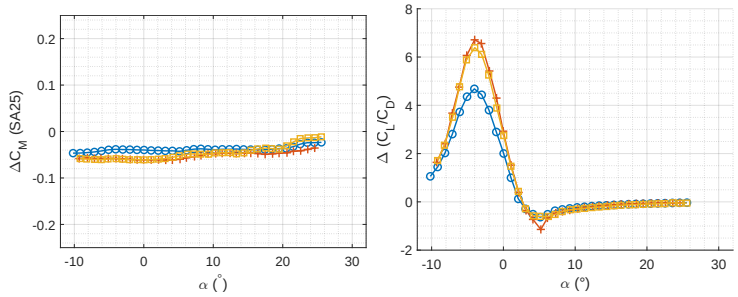
21A model has lower incremental pitching moment variations than UW-S-20A model at two different CG locations in Fig. 2.228c, especially at high angle of attack. Both models have almost identical pitching moment derivative characteristics for zero- and nonzero-flaperon deflections, as Fig. 2.229a show, but they are different in magnitude.

The UW-S-20A mode has "stormy" pitching moment derivative behavior, sharp increase and decrease, at $15^\circ \leq \alpha \leq 25^\circ$ for both zero- and nonzero-flaperon deflections. The UW-S-21A model has smoother pitch moment derivatives than the UW-S-20A model, especially at $\alpha \geq 12^\circ$.

Again, these difference are due to the interaction with the upper wing surface flowflied by the location of nacelles and their effects on the empennage system. That is, the upper wing surface flowfield interactions of the wing and bottom mounted nacelles on the conventional horizontal tail are less than the the upper wing surface flowfield interaction of the wing and top mounted nacelles on the T-tail configuration. The lift-over-drag variations are shown in Fig. 2.229b. As previously discussed, the UW-S-21A model has better lift over drag than the UW-S-20A model. CFD simulations and flow visualization are tools that add insight and help linking flow field characteristics to the behavior of force and moment curves. This is a rich area for future work.

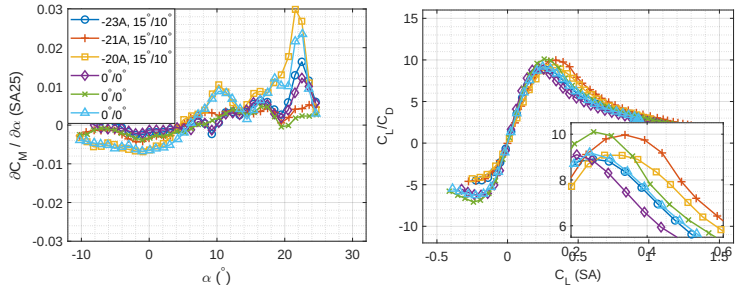


(a) ΔC_L vs. α (b) ΔC_D vs. α



(c) ΔC_M vs. α at $\bar{c} = 25\%$ (d) $\Delta(C_L/C_D)$ vs. α

Figure 2.228: Incremental effects of flaperon deflections on longitudinal forces and moment vs. α for UW-S-21A and UW-S-20A



(a) $dC_M/d\alpha$ vs. α at $\bar{c} = 25\%$ (b) C_L/C_D vs. C_L

Figure 2.229: Effects of flaperon deflections on longitudinal forces and moment vs. α for UW-S-21A and UW-S-20A

2.9 Lateral-Directional Aerodynamics

This section presents selected test results with a focus on the lateral-directional aerodynamics of SCALOS, including comparative effects of configuration differences with notes on configuration parameters that have significant impacts on performance and stability

characteristics at low-speed flight conditions [27].

2.9.1 Configuration Lateral-directional Characteristics

As mentioned previously, several models of the SCALOS having different wings, horizontal, vertical, and canard planforms, as shown in Fig. 2.49, as well as nacelles and their locations, fuselage, forebody, aft-body, aft-deck, etc. were tested for various sideslip angles and angles of attacks. In addition to these configurations, models were tested with various leading and trailing edges flap rotations, flap/flaperon effects, horizontal tail locations and rotations, canard's location, shapes, and deflection angles. Models were tested with various rudders (directional control authority), and aileron (roll control authority), too. Interested readers are referred to Tabs. 2.12-2.18 in §2.2 for different variations of the SCALOS that have been tested up to now. In the section, however, the lateral-directional data for a few models of SCALOS, the configuration variations of which are shown in Tab. 2.27 along with their photos shown in Fig. 2.84, will be discussed. All data are corrected for the wind tunnel blockage walls, wake, etc. effects, as well as the model support tare and interference effects §2.6. In this section, the lateral directional data for six SCALOS models, UW-S-20A, UW-S-20CL, UW-S-21A, UW-S-23E, UW-S-23G, and UW-S-24A, Fig. 2.84, are presented and discussed.

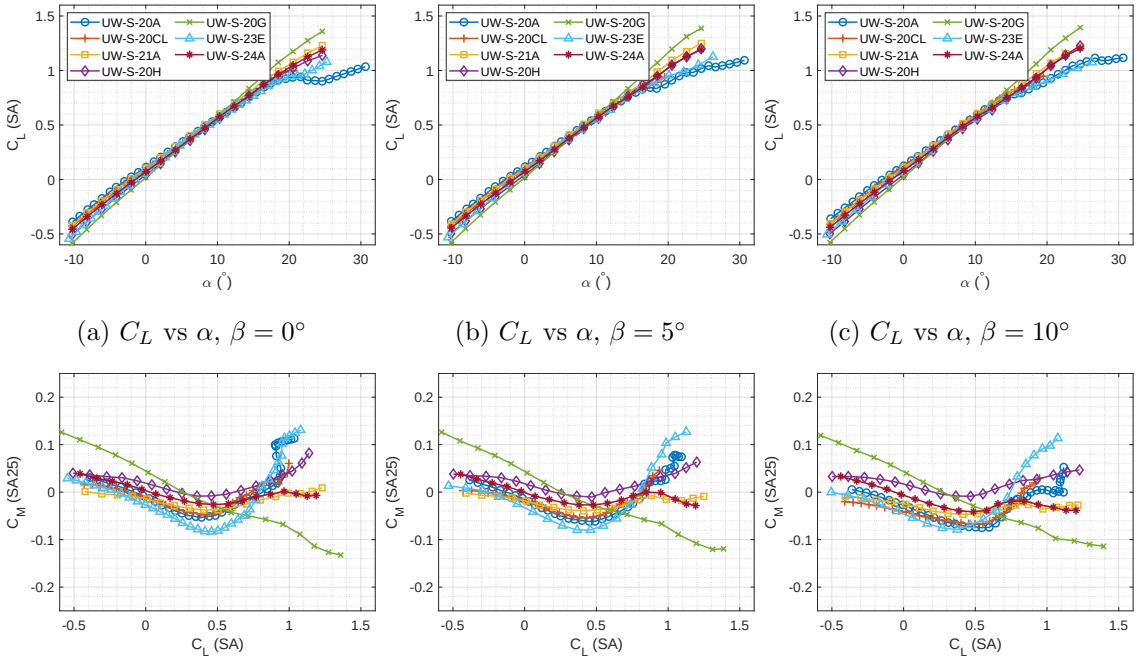
Figure 2.230 shows the effects of SCALOS configurations on the lift and moment at various angles of attacks. The data are also shown for the sideslip angles of $\beta = 0^\circ$, 5°, and 10°. All models were tested at a dynamic pressure of 32 psf corresponding to the Reynolds number of $Re = 2.1x10^6$. However, the UW-S-23E SCALOS model was tested at a dynamic pressure of 6 psf. From Fig. 2.230a it is seen that for $\beta = 0^\circ$ case, all models generate the same lift values for angles of attack of $4^\circ \leq \alpha \leq 12^\circ$, however, for higher angles of attacks, different models show different lift variations for both positive and negative alphas.

The SCALOS models UW-S-21A, UW-S-23G, and UW-S-24A do not show signs of stall at the highest angles of attacks tested, $\alpha \approx 24^\circ$, while other models are seen to stall near $\alpha \approx 20^\circ$. These variations are clearly seen in the pitching moment variations specially on the C_{M_o}, and C_{M_α} values, pitching moment break angles, which are most likely caused by

the addition of different parts, nacelle shape and locations, ventral and dorsal fins, etc. as shown in Tab. 2.27. Similar effects are seen when the models are tested at sideslip angles of $\beta = 5°$, and $10°$ in Figs. 2.230b and 2.230c. Figure 2.230 further shows that the pitch moment behavior of the UW-S-23G that has twin vertical tails and AD16 after deck along with N23.BR nacelle is much different than other SCALOS models. This model does not show any pitch-up or pitch breakdown, for all sideslips and angles of attack tested here, while the other models all show pitch breakdown, statically unstable behavior, near $\alpha \approx 10°$ for all cases shown in Figs. 2.230d, 2.230e, and 2.230f. The pitching moment derivative, $C_{M_\alpha}$for the UW-S-23G model is seen to be negative and constant for angles of attack of up to about $\alpha \approx 20°$ for all cases, while for other models, C_{M_α} is negative and relatively constant up to $\alpha \approx 8.5°$ and create nose up pitch moment, positive C_{M_α}, for higher angles of attack, statically unstable. All models are seen to be stable around zero degrees angle of attack, $C_{M_0} > 0$ with the UW-S-23G model being the most stable one having a relatively large C_{M_0} and negative C_{M_α} for all angles of attack tested. It seems that both UW-S-20A and UW-S-21A tend to regain their static stability around $\alpha \geq 20°$ for all sideslip angles tested.

Figure 2.231 shows the effects of sideslip angles, $\beta = 0°$, $5°$, and $10°$, on the variations of the lateral-directional force and moments coefficients of different SCALOS models shown in Fig. 2.84. At $\beta = 0°$ (Fig. 2.231a-2.231c), all coefficients are zero for all angles of attack tested. The slight deviation from zero values at high angles of attack could be attributed to the model sensitivity to flow separation and unsteady effects. It is seen that UW-S-20A, UW-S-20CL, and UW-S-23E show this type of sensitivity more than other models at high angles of attack. However, the non-zero variations of the lateral-directional force and moment coefficients of UW-S-23E at high angles of attack may be due to the low dynamic pressure, q=6 psf, in which it was tested.

Effects of sideslip angles, $\beta = 5°$ and $10°$ on the lateral-directional force and moments coefficients of the SCALOS models are shown in Figs. 2.231d-2.231f. From these figures, it is seen that for all models both C_Y and C_N have relatively constant non-zero values for angles of attacks of $-10° \leq \alpha \leq 10°$ for both sideslip angles. However, for $\beta = 10°$, variations of C_N vs α is seen to be nonlinear for $\alpha \geq \pm 5°$ which is attributed to the vortex



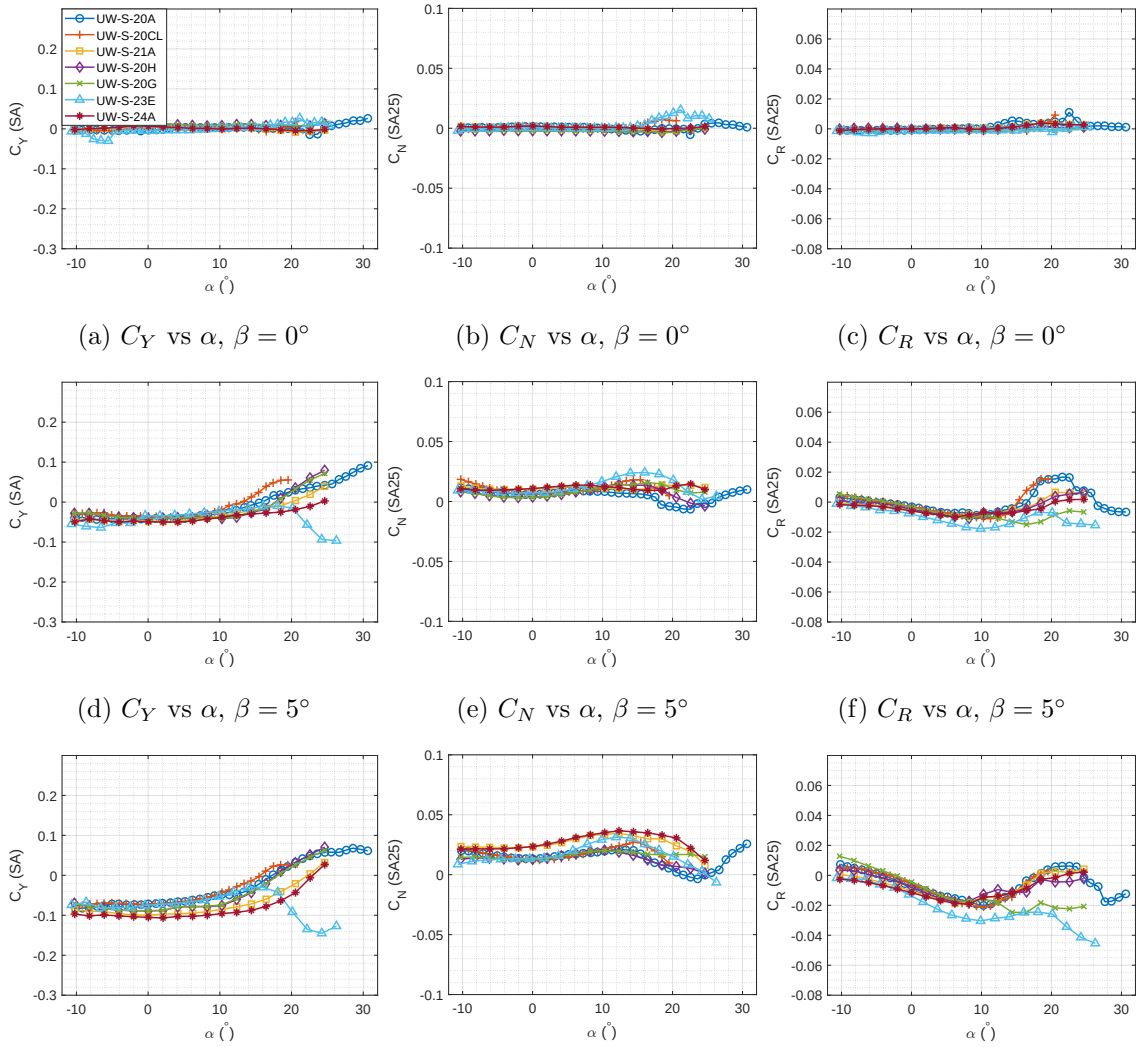
(a) C_L vs α, $\beta = 0°$ (b) C_L vs α, $\beta = 5°$ (c) C_L vs α, $\beta = 10°$

(d) C_M vs. C_L, $\beta = 0°$ (e) C_M vs. C_L, $\beta = 5°$ (f) C_M vs. C_L, $\beta = 10°$

Figure 2.230: Configuration variation longitudinal forces and moments vs. α

formation over the windward wing. For higher angles of attack, this non-linear variation increases with different models showing different values. These nonlinearities are caused by the asymmetrical flow fields as well as the asymmetrical flow separations over different lifting surfaces of the models. All models, except UW-S-23G, are seen to lose their directional control authority when tested at $\beta = 10°$ for angles of attack of $10° \leq \alpha \leq 23°$. For the UW-S-23E that was tested at $q = 6$ psf, the loss of directional control authority occurs between $10° \leq \alpha \leq 19°$ (Fig. 2.231i). Beyond these angles of attack, all models regain their directional control authority as seen in Figs. 2.231h and 2.231i. The UW-S-23G model does not show any loss of directional control authority at all angles of attack and at $\beta = 10°$.

Variations of the lateral-directional force and moment coefficients with sideslip angles for angles of attack of $\alpha = 0°$, $10°$, and $20°$ are shown in Fig. 2.232. As the angle of attack is increased from $0°$ to $10°$, C_{Y_β} remains negative, however, its absolute value for all 4 models decreases. The UW-S-23G model shows an almost linear variation of C_Y vs β for all sideslip angles, while the other three models show slight nonlinearity in their side force variations



(a) C_Y vs α, $\beta = 0°$ (b) C_N vs α, $\beta = 0°$ (c) C_R vs α, $\beta = 0°$

(d) C_Y vs α, $\beta = 5°$ (e) C_N vs α, $\beta = 5°$ (f) C_R vs α, $\beta = 5°$

(g) C_Y vs α, $\beta = 10°$ (h) C_N vs α, $\beta = 10°$ (i) C_R vs α, $\beta = 10°$

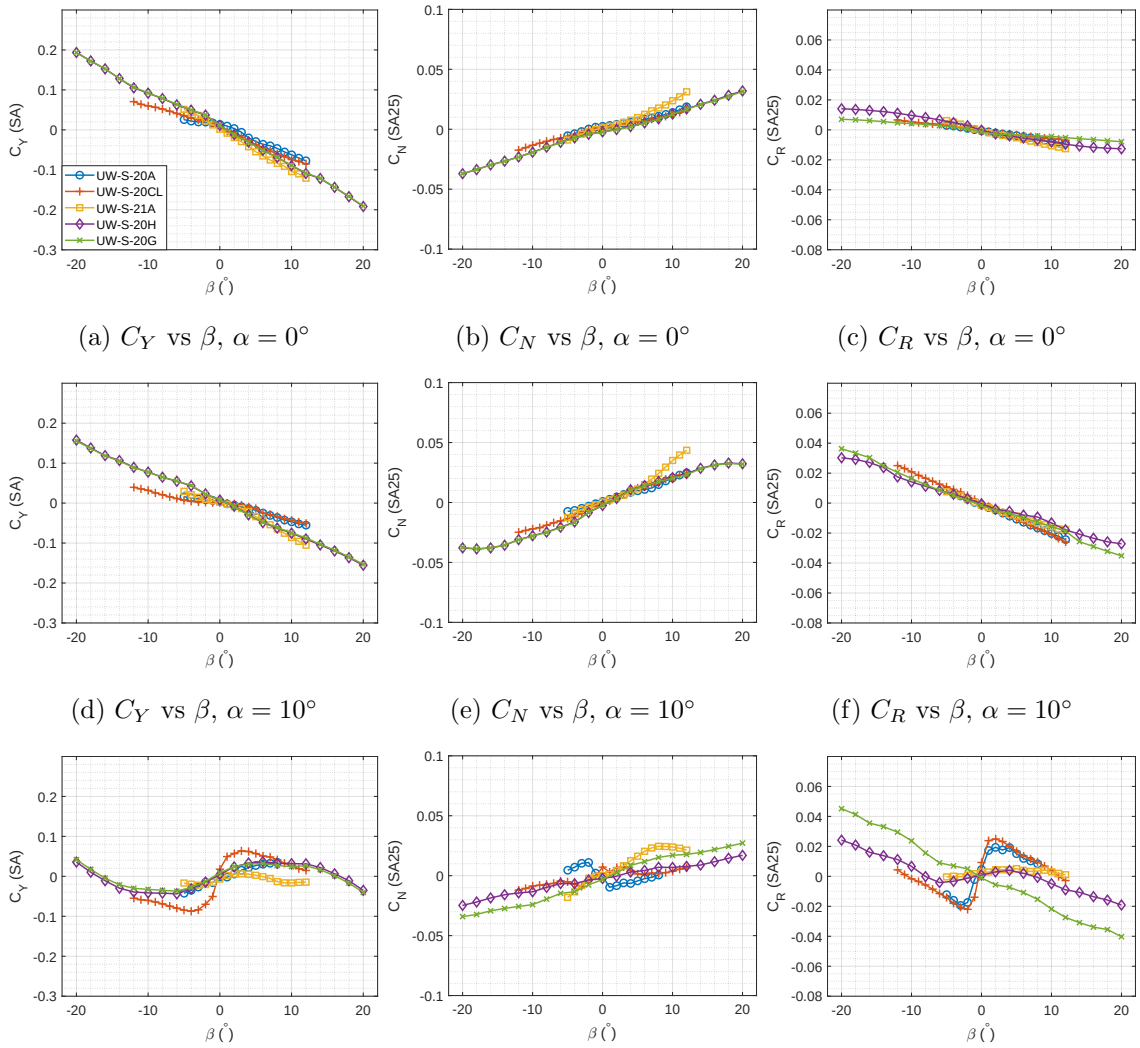
Figure 2.231: Configuration variations lateral directional forces and moments vs. α

with sideslip angle and the non-linearity increases as alpha increases from 0° to 10°.

For the largest angles of attack, $\alpha = 20°$, Fig. 2.232g shows that C_Y for all four SCALOS models varies nonlinearly with sideslip angles. It is clearly seen in Fig. 2.232g that near zero sideslip angle the side force slope becomes very large for the UW-S-20CL model and has positive slopes for the other three models, yaw reversal (directional divergence). For $\beta \geq 3°$, all models tend to regain their negative side force slope, $C_{Y_\beta} < 0$.

The yawing moment coefficient variations for all models show positive C_{N_β} and its value

decreases with increasing angles of attack in Figs. 2.232b, 2.232e, and 2.232h. Similar to the side force coefficient variations near $\beta = 0°$, the UW-S-20A model shows yaw divergence (weathercock instability) but regains its stability for $\beta \geq 2°$ in Fig. 2.232h. The UW-S-23G model is seen to have very close to linear variations of C_N vs β for all angles of attack tested while the other three models show nonlinearity as alpha increases from 0° to 20°. The roll stability of the models for various sideslip angles and for three angles of attack are shown in Figs. 2.232c, 2.232f, and 2.232i. All four models have stable dihedral derivative, $C_{R_\beta} < 0$, for angles of attack of 0° to 20° with almost constant C_{R_β}. The absolute values of C_{R_β} for all models increase as alpha increases from 0° to 10°. Note that the notation C_{R_β} is used here (following the notation used by the KWT) and not the more common C_{l_β} notation for a rolling moment derivative. Both the UW-S-20A and UW-S-20CL models show very large positive C_{R_β} for $-2° \leq \beta \leq 3°$ at $\alpha = 20°$, large roll reversal, like the side force and yaw moment coefficient, Figs. 2.232g and 2.232b, with a loss of directional authority, while C_{R_β} for the UW-S-23G model remains stable. This instability will affect the roll and spiral modes as well as the Dutch roll behavior. Both the UW-S-20A, and UW-S-20CL models regain their directional control authority at $\beta \geq 3°$. Table. 2.12 shows that the UW-S-23G model is equipped with an aft-deck and a twin vertical tail, both of which may have a significant influence on the lateral directional stability of the SCALOS configurations. At $\alpha = 20°$, the leading-edge vortex of the windward wing is reduced by breakdowns, and vortex bursts cover a large portion of the wing surface; hence, reducing the lift force of the windward wing while that of the leeward one might still be only mildly affected. This imbalance of the lift of the windward and leeward wings lift forces creates rolling and yawing moments. Apparently, both aft-deck and twin vertical tails of the UW-S-23G model significantly reduce these nonlinearities. The aft deck produces an extra lift which would counteract the loss of the lift due to vortex bursting and flow separation on the wing surface. In any effort to understand the aerodynamics of SCALOS configurations at sideslip and at high angles of attack, it is important to examine the effects of the front fuselage and the vortex action it creates – by itself and with its canards and chines.



(a) C_Y vs β, $\alpha = 0°$ (b) C_N vs β, $\alpha = 0°$ (c) C_R vs β, $\alpha = 0°$

(d) C_Y vs β, $\alpha = 10°$ (e) C_N vs β, $\alpha = 10°$ (f) C_R vs β, $\alpha = 10°$

(g) C_Y vs β, $\alpha = 20°$ (h) C_N vs β, $\alpha = 20°$ (i) C_R vs β, $\alpha = 20°$

Figure 2.232: Configuration variations lateral directional forces and moments vs. β

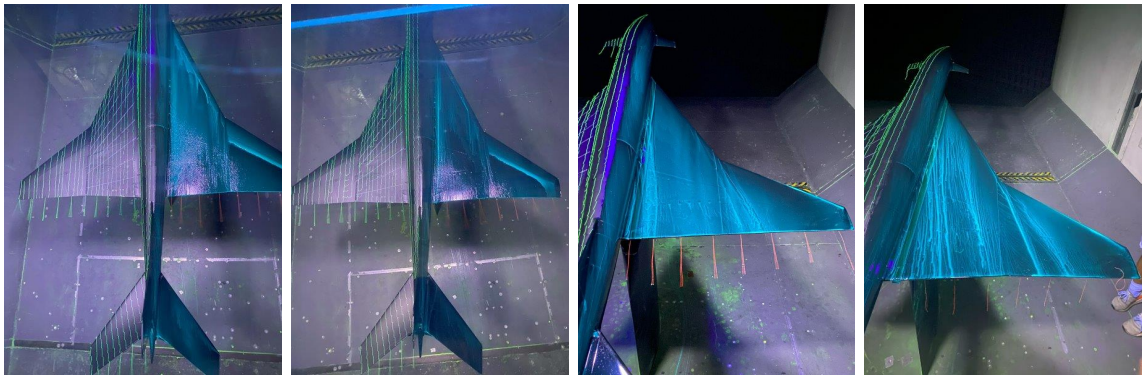
2.9.2 Flow Visualization Correlation

Figures 2.233 - 2.235 show the effects of sideslip angles on the oil flow visualization as well as longitudinal and lateral directional force and moment coefficients of the UW-S-21A SCALOS model at various sideslips and angles of attack. The UW-S-21A model is a three-surface configuration with canards and a conventional empennage system with a single vertical tail and low horizontal tails. Effects of angles of attack on the longitudinal aerodynamic coefficients of this model have been discussed in detail in previous sections §2.7

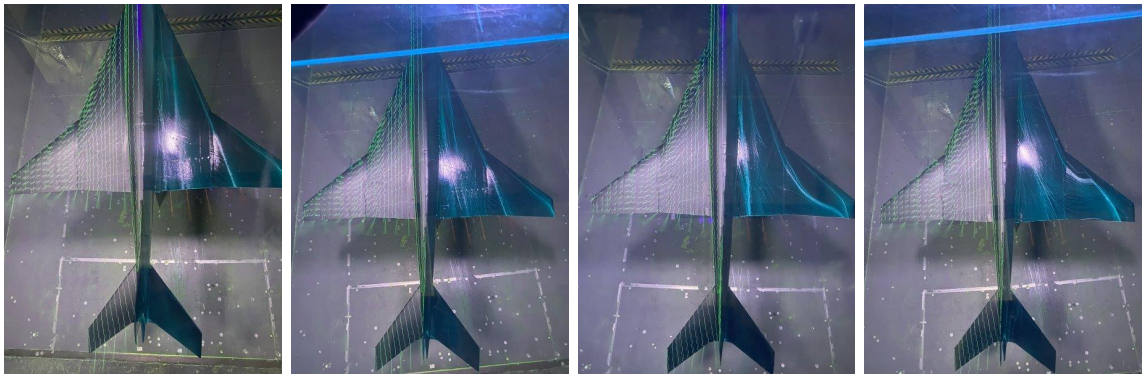
[15, 23, 24, 371, 384]. As the model is yawed, the effective sweep angle of the windward wing decreases while that of the leeward one increases, resulting in asymmetric vortex formation, location, and breakdown. The asymmetries of the vortices result in differences in the lift on each side of the wing with respect to angles of attack. As the angle of attack increases, the windward wing vortex will form and burst sooner at more upstream locations than that of the leeward vortex. These differences are responsible for typical longitudinal, lateral, and directional instabilities, such as a pitch-up, a roll reversal, and directional divergence, respectively.

Minimal differences are shown in the oil flow visualization between $\beta = 0^\circ$ and 5° up to $\alpha < 15^\circ$ in Fig. 2.234. However, distinct differences between the two sideslip angles are shown at $\alpha \geq 15^\circ$. For $\beta = 0^\circ$, the inboard vortex breakdown moves onto the wing surface at $\alpha \approx 15^\circ$ for both left- and right-wing surfaces. For $\beta = 5^\circ$, the windward wing vortex bursts over the wing surface at lower angles of attack than that of the leeward one. The breakdown of both vortices over the wing surface decreases the lift at the wing's trailing edge, resulting in a pitch-up tendency. For $\alpha \geq 20^\circ$, both burst vortices for $\beta = 0^\circ$ and 5° move upstream toward the wing apex, resulting in another strong pitch-up tendency seen in Fig. 2.235.

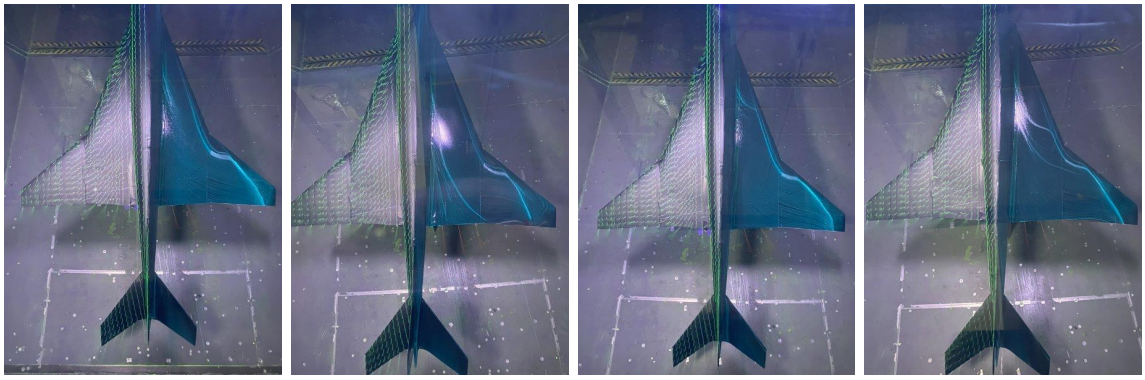
Figure 2.234 shows the effects of sideslip angles on the longitudinal forces and moments of the model. Up to $\alpha \approx 12^\circ$, C_{L_α} does not vary with sideslip angle. For $\alpha \geq 12^\circ$, C_{L_α} decreases slightly with increasing sideslip angle. The maximum lift-to-drag ratio, $C_L/C_{D_{\max}}$, is significantly affected by the sideslip angle in Fig. 2.234c. Figures 2.234d - 2.234f show variations of the lateral directional force and moments coefficients with angles of attack for sideslip angles of $\beta = 0^\circ$, 2°, 5°, and 10°. As the sideslip angle is increased absolute values of all three coefficients at zero degrees angle of attack increase and their variations with angles of attack are seen to be constant for $\beta = 0^\circ$ and 2°, For $\beta = 5^\circ$, both C_Y and C_N do not vary significantly with the angle of attack, while C_R decreases linearly up to $\alpha \approx 10^\circ$. With further increase of alpha, C_R increases and becomes almost zero for $\alpha \geq 18^\circ$. A similar trend is seen for the C_R variations with angles of attack for $\beta = 10^\circ$ in Fig. 2.234f. The slope of the rolling moment coefficient with alpha at $\beta = 5^\circ$ is much smaller than $\beta = 10^\circ$. These differences are due to differences in the strength of the leeward and windward vor-



(a) $\beta = 0°$, $\alpha = 0°$ (b) $\beta = 5°$, $\alpha = 0°$ (c) $\beta = 0°$, $\alpha = 5°$ (d) $\beta = 5°$, $\alpha = 5°$



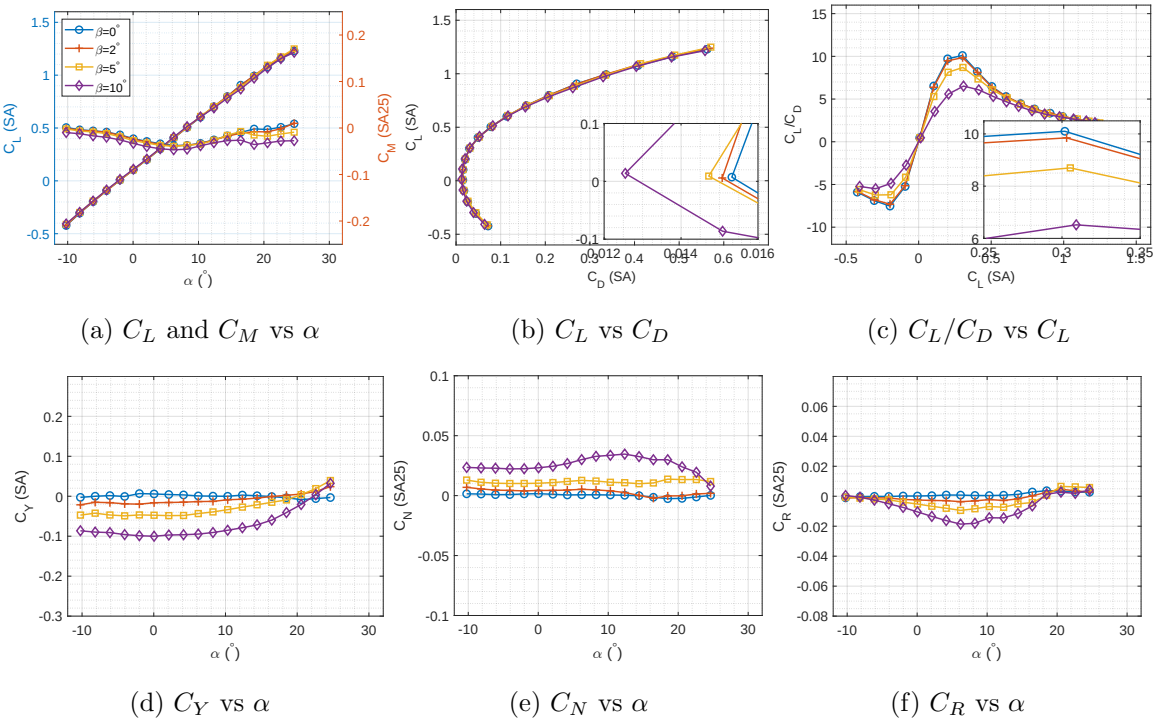
(e) $\beta = 0°$, $\alpha = 10°$ (f) $\beta = 5°$, $\alpha = 10°$ (g) $\beta = 0°$, $\alpha = 15°$ (h) $\beta = 5°$, $\alpha = 15°$



(i) $\beta = 0°$, $\alpha = 20°$ (j) $\beta = 5°$, $\alpha = 20°$ (k) $\beta = 0°$, $\alpha = 25°$ (l) $\beta = 5°$, $\alpha = 25°$

Figure 2.233: UW-S-21A without nacelle Flow Visualization at $\beta = 0°$ and $\beta = 5°$ [27]

tices. For all sideslip angles tested, Fig. 2.234f shows that the rolling moment coefficient becomes almost zero for $\alpha \geq 19°$ which indicates that both windward and leeward vortices are burst over a large portion of the wing surfaces.

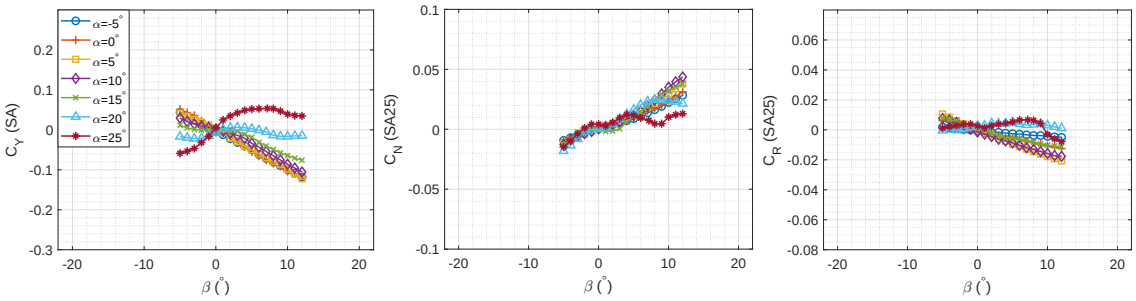


(a) C_L and C_M vs α (b) C_L vs C_D (c) C_L/C_D vs C_L

(d) C_Y vs α (e) C_N vs α (f) C_R vs α

Figure 2.234: UW-S-21A forces and moments vs. α

Figure 2.235 shows the effects of the angle of attack on the variations of the lateral-directional force and moments with sideslip angles. At low angles of attack, $-5° \leq \alpha \leq 5°$, all three coefficients vary almost linearly with sideslip angles. For larger angles of attack, $\alpha \geq 5°$, the variations become non-linear, and the non-linearity increases as alpha is increased. As aforementioned, these non-linear variations are due to the asymmetrical vortices forming over the windward and leeward wing surfaces which create asymmetric lift on the wing surfaces, resulting in the rolling and yawing moment variations.



(a) C_Y vs β (b) C_N vs β (c) C_R vs β

Figure 2.235: UW-S-21A forces and moments vs. β

2.9.3 Canard Deflection

The UW-S-20A model, shown in Fig. 2.220 and Tab. 2.12 in §2.2, is a three-surface configuration with canards, top-mounted nacelles, and a T-tail empennage system. The canard rotations range from $\delta_C = -30°$ to $30°$. Figure 2.236 shows the lift and pitching moment coefficients of this model for different canard rotations at angles of attack at $\beta = 0°$, $5°$, and $10°$. For all sideslip angles tested, the model shows a pitch-up tendency at about $8° \leq \alpha \leq 10°$ as seen from Figs. 2.236d - 2.236f. This pitch-up tendency is caused by the flow separation over the outboard section of the wing surfaces which also reduces C_{L_α}. At $\beta = 0°$, the canard rotations do not change the lift values prior to $\alpha \approx 15°$, which is the angle of attack when both inboard and outboard vortices start to merge over the wing surface as in Fig. 2.233. Beyond $\alpha \approx 15°$, the vortex burst decreases the local lift at the trailing-edge section of the wing, resulting in further pitch-up tendency of the model. The inboard vortex at the inboard section of the wing increases in strength near $\alpha > 15°$ resulting in an increase in the lift for $\delta_C = -15°$ to $+30°$ up to $\alpha \approx 22°$. For $\delta_C = -30°$, the maximum lift, $C_{L_{\max}}$, occurs at $\alpha \approx 18°$ as seen in Fig. 2.236a. For $\delta_C = -15°$ and $-30°$, the reductions of $C_{L_{\max}}$ and $\alpha_{C_{L_{\max}}}$ are due to the massive flow separation over the lower surface of the canard and the corresponding wake it generates, affecting the flow field over the wing surface and reducing the inboard vortex strength.

Overall Fig. 2.236 shows that canard rotation reduces both $C_{L_{\max}}$ and stall angle of attack. The pitching moment variations with angles of attack with canard rotations show that C_{M_0} is proportional to canard rotations but C_{M_α} remain almost constant except for

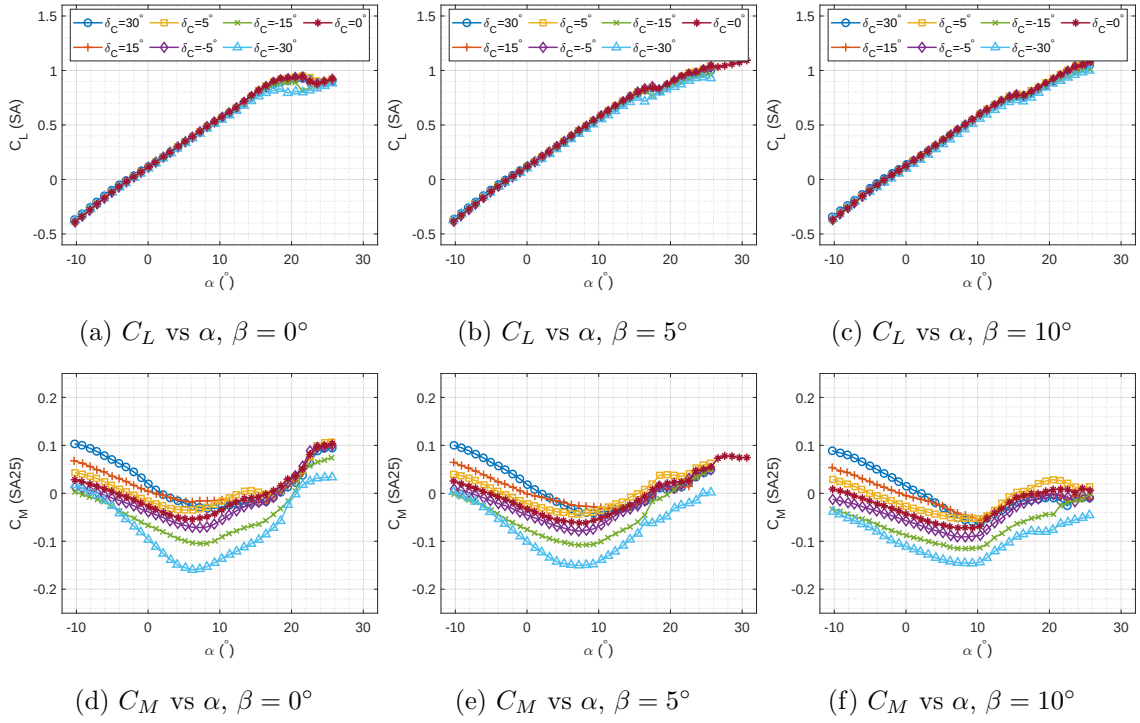
$\delta_C = \pm 30°$. The values of $C_{M_0} > 0$ for all canard rotation angles indicate static longitudinal stability with respect to the chosen moment reference point. For $\beta = 10°$, $C_{M_0} < 0$ for $\delta_C = -5°$, $-15°$, and $-30°$ in Fig. 2.236f, which indicates that for these canard rotation angles the model cannot be trimmed at positive angles of attack at $\beta = 10°$. Positive canard rotations increase C_{M_0} while negative rotations have the reverse effects in Figs 2.236d - 2.236f.

The pitch-up angle (the transition to longitudinal instability) does not vary with canard deflections for $8° \leq \alpha \leq 10°$, but C_{M_α} beyond the pitch-up angle is reduced significantly, especially for $\beta = 10°$ in Fig. 2.236f. Figure 2.236d shows that this T-tail configuration gets into deep stall around $\alpha \approx 22°$ at $\beta = 0°$, caused probably by the wake of the wing affecting the tail.

The lift force coefficients do not vary significantly at $\beta = 0°$ and $5°$. A kink in the C_L variation is observed for $\beta = 5°$ and $10°$. The kink happens at $\alpha \approx 18°$ for $\beta = 5°$ while for $\beta = 10°$, it occurs at $\alpha \approx 15°$. Of course, its location varies slightly with the canard rotation angle too. Beyond the kinks, the lift increases for both sideslip angles with respect to increasing the angle of attack. The present kinks in the lift variation for $\beta \neq 0°$ are due to the asymmetric vortex formation, vortex merging, and vortex burst reaching the windward and leeward portions of the wing surfaces and moving toward the wing apex as the angles of attack are increased. For both sideslip angles shown here, no sign of stalls is seen from Figs. 2.236b and 2.236c while for the zero-sideslip case, a clear stall for all canard rotations is noticed in 2.236a. Figures 2.236d - 2.236f show that the pitch-up break angle of attack has been affected by the sideslip angle too. For the zero-sideslip angle, the pitch-up break angle for all canard rotations occurs at about $8° \leq \alpha \leq 9°$, while for $\beta = 10°$, this happens at $\alpha > 10°$.

Effects of canard rotations on the variations of the lateral-directional force and moment coefficients of the UW-S-20A model with angles of attack for three different sideslip angles of $\beta = 0°$, $5°$, and $10°$ degrees are shown in Figs. 2.237 and 2.238. For all cases examined, this figure shows that canard does not have significant effects on the directional control behavior of this SCALOS model.

For the $\beta = 10°$, it is seen that the value of C_R at $\alpha = 0°$ is affected by the canard

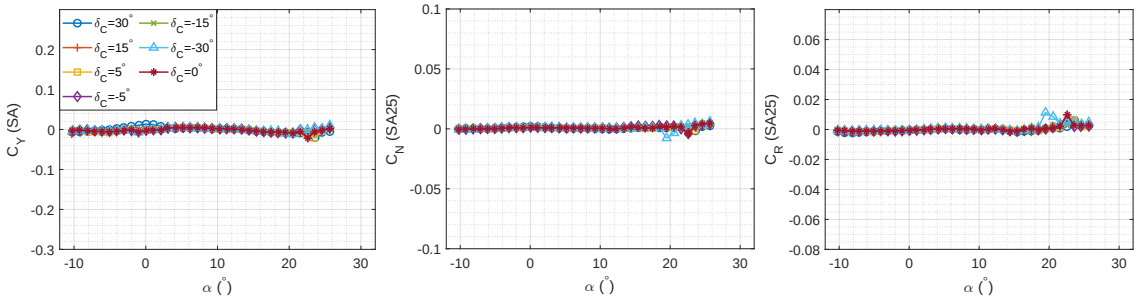


(a) C_L vs α, $\beta = 0°$ (b) C_L vs α, $\beta = 5°$ (c) C_L vs α, $\beta = 10°$

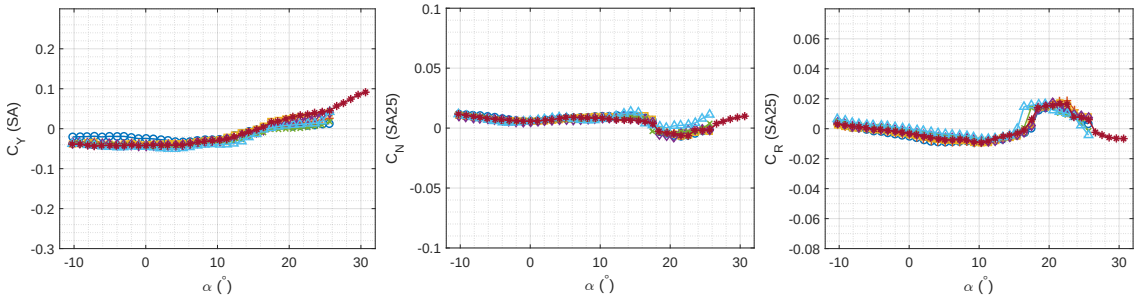
(d) C_M vs α, $\beta = 0°$ (e) C_M vs α, $\beta = 5°$ (f) C_M vs α, $\beta = 10°$

Figure 2.236: UW-S-20A with canard deflections longitudinal forces and moments vs. α

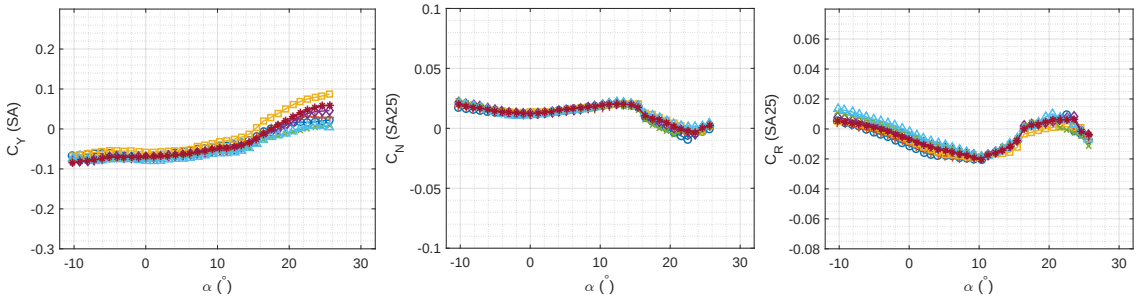
rotation angel while its slope C_{R_β} has not been influenced notably in Fig. 2.237i. For all canard settings, Figs. 2.237f and 2.237i show that this model loses directional roll as well as side weathercock control stability when set to $\beta = 5°$ and $10°$ for $10° < \alpha \leq 20°$. This is most likely caused by the asymmetrical vortex burst moving onto the wing surface toward the wing apex. For higher angles of attack, it seems that the model regains its roll control authority, but C_Y remains positive. Figure 2.238 shows that for $-10° \leq \beta \leq 10°$ at $\alpha = 0°$ and $10°$ this model has directional control force derivatives,$C_{Y_\beta} < 0$, $C_{N_\beta} > 0$, $C_{R_\beta} < 0$, and canard rotation does not have a significant influence on their variations.



(a) C_Y vs α, $\beta = 0°$ (b) C_N vs α, $\beta = 0°$ (c) C_R vs α, $\beta = 0°$

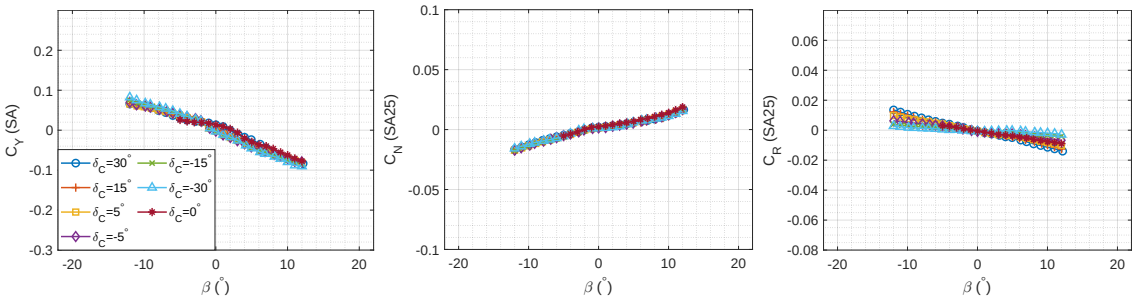


(d) C_Y vs α, $\beta = 5°$ (e) C_N vs α, $\beta = 5°$ (f) C_R vs α, $\beta = 5°$

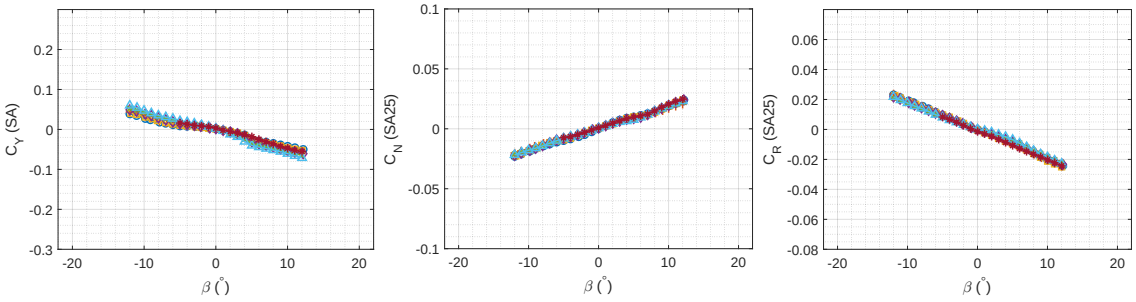


(g) C_Y vs α, $\beta = 10°$ (h) C_N vs α, $\beta = 10°$ (i) C_R vs α, $\beta = 10°$

Figure 2.237: UW-S-20A with canard deflections lateral directional forces and moments vs. α



(a) C_Y vs β, $\alpha = 0°$ (b) C_N vs β, $\alpha = 0°$ (c) C_R vs β, $\alpha = 0°$



(d) C_Y vs β, $\alpha = 10°$ (e) C_N vs β, $\alpha = 10°$ (f) C_R vs β, $\alpha = 10°$

Figure 2.238: UW-S-20A with canard deflections forces and moments vs. β

2.9.4 Directional Control Authority

UW-S-20A

Figure 2.239 shows the UW-S-20A model where its vertical tail is equipped with a rudder that is rotated by $\delta_{\mathrm{R}} = 0°$, $+10°$, and $+20°$. The model has a T-tail configuration and is equipped with both canard and top-mounted nacelles. The effects of angles of attack on the lateral and directional characteristics of this SCALOS configuration at several sideslip angles, $\beta = 0°$, $2°$, $5°$ and $10°$, for the three different rudder rotations mentioned above are shown in Fig. 2.240. Positive rolling and yawing moments indicate a right wing down rotation and a right nose rotation of the aircraft respectively. For an aircraft to be both laterally and directionally stable, $C_{N_\beta} > 0$, and $C_{R_\beta} < 0$. If the sign of these stability derivatives changes, static instability will appear.



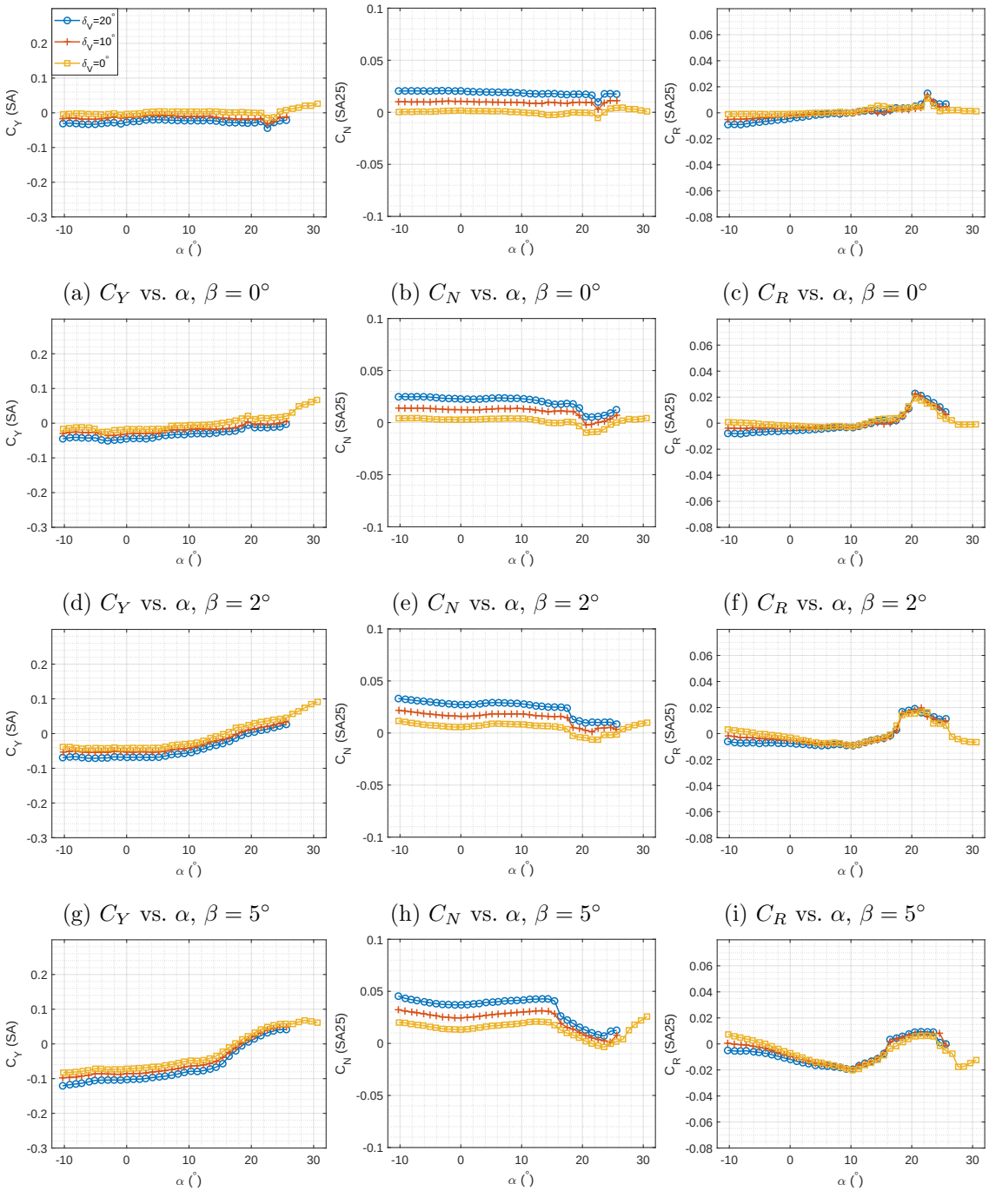
(a) $\delta_R = 0°$ (b) $\delta_R = +10°$ (c) $\delta_R = +20°$

Figure 2.239: UW-S-20A with vertical tail deflections

Figure 2.240 shows that at $-10° \leq \alpha \leq 10°$, the model has both lateral and directional stability for all side slip angles tested. As mentioned before, for these angles of attack, both windward and leeward vortices are stable. Their strength varies due to the larger and smaller wing surface that they cover i.e. the leeward vortices cover a smaller effective wing surface while those of the windward ones cover a larger wing surface. As a result, the lift of the windward side of the wing is larger than that of the leeward one, creating a rolling moment to the right and a nose-right rotation of the aircraft. It should be noted that the windward vortex over a portion of the wing might burst, but the remaining unburst portion of the vortex may be still strong enough to create enough lift that is larger than that of the right wing, leeward wing.

The rudder deflections do not seem to have significant effects on the slope of the lateral and directional characteristics of the model for these angles of attack. As δ_{R} is varied, the curves shift. Note that C_Y, C_N, and C_R are zero at $\beta = 0^\circ$ and $\delta_{\mathrm{R}} = 0^\circ$, but when the $\delta_{\mathrm{R}} \neq 0^\circ$, the values of these coefficients at $\beta = 0^\circ$ change. At $\beta = 5^\circ$ and 10°, Fig. 2.240 shows that rudder rotations did not significantly change the rolling moment variation of the model with angles of attack.

At $\alpha = 20^\circ$, Fig. 2.240 shows that both lateral and directional stability derivatives change signs due to the asymmetric vortex breakdown over the windward and leeward wing sections. The burst leading-edge vortex moves upstream at the windward, reducing the lift of the windward side, which is responsible for the roll reversal. Figure 2.241 shows that for all three rudder rotations lateral directional force and moments vary linearly with sideslip angle variations of $-10^\circ \neq \beta \neq 10^\circ$ for $\alpha = 0^\circ$, 5°, 10°, and 15° with stable values, $C_{Y_\beta} < 0$, $C_{N_\beta} > 0$, $C_{R_\beta} < 0$. When $\alpha \approx 20^\circ$, both C_N ,and C_R show yaw and roll reversals around $-2^\circ \neq \beta \neq 3^\circ$ in Figs. 2.241k and 2.241l, as seen before. For larger sideslip angles, the model regains its lateral-directional stability.



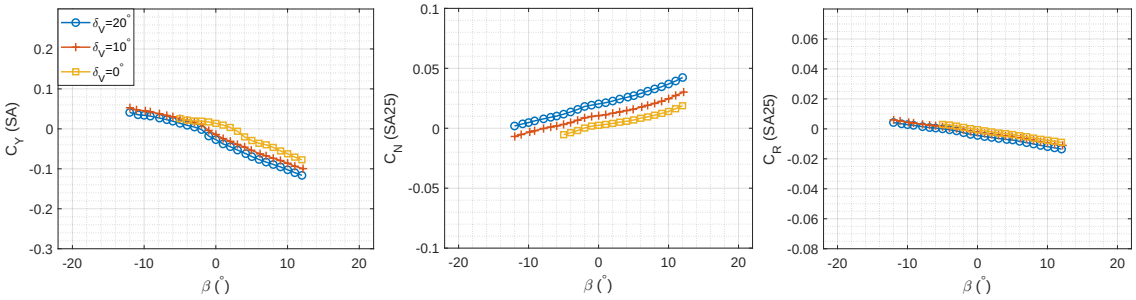
(a) C_Y vs. α, $\beta = 0°$ (b) C_N vs. α, $\beta = 0°$ (c) C_R vs. α, $\beta = 0°$

(d) C_Y vs. α, $\beta = 2°$ (e) C_N vs. α, $\beta = 2°$ (f) C_R vs. α, $\beta = 2°$

(g) C_Y vs. α, $\beta = 5°$ (h) C_N vs. α, $\beta = 5°$ (i) C_R vs. α, $\beta = 5°$

(j) C_Y vs. α, $\beta = 10°$ (k) C_N vs. α, $\beta = 10°$ (l) C_R vs. α, $\beta = 10°$

Figure 2.240: UW-S-20A with rudder deflections forces and moments vs. α



(a) C_Y vs. β, $\alpha = 0°$ (b) C_N vs. β, $\alpha = 0°$ (c) C_R vs. β, $\alpha = 0°$

(d) C_Y vs. β, $\alpha = 10°$ (e) C_N vs. β, $\alpha = 10°$ (f) C_R vs. β, $\alpha = 10°$

(g) C_Y vs. β, $\alpha = 15°$ (h) C_N vs. β, $\alpha = 15°$ (i) C_R vs. β, $\alpha = 15°$

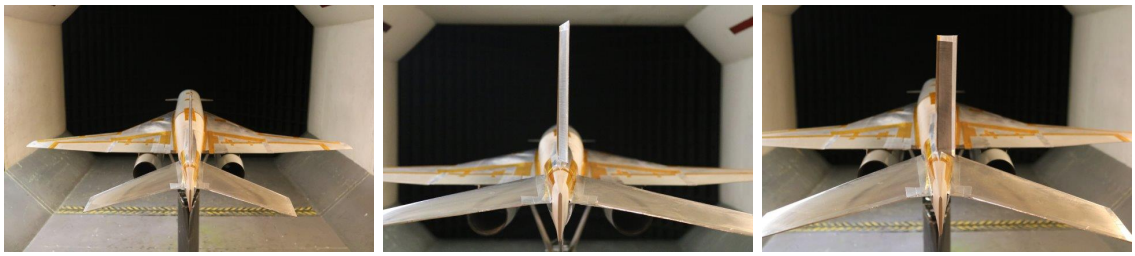
(j) C_Y vs. β, $\alpha = 20°$ (k) C_N vs. β, $\alpha = 20°$ (l) C_R vs. β, $\alpha = 20°$

Figure 2.241: UW-S-20A with rudder deflections forces and moments vs. β

UW-S-21A

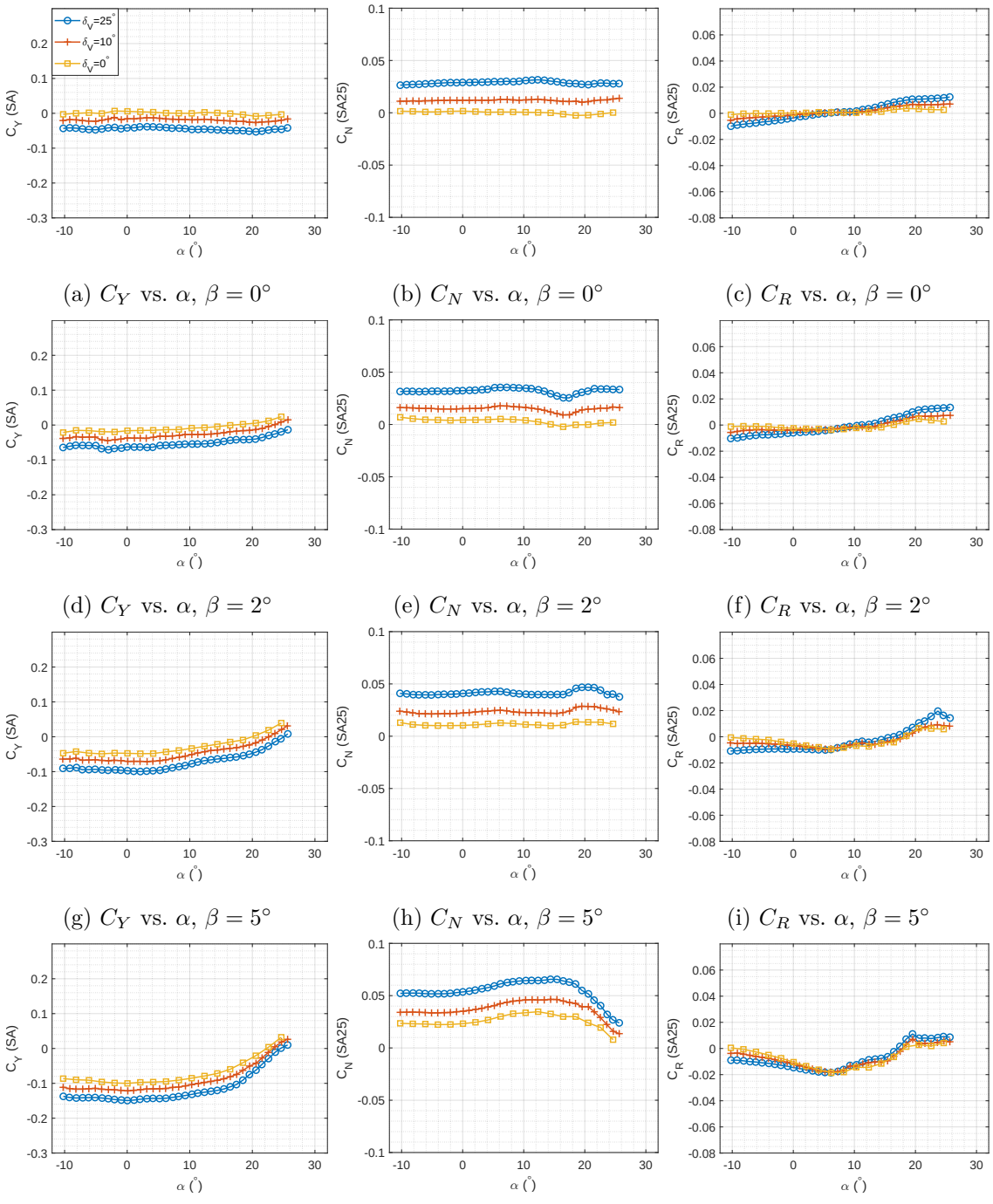
Figure 2.242 shows three photos of the UW-S-21A SCALOS model, which is equipped with bottom nacelles, low-tail empennage system as in Tab. 2.12 in §2.2. The rudder is rotated at $\delta_R = 0°$, $+10°$, and $+20°$. There are some differences between the UW-S-21A and UW-S-20A models (see Fig. 2.49 and Tab. 2.27 for more information). Similar to the UW-S-20A model, the UW-S-21A SCALOS model was tested at various sideslip angles, $\beta = 0°$, $2°$, $5°$ and $10°$, and a range of angles of attack. Figures 2.243 and 2.244 show effects of rudder rotations on the variations of the lateral-directional force and moments with angles of attack for different sideslip angles and with angles of attack of $\alpha = 0°$, $5°$, $10°$, $15°$, and $20°$. The variations of aerodynamic characteristics are very similar to those of the UW-S-20A model shown in Figs. 2.243 and 2.244. It seems that rudder rotations have larger effects on directional stability derivatives. It is noted that the loss of directional control authority seen at $\alpha = 20°$ for a certain range of sideslip angles for the UW-S-20A model in Figs. 2.244k and 2.244l does not exist for this model at similar test conditions in Figs. 2.244k and 2.244l.

At $\alpha = 20°$, $C_{R_\beta} \approx 0$ for all three rudder rotation angles in Fig. 2.244l while $C_{N_\beta} > 0$. There exists a plateau in the C_N vs β curves near $\beta = 0°$ in Figs. 2.244h and 2.244i where C_N remains constant as β is increased at $\alpha = 15°$ and $20°$. In contrast to the dihedral stability derivative, both side force and yaw moment coefficients vary nonlinearly with sideslip angles for angles of attack of $\alpha \geq 10°$ as shown in Fig. 2.244. For $\alpha = 20°$, Fig. 2.244k shows that for sideslip angles $\beta \geq 8°$, $C_{N_\beta} \approx 0$, loss of rudder effectiveness, i.e. as the sideslip angle is increased, these rudder rotations, $\delta_R = +10°$ and $+20°$, are not capable of producing further yaw moment. Apparently, for this large angle of attack, the entire empennage system is immersed in the separated flow of the canard, wing, and fuselage.



(a) $\delta_{VT} = 0°$ (b) $\delta_{VT} = +10°$ (c) $\delta_{VT} = +25°$

Figure 2.242: UW-S-21A with rudder deflections



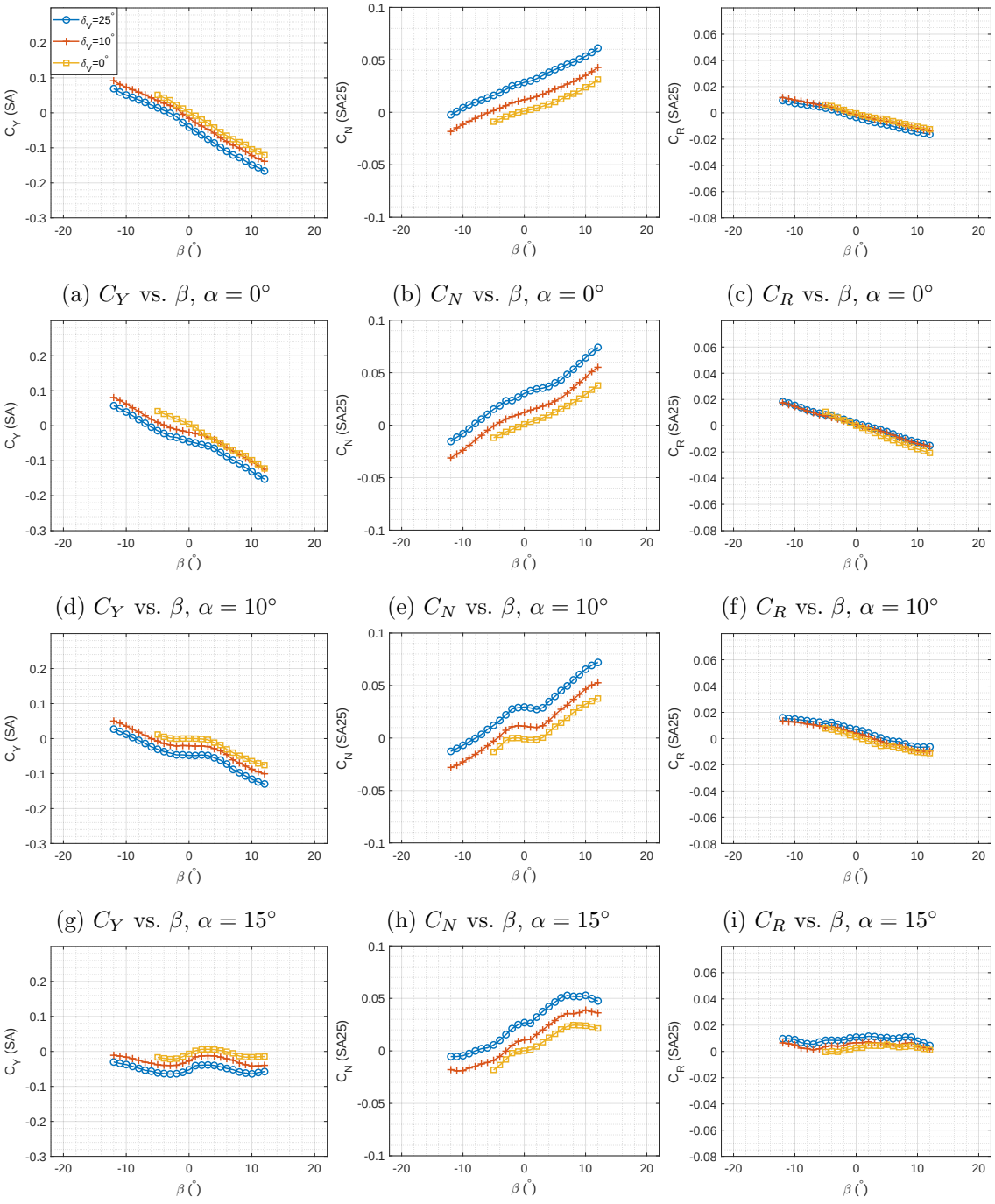
(a) C_Y vs. α, $\beta = 0°$ (b) C_N vs. α, $\beta = 0°$ (c) C_R vs. α, $\beta = 0°$

(d) C_Y vs. α, $\beta = 2°$ (e) C_N vs. α, $\beta = 2°$ (f) C_R vs. α, $\beta = 2°$

(g) C_Y vs. α, $\beta = 5°$ (h) C_N vs. α, $\beta = 5°$ (i) C_R vs. α, $\beta = 5°$

(j) C_Y vs. α, $\beta = 10°$ (k) C_N vs. α, $\beta = 10°$ (l) C_R vs. α, $\beta = 10°$

Figure 2.243: UW-S-21A with vertical tail deflections forces and moments vs. α



(a) C_Y vs. β, $\alpha = 0°$ (b) C_N vs. β, $\alpha = 0°$ (c) C_R vs. β, $\alpha = 0°$

(d) C_Y vs. β, $\alpha = 10°$ (e) C_N vs. β, $\alpha = 10°$ (f) C_R vs. β, $\alpha = 10°$

(g) C_Y vs. β, $\alpha = 15°$ (h) C_N vs. β, $\alpha = 15°$ (i) C_R vs. β, $\alpha = 15°$

(j) C_Y vs. β, $\alpha = 20°$ (k) C_N vs. β, $\alpha = 20°$ (l) C_R vs. β, $\alpha = 20°$

Figure 2.244: UW-S-21A with vertical deflections forces and moments vs. β

2.9.5 Nacelle locations and Engine-out conditions

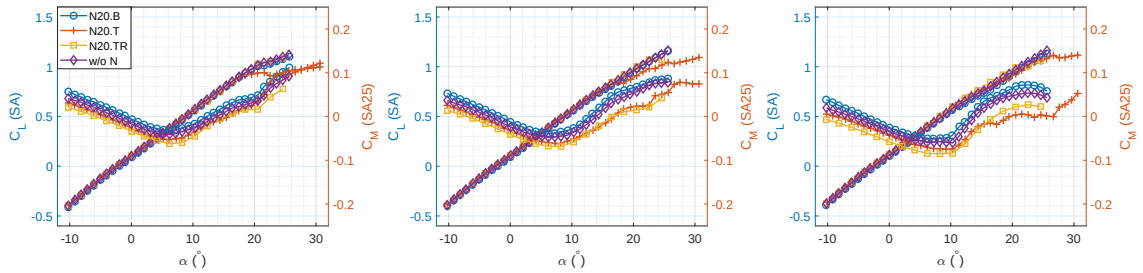
Nacelle locations

In this section, the effects of nacelle locations on the aerodynamic forces and moments of the UW-S-20 models are investigated. Four photos of the UW-S-20A SCALOS models with /without nacelles are shown in Fig. 2.138 in §2.7.7. The nacelles are located on the bottom and top of the wing and on the sides of the fuselage as shown in Figs. 2.138b, 2.138c, and 2.138d, respectively. Details of the models are given in Tab. 2.12 in §2.2. All experimental force and moments are obtained at a dynamic pressure of $q = 32$ psf, corresponding to the Reynolds number of $Re = 2.1 \times 10^6$.

Figure 2.245 shows variations of the lift and moment of the model with different nacelle locations with angles of attack for sideslip angles of $\beta = 0°$, $5°$, and $10°$. The figure shows that nacelle locations do not have significant effects on the lift variations of the model, except for the top-mounted nacelle model, N20.T, which stalls at $\alpha \approx 20°$ for $\beta = 0°$ in Fig. 2.245a. For other nacelle locations, the lift coefficient slopes are seen to be reduced slightly around $\alpha \approx 20°$, but it does not seem that the models are stalled.

For other sideslip angles, variations of the lift coefficient with angles of attack are similar and only C_{L_α}'s are affected by the sideslip angles. As β increases, C_{L_α} for all four cases are seen to be reduced. Nacelle locations have effects on the C_{M_0}, where the model with N20.B has largest C_{M_0} and N20.TR has the smallest C_{M_0}. Nacelle locations do not have significant effects on the slope of the pitching moment curve, C_{M_α}, prior to the pitch-up longitudinal instability initiation angle of attack. The pitch-up occurrence angle of attack for all cases is seen to be at about $\alpha \approx 8°$ and it increases slightly with sideslip angle in Fig. 2.245. Sideslip angle reduces $C_{M_0}$for all models. Therefore, for the models to be trimmable at positive angles of attack when yawed, other means of control, canard deflection, for example, should be employed.

Figure 2.246 shows variations of the lateral-directional force and moment coefficients with angles of attack for side slip angles of $\beta = 0°$, $5°$, and $10°$ for all different nacelle locations. For $\beta = 0°$, all coefficients for all cases are zero for all angles of attack. The slight non-zero values of the coefficients at high angles of attack are caused by massive

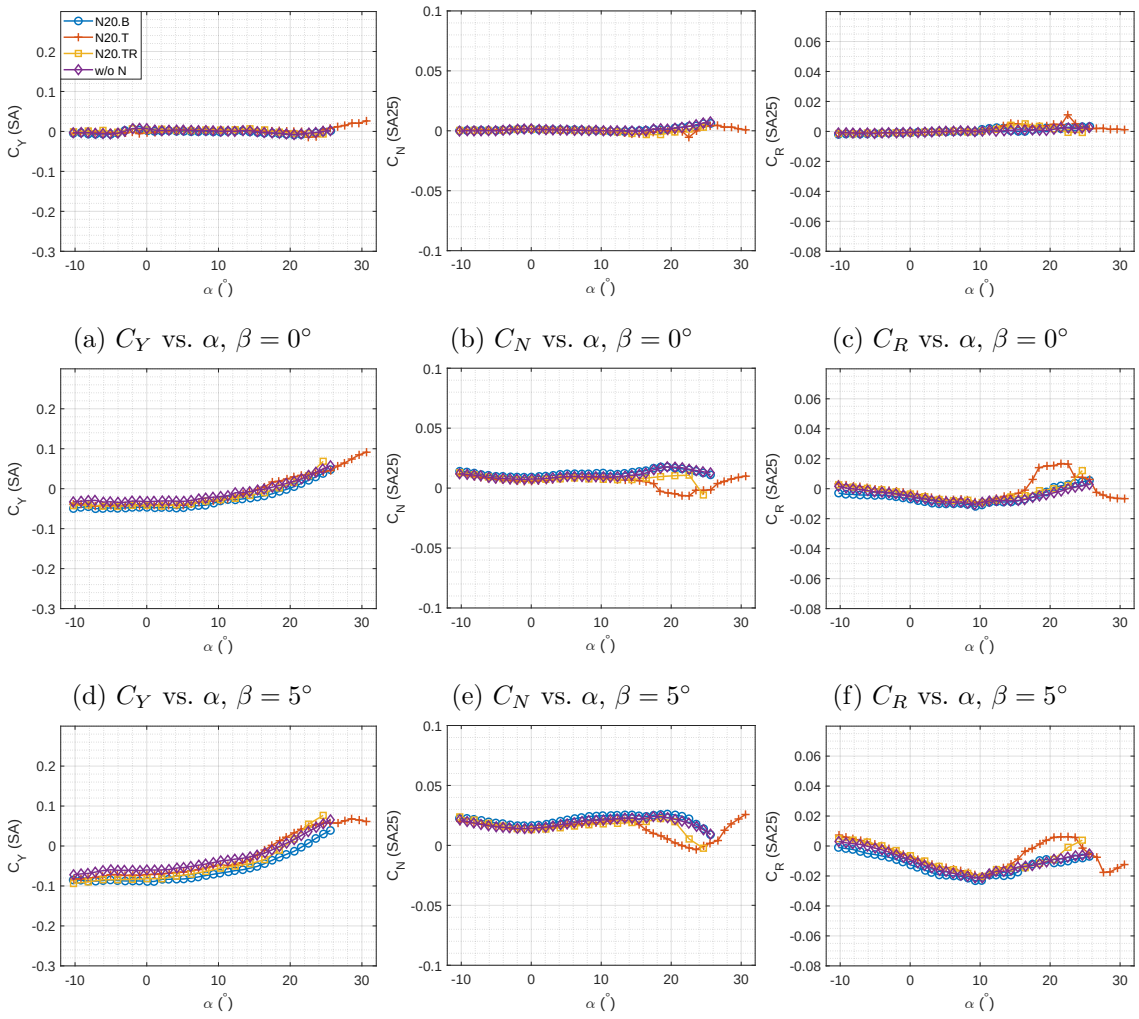


(a) C_L and C_M vs. α, $\beta = 0°$ (b) C_L and C_M vs. α, $\beta = 5°$ (c) C_L and C_M vs. α, $\beta = 10°$

Figure 2.245: UW-S-20 with nacelle location variation longitudinal forces and moments vs. α

separated and unsteady flow. As the sideslip angle is increased to $\beta = 5°$ in Figs. 2.246d - 2.246f, the side force coefficient, which has an initial constant negative value up to about $\alpha \approx 8°$, varies nonlinearly for higher alphas with a positive slope. The yawing moment coefficient C_N stays constant up to about 20 degrees angle of attack for all models, except for the N20.T model where C_N becomes negative for $18° \leq \alpha \leq 24°$, reflecting a loss of weathercock stability. For $\alpha \geq 23°$ the N20.T model regains its weathercock stability. All models show roll stability for $\beta = 5°$, and $10°$ up to $\alpha \approx 10°$, $C_R < 0$ in Fig. 2.246f and 2.246i. For higher angles of attack, $\alpha > 10°$, C_R becomes positive.

All lateral directional stability derivatives show relatively linear variation with sideslip angles, in the range of $-10° \leq \beta \leq 10°$ for $\alpha = 0°$ and $10°$, for top and bottom nacelle locations in Fig. 2.247. The data are shown with the no nacelle model for comparison. It is seen that nacelle addition, whether top or bottom wing mounted, increases lateral directional stability derivatives, making the model more stable. All models are seen to have stable lateral directional behavior for the mentioned sideslips and angles of attack ranges, $C_{Y_\beta} < 0$, $C_{N_\beta} > 0$, and $C_{R_\beta} < 0$.

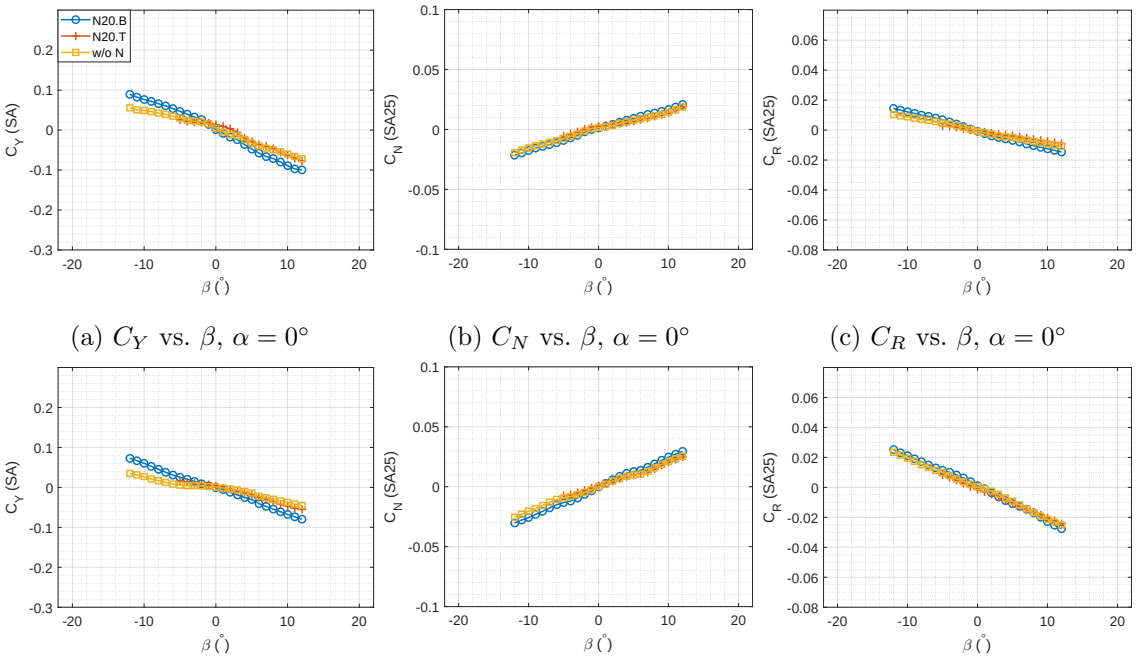


(a) C_Y vs. α, $\beta = 0°$ (b) C_N vs. α, $\beta = 0°$ (c) C_R vs. α, $\beta = 0°$

(d) C_Y vs. α, $\beta = 5°$ (e) C_N vs. α, $\beta = 5°$ (f) C_R vs. α, $\beta = 5°$

(g) C_Y vs. α, $\beta = 10°$ (h) C_N vs. α, $\beta = 10°$ (i) C_R vs. α, $\beta = 10°$

Figure 2.246: UW-S-20 with nacelle location variation: lateral directional forces and moments vs. α



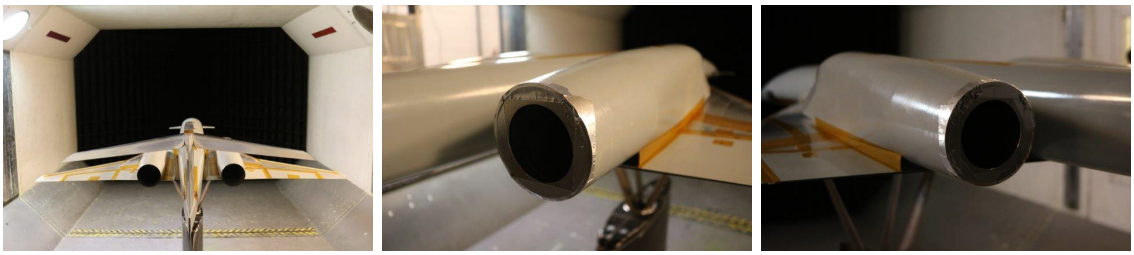
(a) C_Y vs. β, $\alpha = 0°$ (b) C_N vs. β, $\alpha = 0°$ (c) C_R vs. β, $\alpha = 0°$

(d) C_Y vs. β, $\alpha = 10°$ (e) C_N vs. β, $\alpha = 10°$ (f) C_R vs. β, $\alpha = 10°$

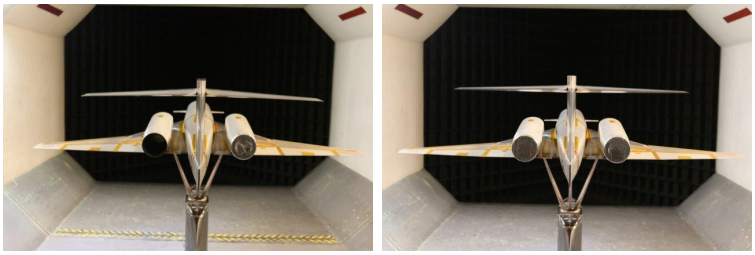
Figure 2.247: UW-S-20 with nacelle location variation: lateral directional forces and moments vs. β

Engine-out simulations

The aerodynamic interference caused by engine operation at reduced throttle setting (or an engine-out situation with seized rotor), was investigated by partially or fully closing off one or both nacelle exits to reduce the air mass flow through the duct. Figure 2.248 shows photos of the UW-S-20A model with fully open nacelles, left nacelle open while right nacelle exit area is reduced by 50%, both right and left nacelle exit areas are reduced by 50%, left nacelle open while right nacelle exit area is fully closed, both left and right nacelle exit areas are fully closed, respectively. All experimental aerodynamic forces and moments were obtained for the same conditions mentioned before.



(a) L/R: 0%/0% (b) L/R: 0%/50% (c) L/R: 50%/50%

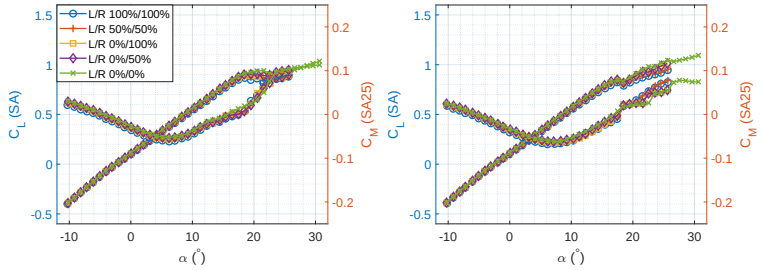


(d) L/R: 0%/100% (e) L/R: 100%/100%

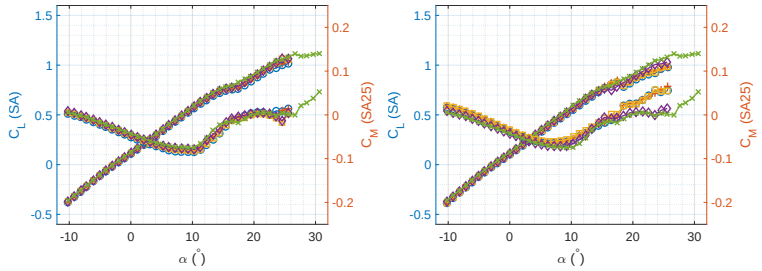
Figure 2.248: UW-S-20A nacelle with reduced nozzle exit areas

Figures 2.249 show variations of the lift and pitching moment coefficients with angles of attack for sideslip angles of $\beta = 0°$, $\pm 5°$, and $\pm 10°$ for all cases of the reduced nozzle exit areas mentioned above. The reduced exit nacelle areas do not seem to have significant effects on both lift and pitching moment variations with angles of attack for zero and positive sideslip angles in Figs. 2.249a - 2.249a. Figure 2.249a shows that the model with fully open exit area nacelles stalls at slightly higher angles of attack. The pitch moment variations are

the same for all cases. The C_{M_0}, C_{M_α}, and pitch-up angles of attack, longitudinal instability, for all cases examined, are the same in Figs. 2.249a - 2.249a. As mentioned before, the deep stall for all cases seems to occur around $\alpha \approx 22°$ in Fig. 2.249a. For the negative sideslip angles Fig. 2.249d shows that C_{M_0} slightly varies with the reduced nacelle exit area. The pitch up for all cases occurs at the same angles of attack, within $8° \leq \alpha \leq 10°$.



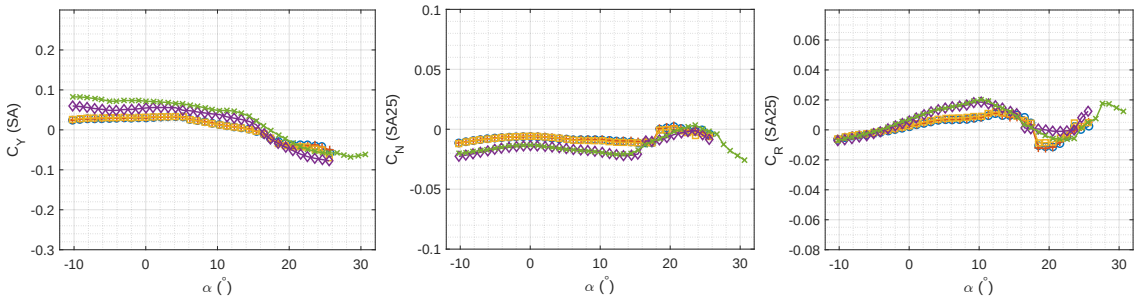
(a) C_L and C_M vs. α, $\beta = 0°$ (b) C_L and C_M vs. α, $\beta = 5°$



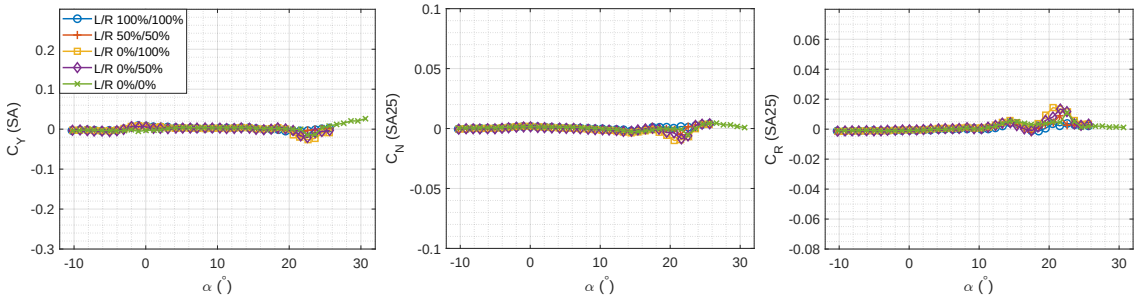
(c) C_L and C_M vs. α, $\beta = 10°$ (d) C_L and C_M vs. α, $\beta = -10°$

Figure 2.249: UW-S-20A with reduced nacelle exit area on the longitudinal forces and moments vs. α

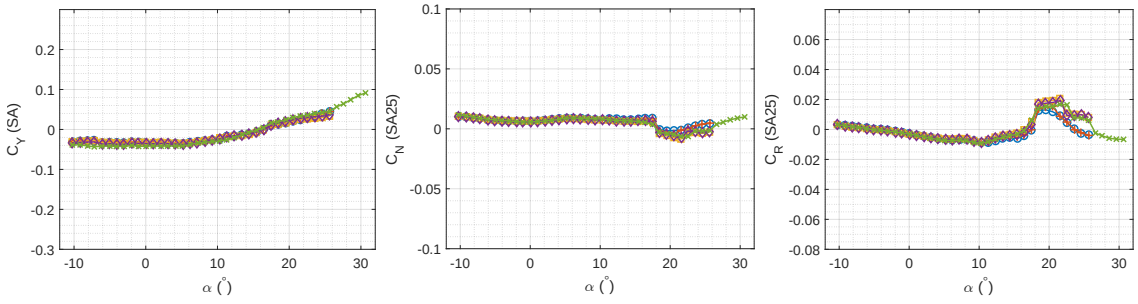
Figure 2.250 shows the effects of nacelle reduced exit areas on the lateral-directional force and moment coefficients. For all sideslip angles tested lateral-directional force and moment coefficients do not show significant changes due to the nacelle reduced exit areas and the variations with angles of attack are the same for all cases.



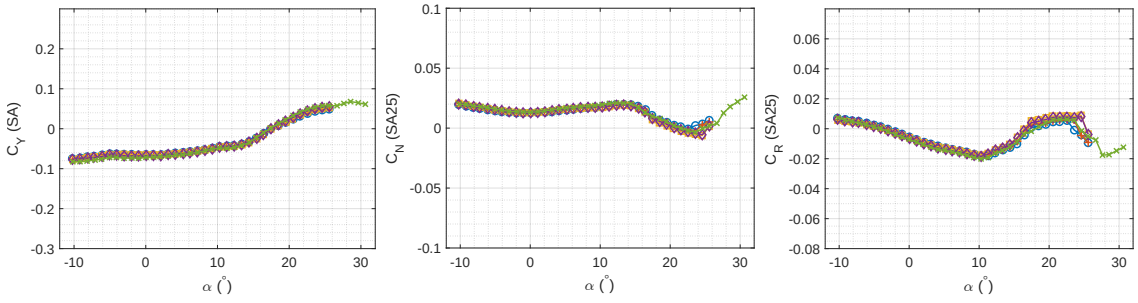
(a) C_Y vs. α, $\beta = -10°$ (b) C_N vs. α, $\beta = -10°$ (c) C_R vs. α, $\beta = -10°$



(d) C_Y vs. α, $\beta = 0°$ (e) C_N vs. α, $\beta = 0°$ (f) C_R vs. α, $\beta = 0°$



(g) C_Y vs. α, $\beta = 5°$ (h) C_N vs. α, $\beta = 5°$ (i) C_R vs. α, $\beta = 5°$



(j) C_Y vs. α, $\beta = 10°$ (k) C_N vs. α, $\beta = 10°$ (l) C_R vs. α, $\beta = 10°$

Figure 2.250: UW-S-20A with reduced nacelle exit area on the lateral directional forces and moments vs. α

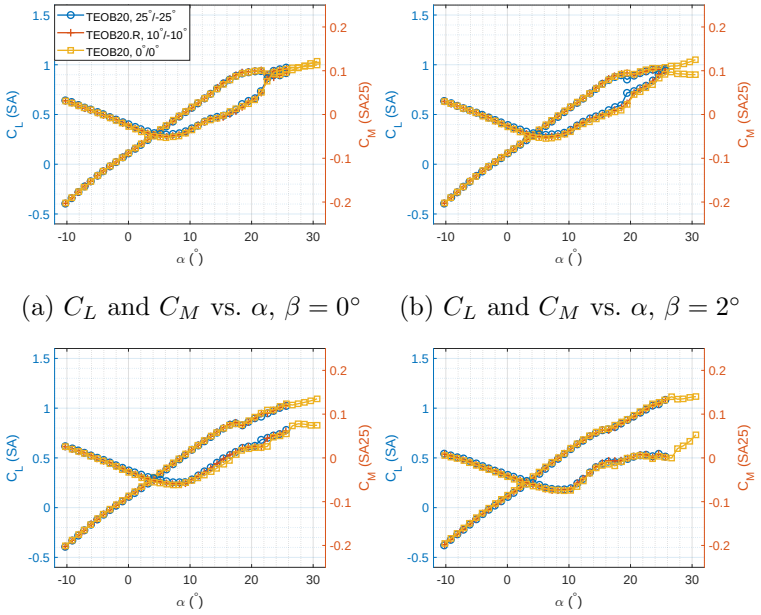
2.9.6 Aileron Deflections

The effects of the trailing-edge outboard aileron (TEOB) rotations on both longitudinal and lateral-directional forces and moment coefficients of the UW-S-20A and UW-S-21A are presented in this section. For both models tests were conducted with full and reduced chord ailerons. The ratio of chords of the reduced chord and full chord ailerons was 2/3. Figures 2.157 and 2.156 in §2.7 show photos of the UW-S-20A and UW-S-21A SCALOS models with full and reduced chord aileron, respectively. Tests were conducted for both positive and negative aileron rotations.

Figures 2.251 and 2.254 show the effects of full and reduced chord aileron rotations on the lift and pitch moment variations of the UW-S-20A and UW-S-21A models with angles of attack for several sideslip angles respectively. For $\beta = 0^\circ$ and 2°, aileron rotations do not have significant effects on the lift and pitch moment variations of the UW-S-20A model which has a T-tail empennage system and bottom nacelle location in Figs. 2.251a and 2.251b. For the $\beta = 5^\circ$, Fig. 2.251c shows that the pitching moment coefficients for both reduced aileron rotations of $\delta = \pm 10^\circ$ and $\pm 20^\circ$, have been slightly shifted, C_{M_0} is slightly increased, while C_{M_α} remains the same for the zero and non-zero aileron rotations.

Similarly, the UW-S-21A model with a low horizontal tail and with top wing mounted nacelles, does not show any significant variations in its lift and pitching moment developments with full or reduced aileron rotations in Fig. 2.254a. Figures 2.254a-2.254c show that aileron rotation significantly reduces C_{M_α} both prior to the pitch-up initiation, $\alpha \approx 10^\circ$, and post pitch up initiation, $10^\circ \leq \alpha \leq 20^\circ$, and the nose-up behavior is smooth and gradual in comparison to the previous case of UW-S-20A model in Fig. 2.251a. Beyond $\alpha \geq 20^\circ$, $C_{M_\alpha} \approx 0$ – a neutrally stable longitudinal behavior in Figs. 2.254a-2.254c.

The trailing-edge aileron rotation has significant effects on the rolling moment variations of both models with angles of attack and sideslip angles. As the aileron is rotated, the value of C_R at $\alpha = 0^\circ$ for all sideslip angles tested increases, creating more rolling moment. The roll dihedral stability derivative, C_{R_β}, at $\alpha = 0^\circ$ is not affected by the aileron deflection in Fig. 2.253c. At $\alpha = 10^\circ$, Fig. 2.253f shows that $|C_{R_\beta}|$ increases with aileron rotation. Figure 2.253f shows that $|C_{R_\beta}|$ does not vary when δ is increased from $\pm 10^\circ$ to $\pm 20^\circ$. It

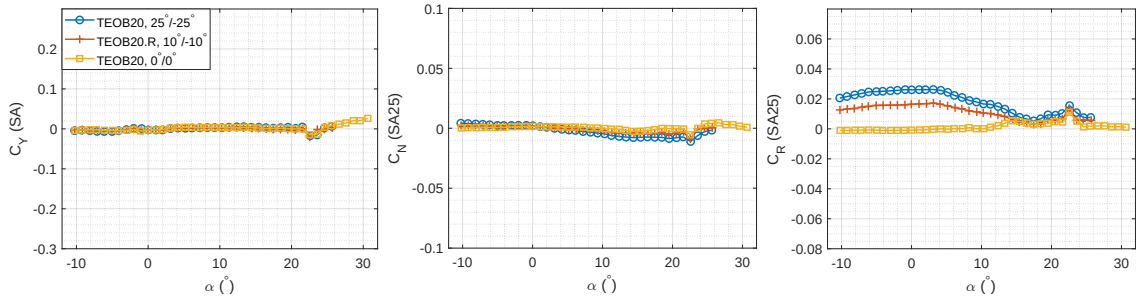


(a) C_L and C_M vs. α, $\beta = 0°$ (b) C_L and C_M vs. α, $\beta = 2°$

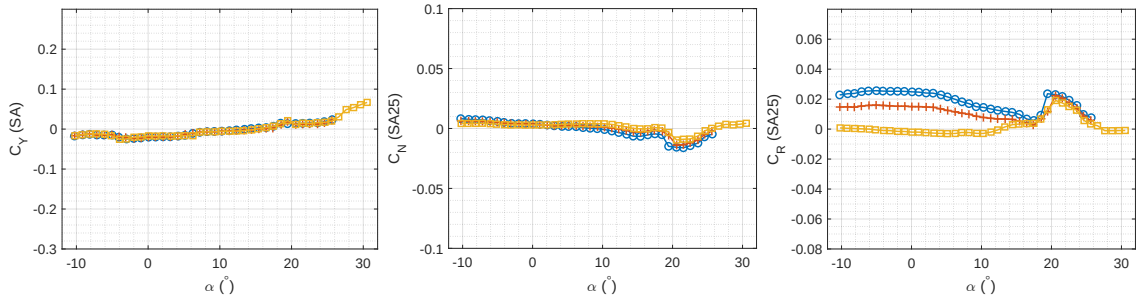
(c) C_L and C_M vs. α, $\beta = 5°$ (d) C_L and C_M vs. α, $\beta = 10°$

Figure 2.251: UW-S-20A with reduced chord ailerons deflections longitudinal forces and moments vs. α

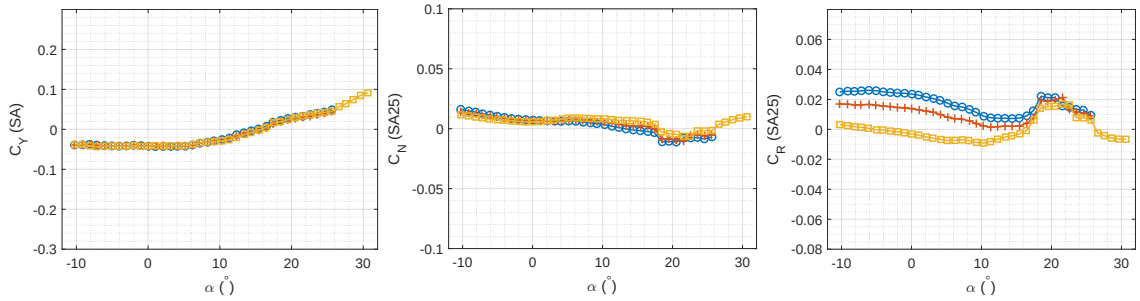
appears that for this angle of attack, ailerons lose their effectiveness when deflected by more than $\delta \geq \pm 10°$. Similar effects are observed for the UW-S-21A model with both full and reduced aileron chords. The shifts in the C_R values at $\alpha = 0°$ for all sideslip angles are more for the full aileron chord. Variations of the C_R with angles of attack are the same for both full and reduced aileron chords in Figs. 2.255f and 2.255i.



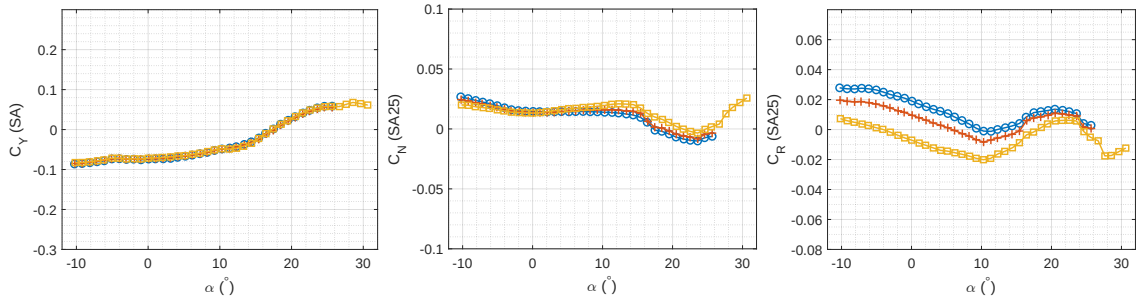
(a) C_Y vs. α, $\beta = 0°$ (b) C_N vs. α, $\beta = 0°$ (c) C_R vs. α, $\beta = 0°$



(d) C_Y vs. α, $\beta = 2°$ (e) C_N vs. α, $\beta = 2°$ (f) C_R vs. α, $\beta = 2°$

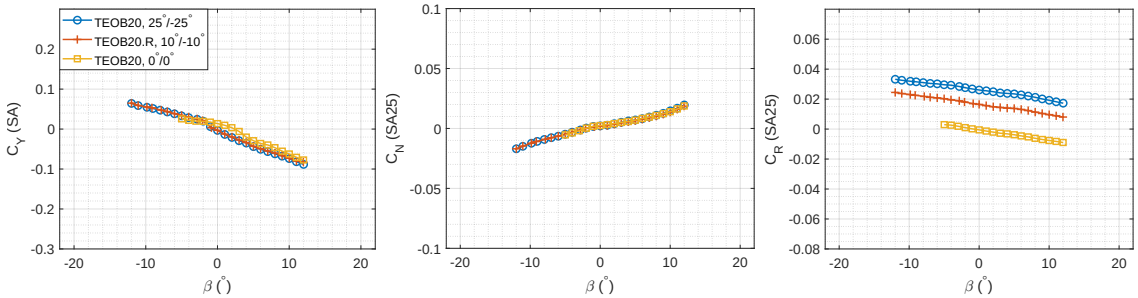


(g) C_Y vs. α, $\beta = 5°$ (h) C_N vs. α, $\beta = 5°$ (i) C_R vs. α, $\beta = 5°$

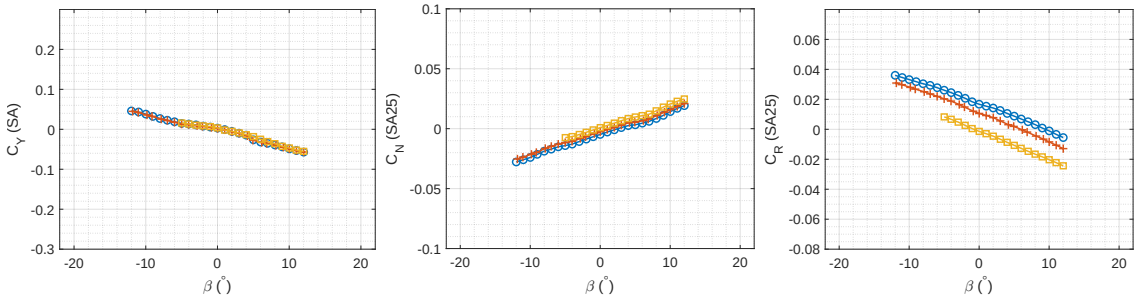


(j) C_Y vs. α, $\beta = 10°$ (k) C_N vs. α, $\beta = 10°$ (l) C_R vs. α, $\beta = 10°$

Figure 2.252: UW-S-20A with reduced ailerons deflections lateral directional forces and moments vs. α

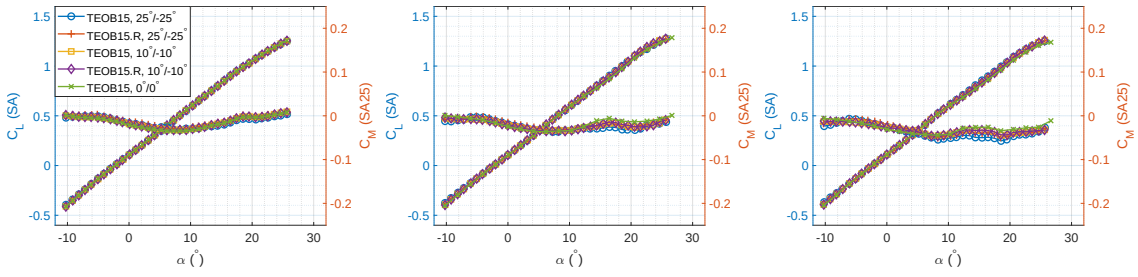


(a) C_Y vs. β, $\alpha = 0°$ (b) C_N vs. β, $\alpha = 0°$ (c) C_R vs. β, $\alpha = 0°$



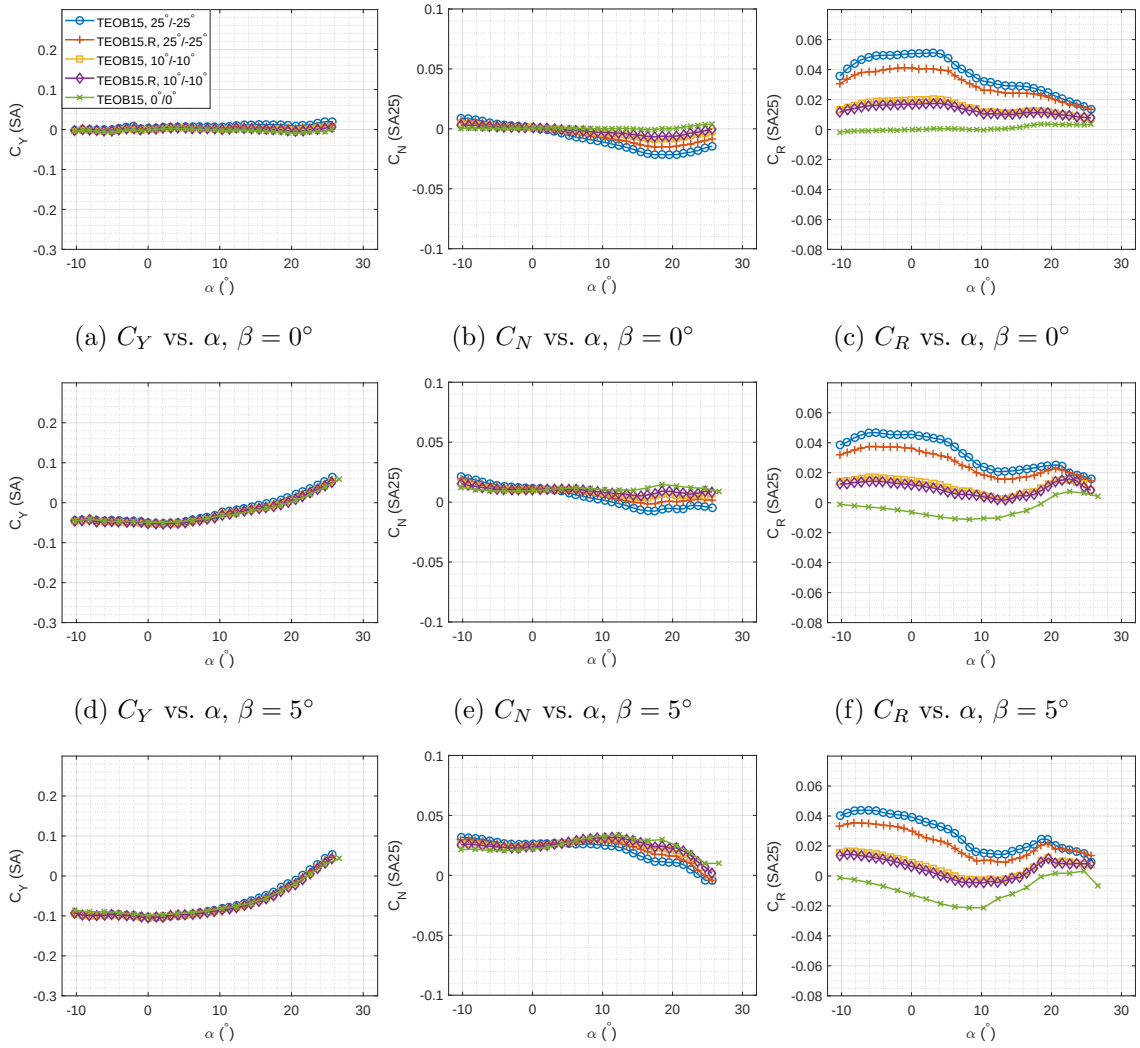
(d) C_Y vs. β, $\alpha = 10°$ (e) C_N vs. β, $\alpha = 10°$ (f) C_R vs. β, $\alpha = 10°$

Figure 2.253: UW-S-20A with reduced ailerons deflections lateral directional forces and moments vs. β



(a) C_L and C_M vs. α, $\beta = 0°$ (b) C_L and C_M vs. α, $\beta = 5°$ (c) C_L and C_M vs. α, $\beta = 10°$

Figure 2.254: UW-S-21A with full and reduced ailerons deflections longitudinal forces and moments vs. α



(a) C_Y vs. α, $\beta = 0°$ (b) C_N vs. α, $\beta = 0°$ (c) C_R vs. α, $\beta = 0°$

(d) C_Y vs. α, $\beta = 5°$ (e) C_N vs. α, $\beta = 5°$ (f) C_R vs. α, $\beta = 5°$

(g) C_Y vs. α, $\beta = 10°$ (h) C_N vs. α, $\beta = 10°$ (i) C_R vs. α, $\beta = 10°$

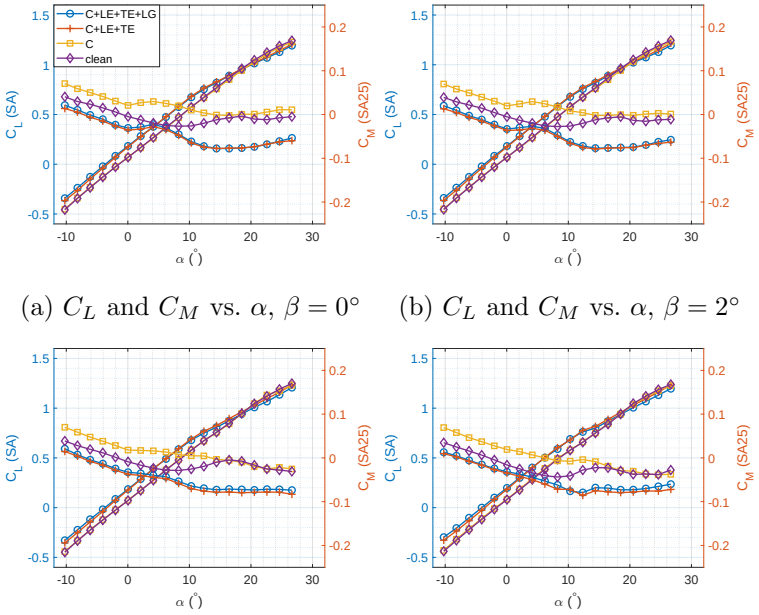
Figure 2.255: UW-S-21A with full and reduced ailerons deflections lateral directional forces and moments vs. α

2.9.7 Take-off and Landing Conditions

Additional wind tunnel tests were carried out to investigate aerodynamic forces and moments of the SCALOS models during take-off and landing. The UW-S-24A model was used for these tests and its photos for different conditions are shown in Fig. 2.194 in §2.7. Variations of the lift and pitching moment with angles of attack for several sideslip angles are shown in Fig. 2.256. The data are for cruise; rotated canards; canard and wing leading and trailing-edge flaps rotated; and canards, wing leading and trailing-edge flaps and landing gears deployed cases. For all sideslip angles tested, Fig. 2.194 shows that canard rotation does not have significant effects on the lift developments of this SCALOS.

For the other two cases tested, C_{L_0} is seen to be shifted as expected. Note that flap deflection increases effective wing camber and effective angle of attack, and, as a result, C_{L_0} increases. For $\alpha \geq 10^\circ$, C_{L_α} of the models with rotated $\delta_C + \delta_{LE} + \delta_{TE}$ and with $\delta_C + \delta_{LE} + \delta_{TE} +$LG24 for all sideslip angles decreases. Beyond $\alpha \geq 20^\circ$ these configurations develop slightly less lift than that of the cruise configuration. No signs of stalls are present in all cases. Canard rotation is seen to increase $|C_{M_0}|$, for all sideslip angles. The $|C_{M_0}|$ of models equipped with $\delta_C + \delta_{LE} + \delta_{TE}$ and $\delta_C + \delta_{LE} + \delta_{TE} +$LG24 reduce $C_{M_0} < 0$, making the configurations not trimmable at positive angle of attack (at least at the reference moment center and untwisted wing). For $\beta = 0^\circ$ and 2°, the models with $\delta_C + \delta_{LE} + \delta_{TE}$ and $\delta_C + \delta_{LE} + \delta_{TE} +$LG24 produce a slight nose up pitching moment, $C_{M_\alpha} > 0$, around $\alpha = 0^\circ$. For $\alpha \geq 5^\circ$ nose down moment is generated in Figs. 2.256a and 2.256c. For $\alpha \geq 14^\circ$ the models with $\delta_C + \delta_{LE} + \delta_{TE}$ and $\delta_C + \delta_{LE} + \delta_{TE} +$ LG24 produce slight nose up pitching moments. The C_{M_α} derivative for the cruise and rotated-canard cases are near zero - a neutral longitudinal stability condition. For larger sideslip angles, $\beta = 5^\circ$ and 10°, Figs. 2.256c and 2.256d, show that $C_{M_\alpha} < 0$ for tests with $\delta_C + \delta_{LE} + \delta_{TE}$ and $\delta_C + \delta_{LE} + \delta_{TE} +$LG24 on, up to about $\alpha = 10^\circ$ and C_{M_α} become nearly zero for $\alpha \geq 10^\circ$.

For the cases of cruise, rotated canards; canards and wing leading and trailing flaps; and canards, wing leading and trailing flaps and landing gears deployed cases, variations of the lateral-directional force and moment coefficient with angles of attack for sideslip angles of $\beta = 0^\circ$, 2°, 5°, and 10° are shown in Fig. 2.258. The only noticeable effects are observed



(a) C_L and C_M vs. α, $\beta = 0°$ (b) C_L and C_M vs. α, $\beta = 2°$

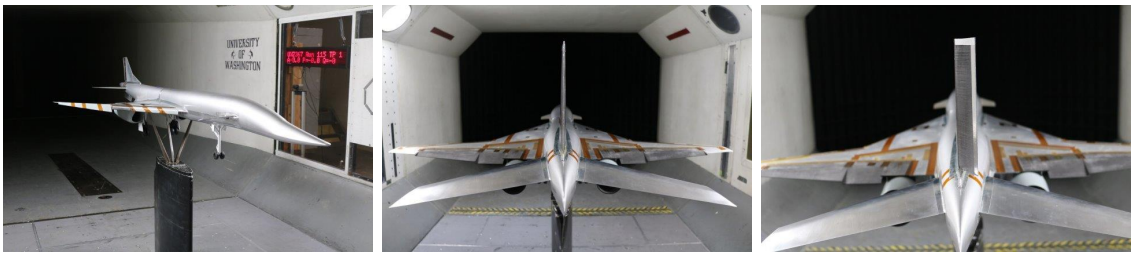
(c) C_L and C_M vs. α, $\beta = 5°$ (d) C_L and C_M vs. α, $\beta = 10°$

Figure 2.256: UW-S-24A with take-off and landing configuration built-up longitudinal forces and moments vs. α

for $\alpha \geq 10°$ and with $\beta = 5°$, and $10°$ in Figs. 2.258h, 2.258i, 2.258k, and 2.258l. The side force coefficient does not vary significantly with the above rotations. In combination with the rudder rotations photos that are shown in Fig. 2.257 and 2.259 show that all lateral directional coefficients are affected while the effects on the rolling moment are seen to be minimal.

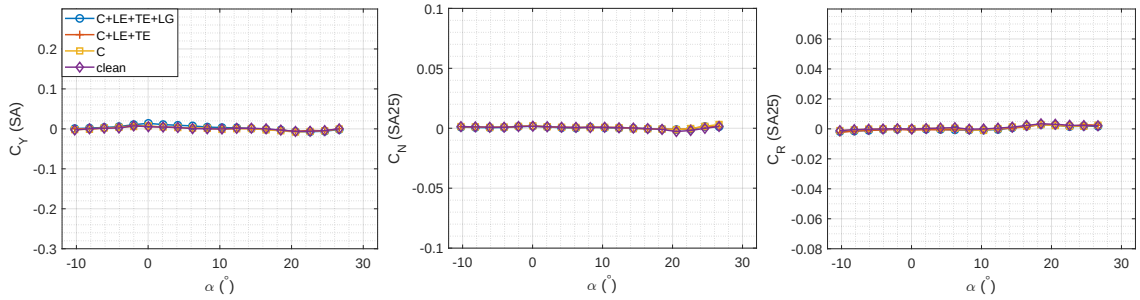
As the rudder is deflected, the vertical tail develops more or less lift (side force), depending on the direction of rudder rotation, and via the moment arm yawing moments change. The resulting small rolling moments are created by the vertical distance from the vertical tail aerodynamic center to the model moment center. Figure 2.259 shows that rudder rotation shifts the side force coefficient at $\beta = 0°$, but the slope of the curve does not vary significantly. Similar effects are seen for the yawing moment variations with sideslip angles for all angles of attack shown in Fig. 2.259, with C_N shifted due to rudder deflection at $\beta = 0°$. Variations of the yawing moment coefficient with sideslip angles for all configurations are highly nonlinear for $\alpha = 0°$ and $20°$ in Figs. 2.259e and 2.259h which is most likely

due to the asymmetrical flow field over the windward and leeward wing surfaces, and the low tail immersed in the canard, wing, and fuselage wake. For the $\alpha = 20°$, Figs. 2.259g and 2.259h show that $C_{Y_\beta} > 0$ while $C_{N_\beta} \approx 0$ - a plateau in the C_N vs β curve, for sideslip angles of $-2° \leq \beta \leq 2°$.

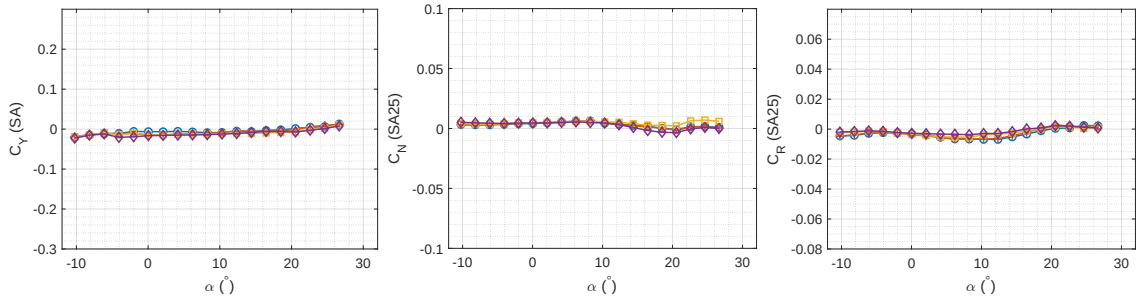


(a) UW-S-24A LTO (b) $\delta_{VT} = 0°$ (c) $\delta_{VT} = +25°$

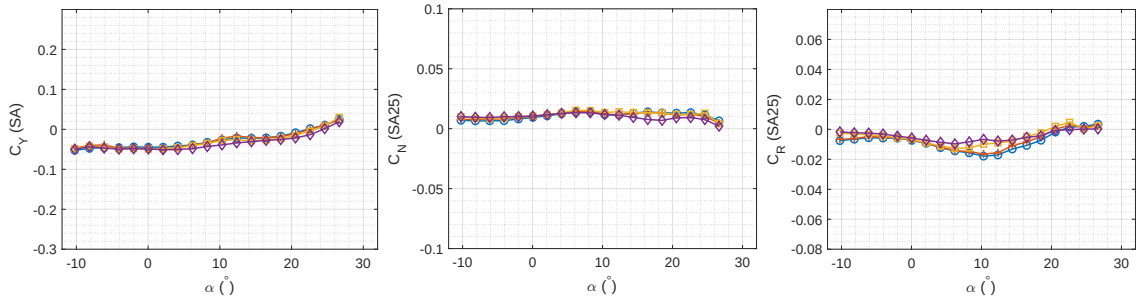
Figure 2.257: UW-S-24A LTO configuration with vertical tail deflections



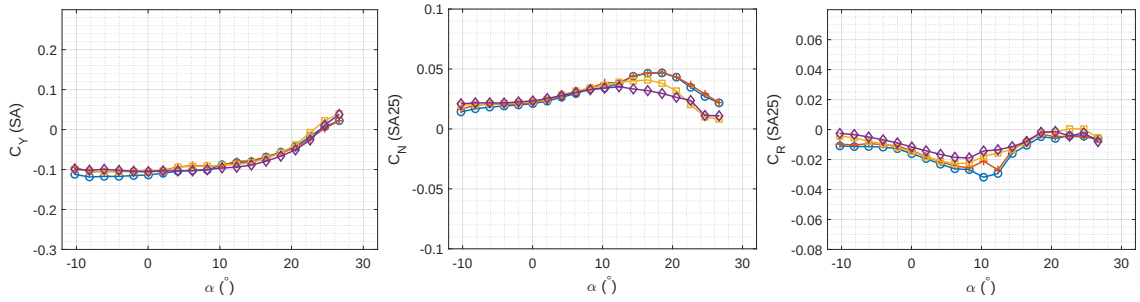
(a) C_Y vs. α, $\beta = 0°$ (b) C_N vs. α, $\beta = 0°$ (c) C_R vs. α, $\beta = 0°$



(d) C_Y vs. α, $\beta = 2°$ (e) C_N vs. α, $\beta = 2°$ (f) C_R vs. α, $\beta = 2°$

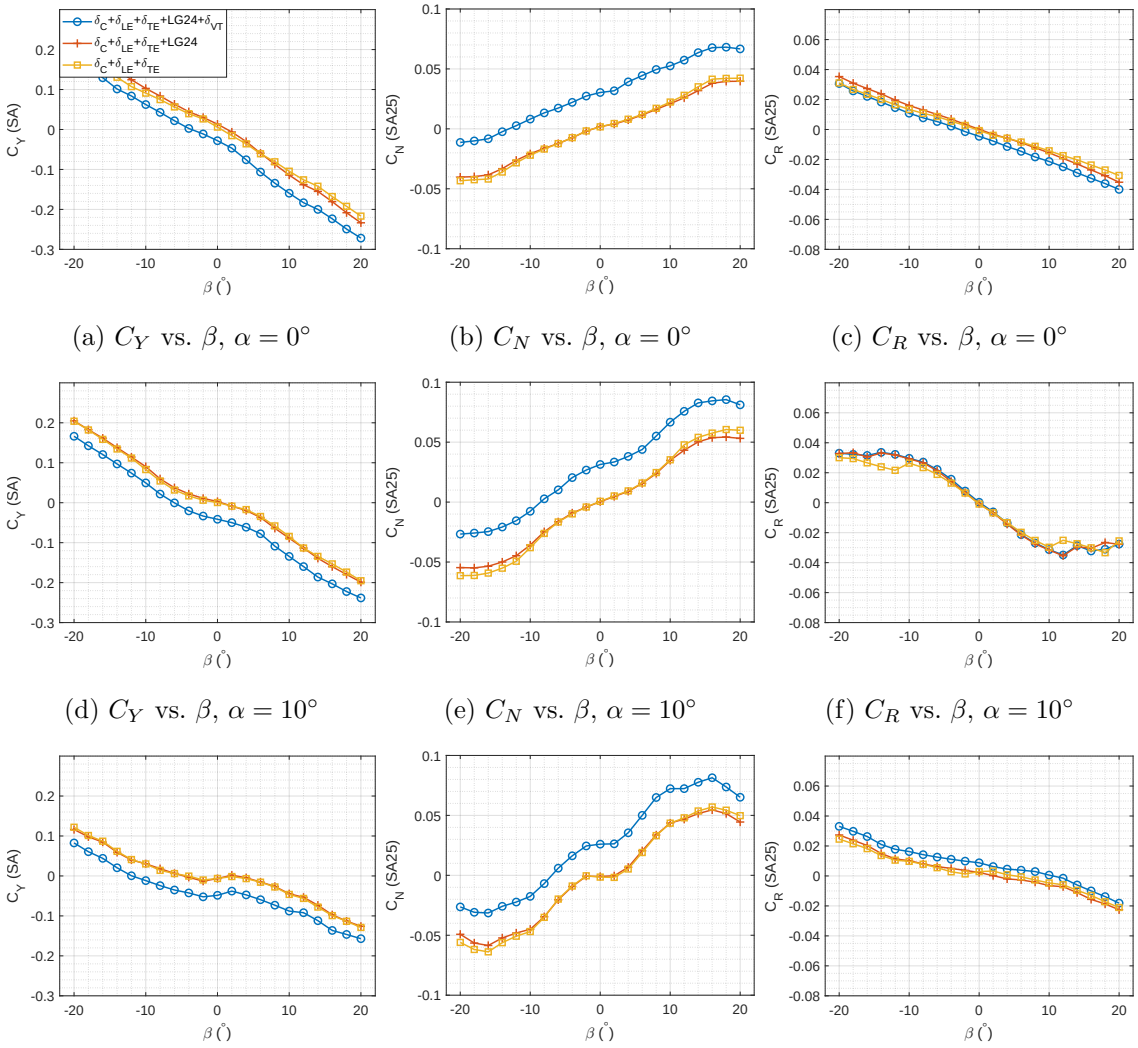


(g) C_Y vs. α, $\beta = 5°$ (h) C_N vs. α, $\beta = 5°$ (i) C_R vs. α, $\beta = 5°$



(j) C_Y vs. α, $\beta = 10°$ (k) C_N vs. α, $\beta = 10°$ (l) C_R vs. α, $\beta = 10°$

Figure 2.258: UW-S-24A with take-off and landing configuration built-up lateraial directional forces and moments vs. β



(a) C_Y vs. β, $\alpha = 0°$ (b) C_N vs. β, $\alpha = 0°$ (c) C_R vs. β, $\alpha = 0°$

(d) C_Y vs. β, $\alpha = 10°$ (e) C_N vs. β, $\alpha = 10°$ (f) C_R vs. β, $\alpha = 10°$

(g) C_Y vs. β, $\alpha = 20°$ (h) C_N vs. β, $\alpha = 20°$ (i) C_R vs. β, $\alpha = 20°$

Figure 2.259: UW-S-24A take-off and landing configuration with rudder deflections lateral directional forces and moments vs. β

2.10 Lessons Learned

The substantial amount of wind tunnel data collected by the SCALOS project and the 5 years of senior capstone design testing and model development before it at the University of Washington makes its possible to study the effects of configuration shape and arrangement on the aerodynamic characteristics of the configurations studied. Actual values of the various aerodynamic derivatives of the different configurations are, of course, important and allow estimating the aerodynamic characteristics of a large number of configurations that fall, in shape and arrangement, into the configuration design space that the tests cover. The results also allow fine-tuning and validation of CFD math models for the resulting CFD technology for this technology to then be used in parametric design studies of new configurations.

This section focuses on general trends and selected insights. In what follows are the studies and presentation of the effects of wing planform, tail configurations, canards, aft-decks, and the location of engine nacelles - that is, the overall configuration without detailed "local" variations in the form of control and high-lift device motions. Trends presented in [377] were used with partially corrected KWT data and are now updated with final SCALOS-specific corrections here. The final fully-corrected data shows essentially equal trends and very similar levels as the pre-final data in earlier papers [377]. The final corrected data is available in the test results database for the replication of the studies shared here and for other studies of the effect of the many configuration variations that were tested on the overall aerodynamic characteristics. It should be noted that unless noted otherwise, all SCALOS data has been reduced using the MAC and reference area of wing W15 (gross projected area and its equivalent trapezoid MAC) in Tab. 2.28 as desrcibed in §2.5.

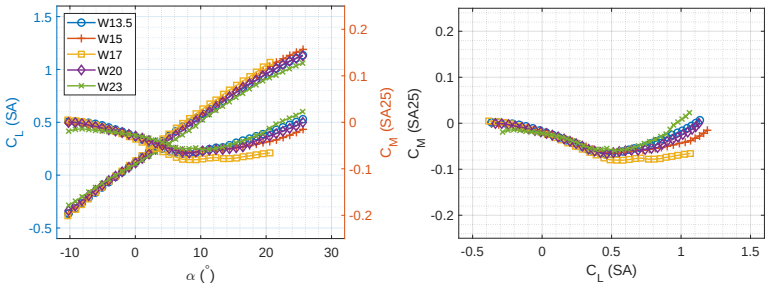
2.10.1 Longitudinal Charateristics

Figures 2.49a and 2.260 show the effects of wing planform shape on the pitching moment coefficient C_M vs. α and C_M vs. C_L curves. The configurations covered by the figures include Wings + Fuselage + VT15 + VentralFin1 + DorsalFin1 components (see tables of components and their designation in the §2.2 and §2.4). There are no canards, nacelles, or

horizontal tails. All wing flaps are at zero. Data is presented in stability-axis orientation with the CG (moment center) at 25% MAC.

The configurations are statically stable up to about 7 degrees angle of attack. The W17 wing becomes statically unstable at about 8 degrees. Note the tendency of W17 to regain static stability at 12 degrees to lose it again at 16 degrees AOA. Around AOA-0 degrees the most statically stable are Wings 13.5 and Wing 17 (See also Ref. [211] for an HSCT-era exploration of wing planforms).

Deflecting leading edge flaps generally improves the stability and drag polar shape of all the planforms by delaying the alpha for leading edge vortex separation (although at some loss in C_L at alpha). As this is fundamentally favorable for landing and takeoff conditions, it is assumed the LTO regime will involve some combination of LE and TE flap settings optimized for trimmed L/D at the operating C_L's. However, planform selection is likely constrained by "flaps-up" characteristics at higher subsonic speeds and certification conditions with various failure scenarios for the flaps and flight controls. In particular, it is desirable for pitch-up to be delayed, the C_M change to be less abrupt, and for the difference in static stability before and after the pitching moment break to be minimized.



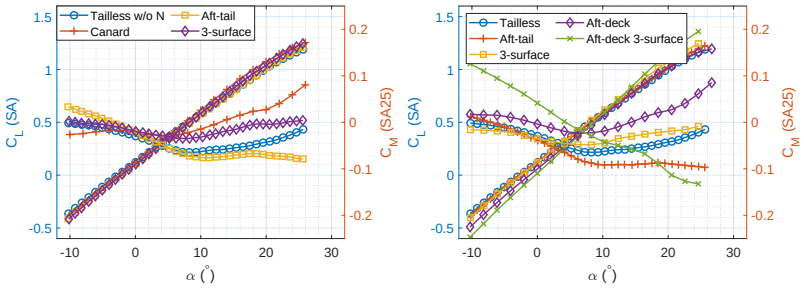
(a) C_L and C_M vs. α (b) C_M vs. C_L

Figure 2.260: Wing planform effects

A study of longitudinal control options is presented in Fig. 2.261a. Shown are C_M (at 0.25 MAC) vs. AOA curves for full configurations with nacelles on, common fuselages, common main wing (W15), no TE/LE flap deflections, based on a common reference area and a common MAC. Note the delay in the start of pitchup, the more moderate pitchup, and the higher static stability at small AOAs of the low-mounted aft-tail case. That case, however,

also shows a region of deep stall from about 20 degrees AOA and higher. The canard, not surprisingly, degrades low AOA static stability without the presence of a horizontal tail and leads to more severe longitudinal instability compared to the other longitudinal control tail options, indicating that a farther forward CG would be needed to retain stability if a canard is employed for pitch trim/control, whether in conjunction with elevons or an aft-tail.

However, it should be noted that the basic planform-dominated shape of the pitching moment curve is relatively unchanged — the lift generated by the canard versus alpha acts to rotate the entire moment curve as though the aircraft was being flown at a farther aft CG. This indicates that equivalent static stability can potentially be recovered by flying at a farther forward CG while retaining the canard's control authority advantage of having a longer "tail arm" from the CG, relative to an aft-tailed configuration. For a given required pitch control / trim authority the canard arrangement may therefore get away with a smaller surface than an equivalent aft tail. It should also be noted that canard configurations have repeatedly shown that the lift generated by canard for trimming at forward CG in the linear alpha region does not increase overall lift because the canard down-wash decreases the wing lift by roughly the same amount. Trim with the canard acts essentially a "couple" in C_M.



(a) Canard and tail options (b) Aft-deck options

Figure 2.261: Longitudinal control: canard, horizontail tail, and aft-deck options C_M vs. α

The effect of adding an aft-deck is shown in Fig. 2.261b. Again, as in the case of the previous figure, a common fuselage and a common main wing (W15) were used, with no LE/TE flap deflections, and with common reference area and reference MAC. The stabilizing effect of the aft deck is obvious. In both the aft-deck and aft tail case as well as the three-surface plus aft deck case, there is practically no loss of longitudinal static stability (except

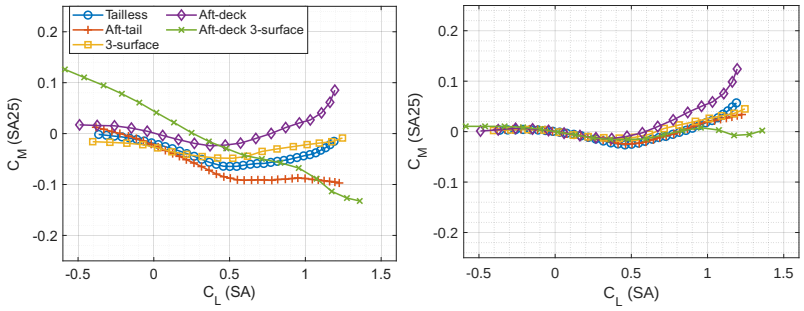
for a small range of AOA between 25 and 27 degrees, where the 3-surface plus aft-deck configuration is marginally stable).

It is likely that this small transitory region of instability could be easily smoothed with fly-by-wire control laws or possibly eliminated during aero detail design. It should be noted that the aft-deck and tailed-aft deck arrangements show excessive static pitch stability about the wing quarter MAC CG location, which could cause high trim drag and larger pitch-control-induced loads on the airframe. This indicates that taking advantage of the aft-deck arrangements requires that the CG be located farther aft. This may be a net-favorable trade-off for some aircraft as the linearity of the pitch stability means that stability at aft CG will not be a limiting factor when operating at higher C_L's. The inherently more linear pitch curve shape of the aft-deck arrangements comes with a penalty in wetted area (C_{D_0}), but increased potential for reducing sonic boom and transonic drag rise, and for integrating upper-surface nacelles for LTO noise shielding. The area-rule characteristics of the aft-deck arrangement can also lead to a somewhat larger cabin cross-section in the forward portion, possibly making this arrangement more attractive for business jet sized applications.

The effect of adding an aft-deck on C_M vs. C_L curves is shown in Fig. 2.262. The aft-deck has a strong stabilizing effect on the low-speed longitudinal static stability. It adds drag, of course. From the aeroelastic perspective it leads to the stiffening of the aft empennage and, therefore, has the potential to alleviate, passively, empennage flutter.

An effort is made in Fig. 2.262b to bring alternative longitudinal configuration arrangements to a common basis. All cases shown in the figure were "balasted" to a reference 5% static margin. They were all trimmed to zero C_{M_0}, with no constraint on CG location and trim drag.

The figure shows that the Aft-deck + stabilator configurations, with or without canard, have nearly linear C_M (at a wetted-area penalty) and no pitchup. Canard lift vs. AOA degrades static margin by ∼4–8% at fixed CG. The 3-surface "tube & wing" general arrangement (similar to RSAC) looks the most unstable in this comparison, has the earliest and most abrupt pitch-up, but has min. trim drag over a greater CG & TE flap deflection range. What's "best" here depends on performance trade-offs and configuration integration / CG constraints.

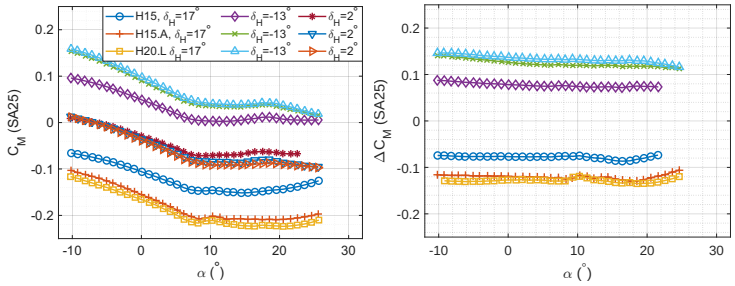


(a) CG at 25%$\bar{c}$ (b) 5% static margin

Figure 2.262: Longitudinal control: canard, horizontail tail, and aft-deck options C_M vs. C_L

Fig. 2.261b shows the contribution of the horizontal stabilizer to longitudinal static stability with and without an aft-deck. As the figure shows, the aft-deck "sponson mounted" stabilizers are very effective while the aft-body-mounted stabilizers help post pitch-up but contribute almost nothing below about 7 degrees AOA.

The effect of horizontal stabilizer area on pitch control authority is studied in Fig. 2.263. It is interesting to note that there is very little change in C_{M_α} static stability for a 50% stabilizer area increase. It seems that the large inboard wing is acting as a strong "flow straightener" (which is similar to the HSCT experience, $d\epsilon/d\alpha$ close to 1). As a result you cannot fix pitch instability by increasing the tail volume $\bar{V}_H$. The increase in pitch authority for adding stabilator area is a ratio of only 4:5, rather than 1:1, which would also have an impact on tail sizing criteria for this class of aircraft.

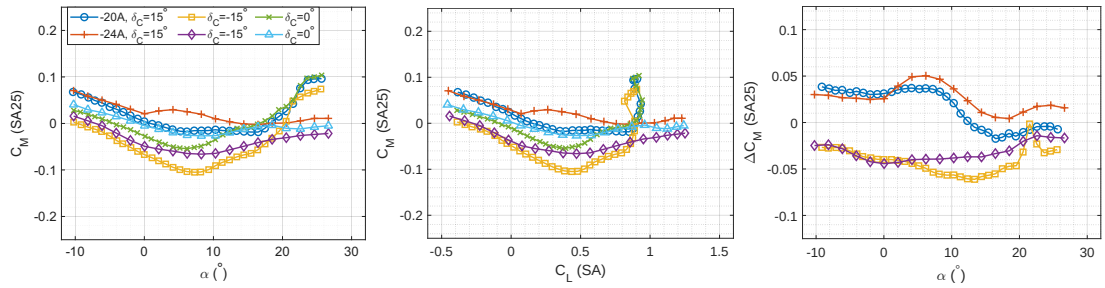


(a) C_M vs. α (b) ΔC_M vs. α

Figure 2.263: Longitudinal control: effect of horizontal tail area

Fig. 2.264 shows an example of canard contributions. The results shown here is based on the SCALOS final corrected data from the campaign than the 2017 data with an aft-deck in original [377]. As can be seen, above a C_L of about 0.8 the canard is not effective due to canard stall. This indicates that a pure-canard (aft-tailless) configuration would also need pitch control from wing elevons to provide adequate pitch authority at high alpha conditions.

Some aft-body + tail configurations show very nonlinear results at larger canard deflections (the '+' orange line here corresponding to the broken red line on the figure in orignal [377]). Testing at UW prior to SCALOS, with various canard planforms and locations, indicated that: (1) this non-linearity can be mitigated to a certain extent by further configuration development, and (2) that selection of the canard planform can impact the canard's own stall behavior (hence pitch-down tendency at large combinations of alpha and canard deflection).



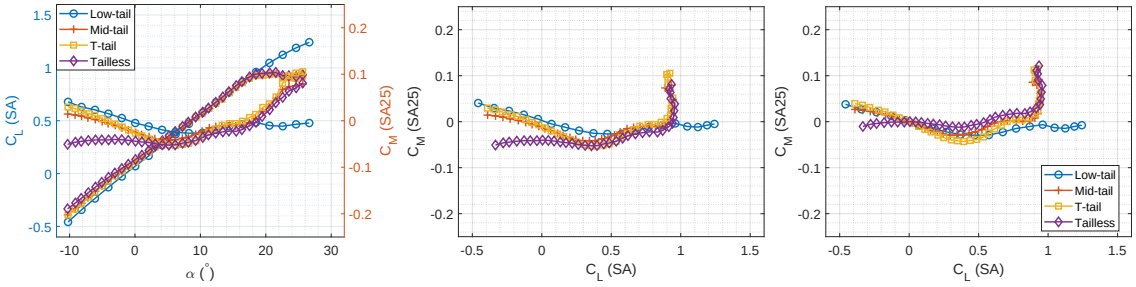
(a) C_M vs. α (b) C_M vs. C_L (c) ΔC_M vs. α

Figure 2.264: Longitudinal control:canard effectiveness

Shifting attention to the effect of vertical location of the horizontal tail, Fig. 2.265 shows C_M vs. AOA curves for T-tail, mid-tail, low-tail, and no-tail configurations based on the common fuselage and W15 with no LE/TE flap deflections. The T-tail provides much more stability at low AOAs and becomes highly unstable above pitch-up. Note the beginning of a turn of the C_M vs. AOA curve around 25 degrees AOA which may lead to deep stall, as is common in the case of T-tail configurations (as the T-tail begins to emerge below the wake of the wing).

The low-tail configuration shows deep stall after about 23 degrees AOA. It is unsta-

ble above 6 degrees AOA and below −6 degrees AOA. The low stability of the tailless configuration relative to the tailed ones is obvious and expected.



(a) C_L and C_M vs. α (b) C_M vs. C_L, untrimmed (c) C_M vs. C_L, pseudo-trimmed

Figure 2.265: Longitudinal control: effect of vertical location of the horizontal tail

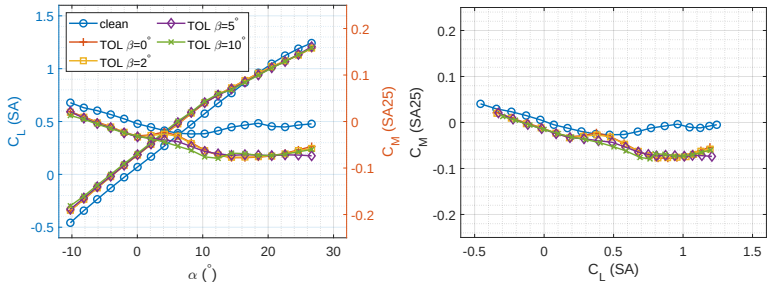
The following figure (Fig. 2.265b) shows C_M vs. C_L curves for the various vertical positions of the horizontal stabilizer for the same configurations as in the previous figure. Data shifted ("pseudo-trimmed") to a common C_{M_0} of zero shows that the T-tail provides much more negative $\partial C_M/\partial C_L$ (static margin) at fixed CG location but is the most unstable post pitch-up.

For the comparison of the partially-corrected versus the final fully-corrected KWT data on the horizontal-tail vertical location, see Figs. 20 and 21 in [377]. The differences in corrected results are minor and the trends are practically the same.

Figure 2.266 shows the effect of using LE/TE flap deflections to improve pitch-up. The "clean" configuration in this case uses the UW-S-24A configuration instead of the UW-S-17A in [377]. The components built up is in Tab. 2.12 in §2.2. Plotting C_M about 0.25 MAC versus C_L for various sideslip angles, the figure links various parts of the C_M vs. C_L curves to important maneuvers. The "approach configuration" includes full-span TEs at 10 deg down, canards at +5 degrees, full span LE flaps at 30 degrees and a stabilizer at zero degrees rotation. The configuration is, thus untrimmed.

It is interesting to note that with flaps down there is about a 70% increase in pitch-up C_L. "Approach" LE/TE C_M in this example looks like that of subsonic aircraft but the pitchup still occurs before $C_{L_{\max}}$. 45 deg bank puts C_L past the local pitch-up instability. That

may mean "special conditions for certification." This example looks favorable, but 25% CG may not be attainable with the full scale airframe (unless the limited region of instability can be smoothed out with fences or other aerodynamic "fixes" during detailed configuration development) and any allowable negative static margin depends on short period dynamics, I_{yy} rotational inertia, and aerodynamic damping coefficients, C_{M_q}. It should be noted that UW-S-24A is selected as the RSAC at the end of the SCALOS program but UW-S-17A appears to be the most "low-speed-friendly" aero characteristics of all the tested planforms.



(a) C_L and C_M vs. α (b) C_M vs. C_L

Figure 2.266: Longitudinal control: clean vs. approach configurations - UW-S-24A

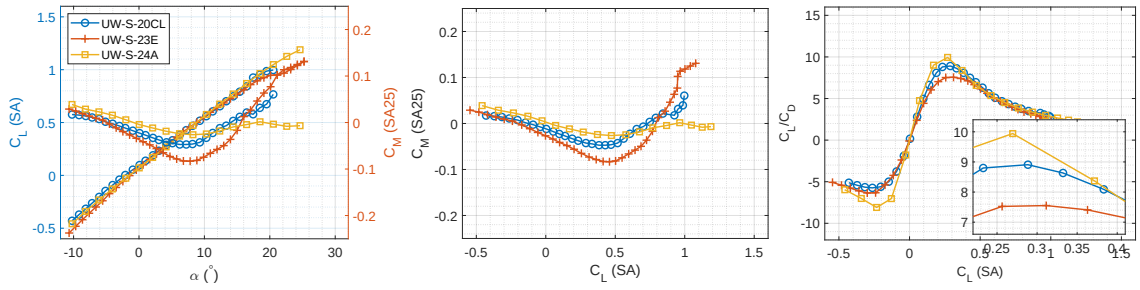
Shifting attention from pitch stability to lift and drag, Fig. 2.267 compares the lift and the Lift/Drag of an RSAC like configuration (UW-S-24) to two low boom concepts.

The figure shows KWT test results at wind tunnel Reynolds numbers for configurations without wing fences, vortex generators, etc. and with no LE/TE flap deflections. Common reference area and MAC are used. The "Icon-2" arrangement is a Boeing-NASA N+3 configuration from the N+3 study ([461]) (based on the general arrangement of the 795-107B) and the SCALOS "Low-Boom" is a UW ogee wing configuration with a longer fuselage, top-mounted nacelles, and a T-Tail. Note the better lift and lift over drag characteristics of the RSAC configuration.

The L/D levels at wind tunnel Reynolds numbers are considerably lower for all of the SCALOS configurations than they would be for a Concorde or HSCT sized aircraft even if only accounting for skin friction differences. However, the comparisons shown here give some idea of the likely penalties incurred at low subsonic conditions when constraining the general arrangement for minimum sonic boom. Although the Icon-II clean configuration shows less

L/D penalty at 0.45–0.65 C_L for LTO/low-noise conditions, the higher wing sweep would tend to make the leading and trailing edge flap deflections relatively less effective, so the L/D gap between it and RSAC would be expected to widen when both are optimized for takeoff and approach field performance and noise.

The longitudinal stability comparison of the RSAC Type configuration is compared to the Low-Boom configurations in Fig. 2.267b. Note that much milder nature of the C_M vs. C_L curve of the RSAC but its somewhat earlier pitch-up.



(a) C_L and C_M vs. α (b) C_M vs. C_L (c) C_L/C_D vs. C_L

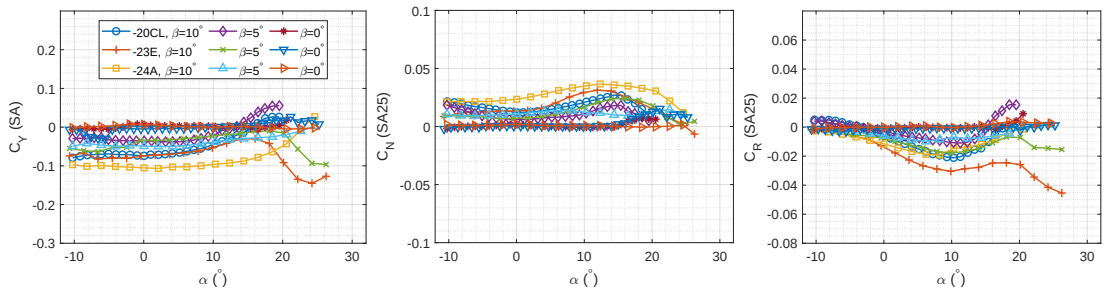
Figure 2.267: Longituidnal aerodynamics comparison of RSAC type with low-boom configurations

A few observations regarding the directional (yaw) stability differences between RSAC type configurations and Low-Boom concepts are made possible by Fig. 2.268b. The ICON2 and the SCALOS Low-Boom configurations are used again to represent low-boom concepts. The SCALOS low-boom has a Nacelle Shock Reflection Deck (NSRD) — a short aft-deck that is the minimum aft deck required on a low-boom configuration (it is similar to the "drool tray" seen under the X-59's engine nozzle). It is important to note that the general arrangement used here was based on Icon-II but that there is no public geometry for that aircraft, only some basic views and an artist rendering.

The figure shows that relative to the two "low-boom" concepts, the RSAC configuration has nearly 2× yaw stability "stiffness" at AOA=0 (but does not increase with AOA). The RSAC configuration does not show "nose slice" instability with AOA at $\beta = 0$.

Moving from static yaw stability to roll stability, comparison of lateral (roll) behavior for RSAC and the two low-boom concepts is shown in Fig. 2.268c. The figure allows us to

find roll moment coefficient derivatives with respect to β (the dihedral effect) at different AOAs. The C_{l_β} (roll due to yaw) cases at AOA=5 degrees and β=5 degrees are -0.002 for the RSAC, -0.0015 for the low-boom SCALOS, and -0.0028 for the V-tail ICON-2 (with a goal of -0.002, but that's only for early design purposes, given that the final value is affected by a combination of flight conditions). The SCALOS low-boom has static roll reversal at about 15 deg. AOA and roll-off at about 18 deg. AOA at zero sideslip. Note: All of the KWT datasets use the designation C_R or C_{rm} for rolling moment coefficient rather than the commonly used C_l.



(a) C_Y vs. α (b) C_N vs. α (c) C_R vs. α

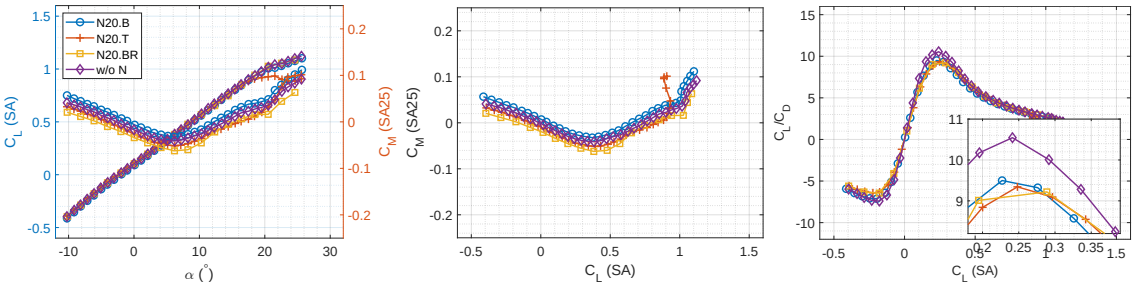
Figure 2.268: Lateral-directional stability comparison of RSAC type with low-boom concepts

Much effort during the development of SCALOS configurations for the configuration design space mapping was dedicated to the effect of engine nacelles and their location. Fig. 2.269a shows the effect of nacelles location on lift. The bottom-mounted nacelles show a slight lift-curve-slope reduction by a higher C_L range. The mounting of nacelles at the rear fuselage has a favorable lift curve slope and the highest C_L at AOA = 25 degrees.

The effect of nacelle location on L/D is shown in Fig. 2.269c. The data used for the figure is untrimmed. The bottom mounted nacelles show some L/D advantage. However test Reynolds number effects may play a role here. There is practically no difference between the top-mounted and aft-body mounted nacelle cases.

The effect of nacelle locations on static pitch stability is shown in Figs. 2.269a (C_M versus AOA) and 2.269b (C_M vs. C_L). The bottom-mounted nacelles show a more positive C_{M_0}. But the pre- and post pitch-up break and the stability levels are similar for all cases.

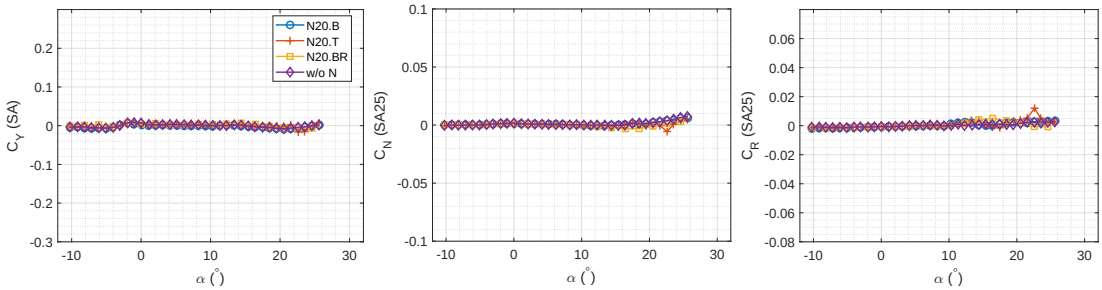
The issue of flow quality into the inlets at high AOAs in the top mounted and aft-fuselage mounted cases is not discussed here. Experience at the University of Washington with top mounted engine nacelles on supersonic configurations in the years 2009 and 2010 (see Fig. 2.3) showed that good to acceptable inlet flow quality could be obtained throughout the flight envelope by placing the nacelles properly longitudinally and laterally. It is important to remember that engines' distance from each other together with the structure that would guarantee that an explosive failure of one engine would not impair the other must be determined simultaneously in an optimal multidisciplinary manner.



(a) C_L and C_M vs. α (b) C_M vs. C_L (c) C_L/C_D vs. C_L

Figure 2.269: Nacelle location: effect longitudinal stability

The Nacelle location impacts on the lat-dir stability characteristics of the configurations tested is shown in Fig. 2.270 for the configurations shown in Fig. 2.138. The top-mounted nacelles appear to have a more non-linear behavior at high AOAs [377].



(a) C_Y vs. α (b) C_N vs. α (c) C_R vs. α

Figure 2.270: Nacelle location: effect lateral-directional stability

Chapter 3

AEROSERVOELASTICITY

3.1 Active Aeroelastic Control

As discussed in §1, aeroservoelastic (ASE) coupling in slender, flexible supersonic transports, presents major challenges. This has led to dedicated wind tunnel testing of active aeroelastic control systems, exemplified by the NASA S4T program. This chapter presents the University of Washington's response to the broader need for low-cost, accessible experimental evaluation of active aeroelastic control: two flexible high-aspect-ratio wing testbeds, and the gust load alleviation and active flutter suppression demonstrated on them using robust control. The goal is to make such aeroservoelastic wind tunnel models available to the developers of ASE control laws for experimental evaluation and feasibility studies on the road to safe active aeroelastic control.

Advances in aerospace control system theory, software, and hardware have made the active control of aeroelastic phenomena in flexible aircraft more practical. Potential benefits include improvements in ride comfort, extension of fatigue life, and overall cost and weight savings [462–466]. The growing power and smaller size of miniature control system hardware, including sensors, actuators, and computers, have made it possible to develop and test wind tunnel [28–32, 467–480] and flight aeroservoelastic models [379] at low costs. This has led to a proliferation of active aeroelastic wind tunnel tests in recent years - an important development that allows rapid evaluation, in tests, of new configurations and new control techniques [481–502].

The pursuit of methods and means for reducing gust response and gust loads in flight goes back to the early days of aviation, with more and more activity in the late 1940s and 1950s including flight tests [503]. Developments in control theory and hardware led to many studies of active gust loads alleviation (GLA), with distinct control systems demonstrated in flight already in the 1960s; GLA has remained an active discipline until today [504].

Numerous theoretical studies of GLA techniques have been published. Many wind tunnel tests have been completed and reported. GLA technology has become an essential part of the development of Multidisciplinary Design Optimization (MDO) of flight vehicles, where the optimization process seeks the best structural, aerodynamic, and control design subject to constraints such as dynamic loads and the ride comfort of crew and passengers due to atmospheric gusts [463]. GLA technology has followed the development of control technology over the years, beginning with classical single-input single-output (SISO) control laws [505], then proceeding to multi-input multi-output (MIMO) designs via Linear Quadratic Regulator (LQR) and Linear Quadratic Gaussian (LQG) control laws, with various robust control approaches also tested; a comprehensive review of aeroservoelastic control is presented in [466].

From the early years of GLA research, it was clear that the capability of an active control system to reduce the response to a sudden gust is significantly limited if the system responds only once the airplane is hit by it. If information about an incoming gust could be known ahead of time, the suppression could be much improved. This triggered the examination of technologies for early detection of incoming gusts, such as LIDAR sensors that measure the velocity of an incoming gust at a distance ahead of the airplane [506, 507]. Preview GLA formulation and simulation [508–523], wind tunnel experiments [469, 524–528], and flight tests [507, 529] have all been explored. Table 3.2 summarizes prior preview GLA works with their control laws and test methods.

With advances made to date in computational modeling and simulation of aeroelastic and aeroservoelastic systems, the uncertainty of such models can still be considerable, making experimental studies timely and valuable. Flight tests of new technologies are costly for full-scale aircraft, and flight tests with small Unmanned Aerial Vehicles are more affordable but challenged by scaling the hardware and operation. In both cases the environments and parameters may not be accurately controllable, and the desired gusts may not be repeatable. Wind tunnel experiments, however, provide controlled and repeatable environments and are cost-effective compared to flight tests. A summary of some aeroelastics testbeds are tabulated in Table 3.1.

As early as the late 1960s and early 1970s, active control technology was studied by tests

not only in wind tunnels but also in flight, using full-size flight vehicles. The B-52 CCV program is an important example [530, 531], in which a multi-task active control system covering Stability Augmentation (SA), Gust Load Alleviation (GLA), Active Flutter Suppression (AFS), and Maneuver Load Alleviation (MLA) was tested in the wind tunnel and in flight. Various forms of aeroelastic active control, such as SA, GLA, and MLA, are now standard on advanced aircraft, while AFS, due to its dangerous nature, has not been fully certified on an operational aircraft despite being demonstrated in wind tunnels and various flight tests. Although flight tests of actively controlled aeroelastic systems are necessary and valuable, testing near and beyond flutter speed is still dangerous, costly, and often infeasible. Techniques for safe flutter testing have been developed over the years, including flutter stoppers [490, 532], the safe-flutter-test method [533, 534], and the destabilize/stabilize approach [31]. At lower costs and with better control of test conditions, wind tunnel tests have therefore been used more extensively for studying active aeroelastic control and for comparing alternative control laws.

Over the years, research has studied a range of control-law synthesis techniques for the AFS problem, including classical SISO methods, root-locus methods, pole placement, Proportional-Integral-Derivative control, Identically Located Accelerometer and Force, and shaping filters; in the MIMO case the Linear Quadratic Regulator and Linear Quadratic Gaussian and their variants; and, driven by an interest in robustness, the $\mathcal{H}_2$, $\mathcal{H}_\infty$, μ-synthesis, and Linear Parameter Varying approaches. A representative summary of the control-law synthesis techniques used thus far in AFS is presented in Table 3.3.

The presence of uncertainty is a central issue in control, where system and model uncertainties can degrade performance and cause closed-loop instability, so it is crucial to examine the closed-loop margins of any designed control system to ensure sufficient robustness. In aeroservoelastic applications the approach to required robustness has generally followed the practices developed in control-systems technology, with conventional gain and phase margins of 6 dB and 45 degrees for SISO systems or a one-loop-at-a-time approach to MIMO systems, halved to 3 dB and 22.5 degrees for multiloop margins [535], as demonstrated in [486, 521, 523, 536–538]. The robust control of the $\mathcal{H}_\infty$ method is thus a natural selection, not only for the stabilization robustness guaranteed via the small gain theorem, but also for

bridging frequency- and time-domain requirements.

The University of Washington's William E. Boeing Department of Aeronautics and Astronautics has developed two aeroservoelastic test articles with gust generation systems (GGS) in two low-speed wind tunnels: a 3 ft by 3 ft low-speed wind tunnel and the 12 ft by 8 ft Kirsten Wind Tunnel [17]. The 3x3 model, the Model of Aeroelastic Response to Gust Excitation (MARGE) [28], was developed as a low-cost, rapid-testing, validation, and risk-reduction testbed, with the larger and more expensive Large model of Aeroelastic Response to Gust Excitation (LARGE) [477] of the KWT used for larger, more complex models. The relevant works on these test articles, control-law synthesis, implementation, and test results are presented in [28–32, 467–469, 476–480].

The rest of the chapter presents the contribution to aeroservoelastic demonstration and experimental evaluation toward flight safety on the MARGE and LARGE testbeds where §3.2 details the experimental setup, §3.3 provides the mathematical backgrounds, §3.4 shows wind tunnel system identification, §3.5 details the control design on gust load alleviation and active flutter suppression, and lastly §3.6 presents the wind tunnel results and closed-loop analysis of the controller performance and evaluation.

Table 3.1: Some aeroelastic testbeds

	Half-wing model	Half-aircraft model	UAV	Aircraft
Wind Tunnel	NASA BACT[539–546]	DC-10 [560]	ITA EOLO [571]	B-52 [531]
	NASA RSW [547]	NASA AFW [561–563]		F-16 [572, 573]
	NASA BSCW [500, 547]	LM/NG HILDA [564]		YF-17 [574–576]
	RWTH HIRENASD [547]	NASA/Boeing IAWTM [565]		POLIMI X-DIA [481–494]
	Duke U NACA0012 [548–550]	NASA/Boeing TTBW [566]		
	Beihang U NACA0015 [551]	JAXA CRM like [567, 568]		
	Nanjing U MAW [552–558]	UW MARGE [28–32, 467–469]		
	UW TLW [470–480]	Beihang U COMAC like [569]		
	Technion Pazy [495, 497–499]	UMich/ Technion AT3B [570]		
	DLR oLAF [559]			
Flight Test	N/A	N/A	NASA DAS [577–581]	B-52 CCV [530, 606–608]
			Lockheed BFF [582]	F-4 [609–611]
			NASA X-56 [583–586]	YF-17/F-18/X-53 [612–614]
			UMich X-HALE [587, 588]	NASA X-29 [615, 616]
			UMinn Mini Mutt[536–538, 589–594]	F-16 [617, 618]
			EU FLEXOP [595–600]	B-1 [619]
			Technion AT3B [496]	E-6 [620]
			ITA EOLO [601]	B-2 [621]
			Nanjing U AFD-1 [602–605]	

Table 3.2: Some preview gust load alleviation works

	Simulation	Wind Tunnel Test	Flight Test
Feedforward	Fezans and Joos [508]	Zhou et al. [569] Hu et al. [528]	Rabadan et al. [507]
Adaptive	Wang et al. [511] Zhao et al. [512]	Wang et al. [524]	N/A
MPC	Giesseler et al. [509] Liu et al. [514]	Barzgaran et al. [525, 526]	N/A
$\mathcal{H}_2$	Hamada [510, 513, 519] Takase et al. [515]	Hamada et al. [527]	Hamada [529] Hamada [622] (plan)
$\mathcal{H}_\infty$	Khalil and Fezans [516–518] Hamada [513, 519] Takase et al. [520] Fezans et al. [522]	Ting et al. [469]	N/A
μ-synthesis	Fournier et al. [521, 523]	N/A	N/A

Table 3.3: Some active flutter suppression works

	Simulation	Wind tunnel test	UAV flight test	Manned flight test
Classical				
Shaping filters		Berg et al. [31, 32]		
Nyquist	Triplett et al. [609, 610]	Peloubet et al. [572, 573]		Peloubet et al. [617]
	Nissim [580]	Huang et al. [574, 575]		Newsom and Pototzky [578]
Root locus	Chipman et al. [615, 616]			
	Waszak and Srinathkumar [562]		Roger et al. [530]	
	Mukhopadhyay [542, 543]			
	Scott and Pado [544]			
	McEver et al. [550]			
PID	Zou et al. [603]			Sensburg et al. [611]
pole placement	Scott and Pado [544]	Adams et al. [561]		
	Yang et al. [557]	Huang et al. [556]		
ILAF	Schmidt [592]	Ricci et al. [486, 487, 490]	Schmidt et al. [537, 593, 594]	
LQR / LQG	Chipman et al. [615, 616]	Huang and Pi [576]		
	Newsom et al. [579]	Adams et al. [561]		
	Miyazawa and Dowell [623]	Mukhopadhyay [563]		
	Nissim [581]	Qian et al. [555]		
	Mukhopadhyay [542, 543]	Ricci et al. [486, 487, 490]		
	Xiong and Yang [624]			
Adaptive	Huang et al. [553]		Danowsky et al. [537, 593, 594]	
(modified LQR)	Danowsky et al. [625]			
$\mathcal{H}_2$	Luspay et al. [597]	Vipperman et al. [548, 549]		
	Micheli [626]			
$\mathcal{H}_\infty$	Mukhopadhyay [542, 543]	Waszak [546]	Theis et al. [594]	
	Theis et al. [536–538, 593]	Berg et al. [31, 32]	(not beyond flutter speed)	
	Waitman et al. [597, 598]			
	Zou et al. [602]			
	Faisee et al. [627, 628]			
	Fournier et al. [629]			
	De Souza et al. [630]			
	Micheli [626]			
μ-synthesis	Moulin et al. [631, 632]	Vipperman et al. [549]		
	Qian et al. [554]	Waszak [546]		
	Patartics et al. [600]	Qian [558]		
LPV	Seiler et al. [583, 614]			
	Takarics and Vanek [599]			
Nonlinear	Xiang et al. [633]			
Neural Network		Scott and Pado [544]		
Others	Wu and Cooper [634]	Adams et al. [561]	Burnett et al. [585]	
or unidentified	Waitz [635]	Haley and Soloway [545]		
	Richards et al. [636]	Ricci et al. [486, 487, 490]		

3.2 Experimental Setup

This section describes the experimental setup for the MARGE and LARGE wind tunnel models, including the hardware and software integration and closed-loop setup for the MARGE model [30, 31, 477, 480, 637].

3.2.1 Aeroelastic Model in 3'x3', MARGE

3'x3' Low-Speed Wind Tunnel and Gust Generation System

The University of Washington's 3'x3' low-speed wind tunnel has a 9-to-1 contraction ratio, 3ft by 3ft by 8ft test section, and a 34-135 mph (15.2-61.7 m/s) wind speed capability. Figure 3.1 shows the schematics of the open-circuit wind tunnel. The gust generation system (GGS) is installed at the extension section between the contraction and test sections. There are two movable gust vanes with NACA-0012 airfoils and 10-inch (0.254-m) chord length each. They are driven together by an electric motor and are installed vertically and spaced evenly, 7 inches (0.18 m) from the centerline. The vanes are designed to be stiff with minimal distortion under load during operation for uniform gust field generation in the test section. The natural frequencies of the vanes, above 20 Hz, are much higher than the frequencies of interest of the aeroservoelastic models tested. Based on hot-wire measurement of turbulence intensity of the tunnel, turbulence intensity (RMS) is 0.2% [638].

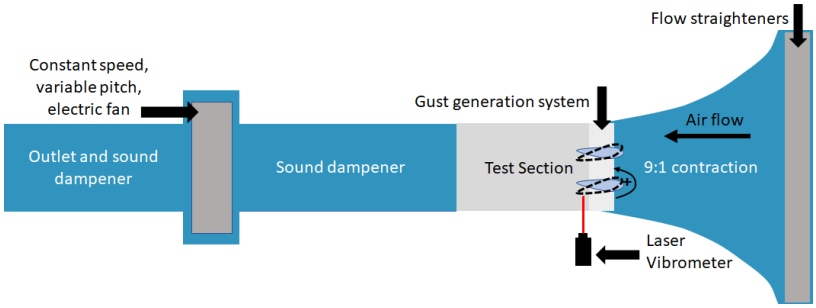
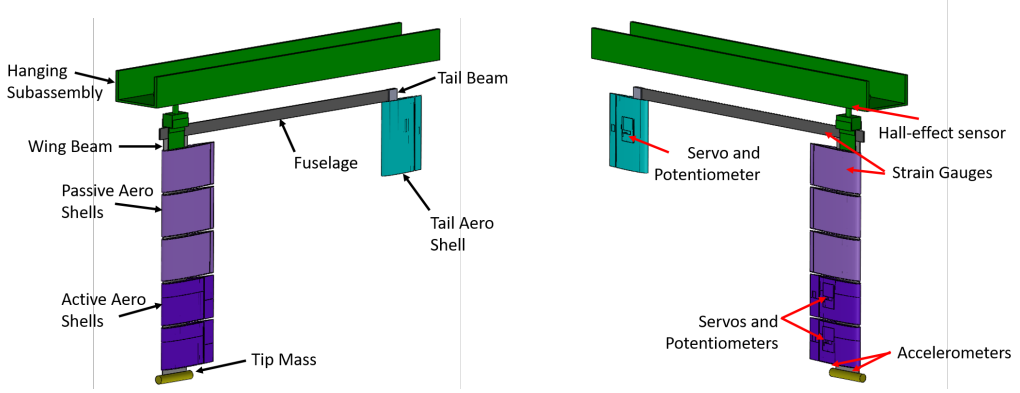


Figure 3.1: Top view of University of Washington's 3ft by 3ft low-speed wind tunnel and gust generation system [28–30]

Model for Aeroelastic Response to Gust Excitation (MARGE)

The Model for Aeroelastic Response to Gust Excitation (MARGE-I), was designed, subject to the wind tunnel's physical constraints, to portray typical aeroelastic coupling of rigid-body and elastic motions of typical wing-fuselage-tail configurations [28]. Figure 3.2 shows the structural, aerodynamic, and system components of MARGE-I. It is a half-span wing-body-tail model vertically mounted to a channel section attached to the wind tunnel ceiling with its wingtip pointing down. MARGE-I is made of three beams: the wing, fuselage, and tail. Both the wing and tail are covered by 3D-printed NACA-0012 airfoil aerodynamic shells, and soft foams between shells to minimize the aerodynamic leaks while preventing shell-to-shell contact from affecting the stiffness of the structure. The tip mass at the wing tip is sized and placed to obtain desired low-frequency modes of motion and natural frequencies. MARGE-I has two wing control surfaces on the two outer shell of the wing and a single full-span elevator. Each control surface is driven by an MKS HV6130 servo motor mounted inside the shell. Seven onboard sensors are shown in Fig. 3.2b including a non-contact Hall-effect sensor for rigid body pitch angle, two accelerometers at the wing tip for bending and torsional motions, and a strain gauge for out-of-plane wing-root bending moment. Rotary potentiometers are installed on each control surface for surface rotations. Some key parameters for MARGE-I are summarized in Tab. 3.4 from Figs. 4 and 5, and Tabs. 1-9 in [28].



(a) Primary components (b) Sensing and actuation components

Figure 3.2: Model of aeroeslatic response to gust excitation [28]

Table 3.4: Overview of MARGE's key parameters [28, 29, 31, 32]

(a) Structural components

Components	Material	Weight (lb/ kg)
Wing beam	Aluminum 6061-T6	0.367 / 0.166
Tip cylinder	Brass	0.276 / 0.125
Active aero-Shell	Polyactic acid (PLA)	0.209 / 0.095
Passive aero-Shell	Polyactic acid (PLA)	0.132 / 0.060
Fuselage beam	Low carbon steel	0.986 / 0.447
Tail beam	Aluminum 6061-T6	0.146 / 0.066

(b) Model Geomteries

Parameter	Value
Span	20.55 in (0.52 m)
Chord	6.55 in (0.17 m)
Sweep	0°
Aspect ratio	6.28
Flap-chord ratio	0.22

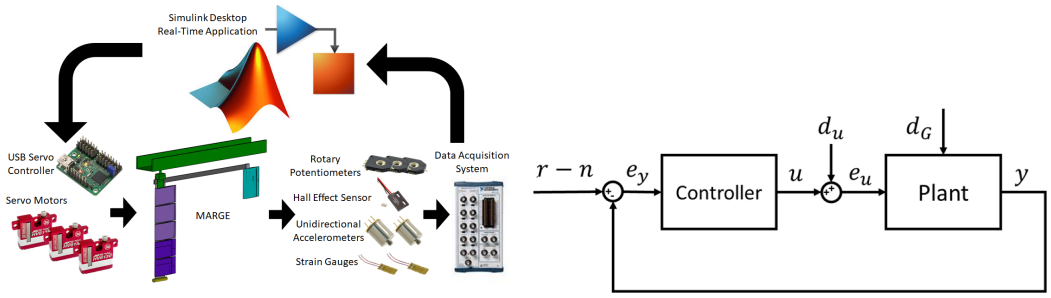
(c) Mode characteristics

Mode (Hz)	NASTRAN	GVT
1^{st} wing	1.4440	1.422
2^{nd} wing	10.4867	10.142
1^{st} fuselage	16.6383	19.897
1^{st} wing twisting	19.1997	18.094
1^{st} fuselage in-plane	21.9480	19.893
3^{rd} wing	32.3108	32.545

Hardware and Software Integration and Closed-loop Setup

A dedicated computer is used for the test setup, including the wind tunnel data acquisition (DAQ), GGS command, Simulink Desktop Real-Time Application, and MARGE-I DAQ. The Simulink Desktop Real-Time Application interacts with the MARGE-I wind tunnel model as shown in Fig. 3.3a. While the simulation interacts with the state space model, the hardware-in-the-loop interacts with MARGE-I through a custom circuit board for signal conditioning with 1st-order anti-aliasing filters on all signals with a cutoff frequency at 25 Hz.

Then the differential signals are connected to a National Instruments (NI) BNC 2110 board and NI PCIe 6320 DAQ to the dedicated computers. The DAQ board has 16 differential channels for seven onboard sensors and a separate laser vibrometer. The measured signals (y) could be processed with optional output filters in the estimated output ($\hat{y}$) and then passed to a Kalman filter for state estimation ($\hat{x}$). Output feedback is used for both gust load alleviation and active flutter suppression. As such, a Kalman filter and the gust input (d_G) are not utilized for the work described here. The closed-loop control block diagram is shown in Fig. 3.3b where r is the reference output, e_y is the error output, u is the control input, d_u is the input disturbance, and e_u is the actual input.



(a) Closed-loop signal flow [29] (b) Output feedback control block diagram

Figure 3.3: MARGE-I hardware-in-the-loop and control block diagram setup

3.2.2 Aeroelastic Model in Kirsten Wind Tunnel (KWT), LARGE

The LARGE flexible wing aeroservoelastic wind tunnel model

The LARGE system is described in Refs. [477] and [475].

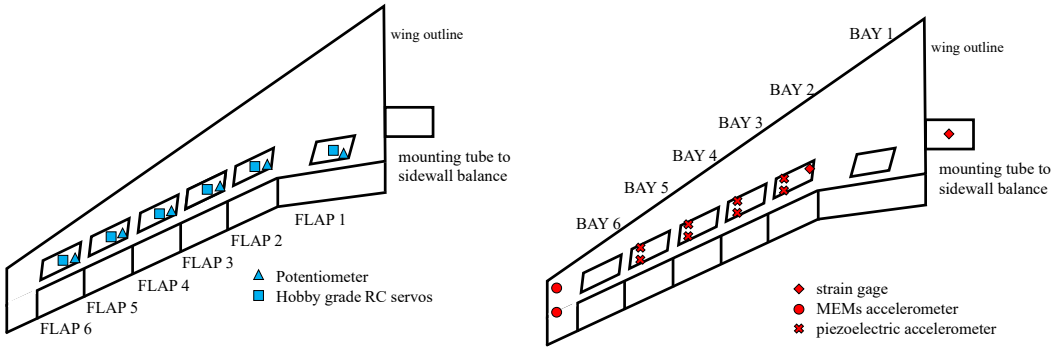
The wing was built to the planform, airfoil shape, and twist distributions of the Common Research Model (CRM) wing [639] with overall flexibility that would be similar to that of a current advanced commercial large airplane with composite wings. LARGE is 85 inches in span from root to wing tip with continuous skin design [470–477] (not common in low-speed aeroelastic wind tunnel mode). That is, it is not made from a core spar and its selected EI and GJ distributions, plus a distribution of masses, all covered by aerodynamic fairing sector for the aerodynamic shape. The goal was to build a Variable Camber Continuous

Trailing Edge Flapped (VCCTEF) aeroelastic model that would allow testing that would be both aeroelastic, for gust load alleviation, but also classic aerodynamic for drag and lift.

The first wing bending natural frequency of LARGE, 2.5 Hz, is well within its actuation and GGS frequency bandwidths. A detailed NASTRAN model / test correlation was presented in [475]. Trailing edge flexible transition strips connecting flaps spanwise and the two innermost flaps camber variable features were removed in the redesign in 2021 [477].

LARGE has six spanwise flaps as shown in Fig. 3.4a and the sensors are placed inside the bays underside of the LARGE - Fig. 3.4b. A metal strip-spar from wing root to wing tip not only provides strength and flexibility for the wing but also serves as support for actuator and sensor placements. The bays are separated spanwise by the mental ribs. The volume of the wing is made of foam. The wing surface is covered by thin fiberglass skins.

Wing sensors in LARGE remain the same as the in the 2021 design [477], with two MEMs ADXL356BZ accelerometers at the wingtip, eight piezoelectric TE805M1 accelerometers from TE Connectivity in bays, one 350 Ω, 3%, strain gauge from Micro-Measurements installed in bay two, and a single ZX-PA-1.5-A string potentiometer from Unimeasure at each flap in Fig. 3.4. The three-axis force and moments at the wing root are measured by the sidewall balance (SWB) in the Kirsten Wind Tunnel (KWT) as presented §2.4.1.



(a) Actuation Components (b) Sensor Components

Figure 3.4: LARGE – bottom view of onboard actuators and sensors with accessing bays.

A dedicated computer is used for Simulink Desktop Real-Time Application, LARGE DAQ, and GGS command. The Simulink Desktop Real-Time Application collects sensor measurements and sends actuation commands to the LARGE model in the wind tunnel.

A dedicated desktop personal computer runs the realtime desktop environments and stores collected test data through National Instruments (NI) PCIE-6323, 32 single-ended channels or 16 differential channels, and two NI BNC 2100 DAQ for input and output (I/O) signals at 500 Hz sampling of analog signals. Custom instrumentation circuit boards perform signal conditioning prior to sampling by the NI DAQ. The custom instrumentation circuit boards also apply the second-order analog anti-aliasing filters with a -3 dB frequency of 40 Hz updated from 25 Hz due to the actuator improvement (see §3.2.2). The measured signals are filtered and then can be further estimated by a Kalman filter for state reconstruction which is not part of the work reported here. The flowchart of the closed-loop control process is shown in Fig. 3.3b. The Simulink environment is a more capable version of what is used for MARGE-I in the 3x3 tunnel in Fig. 3.3a [28, 477].

TLW Hardware and Modeling Update

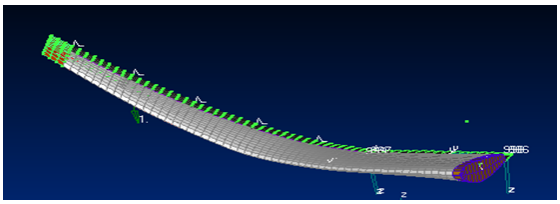
The 2024 system improvement of LARGE focused on the servo-actuation and side-wall balance integration. The flap 3 to 6 hobby-grade servos, HS-9360TH by Hitec RCD, were replaced by the MKS HBL880 with approximately double the bandwidth. The linkage systems from flap 3 to 6 were also replaced with servo horns and longer moment arms by extruding outside of the wing bay covers that house the actuators. The flap connections were replaced with custom 3D-printed parts. The updated servo-actuation system reduced the free play angles to less than 0.25°.

The side-wall balance integration allowed three-axis force and moment data collected by the KWT to be viewed in real-time in Simulink. It was done via UDP protocol. In the tests presented here no direct sidewall loads are used for feedback. Strain gauge information in the wing root area, calibrated to provide bending moment along the wing's elastic axis was used as the internal gust response loads output to be reduced by the active control system together with vibration response reduction based on accelerometer measurements.

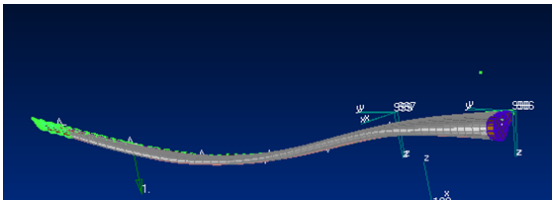
The NASTRAN finite element model (FEM) of the LARGE system has 3322 elements and 13 materials. Element types include membrane elements for the skins; 3D elements for the foam core, wingtip, and reinforcements' spring elements for control surface attachments;

and beam elements for the strip spar. The first five modes are shown in Fig. 3.5 with frequencies tabulated in Tab. 3.5. More detail of the FEM can be found in [477]. Unsteady aerodynamic forces were produced by the Doublet Lattice Method (DLM) capabilities of NASTRAN. NASTRAN capabilities were also used for the transformation between the DLM and structural NASTRAN FE meshes.

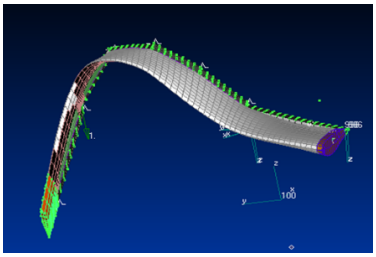
It is important to note here that the FE/DLM model of the system includes the wing, the walls of the test section, and the gust vanes ahead of the wing. Various Doublet Lattice aerodynamic meshes were studied before the final mesh was selected. A number of ground vibration tests during the development of the wing, in the lab and in the wind tunnel test section, led to improvements, by fine-tuning, of the FE NASTRAN model. The focus of the wind tunnel tests of 2024 was on gust loads and vibration suppression of the response in the first bending mode of the wing.



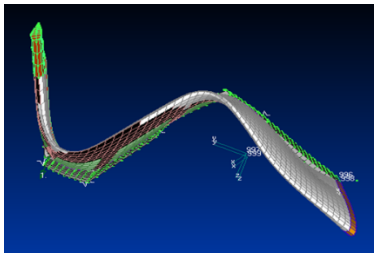
(a) Mode 1: 1st wing bending



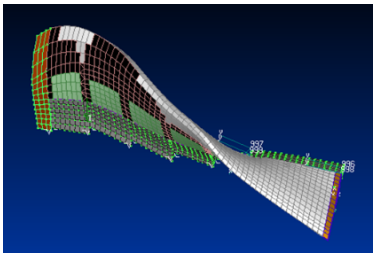
(b) Mode 2: in-plane bending



(c) Mode 3: 2nd wing bending



(d) Mode 4: Bending and torsion



(e) Mode 5: Torsion

Figure 3.5: LARGE - finite element model modes shapes

Table 3.5: LARGE - finite element model mode characteristic

Mode #	Mode shape	NASTRAN (Hz)
1	1st bending	2.2
2	in-plane bending	9.4
3	2nd bending	10.8
4	bending and torsion	24
5	torsion	29

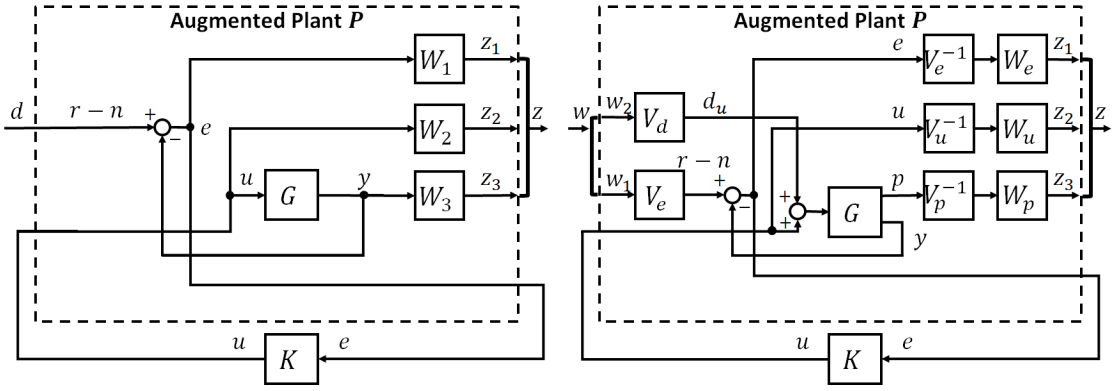
3.3 Background Mathematics

This section provides the mathematical background for the control design and analysis in this chapter, including robust control theory, destabilization/stabilization techniques, and the use of the Chirp-Z Transform (CZT) for both open-loop system identification and closed-loop evlaution [30, 31, 480, 637].

3.3.1 Robust Control

A Summary of the Key Elements of the $\mathcal{H}_\infty$ control method

Feedback Formulation



(a) Mixed-sensitivity $\mathcal{H}_\infty$ loop shaping [640–642] (b) Robust modal damping control [536, 538]

Figure 3.6: Robust $\mathcal{H}_\infty$ control

The continuous LTI system model with modeled regulated output and disturbances assumes the form,

$$\begin{aligned} \dot{x}(t) &= Ax(t) + B_1 d(t) + B_2 u(t) \\ z(t) &= C_1 x(t) + D_{11} d(t) + D_{12} u(t) \\ y(t) &= C_2 x(t) + D_{21} d(t) + D_{22} u(t) \end{aligned} \tag{3.1}$$

where $x(t) \in \mathbb{R}^{n_x}$, $d(t) \in \mathbb{R}^{n_d}$, and $u(t) \in \mathbb{R}^{n_u}$ are the state vector, exogenous/disturbance input vector, and the control input vector. The variables $z(t) \in \mathbb{R}^{n_z}$ and $y(t) \in \mathbb{R}^{n_y}$ denote the regulated outputs and observed outputs, respectively. The regulated outputs are not necessarily fed back to the closed-loop system; on the other hand, the observed outputs are used for feedback control.

The transfer matrix/ generalized plant representation of Eq. (3.1) is as follows:

$$G(s) = \left[\begin{array}{c|cc} A & B_1 & B_2 \\ \hline C_1 & D_{11} & D_{12} \\ C_2 & D_{21} & D_{22} \end{array}\right]. \tag{3.2}$$

By constructing the generalized plant, the general control problem can be solved as a standard $\mathcal{H}_\infty$ problem [643, 644]. The $\mathcal{H}_\infty$ is the set of stable and proper transfer functions with bounded ∞-norm, and the $\infty-$ norm of the system in Eq. (3.2) is

$$\left\| G(s) \right\|_\infty \triangleq \sup_\omega \sigma_{\max} \left| G(j\omega) \right| = \sup_{d(t)\neq 0} \frac{\left\| z(t) \right\|_2}{\left\| d(t) \right\|_2} = \sup_{||d(t)||_2 = 1} \left\| z(t) \right\|_2, \tag{3.3}$$

where ω and t denote the frequency and time spaces, respectively. The frequency and time domain interpretations are related based on the induced 2-norm and Parseval's Theorem.

In the frequency domain, minimizing the $\mathcal{H}_\infty$ norm reduces the largest singular value at the *worst* direction and frequency, while in the time domain minimizing $\mathcal{H}_\infty$ norm mitigates the *worst* response of the system. The general control structure of the $\mathcal{H}_\infty$ control problem is represented as

$$\begin{bmatrix} z \\ y \end{bmatrix} = G(s) \begin{bmatrix} d \\ u \end{bmatrix} = \begin{bmatrix} G_{11}(s) & G_{12}(s) \\ G_{21}(s) & G_{22}(s) \end{bmatrix} \begin{bmatrix} d \\ u \end{bmatrix}, \tag{3.4}$$

$$u = K(s) y, \tag{3.5}$$

without state variables (see Eqs. (3.1) and (3.2)). The closed-loop transfer function from the exogenous signal, d, to regulated output, z, is given by the linear fractional transformation of the plant, G, and controller, K, as

$$\begin{aligned} z &= F_l(G,K)d, \\ F_l(G,K) &= G_{11} + G_{12}K(I - G_{22}K)^{-1}G_{21}, \end{aligned} \tag{3.6}$$

where $F_l(G,K)$ is often denoted as T_{zw} in the literature and the $\mathcal{H}_\infty$ controller minimizes the $\mathcal{H}_\infty$ norms of $F_l(G,K)$.

The mixed-sensitivity $\mathcal{H}_\infty$ loop shaping formulates the $\mathcal{H}_\infty$ control problem in Eq. (3.4) as

$$\begin{bmatrix} z_1 \\ z_2 \\ z_3 \\ y \end{bmatrix} = \left[\begin{array}{c|c} W_1 & -W_1G \\ 0 & W_2G \\ 0 & W_3 \\ \hline I & -G \end{array}\right] \begin{bmatrix} d \\ u \end{bmatrix} \tag{3.7}$$

and minimize the $S/KS/T$ of the augmented system P in Fig. 3.6a (also see: [640–642]

$$\|F_l(P,K)\|_\infty = \left\| \begin{bmatrix} W_1S \\ W_2KS \\ W_3T \end{bmatrix} \right\|_\infty \tag{3.8}$$

where $S = (I + GK)^{-1}$ and $T = GK(I + GK)^{-1}$ are the sensitivity and complementary sensitivity functions, respectively.

The proposed method of [536, 538] imposes normalization and adds input disturbance, d_u, to the augmented plant P

$$\begin{bmatrix} z_1 \\ z_2 \\ z_3 \\ y \end{bmatrix} = \left[\begin{array}{cc|c} W_e & WeVe^{-1}G_yV_d & -W_eV_e^{-1}Gy \\ 0 & 0 & W_uV_u^{-1} \\ 0 & W_pV_p^{-1}G_pV_d & W_pV_p^{-1}G_p \\ \hline V_e & -G_yV_d & -Gy \end{array}\right] \begin{bmatrix} w_1 \\ w_2 \\ u \end{bmatrix}. \tag{3.9}$$

where G_y and G_p are the observation transfer function and performance transfer function, respectively. The signal vector $p \in \mathbb{R}^{n_p}$ is an additional performance output. The variable V is the static weight normalizing the corresponding signals. Contrasting the pre-scaling of

the system in [30, 644], the method of [536, 538] incorporates the normalization scaling as part of the weighting filter in the synthesis process. The control problem presented in Fig. 3.6b becomes the minimization of the linear fractional transformation below

$$\|F_l(P,K)\|_\infty = \left\| \begin{bmatrix} W_e V_e^{-1} S_o V e & -W_e V_e^{-1} G_y S_i V_d \\ W_u V_u^{-1} K S_o V_e & -W_u V_u^{-1} K G_y S_i V_d \\ W_p V_p^{-1} G_p K S_o V_e & W_p V_p^{-1} G_p S_i V_d \end{bmatrix} \right\|_\infty \tag{3.10}$$

where the subscripts $_i$ and $_o$ represent the input and output of the sensitivity function, respectively. It is important to note that the regulated output z is normalized in Fig. 3.6b as opposed to Fig. 3.6a.

Preview Formulation

The preview augmentation is presented in discrete-time LTI system form. Equation (3.1) replaces the time variable (t) by a time-step subscript k. The disturbance is:

$$d_{p,k} := d_{k+h}. \tag{3.11}$$

where $d_{p,k} = d_{k+h}$, the last disturbance, is observed and known, and h is the preview step.

Substituting Eq. (3.11) into the discrete form of Eq. (3.1) yields:

$$\begin{aligned} x_{k+1} &= Ax_k + B_1 d_{p,k-h} + B_2 u_k, \\ z_k &= C_1 x_k + D_{11} d_{p,k-h} + D_{12} u_k, \\ y_k &= C_2 x_k + D_{21} d_{p,k-h} + D_{22} u_k. \end{aligned} \tag{3.12}$$

The disturbance vector is redefined from Eq. (3.11) as:

$$x_{d,k} = \begin{bmatrix} d_k & d_{k+1} & \cdots & d_{k+h} \end{bmatrix}^\intercal = \begin{bmatrix} d_{p,k-h} & d_{p,k-h+1} & \cdots & d_{p,k-1} \end{bmatrix}^\intercal \in \mathbb{R}^{l \times h} \tag{3.13}$$

where the disturbance dynamics is modeled as:

$$\begin{aligned} x_{d,k+1} &= A_d x_{d,k} + B_d d_{p,k}, \\ y_{d,k} &= C_d x_{d,k} + D_d d_{p,k}. \end{aligned} \tag{3.14}$$

The disturbance dynamics matrices are partitioned as follows (with their dimensions):

$$A_d = \left[\begin{array}{c|c} 0_{h-1\times 1} & I_{h-1\times h-1} \\ \hline 0 & 0_{1\times h-1} \end{array}\right], B_d = \left[\begin{array}{c} 0_{h-1\times l} \\ \hline I \end{array}\right], C_d = \left[\begin{array}{c} I_{h\times h} \\ \hline 0_{1\times h} \end{array}\right], D_d = \left[\begin{array}{c} 0_{h\times l} \\ \hline I \end{array}\right]. \quad (3.15)$$

The new state vector is the original state vector augmented with known previewed disturbance states, $\tilde{x}_k = [x_k^\mathsf{T} \quad x_{d,k}^\mathsf{T}]^\mathsf{T}$, and the augmented generalized plant in partition form becomes:

$$\tilde{x}_{k+1} = \left[\begin{array}{c|cc} A & B_1 & 0_{n\times h-1} \\ \hline 0_{h\times n} & \multicolumn{2}{c}{A_d} \end{array}\right] \begin{bmatrix} x_k \\ x_{d,k} \end{bmatrix} + \left[\begin{array}{c} 0_{n\times l} \\ \hline B_d \end{array}\right] d_{p,k} + \left[\begin{array}{c} B_2 \\ \hline 0_{h\times m} \end{array}\right] u_k, \quad (3.16)$$

$$\tilde{z}_k = \left[\begin{array}{c|cc} C_1 & D_{11} & 0_{p\times h-1} \end{array}\right] \begin{bmatrix} x_k \\ x_{d,k} \end{bmatrix} + \begin{bmatrix} 0_{p\times l} \end{bmatrix} d_{p,k} + D_{12} u_k, \quad (3.17)$$

$$\tilde{y}_k = \left[\begin{array}{c|cc} C_2 & D_{21} & 0_{q\times h-1} \\ \hline 0_{h+1\times n} & \multicolumn{2}{c}{C_d} \end{array}\right] \begin{bmatrix} x_k \\ x_{d,k} \end{bmatrix} + \left[\begin{array}{c} 0_{q\times l} \\ \hline D_d \end{array}\right] d_{p,k} + \left[\begin{array}{c} D_{22} \\ \hline 0_{h+1\times m} \end{array}\right] u_k. \quad (3.18)$$

This formulation allows the preview problem to be solved as a standard $\mathcal{H}_2$ or $\mathcal{H}_\infty$ problem as in Eq. (3.4).

3.3.2 The Destabilize/Stabilize Approach

A short summary of the destabilize/Stabilize approach from [31, 32]: Take Laplace transformed of a linear time invariant (LTI) state space model of an aeroservoelastic system as in Eq. (3.39) is

$$\begin{aligned} sX &= AX + BU \\ Y &= CX \end{aligned} \quad (3.19)$$

where U is the control input and Y is the measured outputs. The model in Eq. (3.19) represents the strictly proper transfer function of the aeroelastic state space model including dynamics of the bare-airframe, actuators, sensors, and any filters added, i.e. anti-aliasing, low-pass, and band pass filers.

The input and output vectors could be partitioned into $U = [U_1 \quad U_2]^\mathsf{T}$ and $Y = [Y_1 \quad Y_2]^\mathsf{T}$ where the partition size of U_1, U_2, Y_1 and Y_2 may be different. The partitioned transfer

function of Eq. (3.19) becomes

$$\begin{aligned} sX &= AX + \begin{bmatrix} B_1 & B_2 \end{bmatrix} \begin{bmatrix} U_1 \\ U_2 \end{bmatrix} \\ \begin{bmatrix} Y_1 \\ Y_2 \end{bmatrix} &= \begin{bmatrix} C_1 \\ C_2 \end{bmatrix} X \end{aligned} \tag{3.20}$$

Let a general linear control law with input Y_1 and output U_1 be in the form of

$$\begin{aligned} sZ &= A_{ds}Z + B_{ds}Y_1 \\ U_1 &= C_{ds}Z + D_{ds}Y_1 \end{aligned} \tag{3.21}$$

where the subscript $_{ds}$ stands for destabilizing. The control law intends to shape the overall system with some desired flutter mechanics and flutter boundaries. Substitution of Eq. (3.21) into Eq. (3.20) with appending the controller state Z , the closed-loop system is then

$$\begin{aligned} s \begin{bmatrix} X \\ Z \end{bmatrix} &= \begin{bmatrix} A + B_1 D_{ds} C_1 & B_1 C_{ds} \\ B_{ds} C_1 & A_d s \end{bmatrix} \begin{bmatrix} X \\ Z \end{bmatrix} + \begin{bmatrix} B_2 \\ 0 \end{bmatrix} U_2 \\ \begin{bmatrix} Y_2 \\ 0 \end{bmatrix} &= \begin{bmatrix} C_2 \\ 0 \end{bmatrix} \begin{bmatrix} X \\ Z \end{bmatrix} \end{aligned} \tag{3.22}$$

which is equivalent to the new unstable system as follows

$$\begin{aligned} s\bar{X} &= \bar{A}\bar{X} + \bar{B}\bar{U} \\ \bar{Y} &= \bar{C}\bar{X}. \end{aligned} \tag{3.23}$$

The original aeroservoelastic system in Eq. (3.19), controlled by the destabilizing control laws in Eq. (3.21), becomes the new unstable aeroservoelastic system in Eq. (3.23) available for active control studies. Note that the test of the active flutter suppression is in a controlled environment where instability could be eliminated via breaking the loop of the control laws without any tunnel shut down or using flutter stoppers. Interested readers could refer to [31] for two different types of flutter mechanism created by this approach.

3.3.3 Chirp Z-Transform

A Summary of the Chirp Z-transform (CZT) from [49].

The finite Fourier transform takes nonperiodic time-based input and output signals $x(t)$ and $y(t)$, respectively, and transforms them into two equivalent frequency based signals $X(f)$ and $Y(f)$ from $t = 0$ to $t = T$

$$X(f,T) = \int_0^T x(t)e^{-j2\pi ft}dt \tag{3.24}$$

and the discrete version in

$$X(f_k) = \Delta t \sum_{n=0}^{N-1} x_n e^{\frac{-j2\pi kn}{N}} dt \tag{3.25}$$

where $X(f_k)$ is the Fourier coefficient, $x_n = x(n\Delta t)$ is the discrete data, and $\Delta f = 1/N\Delta t$ is the frequency resolution. The *rough estimates* (denoted by $\tilde{}$) of the autospectrum from the Fourier coefficients are

$$\tilde{G}_{xx}(f) = \frac{2}{T}\left|X(f)\right|^2 \tag{3.26}$$

$$\tilde{G}_{yy}(f) = \frac{2}{T}\left|Y(f)\right|^2 \tag{3.27}$$

$$\tilde{G}_{xy}(f) = \frac{2}{T}\left|X^*(f)Y(f)\right| \tag{3.28}$$

where $\tilde{G}_{xx}$, $\tilde{G}_{yy}$, and $\tilde{G}_{xy}$ are the input, output, and cross spectrum, respectively. The *smooth estimate* (denoted by $\hat{}$) is done through overlapping windowing and becomes

$$\hat{G}_{xx}(f) = \frac{1}{Un_r}\sum_{k=1}^{n_r} \tilde{G}_{xx,k}(f) \tag{3.29}$$

$$\hat{G}_{yy}(f) = \frac{1}{Un_r}\sum_{k=1}^{n_r} \tilde{G}_{yy,k}(f) \tag{3.30}$$

$$\hat{G}_{xy}(f) = \frac{1}{Un_r}\sum_{k=1}^{n_r} \tilde{G}_{xy,k}(f) \tag{3.31}$$

where n_r is the overlapped window segments and $U = \sqrt{3/8}$ is the Hanning window corrections.

The frequency response function $H(f)$ can be estimated directly from the spectral function estimate above

$$\hat{H}_1(f) = \frac{\hat{G}_{xy}}{\hat{G}_{xx}} \tag{3.32}$$

$$\hat{H}_2(f) = \frac{\hat{G}_{yy}}{\hat{G}_{yx}} \tag{3.33}$$

and the coherence function is

$$\hat{\gamma}_{xy}^2(f) = \frac{\left|\hat{G}_{xy}(f)\right|^2}{\left|\hat{G}_{xx}(f)\right| \left|\hat{G}_{yy}(f)\right|}. \tag{3.34}$$

Note that [49] suggests that the coherence function can be interpreted physically as the function of the output spectrum that is linearly attributable to the input spectrum at a frequency, and the guideline is $\gamma_{xy}^2 \geq 0.6$.

The quantitative estimate of the expected normalized random error is

$$\epsilon_r = C_\epsilon \frac{\left(1 - \gamma_{xy}^2\right)^{1/2}}{|\gamma_{xy}| \sqrt{2n_d}} \tag{3.35}$$

where C_ϵ accounts window overlap and n_d is the non-overlapping window segments. The frequency response uncertainty could be estimated by the normalized random error function with 95% confidence bounds as

$$\left|\hat{H}\right| (1 - 2\epsilon_r) \leq |H| \leq \left|\hat{H}\right| (1 + 2\epsilon_r) \tag{3.36}$$

$$(\hat{\phi}_{\text{rad}} - 2\epsilon_r) \leq |\phi_{\text{rad}}| \leq (\hat{\phi}_{\text{rad}} + 2\epsilon_r) \tag{3.37}$$

where the uncertainty in the phase estimate of the frequency response $\Delta\hat{\phi}_{\text{rad}} = \epsilon_r$. Note the $\epsilon_r \leq 0.1$ are used for uncertainty quantification.

3.4 Wind Tunnel System Identification

This section presents the system identification process for the MARGE and LARGE wind tunnel models, including the time-domain and frequency-domain responses and correlations [30, 31, 477, 480, 637].

3.4.1 MARGE

2019 MARGE

Commonly used techniques for generating state space models of linear aeroservoelastic systems are used in this work [645–648]. Ref [28] detailed the mathematical modeling process, which mainly followed [646]. For the structural dynamics part, rigid body and elastic motions were decoupled. The two dynamics are then coupled by aerodynamic loads that are

dependent on both structural deformation and rigid body motions. Small structural deflection and small aerodynamic incident angles are assumed. For the work presented here, after studying the aeroelastic behavior of the system numerically and comparing to test results, it was found that a linear time-invariant (LTI) state-space model without aerodynamic lag terms was sufficient [649]. The structural dynamic part of the model was based on a NASTRAN® finite element model of quenzer2019MARGE, as shown in [649]. The LTI state-space model is shown in the standard form of $\dot{x} = Ax(t) + Bu(t)$, where $x \in \mathbb{R}^n$ is the time-dependent state vector and $u \in \mathbb{R}^m$ is the time-dependent control inputs vector. The matrices A and B are system state and control input matrices, respectively. The states used in the approximate model include contributions from the angle of attack, pitch rate, and the motions in the first two structural elastic modes and their time rates of change. Generalized modal displacements serve as a reduced order basis to approximate the motions of the elastic structure: $q \approx \Phi\eta$, where Φ is a normal modes matrix and η is the vector of generalized modal displacements. The system matrix can be partitioned into a part associated with the rigid body motions about the root, a part for the motions in the elastic degrees of freedom, and sub-matrices of coupling between rigid body and elastic motions, namely,

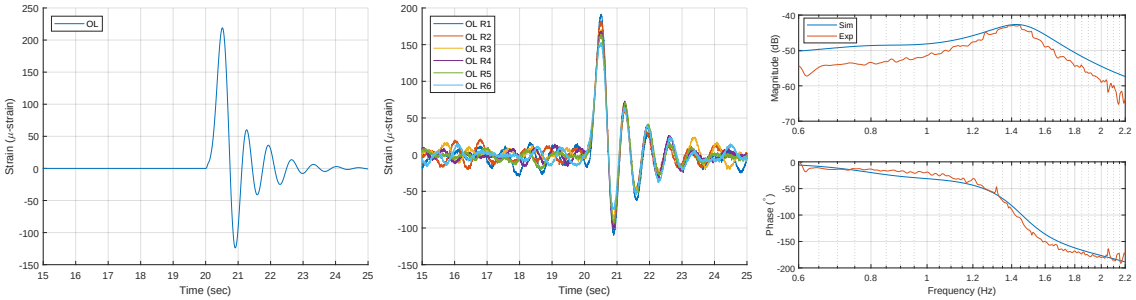
$$A = \begin{bmatrix} A_{\mathrm{r}} & A_{\mathrm{re}} \\ A_{\mathrm{er}} & A_{\mathrm{e}} \end{bmatrix}, \tag{3.38}$$

where the matrix $A_{\mathrm{r}} \in \mathbb{R}^{2\times 2}$ contains the linearized aeroelastic rigid-body dynamics, the matrix $A_{\mathrm{e}} \in \mathbb{R}^{4\times 4}$ models the elastic aeroelastic contributions, and $A_{\mathrm{re}} \in \mathbb{R}^{2\times 4}$ and the $A_{\mathrm{er}} \in \mathbb{R}^{4\times 2}$ account for coupled rigid body / elastic dynamic behavior. A detailed description of the mathematical model, including states, inputs, and outputs, as well as the system matrices, is given in the Appendix [30]. The model was fine-tuned by frequency sweep input-output tests in the wind tunnel.

Figure 3.7 shows the time history of simulation and experimental results of open-loop wing-root strain response to gust excitation whose profile is a 1-cos input with a 4° amplitude starting at 20 s and with a duration tailored to excite the first wing bending mode at 1.4 Hz. The experimental time domain results in Fig. 3.7b are for repeated test runs and show the effects of the wind tunnel's natural turbulence. The deterministic results from the

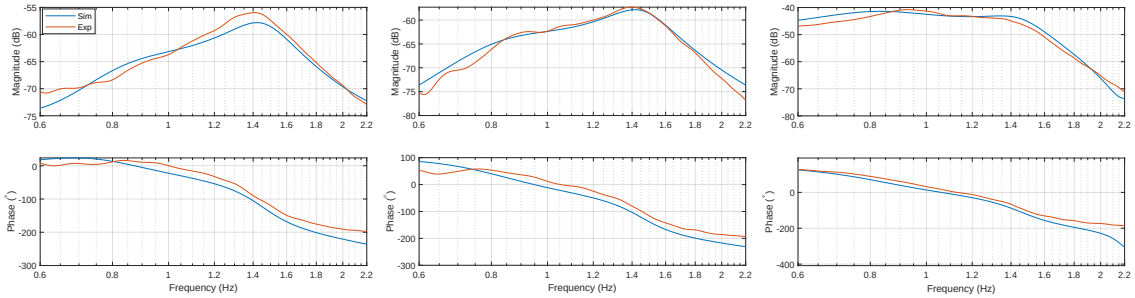
simulation do not account for this effect in the cases studied here. The turbulence effects can be added to the simulations using conventional techniques of modeling the effects of random and discrete gusts on aeroservoelastic systems [650–652]. The gust inputs reported here are much larger in amplitude compared to the excitation by the natural turbulence of the wind tunnel such that the effect of the natural turbulence was not included directly in the stat space simulations, but was included indirectly via the standard approaches to according to the noise in allowable magnitude in the modern control law synthesis.

Figure 3.7c shows wing-root strain frequency response function comparisons between experiment and simulation over the frequency range of interest, which is determined by the frequency capacity of the actuators. And the selected frequency response excited by individual control surfaces in both simulation and experiments are shown in Fig. 3.8.



(a) Simulation (b) Experiment (c) Frequency response

Figure 3.7: Time history and frequency response of open-loop wing-root strain response to a 1-cos gust of 4° amplitude and a period equivalent to 1.4 Hz (*OL* stands for open loop and *R* stands for the run number)



(a) Outboard aileron (b) Inboard aileron (c) Elevator

Figure 3.8: Frequency response of wing-root strain response to control inputs (*Sim* stands for simulation and *Exp* stands for experiment)

MARGE Hardware and Modelling Update

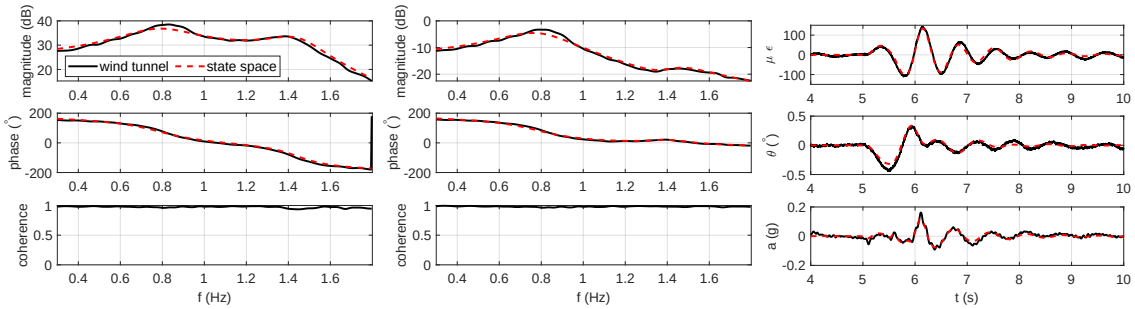
The MARGE-I system was initially designed, completed, and tested in 2019 [28]. The model was later updated with new sensors, actuators, and root pitch-axis housing. A differential pressure sensor for dynamic pressure measurement was added to the wind tunnel [31]. The state space model was developed based on a NASTRAN Finite Element Model (FEM), Doublet Lattice Method (DLM) unsteady aerodynamics, Ground Vibration Test (GVT), and wind tunnel tests for overall system identification using the Comprehensive Identification from Frequency Responses (CIFER) code [31]. The wind tunnel system identification was done using control surfaces frequency sweeps from 0.1 Hz to 2.5 Hz at $q = 68, 94, 169, 209, 283$, and 343 Pa, where the open-loop flutter is at $q = 450$ Pa at 12 Hz (beyond actuator bandwidth). CIFER is a frequency-domain-based system identification code that is typically used for aircraft and rotorcraft parameter identification via pattern search instead of a gradient-based method [49, 535]. In the MARGE-I case, CIFER used the NASTRAN-DLM state space model as the initial starting point in the process of matching a low-order aeroelastic state space model (SSM) to the test results. Knowing the transfer functions of the actuators, sensors, and filters in the system, it was possible to focus the CIFER effort on the fine-tuning of the "pure" aeroelastic model. Because of the narrow range of frequencies (and reduced frequencies) of interest in the MARGE-I case, there was no need to include the aerodynamic lag terms in the aeroelastic SSM [31].

The structure of the aeroelastic state space model assumes the form of

$$\begin{aligned} \dot{x} &= Ax + Bu \\ y &= Cx + Du, \end{aligned} \tag{3.39}$$

where the state, input, and output vectors are, respectively, $x = [\theta \quad \dot{\theta} \quad \eta \quad \dot{\eta}]^T$, $u = [\delta_{\mathrm{E}} \quad \delta_{\mathrm{OB}}^T \quad \delta_{\mathrm{IB}} \quad \delta_{\mathrm{G}}]^T$, and $y = [\mu\epsilon \quad \theta \quad a]^T$. The state variables θ and η are the root pitch rotation and the generalized displacement of the first wing bending mode, respectively. The input variables of δ are the control surface rotations, with subscripts denoting elevator (δ_{E}), outboard aileron (δ_{OB}), inboard aileron (δ_{IB}), and gust vane rotations (δ_{G}). The output variables $\mu\epsilon$ and a are the wing root strain in micro units and the wing tip acceleration in g, respectively.

The SSM of the aeroelastic system is appended with the identified actuator dynamics for each control surface. The sensors' bandwidths are beyond the frequency range pertaining to actuators' "action" and as such, are not included in the overall SSM. Transfer function predictions by the fine-tuned state space model and experimental results, in the frequency and time domains, for the cases of elevator to wing root strain and pitch rotation are shown in Figure 3.9. The SSM captures the dynamics of the system well over the range of frequencies of interest with two modes affecting the dynamics of the system: a "short period" mode (rigid body rotation) and a first-bending mode. When the frequencies of these modes are close, and depending on the mode shapes, a flutter mechanism known as Body Freedom Flutter (BFF) may appear [464]. More details can be found in [31, 32].



(a) Frequency response of elevator to wing-root strain

(b) Frequency response of elevator to pitch rotation

(c) Time history response of elevator doublet to sensor output

Figure 3.9: Frequency and time response of elevator to wing-root strain and pitch rotation [31]

Destabilization/Stabilization Approach and the Flutter Case Used for AFS

When an aeroelastic configuration has multiple control surfaces and sensors, then, subject to controllability and observability constraints and operating well below the actual flutter speed of the system, a subset of control surfaces and sensors can be used to create flutter mechanisms of desired characteristics using closed-loop control while the other sensors and control surfaces can be used, via AFS, to suppress those flutter mechanisms shown in Fig. 3.10. Since the ailerons are next to each other, to avoid a trivial solution, the destabilizing control used pitch rotation and elevator as I/O, and the stabilizing AFS used the strain gauge and outboard aileron as I/O. Note that there is only one mode, first wing-bending, within the actuation bandwidth, such that even with a MIMO controller, both the inboard and outboard ailerons would likely move in the same direction with a gain difference. Thus, two SISO controllers are designed for destabilization and stabilization. The method was presented in [31]. Since the instability is deliberately synthesized using closed-loop control, safe testing requires no "flutter stoppers" or other safety devices. If the tested AFS control laws do not suppress the instability they were designed to suppress in the first place, and if large oscillations develop that would risk the integrity of the system, active control can be disconnected instantaneously (both the destabilizing and the AFS controllers); in this case, the system would return to its stable open-loop state.

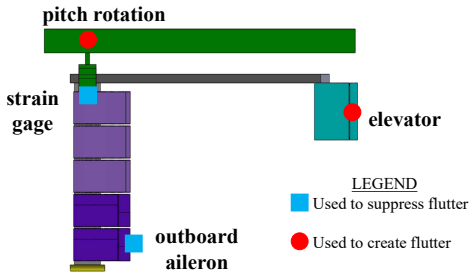


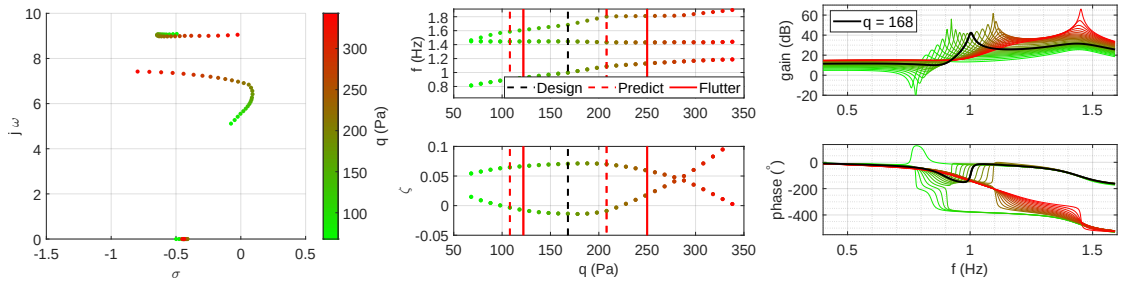
Figure 3.10: Control surfaces and sensors used for both the destabilizing and stabilizing control laws [31].

The destabilization controller that was used to create flutter in the case presented here used the root pitch rotation as input and the elevator commanded rotation as the output:

$$\delta_{\mathrm{E}}(s) = -4.5 \left(\frac{s}{s+1} \right) \left(\frac{7}{s+7} \right) \theta(s), \tag{3.40}$$

where, together with a simple band pass filter concentrated near the rigid body frequency, a hump-mode style flutter mechanism was created as shown in Fig. 3.11. Both root locus analysis and model damping show that the SSM is unstable over a range of dynamic pressures, 108 Pa $\leq q \leq$ 208 Pa. The discrepancy in the figure between simulation and test results for the lowest damping in the system is probably due to the difficulty in measuring damping in tests when the overall level of damping is very low in Fig. 3.12c. In such cases, it is difficult to distinguish the response of the system to deliberate excitations (by control surface frequency sweeps, for example) from its response to the natural turbulence of the flow and other sources of noise. Figure 3.12c shows that the destabilized system remained unstable up to $q = 252$ Pa, and the flutter line is plotted in Fig. 3.11b. Figure 3.11c illustrates the destabilized system response with respect to dynamic pressure, and $q = 168$ Pa is highlighted for control design later in §3.5.2.

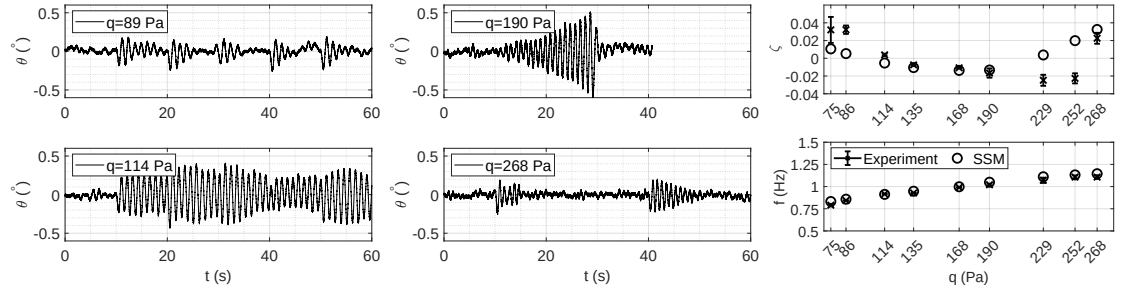
Figure 3.12 shows the pitch rotation measurements at selected dynamic pressure between 89 Pa $\leq q \leq$ 268 Pa. At different dynamic pressures, the system is repeatedly excited by the inputs of control surface. Over the hump-mode range of speeds where the closed-loop destabilized system is unstable, the destabilizing controller is engaged repeatedly for short periods of time to allow measurements of the resulting divergent motions of the system before it gets deactivated again to keep the system safe. The time history in Fig. 3.12



(a) Root locus (b) Modal damping and frequency (c) Bode plot from δ_{OB} to $\mu\epsilon$

Figure 3.11: State space model root locus, modal frequency, modal damping, and Bode plot for the destabilized system at 68 Pa $\leq q \leq$ 338 Pa with increment of 10 Pa [31]

shows that the system was stable at $q = 89$ Pa, unstable at $q = 114, 190$ Pa, and stable again at $q = 268$ Pa, agreeing with the designed closed-loop hump-mode flutter of the system in Fig. 3.11. Note that the nonlinear effect may occur when flutter happens, where the model is moving away from the linearization. The two safety triggers are pitch rotation (θ) and strain gage ($\mu\epsilon$), and the thresholds are $|\theta| \leq 0.5°$ or $|\mu\epsilon| \leq 100$, respectively. Figure 3.12b indicates that the safety disconnected the destabilizing controller after $|\theta| > 0.5°$. The two safety triggers were set within a small range, ensuring that nonlinearities are minimal.



(a) Time history of pitch rotation (b) Time history of pitch rotation (c) Modal damping & frequency

Figure 3.12: Experimental time history of closed-loop hump-mode system at selected dynamic pressures (destabilizing controller is engaged after 10 s with pulses every 10 s) and modal frequency and damping ratio [31]

3.4.2 LARGE

2022 LARGE

System Identification Figure 3.13 shows the multi-flap configuration from commanded aileron input to acceleration output. Also, highlighted in Fig. 3.13 is the SISO nature of the multi-flap plant tested, actively, in the exploratory tests described here. Although not novel, the SISO multi-flap plant begets simple, and effective, SISO controllers and their associated intuitive stability and robustness properties. The insights and standard tools offered by classic SISO control law designs were the motivation for the testing of such laws on the large flexible wing before proceeding to full MIMO designs. The identical location of accelerations and forces (ILAF) control idea arose in the 1960's for modal suppression [505]. The inner-loop servo controllers are not shown but exist between the scaling factors and the plant input shown in Fig. 3.13. The dynamics of these inner-loop servo controllers were implicitly included in the overall SISO multi-flap plant.

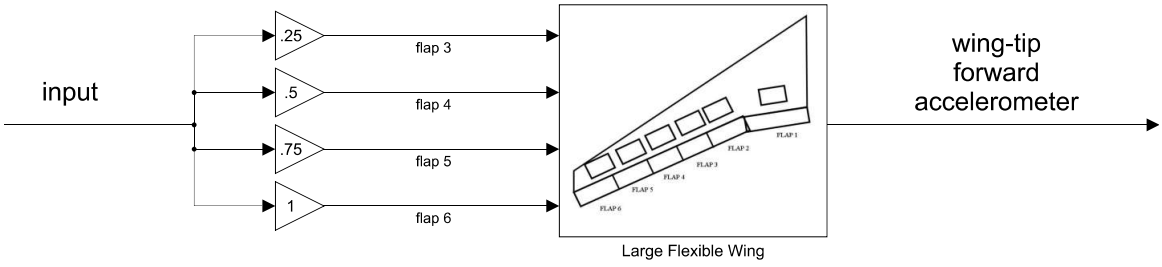


Figure 3.13: Multi-flap SISO plant. The outboard flap receives 100 % of the commanded signal, while the inboard flap receives 25 % of the commanded signal.

Frequency sweeps, or chirps, were applied to the multi-flap SISO plant using a starting frequency of 0.5 Hz and an ending frequency of 6 Hz, as shown in Fig. 3.14. These frequencies were chosen as they placed the aeroelastic 1st-wing bending frequency of about 2.5 Hz in the middle of their range. The ILAF control scheme is inherently a modal suppression scheme and, in this case, the target mode was first-wing bending. Achieving a good fit between experimental data and the identified model (as well as the analytical model), over

these frequencies, was critical for good modal suppression and load alleviation. Figure 3.14a shows the full duration of a sweep, the various amplitudes, and also the different performance achieved by the inner-loop servo actuator controllers. The different amplitudes for each flap are more pronounced in Fig. 3.14b, where the nonlinearities associated with the actuator free-play are in plain view. It is important to point out that, although nonlinearities are present in the flap motions, these effects do not overly impinge on the performance of the system identification or the associated GLA controller. This is a consequence of the system identification being performed from command input to acceleration output, rather than the particular flap motions to the accelerations that would normally be standard for identifying a model.

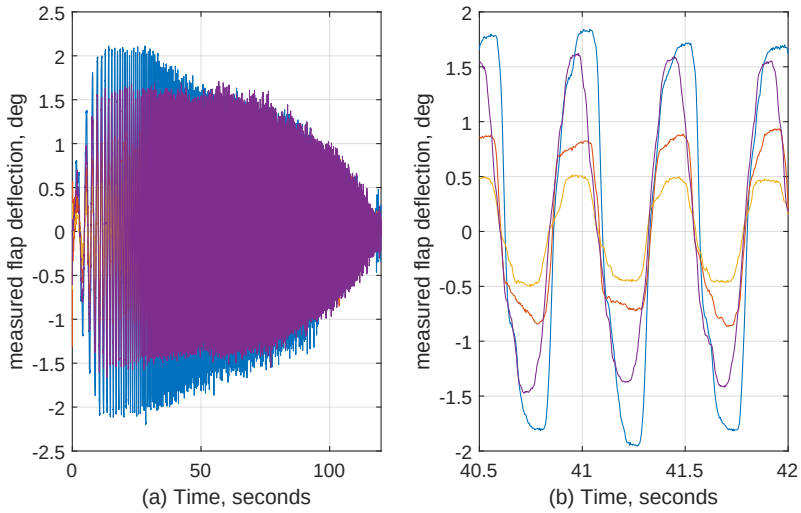


Figure 3.14: (a): Overlay of all four flaps performing a frequency sweep. (b): Close-in view of the flaps during the sweep highlighting the different amplitudes of each flap.

Figure 3.15 shows the accelerometer time response resulting from the frequency sweep input as well as the measured corresponding frequency response and the identified model. The accelerometer time response shown in Fig. 3.15a indicates a peak magnitude of approximately ±0.6 g, well below the 2g limit defined in the safety-check block. The frequency response shown in 3.15b exhibits excellent coherence resulting in gain and phase curves that can be trusted with high confidence. Consequently, the frequency response shown in Fig.

3.15b can be considered to accurately capture the model's behavior in the frequency range from 0.5 Hz to 5.0 Hz, which is where the coherence starts to drop off. The model identified from the frequency response data, shown in Fig. 3.15b, was identified using MATLAB's TFEST function with an 84% fit to the estimation data over the region from approximately 1 Hz to 4 Hz. Correlation between the measured and analytically predicted frequency response will be shown in a subsequent section.

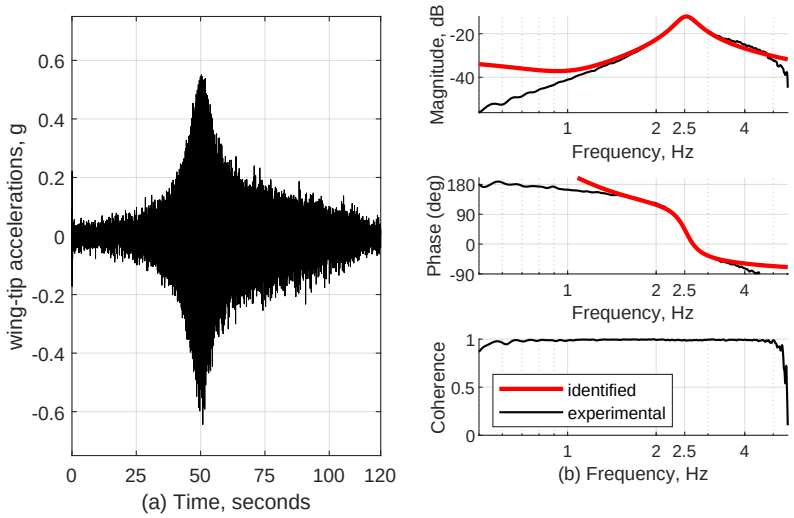
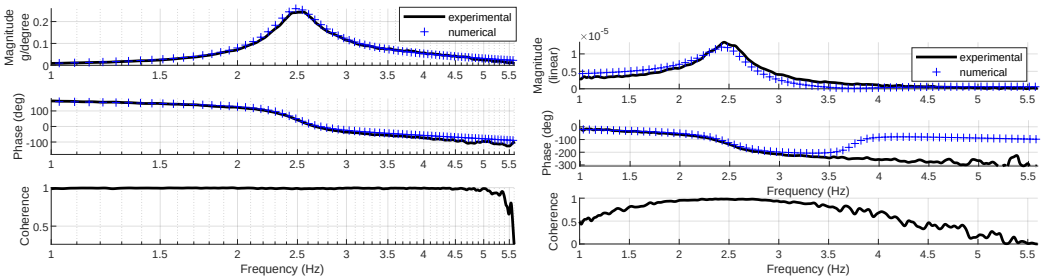


Figure 3.15: (a): Time response of the forward wing-tip accelerometer to the multi-flap sine-sweep input. (b): Frequency response and identified model for the multi-flap SISO plant.

Frequency Response Comparison Figure 3.16a shows the frequency response of the multi-flap input to wing-tip accelerometers derived from experimental data and compared against the frequency response of the twelve-mode aeroservoelastic model. Both the numerical model and the experimental data shown in Fig. 3.16a contain the effects of the inner-loop servo control for each flap individually. A comparison of the numerical and experimental frequency response for the multi-flap input to the strain output is shown in Fig. 3.16b. The comparisons shown in Fig. 3.16a and Fig. 3.16b reveals the numerical model to be quite accurate across the frequency range considered with the exception of higher frequency phase uncertainty seen in the strain response. The gust-response in Fig. 3.17a

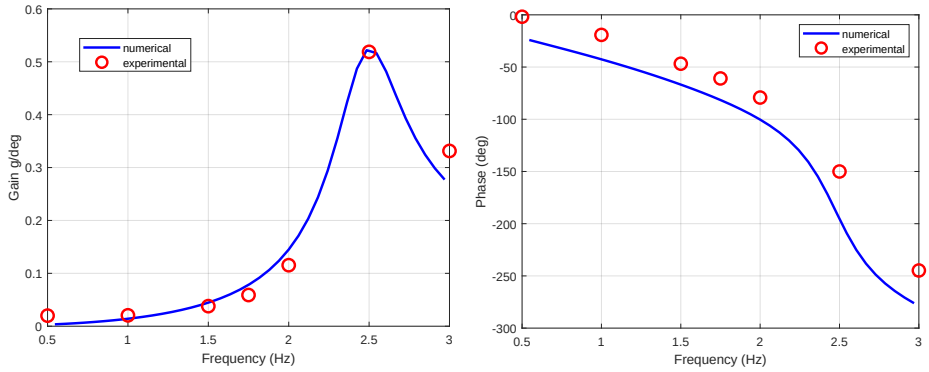
and Fig. 3.17b , however, does exhibit slightly more uncertainty. The gust generation



(a) Wing-tip accelerometer (b) Bay two strain

Figure 3.16: Frequency response comparison between the numerical model of the multi-flap SISO plant and the experimental data.

system was not capable of frequency sweeps, therefore, frequency dwells were conducted at seven separate frequencies in an effort to recreate the frequency response. The frequency response of the gain, for gust to wing-tip accelerometers, Fig. 3.17a, shows a good fit up to and including the 2.5 Hz 1st-wing bending frequency. However, a worse match is seen beyond 2.5 Hz. Figure 3.17b shows the frequency response of the phase, for gust to wing-tip accelerometers, to have a fairly constant phase offset.



(a) Gain (b) Phase

Figure 3.17: Comparison of the gust-to-wing-tip accelerometer frequency response for the numerical model and the experimental data.

Time-Response Comparison: Open Loop Figure 3.18, below, shows a comparison between the wing-tip accelerations on the numerical model and the experimental data for a continuous, sinusoidal, gust at 2.5 Hz. A slight phase advance is seen in Fig. 3.18b, and the magnitude shown in both Fig. 3.18a and 3.18b is approximately 8% higher. Aside from these differences, the twelve-mode model matches the experimental data quite well.

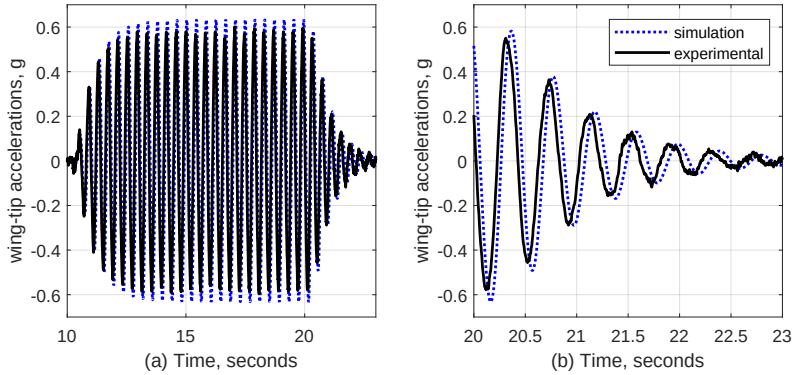


Figure 3.18: (a): Comparison of wing-tip acceleration between the Numerical model and the experimental data during a continuous gust excitation at 2.5 Hz. (b): Close-in view showing the decay at the end of the continuous gust.

Figure 3.19 shows the strain response to the continuous gust excitation at 2.5 Hz. The DC offset present in Fig. 3.19 is a result of the experiment being conducted before the application of the washout/high-pass filters. These filters were later added to all measurement channels. The strain response in Fig. 3.19 shows a slightly higher magnitude than the experimental data. Uncertainties such as these are expected given the exploratory nature of this work. Figure 3.19 also shows the strain response to exhibit very little noise considering the milli-volt level signal must travel roughly 10 feet in a noisy wind-tunnel environment before signal conditioning. The wing-tip accelerometer time response to a discrete, 1 - cosine, gust can be seen in Fig. 3.20a. Similar to Fig. 3.18, the time response in Fig. 3.20a exhibits phase advance and a slightly greater peak magnitude. Despite these differences, the twelve-mode model matches well and appears to have a similar damping ratio and natural frequency to the physical hardware. The strain response to a 1 - cosine gust event can be seen in Fig. 3.20b. The strain response seen in Fig. 3.20b shows a larger peak. This differ-

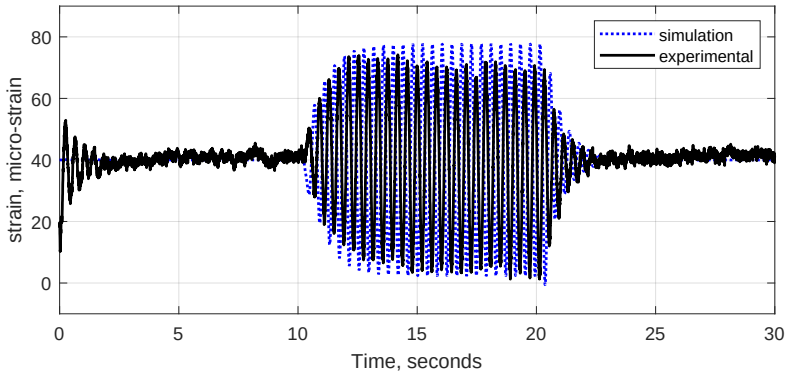
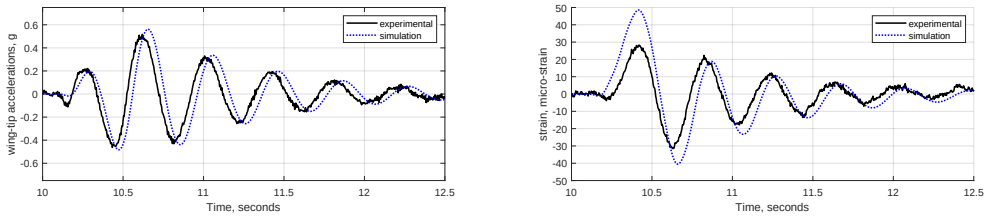


Figure 3.19: Open loop strain response, measured in bay two, to a sinusoidal gust at 2.5 Hz.

ence could be attributed to the challenges associated with exactly modeling the location of the strain gage inside the flexible wind-tunnel model.



(a) Wing-tip accelerometer (b) Bay two strain

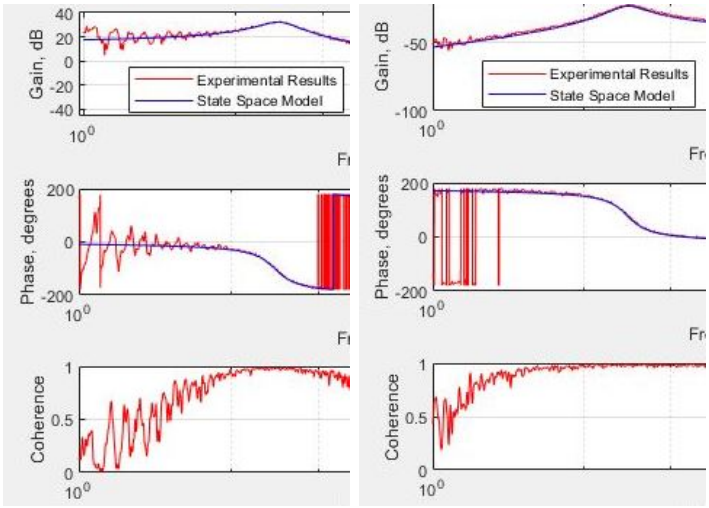
Figure 3.20: Open loop response to a 1-cosine gust event at 2.5 Hz.

2024 LARGE

State space models of various orders were studied for their capability to accurately capture the system ID test results and for their order, which would affect the synthesis of the control laws and their performance. Elements of the state space modeling that were covered included the number of modes to use, static aeroelastic corrections, and the number of aerodynamic lag terms used for the rational function approximation (RFA) of the unsteady aerodynamic force matrices. With knowledge of the transfer functions of actuators (measured in separate tests) and various filters (such as the anti-aliasing filter, low-pass filters to limit the active control effort to responses by the first mode, and other filters for focusing on the frequency

range of interest), and with access in the tests to the actual motions of the excitation-driving control surfaces and gust vanes, the fine-tuning of the simulation of the "pure" aeroelastic system was done first before the actuator and filter state space models were added to create the final state space models of the full system.

The wing was tested for I/O measurements at a number of dynamic pressures and root angles of attack. For the exploratory studies presented here, data for the 8 psf dynamic pressure at 3 degrees angle of attack (AOA) test conditions were used. Despite the relatively low dynamic pressure and angle of attack, there is enough load on the wing to bend it up and also preload the control surfaces. Selected comparisons of SSM simulations and measured test data are shown in the next few figures. Figure 3.21 shows frequency response functions (FrFs) for inputs by Active Flap 6 - the most outboard control surface - and the bending strain at Bay 2 as well as the vertical acceleration at the forward tip accelerometer location.



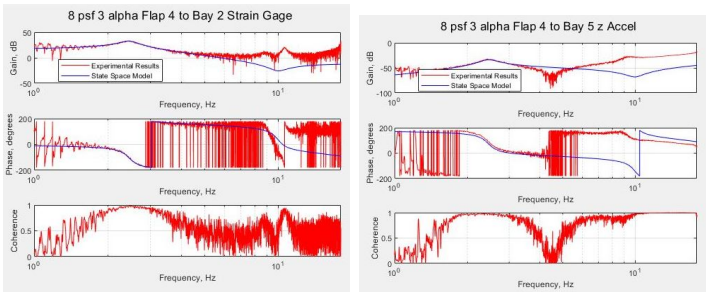
(a) Inboard bending strain (b) Fwd tip accelerometer

Figure 3.21: Frequency response to flap 6 frequency sweep inputs

Several FRFs involving inputs by Active Flap 4 are shown in Figures 3.22 and 3.23.

Simulation/Test FRF comparisons for the gust vanes as the input are shown in Figure 3.24.

The fine-tuned state space model for the 8 psf dynamic pressure and 3 degrees root AOA case matches test results quite well over the frequency range of interest for the gust



(a) Inboard bending strain (b) Bay 5 acceleration

Figure 3.22: Frequency response to flap 4 frequency sweep inputs

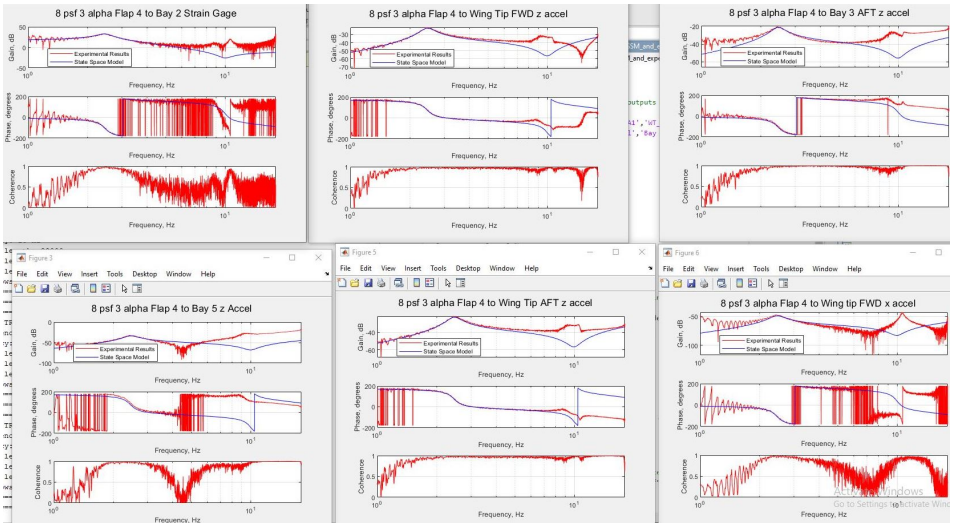
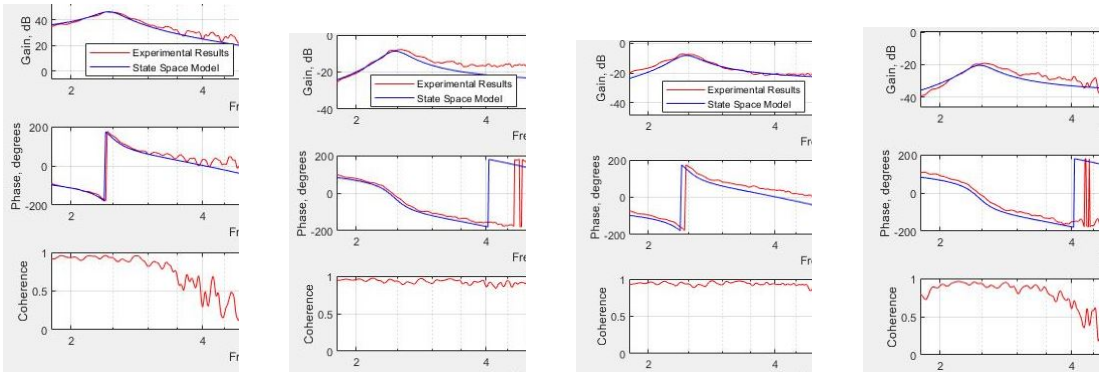


Figure 3.23: Frequency response to flap 4 input

alleviation active control studies reported here. It is based on a single degree of freedom aeroelastic model (just the first bending mode with some corrections for static aeroelastic effects). It has 27 states, which include actuators' states. It has 6 inputs and 6 outputs. The inputs include active flaps 2 to 6 and the gust vane input. The outputs include vertical accelerations measured by forward and aft wing tip accelerometers, x-direction acceleration at the wingtip, vertical accelerations at wing bay 5 and the aft accelerometer location in wing bay 3, and the bending moment strain gauge which is located in the Bay 2 area.

Note that some of the FRF figures shown above include test results beyond the 4 Hz to 5 Hz upper limit on the control law synthesis and active control in the studies reported here.



(a) Inboard strain (b) Fwd tip accel (c) Bay 3 Aft accel (d) Bay 5 accel

Figure 3.24: Frequency response to gust vane inputs

The 1-mode state space model cannot capture the behavior of the system at those higher frequencies. Low pass filtering is used in the tests to filter out high-frequency contributions by modes 3 and higher. The actuators and their low-pass nature contribute to this filtering. The system is capable of testing in the frequency range that would cover at least the first 3 modes of the wing. Expansion of the work reported here to such cases, with richer dynamics and more demanding math modeling and control law synthesis, will be pursued in future work.

3.5 Control Design

This section details the control design process for the MARGE and LARGE wind tunnel models, including the design of the signal-based preview robust gust load alleviation control [30], mixed-sensitivity robust active flutter suppression control with modal damping [31, 637], and preview mixed-sensitivity robust gust load alleviation control with modal damping [480].

3.5.1 MARGE GLA

Closed Loop

The selected regulated outputs were the wing-root strain, inboard, and outboard ailerons. The generalized plant is normalized to bound maximum allowed control inputs and regu-

lated outputs as described in §3.5. The wing-root strain is normalized by the maximum absolute open-loop response, $\hat{y}_{\max}$, and the ailerons are normalized by the maximum physically allowable deflections, $|\hat{u}_{\max}| = 20°$. Both static and frequency weights for wing-root strain were tuned such that the corresponding norms decreased monotonically with respect to preview steps. Outboard and inboard ailerons used the same frequency weight to penalize high-frequency actuation due to the bandwidth limitation of the actuators.

The static weight was tested early in this research work such that neither the output filters nor the reduced-order controllers were incorporated. The static weight was subsequently updated to frequency weight to further target the first wing bending mode and constrain actuation, and the output filters were included in the model, accounting for gain attenuation and phase delay to increase model fidelity for controller synthesis. The detailed information on filters are tabulated in Tab. 3.6 and depicted in Fig. 3.25a.

The order of the plant is six for static weight and is increased to twenty-two states for the frequency weight incorporating two third-order band-pass and two second-order low-pass Butterworth filters. The weights for regulated channels increase the number of states to eight for the static weighted wing-root strain and twenty-five for the frequency weighted wing-root strain, first-order frequency weights for the actuator, and the augmented preview plants are $8+h$ and $25+h$ states with respect to h preview steps. The weights on regulated channels increase the number of states to 8 for the static-weighted wing-root strain and 25 for the frequency-weighted wing-root strain and first-order frequency-weighted actuators. The numbers of states for the augmented preview plants are 8 + h and 25 + h states, where h is preview steps, for the static-weighted wing-root strain and the frequency-weighted wing-root strain and first-order frequency-weighted actuators, respectively. The full-order controllers were synthesized so that the controllers have the same order as the augmented preview plant's order, while the reduced-order controllers have specified reduced order for the frequency-weighted wing-root strain. In the following figures, the *FB* stands for feedback control and *PC*s stand for preview control with following preview duration. *IB* and *OB* stands for inboard and outboard ailerons, respectively. The *SW* and *FW* stand for static weight and frequency weight, respectively, and are referred to the wing-root strain weights. The *Sim* and *Exp* refer to simulated and experimental results, respectively.

Table 3.6: Generalized plant filters

(a) Output channel filters

Output channels	Filter type (Butterworth)	Order	Crossover frequency (Hz)
Forward accelerometer	Band-pass	3rd	0.5, 20
Afterward accelerometer	Band-pass	3rd	0.5, 20
Wing-root strain	Low-pass	2nd	15
Hall effect sensor	Low-pass	2nd	10

(b) Regulated channel filters - static

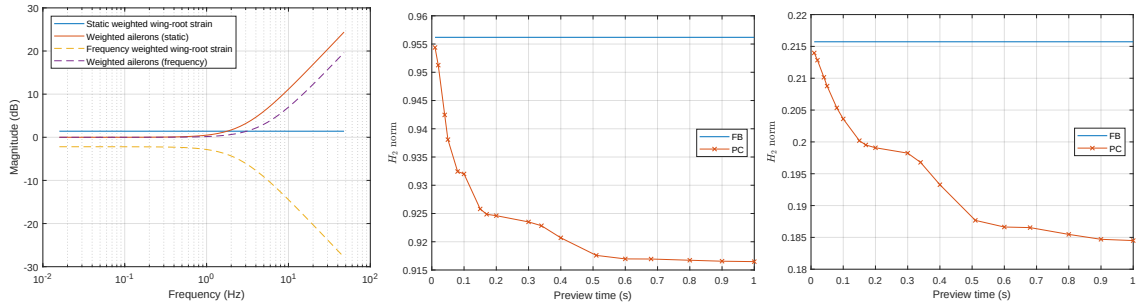
Regulated channels	Filter type	Order	DC gain (dB)	Crossover frequency (Hz) & gain (dB)
Wing-root strain	Static	N/A	1.412	N/A
Outboard aileron	High-pass	1st	1	5, 6
Inboard aileron	High-pass	1st	1	5, 6

(c) Regulated channel filters - frequency

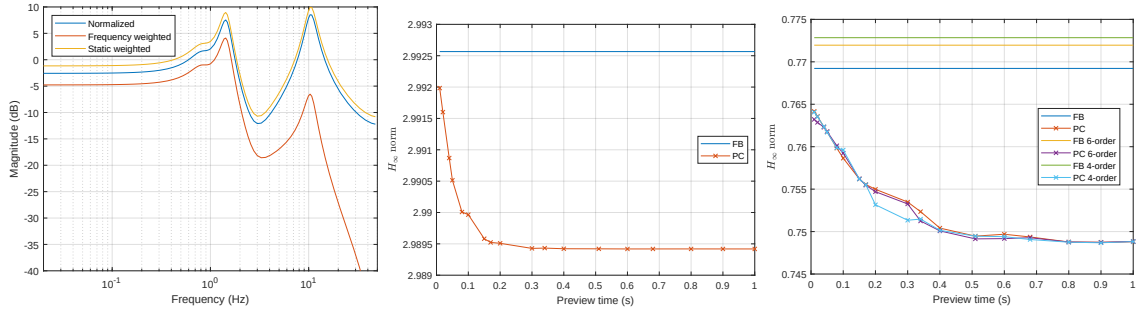
Regulated channels	Filter type	Order	DC gain (dB)	Crossover frequency (Hz) & gain (mag)
Wing-root strain	Low-pass	1st	-2.216	2.5, -3
Outboard aileron	High-pass	1st	1	5, 3
Inboard aileron	High-pass	1st	1	5, 3

The weighted wing-root strains are shown in Fig. 3.25d where the static weight shifted the magnitude of response and low-pass frequency weight rolled off the second wing bending mode. Fig. 3.25 also displays the closed-loop norms of the transfer functions reduced with respect to increased preview length [516, 653]. The corresponding transfer functions with the given preview information are shown in Fig. 3.26. Table 3.7 summarizes the designed and tested controllers.

For the static weighted wing-root strain, the $\mathcal{H}_2$ and $\mathcal{H}_\infty$ closed-loop wing-root strain responses behave almost identically. Figure 3.25d shows the open loop and static weighted wing-root strain have a higher response in magnitude at the second wing bending mode than the first. The $\mathcal{H}_2$ control minimizes the overall energy of the system as mentioned in



(a) Regulated channel filters (b) Static weighted $\mathcal{H}_2$ norms (c) Frequency weighted $\mathcal{H}_2$ norms



(d) Weighted wing-root strain (e) Static weighted $\mathcal{H}_\infty$ norms (f) Frequency weighted $\mathcal{H}_\infty$ norms

Figure 3.25: Transfer function of weighted filters and weighted open-loop wing-root strain to gust excitation, and norms of $\mathcal{H}_2$ and $\mathcal{H}_\infty$ closed-loop transfer functions given preview information

Table 3.7: $\mathcal{H}_2$ and $\mathcal{H}_\infty$ controllers examined in this work: $\odot$ designates designed and tested, $\otimes$ designates designed and tested yet unstable, and $\oslash$ designates designed but not tested

Controllers	FB	PC=0.17s	PC=0.34s	PC=0.51s	PC=0.68s	PC=0.80s	PC=0.90s	PC=1.00s
Static weighted $\mathcal{H}_2$	$\odot$	$\odot$	$\odot$	$\odot$	$\odot$	$\odot$	$\odot$	$\odot$
Static weighted $\mathcal{H}_\infty$	$\odot$	$\odot$	$\odot$	$\odot$	$\odot$	$\odot$	$\odot$	$\odot$
Frequency weighted $\mathcal{H}_2$	$\odot$	$\odot$	$\odot$	$\odot$	$\odot$	$\odot$	$\odot$	$\odot$
Frequency weighted $\mathcal{H}_\infty$	$\odot$	$\odot$	$\odot$	$\odot$	$\odot$	$\odot$	$\odot$	$\odot$
Frequency weighted $\mathcal{H}_\infty$ 6-order	$\otimes$	$\odot$	$\odot$	$\odot$	$\odot$	$\odot$	$\odot$	$\odot$
Frequency weighted $\mathcal{H}_\infty$ 4-order	$\oslash$	$\oslash$	$\otimes$	$\odot$	$\odot$	$\odot$	$\odot$	$\odot$

Appendix. With frequency weighted actuators, the actuation at the second wing bending mode is constrained and the second wing bending mode is gradually and slightly suppressed as shown in Fig. 3.26a, while the first wing bending mode is minimized and reduced with

respect to the preview length. The $\mathcal{H}_\infty$ control minimizes the *largest* response of the system suppressing the second bending mode, while the control inputs are constrained by the actuation weights as shown in Fig. 3.26d.

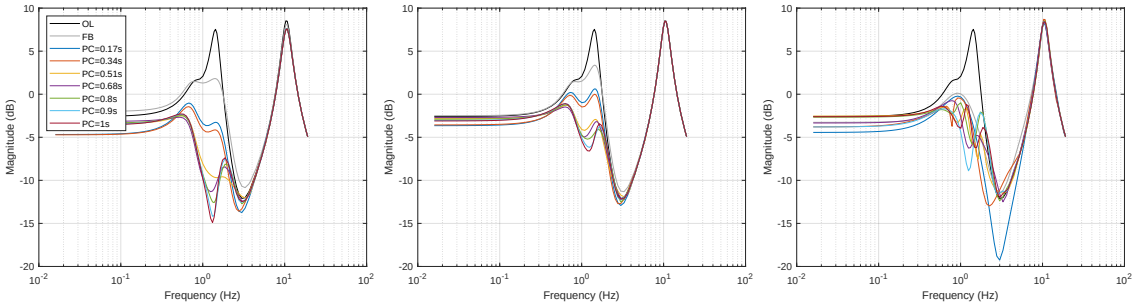
The frequency weighted actuations constrain and penalize further reduction at the second wing bending. Thus the first wing bending is minimized and reduced with respect to preview length similar to the $\mathcal{H}_2$ control. Figure 3.25 shows the norm reductions are minimal for $\mathcal{H}_2$ and hardly for $\mathcal{H}_\infty$ because the $\mathcal{H}_2$ norm is measured by the sum of squared singular values over all frequencies and the $\mathcal{H}_\infty$ norm is measured by the largest singular value which is at the second wind bending mode constrained by the actuation weights. The updated frequency weights are applied to wing-root strain, rolling off the second wing bending mode in Figs. 3.25a and 3.25d. Constrained by the actuation penalty and the second wind bending roll-off, Figs. 3.26b and 3.26e present the distinctive behaviors of the $\mathcal{H}_2$ and $\mathcal{H}_\infty$ control, where the $\mathcal{H}_2$ control attenuates the first wing bending mode gradually and the $\mathcal{H}_\infty$ control immediately suppresses the first wing bending mode and further decrease the norm, given preview information, in Figs. 3.25c, 3.25f, 3.26b, and 3.26e. Figures 3.26c and 3.26f present the closed-loop response of the reduced-order controllers. Note that the closed loop performance improves for higher order feedback control.

3.5.2 MARGE AFS

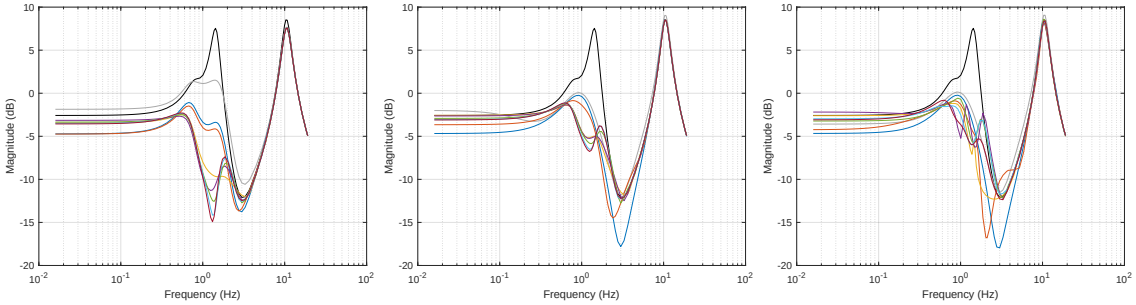
Controller Synthesis

The destabilization controller used pitch rotation and elevator as input and output, respectively, in §3.4.1. To avoid a trivial solution, the AFS controller presented here uses strain measurement and outboard aileron for input and output for stabilization. The goal was to stabilize the hump mode of the system in the unstable region of 108 Pa $\leq q \leq$ 208 Pa and stay stable elsewhere. The hardware setup and approach of partitioning of stabilization and destabilization constrain the controller to be of the SISO type.

The aeroelastic wind tunnel model has the rigid body pitch and aeroelastic first wing bending mode degrees of freedom, see §3.2. The test-identified MKS HV6130 actuator dynamic is shown in Fig. 3.27a. The sensor dynamics and the anti-aliasing filter cutoff



(a) Static weighted $\mathcal{H}_2$ (b) Frequency weighted $\mathcal{H}_2$ (c) Frequency weighted 4th-order $\mathcal{H}_\infty$



(d) Static weighted $\mathcal{H}_\infty$ (e) Frequency weighted $\mathcal{H}_\infty$ (f) Frequency weighted 6th-order $\mathcal{H}_\infty$

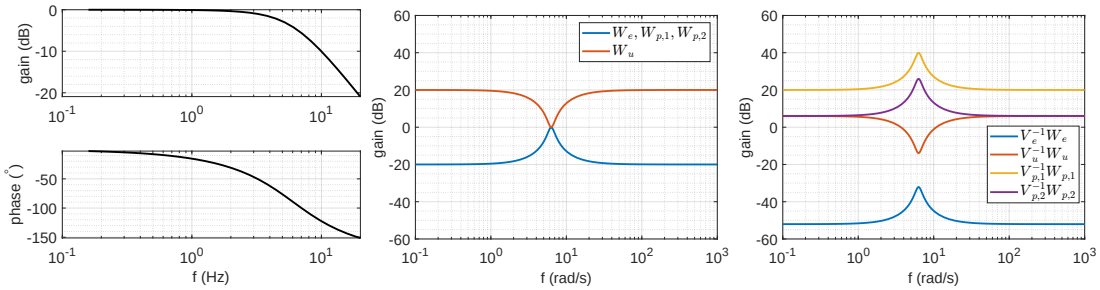
Figure 3.26: Simulated transfer functions of $\mathcal{H}_2$ and $\mathcal{H}_\infty$ closed-loop wing-root strain response to gust excitation

frequency are beyond the frequency region of interest, around 0.5 Hz to 2 Hz in Fig. 3.9, and have minimal impact on gain attenuation and phase delay. They are, therefore, omitted from the state space model.

The nominal plant model for control law synthesis was chosen at the dynamic pressure of $q = 168$ Pa where the unstable poles are furthest away from the imaginary axis in Fig 3.11a. A fixed-controller was sought to avoid gain scheduling. The performance channel was selected with the model's first mode and its corresponding derivative. The normalization scaling used the values listed below:

$$V_u = V_d = 5, \quad V_e = 40, \quad V_p = \begin{bmatrix} 0.01 & 0 \\ 0 & 0.05 \end{bmatrix}.$$

The scaling value V_u was chosen based on constraining the outboard aileron actuation,



(a) Identified actuator dynamics [28]

(b) Weighting functions

(c) Combined scaling and weighting

Figure 3.27: Actuator dynamics and H_∞ weighting and scaling functions

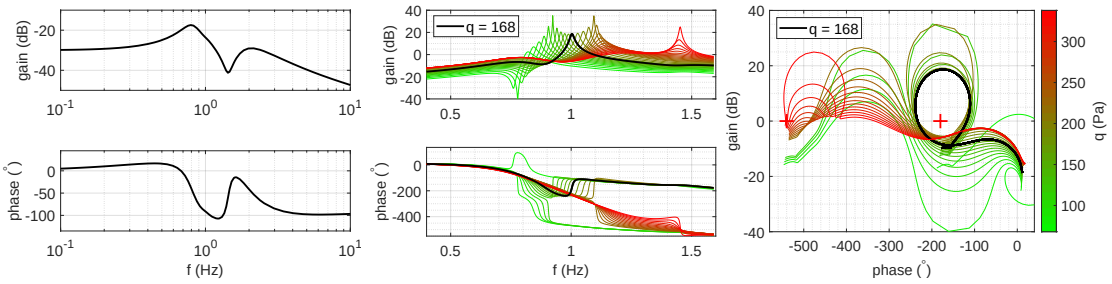
$|\delta_{\text{OB}}| \leq 5°$, and V_d was set equal to V_u to ensure incorporating the input uncertainty. The scaling V_e sets the maximum allowable excitation of the wing root strain, $|\epsilon| \leq 40\mu$, when AFS is engaged. Note that the excitation of the wing root strain from wind tunnel turbulence is $|\epsilon| \leq 20\mu$ [30]. The maximum allowable excitation doubled the turbulence excitation at stable conditions. Lastly, V_p was selected based on the open-loop simulation where the system's initial state is randomly perturbed, and the V_p normalizes the states, η_1 and $\dot{\eta}_1$, to be less than unity.

The weight functions for each channel are

$$W_u = 10\frac{s^2 + 10^{-1}2\omega_f s + \omega_f^2}{s^2 + 2\omega_f s + \omega_f^2} \quad \text{and} \quad W_e = W_{p_{1,2}} = \frac{1}{10}\frac{s^2 + 2\omega_f s + \omega_f^2}{s^2 + 10^{-1}2\omega_f s + \omega_f^2},$$

where $\omega_f = 6.3$ rad/s is the unstable mode frequency and the weighting functions are shown in Fig. 3.27. Note that the notch filters of error, performance, and control channels targeted the unstable flutter of the hump mode at 6.3 rad/s $\approx$ 1.00 Hz. The structure in Fig. 3.6b was constructed in MATLAB® via the command *connect*, and the full-order controller was synthesized using the *hinfsyn* function. Figure 3.28 shows the Bode plot of the controller, the Bode plot of the loop transfer function, and the Nichols plot of the loop transfer function. The 18th-order controller in Fig. 3.28a is the result of four states for the aeroelastic model in Eq (3.39); second-order actuator dynamics for elevator and outboard ailerons in Fig. 3.27a; second-order destabilizing controller in Eq. (3.40); second-order weighting filters for outboard aileron, error output, and modal suppression for η_1 and $\dot{\eta}_1$

in Fig. 3.27c. Figures 3.28b and 3.28c illustrate the Bode and Nichols plots of the loop transfer function from aileron to strain response. The right-half-plane (RHP) poles of the hump mode at $108 \leq q \leq 208$ Pa are shown as positive phase shifts in Fig. 3.28b and as the encirclements of the origin in Fig. 3.28c.

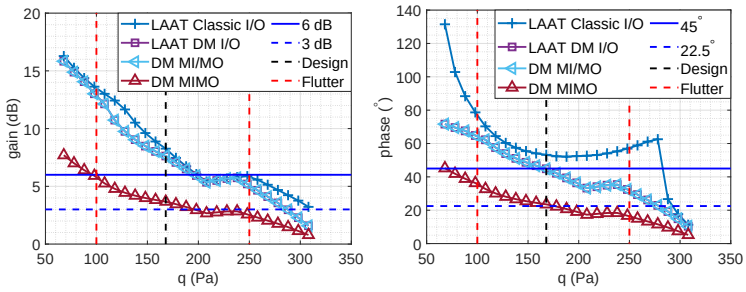


(a) Bode plot of controller (b) Bode plot of loop transfer function (c) Nichols plot of loop transfer function

Figure 3.28: Bode plots of controller and loop transfer function, and Nichols plot of loop transfer function at 68 Pa $\leq q \leq$ 338 Pa with increment of 10 Pa

The synthesized controller is evaluated across the dynamic pressures to ensure closed-loop stability and proper robust margins. Loop-at-a-time (LAAT), multiloop gain and phase margin (GM and PM, respectively), and disk margin (DM) were used to analyze robustness margins. Common practice margins, 6 dB GM and 45° for LAAT and 3 dB GM and 22.5° for multi-loop, were used [49]. More details and insights on the margin relationships can be found in [30, 536]. The results for the robustness margins are shown in Fig. 3.29. In the case of the SISO system, the classical loop-at-a-time at input is equivalent to output. The loop-at-a-time disk margin at either input or output is equivalent to the multi-loop disk margin at either input or output. Furthermore, the disk margin at the input is equivalent to the disk margin at the output. For simplicity, the loop-at-a-time and multi-loop disk margin at either input or output are equivalent in this work here and are referred to as disk margin for the rest of the chapter. Note that this analysis can be generalized to a MIMO system. Figure 3.29a shows that both classic and disk margins have sufficient margins except at $q = 208$ Pa and Figure 3.29b has sufficient classical phase margin across all dynamic pressures. Although the disk margin falls below 45°, it refers to the simultaneous perturbation of

gain and phase. The mixed-sensitiveness loop-shaping method adds frequency-weight filters to shape the corresponding input and output sensitivity, complementary sensitivity, and disturbance-to-control functions. While frequency-weight filters do the loop shaping, the static weights tune the appropriate margins. Additional grid search on control weighting (W_u) could be performed to search for an appropriate weight satisfying flutter suppression over the dynamic pressure range.



(a) Gain margin (b) Phase margin

Figure 3.29: Summary of simulation-results minimum gain and phase margin vs. dynamic pressure for the $\mathcal{H}_\infty$ AFS control.

3.5.3 LARGE GLA

Control Design

The control strategy used here combines the aforementioned mixed-sensitivity $\mathcal{H}_\infty$ loop shaping and preview control. Reference [30, 469] uses a signal-based approach that directly minimizes gust input to strain output. The mixed-sensitivity $\mathcal{H}_\infty$ loop shaping here augments the minimization of sensitivity (S), complementary sensitivity (T), and disturbance to gain (KS) functions. The preview $\mathcal{H}_\infty$ loop shaping first incorporates the disturbance dynamics in Eq. (3.15) into the augmented plant as in Eqs. (3.16)-(3.18) and then constructs the preview augmented plants with weighting and scaling functions as in Fig. 3.6b. Note that digital Butterworth filters are applied to sensors so that the plant includes filters in the control design to account for gain and phase shifts.

For the exploratory work described here the selected actuator and sensor are flap 5

of the large flexible wing and its forward wingtip MEMs accelerometer (Fig. 3.4). The performance channel focused on is the wing inboard section bending strain as in [30, 469]. The V_u was chosen based on constraining the flap actuation, $\delta \leq 5°$, and the V_d was set as the gust excitation, 4°. The V_e and V_p set the maximum allowable the wingtip acceleration ($V_e \approx 0.24g$) and inboard wing bending strain ($V_p \approx 188\mu$), respectively, from the open-loop simulation. Note that V_u, V_e, V_d, and V_p normalize the plants so that the disturbance inputs to outputs are less than unity.

The weighting filters, W_e, W_u, and W_p are applied as shown in Fig. 3.6b. The W_u represents two second-order notch filters that target the first wing bending mode at 2.45 Hz and in the reverse direction at 60 Hz filtering out high frequency noise. The W_e and W_p are inverse of W_u that target the first wing bending mode and additional notch on 60 Hz content.

The structure presented in Fig. 3.6b was constructed in MATLAB® via the command of *connect*, and the full order controller was synthesized using the *hinfsyn* function. The feedback controller is tuned to ensure closed-loop stability and robust margins and the norm of the preview control decreases monotonically with respect to preview lengths.

Loop-at-a-time (LAAT), multi-loop gain and phase margins (GM and PM, respectively) and disk margin (DM) were used to analyze robust margin and common practice of margins (8 dB GM and 60° for LAAT and 4 dB GM and 30° for multiloop) in [535] were followed to ensure robustness. More detail and interpretation of the robustness margins can be found in [30, 536].

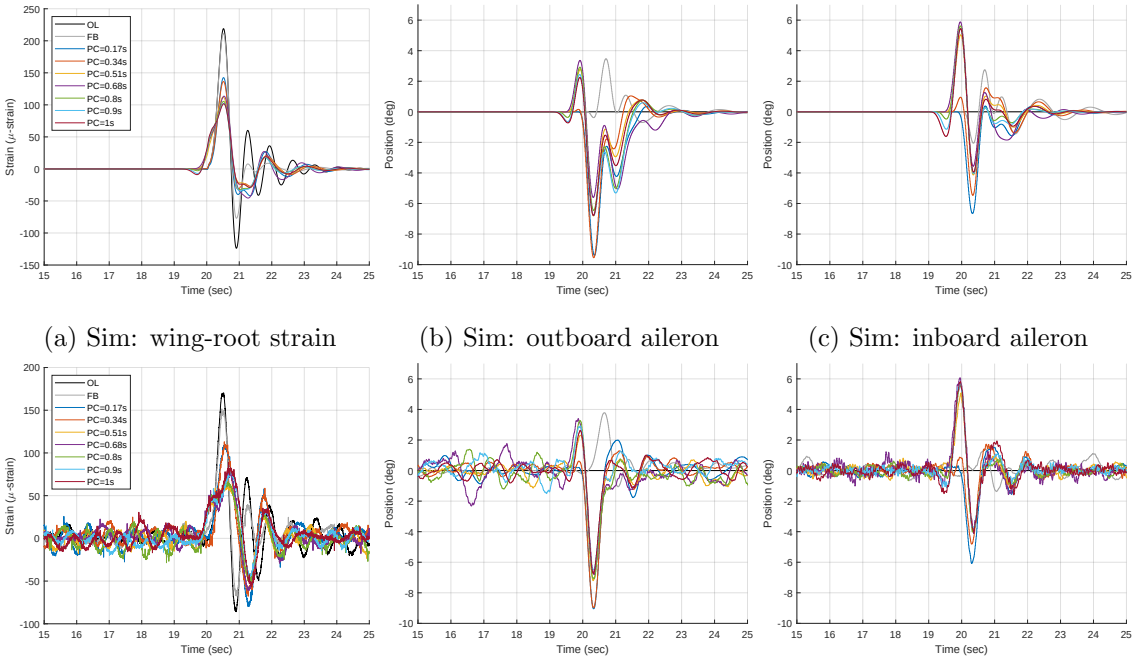
3.6 Wind Tunnel Results

This section shows the wind tunnel results for the MARGE and LARGE models, including the performance of the designed controllers with respect to closed-loop performance and robustness evaluation [30, 31, 480, 637].

3.6.1 MARGE GLA

Time History

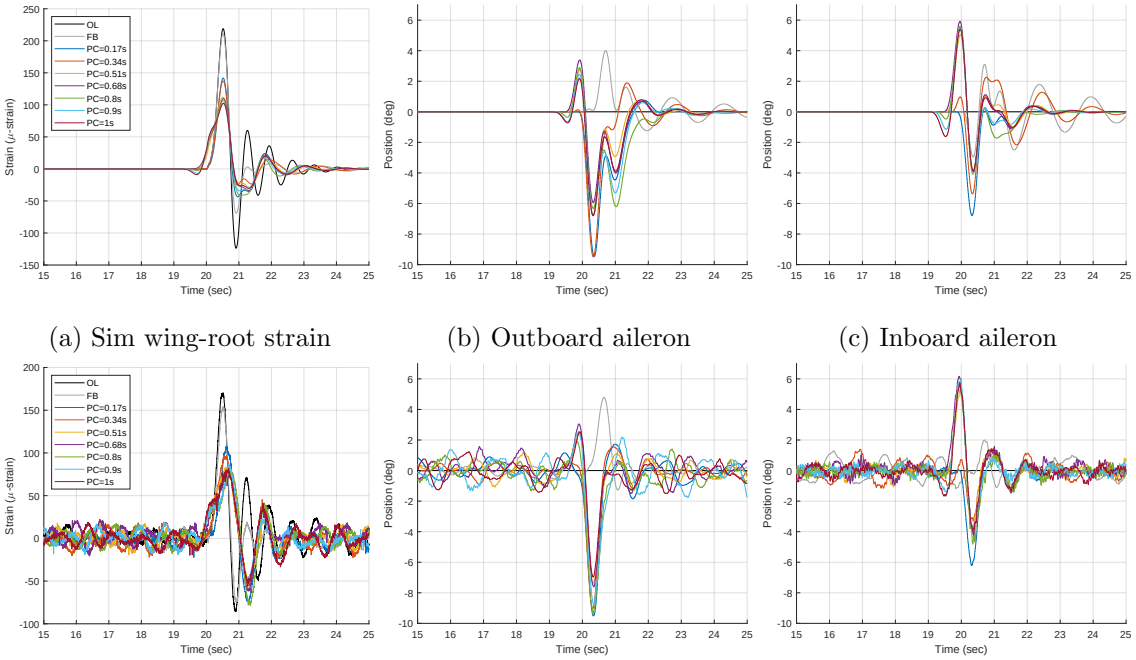
Static weighted wing-root-strain without output filters The $\mathcal{H}_2$ and $\mathcal{H}_\infty$ closed-loop responses for simulation and experiments are shown in Figs. 3.30 and 3.31 whose wing-root strains are minimized with respect to the preview length. These figures show a good correlation between experiments and simulations and demonstrate the benefits of preview information on reducing the wing-root strain. The experimental results of both $\mathcal{H}_2$ and $\mathcal{H}_\infty$ feedback wing-root strain reductions exceed simulation results and the preview control display good correlation, overall, between experimental and simulation results. Despite good correlation and analytic modeling of the time dependence response of the first and second modes in Fig. 3.8, there are however small differences in amplitude. Test / simulation differences are due to the imperfect models of the system, errors in system identification, the linearity of the analytic model in presence of nonlienarities such as small freeplay, model reduction, and unmodeled high frequency dynamics, for both $\mathcal{H}_2$ and $\mathcal{H}_\infty$ actuation time histories.



(a) Sim: wing-root strain (b) Sim: outboard aileron (c) Sim: inboard aileron

(d) Exp: wing-root strain (e) Exp: outboard aileron (f) Exp: inboard aileron

Figure 3.30: Time history of $\mathcal{H}_2$ static weighted closed-loop response with a discrete gust disturbance



(a) Sim wing-root strain (b) Outboard aileron (c) Inboard aileron

(d) Wing-root strain (e) Outboard aileron (f) Inboard aileron

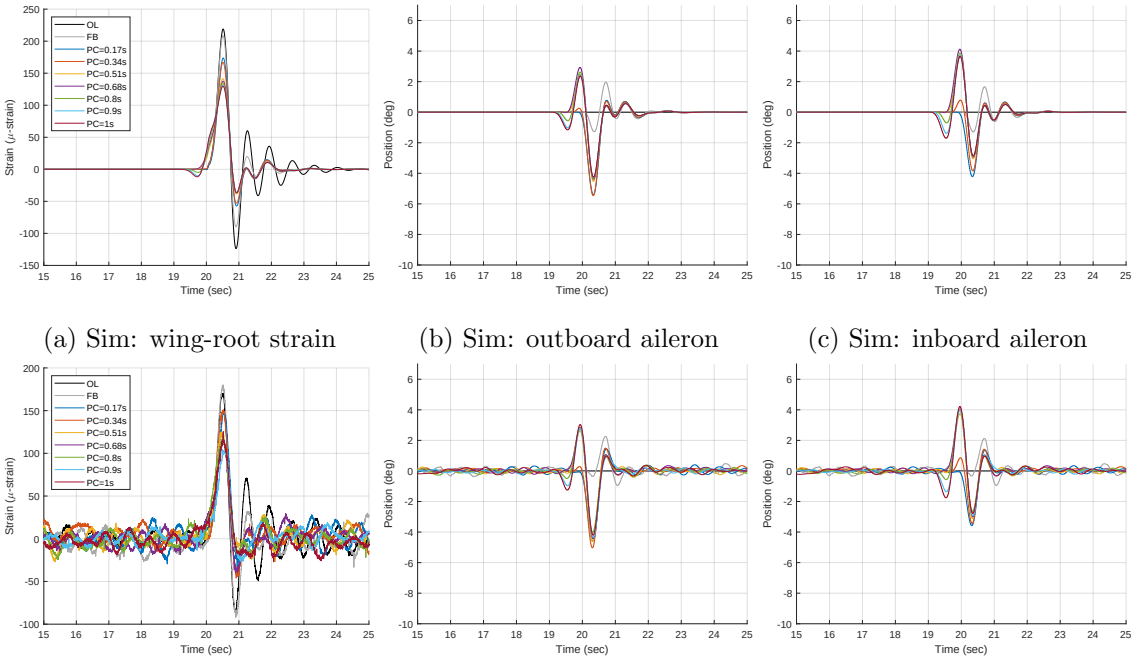
Figure 3.31: Time history of $\mathcal{H}_\infty$ static weighted closed-loop response with a discrete gust disturbance

Frequency weighted wing-root-strain with output filters The $\mathcal{H}_2$, $\mathcal{H}_\infty$, and reduced-order $\mathcal{H}_\infty$ closed-loop responses for simulation and experiments are shown in Figs. 3.32 to 3.35. Similar to the static weighted wing-root strain, the frequency weighted wing-root strains are reduced with respect to preview length. Figures 3.32 and 3.33 show good correlations between experiments and simulations in preview controls but not in just feedback control. There may be several reasons causing the worsened performance of the experimental $\mathcal{H}_2$ feedback compared to the open loop. First, the normalization process in §3.5 equally scales the control inputs and regulated output to unity with respect to individual maximum allowable values, and the additional weights in §3.5 and §3.5.1 further shape the normalized plant and penalize the regulated outputs of wing-root strain and the actuation of the ailerons. The low-pass weighted wing-root strain weights less than the high-pass weighted control actuation before roll-off in Fig. 3.25a. The weights penalized the actuations more than the wing-root strain resulting in less actuation in Fig. 3.32 comparing to the time history corresponding to static weight in Fig. 3.30. Second, let us note the effect of the wind tunnel's turbulence. This is presented in Fig. 3.7b of §3.2.1, which shows the mean and deviation of the wing-root strain variations. Lastly, there exists $\pm 1^\circ$ freeplay in the ailerons and elevator actuation. The effect is negligible when the actuation is large. However, free play may pose simulation/test correlation issues when the actuation is small. Despite some test / simulation differences, the experiments, overall, successfully demonstrated the feasibility and benefits of the preview control.

For the $\mathcal{H}_\infty$ control, the same filters, in Fig. 3.25a, were applied for $\mathcal{H}_\infty$ controller synthesis. The weight in $\mathcal{H}_\infty$ control achieved similar performance as $\mathcal{H}_2$ control in less actuation authorities and less strain reductions in Fig. 3.33 compared to static weight time history in Fig. 3.31. Although the $\mathcal{H}_\infty$ feedback reduced wing-root strain comparing to open loop, the reduction is minimal compared to simulation and is almost unstable as shown in Fig. 3.33e and 3.33f. This instability is further analyzed and addressed in the next section §3.6.1.

Figures 3.34 and 3.35 present the reduced-order $\mathcal{H}_\infty$ control using the *hinfstruct* function in MATLAB® Robust Control Toolbox [640–642] mentioned in §3.5 with detailed solution in [643, 654, 655]. The experimental 6th-order $\mathcal{H}_\infty$ feedback and experimental 4th-order $\mathcal{H}_\infty$

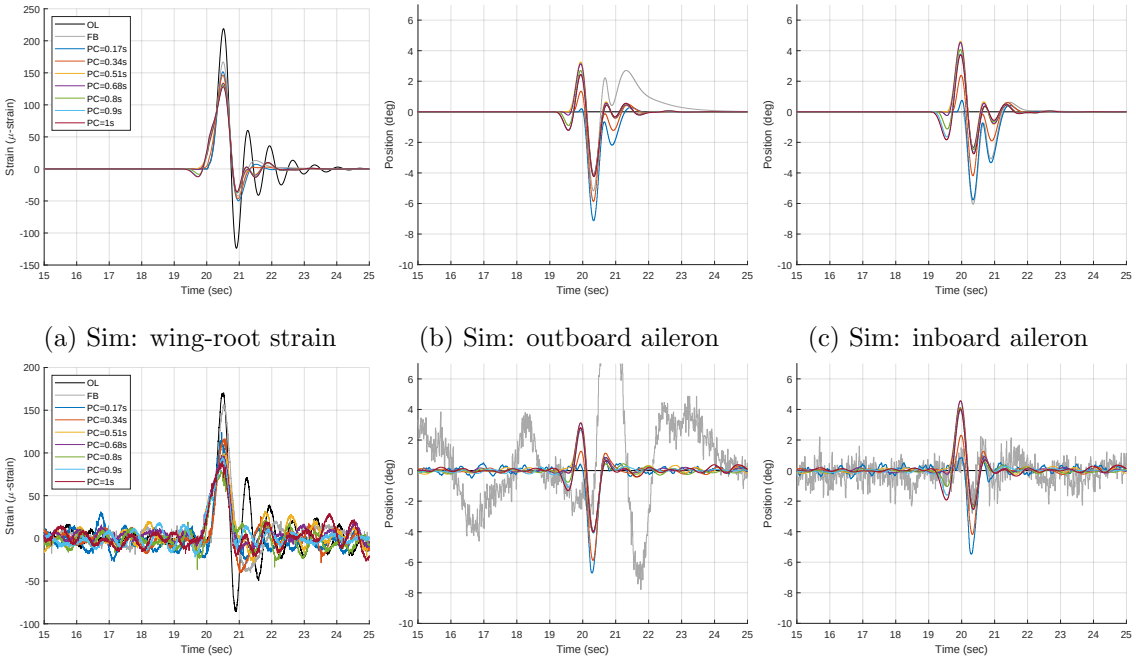
preview control with 0.34s preview are unstable and not plotted. The testing was aborted for 4th-order $\mathcal{H}_\infty$ feedback and preview control with 0.17s preview due to instability of preview control with 0.34s preview. These instability issues are addressed and discussed in §3.6.1. Except for the unstable closed-loop control, the differences between simulation and experimental are minor. The preview controls pre-loaded the wing to reduce wing load upon gust excitation shown in Figs. 3.32 to 3.35.



(a) Sim: wing-root strain (b) Sim: outboard aileron (c) Sim: inboard aileron

(d) Exp: wing-root strain (e) Exp: outboard aileron (f) Exp: inboard aileron

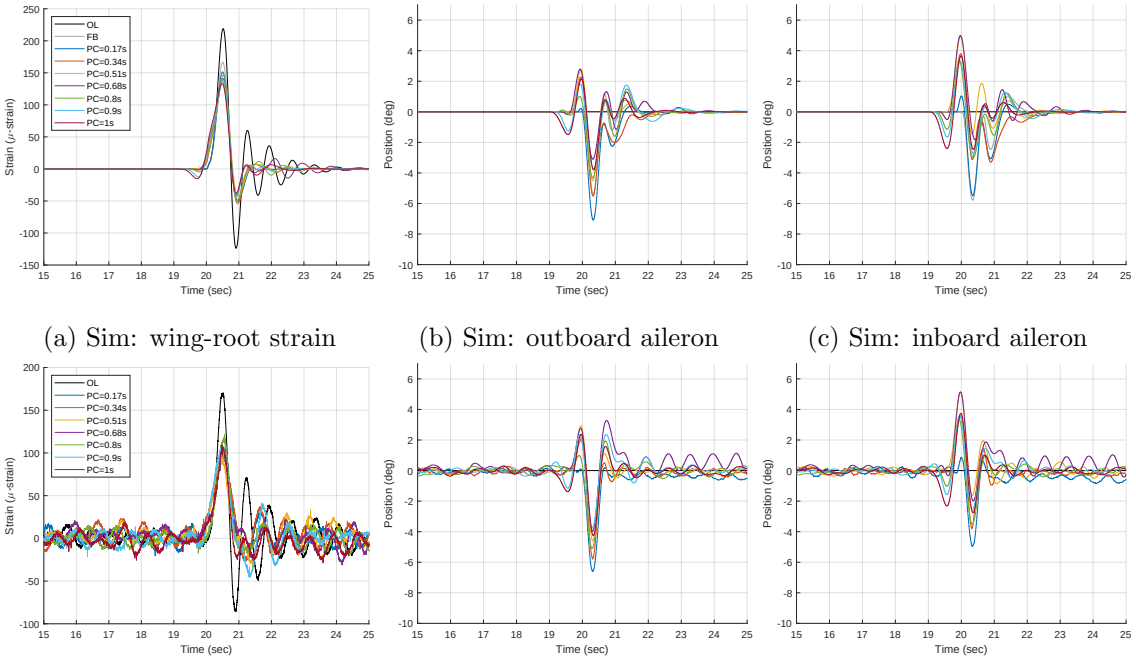
Figure 3.32: Time history of $\mathcal{H}_2$ frequency weighted closed-loop response with a discrete gust disturbance



(a) Sim: wing-root strain (b) Sim: outboard aileron (c) Sim: inboard aileron

(d) Exp: wing-root strain (e) Exp: outboard aileron (f) Exp: inboard aileron

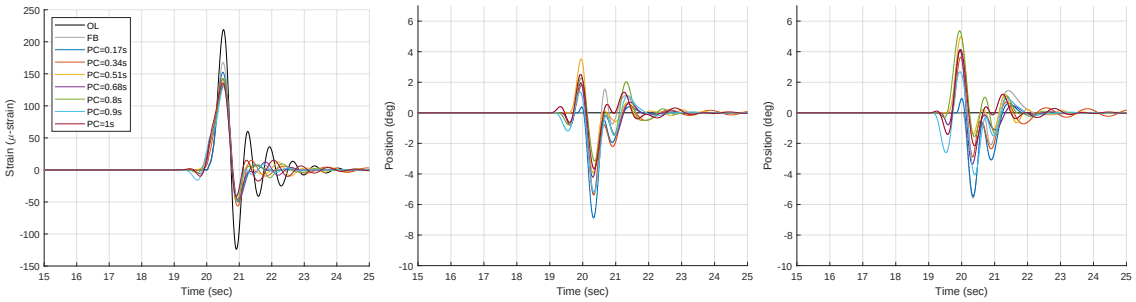
Figure 3.33: Time history of $\mathcal{H}_\infty$ frequency weighted closed-loop response with a discrete gust disturbance



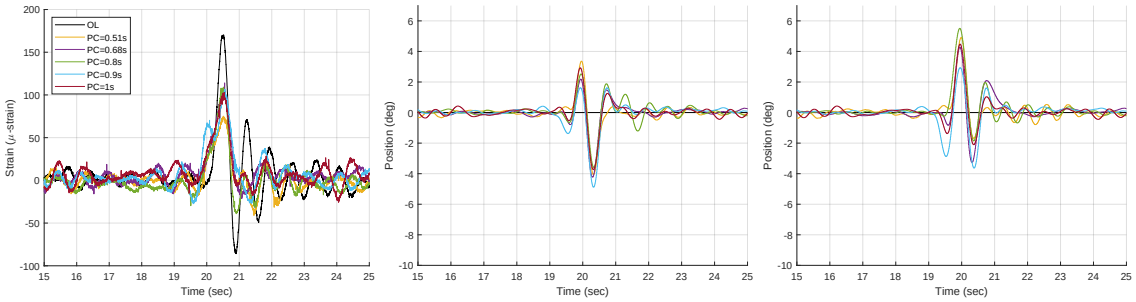
(a) Sim: wing-root strain (b) Sim: outboard aileron (c) Sim: inboard aileron

(d) Exp: wing-root strain (e) Exp: outboard aileron (f) Exp: inboard aileron

Figure 3.34: Time history of 6th-order $\mathcal{H}_\infty$ frequency weighted closed-loop response with a discrete gust disturbance



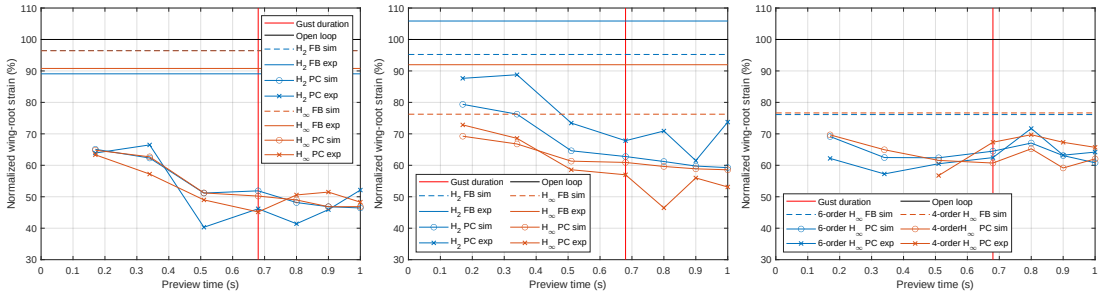
(a) Sim: wing-root strain (b) Sim: outboard aileron (c) Sim: inboard aileron



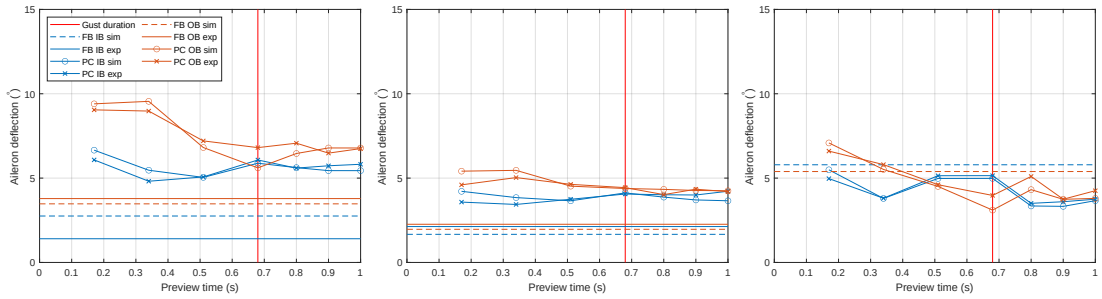
(d) Exp: wing-root strain (e) Exp: outboard aileron (f) Exp: inboard aileron

Figure 3.35: Time history of 4th-order $\mathcal{H}_\infty$ frequency weighted closed-loop response with a discrete gust disturbance

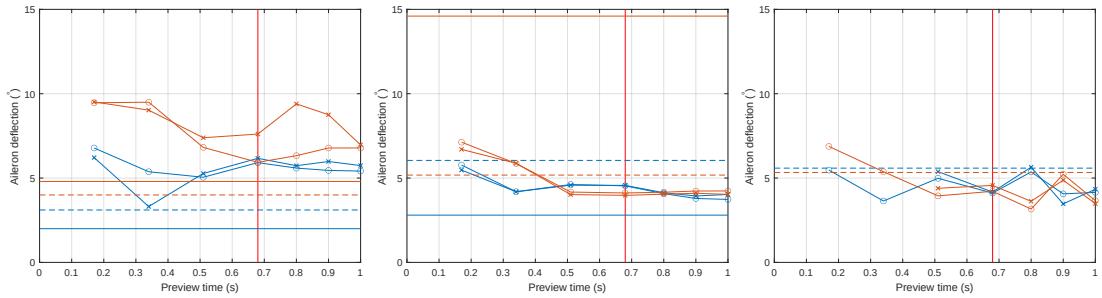
Summary of simulations and experiments Figure 3.36 summarizes the maximum absolute values of the close-loop time history response with respect to preview times from §3.6.1 and 3.6.1. Figures 3.36a to 3.36c show the maximum absolute wing-root strains decreasing with increasing preview information, correlating with Figs. 3.25b, 3.25c, 3.25e, and 3.25f. In the mean time, the wing-root strains of simulated results decrease monotonically with preview time. Although the experiments are affected by the turbulence within the wind tunnel as shown in Fig. 3.7b, the trend of experimental wing-root strains decrease with preview time. Figures 3.36d to 3.36i summarize the control surfaces' maximum absolute deflection of the closed-loop response time history. The line style and color are the same for Fig. 3.36d to 3.36i and the legends are omitted for Fig. 3.36e to 3.36i. Experimental feedback results are not plotted in Fig. 3.36c, 3.36f and 3.36i due to instabilities as mentioned in §3.6.1. Both simulated and experimental results confirm the bounds, $|\hat{u}_{\max}| < 20^{\circ}$, of the normalization process from §3.5 and §3.5.1 even when the frequency weighted full-order feedback control was almost unstable as shown in Fig. 3.36h.



(a) SW strain reduction (b) FW strain reduction (c) FW reduced-order strain reduction



(d) SW $\mathcal{H}_2$ actuation (e) FW $\mathcal{H}_2$ actuation (f) FW sixth-order $\mathcal{H}_\infty$ actuation



(g) SW $\mathcal{H}_\infty$ actuation (h) FW $\mathcal{H}_\infty$ actuation (i) FW fourth-order $\mathcal{H}_\infty$ actuation

Figure 3.36: Summary of static and frequency weighted normalized strain reduction and control actuation, on the y-axis, given preview information, on the x-axis, for variation of $\mathcal{H}_2$ and $\mathcal{H}_\infty$ in feedback and preview closed-loop control of simulation and experimental results

Controller Robustness Analysis

Going into experimental validations, it was clear that the analytic models used for control law synthesis were not perfect and that some uncertainty was present due to current math-

ematical aeroservoelastic modelling technology not capturing the dynamics of the systems perfectly, for example due to model order reduction and presence of unmodelled dynamics. Other sources of analytic model / physical system mismatch are variations in the dynamics of the actual system over time, with temperature changes that affect flow characteristics as well as structural damping levels, the gradual loosening of structural joints and their periodic tightening, etc. This is always the case with full size aircraft over their maintenance and operations cycles, as well as modeling uncertainty due to unsteady aerodynamic forces, structural dynamics, and the dynamics of sensors and actuators.

While the control laws that were synthesized for the research work here performed well overall in repeated wind tunnel tests, it was important to evaluate their robustness properties analytically for a better insights regarding their characteristics. Various measures are commonly used for quantifying robustness of linear control laws. Loop-at-a-time and multi-loop gain and phase margin measures (GM and PM, respectively) and a Disk Margin (DM) measure were used in the exploratory work reported here.

The work reported here followed the common practice presented in [535] of tightening the measures from loop-at-a-time magnitudes of 6 dB GM and 45° PM to, in the case of multi-loop measures, 3 dB GM and 22.5° PM at either input or output. The closed-loop margins of the feedback and preview controllers from §3.6.1 and 3.6.1 are shown in Figs. 3.37 and 3.38. It is important to note that the feedback is plotted at given preview information at 0 s for visual representation; however, the feedback control has no information of the preview gust at 0 s. The classical gain and phase margin are plotted in black dotted line and multiloop margins are plotted in red dotted line as requirements. The loop-at-a-time DM is more conservative than the loop-at-a-time GM and PM due to considering simultaneous variations in gain and phase by fitting a maximum disk for the closed-loop system in the Nyquist plot. Furthermore, the multiloop DM at either input or output is more conservative than loop-at-a-time DM. Ultimately, the multiloop input and output DM accounts simultaneously for gain and phase margins in all loops at both input and output of the plant. The relationships between these margins are,

$$GM \geq DM_{\text{loop-at-a-time}} \geq DM_{\text{multiloop}} \geq DM_{\text{multiloop I/O}}, \tag{3.41}$$

and

$$PM \geq DM_{\text{loop-at-a-time}} \geq DM_{\text{multiloop}} \geq DM_{\text{multiloop I/O}}, \tag{3.42}$$

where the DMs in Eq. (3.41) and (3.42) are the respective gain and phase margins computed through simultaneous gain and phase variation distinguished from the traditional gain and phase margins.

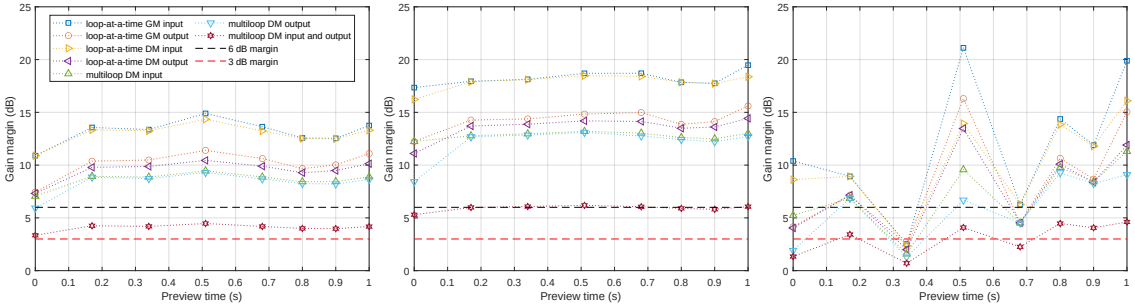
In Figs. 3.37 and 3.38, the loop-at-a-time GM and PM at input and output are computed and plotted for the smallest GM and PM of all loops using Matlab® function *allmargin* from the Robust Control Toolbox [640, 641]. The loop-at-a-time, multiloop, and multiloop input and output DM are computed and plotted using Matlab® function *diskmargin* from the Robust Control Toolbox [640, 641]. The loop-at-a-time GM and PM are omitted when they are infinite. Figures 3.37a, 3.38a, 3.37d, and 3.38d show that the static weighted $\mathcal{H}_2$ and $\mathcal{H}_\infty$ controllers have sufficient margins. Although the static weighted $\mathcal{H}_2$ and $\mathcal{H}_\infty$ feedback loop-at-a-time DM at output is lower than 6 dB and 45°, the multiloop margins at either input or output satisfy the requirements and the preview control satisfies the above expectation where the multiloop margins are doubled.

Figures 3.37b and 3.38b present the frequency weighted $\mathcal{H}_2$ controls whose margins are all within the desired range. However, this is not the case for the frequency weighted $\mathcal{H}_\infty$ control. Relative to the commonly used levels listed above, all the the margins are insufficient for the frequency weighted $\mathcal{H}_\infty$ feedback control in Figs. 3.37e and 3.38e and this correlates with the almost unstable time history in Figs. 3.33e and 3.33f from §3.6.1.

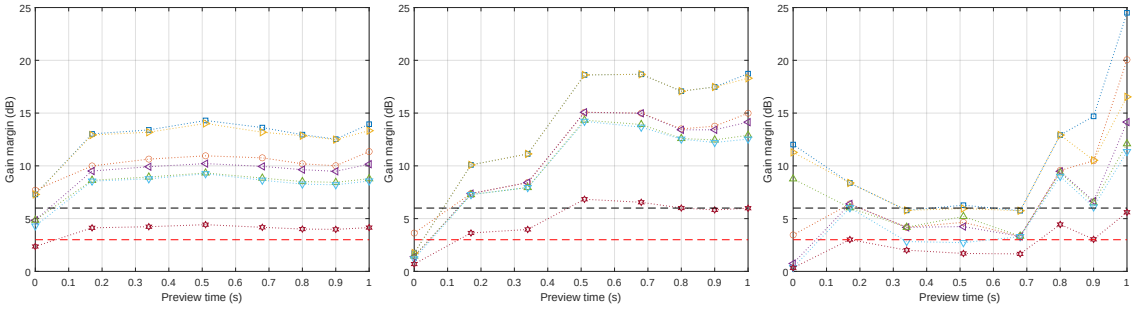
All simulations are deterministic in the absence of noise and the corresponding closed-loop system is stable, i.e., Figs. 3.33b and 3.33c. The preview augmentation increases the margins and the frequency weighted $\mathcal{H}_\infty$ preview controls meet all margin requirements. This is not the case, however, for the reduced-order controls. Figures 3.37c, 3.38c, 3.37f, and 3.38f show the margins of the frequency weighted 4th-order and 6th-order $\mathcal{H}_\infty$ control.

The robustness analysis of the reduced order laws here correlates with the experiments described in §3.6.1 and §3.6.1 whose 6th-order $\mathcal{H}_\infty$ feedback and 4th-order $\mathcal{H}_\infty$ preview controllers with 0.34 s preview were found to be unstable due to insufficient margins. It is of interest that although the 4th-order $\mathcal{H}_\infty$ preview control with 0.17 s preview has

the required margins, the shift to 0.34 s preview led to instability in the wind tunnel and the testing had to be aborted. This is due to the order reduction on the full-order controller yielding *a* reduced-order controller, but not *the* optimal reduced-order controller nor preserving robustness as that of the full-order controller. Therefore, both performance and margins of the reduced-order controllers are not guaranteed. Note that during the reduced-order controller synthesis, a good initial guess, say through the full-order controller value, would expedite the synthesis process and improve the performance of the reduced controller like the full-order one.

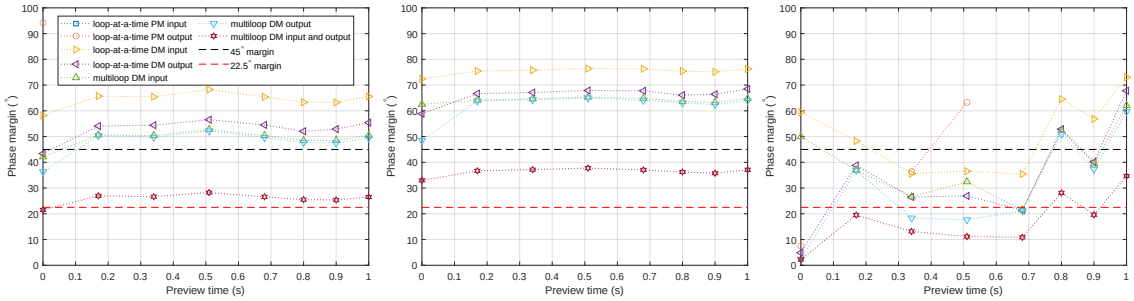


(a) Static weighted $\mathcal{H}_2$ (b) Frequency weighted $\mathcal{H}_2$ (c) Frequency weighted fourth-order $\mathcal{H}_\infty$

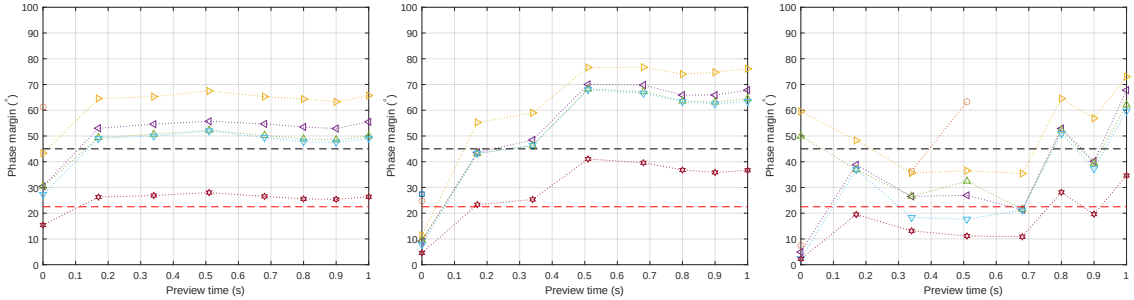


(d) Static weighted $\mathcal{H}_\infty$ (e) Frequency weighted $\mathcal{H}_\infty$ (f) Frequency weighted sixth-order $\mathcal{H}_\infty$

Figure 3.37: Summary of minimum gain margin, on the y-axis, given preview information, on the x-axis, for variation of $\mathcal{H}_2$ and $\mathcal{H}_\infty$ in feedback and preview closed-loop control results



(a) Static weighted $\mathcal{H}_2$ (b) Frequency weighted $\mathcal{H}_2$ (c) Frequency weighted fourth-order $\mathcal{H}_\infty$



(d) Static weighted $\mathcal{H}_\infty$ (e) Frequency weighted $\mathcal{H}_\infty$ (f) Frequency weighted sixth-order $\mathcal{H}_\infty$

Figure 3.38: Summary of minimum phase margin, on the y-axis, given preview information, on the x-axis, for variation of $\mathcal{H}_2$ and $\mathcal{H}_\infty$ in feedback and preview closed-loop control results

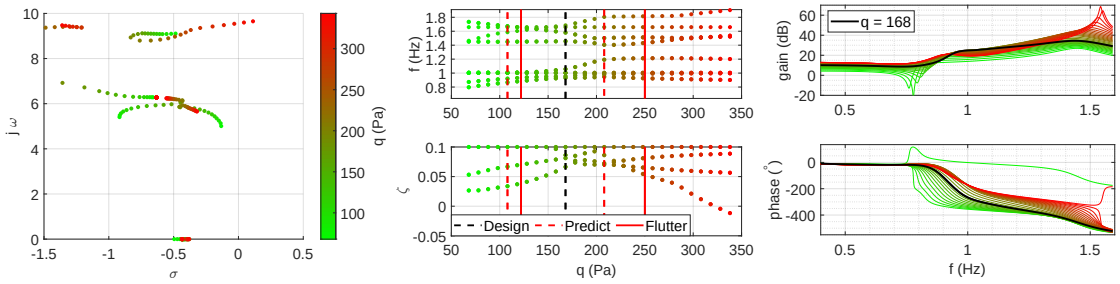
3.6.2 MARGE AFS

In the following sections, the simulation and experimental results are presented. The simulations were carried out in the Simulink environment in §3.2.1, and the wind tunnel tests were carried out at the University of Washington's 3'x3' low-speed wind tunnel, described in §3.2.1. The destabilizing closed-loop system used to create the flutter mechanism that was the focus of AFS research is presented in §3.4.1. The stabilization AFS controller, designed to suppress flutter, is presented in §3.3 and §3.5.2.

Simulation Evaluation

The AFS controller studied here is built upon a mixed-sensitivity $\mathcal{H}_\infty$ strategy to design a single SISO control law to be used across all dynamic pressures in §3.5. The destabilizing

control law, synthesizing the desired flutter behavior, used the elevator and root pitch rotation as described in Eq. (3.40) from §3.4.1. The AFS system used the wing-root strain gauge as the input and the outboard aileron command as the output for the stabilizing control law in §3.5.2. Figure 3.39 shows the behavior of the closed-loop stabilized hump-mode-type system using root locus, frequency, and damping, and Bode plots. The root locus in Fig. 3.39a shows that the hump mode in Fig. 3.11a, unstable from 108 Pa $\leq q \leq$ 208 Pa, is fully suppressed, but it lowered the second flutter mode instability from $q \approx 350$ Pa to $q \approx 318$ Pa. The damping ratio evolution with dynamic pressure in Fig. 3.39b shows that the AFS-stabilized closed-loop system increased damping at 108 Pa $\leq q \leq$ 208 and loses damping at $q \approx 318$ Pa. Although the AFS controller lowers the flutter dynamic pressure of the second mode, the successful stabilization of the hump mode is clearly evident.



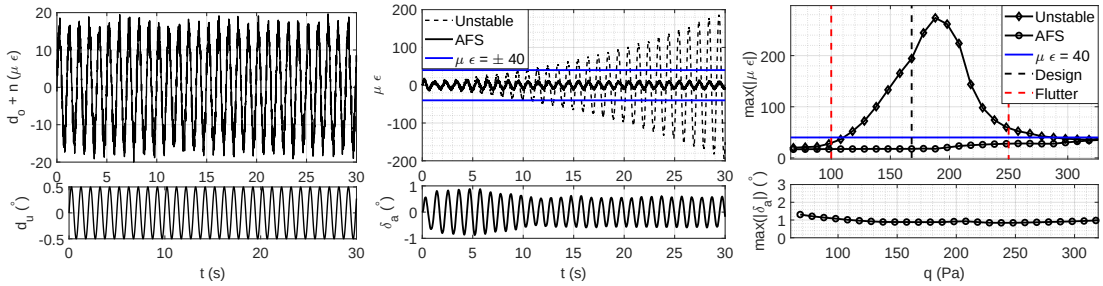
(a) Root locus [31] (b) Modal frequency and damping (c) Bode plot from d_i to $\mu\epsilon$

Figure 3.39: State space model root locus, modal frequency, modal damping, Bode plot for stabilized system by active flutter suppression at 68 Pa $\leq q \leq$ 338 Pa with increment of 10 Pa

Figure 3.40 shows the simulation results with the designed active flutter suppression controller. The time histories of the simulated disturbances are plotted in Fig. 3.40a, where the input and output are referenced to Fig. 3.6b in §3.3. The output disturbance is modeled at the sensor output of the wing-root strain targeting the unstable mode at the dynamic pressure of $q = 168$ Pa with an amplitude of $|\epsilon| \leq 15\mu$ and all frequency noise with an amplitude of $|\epsilon| \leq 5\mu$ so that the resulting output disturbance and noise are approximated at the amplitude of $|\epsilon| \leq 20\mu$ as described in §3.5.2 and in [30]. The input

disturbance at the outboard aileron also focuses on the natural frequency at the dynamic pressure presented. The freeplay of the aileron was found to be less than a degree peak-to-peak, so that the disturbance amplitude is $|\Delta\delta_{\text{OB}}| \leq 0.5°$. Note that the input and output disturbance here are magnified to focus on the natural frequency. In reality, the frequency spectrum of disturbances would be across all frequencies. However, for robustness analysis, the disturbances at input and output both focus on the lowest-damped natural frequency at the dynamic pressure presented here for worst-case scenario analysis as in Fig. 3.40a.

Figure 3.40b shows the simulated results of the unstable system and the stabilized system with AFS at the designed dynamic pressure of $q = 168$ Pa. The dashed line is the unstable system response to the disturbance input from Fig. 3.40a. The solid line is the response of the stabilized system with AFS and is bounded by the design criteria of $|\epsilon| \leq 40\mu$ for wing root strain. Figure 3.40b also shows the level of activity of the aileron in suppressing the unstable system. It is, indeed, bounded as required by the design criteria of the $|\delta_{\text{OB}}| \leq 5°$ specified in §3.5.2. Figure 3.40c shows the maximum wing-root strain response of the unstable and stabilized systems over a range of dynamic pressures, 68 Pa $\leq q \leq$ 338 Pa, where the disturbance input in Fig. 3.40a are adjusted to fall on the natural frequency at each simulated dynamic pressure as in Fig. 3.11. Note that the maximum wing-root strain plotted in Fig. 3.40c are the maximum value within the 30 s of simulation illustrated in Fig. 3.40b. That is, the amplitudes in the unstable cases where the oscillation is divergent are taken as the amplitudes at $t \leq 30$ s. Figure 3.40c shows that the maximum wing-root strain and actuation input in the AFS case are bounded according to the design criteria.



(a) Disturbances and noise at q=168 Pa (b) Time history at q=168 Pa (c) Maximum input and strain vs. q

Figure 3.40: Time history of simulated unstable and stabilized systems with disturbance and noise input at given dynamic pressure

Experimental Evaluation

Figure 3.41 shows the experimental time history from the wind tunnel studies of the designed $\mathcal{H}_\infty$ AFS controller. To reemphasize, the instability was created by feedback, and so the unstable feedback controller must be engaged. The destabilizing controller in Eq. (3.40) was activated after 10 seconds and the AFS controller was engaged shortly thereafter. Figure 3.41 shows aileron pulses of $\delta_{\text{OB}} = 2^\circ$ that were added to the control input to obtain sufficient model excitation. The bottom plot of Fig. 3.41 shows the dynamic pressure variation with time, which began near $q = 90$ Pa, passed through the predicted hump mode instability range of dynamic pressures, and reached about $q = 270$ Pa. The "destabilized" system was stable at $t < 42$s, unstable at $42s < t < 126s$, and stable again after $t > 126s$ - shown by the red dashed line. The $\mathcal{H}_\infty$ AFS controller was engaged after the first pulse to stabilize the unstable system and disengaged after $t \approx 142s$ to demonstrate the stability of the hump mode at its high-speed stable domain. The time history demonstrates that the closed-loop system was stabilized across the instability range of dynamic pressures of the hump mode and that the maximum control actuation bounds were not violated, as designed. A few rounds of wind tunnel experiments were carried out. All test results were properly stabilized and bounded. Figure 3.41 is representative of the test results.

Table 3.8 lists frequency sweeps that were used in the test. Those sweeps–forced sinusoidal sweeps by the ailerons–are superimposed on the activity of the aileron for the AFS

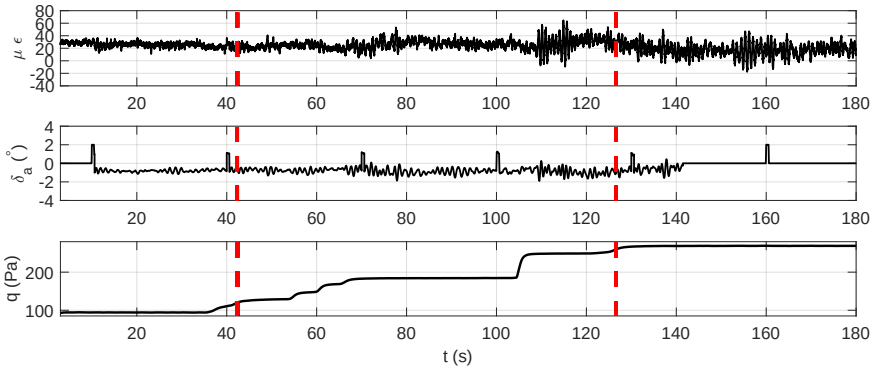


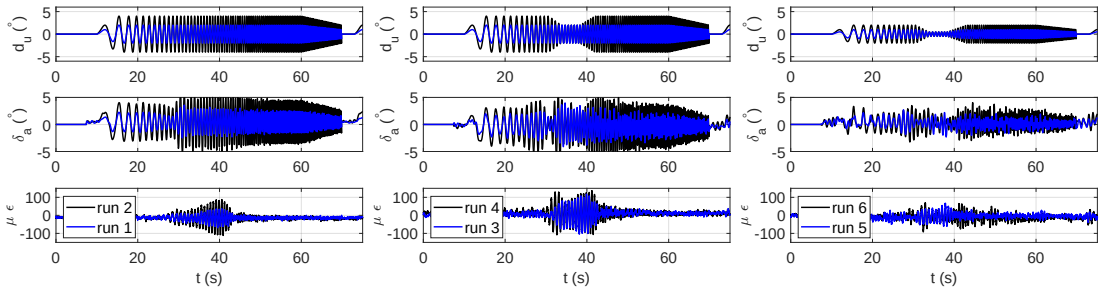
Figure 3.41: Time history of the unstable hump-mode system stabilized by the AFS controller [31]

controller; frequency sweeps are another way, like the pulses, to excite the system. If slow enough, they produce frequency response functions directly. Three dynamic pressures were selected for the input sweeps. Table 3.8 shows the dynamic pressure, amplitude, input filter, sweep number, and duration of sweep. All the sweeps have a duration of 200 s, consisting of three individual sweeps from 0.1 Hz to 3 Hz in a single run. Representative time histories of the sweeps are shown in Fig. 3.42. Note the rise in strain response, bottom figures, as the excitation frequency reaches and passes a natural frequency of a pole. Note also that different excitation amplitudes were used and that at the highest dynamic pressure shown in Fig. 3.42c, the level of excitation was reduced to anticipate a higher response level.

Table 3.8: Experimental closed-loop frequency sweeps

Frequency sweep	1	2	3	4	5	6
q (Pa)	97	97	171	171	235	235
amplitude (°)	2	4	2	4	1	2
notched input	N	N	N	Y	Y	Y
sweep number	3	3	3	3	3	3
duration	200	200	200	200	200	200

Figure 3.42 shows the time history of sweep input, aileron deflection, and wing-root strain output from top to bottom of the figure. The different runs are color-coded with sweep details in Tab. 3.8. The sweep input and aileron deflection are used to estimate the stabilized closed-loop transfer function and margin from the wind tunnel data and compare



(a) q = 97 Pa (b) q = 171 Pa (c) q = 235 Pa

Figure 3.42: Experimental frequency sweep: time history of input and output

with the state space prediction. The loop transfer function could be derived from an indirect estimate of input error response as in Fig. 3.3b in §3.2. The broken loop transfer function in Fig. 3.3b from d_u to e_u is the sensitivity function S as

$$\frac{e_u}{d_u}(s) = \frac{1}{1+GK} = S \tag{3.43}$$

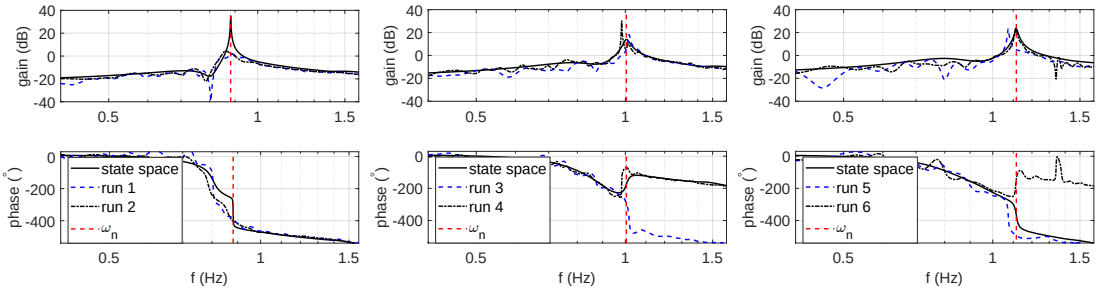
and rearranging Eq. (3.43), the loop transfer function L is

$$GK(f) = \frac{1}{e_u(f)/d_u(f)} - 1 = L, \tag{3.44}$$

where the f here denotes the experimental frequency range. The method used here adopts the Chirp Z-transform [49], originally from [656, 657]. A summary is presented in the Appendix. The sensitivity functions are omitted from the plots because they are the intermediate step to the loop transfer function.

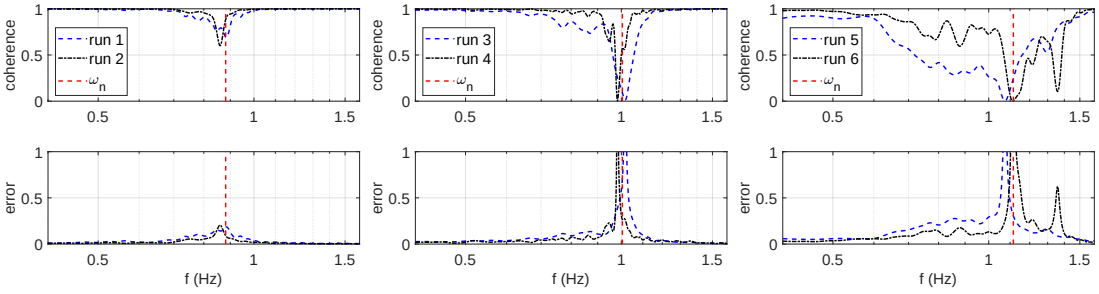
Figure 3.43 shows the Bode plots of the loop transfer function of each sweep in Tab. 3.8. It is important to note the importance of the signal-to-noise ratio for the frequency responses, where two different amplitudes were tested at each dynamic pressure. The window lengths also play an important role in the results, and the results here are adjusted to minimize noise and best represent the experimental transfer function, see Ref. [49] for more details. The coherence is plotted in Fig. 3.44 according to Eq. (3.34), which is *the fraction of the output spectrum that is linearly attributable to the input spectrum at the frequency* [49]. The ideal coherence is 1; however, in reality, it would be less than 1 because of noise and nonlinearities. A rule of thumb recommended by [49] is: Coherence $\gamma_{xy}^2 \geq 0.6$. The blue lines in Fig. 3.44 present the runs with less coherence and poorly represent the closed-loop transfer function,

especially in Figs. 3.44b and 3.44c, where instabilities were presented as stable conditions and vice versa. Aforementioned in §3.4.1 that the destabilized plant is unstable at $q = 171$ and $q = 235$, where $q = 235$ should have been stable but not due to uncertainty in Fig. 3.12c. The black dashed lines are frequency sweeps with doubled amplitude, resulting in a better signal-to-noise ratio and coherence. The coherence led to differences in identification for both black and blue lines in Figs. 3.43b and 3.43c, where the black lines had a positive phase shift indicating RHP poles, while dashed blue lines did not capture the RHP poles behaviors. Note that this poor coherence near the natural frequency is the result of noise driving the low-damped closed-loop system. This is a known phenomenon in flight flutter tests near the flutter speeds, when damping ratios become very small [618].



(a) q = 97 Pa (b) q = 171 Pa (c) q = 235 Pa

Figure 3.43: Experimental frequency sweep: loop transfer function frequency response

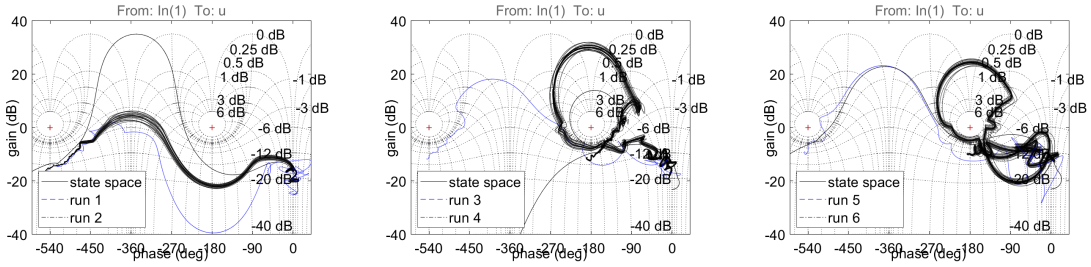


(a) q = 97 Pa (b) q = 171 Pa (c) q = 235 Pa

Figure 3.44: Experimental frequency sweep: loop transfer function coherence and error

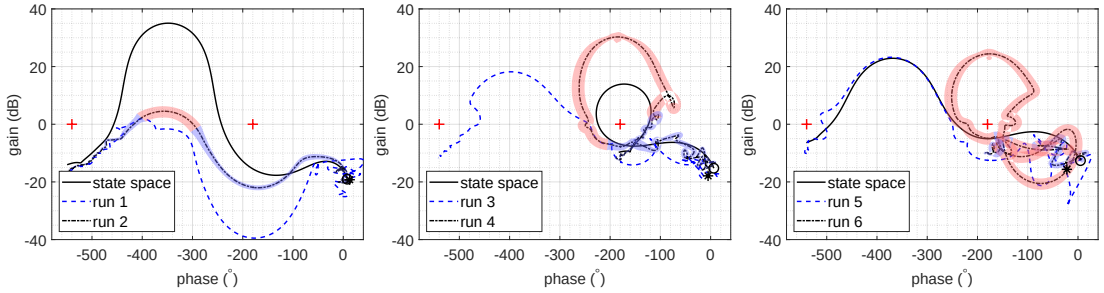
The gain and phase of Fig. 3.43 are plotted on Nichols plots in Figs. 3.45 and 3.46, where the solid lines represent the SSM and two dashed lines are the experimental frequency sweeps

from Tab. 3.8. The Nichols plots further confirm the identification of stabilization of the unstable system at $q = 171$ and $q = 235$, where the origin is encircled clockwise, suggesting RHP open-loop pole. The dashed blue line did not encircle the origin, missing the RHP open-loop poles identification. The Nichols plots are plotted again with uncertainty bounds according to Eq. (3.36), where only the best coherence runs at each dynamic pressure are plotted with uncertainty bounds. The shaded blue regions show 95% confidence bounds, where the expected normalized random error is small, $\epsilon_r \leq 0.1$, and is approximately equal to the random error in Eq. (3.35), and the red shaded regions show where $\epsilon_r > 0.1$, which is replaced with $\epsilon_r = 0.1$. Note that the expected normalized random error, ϵ, should be less than unity; however, where the coherence drops to zero near the natural frequencies of low-damped poles, resulting in ϵ "blowing up" according to Eq. (3.35). This is a direct result of the stabilized low-damped closed-loop system, so that the $\epsilon_r > 0.1$ are replaced with $\epsilon_r = 0.1$. Further note that the uncertainties in gain and phase with respect to frequency are replaced with disk-based gain variations through MATLAB's command *getDGM*. An uncertain system could be built with the nominal experimental identified loop transfer function system with disk-based gain variations as in Fig. 3.45. The approach here took the disk-based gain variations and plotted them normal to the nominal experimental identified Nichols plot in magnitude and radians first, then converted into decibels and degrees as in Fig. 3.46. The wind tunnel results agree with the state space prediction for $q = 97$ and 171 Pa but not $q = 235$ Pa, in Figs. 3.45 and 3.46. Fig. 3.46b showed that the poor noise-to-signal ratio could potentially lead to large errors in identification. The result in Fig. 3.46c agreed with the experimental identification in Fig. 3.12c [31], but, as expected, less well with the SSM in §3.4.1. The nominal closed-loop estimations were analyzed with classical and disk margin and plotted in Fig. 3.47 compared with state space closed-loops margins from Fig. 3.29. The loop-at-a-time (LAAT) results show higher margins except at $q = 235$ Pa where it was actually unstable, and the disk margin follows predictions closely. The disk margins of the inner and outer bounds in the Nichols plot in Fig. 3.46 were analyzed and plotted as error bars in Fig. 3.47 to represent uncertainty margin bounds.



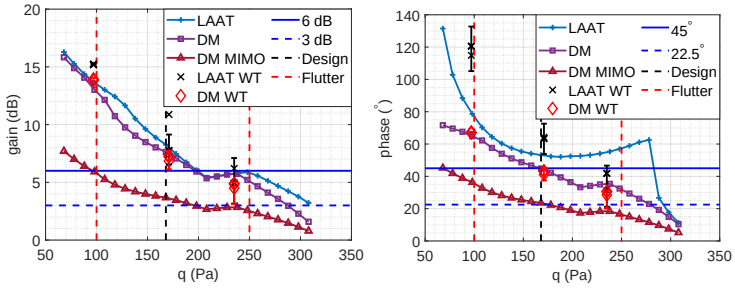
(a) q = 97 Pa (b) q = 171 Pa (c) q = 235 Pa

Figure 3.45: Experimental frequency sweep: Nichols chart of uncertain system



(a) q = 97 Pa (b) q = 171 Pa (c) q = 235 Pa

Figure 3.46: Experimental frequency sweep: Nichols chart of uncertain system with bounds



(a) Gain margin (b) Phase margin

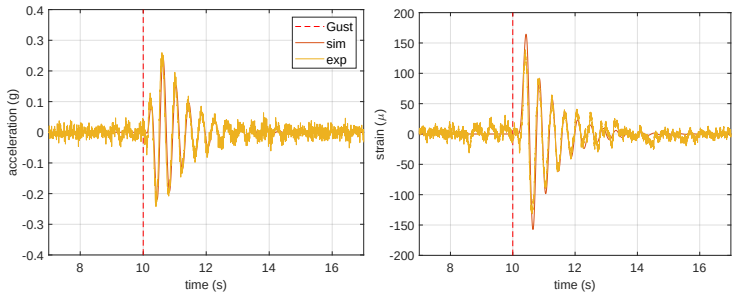
Figure 3.47: Summary of minimum gain and phase margin vs. dynamic pressure for the $\mathcal{H}_\infty$ AFS control

3.6.3 LARGE GLA

The results presented here are from [480], where mixed-sensitivity preview $\mathcal{H}_\infty$ control is combined with feedforward control on the LARGE testbed.

Simulation and Experimental Results

Figure 3.48 shows the open loop simulation and experimental results of wing inboard section bending strain and wingtip accelerometer response to gust excitation whose profile is 1-cos with 4° amplitude at 2.45 Hz. This 1-cos gust was selected deliberately for maximum excitation of the first wing bending mode at 10 s. Figure 3.48 shows a close match between test and simulation correlation.



(a) Wingtip accelerometer (b) Wing root strain gauge

Figure 3.48: Time history of system response to 1-cosine gust, simulation vs. experimental

Figures 3.49 - 3.51 present simulation and experimental results where the phrases sim and exp denote the simulation and experimental results, respectively. In the figures, OL is open loop, FB is feedback control, FF is feedforward control, and PC is preview control with the corresponding preview duration. The preview times of 0.2 s, 0.4 s, and 0.6 s were selected based on the norm reduction, where the norm is plateaued beyond 0.5 s. Note that the feedforward control here is the minimum realization of the gust to wingtip accelerometer divided by flap to wing-tip accelerometer. Since the plant is a minimum phase and stable system, the SISO inversion can be realized. The maximum feedforward flap amplitude was set to $\delta = 5°$.

Figure 3.49 presents the result of feedback and feedback with feedforward inputs, where the feedforward commands significantly reduced the wing inboard strain in both simulation and experiments.

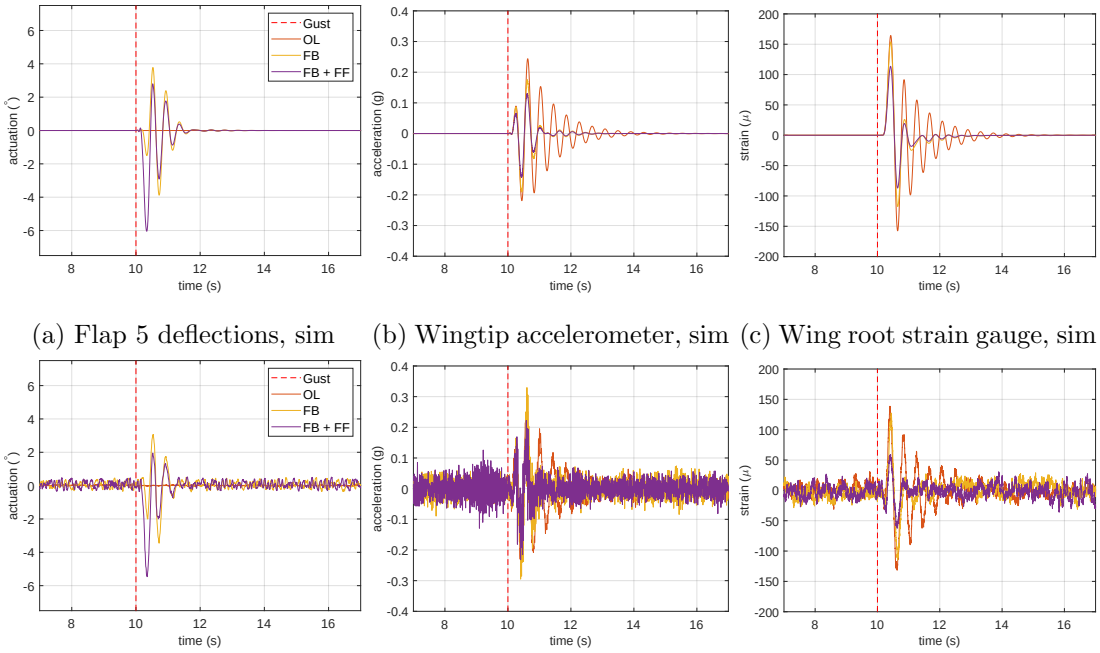
Figure 3.50 compares the results of feedback and preview control with different preview lengths. The preview control reduces the wing inboard bending strain more than the

feedback control. It is interesting to note that the strain reduction is the same with preview control across the range of preview durations of 0.2 - 0.6 s, the actuation magnitudes decrease with preview, and this correlates with the norm reduction.

Figure 3.51 adds the feedforward to preview control. Some experimental work was pursued here by adding the feedforward signal to the preview control. In the simulation, the feedforward has comparable results to those of the preview control. The actuation, however, exceeded the 5° design constraints. The strain was further reduced by adding the feedforward commands but at the expense of the actuation cost. It is also interesting to note that the feedforward and preview with 0.2 s duration had conflicting commands at $t \approx 10.3$ s in Fig. 3.51a resulting in wingtip excitation in Figs. 3.51b and 3.51e.

Figure 3.52 summarizes the maximum absolute values of the close-loop time history responses with respect to preview times. Good overall correlation between simulation and experiments for the Flap 5 input / Tip acceleration output cases that were considered was obtained.

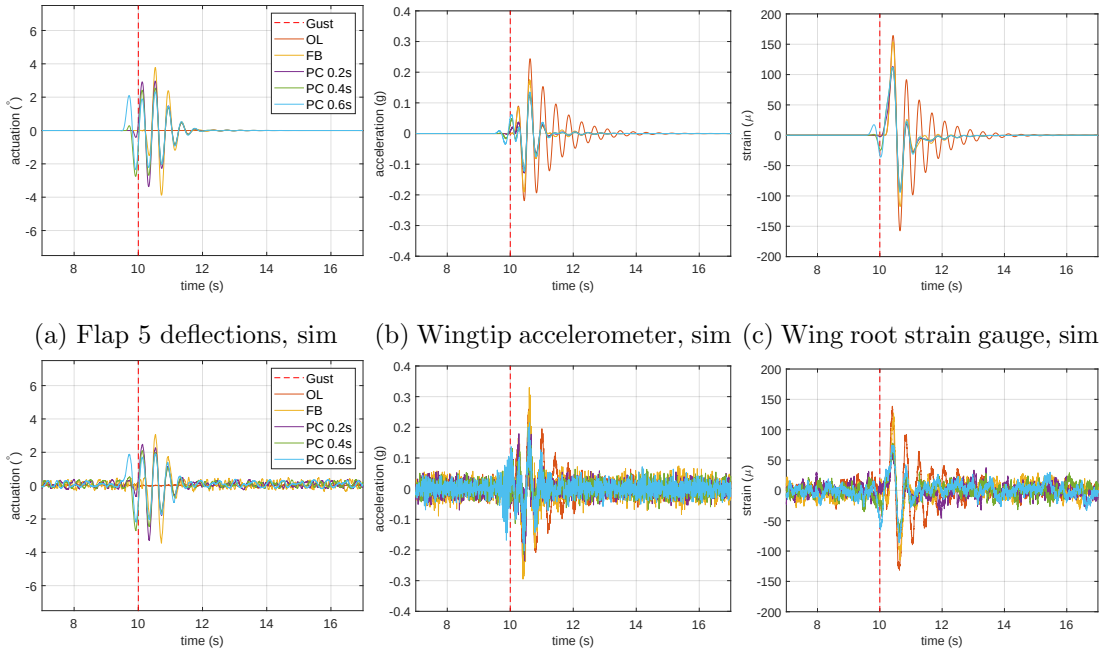
It is important to note here that in the tests described here a significant level of noise was present in the accelerometer measurements. Onboard digital filters were used, but still the wingtip acceleration measurements were quite noisy. A better understanding of the sources of this measurement noise is required as well as more work on solutions that would improve the simulation/test correlations.



(a) Flap 5 deflections, sim (b) Wingtip accelerometer, sim (c) Wing root strain gauge, sim

(d) Flap 5 deflections, exp (e) Wingtip accelerometer, exp (f) Wing root strain gauge, exp

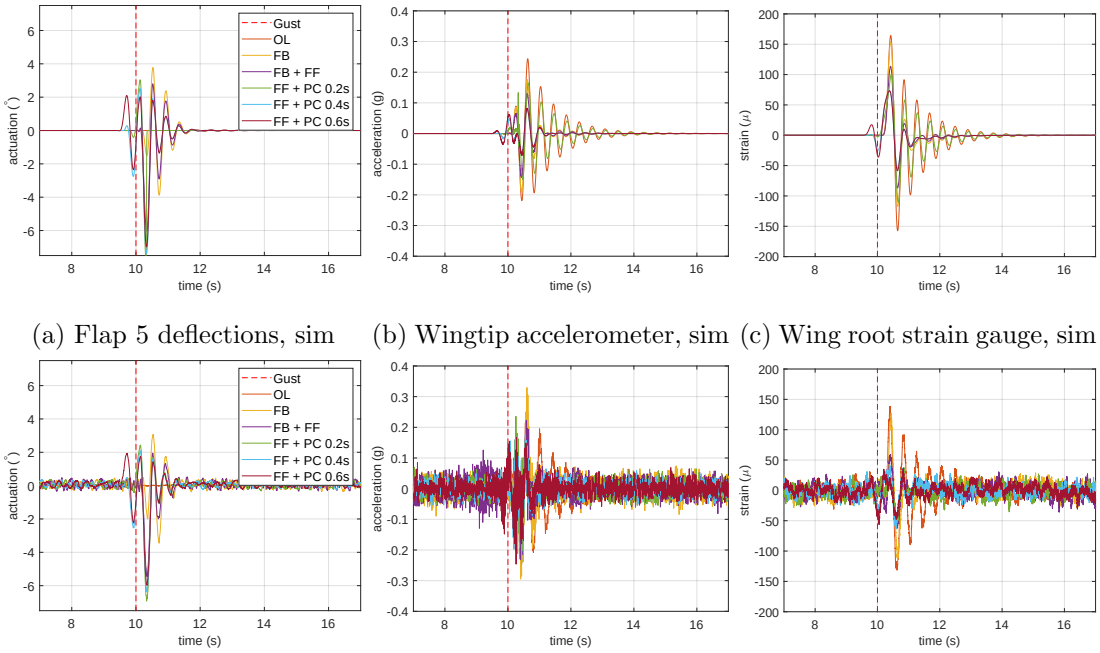
Figure 3.49: Closed-loop feedback and feedforward mixed sensitivity $\mathcal{H}_\infty$ simulation vs. experiment.



(a) Flap 5 deflections, sim (b) Wingtip accelerometer, sim (c) Wing root strain gauge, sim

(d) Flap 5 deflections, exp (e) Wingtip accelerometer, exp (f) Wing root strain gauge, exp

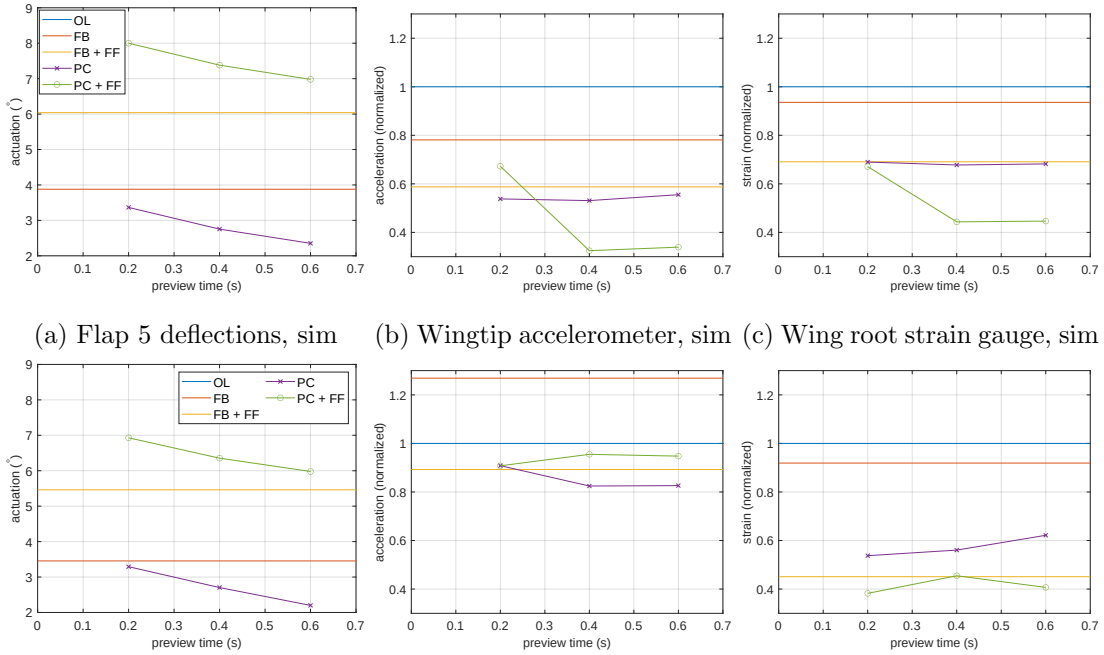
Figure 3.50: Closed-loop feedback and preview mixed sensitivity $\mathcal{H}_\infty$ simulation vs. experiment.



(a) Flap 5 deflections, sim (b) Wingtip accelerometer, sim (c) Wing root strain gauge, sim

(d) Flap 5 deflections, exp (e) Wingtip accelerometer, exp (f) Wing root strain gauge, exp

Figure 3.51: Closed-loop feedback, feedforward, and preview mixed sensitivity $\mathcal{H}_\infty$ simulation vs. experiment.



(a) Flap 5 deflections, sim (b) Wingtip accelerometer, sim (c) Wing root strain gauge, sim

(d) Flap 5 deflections, exp (e) Wingtip accelerometer, exp (f) Wing root strain gauge, exp

Figure 3.52: Closed-loop feedback, feedforward, and preview mixed sensitivity $\mathcal{H}_\infty$ simulation vs. experiment

Chapter 4

CONCLUSION

This dissertation addresses two gaps in the development of the next generation of commercial supersonic aircraft: the lack of publicly accessible low-speed aerodynamic data for slender, low-boom-shaped configurations, and the limited experimental evaluation of the active aeroservoelastic control of flexible aircraft - one of the central issues at the end of HSCT.

On the aerodynamics side, the SCALOS project first established the limitations of low-speed aerodynamic prediction across simulation methods of different fidelity and showed where wind tunnel testing remains necessary. A design space survey of existing supersonic transport designs guided the selection of configurations and components for testing. Over a five-year wind tunnel campaign of eight entries, 1415 runs, and 61.5 occupancy test days at the Kirsten Wind Tunnel, a low-speed aerodynamic results database of supersonic configurations and their parametric variations was generated. Dedicated tare-and-interference corrections were developed for the slender SCALOS geometries, for which the standard wind tunnel corrections were found to be inadequate, and the longitudinal and lateral-directional aerodynamic effects of wing planforms, fuselages, canards, tails, nacelles, leading and trailing edge devices, and take-off and landing configurations were characterized and published.

On the aeroservoelastic side, two low-cost wind tunnel testbeds, MARGE and LARGE, built around flexible high-aspect-ratio wings, were used to study active control of flexible aircraft and to establish, by experimental evaluation, the quality and feasibility of active aeroelastic control technology toward certification. The control methodology, established and tested ,is transferable across flexible configurations including future commercial supersonic transports. Gust load alleviation was demonstrated with preview $\mathcal{H}_2$ and $\mathcal{H}_\infty$ control, quantifying the benefits of gust preview information. Active flutter suppression was demonstrated by a destabilize/stabilize approach, in which control surfaces deliberately create

a flutter mechanism of interest that are then suppressed with mixed-sensitivity $\mathcal{H}\infty$ control with modal damping in the safe and controlled environment of the wind tunnel. The emphasis was placed on the closed-loop robustness of the designed controllers and on the correlation between simulation and experiment.

The accomplishments of and lessons from this work call for additional research and technology development. Near-term efforts, for which the data have been reprocessed and journal preparation is under way, include journal papers on the SCALOS project overview and lessons learned, on the tare-and-interference corrections, and on the downwash characteristics of the tested configurations. In addition, with the data that are now available, machine-learning-based prediction of the SCALOS aerodynamic coefficients, including configuration matrix completion, should be developed. A paper abstract on this has been submitted. A journal paper on the active flutter suppression results has just been published.

Proposed longer-term follow-on work utilizing the SCALOS database includes nonlinear three and six-degree-of-freedom rigid-aircraft dynamic models built based on the wind tunnel database. Take-off and landing trajectory optimization (using sequential convex programming, for example) should be developed, taking emergency scenarios into account as well as aeroelastic and noise considerations.

On the aeroservoelastic side, future R&D directions include image-based (computer-vision) system identification of the flexible model for use in feedback control, motivated by the measurement-noise limitations encountered with the onboard accelerometers in the tests described here. The application of μ-synthesis and linear-parameter-varying (LPV) control to both gust load alleviation and active flutter suppression across the flight envelope should be explored. Online data-driven control that accounts for model uncertainty, together with backup control strategies for conditions in which the system shifts away from its trim point should also be pursued.

BIBLIOGRAPHY

[1] Florance, J., Scott, R., Keller, D., Sanetrik, M., Silva, W., and Perry, B., "Lessons in the Design and Characterization Testing of the Semi-span Super-sonic Transport (S4T) Wind-tunnel Model," *53rd AIAA/ASME/ASCE/AHS/ASC Structures, Structural Dynamics and Materials Conference 20th AIAA/ASME/AHS Adaptive Structures Conference 14th AIAA*, AIAA, 2012, p. 1553. https://doi.org/10.2514/6.2012-1553.

[2] Furukawa, T., and Makino, Y., "Conceptual Design and Aerodynamic Optimization of Silent Supersonic Aircraft at JAXA," *25th AIAA Applied Aerodynamics Conference*, AIAA, 2007, p. 4166. https://doi.org/10.2514/6.2007-4166.

[3] Buckner, J., Hill, P., and Benepe, D., "Aerodynamic Design Evolution of the YF-16," *6th Aircraft Design, Flight Test and Operations Meeting*, AIAA, 1974, p. 935. https://doi.org/10.2514/6.1974-935.

[4] Nelson, C. P., Ting, K.-Y., Mavriplis, N., Soltani, R., and Livne, E., "Supersonic Configurations at Low Speeds (SCALOS): Project Background and Progress at University of Washington," *SciTech 2022 Forum*, AIAA, 2022, p. 1803. https://doi.org/10.2514/6.2022-1803.

[5] NASA, "Critical Propulsion Components," Tech. Rep. CR-2005-213584, NASA, 2005. URL https://ntrs.nasa.gov/citations/20050185247.

[6] Welge, H. R., Bonet, J., Magee, T., Chen, D., Hollowell, S., Kutzmann, A., Mortlock, A., Stengle, J., Nelson, C., Adamson, E., Baughcum, S., Britt, R. T., Miller, G., and Tai, J., "N+2 Supersonic Concept Development and Systems Integration," Tech. Rep. CR-2010-216842, NASA, 2010. URL https://ntrs.nasa.gov/citations/20100030607.

[7] Bruner, S., Baber, S., Harris, C., Caldwell, N., Keding, P., Rahrig, K., Pho, L., and Wlezian, R., "NASA N+ 3 Subsonic Fixed Wing Silent Efficient Low-emissions Commercial Transport (SELECT) Vehicle Study," Tech. Rep. 2010-216798, NASA, 2010. URL https://ntrs.nasa.gov/citations/20100042399.

[8] Welge, H., Nelson, C., and Bonet, J., "Supersonic Vehicle Systems for the 2020 to 2035

Timeframe," *28th AIAA Applied Aerodynamics Conference*, AIAA, 2010, p. 4930. https://doi.org/10.2514/6.2010-4930.

[9] Morgenstern, J., Norstrud, N., Sokhey, J., Martens, S., and Alonso, J., "Advanced Concept Studies for Supersonic Commercial Transports Entering Service in the 2018 to 2020 Period, Phase I Final Report," Tech. Rep. CR-2013-217820, NASA, 2013. URL https://ntrs.nasa.gov/citations/20130010174.

[10] Morgenstern, J., Buonanno, M., Yao, J., Murugappan, M., Paliath, U., Cheung, L., Malcevic, I., Ramakrishnan, K., Pastouchenko, N., Wood, T., Martens, S., Viars, P., Tersmette, T., Lee, J., Simmons, R., Plybon, D., Alonso, J., Palacios, F., Lukaczyk, T., and Carrier, G., "Advanced Concept Studies for Supersonic Commercial Transports Entering Service in the 2018 to 2020 Period Phase 2," Tech. Rep. CR-2015-218719, NASA, 2015. URL https://ntrs.nasa.gov/citations/20150015837.

[11] Trefny, C. J., Hirt, S. M., Anderson, B. H., Fink, L., and Magee, T., "Performance of a Supersonic Over-Wing Inlet with Application to a Low-Sonic-Boom Aircraft," *50th AIAA/ASME/SAE/ASEE Joint Propulsion Conference*, AIAA, 2014, p. 3802. https://doi.org/10.2514/6.2014-3802.

[12] "National Aeronautics and Space Administration," , 1959-presenet. URL https://ntrs.nasa.gov/, accessed: December 1str, 2023.

[13] Nelson, C. P., Ting, K.-Y., Ignacio, J., Mavriplis, N., Soltani, R., and Livne, E., "Supersonic Configurations at Low Speeds (SCALOS): Configuration Comparison of SCALOS to Existing Designs," *SciTech 2023 Forum*, AIAA, 2023, p. 0228. https://doi.org/10.2514/6.2023-0228.

[14] Mavriplis, N., Ting, K.-Y., Moustafa, A., Hill, C., Soltani, R. M., Nelson, C. P., and Livne, E., "Supersonic Configurations at Low Speeds (SCALOS): Test / Simulation Correlation Studies," *SciTech 2022 Forum*, AIAA, 2022, p. 1801. https://doi.org/10.2514/6.2022-1801.

[15] Magee, T. E., Hayes, P. J., Dorgan, A. J., and Khodadoust, A., "Dynamic Stability Characteristics for Commercial Supersonic Configurations at Low-Speed Flight Conditions," *SciTech 2022 Forum*, AIAA, 2022, p. 1802. https://doi.org/10.2514/6.2022-1802.

[16] Guimarães, T. A., Cesnik, C. E., and Kolmanovsky, I. V., "An Integrated Low-Speed Aeroelastic-Flight-Dynamics Framework for Modeling Supersonic Aircraft," *SciTech 2022 Forum*, AIAA, 2022, p. 2175. https://doi.org/10.2514/6.2022-2175.

[17] "The University of Washington's Kirsten Wind Tunnel," , 1936-present. URL https://www.aa.washington.edu/AERL/KWT, accessed: December 1str, 2023.

[18] Mavriplis, N., Ting, K.-Y., Soltani, R. M., Nelson, C. P., and Livne, E., "Supersonic Configurations at Low Speeds (SCALOS): CFD Aided Wind Tunnel Data Corrections," *SciTech 2023 Forum*, AIAA, 2023, p. 0231. https://doi.org/https://doi.org/10.2514/6.2023-0231.

[19] Ting, K.-Y., Nelson, C. P., and Livne, E., "Supersonic Configurations at Low Speeds (SCALOS): Tare & Interference Corrections for SCALOS Configurations tested at the University of Washington's KirstenWind Tunnel," *SciTech 2024 Forum*, AIAA, 2024, p. 0899. https://doi.org/https://doi.org/10.2514/6.2024-0899.

[20] Zafarghandi, F., and Soltani, M., "An Experimental Investigation of the Vortex Merging over a Cranked-Delta Wing at Subsonic Speed," *Journal of Aerospace Engineering and Mechanics*, Vol. 5, No. 1, 2021, pp. 400–416. https://doi.org/10.36959/422/453.

[21] Pfnür, S., Hövelmann, A., Sedlacek, D., and Breitsamter, C., "Vortex Flow Interaction Phenomena on Multi Swept Delta Wings at Subsonic Speeds," Tech. rep., STO-MP-AVT-307, 20, 2019.

[22] Hamizi, I. B., and Khan, S. A., "Aerodynamics Investigation of Delta Wing at Low Reynolds Number," *CFD Letters*, Vol. 11, No. 2, 2019, pp. 32–41.

[23] Ting, K.-Y., Mavriplis, N., Soltani, R. M., Nelson, C. P., and Livne, E., "Supersonic Configurations at Low Speeds (SCALOS): Model Geometry and Aerodynamic Results," *SciTech 2022 Forum*, AIAA, 2022, p. 1800. https://doi.org/10.2514/6.2022-1800.

[24] Ting, K.-Y., Wiersema, K., Nelson, C. P., and Livne, E., "Supersonic Configurations at Low Speeds (SCALOS): Progress at the University of Washington," *SciTech 2024 Forum*, AIAA, 2024, p. 0898. https://doi.org/https://doi.org/10.2514/6.2024-0898.

[25] Ting, K.-Y., Wiersema, K. C., Soltani, R., Nelson, C. P., and Livne, E., "Supersonic Configurations at Low Speeds (SCALOS): Results and Insights from the 2024 Wind Tunnel Test Campaign," *AIAA SCITECH 2026 Forum*, 2026, p. 2639. https://doi.org/10.2514/6.2026-2639.

[26] Ting, K.-Y., Mavriplis, N., Soltani, R. M., Nelson, C. P., and Livne, E., "Supersonic Configurations at Low Speeds (SCALOS): The Aerodynamic Effects of Control Surfaces," *SciTech 2023 Forum*, AIAA, 2023, p. 0229. https://doi.org/10.2514/6.2023-0229.

[27] Ting, K.-Y., Soltani, R. M., Wiersema, K., Nelson, C. P., and Livne, E., "Supersonic Configurations at Low Speeds (SCALOS): Lateral-directional Aerodynamics: Configuration Variations and Control Surface Effects," *AIAA SciTech 2025 Forum*, 2025, p. 2361. https://doi.org/10.2514/6.2025-2361.

[28] Quenzer, J. D., Zongolowicz, A., Hinson, K. A., Barzgaran, B., Livne, E., Mesbahi, M., and Morgansen, K., "Model for Aeroelastic Response to Gust Excitation," *SciTech 2019 Forum*, AIAA, 2019, p. 2031. https://doi.org/10.2514/6.2019-2031.

[29] Barzgaran, B., Quenzer, J. D., Zongolowicz, A., Hinson, K. A., Mesbahi, M., Morgansen, K., and Livne, E., "Low-cost Wind Tunnel Studies of Gust Alleviation Control Techniques," *18th International Forum on Aeroelasticity and Structural Dynamics*, International Forum on Aeroelasticity and Structural Dynamics (IFASD), 2019, p. 008. URL https://www.asdjournal.org/public/Proceedings/IFASD_2019/IFASD-2019-008.pdf.

[30] Ting, K., Mesbahi, M., and Livne, E., "Aeroservoelastic Wind Tunnel Evaluation of Preview H2 and H-infinity Gust Load Alleviation," *Journal of Guidance, Control, and Dynamics*, Vol. 46, 2023. https://doi.org/10.2514/1.G007450.

[31] Berg, J. K., Ting, K.-Y., Livne, E., and Morgansen, K., "Destabilize/Stabilize Approach to Experimental Active Flutter Suppression Technology Development," *Journal of Guidance, Control, and Dynamics*, 2025. https://doi.org/10.2514/1.G008589.

[32] Berg, J., Ting, K.-Y., Livne, E., and Morgansen, K. A., "A Destabilize/Stabilize Approach to Experimental Active Flutter Suppression Technology Development," *SciTech 2025 Forum*, AIAA, 2025, p. 1852. https://doi.org/10.2514/6.2025-1852.

[33] "National Advisory Committee for Aeronautics," , 1917-1958. URL https://ntrs.nasa.gov/, accessed: December 1str, 2023.

[34] Smetana, F. O., Summery, D., and Johnson, W. D., "Riding and Handling Qualities of Flight Aircraft: A Review and Analysis," Tech. Rep. CR-1975, NASA, 1975. URL https://ntrs.nasa.gov/citations/19720018355.

[35] "Aeronautical Research Council Reports & Memoranda," , 1909-1979. URL https://reports.aerade.cranfield.ac.uk/, accessed: December 1str, 2023.

[36] "ESDU (Engineering Sciences Data Unit) Aerodynamics," , 1964-present. URL https://esdu.com/cgi-bin/ps.pl?sess=unlicensed_1210526230324pwb&t=ser&p=ser_aero, accessed: December 1str, 2023.

[37] Finck, R. D., Ellison, D. E., and Malthan, L. V. P. I. .-., "USAF (United States Air Force) Stability and Control DATCOM (Data Compendium)," Tech. Rep. TR-83-3048, Air Force Wright Aeronautical Laboratories, 1978. AD B072483.

[38] Hoerner, S. F., and Borst, H. V., "Fluid-dynamic Lift: Practical Information on Aerodynamic and Hydrodynamic Lift," *NASA STI/Recon Technical Report A*, Vol. 76, 1975, p. 32167.

[39] Hoerner, S. F., "Fluid-Dynamic Drag: Practical Information on Aerodynamic Drag and Hydrodynamic Resistance," *The Aeronautical Journal*, Vol. 80, No. 788, 1976, pp. 371–371.

[40] Roskam, J., *Methods for Estimating Drag Polars of Subsonic Airplanes*, Roskam Aviation and Engineering Corporation, 1971.

[41] Roskam, J., *Airplane Design*, DARcorporation, 1985.

[42] Roskam, J., and Lan, C.-T. E., *Airplane Aerodynamics and Performance*, DARcorporation, 1997.

[43] Nelson, R. C., et al., *Flight Stability and Automatic Control*, Vol. 2, McGraw-Hill, 1998.

[44] Anderson, J. D., *Aircraft Performance and Design*, Vol. 1, McGraw-Hill, 1999.

[45] Pamadi, B. N., *Performance, Stability, Dynamics, and Control of Airplanes*, AIAA, 2004.

[46] Anderson, J. D., and Bowden, M. L., *Introduction to flight*, McGraw-Hill, 2005.

[47] Stengel, R. F., *Flight dynamics*, Princeton university press, 2005.

[48] Raymer, D., *Aircraft Design: a Conceptual Approach*, AIAA, 2012.

[49] Tischler, M. B., and Remple, R. K., *Aircraft and Rotorcraft System Identification*, AIAA, 2012.

[50] Stevens, B. L., Lewis, F. L., and Johnson, E. N., *Aircraft Control and Simulation: Dynamics, Controls Design, and Autonomous Systems*, John Wiley & Sons, 2015.

[51] Morelli, E. A., and Klein, V., *Aircraft System Identification: Theory and Practice*, Vol. 2, Sunflyte Enterprises, 2016.

[52] Day, R. E., *Coupling Dynamics in Aircraft: a Historical Perspective*, Vol. 532, NASA, 1997. URL https://ntrs.nasa.gov/citations/19970019603.

[53] Ericsson, L. E., and Reding, J. P., "Unsteady Aerodynamics of Slender Delta Wings at Large Angles of Attack," *Journal of Aircraft*, Vol. 12, No. 9, 1975, pp. 721–729. https://doi.org/10.2514/3.59863.

[54] Benepe, D. B., "Development of Aerodynamic Prediction Methods for Irregular Planform Wings," Tech. Rep. CR-3664, NASA, 1983. URL https://ntrs.nasa.gov/citations/19830009244.

[55] LeMay, S. P., Batill, S. M., and Nelson, R. C., "Vortex Dynamics on a Pitching Delta Wing," *Journal of Aircraft*, Vol. 27, No. 2, 1990, pp. 131–138. https://doi.org/10.2514/3.45908.

[56] Bragg, M. B., and Soltani, M. R., "Measured Forces and Moments on a Delta Wing During Pitch-up," *Journal of Aircraft*, Vol. 27, No. 3, 1990, pp. 262–267. https://doi.org/10.2514/3.45928.

[57] Soltani, M. R., Bragg, M. B., and Brandon, J. M., "Measurements on an Oscillating 70-deg Delta Wing in Subsonic Flow," *Journal of Aircraft*, Vol. 27, No. 3, 1990, pp. 211–217. https://doi.org/10.2514/3.45921.

[58] Soltani, M. R., and Bragg, M. B., "Early Vortex Burst on a Delta Wing in Pitch," *AIAA Journal*, Vol. 31, No. 12, 1993, pp. 2283–2289. https://doi.org/10.2514/3.11926.

[59] Chu, J., and Luckring, J. M., "Experimental Surface Pressure Data Obtained on 65 Degree Delta Wing Aross Reynolds Number and Mach Number Ranges," Tech. Rep. TM-4645, NASA, 1996. URL https://ntrs.nasa.gov/citations/19960025648.

[60] Mc Mahon, M. C., and Wentz Jr, W. H., "An Experimental Investigation of the Flow Fields About Delta and Double-delta Wings at Low Speeds," Tech. Rep. CR-521, NASA, 1966. URL https://ntrs.nasa.gov/citations/19660025758.

[61] Coe Jr, P. L., Kjelgaard, S. O., and Gentry Jr, G. L., "Low-speed Aerodynamic Characteristics of a Highly Swept, Untwisted Uncambered Arrow Wing," Tech. Rep. TP-2176, NASA, 1983. URL https://ntrs.nasa.gov/citations/19830027729.

[62] Reuther, J., Cliff, S., Hicks, R., and Van Dam, C., "Practical Design Optimization of Wing/-body Configurations Using the Euler Equations," *10th Applied aerodynamics conference*, AIAA, 1992, p. 2633. https://doi.org/0.2514/6.1992-2633.

[63] Polhamus, E. C., "A Concept of the Vortex Lift of Sharp-edge Delta Wings Based on a Leading-edge-suction Analogy," Tech. Rep. TN D-3767, NASA, 1967. URL https://ntrs.nasa.gov/citations/19670003842.

[64] Lan, C. E., and Su, I., "Effect of a Round Airfoil Nose on Leading-edge Suction," *Journal of aircraft*, Vol. 24, No. 7, 1987, pp. 472–474. URL https://ntrs.nasa.gov/citations/19870066510.

[65] Carlson, H. W., McElory, M. O., Lessard, W. B., and McCullers, L. A., "Improved Method for Prediction of Attainable Wing Leading-edge Thrust," Tech. Rep. 3557, NASA, 1996. URL https://ntrs.nasa.gov/citations/19960023729.

[66] Kulfan, R., "Wing Geometry Effects on Leading-edge Vortices," *AIAA Paper 1979-1872*, 1979. https://doi.org/10.2514/6.1979-1872.

[67] Sams, H., "F-15 Propulsion System Design and Development," *Aircraft Systems and Technology Meeting*, AIAA, 1975, p. 1042. https://doi.org/10.2514/6.1975-1042.

[68] Imfeld, W. F., "Development Program for the F-15 Inlet," *Journal of Aircraft*, Vol. 13, No. 4, 1976, pp. 286–291. https://doi.org/10.2514/3.58657.

[69] Katz, H., Foppe, G., and Grossman, D. T., "F-15 Flight Flutter Test Program," Tech. Rep. CP, NASA, 1976. URL https://ntrs.nasa.gov/citations/19770014093.

[70] Stevens, C., Spong, E., and Hammock, M., "F-15 inlet/engine test techniques and distortion methodologies studies. Volume 1: Technical discussion," Tech. Rep. CR-144866, NASA, 1978. URL https://ntrs.nasa.gov/citations/19780022180.

[71] Stevens, C., Spong, E., and Hammock, M., "F-15 inlet/engine test techniques and distortion methodologies studies. Volume 2: Time variant data quality analysis plots," Tech. Rep. CR-14487, NASA, 1978. URL https://ntrs.nasa.gov/citations/19780022181.

[72] LorincZ, D., and Friend, E., "Water Tunnel Visualization of the Vortex Flows of the F-15," *5th Atmospheric Flight Mechanics Conference for Future Space Systems*, AIAA, 1979, p. 1649. https://doi.org/10.2514/6.1979-1649.

[73] Burcham Jr., F. W., Maine, T., and Wolf, T., "Flight Testing and Simulation of an F-15 Airplane Using Throttles for Flight Control," *6th AIAA Biennial Flight Test Conference*, AIAA, 1992, p. 4109. https://doi.org/10.2514/6.1992-4109.

[74] Corda, S., "Dynamic Ground Effects Flight Test of an F-15 Aircraft," Tech. Rep. TM-4604, NASA, 1994. URL https://ntrs.nasa.gov/citations/19950005778.

[75] Dietz, W., and Bailey, W., "Influence of Prototype Concept and Cost Ceilings on Airframe Design and Manufacture of the YF-16 Lightweight Fighter," Tech. rep., SAE Technical Paper, 1973. https://doi.org/10.4271/730888.

[76] Buckner, J., and Webb, J., "Selected Results from the YF-16 Wind Tunnel Test Program," *8th Aerodynamic Testing Conference*, AIAA, 1974, p. 619. https://doi.org/10.2514/6.1974-619.

[77] Lamers, J. P., "Design for Departure Prevention in the YF-16," *Mechanics and Control of Flight Conference*, AIAA, 1974, p. 794. https://doi.org/10.2514/6.1974-794.

[78] Livingston, E. C., "Fly-by-wire Flight Control System Design Considerations for Fighter Aircraft," *SAE transactions*, 1975, pp. 2881–2887. https://doi.org/10.4271/751046.

[79] Hawkins, J., "YF-16 Inlet Design and Performance," *Journal of Aircraft*, Vol. 13, No. 6, 1976, pp. 436–441. https://doi.org/10.2514/3.58675.

[80] Anderson, C. A., and Operation, F. W., "Development of an Active Fly-by-wire Flight Control System," Tech. Rep. N76-31138, NASA, 1976. URL https://ntrs.nasa.gov/citations/19760024050.

[81] Merkel, P., and Whitmoyer, R., "Development and Evaluation of Precision Control Modes for Fighter Aircraft," *Guidance and Control Conference*, AIAA, 1976, p. 1950. https://doi.org/10.2514/6.1976-1950.

[82] Swortzel, F. R., and Barfield, A. F., "The Fighter CCV Program-demonstrating New Control Methods for Tactical Aircraft," *Aircraft Systems and Technology Meeting*, AIAA, 1976, p. 889. https://doi.org/10.2514/6.1976-889.

[83] Gilbert, W. P., Nguyen, L. T., and Vangunst, R. W., "Simulator Study of the Effectiveness of an Automatic Control System Designed to Improve the High-angle-of-attack Characteristics of a Fighter Airplane," Tech. Rep. TN D-8176, NASA, 1976. URL https://ntrs.nasa.gov/citations/19760017178.

[84] Nguyen, L. T., "Simulator Study of Stall/post-stall Characteristics of a Fighter Airplane with Relaxed Longitudinal Static Stability," Tech. Rep. TP-1538, NASA, 1979. URL https://ntrs.nasa.gov/citations/19800005879.

[85] Smith, C. W., Ralston, J. N., and Mann, H. W., "Aerodynamic characteristics of forebody and nose strakes based on F-16 wind tunnel test experience. Volume 1: Summary and analysis," Tech. Rep. CR-3053, NASA, 1978. URL https://ntrs.nasa.gov/citations/19790019972.

[86] Smith, C. W., and Bhateley, I. C., "Aerodynamic characteristics of forebody and nose strakes based on F-16 wind tunnel test experience. Volume 2: Data base," Tech. Rep. CR-158922, NASA, 1978. URL https://ntrs.nasa.gov/citations/19790003895.

[87] Ammons, E., "F-16 Flight Control System Redundancy Concepts," *Guidance and control conference*, AIAA, 1979, p. 1771. https://doi.org/0.2514/6.1979-1771.

[88] Hunter, L. G., and Hawkins, J., "F-16 Variable-geometry Inlet Design and Performance," *17th Joint Propulsion Conference*, AIAA, 1981, p. 1394. https://doi.org/10.2514/6.1979-1771.

[89] Hagseth, P., "F-16 Modular Common Inlet Design Concept," *23rd Joint Propulsion Conference*, AIAA, 1987, p. 1748. https://doi.org/10.2514/6.1987-1748.

[90] Erickson, G. E., "Water Tunnel Flow Visualization: Insight into Complex Three-dimensional Flowfields," *Journal of Aircraft*, Vol. 17, No. 9, 1980, pp. 656–662. https://doi.org/10.2514/3.57952.

[91] Frink, N. T., and Lamar, J. E., "Water-tunnel and Analytical Investigation of the Effect of Strake Design Variables on Strake Vortex Breakdown Characteristics," Tech. Rep. TP-1676, NASA, 1980. URL https://ntrs.nasa.gov/citations/19800019803.

[92] Erickson, G. E., "Water-tunnel Studies of Leading-edge Vortices," *Journal of aircraft*, Vol. 19, No. 6, 1982, pp. 442–448. https://doi.org/10.2514/3.57414.

[93] Hebbar, S., Platzer, M., and Cavazos, O., "A Water Tunnel Investigation of the Effects of Pitch Rate and Yaw Onlex Generated Vortices of an F/A-18 Fighter Aircraft Model," *29th Aerospace Sciences Meeting*, AIAA, 1991, p. 280. https://doi.org/10.2514/6.1991-280.

[94] Suarez, C., and Malcolm, G., "Water Tunnel Force and Moment Measurements on an F/A-18," *12th Applied Aerodynamics Conference*, AIAA, 1994, p. 1802. https://doi.org/10.2514/6.1994-1802.

[95] Beyers, M. E., and Ericsson, L. E., "Implications of Recent Rotary Rig Results for Flight Prediction," *Journal of aircraft*, Vol. 37, No. 4, 2000, pp. 545–553. https://doi.org/10.2514/2.2643.

[96] Niewoehner, R., and Filbey, J., "A computational study of F/A-18 E/F wing-drop in the approach configuration," *AIAA Atmospheric Flight Mechanics Conference and Exhibit*, AIAA, 2001, p. 4194. https://doi.org/10.2514/6.2001-4194.

[97] Beyers, M. E., "From water tunnel to poststall flight simulation: The F/A-18 Investigation," *Journal of aircraft*, Vol. 39, No. 6, 2002, pp. 913–926. https://doi.org/10.2514/2.3026.

[98] Owens, D. B., Bryant, E. M., and Barlow, J. B., "Free-to-roll Investigation of the Preproduction F/A-18E Powered-approach Wing Drop," *Journal of aircraft*, Vol. 43, No. 2, 2006, pp. 466–470. https://doi.org/10.2514/1.15721.

[99] Mullin, S., "The evolution of the F-22 advanced tactical fighter (1992 Wright Brothers Lecture)," *Flight simulation technologies conference*, AIAA, 1992, p. 4188. https://doi.org/10.2514/6.1992-4188.

[100] Barham, R., "Thrust Vector Aided Maneuvering of the YF-22 Advanced Tactical Fighter Prototype," *Biennial flight test conference*, AIAA, 1994, p. 2105. https://doi.org/10.2514/6.1994-2105.

[101] Harris, J., and Black, G., "F-22 Control Law Development and Flying Qualities," *21st atmospheric flight mechanics conference*, AIAA, 1996, p. 3379. https://doi.org/10.2514/6.1996-3379.

[102] Piccirillo, A., "Origins of the F-22 Raptor," *AIAA and SAE, 1998 World Aviation Conference*, AIAA, 1998, p. 5566. https://doi.org/10.2514/6.1998-5566.

[103] Gillard, W., "AFRL F-22 Dynamic Wind Tunnel Test Results," *24th Atmospheric Flight Mechanics Conference*, AIAA, 1999, p. 4015. https://doi.org/10.2514/6.1999-4015.

[104] Josyula, E., and Gordnier, R. E., "Computational Simulation of the F-22 Aircraft," *Journal of aircraft*, Vol. 36, No. 3, 1999, pp. 614–616. https://doi.org/10.2514/6.1998-526.

[105] Ericsson, L., and Beyers, M., "High-alpha Aerodynamics of a Slender Tailless Aircraft," *40th AIAA Aerospace Sciences Meeting & Exhibit*, AIAA, 1992, p. 94. https://doi.org/10.2514/6.2002-94.

[106] Colgren, R., and Loschke, R., "To Tail or Two Tails?-the Effective Design and Modeling of Yaw Control Devices," *AIAA Modeling and Simulation Technologies Conference and Exhibit*, AIAA, 2002, p. 4609. https://doi.org/10.2514/6.2002-4609.

[107] Anderson, W., and Mortara, S., "Maximum Control Surface Freeplay, Design and Flight Testing Approach on the F-22," *48th AIAA/ASME/ASCE/AHS/ASC structures, structural dynamics, and materials conference*, AIAA, 2007, p. 1767. https://doi.org/10.2514/6.2007-1767.

[108] Walker, G., and Allen, D., "X-35B STOVL Flight Control Law Design and Flying Qualities," *2002 Biennial international powered lift conference and exhibit*, AIAA, 2002, p. 6018. https://doi.org/10.2514/6.2002-6018.

[109] Bevilaqua, P. M., "Genesis of the F-35 Joint Strike Fighter," *Journal of Aircraft*, Vol. 46, No. 6, 2009, pp. 1825–1836. https://doi.org/10.2514/1.42903.

[110] Bevilaqua, P., "Inventing the F-35 Joint Strike Fighter," *47th AIAA aerospace sciences meeting including the new horizons forum and aerospace exposition*, AIAA, 2009, p. 1650. https://doi.org/10.2514/6.2009-1650.

[111] Parsons, D., Eckstein, A., and Azevedo, J., "F-35 Aerodynamic Performance Verification," *2018 Aviation Technology, Integration, and Operations Conference*, AIAA, 2018, p. 3679. https://doi.org/10.2514/6.2018-3679.

[112] Wiegand, C., "F-35 Air Vehicle Technology Overview," *2018 Aviation Technology, Integration, and Operations Conference*, AIAA, 2018, p. 3368. https://doi.org/10.2514/5.9781624105678.0121.0160.

[113] Ellis, R. M., Gross, P., Yates, J. B., Casement, J. R., Chichester, R. H., and Nesmith, K., "F-35 Structural Design, Development, and Verification," *2018 Aviation Technology, Integration, and Operations Conference*, AIAA, 2018, p. 3515. https://doi.org/10.2514/6.2018-3515.

[114] Frey, T. L., Aguilar, C., Engebretson, K., Faulk, D., and Lenning, L. G., "F-35 information fusion," *2018 Aviation Technology, Integration, and Operations Conference*, AIAA, 2018, p. 3520. https://doi.org/10.2514/6.2018-3520.

[115] Harris, J. J., "F-35 Flight Control Law Design, Development and Verification," *2018 Aviation Technology, Integration, and Operations Conference*, AIAA, 2018, p. 3516. https://doi.org/10.2514/5.9781624105678.0287.0312.

[116] Robbins, D., Bobalik, J., De Stena, D., Martin, N., Plag, K., Rail, K., and Wall, K., "F-35 Subsystems Design, Development & Verification," *2018 Aviation Technology, Integration, and Operations Conference*, AIAA, 2018, p. 3518. https://doi.org/10.2514/5.9781624105678.0365.0398.

[117] Wurth, S. P., "F-35 Propulsion System Integration, Development & Verification," *2018 Aviation Technology, Integration, and Operations Conference*, AIAA, 2018, p. 3517. https://doi.org/10.2514/6.2018-3517.

[118] Chin, J., Berman, H., and Ellinwood, J., "X-29A Flight Control System Design Experiences," *Guidance and Control Conference*, AIAA, 1982, p. 1538. https://doi.org/10.2514/6.1982-1538.

[119] Putnam, T., "X-29 Flight Research Program," Tech. Rep. TM-860256, NASA, 1984. URL https://ntrs.nasa.gov/citations/19840030937.

[120] Moore, M., and Frei, D., "X-29 Forward Swept Wing Aerodynamic Overview," *Applied Aerodynamics Conference*, AIAA, 1983, p. 1834. https://doi.org/10.2514/6.1983-1834.

[121] WeekS, T., "X-29 Advanced Technology Integration for Tomorrow's Fighter Aircraft," *Aircraft Systems, Design and Technology Meeting*, AIAA, 1986, p. 2613. https://doi.org/10.2514/6.1986-2613.

[122] Chin, J., Chacon, V., and Gera, J., "X-29A Flight Control System Performance During Flight Test," *Aircraft Design, Systems and Operations Meeting*, AIAA, 1987, p. 2878. https://doi.org/10.2514/6.1987-2878.

[123] Ashworth, J., Mouch, T., and Luttges, M., "Application of Forced Unsteady Aerodynamics to a Forward Swept Wing X-29 Model," *26th Aerospace Sciences Meeting*, AIAA, 1988, p. 563. https://doi.org/10.2514/6.1988-563.

[124] Ashworth, J., Mouch, T., and Luttges, M., "Visualization and Anemometry Analyses of Forced Unsteady Flows Aboutan X-29 Model," *6th Applied Aerodynamics Conference*, AIAA, 1988, p. 2570. https://doi.org/10.2514/6.1988-2570.

[125] Del Frate, J., and Saltzman, J., "In-flight Flow Visualization Results from the X-29A Aircraft at Highangles of Attack," *6th AIAA Biennial Flight Test Conference*, AIAA, 1992, p. 4102. https://doi.org/10.2514/6.1992-4102.

[126] Smith, W., and Pellicano, P., "X-29 High Angle-of-attack Military Utility Flight Test Results," *6th AIAA Biennial Flight Test Conference*, AIAA, 1992, p. 4080. https://doi.org/10.2514/6.1992-4080.

[127] Bosworth, J. T., "Linearized Aerodynamic and Control Law Models of the X-29A Airplane and Comparison with Flight Data," Tech. Rep. TM-4356, NASA, 1991. URL https://ntrs.nasa.gov/citations/19920009932.

[128] Tindell, R., and Hill Jr, W., "CFD Analysis of the X-29 Inlet at High Angle of Attack," *Journal of aircraft*, Vol. 30, No. 4, 1993, pp. 480–487. https://doi.org/10.2514/3.56892.

[129] Snell, S., Garrard, W., and Enns, D., "Nonlinear Control of a Supermaneuverable Aircraft," *Guidance, Navigation and Control Conference*, AIAA, 1989, p. 2171. https://doi.org/10.2514/6.1989-3486.

[130] Hebbar, S. K., Platzer, M. F., and Kwon, H. M., "Static and Dynamic Water Tunnel Flow Visualization Studies of a Canard Configured X-31a-like Fighter Aircraft Model," *AIAA 22nd Fluid Dynamics, Plasma Dynamics and Lasers Conference, 1991*, AIAA, 1991, p. 1629. https://doi.org/10.2514/6.1991-1629.

[131] Klein, V., and Noderer, K., "Aerodynamic Parameters of the X-31 Drop Model Estimated from Flight Data at High Angles of Attack," *Guidance, Navigation and Control Conference*, AIAA, 1992, p. 4357. https://doi.org/10.2514/6.1992-4357.

[132] Mackall, D., Norlin, K., Cohen, D., Kellogg, G., Schilling, L., and Sheen, J., "Rapid Development of the X-31 Simulation to Support Flight-testing," *Flight Simulation Technologies Conference*, AIAA, 1992, p. 4176. https://doi.org/10.2514/6.1992-4176.

[133] Noderer, K., "An Overview of the System Identification Procedure with Applicationsto the X-31 Drop Model," *31st Aerospace Sciences Meeting*, AIAA, 1993, p. 10. https://doi.org/10.2514/6.1993-10.

[134] Hodson, C. H., Dobbs, S. K., Brosnan, M. J., and Chen, J. B., "X-31A Flight Flutter Test Excitation by Control Surfaces," *34th Structures, Structural Dynamics and Materials Conference*, AIAA, 1993, p. 1538. https://doi.org/10.2514/6.1993-1538.

[135] Croom, M. A., Fratello, D. J., Whipple, R. D., O'rourke, M. J., and Trilling, T. W., "Dynamic Model Testing of the X-31 Configuration for High-angle-of-attack Flight Dynamics Research," *Flight Simulation and Technologies*, AIAA, 1993, pp. 488–506. https://doi.org/10.2514/6.1993-3674.

[136] Cobleigh, B. R., "High-angle-of-attack Yawing Moment Asymmetry of the X-31 Aircraft from Flight Test," *12th Applied Aerodynamics Conference*, AIAA, 1994, pp. 25–48. https://doi.org/10.2514/6.1994-1803.

[137] Williams, D., II, Nelson, R., and Fisher, D., "An Investigation of X-31 Roll Characteristics at High Angle-of-attack Through Subscale Model Testing," *32nd Aerospace Sciences Meeting and Exhibit*, AIAA, 1994, p. 806. https://doi.org/10.2514/6.1994-806.

[138] Canter, D., and Groves, A., "X-31 Post-stall Envelope Expansion and Tactical Utility Testing," *Biennial Flight Test Conference*, AIAA, 1994, p. 2171. https://doi.org/10.2514/6.1994-2171.

[139] Huber, P., "Control Law Design for Tailless Configurations and In-flight Simulation Using the X-31 Aircraft," *Guidance, Navigation, and Control Conference*, AIAA, 1995, pp. 247–257. https://doi.org/10.2514/6.1995-3199.

[140] Grohs, T., Fischer, B., Heinzinger, O., and Brieger, O., "X-31 VECTOR control law design for ESTOL to the ground," *Guidance, Navigation, and Control Conference and Exhibit*, AIAA, 2003, p. 5406. https://doi.org/10.2514/6.2003-5406.

[141] Grohs, T., Fischer, B., Heinzinger, O., and Brieger, O., "X-31 VECTOR-ESTOL to the Ground Flight Test Results and Lessons Learned," *Guidance, Navigation, and Control Conference and Exhibit*, AIAA, 2004, p. 5029. https://doi.org/10.2514/6.2004-5029.

[142] Tamrat, B., "The X-31: A post-Stall Technology (PST) fighter close-in-combat results assessment, and a look at new CIC performance evaluation metrics," *Atmospheric Flight Mechanics Conference*, AIAA, 2004, pp. 1002–1022. https://doi.org/10.2514/6.2004-5173.

[143] Rohlf, D., "Global model approach for X-31 VECTOR system identification," *Journal of aircraft*, Vol. 42, No. 1, 2005, pp. 54–62. https://doi.org/10.2514/1.6147.

[144] Rein, M., Höhler, G., Schütte, A., Bergmann, A., and Löser, T., "Ground-based Simulation of Complex Maneuvers of a Delta-wing Aircraft," *Journal of Aircraft*, Vol. 45, No. 1, 2008, pp. 286–291. https://doi.org/10.2514/1.30033.

[145] Jirásek, A., and Cummings, R., "Application of Volterra functions to X-31 aircraft model motion," *27th AIAA Applied Aerodynamics Conference*, AIAA, 2009, p. 3629. https://doi.org/10.2514/6.2009-3629.

[146] Nangia, R., "X-31 Vector Aircraft, Low Speed Stability & Control, Comparisons of Wind Tunnel Data & Theory (Focus on Linear & Panel Codes)," *39th AIAA Fluid Dynamics Conference*, AIAA, 2009, p. 3898. https://doi.org/10.2514/6.2009-3898.

[147] Jirásek, A., and Cummings, R., "Assessment of sting effect on X-31 aircraft model using CFD," *48th AIAA aerospace sciences meeting including the New Horizons Forum and Aerospace Exposition*, AIAA, 2010, p. 1040. https://doi.org/10.2514/6.2010-1040.

[148] Schütte, A., Boelens, O. J., Loeser, T., and Oehlke, M., "Prediction of the flow around the X-31 aircraft using two different CFD methods," *28th AIAA Applied Aerodynamics Conference*, AIAA, 2010, p. 4692. https://doi.org/10.2514/6.2010-4692.

[149] Tomac, M., and Rizzi, A., "Creation of Aerodynamic Database for the X-31," *48th AIAA Aerospace Sciences Meeting Including the New Horizons Forum and Aerospace Exposition*, AIAA, 2010, p. 501. https://doi.org/10.2514/6.2010-501.

[150] Tomac, M., Rizzi, A., Nangia, R., and Mendenhall, M., "Comparing and Benchmarking Engineering Methods on the Prediction of X-31 Aerodynamics," *28th AIAA Applied Aerodynamics Conference*, AIAA, 2010, p. 4694. https://doi.org/10.2514/6.2010-4694.

[151] Jirásek, A., and Cummings, R. M., "Reduced Order Modeling of X-31 Wind Tunnel Model Aerodynamic Loads," *Aerospace Science and Technology*, Vol. 20, No. 1, 2012, pp. 52–60. https://doi.org/10.2514/6.2010-4693.

[152] Boelens, O. J., "CFD Analysis of the Flow Around the X-31 Aircraft at High Angle of Attack," *Aerospace Science and Technology*, Vol. 20, No. 1, 2012, pp. 38–51. https://doi.org/10.2514/6.2009-3628.

[153] Ghoreyshi, M., Post, M., Cummings, R., Da Ronch, A., and Badcock, K., "Transonic Aerodynamic Loads Modeling of X-31 Aircraft," *30th AIAA Applied Aerodynamics Conference*, AIAA, 2012, p. 3127. https://doi.org/10.2514/6.2012-3127.

[154] Ghoreyshi, M., Cummings, R. M., Ronch, A. D., and Badcock, K. J., "Transonic Aerodynamic Load Modeling of X-31 Aircraft Pitching Motions," *AIAA journal*, Vol. 51, No. 10, 2013, pp. 2447–2464. https://doi.org/10.2514/1.J052309.

[155] Ghoreyshi, M., Jirasek, A., and Cummings, R. M., "Validation of CFD models for simulating a maneuvering X-31 with flight test data," *52nd Aerospace Sciences Meeting*, AIAA, 2014, p. 0048. https://doi.org/10.2514/6.2014-0048.

[156] Walker, L. A., "Flight Testing the X-36: The Test Pilots Perspective," Tech. Rep. CR-198058, NASA, 1997. URL https://ntrs.nasa.gov/citations/19970031950.

[157] Harris, W., and Harris, W., "X-36 Tailless Agility Aircraft Subsystems Integration," *1997 World Aviation Congress*, AIAA, 1997, p. 5505. https://doi.org/10.2514/6.1997-5505.

[158] Balough, D., "Determination of X-36 Stability Margins Using Real-time Frequency Response Techniques," *23rd Atmospheric Flight Mechanics Conference*, AIAA, 1998, p. 4154. https://doi.org/10.2514/6.1998-4154.

[159] Brinker, J. S., and Wise, K. A., "Flight Testing of Reconfigurable Control Law on the X-36 Tailless Aircraft," *Journal of Guidance, Control, and Dynamics*, Vol. 24, No. 5, 2001, pp. 903–909. https://doi.org/10.2514/2.4826.

[160] Carter, D., "The Integration of Wind Tunnel and Water Tunnel Results for a New In-flight Simulator Configuration," *15th Aerodynamic Testing Conference*, AIAA, 1988, p. 2045. https://doi.org/10.2514/6.1988-2045.

[161] Cotting, M. C., Stephens, S. S., Cole, J., Barricklow, J., and Gray, W., "X-62 VISTA Capabilities and Architecture," *SciTech 2023 Forum*, AIAA, 2023, p. 1744. https://doi.org/10.2514/6.2023-1744.

[162] Haus, P. J., Konopka, B., and Faught, D., "The New VISTA Simulation System (VSS) Design and Implementation," *SciTech 2023 Forum*, AIAA, 2023, p. 1745. https://doi.org/10.2514/6.2023-1745.

[163] Caraway, D. J., Harris, Q. C., and Cotting, M. C., "VISTA X-62A Model Following Algorithm Overview," *SciTech 2023 Forum*, AIAA, 2023, p. 1746. https://doi.org/10.2514/6.2023-1746.

[164] Harris, Q. C., and Caraway, D. J., "Model Following Control Allocation For The X-62A," *SciTech 2023 Forum*, AIAA, 2023, p. 1747. https://doi.org/10.2514/6.2023-1747.

[165] Schiavone, A., Babala, P., Hartwig, L., and Cotting, M. C., "X-62 VISTA System for the Autonomous Control of the Simulation Design and Implementation," *SciTech 2023 Forum*, AIAA, 2023, p. 1926. https://doi.org/10.2514/6.2023-1926.

[166] Haus, P. J., "Ground and Flight Testing the New VISTA Simulation System (VSS)," *SciTech 2023 Forum*, AIAA, 2023, p. 1927. https://doi.org/10.2514/6.2023-1927.

[167] Cotting, M. C., Stephens, S. S., Cole, J., Gray, W., Hartwig, L., Caraway, D. J., Harris, Q., Schiavone, A., Babala, P., and Picard, R., "X-62 VISTA Simulation and Autonomy Flight Testing," *SciTech 2023 Forum*, AIAA, 2023, p. 1928. https://doi.org/10.2514/6.2023-1928.

[168] Hobbs, K. L., Heiner, B., Busse, L., Dunlap, K., Rowanhill, J., Hocking, A. B., and Zutshi, A., "Systems Theoretic Process Analysis of a Run Time Assured Neural Network Control System," *SciTech 2023 Forum*, AIAA, 2023, p. 2664. https://doi.org/10.2514/6.2023-2664.

[169] Leyman, C., "A Review of the Technical Development of Concorde," *Progress in Aerospace Sciences*, Vol. 23, No. 3, 1986, pp. 185–238. https://doi.org/10.1016/0376-0421(86)90007-2.

[170] Swihart, J. M., "Transonic Aerodynamic Characteristics of a 1/15-Scale Model of the Convair B-58 Airplane," Tech. Rep. RM-SL56J22, NACA, 1956. URL https://ntrs.nasa.gov/citations/19710076499.

[171] Smith, L., and Rogers, C., "Bonded Bomber—B-58," *SAE Transactions*, Vol. 70, 1962, pp. 477–486. URL https://www.jstor.org/stable/44469505.

[172] Preston, L., "Contract Negotiations and Results in Aircraft Procurement: Case Studies of the B-52 and B-58," Tech. Rep. RM-3254-PR, Rand Corporation, 1962. https://doi.org/10.7249/RM3254.

[173] Walker, H. J., "Performance Evaluation Method for Dissimilar Aircraft Designs," Tech. Rep. RP-1041, NASA, 1979. URL https://ntrs.nasa.gov/citations/19790021968.

[174] Tinetti, A. F., Maglieri, D. J., Driver, C., and Bobbitt, P. J., "Equivalent Longitudinal Area Distributions of the B-58 and XB-70-1 Airplanes for Use in Wave Drag and Sonic Boom Calculations," Tech. Rep. CR–2011-217078, NASA, 2011. URL https://ntrs.nasa.gov/citations/20110008473.

[175] Rogerson, D. B., "Technological Advancements Resulting from XB-70 Performance Requirements," Tech. rep., SAE Technical Paper, 1965. https://doi.org/10.4271/650798.

[176] Andrews, W. H., "Summary of Preliminary Data Derived From the XB-70 Airplanes," Tech. Rep. TM-X-1240, NASA, 1966. URL https://ntrs.nasa.gov/citations/19660018723.

[177] Kordes, E. E., and Love, B. J., "Preliminary Evaluation of XB-70 Airplane Encounters with High-altitude Turbulence," Tech. Rep. TN-D-4209, NASA, 1967. URL https://ntrs.nasa.gov/citations/19670030390.

[178] Fulton Jr, F. L., "Lessons from the XB-70 as Applied to the Supersonic Transport," Tech. Rep. NASA-TM-X-56014, NASA, 1968. URL https://ntrs.nasa.gov/citations/19670030390.

[179] Irwin, K. S., and Andrews, W. H., "Summary of XB-70 Airplane Cockpit Environmental Data," Tech. Rep. TN-D-5439, NASA, 1969. URL https://ntrs.nasa.gov/citations/19730023226.

[180] Wykes, J. H., and Mori, A. S., "XB-70 Aerodynamic, Geometric, Mass, and Symmetric Structural Mode Data," Tech. Rep. CR-116773, NASA, 1970. URL https://ntrs.nasa.gov/citations/19720004294.

[181] Larson, T. J., and Schweikhard, W. G., "Verification of Takeoff Performance Predictions for the XB-70 Airplane," Tech. Rep. TM-X-2215, NASA, 1971. URL https://ntrs.nasa.gov/citations/19710009034.

[182] Lock, W. P., Kordes, E. E., and McKay, J. M., "Flight Investigation of a Structural Mode Control System for the XB-70 Aircraft," Tech. Rep. TN-D-7420, NASA, 1973. URL https://ntrs.nasa.gov/citations/19730023218.

[183] McKay, J. M., and Kordes, E. E., "Flight Investigation of XB-70 Structural Response to Oscillatory Aerodynamic Shaker Excitation and Correlation with Analytical Results," Tech. Rep. TN-D-7227, NASA, 1973. URL https://ntrs.nasa.gov/citations/19730016165.

[184] Wolowicz, C. H., and Yancey, R. B., "Summary of Stability and Control Characteristics of the XB-70 Airplane," Tech. Rep. TM-X-7933, NASA, 1973. URL https://ntrs.nasa.gov/citations/19730023226.

[185] Ross, J., and Rogerson, D., "XB-70 technology advancements," *Aircraft Prototype and Technology Demonstrator Symposium*, AIAA, 1983, p. 1048. https://doi.org/10.2514/6.1983-1048.

[186] Maglieri, J., and Sothcott, E., "A Summary of XB-70 Sonic Boom Signature Data," Tech. Rep. CR–189630, NASA, 1992. URL https://ntrs.nasa.gov/citations/19920015557.

[187] Razgonyaev, V., and Mason, W., "An Evaluation of Aerodynamic Prediction Methods Applied to the XB-70 for Use in High Speed Aircraft Stability and Control System Design," *33rd Aerospace Sciences Meeting and Exhibit*, AIAA, 1995, p. 759. https://doi.org/10.2514/6.1995-759.

[188] Maglieri, D. J., Henderson, H. R., and Tinetti, A. F., "Measured Sonic Boom Signatures Above and Below the XB-70 Airplane Flying at Mach 1.5 and 37,000 Feet," Tech. Rep. CR–2011-217077, NASA, 2011. URL https://ntrs.nasa.gov/citations/20110011170.

[189] Sigalla, A., and Hallstaff, T., "Aerodynamics of Powerplant Installation on Supersonic Aircraft," *Journal of Aircraft*, Vol. 4, No. 4, July 1967, pp. 273–277. https://doi.org/10.2514/3.43834.

[190] Company, T. B., "General Description of Boeing SST 2707," Tech. rep., The Boeing Company, 1969.

[191] Carlson, H. W., Barger, R. L., and Mack, R. J., "Application of Sonic-boom Minimization Concepts in Supersonic Transport Design," Tech. Rep. TN-D-7218, NASA, 1973. URL https://ntrs.nasa.gov/citations/19730015338.

[192] FitzSimmons, R., and Roensch, R., "Advanced supersonic transport," Tech. rep., SAE Technical Paper, 1975. https://doi.org/10.4271/750617.

[193] Wood, R., Niedling, L., Miller, D., Klein, J., and Hahne, D., "Status Review of a Supersonically Biased Fighter Wing Design Study," *Journal of Aircraft*, Vol. 21, No. 10, 1984, pp. 767–775. https://doi.org/10.2514/3.45040.

[194] McLean, F. E., "SCAR program overview," Tech. rep., NASA, 1976. URL https://ntrs.nasa.gov/citations/19770011053.

[195] Carlson, H. W., "Simplified Sonic-Boom Prediction," Tech. Rep. TP-1122, NASA, 1978. URL https://ntrs.nasa.gov/citations/19780012135.

[196] Radkey, R., Welge, H., and Roensch, R., "Aerodynamic Design of a Mach 2.2 Supersonic Cruise Aircraft," *Journal of Aircraft*, Vol. 15, No. 6, 1978, pp. 351–357. https://doi.org/10.2514/3.58369.

[197] Kulfan, R. M., and Sigalla, A., "Real Flow Limitations in Supersonic Airplane Design," *Journal of Aircraft*, Vol. 16, No. 10, 1979, pp. 645–658. https://doi.org/10.2514/3.58585.

[198] Fishbach, L., Stitt, L., Stone, J., and Whitlow Jr., J., "NASA Research in Supersonic Propulsion-a Decade of Progress," *18th Joint Propulsion Conference*, AIAA, 1982, p. 1048. https://doi.org/10.2514/6.1982-1048.

[199] McLean, F. E., *Supersonic cruise technology*, Vol. 472, NASA STI, 1985. URL https://ntrs.nasa.gov/citations/19850020600.

[200] Williams, M. S., Owens Jr, L. R., and Chu, J., "A Reynolds Number Study of Wing Leading-Edge Effects on a Supersonic Transport Model at Mach 0.3," Tech. rep., NASA, 1999. URL https://ntrs.nasa.gov/citations/20000033218.

[201] Allen H. Whitehead, J., "First Annual High-Speed Research Workshop," Tech. Rep. CP-10087, NASA, 1991. URL https://ntrs.nasa.gov/citations/19940028941.

[202] Darden, C. M., "High-Speed Research: Sonic Boom," Tech. Rep. CP-3172, NASA, 1992. URL https://ntrs.nasa.gov/citations/19920024630.

[203] Edwards, T. A., "High-Speed Research: Sonic Boom," Tech. Rep. CP-10132, NASA, 1992. URL https://ntrs.nasa.gov/citations/19940023685.

[204] McCurdy, D. A., "High-Speed Research: 1994 Sonic Boom Workshop. Configuration, Design, Analysis and Testing," Tech. Rep. CP-1999-209699, NASA, 1994. URL https://ntrs.nasa.gov/citations/20000027440.

[205] Baize, D. G., "High-Speed Research: 1994 Sonic Boom Workshop. Configuration, Design, Analysis and Testing," Tech. Rep. CP-3335, NASA, 1995. URL https://ntrs.nasa.gov/citations/19960055049.

[206] Baize, D. G., "NASA High-Speed Research Program Aerodynamic Performance Workshop: Configuration Aerodynamics," Tech. Rep. CP-1999-209691, NASA, 1997. URL https://ntrs.nasa.gov/citations/20000045988.

[207] McMillin, S. N., "NASA High-Speed Research Program Aerodynamic Performance Workshop," Tech. Rep. CP-1999-2096962, NASA, 1998. URL https://ntrs.nasa.gov/citations/20000031532.

[208] Wood, R. M., "First NASA/Industry High-Speed Research Configuration Aerodynamics Workshop," Tech. Rep. CP-1999-209690, NASA, 1999. URL https://ntrs.nasa.gov/citations/20000044865.

[209] Hahne, D. E., "NASA High-Speed Research Program Aerodynamic Performance Workshop: Configuration Aerodynamics," Tech. Rep. CP-1999-209704, NASA, 1999. URL https://ntrs.nasa.gov/citations/20000020876.

[210] Airpalnes, B. C., "High-speed Civil Transport Study," Tech. Rep. CR-4233, NASA, 1989. URL https://ntrs.nasa.gov/citations/19890018277.

[211] Nelson, C., "Effects of Wing Planform on HSCT Off-design Aerodynamics," *10th Applied Aerodynamics Conference*, AIAA, 1992, p. 2629. https://doi.org/10.2514/6.1992-2629.

[212] Antani, D., and Morgenstern, J., "HSCT High-lift Aerodynamic Technology Requirements," *Guidance, Navigation and Control Conference*, AIAA, 1992, p. 4228. https://doi.org/10.2514/6.1992-4228.

[213] Haglund, G. T., and Ogg, S. S., "Two HSCT Mach 1.7 low sonic boom designs," Tech. Rep. CR, NASA, 1992. URL https://ntrs.nasa.gov/citations/19920076746.

[214] Benoliel, A., and Mason, W., "Pitch-up Characteristics for HSCT class Planforms - Survey and Estimation," *12th Applied Aerodynamics Conference*, AIAA, 1994, p. 1819. https://doi.org/10.2514/6.1994-1819.

[215] Mejia, K., "A comprehensive review of high speed wind tunnel performance data from the Boeing High Speed Civil Transport Program," *39th Aerospace Sciences Meeting and Exhibit*, AIAA, 2001, p. 453. https://doi.org/10.2514/6.2001-453.

[216] Owens, L., and Wahls, R., "Reynolds Number Effects on a Supersonic Transport at Subsonic High-lift Conditions," *39th Aerospace Sciences Meeting and Exhibit*, AIAA, 2001, p. 911. https://doi.org/10.2514/6.2001-911.

[217] Kulfan, B., "Reynolds Numbers Considerations for Supersonic Flight," *32nd AIAA Fluid Dynamics Conference and Exhibit*, AIAA, 2002, p. 2839. https://doi.org/10.2514/6.2002-2839.

[218] Mavris, D. N., and Bandte, O., "Economic Uncertainty Assessment Using a Combined Design of Experiments Monte Carlo Simulation Approach with Application to an HSCT," *17th Annual Conference of the International Society of Parametric Analysts*, 1995. URL http://hdl.handle.net/1853/6317.

[219] Schrage, D. P., Craig, J. I., Fulton, R. E., and Mistree, F., "New Approaches to HSCT Multidisciplinary Design and Optimization," Tech. Rep. NGT-51102L, NASA, 1995. URL https://ntrs.nasa.gov/citations/19990061937.

[220] Mavris, D., Bandte, O., and Schrage, D., "Application of Probabilistic Methods for the Determination of an Economically Robust HSCT Configuration," *6th Symposium on Multidisciplinary Analysis and Optimization*, AIAA, 1996, p. 4090. https://doi.org/10.2514/6.1996-4090.

[221] Kaminer, I. I., Howard, R. M., and Buttrill, C. S., "Development of Closed -loop Tail -sizing Criteria for a High Speed Civil Transport," *Journal of Aircraft*, Vol. 34, No. 5, 1997, pp. 658–664. https://doi.org/10.2514/2.2226.

[222] Daberkow, D. D., and Mavris, D. N., "New Approaches to Conceptual and Preliminary Aircraft Design : A Comparative Assessment of a Neural Network Formulation and a Response Surface Methodology," *SAE Technical Paper*, 1998, p. 985509. https://doi.org/10.4271/985509.

[223] Patnaik, S. N., Guptill, J. D., Hopkins, D. A., and Lavelle, T. M., "Neural Network and Regression Approximations in High -speed Civil Aircraft Design Optimization," *Journal of Aircraft*, Vol. 35, No. 6, 1998, pp. 839–850. https://doi.org/10.2514/2.2395.

[224] Koch, P. N., Simpson, T. W., Allen, J. K., and Mistree, F., "Statistical Approximations for Multidisciplinary Design Optimization: The Problem of Size," *Journal of Aircraft*, Vol. 36, No. 1, 1999, pp. 275–286. https://doi.org/10.2514/2.2435.

[225] Zang, T., and Green, L., "Multidisciplinary Design Optimization Techniques - Implications and Opportunities for Fluid Dynamics Research," *30th Fluid Dynamics Conference*, AIAA, 1999, p. 3798. https://doi.org/10.2514/6.1999-3798.

[226] Solies, U., "Low speed handling qualities of the High Speed Civil Transport," *Aircraft Engineering, Technology, and Operations Congress*, AIAA, 1995, p. 3912. https://doi.org/10.2514/6.1995-3912.

[227] Englar, J., "Application of Pneumatic Lift and Control Surface Technology to Advanced Transport Aircraft," Tech. rep., NASA, 1996. URL https://ntrs.nasa.gov/citations/19960023623.

[228] Kandil, O., Adam, I., and Wong, T.-C., "Far-field Turbulent Vortex-wake/exhaust Plume Interaction for Subsonic and HSCT Airplanes," *Fluid Dynamics Conference*, AIAA, 1996, p. 1962. https://doi.org/10.2514/6.1996-1962.

[229] Cox, T. H., and Jackson, D. W., "Evaluation of High -speed Civil Transport Handling Qualities Criteria With Supersonic Flight Data," Tech. Rep. TM-4791, NASA, 1997. URL https://ntrs.nasa.gov/citations/19970014738.

[230] Newman, B., "Investigation of Inner Loop Flight Control Strategies for High -speed Research," Tech. Rep. CR-1999-209522, NASA, 1999. URL https://ntrs.nasa.gov/citations/20000023185.

[231] Newman, B. A., "Multivariable Techniques for High -speed Research Flight Control Systems," Tech. Rep. CR-1999-209528, NASA, 1999. URL https://ntrs.nasa.gov/citations/20000012320.

[232] Owens, L., Wahls, R., Elzey, M., and Hamner, M., "Reynolds Number Effects on the Stability and Control Characteristics of a Supersonic Transport," *40th AIAA Aerospace Sciences Meeting & Exhibit*, AIAA, 2002, p. 417. https://doi.org/10.2514/6.2002-417.

[233] Raney, L., Jackson, E. B., and Buttrill, C. S., "Simulation Study of Impact of Aeroelastic Characteristics on Flying Qualities of a High Speed Civil Transport," Tech. Rep. TP-2002-211943, NASA, 2002. URL https://ntrs.nasa.gov/citations/20020084988.

[234] Owens, L. R., Wahls, R. A., Elzey, M. B., and Hamner, M. P., "Reynolds Number Effects on Off -design Stability and Control Characteristics of Supersonic Transports," *Journal of Aircraft*, Vol. 44, No. 1, 2007, pp. 134–143. https://doi.org/10.2514/1.22519.

[235] Issac, J., Kapania, R., and Barthelemy, J.-F., "Sensitivity Analysis of Flutter Response of a Wing Incorporating Finite-span Corrections," *5th Symposium on Multidisciplinary Analysis and Optimization*, AIAA, 1994, p. 4398. https://doi.org/10.2514/6.1994-4398.

[236] Newman, B., and Buttrill, C., "Conventional Flight Control for an Aeroelastic, Relaxed Static Stability High-Speed Transport," *Guidance, Navigation, and Control Conference*, AIAA, 1995, p. 3250. https://doi.org/10.2514/6.1995-3250.

[237] Joshi, M., and Kelkar, A. G., "On Longitudinal Control of High Speed Aircraft in the Presence of Aeroelastic Modes," Tech. Rep. TM-110254, NASA, 1996. URL https://ntrs.nasa.gov/citations/19960028563.

[238] McMinn, J., "Extension of a Kolmogorov Atmospheric Turbulence Model for Time-Based Simulation Implementation," *Guidance, Navigation, and Control Conference*, 1997, p. 3532. https://doi.org/10.2514/6.1997-3532.

[239] Baker, M., and Lenkey, P., "High Speed Research - Airframe Technology Airframe Materials & Structures 4.2.6 - Aeroelasticity," Tech. Rep. TR-3342, NASA, 1997. URL https://ntrs.nasa.gov/citations/20100033318.

[240] The Boeing Company, "HSR Task 20 – Aeroelastic Concept Engineering (ACE): Inputs to Preliminary Technology Configuration," Tech. Rep. HSR-II Task 20, WBS 2.1.3, Contract NAS1-20220, NASA, 1997. URL https://ntrs.nasa.gov/citations/20205005427.

[241] Bharadvaj, B. K., and Welge, H. R., "High Speed Research Program (HSR II) – Airframe Task 20, Tasks 2.1 – Technology Integration, SubTask 2.1.3 Aeroelastic Concept Engineering (ACE), Preliminary Aeroelastic Concept," Tech. Rep. HSR-II Task 20, WBS 2.1.3, Contract NAS1-20220, NASA, 1997. URL https://ntrs.nasa.gov/api/citations/20205005396/downloads/20205005396%20-%20PRELIMINARY%20AEROELASTIC%20CONCEPT_Redacted.pdf.

[242] The Boeing Company, "HSR Task 20 – Aeroelastic Concept Engineering (ACE): Preliminary Aeroelastic Concept (WBS 2.1.3.2), Boeing ACE Structures/Weights Team Final Report," Tech. Rep. HSR-II Task 20, WBS 2.1.3.2, Contract NAS1-20220, NASA, 1997. URL https://ntrs.nasa.gov/citations/20205005414.

[243] Borland, C., Giesing, J., and Knoernschild, D., "High Speed Research Program (HSR II) – Airframe Task 20 Tasks 2.1 – Technology Integration SubTask 2.1.3 Aeroelastic Concept Engineering (ACE), ACE Final Report," Tech. Rep. HSR-II Task 20, WBS 2.1.3, Contract NAS1-20220, NASA, 1998. Not publicly available.

[244] Nagaraja, K. S., and Kraft, R. H., "Technology Integration (Task 20) Aeroservoelastic Modeling and Design Studies: Evaluation of Aeroservoelastic Effects on Flutter and Dynamic Gust Response-Part A," Tech. Rep. TI4D1502, NASA, 1999. URL https://ntrs.nasa.gov/citations/20100033317.

[245] Edwards, J., Schuster, D., Spain, C., Keller, D., and Moses, R., "MAVRIC Flutter Model Transonic Limit Cycle Oscillation Test," *19th AIAA Applied Aerodynamics Conference*, AIAA, 2001, p. 1291. https://doi.org/10.2514/6.2001-1291.

[246] Gregory, I., "Stability Result for Dynamic Inversion Devised to Control Large Flexible Aircraft," *AIAA Guidance, Navigation, and Control Conference and Exhibit*, AIAA, 2001, p. 4284. https://doi.org/10.2514/6.2001-4284.

[247] Hajj, M. R., and Silva, W. A., "Nonlinear Flutter Aspects of the Flexible HSCT Semispan Model," *44th AIAA/ASME/ASCE/AHS/ASC Structures, Structural Dynamics and Materials Conference*, AIAA, 2003, p. 1515. https://doi.org/10.2514/1.2225.

[248] Walsh, J. L., Dunn, H. J., Stroud, W. J., Barthelemy, J.-F. M., Weston, R. P., Martin, C. J., and Bennett, R. M., "Aeroelastic Sizing for High-Speed Research (HSR) Longitudinal Control Alternatives Project (LCAP)," Tech. Rep. TP-2005-213533, NASA, 2005. URL https://ntrs.nasa.gov/citations/20050229941.

[249] Silva, W., Perry, B., Florance, J., Sanetrik, M., Wieseman, C., Stevens, W., Funk, C., Hur, J., Christhilf, D., and Coulson, D., "An Overview of the Semi -span Super -sonic Transport (S4T) Wind -tunnel Model Program," *53rd AIAA/ASME/ASCE/AHS/ASC Structures, Structural Dynamics and Materials Conference 20th AIAA/ASME/AHS Adaptive Structures Conference 14th AIAA*, AIAA, 2012, p. 1552. https://doi.org/10.2514/6.2012-1552.

[250] Heeg, J., and Wieseman, C. D., "System Identification and Uncertainty Quantification Using Orthogonal Excitations and the Semi-Span Supersonic Transport (S4T) Model," *53rd AIAA/ASME/ASCE/AHS/ASC Structures, Structural Dynamics and Materials Conference*, AIAA, 2012, p. 1404. https://doi.org/10.2514/6.2012-1404.

[251] Kukreja, S. L., "Data-driven model development for the supersonic semispan transport," *AIAA journal*, Vol. 51, No. 6, 2013, pp. 1333–1341. https://doi.org/10.2514/1.J051721.

[252] Glaab, L. J., "Initial Piloted Simulation Evaluation of the Reference-H High-Speed Civil Transport Design During Takeoff and Recovery From Limit Flight Conditions," Tech. Rep. CR-1999-209523, NASA, 1999. URL https://ntrs.nasa.gov/citations/20000011419.

[253] Jackson, E. B., Raney, D. L., Hahne, D. E., Derry, S. D., and Glaab, L. J., "Reference H Piloted Assessment (LaRC. 1) Pilot Briefing Guide," Tech. Rep. TM-1999-20533, NASA, 1999. URL https://ntrs.nasa.gov/citations/20000025434.

[254] Bailey, L., "Pilot Comments for High Speed Research Cycle 3 Simulation Study (Larc.1)," Tech. Rep. CR-2000-210306, NASA, 2000. URL https://ntrs.nasa.gov/citations/20000080528.

[255] Bruce, E., and Raney, L., "Piloted Simulation Assessment of a High - Speed Civil Transport Configuration," Tech. Rep. TI4D1502, NASA, 2002. URL https://ntrs.nasa.gov/citations/20100033317.

[256] Stringer, M. T., Cowen, B., Hoffler, K. D., Ogburn, M. E., and Diebler, C., "Piloted Simulation Assessment of the Impact of Flexible Structures on Handling Qualities of Generic Supersonic Aircraft," *AIAA Atmospheric Flight Mechanics (AFM) Conference*, AIAA, 2013, p. 4606. https://doi.org/10.2514/6.2013-4606.

[257] Ray, J., Carlin, C., and Lambregts, A., "High-speed Civil Transport Flight-and Propulsion-control Technological Issues," Tech. Rep. CR-186015, NASA, 1992. URL https://ntrs.nasa.gov/citations/19920012010.

[258] Shaw, R. J., Gilkey, S., and Hines, R., "Engine Technology Challenges for a 21st Century High-Speed Civil Transport," Tech. Rep. TM-106216, NASA, 2002. URL https://ntrs.nasa.gov/citations/19930070043.

[259] Cole, G. L., Chicatelli, A. K., and Melcher, K. J., "Computational Methods for HSCT - inlet Controls/cfd Interdisciplinary Research," *30th Joint Propulsion Conference and Exhibit*, AIAA, 1994, p. 3209. https://doi.org/10.2514/6.1994-3209.

[260] Shaw, R. J., Koops, L., and Hines, R., "PROGRESS TOWARD MEETING THE PROPULSION TECHNOLOGY CHALLENGES FOR A 21ST CENTURY HIGH -SPEED CIVIL TRANSPORT," Tech. Rep. TM-113161, NASA, 2002. URL https://ntrs.nasa.gov/citations/19970037587.

[261] Plencner, R., Misra, A., Graber, E., Jr., Shaw, R., and Seng, G., "Engine Technology Challenges for the High -speed Civil Transport Plane," *20th AIAA Advanced Measurement and Ground Testing Technology Conference*, AIAA, 1998, p. 2505. https://doi.org/10.2514/6.1998-2505.

[262] Midea, A. C., Austin, T., Pao, S. P., DeBonis, J. R., and Mani, M., "High Speed Civil Transport (HSCT) Isolated Nacelle Transonic Boattail Drag Study and Results Using Computational Fluid Dynamics (CFD)," Tech. Rep. CP, NASA, 1999. URL https://ntrs.nasa.gov/citations/20000044627.

[263] Chaney, S., "HSCT Propulsion Airframe Integration," Tech. Rep. CP, NASA, 1999. URL https://ntrs.nasa.gov/citations/20000044624.

[264] Stern, M., "HSCT nozzle source noise programs at Pratt and Whitney," Tech. Rep. CP, NASA, 1994. URL https://ntrs.nasa.gov/citations/19940028959.

[265] Glaab, J., Riley, R., Brandon, J. M., Person, L. H., and Glaab, C., "Piloted Simulation Study of the Effect of High -lift Aerodynamics on the Takeoff Noise of a Representative High -speed Civil Transport," Tech. Rep. TP-1999-290696, NASA, 1999. URL https://ntrs.nasa.gov/citations/20000024908.

[266] Anderson, D. J., and Mizukami, M., "Bibliography on Propulsion Airframe Integration Technologies for High-speed Civil Transport Applications, 1980-1991," Tech. Rep. TM-105602, NASA, 1993. URL https://ntrs.nasa.gov/citations/19930016947.

[267] Morgenstern, J., Buonanno, M., and Norstrud, N., "N+2 Low Boom Wind Tunnel Model Design and Validation," *30th AIAA Applied Aerodynamics Conference*, AIAA, 2012, p. 3217. https://doi.org/10.2514/6.2012-3217.

[268] Magee, T., Shaw, S., and Fugal, S., "Experimental Validations of a Low Boom Aircraft Design," *51st AIAA Aerospace Sciences Meeting including the New Horizons Forum and Aerospace Exposition*, AIAA, 2013, p. 646. https://doi.org/10.2514/6.2013-646.

[269] Magee, T. E., Wilcox, P. A., Fugal, S. R., Acheson, K. E., Adamson, E. E., Bidwell, A. L., and Shaw, S. G., "System-level Experimental Validations for Supersonic Commercial Transport Aircraft Entering Service in the 2018-2020 Time Period," Tech. Rep. CR–2013-217797, NASA, 2013. URL https://ntrs.nasa.gov/citations/20130011026.

[270] Morgenstern, J., Norstrud, N., Sokhey, J., Martens, S., and Alonso, J. J., "Advanced Concept Studies for Supersonic Commercial Transports Entering Service in the 2018 to 2020 Period: Phase I Final Report," Tech. Rep. CR-2013-217820, NASA, 2013. URL https://ntrs.nasa.gov/citations/20130010174.

[271] Benson, L. R., *Quieting the Boom: The Shaped Sonic Boom Demonstrator and the Quest for Quiet Supersonic Flight*, NASA, 2013. URL https://www.nasa.gov/aeronautics/quieting-the-boom-the-shaped-sonic-boom-demonstrator-and-the-quest-for-quiet-supersonic-flight/.

[272] Buonanno, M., Chai, S., Marconi, F., and Morgenstern, J. M., "Overview of Sonic Boom Reduction Efforts on the Lockheed Martin N+2 Supersonic Validations Program," *32nd AIAA Applied Aerodynamics Conference*, AIAA, 2014, p. 2138. https://doi.org/10.2514/6.2014-2138.

[273] Durston, D. A., Elmiligui, A. A., Cliff, S. E., Winski, C., Carter, M. B., and Walker, E., "Experimental and computational sonic boom assessment of Boeing N+ 2 low boom models," *32nd AIAA Applied Aerodynamics Conference*, AIAA, 2014, p. 2140. https://doi.org/10.2514/6.2014-2140.

[274] Locatelli, D., Mulani, S. B., Liu, Q., Tamijani, A. Y., and Kapania, R. K., "Supersonic Wing Optimization Using SpaRibs," Tech. Rep. CR–2014-218537, NASA, 2014. URL https://ntrs.nasa.gov/citations/20140013263.

[275] Morgenstern, J., Buonanno, M., Yao, J., Murugappan, M., Paliath, U., Cheung, L., Malcevic, I., Ramakrishnan, K., Pastouchenko, N., Wood, T., et al., "Advanced Concept Studies for Supersonic Commercial Transports Entering Service in the 2018-2020 Period Phase 2," Tech. Rep. CR–2015-218719, NASA, 2015. URL https://ntrs.nasa.gov/citations/20150015837.

[276] Pak, C.-g., "Aeroelastic Tailoring Study of an N+2 Low-boom Supersonic Commercial Transport Aircraft," *16th AIAA/ISSMO Multidisciplinary Analysis and Optimization Conference*, AIAA, 2015, p. 2791. https://doi.org/10.2514/6.2015-2791.

[277] Connolly, J. W., Kopasakis, G., Carlson, J.-R., and Woolwine, K., "Nonlinear Dynamic Modeling of a Supersonic Commercial Transport Turbo-Machinery Propulsion System for Aero-Propulso-Servo-Elasticity Research," *51st AIAA/SAE/ASEE Joint Propulsion Conference*, AIAA, 2015, p. 4031. https://doi.org/10.2514/6.2015-4031.

[278] Bridges, J. E., Brown, C. A., Henderson, B. S., and Seidel, J. A., "NASA's Pursuit of Low-Noise Propulsion for Low-Boom Commercial Supersonic Vehicles," *2018 AIAA Aerospace Sciences Meeting*, AIAA, 2018, p. 0265. https://doi.org/10.2514/6.2018-0265.

[279] Carter, M. B., Elmiligui, A. A., Park, M. A., Shea, P. R., Winski, C. S., Durston, D. A., Jensen, J. C., Wagner, J. M., Neuhoff, S. M., and Wolter, J. D., "Experimental and Computational Study of the X-59 Wind Tunnel Model at Glenn Research Center 8- by 6-foot Supersonic Wind Tunnel," Tech. Rep. TM–20220011496, NASA, 2022. URL https://ntrs.nasa.gov/citations/20220011496.

[280] Magee, T. E., Serrano, L., Mendoza, R., Gonzalez, A., Muscalus, D. R., Jones, A. M., Peyton, M., and Shaw, S. G., "X-59 CFD and Wind Tunnel Data Comparisons," *Aviation 2023 Forum*, AIAA, 2023, p. 4320. https://doi.org/10.2514/6.2023-4320.

[281] Durston, D. A., Wolter, J. D., Shea, P., Winski, C. S., Elmiligui, A. A., Carter, M. B., Langston, S., and Bozeman, M. D., "X-59 Sonic Boom Test Results from the NASA Glenn 8- by 6-Foot Supersonic Wind Tunnel," *Aviation 2023 Forum*, AIAA, 2023, p. 4317. https://doi.org/10.2514/6.2023-4317.

[282] Ahmad, N. N., Park, M. A., Nishikawa, H., Wang, L., and Elmiligui, A. A., "Evaluation of Limiter Functions for Supersonic Applications," *Aviation 2023 Forum*, AIAA, 2023, p. 4405. https://doi.org/10.2514/6.2023-4405.

[283] Neuhoff, S., Ashby, C., Housman, J., and Duensing, J., "Enhanced Simulation Techniques in Predicting Sonic Boom Loudness Using CFD," *12th International Conference on Computational Fluid Dynamics (ICCFD12)*, ICCFD, 2024, pp. 1–B–03. URL https://ntrs.nasa.gov/citations/20240008312.

[284] Carpenter, F. L., Hantsche, L. J., Cliatt, L. J., and Haering, E. A., "Supersonic Flight Testing to Assess Ground Recording Systems for NASA's Low Boom Flight Demonstrator," *SciTech 2025 Forum*, AIAA, 2025, p. 0194. https://doi.org/10.2514/6.2025-0194.

[285] Lovell, D., "European Research to Reduce Drag for Supersonic Transport Aircraft," *17th Applied Aerodynamics Conference*, AIAA, 1999, pp. 117–132. https://doi.org/10.2514/6.1999-3100.

[286] McParlin, S. C., "Drag extraction for Supersonic Civil Transports," Tech. Rep. DER-A/MSS/MSFC1/CR011012, Group For Aeronautical Research and Technology in Europe, 2001. URL https://www.researchgate.net/publication/256842603_Drag_prediction_for_civil_supersonic_transport_aircraft_at_low-speed_transonic_and_supersonic_conditions.

[287] Herrmann, U., and Radespiel, R., "Low-Speed Characteristics of Supersonic Transport Aircraft," *European Congress on Computational Methods in Applied Sciences and Engineering*, ECCOMAS, 2011, p. 48. URL https://elib.dlr.de/72034/.

[288] Herrmann, U., "Supersonic Commercial Transport Low Speed Performance," *3rd SST-CFD Workshop*, JAXA, 2001, p. 486. URL https://jaxa.repo.nii.ac.jp/record/5793/files/63609062.pdf.

[289] Herrmann, U., Press, A., Newbold, C., Kaurinkoski, P., Artiles, C., Van Muijden, J., and Carrier, G., "Validation of European CFD Codes for SCT Low-speed High-lift Computation," *19th AIAA Applied Aerodynamics Conference*, AIAA, 2001, p. 2405. https://doi.org/10.2514/6.2001-2405.

[290] Van Muijden, J., and Elsenaar, B., "Numerical Prediction Capabilities and Analysis of Flow Development for a Supersonic Civil Transport at Low Speed," Tech. Rep. NLR-TP-2002-496, NLR, 2002.

[291] Brandi, V., "Low-Speed High-Lift Performance Improvements obtained and validated by the EC-project EPISTLE," *24th International Congress of the Aeronautical Sciences*, ICAS, 2004, p. 269. URL https://www.icas.org/icas_archive/ICAS2004/ABSTRACTS/269.HTM.

[292] Brandi, V., "Navier-Stokes Analysis for SCT Low-Speed High-Lift Flight and Wind Tunnel Configurations," *24th International Congress of the Aeronautical Sciences*, ICAS, 2004, p. 74. URL https://www.icas.org/icas_archive/ICAS2004/ABSTRACTS/074.HTM.

[293] Herrmann, U., "EPISTLE: High Lift System Design for Low-noise Applied to a Supersonic Aircraft," *The Aeronautical Journal*, Vol. 110, No. 1107, 2006, pp. 327–331. https://doi.org/10.1017/S0001924000013191.

[294] Van Muijden, J., "Improvement and Verification of Low-speed Aerodynamic Characteristics of a Supersonic Civil Transport Aircraft," *Proceedings of the Institution of Mechanical Engineers, Part G: Journal of Aerospace Engineering*, Vol. 220, No. 6, 2006, pp. 569–580. https://doi.org/10.1243/09544100JAERO87.

[295] Herrmann, U., "Multiple Discipline Optimization and Aerodynamic Off-Design Analysis of Supersonic Transport Aircraft," *Journal of Aircraft*, Vol. 45, No. 5, 2008, pp. 1474–1480. https://doi.org/10.2514/1.32673.

[296] Gaffuri, M., and Brezillon, J., "Unstructured Mesh Capabilities for Supersonic Wing Design at Low Speed Conditions," *European Congress on Computational Methods in Applied Sciences and Engineering*, ECCMOS, 2011, p. 48. URL https://elib.dlr.de/72034/.

[297] Martin, S., "Publishable Activity Report," Tech. Rep. HISAC-T-6-26-1, Dassault Aviation, 2008. URL https://cordis.europa.eu/project/id/516132/reporting.

[298] European Union, "(LTO) noiSe and EmissioNs of supErsoniC Aicraft (SENECA)," , 2021-2024. URL https://seneca-project.eu/, accessed: April 28th, 2025.

[299] European Union, "(LTO) noiSe and EmissioNs of supErsoniC Aicraft (SENECA)," , 2021-2025. URL https://cordis.europa.eu/project/id/101006856/de, accessed: April 28th, 2025.

[300] Nöding, M., Schuermann, M., Bertsch, L., Koch, M., Plohr, M., Jaron, R., and Berton, J. J., "Simulation of Landing and Take-Off Noise for Supersonic Transport Aircraft at a Conceptual Design Fidelity Level," *Aerospace*, Vol. 9, No. 1, 2921, p. 9. https://doi.org/10.3390/aerospace9010009.

[301] Villena Munoz, C., Bonavolontà, G., Lawson, C., and Riaz, A., "Conceptual Design of a Next Generation Supersonic Airliner for Low Noise and Emissions," *SciTech 2023 Forum*, AIAA, 2023, p. 0215. https://doi.org/10.2514/6.2023-0215.

[302] Muller, M., and Terrenoire, E., "Near-field Mesh Adaptation for Contrail Modeling of a Supersonic Aircraft," *57th 3AF International Conference on Applied Aerodynamics*, International Conference on Applied Aerodynamics, 2023, p. 79. URL https://hal.science/hal-04066172/.

[303] Mourouzidis, C., Del Gatto, D., Adamidis, S., Villena Munoz, C., Lawson, C., Martinez Corzo, B., Leyland, P., Marsh, D., Lim, L., Owen, B., Terrenoire, E., Atinault, O., LeGriffon, I., Huet, M., Schaefer, M., Plohr, M., Bake, S., and Madden, P., "Preliminary Design of Next Generation Mach 1.6 Supersonic Business Jets to Investigate Landing & Take-off (LTO) Noise and Emissions – SENECA ." *Journal of Physics: Conference Series*, Vol. 2526, No. 1, 2023, p. 012011. https://doi.org/10.1088/1742-6596/2526/1/012011.

[304] Bonavolontà, G., Lawson, C., and Riaz, A., "Review of Sonic Boom Prediction and Reduction Methods for Next Generation of Supersonic Aircraft," *Aerospace*, Vol. 10, No. 11, 2023, p. 917. https://doi.org/10.3390/aerospace10110917.

[305] Bonavolontà, G., Manoj, A., Villena Munoz, C., Tajesh Chilukuri, S., Lawson, C., and Riaz, A., "Toward Quieter and More Efficient Supersonic Flight: Multi-Objective Optimization of a Bell-Shaped Lift Distribution Wing SSBJ," *SciTech 2024 Forum*, AIAA, 2024, p. 2114. https://doi.org/10.2514/6.2024-2114.

[306] Villena Munoz, C., Lawson, C., Riaz, A., and Jaron, R., "Conceptual Design of Supersonic Aircraft to Investigate Environmental Impact," *SciTech 2024 Forum*, AIAA, 2024, p. 2115. https://doi.org/10.2514/6.2024-2115.

[307] Graebert, M., Jaron, R., Plohr, M., Zenkner, S., Richter, C., Stohrer, C., and Munoz, C. V., "Landing and Takeoff Noise Prediction of Conceptual Supersonic Aircraft," *34th Congress of the International Council of the Aeronautical Science*, ICAS, 2024, p. 0121. URL https://www.icas.org/icas_archive/icas2024/data/preview/icas2024_0121.htm.

[308] Plohr, M., Zenkner, S., Bake, S., and Zeitz, D., "Thermodynamic Design and Emission Model of a Mach 1.8 Supersonic Airliner Engine," *34th Congress of the International Council of the Aeronautical Science*, ICAS, 2024, p. 0129. URL https://www.icas.org/icas_archive/icas2024/data/preview/icas2024_0129.htm.

[309] Muñoz, C. V., Lawson, C., Riaz, A., and Sharma, A., "Design of the SENECA Mach 1.8 Supersonic Airliner with Multi-Fidelity Aerodynamic Analysis for Noise-Optimized Take-Off Trajectories," *34th Congress of the International Council of the Aeronautical Science*, ICAS,

2024, p. 0758. URL https://www.icas.org/icas_archive/icas2024/data/preview/icas2024_0758.htm.

[310] Jaron, R., and Viola, N., "The Future of Civil Supersonic Transport in Europe The SENECA and MORE&LESS Projects," *34th Congress of the International Council of the Aeronautical Science*, ICAS, 2024, p. 0820. URL https://www.icas.org/icas_archive/icas2024/data/preview/icas2024_0820.htm.

[311] Terrenoire, E., Muller, M., Correra, E. R., Leyland, P., Synylo, K., Krupko, A., Zaporozhets, O., Lee, D., Owen, B., Lim, L., and Skowron, A., "Seneca's Aircraft Emissions Evaluation and Theirs Environmental," *34th Congress of the International Council of the Aeronautical Science*, ICAS, 2024, p. 0975. URL https://www.icas.org/icas_archive/icas2024/data/preview/icas2024_0975.htm.

[312] Synylo, K., Krupko, A., and Zanorozhets, O., "Local Air Quality Studies for Supersonic Aircraft," *2024 New Trends in Aviation Development (NTAD)*, IEEE, 2024, pp. 176–180. https://doi.org/10.1109/NTAD63796.2024.10850156.

[313] Zaporozhets, O., Makarenko, V., Tokarev, V., and Kazhan, K., "Engine Installation Effect Contribution in Noise Performances of the New Supersonic Airplane," *2024 New Trends in Aviation Development (NTAD)*, IEEE, 2024, pp. 230–235. https://doi.org/10.1109/NTAD63796.2024.10850272.

[314] Bertsch, L., Loessle, F., Noeding, M., Schaeffer, B., and Mulani, S. B., "Considerations Toward Uncertainty Quantification of Single Event Noise Predictions for Novel SST Concept Aircraft," *SciTech 2025 Forum*, 2025, p. 1797. https://doi.org/10.2514/6.2025-1797.

[315] Graebert, M., Jaron, R., Villena Munoz, C., Plohr, M., and Moreau, A., "Single- and Two-Stage Fan Designs for a Supersonic Airliner with Focus on Certification Noise Reduction," *SciTech 2025 Forum*, 2025, p. 2680. https://doi.org/10.2514/6.2025-2680.

[316] Adamidis, S., Gatto, D. D., Mourouzidis, C., Brown, S., and Pachidis, V., "Installation Effects of Supersonic Inlets on Next-Generation SST Turbofan Engines," *Engineering Proceedings*, Vol. 90, No. 1, 2025, p. 50. https://doi.org/10.3390/engproc2025090050.

[317] Piccirillo, G., Graziani, S., Fusaro, R., and Viola, N., "LTO Noise and Sonic Boom Predictions in Early Conceptual Design Phases," *33th Congress of the International Council of the Aero-*

nautical Science, ICAS, 2022, p. 0498. URL https://www.icas.org/icas_archive/ICAS2022/data/preview/ICAS2022_0498.htm.

[318] Gori, O., "Simplified Models for the Preliminary Aerodynamic Characterization of High-speed Vehicles to Support Mission Analysis," *33th Congress of the International Council of the Aeronautical Science*, ICAS, 2022, p. 0551. URL https://www.icas.org/icas_archive/ICAS2022/data/preview/ICAS2022_0551.htm.

[319] Viola, N., Fusaro, R., Ferretto, D., Gori, O., Marini, M., Roncioni, P., Cakir, B. O., Ispir, A. C., and Saracoglu, B. H., "Hypersonic aircraft and mission concept re-design to move from Mach 8 to Mach 5 operations," *33th Congress of the International Council of the Aeronautical Science*, ICAS, 2022, p. 0572. URL https://www.icas.org/icas_archive/ICAS2022/data/preview/ICAS2022_0572.htm.

[320] Saccone, G., and Marini, M., "High Pressure Hydrogen Oxygen Combustion Kinetic Assessment for Air-breathing Propulsion Supersonic Green Aviation," *33th Congress of the International Council of the Aeronautical Science*, ICAS, 2022, p. 0845. URL https://www.icas.org/icas_archive/ICAS2022/data/preview/ICAS2022_0845.htm.

[321] Rötger, T., Eyers, C., and Fusaro, R., "A Review of the Current Regulatory Framework for Supersonic Civil Aircraft: Noise and Emissions Regulations," *Aerospace*, Vol. 11, No. 1, 2023, p. 19. https://doi.org/10.3390/aerospace11010019.

[322] Roncioni, P., Marini, M., Gori, O., Fusaro, R., and Viola, N., "Aerodatabase Development and Integration and Mission Analysis of a Mach 2 Supersonic Civil Aircraft," *Aerospace*, Vol. 11, No. 2, 2024, p. 111. https://doi.org/10.3390/aerospace11020111.

[323] Yoshida, K., and Hayama, K., "Experimental and Numerical Study of Aerodynamic Characteristics for Second Generation SST," *SAE Transactions*, 1991, pp. 2224–2236. https://doi.org/10.4271/912056.

[324] Yoshida, K., Yoshikazu, M., and Shimbo, Y., "An Experimental Study on Unmanned Scaled Supersonic Experimental Airplane," *32nd AIAA Fluid Dynamics Conference and Exhibit*, 10.2514/6.2002-2842, 2002, p. 2842. https://doi.org/10.2514/6.2002-2842.

[325] Kwak, D.-Y., Miyata, K., Noguchi, M., Rinoie, K., and Fujita, T., "Aerodynamic Characteristics of Rolled SST Configuraton with LE and TE Flaps at High Angles of Attack," *21st AIAA Applied Aerodynamics Conference*, AIAA, 2003, p. 3413. https://doi.org/10.2514/6.2003-3413.

[326] Kwak, D.-Y., Shirotake, M., and Rinoie, K., "Vortex Behaviors over a Cranked Arrow Wing Configuration at High Angles of Attack," *24th Congress of the International Council of the Aeronautical Sciences*, ICAS, 2004, p. 387. URL https://www.icas.org/icas_archive/ICAS2004/ABSTRACTS/387.HTM.

[327] Rinoie, K., Miyata, K., Kwak, D. Y., and Noguchi, M., "Studies on Vortex Flaps with Rounded Leading Edges for Supersonic Transport Configuration," *Journal of Aircraft*, Vol. 41, No. 4, 2004, pp. 829–838. https://doi.org/10.2514/1.264.

[328] Horinouchi, S., "Conceptual Design of a Low Boom SSBJ," *43rd AIAA Aerospace Sciences Meeting and Exhibit*, AIAA, 2005, p. 1018. https://doi.org/10.2514/6.2005-1018.

[329] Lei, Z., and Kwak, D.-Y., "Numerical Investigation of Leading Edge Flap on Cranked Arrow Wing," *23rd AIAA Applied Aerodynamics Conference*, AIAA, 2005, p. 5087. https://doi.org/10.2514/6.2005-5087.

[330] Ohnuki, T., Hirako, K., and Sakata, K., "National Experimental Supersonic Transport Project," *25th Congress of the International Council of the Aeronautical Sciences*, ICAS, 2006, p. 760. URL https://www.icas.org/icas_archive/ICAS2006/ABSTRACTS/760.HTM.

[331] Higuchi, K., Rinoie, K., Lei, Z., and Kwak, D., "A Low Fidelity Method for Flap Aerodynamic Design of a Cranked-Arrow Wing," *25th AIAA Applied Aerodynamics Conference*, AIAA, 2007, p. 4178. https://doi.org/10.2514/6.2007-4178.

[332] Lei, Z., "Flow Simulation of an Supersonic Transport Configuration at Low-Speed and High-Lift Conditions," *Journal of aircraft*, Vol. 45, No. 5, 2008, pp. 1514–1521. https://doi.org/10.2514/1.33856.

[333] Hirai, K., Kwak, D.-Y., and Rinoie, K., "Vortex Behaviors of Cranked Arrow Wing Configurations with Different Wing Planforms," *26th Congress of the International Council of the Aeronautical Sciences*, ICAS, 2008, p. 387. URL https://www.icas.org/icas_archive/ICAS2008/ABSTRACTS/387.HTM.

[334] Kwak, D., Hirai, K., Rinoie, K., and Kato, H., "Rolling Moment Characteristics at High Alpha on Several Planforms of Cranked Arrow Wing Configuration," *27th AIAA Applied Aerodynamics Conference*, AIAA, 2009, p. 3937. https://doi.org/10.2514/6.2009-3937.

[335] Lei, Z., and Kwak, D.-Y., "Numerical Optimization of Leading-Edge Deflection Angles for an SST Configuration at Low Speed," *27th International Congress of the Aeronautical Sciences*, AIAA, 2011, p. 238. https://doi.org/10.2514/6.2013-238.

[336] Lei, Z., Kwak, D., Higuchi, K., and Rinoie, K., "Experimental Investigation of a Segmented Flap System of a Cranked-Arrow Wing," *Transactions of the Japan Society for Aeronautical and Space Sciences*, Vol. 55, No. 5, 2012, pp. 304–312. https://doi.org/10.2322/tjsass.55.304.

[337] Zhao, W., Kwak, D., and Rinoie, K., "Studies on Improvement of Nonlinear Pitching Moment Characteristics of Cranked-Arrow Wing," *28th Congress of the International Council of the Aeronautical Sciences*, ICAS, 2012, p. 262. URL https://www.icas.org/icas_archive/ICAS2012/ABSTRACTS/262.HTM.

[338] Lei, Z., Kwak, D.-y., and Rinoie, K., "Experimental Optimization of Leading-Edge Deflection Angles for an SST Configuration at Low Speed," *51st AIAA Aerospace Sciences Meeting including the New Horizons Forum and Aerospace Exposition*, AIAA, 2013, p. 238. https://doi.org/10.2514/6.2013-238.

[339] Toyoda, K., Kwak, D., Noguchi, M., and Rinoie, K., "Aerodynamic Interference Caused by the Inboard Leading-Edge Flap on the Outboard Area of the Cranked Arrow Wing," *Procedia Engineering*, Vol. 99, 2015, pp. 1642–1646. https://doi.org/10.1016/j.proeng.2015.06.050.

[340] Kwak, D., Gaffuri, M., Ohira, K., and Brezillon, J., "Numerical Study of the Reynolds Number Effect on Low Aspect Ratio Wings at Low Speed," *28th International Congress of the Aeronautical Sciences*, ICAS, 2012, p. 023. URL https://www.icas.org/icas_archive/ICAS2012/ABSTRACTS/023.HTM.

[341] Kwak, D.-Y., Ohira, K., Gaffuri, M., and Brezillon, J., "CFD Validation for the Supersonic Transport Configuration at Low-Speed and High Alpha Flight Condition," *31st AIAA Applied Aerodynamics Conference*, AIAA, 2013, p. 3030. https://doi.org/10.2514/6.2013-3030.

[342] Ohira, K., and Kwak, D.-Y., "Investigation of Turbulence Models for the Supersonic Transport Configuration at Low-Speed and High Alpha Flight Condition," *32nd AIAA Applied Aerodynamics Conference*, AIAA, 2014, p. 3098. https://doi.org/10.2514/6.2014-3098.

[343] Japanese Exploration Agency, "D-SEND Database," , 2010-2013. URL https://d-send.jaxa.jp/d_send_e/index.html, accessed: April 28th, 2025.

[344] Honda, M., and Yoshida, K., "D-SEND Project for Low Sonic Boom Design Technology," *28th Congress of the International Council of the Aeronautical Sciences*, ICAS, 2012, p. 941. URL https://www.icas.org/icas_archive/ICAS2012/ABSTRACTS/941.HTM.

[345] Ninomiya, T., Suzuki, H., and Kawaguchi, J., "Dynamic Inversion Controller Design for Balloon-Launched Supersonic Aircraft," *Transactions of the Japan Society for Aeronautical and Space Sciences*, Vol. 61, No. 6, 2018, pp. 248–257. https://doi.org/10.2322/tjsass.61.248.

[346] Karino, H., Yairi, T., Ninomiya, T., and Hori, K., "Estimating Aerodynamic Coefficients from Uncertain Data of D-SEND Aircraft with Gaussian Process Regression," *Transactions of the Japan Society for Aeronautical and Space Sciences*, Vol. 63, No. 6, 2020, pp. 257–264. https://doi.org/10.2322/tjsass.63.257.

[347] Kwak, D., and Ohira, K., "Preliminary Study of the Aerodynamic Characteristic of Kruger Flap on the SST Configuration," *31th International Congress of the Aeronautical Sciences*, ICAS, 2018, p. 0098. URL https://www.icas.org/icas_archive/ICAS2018/data/papers/ICAS2018_0098_paper.pdf.

[348] Setoguchi, N., and Kanazaki, M., "Low-Speed and High Angle of Attack Aerodynamic Characteristics of Supersonic Business Jet with Forward Swept Wing," *Scitech 2020 Forum*, AIAA, 2020, p. 0534. https://doi.org/10.2514/6.2020-0534.

[349] Duong Nguyen, T., Kashitani, M., Kusunose, K., Taguchi, M., and Takita, Y., "Analysis of a Wing–Fuselage Biplane with Trailing-Edge Flaps in Low-Speed Flow," *Journal of Aircraft*, Vol. 59, No. 2, 2022, pp. 350–363. https://doi.org/10.2514/1.C036154.

[350] Akatsuka, J., Koganezawa, S., Kondoh, S., Ishikawa, H., Makino, Y., and Nagai, S., "Near-Field Pressure Signature Measurements of NASA X-59 in JAXA 1 m × 1 m Supersonic Wind Tunnel," *Aviation 2023 Forum*, AIAA, 2023, p. 4318. https://doi.org/10.2514/6.2023-4318, URL https://arc.aiaa.org/doi/10.2514/6.2023-4318.

[351] Koganezawa, S., Ishikawa, H., Kondoh, S., Akatsuka, J., and Makino, Y., "Near-Field Pressure Signature Prediction of NASA X-59 using JAXA's Unstructured Grid Solver FaSTAR," *Aviation 2023 Forum*, AIAA, 2023, p. 4319. https://doi.org/10.2514/6.2023-4319.

[352] Akatsuka, J., Ueno, A., and Makino, Y., "System Noise Assessment and Prediction Methodology Uncertainty Analysis for JAXA's Supersonic Conceptual Aircraft With Variable Noise Re-

duction System," *SciTech 2025 Forum*, AIAA, 2025, p. 1796. https://doi.org/10.2514/6.2025-1796.

[353] Kawazoe, H., Abe, S., Matsuno, T., Yamada, G., and Obayashi, S., "Low-speed Aerodynamic Characteristics of a Busemann-type Silent Supersonic Biplane," *27th Congress of the International Council of the Aeronautical Sciences*, ICAS, 2010, p. 612. URL https://www.icas.org/icas_archive/ICAS2010/ABSTRACTS/612.HTM.

[354] Lan, C. E., "VORSTAB: a Computer Program for Calculating Lateral-directional Stability Derivatives with Vortex Flow Effect," Tech. Rep. CR-172501, NASA, 1985. URL https://ntrs.nasa.gov/citations/19870008896.

[355] Snyder, L. D., and Erickson, L. L., "PAN AIR prediction of NASA Ames 12-foot pressure wind-tunnel interference on a fighter configuration," *22nd Aerospace Sciences Meeting*, AIAA, 1984, p. 219. https://doi.org/10.2514/6.1984-219.

[356] Johnson, F., Samant, S., Bieterman, M., Melvin, R., Young, D., Bussoletti, J., and Hilmes, C., "TranAir: A full-potential, solution-adaptive, rectangular grid code for predicting subsonic, transonic, and supersonic flows about arbitrary configurations. User's manual," Tech. Rep. CR-4349, NASA, 1992. URL https://ntrs.nasa.gov/citations/19950021809.

[357] Gloudemans, J., Davis, P., and Gelhausen, P., "A Rapid Geometry Modeler for Conceptual Aircraft," *34th aerospace sciences meeting and exhibit*, AIAA, 1996, p. 52. https://doi.org/10.2514/6.1996-52.

[358] Johnson, F., Tinoco, E., and Yu, J., "Thirty Years of Development and Application of CFD at Boeing Commercial Airplanes, Seattle," *16th AIAA Computational Fluid Dynamics Conference*, AIAA, 2003, p. 3439. https://doi.org/10.2514/6.2003-3439.

[359] Hahn, A., "Vehicle Sketch Pad: a Parametric Geometry Modeler for Conceptual Aircraft Design," *48th AIAA Aerospace Sciences Meeting Including the New Horizons Forum and Aerospace Exposition*, AIAA, 2010, p. 657. https://doi.org/10.2514/6.2010-657.

[360] Palacios, F., Alonso, J., Duraisamy, K., Colonno, M., Hicken, J., Aranake, A., Campos, A., Copeland, S., Economon, T., Lonkar, A., Lukaczyk, T., and Taylor, T., "Stanford University Unstructured (SUˆ2): An open-source integrated computational environment for multi-physics simulation and design," *51st AIAA Aerospace Sciences Meeting including the New Horizons Forum and Aerospace Exposition*, AIAA, 2013, p. 287. https://doi.org/10.2514/6.2013-287.

[361] McDonald, R. A., and Gloudemans, J. R., "Open Vehicle Sketch Pad: An Open Source Parametric Geometry and Analysis Tool for Conceptual Aircraft Design," *SciTech 2022 Forum*, AIAA, 2022, p. 4. https://doi.org/10.2514/6.2022-0004.

[362] Mani, M., and Dorgan, A. J., "A Perspective on the State of Aerospace Computational Fluid Dynamics Technology," *Annual Review of Fluid Mechanics*, Vol. 55, No. 1, 2023, pp. 431–457. https://doi.org/10.1146/annurev-fluid-120720-124800.

[363] "OpenFOAM," , 2004-present. URL https://www.openfoam.com/, accessed: December 1str, 2023.

[364] "STAR-CCM+," , 2004-present. URL https://www.plm.automation.siemens.com/global/en/products/simcenter/STAR-CCM.html, accessed: December 1str, 2023.

[365] Rumsey, C. L., and Ying, S. X., "Prediction of High Lift: Review of Present CFD Capability," *Progress in Aerospace sciences*, Vol. 38, No. 2, 2002, pp. 145–180. https://doi.org/10.1016/S0376-0421(02)00003-9.

[366] Fujii, K., "Progress and Future Prospects of CFD in Aerospace—wind Tunnel and Beyond," *Progress in Aerospace Sciences*, Vol. 41, No. 6, 2005, pp. 455–470. https://doi.org/10.1016/j.paerosci.2005.09.001.

[367] Slotnick, J. P., Khodadoust, A., Alonso, J., Darmofal, D., Gropp, W., Lurie, E., and Mavriplis, D. J., "CFD Vision 2030 Study: a Path to Revolutionary Computational Aerosciences," Tech. Rep. CR–2014-218178, NASA, 2014. URL https://ntrs.nasa.gov/citations/20140003093.

[368] Malik, M. R., "CFD Vision 2030 CFD Study: A Pathway to Revolutionary Computational Aeroscienes," , 2015.

[369] Joshi, H., and Thomas, P., "Review of Vortex Lattice Method for Supersonic Aircraft Design," *The Aeronautical Journal*, Vol. 127, No. 1317, 2023, pp. 1869–1903. https://doi.org/10.1017/aer.2023.25.

[370] Leishman, J. G., *Introduction to Aerospace Flight Vehicles*, Embry-Riddle Aeronautical University, 2023.

[371] Ting, K.-Y., Mavriplis, N., Soltani, R. M., Nelson, C. P., and Livne, E., "Supersonic Configurations at Low Speeds (SCALOS) Longitudinal Aerodynamics: Configuration Vari-

ations and Control Surfaces Effects," *SciTech 2023 Forum*, AIAA, 2023, p. 0230. https://doi.org/10.2514/6.2023-0230.

[372] Nelson, C. P., and Wiersema, K., "The NASA SCALOS Project – Final Report – Appendix F: RSAC – A Reference Supersonic Airliner Concept," Tech. rep., University of Washington, 2024. Submitted to NASA (not yet available online).

[373] Ting, K.-Y., Wiersema, K., Soltani, R. M., Nelson, C. P., and Livne, E., "The NASA SCALOS Project – Final Report – Appendix G: Data User Guide," Tech. rep., University of Washington, 2024. Submitted to NASA (not yet available online).

[374] Ting, K.-Y., Wiersema, K., Soltani, R. M., Nelson, C. P., and Livne, E., "The NASA SCALOS Project – Final Report - Appendix H: Test Data Reduction," Tech. rep., University of Washington, 2024. Submitted to NASA (not yet available online).

[375] Ting, K.-Y., Wiersema, K., Soltani, R. M., Nelson, C. P., and Livne, E., "The NASA SCALOS Project – Final Report – Appendix I: Model and Part Geometry and Dimensions," Tech. rep., University of Washington, 2024. Submitted to NASA (not yet available online).

[376] Ting, K.-Y., Wiersema, K., Soltani, R. M., Nelson, C. P., and Livne, E., "The NASA SCALOS Project – Final Report – Appendix J: Wind Tunnel Parts," Tech. rep., University of Washington, 2024. Submitted to NASA (not yet available online).

[377] Ting, K.-Y., Nelson, C. P., Wiersema, K., and Livne, E., "Supersonic Configurations at Low Speeds (SCALOS): Wind Tunnel Tests at the University of Washington - an Overview and Some Key Insights," *AIAA SciTech 2025 Forum*, 2025, p. 2359. https://doi.org/10.2514/6.2025-2359.

[378] Livne, E., Nelson, C. P., Soltani, R. M., Ting, K.-Y., Mavriplis, N., Wiersema, K., Cesnik, C. E., Kolmanovsky, I., Martins, J. R., Guimaraes, T. A., et al., "Compilation of Supersonic Configurations at Low Speeds (SCALOS) Final Report and Appendices A–F," Tech. Rep. 20250006613, CG-80NSSC19K1661, NASA, 2025. URL https://ntrs.nasa.gov/citations/20250006613.

[379] Livne, E., and Nelson, C., "From Blank Slate to Flight Ready New Small Research UAVs in Twenty Weeks-Undergraduate Airplane Design at the University of Washington," *50th AIAA Aerospace Sciences Meeting including the New Horizons Forum and Aerospace Exposition*, AIAA, 2012, p. 845. https://doi.org/10.2514/6.2012-845.

[380] Langston, S., Nelson, C. P., and Livne, E., "Low-Speed Stability and Control of a Reduced Scale Long-Range Supersonic Configuration with Reduced-Size or No Vertical Tail," *AIAA Atmospheric Flight Mechanics Conference*, AIAA, 2016, p. 1036. https://doi.org/10.2514/6.2016-1036.

[381] Mavriplis, N., "RANS-CFD Based Assessment of Corrections Applied to the Measured Characteristics of Supersonic Configurations in a Low Speed Wind Tunnel," Master's thesis, University of Washington, 2022. URL http://hdl.handle.net/1773/49591.

[382] Wiersema, K., Ting, K.-Y., Nelson, C., and Livne, E., "Supersonic Configurations at Low Speeds(SCALOS): Correlation of CFD / Wind Tunnel Test Results," *AIAA SciTech 2025 Forum*, 2025, p. 2362. https://doi.org/10.2514/6.2025-2362.

[383] Wiersema, K. C., Ting, K.-Y., Livne, E., Nelson, C. P., and Soltani, R., "Wind Tunnel Low-Speed Tare and Interference Corrections: CFD vs Test Results-The Supersonic Configurations (SCALOS) Cases," *AIAA SCITECH 2026 Forum*, 2026, p. 2640. https://doi.org/10.2514/6.2026-2640.

[384] Magee, T. E., Hayes, P. J., Dorgan, A. J., and Khodadoust, A., "Dynamic Stability Characteristics for Commercial Supersonic Configurations at Low-Speed Flight Conditions–Part II," *SciTech 2024 Forum*, AIAA, 2024, p. 0900. https://doi.org/10.2514/6.2024-0900.

[385] Magee, T. E., Hayes, P. J., and Khodadoust, A., "The NASA SCALOS Project – Final Report – Appendix C: BR&T Final Report," Tech. rep., Boeing Research & Technology, 2024. Submitted to NASA (not yet available online).

[386] Magee, T. E., Hayes, P. J., and Khodadoust, A., "Dynamic Stability Characteristics for Commercial Supersonic Configurations at Low-Speed Flight Conditions – Part III," *AIAA SciTech 2025 Forum*, 2025, p. 2363. https://doi.org/10.2514/6.2025-2363.

[387] Guimarães, T. A., Cesnik, C. E., and Kolmanovsky, I., "Low Speed Aerodynamic Modeling for Control-related Considerations in Supersonic Aircraft Design," *Aviation 2021 Forum*, AIAA, 2021, p. 2351. https://doi.org/10.2514/6.2021-2531.

[388] Seraj, S., and Martins, J. R., "Predicting the High Angle of Attack Characteristics of a Delta Wing at Low Speed," *Aviation 2021 Forum*, AIAA, 2021, p. 2612. https://doi.org/10.2514/6.2021-2612.

[389] Bertolin, R., Chaves Barbosa, G., Cunis, T., Kolmanovsky, I. V., and Cesnik, C. E., "Gust Rejection of a Supersonic Aircraft During Final Approach," *SciTech 2022 Forum*, AIAA, 2022, p. 2174. https://doi.org/10.2514/6.2022-2174.

[390] Cunis, T., Kolmanovsky, I. V., and Cesnik, C. E., "Control Co-Design Optimization: Integrating nonlinear controllability into a multidisciplinary design process," *SciTech 2022 Forum*, AIAA, 2022, p. 2176. https://doi.org/10.2514/6.2022-2176.

[391] Seraj, S., and Martins, J. R., "Aerodynamic Shape Optimization of a Supersonic Transport Considering Low-Speed Stability," *SciTech 2022 Forum*, AIAA, 2022, p. 2177. https://doi.org/10.2514/6.2022-2177.

[392] Seraj, S., and Martins, J. R. R. A., "Predicting the High-Angle-of-Attack Characteristics of a Delta Wing at Low Speed," *Journal of Aircraft*, Vol. 59, No. 4, 2022, pp. 1071–1081. https://doi.org/10.2514/1.C036618.

[393] Seraj, S., Yildirim, A., Anibal, J. L., and Martins, J., "Improving the Performance of a Compressible RANS Solver for Low and High Mach Number Flows," *11th International Conference on Computational Fluid Dynamics (ICCFD11)*, 2022, p. 1702. URL https://www.iccfd.org/iccfd11/assets/pdf/papers/ICCFD11_Paper-1702.pdf.

[394] Guimarães, T. A., Cesnik, C. E., and Kolmanovsky, I., "Unsteady Vortex Lattice Linearization and Sensitivity Analyses for Control Models in Supersonic Aircraft Design," *SciTech 2023 Forum*, AIAA, 2023, p. 0416. https://doi.org/10.2514/6.2023-0416.

[395] Guimarães, T. A., Cesnik, C. E., and Kolmanovsky, I., "Flexibility Assessment of the Aeroelastic-flight-dynamic Behavior for Supersonic Aircraft," *SciTech 2023 Forum*, AIAA, 2023, p. 0417. https://doi.org/10.2514/6.2023-0417.

[396] Seraj, S., and Martins, J. R., "Minimum Trim Drag for a Three-Surface Supersonic Transport Aircraft," *SciTech 2023 Forum*, AIAA, 2023, p. 3472. https://doi.org/10.2514/6.2023-3472.

[397] Seraj, S., Yildirim, A., Anibal, J. L., and Martins, J. R., "Dissipation and Time Step Scaling Strategies for Low and High Mach Number Flows," *Journal of Computational Physics*, Vol. 491, 2023, p. 112358. https://doi.org/10.1016/j.jcp.2023.112358.

[398] Hajdik, H. M., Yildirim, A., Wu, E., Brelje, B. J., Seraj, S., Mangano, M., Anibal, J. L., Jonsson, E., Adler, E. J., Mader, C. A., et al., "Pygeo: a Geometry Package for Multidisciplinary Design Optimization," *Journal of Open Source Software*, Vol. 8, No. 87, 2023, p. 5319.

[399] Guimarães, T. A., and Cesnik, C. E., "The Impact of Vortex Breakdown on the Longitudinal Flight Behavior of the SCALOS Aircraft," *SciTech 2024 Forum*, AIAA, 2024, p. 0902. https://doi.org/https://doi.org/10.2514/6.2024-0902.

[400] Monteiro, B. B., Kolmanovsky, I., and Cesnik, C. E., "Controller Agnostic Design Metricsfor Stochastic Disturbance Rejection," *SciTech 2024 Forum*, AIAA, 2024, p. 0901. https://doi.org/https://doi.org/10.2514/6.2024-0901.

[401] Seraj, S., "Aerodynamic Design Optimization of a Supersonic Transport Aircraft Considering Low-Speed Stability," Ph.D. thesis, University of Michigan, 2024. https://doi.org/10.7302/22987.

[402] Bahia Monteiro, B., "Control Related Metrics for Multidisciplinary Design Optimization," Ph.D. thesis, University of Michigan, 2024. https://doi.org/10.7302/23748.

[403] Bahia Monteiro, B., Seraj, S., Cunis, T., Bertolin, R., Guimarães, T. A., Martins, J. R. R. A., Kolmanovsky, I. V., and Cesnik, C. E., "The NASA SCALOS Project – Final Report – Appendix A: Modeling of Low-Speed Flight Characteristics for Integrated Configuration Shaping of Commercial Supersonic Aircraft," Tech. rep., University of Michigan, 2024. Submitted to NASA (not yet available online).

[404] Shanbhag, T. K., Zhou, B. Y., Molina, E., and Alonso, J., "A Comparison of Jet Acoustic Analysis Methods," *Aviation 2021 Forum*, AIAA, 2021, p. 2102. https://doi.org/10.2514/6.2021-2102.

[405] Shen, Y., Shanbhag, T. K., Kroo, I., and Alonso, J. J., "The NASA SCALOS Project – Final Report – Appendix C: Stanford University Final Report," Tech. rep., Standford University, 2024. Submitted to NASA (not yet available online).

[406] Shen, Y., and Alonso, J. J., "Performance Evaluation of a Graph Neural Network-Augmented Multi-Fidelity Workflow for Predicting Aerodynamic Coefficients on Delta Wings at Low Speed," *AIAA SciTech 2025 Forum*, 2025, p. 2360. https://doi.org/10.2514/6.2025-2360.

[407] Shen, Y., Needels, J. T., and Alonso, J. J., "VortexNet: A Graph Neural Network-Based Multi-Fidelity Surrogate Model for Field Predictions," *AIAA SciTech 2025 Forum*, 2025, p. 0494. https://doi.org/10.2514/6.2025-0494.

[408] Shen, Y., and Alonso, J. J., "A Multi-Fidelity Double-Delta Wing Dataset and Empirical Scaling Laws for GNN-based Aerodynamic Field Surrogates," *AIAA SCITECH 2026 Forum*, 2026, p. 0686. https://doi.org/10.2514/6.2026-0686.

[409] Baize, D., "1997 NASA High-Speed Research Program Aerodynamic Performance Workshop," Tech. Rep. CP-1999-209691, NASA, 1997. URL https://ntrs.nasa.gov/citations/20000045988.

[410] Hahne, D., "1999 NASA High-Speed Research Program Aerodynamic Performance Workshop," Tech. Rep. CP-1999-209704, NASA, 1999. URL https://ntrs.nasa.gov/citations/20000014369.

[411] "Civil Supersonic Aircraft Technical Workshop 2003: Boeing Airframe Focus," , 2003. URL https://www.faa.gov/about/office_org/headquarters_offices/apl/noise_emissions/supersonic_aircraft_noise, accessed: 2021-12-06.

[412] "Supersonic Aerospace International," , 1959-present. URL http://www.sai-qsstx.com/, accessed: 2021-12-06.

[413] Howe, D., Simmons III, F., and Freund, D., "Development of the Gulfstream Quiet Spike TM for Sonic Boom Minimization," *46th AIAA Aerospace Sciences Meeting and Exhibit*, 2008, p. 124. https://doi.org/10.2514/6.2008-124.

[414] Sun, Y., and Smith, H., "Review and Prospect of Supersonic Business Jet Design," *Progress in Aerospace Sciences*, Vol. 90, 2017, pp. 12–38. https://doi.org/10.1016/j.paerosci.2016.12.003.

[415] NASA, "Critical Propulsion Components," Tech. Rep. CR-2005-213584, NASA, 2005.

[416] Welge, H., Bonet, J., Magree, T., Chen, D., Hollowell, S., Kutzmann, A., Mortlock, A., Stengle, J., Nelson., C., Adamson, E., Baughcum, S., Britt, R., Miller, G., and Tai, J., "N+2 Supersonic Concept Development and Systems Integration," Tech. Rep. CR-2010-216842, NASA, 2010.

[417] Durston, D. A., Elmiligui, A. A., Cliff, S. E., Winski, C., Carter, M. B., and Walker, E., "Experimental and computational sonic boom assessment of Boeing N+ 2 low boom models," *32nd AIAA Applied Aerodynamics Conference*, 2014, p. 2140.

[418] Furukawa, T., and Makino, Y., "Conceptual Design and Aerodynamic Optimization of Silent Supersonic Aircraft at JAXA," *25th AIAA Applied Aerodynamics Conference*, 2007, p. 4166. https://doi.org/10.2514/6.2007-4166.

[419] Honda, M., and Yoshida, K., "D-SEND project for low sonic boom design technology," *28th International Congress of the Aeronautical Sciences*, 2012, pp. 2012–1.

[420] Honda, M., and Yoshida, K., "D-SEND project for low sonic boom design technology," *29th International Congress of the Aeronautical Sciences*, 2014, p. 6.

[421] "Concept for the Next-generation Supersonic Civil Transport," JAXA, 2013. URL https://www.aero.jaxa.jp/eng/research/frontier/sst/concept/, accessed: December 1str, 2023.

[422] "Aerion Supersonic Business Jet: AS1," Aerion Corporation, 2004-2021. URL https://web.archive.org/web/20140103223046/http://aerioncorp.com/jet#specs, accessed: December 1str, 2023.

[423] "Aerion Supersonic Business Jet: AS2," Aerion Corporation, 2004-2021. URL https://web.archive.org/web/20171217014146/https://www.aerionsupersonic.com/, accessed: 2021-05-30.

[424] "Supersonic airliner could fly LA to Tokyo in under three hours," CNN, 2021-05-30. URL https://edition.cnn.com/travel/article/aerion-as3-supersonic-jet/index.html, accessed: 2021-05-30.

[425] Wolz, R., "A summary of recent supersonic vehicle studies at Gulfstream Aerospace," *AIAA Paper 2003-558*, 2003. https://doi.org/10.2514/6.2003-558, 41st Aerospace Sciences Meeting and Exhibit.

[426] Freund, D., Simmons, F., Spivey, N., and Schuster, L., "Quiet Spike Prototype Flight Test Results," *AIAA Paper 2007-1778*, 2007. https://doi.org/10.2514/6.2007-1778, 48th AIAA/ASME/ASCE/AHS/ASC Structures, Structural Dynamics, and Materials Conference.

[427] Maglieri, D. J., "Compilation and Review of Supersonic Business Jet Studies from 1963 through 1995," Tech. Rep. CR–2011-217144, NASA, 2011.

[428] "S-512 Specifications & Performance," Spike Aerospace, 2013-present. URL https://www.spikeaerospace.com/s-512-supersonic-jet/specifications-performance/, accessed: December 1str, 2023.

[429] "Supersonic Passenger Flight by 2029 — SVP of Overture Development," Boom Supersonic, 2014-present. URL https://boomsupersonic.com/overture, accessed: 2021-05-30.

[430] "Exclusive look at designs for US supersonic presidential jet," CNN, 2021-04-21. URL https://www.cnn.com/travel/article/supersonic-air-force-one-exosonic-cabin-interior/index.html, accessed: 2021-05-30.

[431] "HyperMach unveils SonicStar supersonic business jet concept," New Atlas, 2011-06-21. URL https://newatlas.com/hypermach-sonicstar-ssbj-concept/18974/, accessed: 2021-05-30.

[432] "Tupolev Tu-444," Wikipedia, 2016-03-22. URL https://ipfs.io/ipfs/QmXoypizjW3WknFiJnKLwHCnL72vedxjQkDDP1mXWo6uco/wiki/Tupolev_Tu-444.html, accessed: 2021-05-30.

[433] Sun, Y., and Smith, H., "Supersonic business jet conceptual design in a multidisciplinary design analysis optimization environment," *2018 AIAA/ASCE/AHS/ASC Structures, Structural Dynamics, and Materials Conference*, 2018, p. 1651.

[434] Sun, Y., and Smith, H., "Low-Boom Low-Drag Solutions through the Evaluation of Different Supersonic Business Jet Concepts," *The Aeronautical Journal*, 2019, p. 25.

[435] "X-59 Research Aircraft," NASA, 2019-05-19. URL https://www.nasa.gov/aero/x-59-research-aircraft-overview, accessed: 2021-05-30.

[436] "NASA Takes Delivery of GE Jet Engine for X-59," NASA, 2020. URL https://www.nasa.gov/feature/nasa-takes-delivery-of-ge-jet-engine-for-x-59, accessed: 2022-08-03.

[437] "Airframe Dimensions," Heritage Concorde, 2010-present. URL https://www.heritageconcorde.com/airframe-dimensions, accessed: 2022-07-25.

[438] "Concorde," Concorde SST, 2001. URL https://www.concordesst.com/dimentions.html, accessed: 2022-07-26.

[439] Bohannon, R., "NAC-60 SST Navigation and Traffic Control," *Navigation*, Vol. 11, No. 3, 1964, pp. 177–186.

[440] "Lockheed L-2000," Wikipedia, 2003. URL https://en.wikipedia.org/wiki/Lockheed_L-2000, accessed: 2022-08-23.

[441] "Tu-144 SST," Tu-144 SST, 2003. URL http://www.tu144sst.com/techspecs/performance.html, accessed: 2022-08-01.

[442] "Kolesov RD-36," Wikipedia, 2008. URL https://en.wikipedia.org/wiki/Kolesov_RD-36, accessed: 2022-08-01.

[443] "XB-70, SR-71, & TU-144 Large Supersonic Transports," Virginia Tech, 2006. URL http://www.dept.aoe.vt.edu/~mason/Mason_f/XB70SR71TU144.pdf, accessed: 2022-08-01.

[444] Rivers, R. A., and Jackson, E. B., "A Qualitative Piloted Evaluation of the Tupolev Tu-144 Supersonic Transport," *NASA/TM-2000-209850*, 2000, p. 44.

[445] "Conceptual Design of a Quiet Supersonic Technology Airliner," NASA, 2019. URL https://lbpw-ftp.larc.nasa.gov/aviation-2019/buonanno-lockheed-martin-conceptual-design-supersonic-airliner.pdf, accessed: 2022-08-02.

[446] Sun, Y., and Smith, H., "Low-Boom Low-Drag Solutions through the Evaluation of Different Supersonic Business Jet Concepts," *The Aeronautical Journal*, 2019, p. 25.

[447] Honda, M., and Yoshida, K., "D-SEND project for low sonic boom design technology," *29th International Congress of the Aeronautical Sciences*, 2014, p. 6.

[448] "Sukhoi-Gulfstream S-21," Wikipedia, 2012. URL https://en.wikipedia.org/wiki/Sukhoi-Gulfstream_S-21, accessed: 2021-05-30.

[449] Galbraith, B., *DATCOM+ Pro User's Manual*, Holy Cows, Inc., 2020. URL http://www.holycows.net/datcom/, version 3.7.

[450] Lan, C. E., Emdad, H., Chin, S., Sundaram, P., and Mehrotra, S., "Calculation of High Angle-of-Attack Aerodynamics of Fighter Configurations," *7th Applied Aerodynamics Conference*, 1989, p. 2188. https://doi.org/10.2514/6.1989-2188.

[451] Carlson, H. W., Mack, R. J., and Barger, R. L., "Estimation of Attainable Leading-Edge Thrust for Wings at Subsonic and Supersonic Speeds," Tech. Rep. TP-1500, NASA, 1979. URL https://ntrs.nasa.gov/citations/19790018939.

[452] Lan, C. E., and Chang, J.-F., "Calculation of Vortex Lift Effect for Cambered Wings by the Suction Analogy," Tech. Rep. CR-3449, NASA, 1981. URL https://ntrs.nasa.gov/citations/19820001317.

[453] NASA Langley Research Center, "Turbulence Modeling Resource: ONERA M6 Wing Numerical Validation," , 2021. URL https://turbmodels.larc.nasa.gov/onerawingnumerics_val.html, accessed: 2021-12-06.

[454] Seraj, S., and Martins, J. R. R. A., "Aerodynamic Shape Optimization of a Supersonic Transport Considering Low-Speed Stability," *AIAA SciTech 2022 Forum*, 2022, p. 2177. https://doi.org/10.2514/6.2022-2177.

[455] Barlow, J. B., Rae, W. H., and Pope, A., *Low-speed Wind Tunnel Testing*, 3rd ed., John wiley & sons, 1999.

[456] University of Washington Aeronautics & Astronautics, "Kirsten Wind Tunnel Technical Guide - Model Mounting," , 1936-present. URL https://www.aa.washington.edu/AERL/KWT/techguide#mounting, accessed: December 1st, 2023.

[457] Britt, R., Ortega, D., Mc Tigue, J., and Scott, M., "Wind Tunnel Test of a Very Flexible Aircraft Wing," *53rd AIAA/ASME/ASCE/AHS/ASC Structures, Structural Dynamics and Materials Conference 20th AIAA/ASME/AHS Adaptive Structures Conference 14th AIAA*, AIAA Paper 2012-1464, 2012. https://doi.org/10.2514/6.2012-1464.

[458] Polhamus, E. C., "A concept of the vortex lift of sharp-edge delta wings based on a leading-edge-suction analogy," Tech. Rep. TN D-3767, NASA, 1966.

[459] "Developing Airframe Design Technology to Reduce Sonic Booms," JAXA, Unspecified year. URL https://global.jaxa.jp/activity/pr/jaxas/no085/03.html, accessed: December 1str, 2023.

[460] Richardson, J. D., and A'Harrah, R. C., "Application of Flight Simulators to the Development of the A-5A Vigilante," *Journal of Aircraft*, Vol. 1, No. 4, 1964, pp. 171–177.

[461] Welge, H. R., Bonet, J., Magee, T., Tompkins, D., Britt, T. R., Nelson, C., Miller, G., Stenson, D., Staubach, J. B., Bala, N., Duge, R., O'Brien, M., Cedoz, R., Barlow, A., Martins, S., Viars, P., Rasheed, A., Kirby, M., Raczynski, C., Roughen, K., Doyle, S., Alston, K., Page, J., and Plotkin, K. J., "N+3 Advanced Concept Studies for Supersonic Commercial Transport Aircraft Entering Service in the 2030-2035 Period," Tech. Rep. NASA CR-2011-217084, NASA, April 2011. URL https://ntrs.nasa.gov/api/citations/20110010973/downloads/20110010973.pdf.

[462] Livne, E., Schmit, L. A., and Friedmann, P. P., "Towards an Integrated Approach to the Optimum Design of Actively Controlled Composite Wings," *Journal of Aircraft special issue on Multidisciplinary Optimization of Aeronautical Systems*, Vol. 27, No. 12, 1990, pp. 979–992. https://doi.org/10.2514/3.45972.

[463] Livne, E., "Integrated Aeroservoelastic Optimization: Status and Direction," *Journal of Aircraft*, Vol. 36, No. 1, 1999, pp. 122–145. https://doi.org/10.2514/2.2419.

[464] Livne, E., and Weisshaar, T. A., "Aeroelasticity of Nonconventional Airplane Configurations-past and Future," *Journal of aircraft*, Vol. 40, No. 6, 2003, pp. 1047–1065. https://doi.org/10.2514/2.7217.

[465] Livne, E., "Future of Airplane Aeroelasticity," *Journal of Aircraft*, Vol. 40, No. 6, 2003, pp. 1066–1092. https://doi.org/10.2514/2.7218.

[466] Livne, E., "Aircraft Active Flutter Suppression: State of the Art and Technology Maturation Needs," *Journal of Aircraft*, Vol. 55, 2018, pp. 410–450. https://doi.org/10.2514/1.C034442.

[467] Barzgaran, B., and Mesbahi, M., "Robust Analysis and Sensitivity Design of Model Predictive Control," *IFAC-PapersOnLine*, Vol. 53, No. 2, 2020, pp. 7111–7116. https://doi.org/10.1016/j.ifacol.2020.12.510.

[468] Barzgaran, B., Quenzer, Mesbahi, M., Morgansen, K., and Livne, E., "Real-time Model Predictive Control for Gust Load Alleviation on an Aeroelastic Wind Tunnel Test Article," *SciTech 2021 Forum*, AIAA, 2021, p. 0500. https://doi.org/10.2514/6.2021-0500.

[469] Ting, K.-Y., Mesbahi, M., Livne, E., and Morgansen, K. A., "Wind Tunnel Study of Preview H_2 and H_∞ Control for Gust Load Alleviation for Flexible Aircraft," *SciTech 2022 Forum*, AIAA, 2022, p. 2489. https://doi.org/10.2514/6.2022-2489.

[470] Livne, E., Precup, N., and Mor, M., "Design, Construction, and Tests of an Aeroelastic Wind Tunnel Model of a Variable Camber Continuous Trailing Edge Flap (VCCTEF) Concept Wing," *32nd AIAA Applied Aerodynamics Conference*, AIAA, 2014, p. 2442. https://doi.org/10.2514/6.2014-2442.

[471] Nguyen, N. T., Livne, E., Precup, N., Urnes, J. M., Nelson, C., Ting, E., and Lebofsky, S., "Experimental Investigation of a Flexible Wing with a Variable Camber Continuous Trailing Edge Flap Design," *32nd AIAA Applied Aerodynamics Conference*, AIAA, 2014, p. 2441. https://doi.org/10.2514/6.2014-2441.

[472] Precup, N., Mor, M., and Livne, E., "The Design, Construction, and Tests of a Concept Aeroelastic Wind Tunnel Model of a High-Lift Variable Camber Continuous Trailing Edge Flap (HL-VCCTEF) Wing Configuration," *56th AIAA/ASCE/AHS/ASC Structures, Structural Dynamics, and Materials Conference*, AIAA, 2015, p. 1406. https://doi.org/10.2514/6.2015-1406.

[473] Nguyen, N. T., Precup, N., Livne, E., Urnes, J. M., Dickey, E., Nelson, C., Chiew, J., Rodriguez, D. L., Ting, E., and Lebofsky, S., "Wind Tunnel Investigation of a Flexible Wing High-Lift Configuration with a Variable Camber Continuous Trailing Edge Flap Design," *33rd AIAA Applied Aerodynamics Conference*, AIAA, 2015, p. 2417. https://doi.org/10.2514/6.2015-2417.

[474] Precup, N., Mor, M., and Livne, E., "An Active Variable Camber Continuous Trailing Edge Flapped Wing Wind Tunnel Model for Aeroelastic "In-Flight" Shape Optimization Tests," *2018 Multidisciplinary Analysis and Optimization Conference*, AIAA, 2018, p. 3106. https://doi.org/10.2514/6.2018-3106.

[475] Mundt, T., "Development of an Active Aeroelastic Continuous Trailing Edge Wind Tunnel Wing Model for Drag and Gust Load Minimization," Master's thesis, University of Washington, 2019. MSAA Thesis.

[476] Nguyen, N. T., Cramer, N. B., Hashemi, K. E., Drew, M. C., Xiong, J., Mundt, T., Mor, M., and Livne, E., "Progress on Gust Load Alleviation Wind Tunnel Experiment and Aeroservoelastic Model Validation for a Flexible Wing with Variable Camber Continuous Trailing Edge Flap System," *SciTech 2020 Forum*, 2020, pp. 2020–0214. https://doi.org/10.2514/6.2020-0214.

[477] Berg, J., Ting, K.-Y., Mundt, T. J., Mor, M., Livne, E., and Morgansen, K. A., "Exploratory Wind Tunnel Gust Alleviation Tests of a Multiple-Flap Flexible Wing," *SciTech 2025 Forum*, 2022, pp. 2022–2488. https://doi.org/10.2514/6.2022-2488.

[478] Hinson, K. A., Morgansen, K. A., and Livne, E., "Autocovariance Least Squares Noise Covariance Estimation for a Gust Load Alleviation Test-Bed," *SciTech 2022 Forum*, AIAA, 2022, p. 0617. https://doi.org/10.2514/6.2022-0617.

[479] Hinson, K. A., and Morgansen, K. A., "Ill-Conditioned Autocovariance Least Square Noise Covariance Identification for Colored Noise Gust Estimation," *SciTech 2024 Forum*, AIAA, 2024, p. 0961. https://doi.org/10.2514/6.2024-0961.

[480] Berg, J., Ting, K.-Y., Mor, M., and Livne, E., "Test/Analysis Active Control Exploration Using the University of Washington's Multiple Control Surface Large Flexible Wing," *SciTech 2025 Forum*, 2025, p. 1854. https://doi.org/10.2514/6.2025-1854.

[481] Fonte, F., Riccobene, L., Ricci, S., Adden, S., and Martegani, M., "Design, Manufacturing and Validation of a Gust Generator for wind tunnel test of a Large Scale Aeroelastic Model,"

30TH ICAS The International Council for the Aerospace Sciences, 2016, p. 0676. URL https://www.icas.org/icas_archive/ICAS2016/data/papers/2016_0676_paper.pdf.

[482] Ricci, S., Gaspari, A. D., Riccobene, L., and Fonte, F., "Design and Wind Tunnel Test Validation of Gust Load Alleviation Systems," *58th AIAA/ASCE/AHS/ASC Structures, Structural Dynamics, and Materials Conference*, AIAA, 2017, p. 1818. https://doi.org/10.2514/6.2017-1818.

[483] Ricci, S., Fonte, F., De Gaspari, A., Riccobene, L., Mantegazza, P., Toffol, F., and Livne, E., "Development of a Wind Tunnel Model for Active Flutter Suppression Studies," *AIAA Scitech 2019 Forum*, AIAA, 2019, p. 2029. https://doi.org/10.2514/6.2019-2029.

[484] Fonte, F., De Gaspari, A., Riccobene, L., Toffol, F., Malik, S., Marchetti, L., Ricci, S., Mantegazza, P., Livne, E., et al., "Numerical and Experimental Investigations on Active Flutter Suppression Technologies," *18th International Forum on Aeroelasticity and Structural Dynamics (IFASD 2019)*, IFASD, 2019, pp. 1–19. URL https://re.public.polimi.it/retrieve/e0c31c11-381e-4599-e053-1705fe0aef77/FONTF04-19.pdf.

[485] Marchetti, L., De Gaspari, A., Riccobene, L., Toffol, F., Fonte, F., Ricci, S., Mantegazza, P., Livne, E., and Hinson, K. A., "Active Flutter Suppression Analysis and Wind Tunnel Studies of a Commercial Transport Configuration," *Scitech 2020 Forum*, AIAA, 2020, p. 1677. https://doi.org/10.2514/6.2020-1677.

[486] Berg, J., Morgansen, K. A., Livne, E., Riccobene, L., Fonte, F., Toffol, F., De Gaspari, A., Marchetti, L., Ricci, S., and Mantegazza, P., "Analytical and Experimental Evaluation of Multivariable Stability Margins in Active Flutter Suppression Wind Tunnel Tests," *SciTech 2021 Forum*, AIAA, 2021, p. 1261. https://doi.org/10.2514/6.2021-1261.

[487] Ricci, S., Marchetti, L., Riccobene, L., De Gaspari, A., Toffol, F., Fonte, F., Mantegazza, P., Berg, J., Morgansen, K. A., and Livne, E., "An Active Flutter Suppression (AFS) Project: Overview, Results and Lessons Learned," *SciTech 2021 Forum*, 2021, p. 0908. https://doi.org/10.2514/6.2021-0908.

[488] Di Leone, D., Lo Balbo, F., De Gaspari, A., and Ricci, S., "Model Updating and Aeroelastic Correlation of a Scaled Wind Tunnel Model for Active Flutter Suppression Test," *Aerospace*, Vol. 8, No. 11, 2021, p. 334. https://doi.org/10.3390/aerospace8110334.

[489] Fonzi, N., Ricci, S., and Livne, E., "Numerical and experimental investigations on freeplay-based LCO phenomena on a T-tail model," *SciTech 2022 Forum*, 2022, p. 1346. https://doi.org/10.2514/6.2022-1346.

[490] Ricci, S., Toffol, F., De Gaspari, A., Marchetti, L., Fonte, F., Riccobene, L., Mantegazza, P., Berg, J., Livne, E., and Morgansen, K., "Wind Tunnel System for Active Flutter Suppression Research: Overview and Insights," *AIAA Journal*, Vol. 60, 2022, pp. 6692–6714. https://doi.org/10.2514/1.J061985.

[491] Ricci, S., et al., "Ten Years of Aero-servo-elastic Tests at Large Polimi's Wind Tunnel for Active Flutter Control and Loads Alleviation," *Aeronautics and Astronautics: AIDAA XXVII International Congress*, Vol. 37, Materials Research Forum LLC, 2023, p. 48. URL https://mrforum.com/product/9781644902813/.

[492] Toffol, F., Fonzi, N., Ricci, S., Berg, J., and Livne, E., "Experimental Identification and Control of Flutter beyond the First Flutter Mechanism," *SciTech 2024 Forum*, 2024, p. 1268. https://doi.org/10.2514/6.2024-1268.

[493] Fonzi, N., Ricci, S., and Livne, E., "Wind Tunnel Tests of an Aeroelastic Model with Multiple Control Surface Freeplay nonlinearities," *SciTech 2024 Forum*, 2024, p. 1269. https://doi.org/10.2514/6.2024-1269.

[494] Toffol, F., Paolini, M., Riccobene, L., Grassi, D., Ricci, S., Berg, J., and Livne, E., "Study on Interaction Between a Stability Augmentation System and an Active Flutter Suppression Controller," *SciTech 2025 Forum*, 2025, p. 1853. https://doi.org/10.2514/6.2025-1853.

[495] Freydin, M., Rattner, M. K., Raveh, D. E., Kressel, I., Davidi, R., and Tur, M., "Fiber-optics-based Aeroelastic Shape Sensing," *AIAA Journal*, Vol. 57, No. 12, 2019, pp. 5094–5103. https://doi.org/10.2514/1.J057944.

[496] Joels, T., Yechieli, N., Edery-Azulay, L., and Raveh, D. E., "Design, Analyses, and Flutter Testing of the Active Aeroelastic Aircraft Testbed (A3TB) Platform," *SciTech 2022 Forum*, 2022, p. 2419. https://doi.org/10.2514/6.2022-2419.

[497] Avin, O., Raveh, D. E., Drachinsky, A., Ben-Shmuel, Y., and Tur, M., "Experimental Aeroelastic Benchmark of a Very Flexible Wing," *AIAA Journal*, Vol. 60, No. 3, 2022, pp. 1745–1768. https://doi.org/10.2514/1.J060621.

[498] Simbuerger, M., Raveh, D., and Tur, M., "Aeroelastic Shape Control Using Fiber-Optic-Measured Strain Data and Multiple Control Surfaces," *Journal of Aircraft*, Vol. 59, 2022, pp. 1545–1561. https://doi.org/10.2514/1.C036626.

[499] Ritter, M., Hilger, J., Ribeiro, A., Öngüt, A. E., Righi, M., Raveh, D. E., dos Santos, L. G. P., Drachinsky, A., Riso, C., Cesnik, C. E., et al., "Collaborative Pazy Wing Analyses for the Third Aeroelastic Prediction Workshop," *SciTech 2024 Forum*, 2024, p. 0419. https://doi.org/10.2514/6.2024-0419.

[500] Chwalowski, P., Stanford, B., Jacobson, K., Poplingher, L., Raveh, D. E., Jirasek, A., Pagliuca, G., and Marcello, R., "Flutter Prediction Report in Support of the High Angle Working Group at the Third Aeroelastic Prediction Workshop," *SciTech 2024 Forum*, 2024, p. 0418. https://doi.org/10.2514/6.2024-0418.

[501] Ben Asher, T., and Raveh, D. E., "Aeroelastic System Identification for Flutter Prediction via Multi-Output Autoregressive Modeling," *Journal of Aircraft*, Vol. 61, No. 2, 2024, pp. 470–484. https://doi.org/10.2514/1.C037477.

[502] Revivo, B., and Raveh, D. E., "Static Aeroelasticity and Stability of Very Flexible Swept Wings," *SciTech 2025 Forum*, 2025, p. 1018. https://doi.org/10.2514/6.2025-1018.

[503] Phillips, W., "Gust Alleviation. Performance and Dynamics of Aerospace Vehicles," Tech. Rep. SP–258, NASA, 1971. URL https://ntrs.nasa.gov/citations/19710015233.

[504] Regan, C., and Jutte, C., "Survey of Applications of Active Control Technology for Gust Alleviation and New Challenges for Lighter-weight Aircraft," Tech. Rep. TM-2012-216008, NASA, 2012. URL https://ntrs.nasa.gov/citations/20120013450.

[505] Wykes, J., and Mori, A., "Techniques and Results of an Analytical Investigation into Controlling the Structural Modes of Flexible Aircraft," *Symposium on Structural Dynamics and Aeroelasticity*, AIAA, 1965, p. 1140. https://doi.org/10.2514/6.1965-1140.

[506] Schmitt, N. P., Rehm, W., Pistner, T., Zeller, P., Reithmeier, G., Stilkerich, S., Schertler, K., Diehl, H., and Zinner, H., "The AWIATOR Airborne LIDAR Turbulence Sensor," *Aerospace Science and Technology*, Vol. 11, No. 7-8, 2007, pp. 546–552. https://doi.org/10.1016/j.ast.2007.03.006.

[507] Rabadan, G., Schmitt, N., Pistner, T., and Rehm, W., "Airborne LIDAR for Automatic Feedforward Control of Turbulent In-Flight Phenomena," *Journal of Aircraft*, Vol. 47, No. 2, 2010, pp. 392–403. https://doi.org/10.2514/1.44950.

[508] Fezans, N. and Joos, H., "Combined Feedback and LIDAR-based Feedforward Active Load Alleviation," *Atmospheric Flight Mechanics Conference*, AIAA, 2017, p. 3548. https://doi.org/10.2514/6.2017-3548.

[509] Giesseler, H.-G., Kopf, M., Faulwasser, T., Varutti, P., and Findeisen, R., "Model Predictive Control for Gust Load Alleviation," *IFAC Proceedings Volumes*, Vol. 45, No. 17, 2012, pp. 27–32. https://doi.org/10.3182/20120823-5-NL-3013.00049.

[510] Hamada, Y., "Aircraft Gust Alleviation using Discrete-Time Preview Controller with Prior Gust Information," *The SICE Annual Conference 2013*, IEEE, 2013, pp. 1907–1912. URL https://ieeexplore.ieee.org/document/6736312.

[511] Wang, Y., Li, F., and Da Ronch, A., "Adaptive Feedforward Control Design For Gust Loads Alleviation of Highly Flexible Aircraft," *Atmospheric Flight Mechanics Conference*, AIAA, 2015, p. 2243. https://doi.org/10.2514/6.2015-2243.

[512] Zhao, Y., Yue, C., and Hu, H., "Gust Load Alleviation on a Large Transport Airplane," *Journal of Aircraft*, Vol. 53, No. 6, 2016, pp. 1932–1946. https://doi.org/10.2514/1.C033713.

[513] Hamada, Y., "Preview Feedforward Compensation: LMI Synthesis and Flight Simulation," *IFAC-PapersOnLine*, Vol. 49, No. 17, 2016, pp. 397–402. https://doi.org/10.1016/j.ifacol.2016.09.068.

[514] Liu, X., Sun, Q., and Cooper, J., "LQG Based Model Predictive Control for Gust Load Alleviation," *Aerospace science and Technology*, Vol. 71, 2017, pp. 499–509. https://doi.org/10.1016/j.ast.2017.10.006.

[515] Takase, R., Hamada, Y., and Shimomura, T., "Aircraft Gust Alleviation Preview Control with a Discrete-Time LPV Model," *SICE Journal of Control, Measurement, and System Integration*, Vol. 11, No. 3, 2018, pp. 190–197. https://doi.org/10.23919/SICE.2017.8105493.

[516] Khalil, A. and Fezans, N., "Performance Enhancement of Gust Load Alleviation Systems for Flexible Aircraft using H_∞ Optimal Control with Preview," *SciTech 2019 Forum*, AIAA, 2019, p. 0822. https://doi.org/10.2514/6.2019-0822.

[517] Khalil, A., and Fezans, N., "A Multi-Channel H_∞ Preview Control Approach to Load Alleviation Function Design," *CEAS Aeronautical Journal*, Vol. 12, No. 2, 2021, pp. 401–412. https://doi.org/10.1007/s13272-021-00503-z.

[518] Khalil, A., and Fezans, N., "Gust Load Alleviation for Flexible Aircraft using Discrete-Time Preview Control," *The Aeronautical Journal*, Vol. 125, No. 1284, 2021, pp. 341–364. https://doi.org/10.1017/aer.2020.85.

[519] Hamada, Y., "New LMI-based Conditions for Preview Feedforward Synthesis," *Control Engineering Practice*, Vol. 90, 2019, pp. 19–26. https://doi.org/10.1016/j.conengprac.2019.05.014.

[520] Takase, R., Fujita, K., Hamada, Y., Tsuchiya, T., Shimomura, T., and Suzuki, S., "Robust C* Control Law Design Augmented with LIDAR-Based Gust Information," *IFAC-PapersOnLine*, Vol. 52, No. 12, 2019, pp. 122–127. https://doi.org/10.1016/j.ifacol.2019.11.119.

[521] Fournier, H., Massioni, P., Tu Pham, M., Bako, L., Vernay, R., and Colombo, M., "Robust Gust Load Alleviation of Flexible Aircraft Equipped with LIDAR," *Journal of Guidance, Control, and Dynamics*, 2021, pp. 1–15. https://doi.org/10.2514/1.G006084.

[522] Fezans, N., Wallace, C., Kiehn, D., Cavaliere, D., and Vrancken, P., "Lidar-Based Gust Load Alleviation-Results Obtained on the Clean Sky 2 Load Alleviation Benchmark," *19th International Forum on Aeroelasticity and Structural Dynamics*, International Forum on Aeroelasticity and Structural Dynamics (IFASD), 2022, p. 0155. URL https://elib.dlr.de/187462/.

[523] Fournier, H., Massioni, P., Pham, M. T., Bako, L., Vernay, R., and Colombo, M., "Robust Gust Load Alleviation at Different Flight Points and Mass configurations," *SciTech 2022 Forum*, AIAA, 2022, p. 0285. https://doi.org/10.2514/6.2022-0285.

[524] Wang, Y., Da Ronch, A., and Ghandchi Tehrani, M., "Adaptive Feedforward Control for Gust-induced Aeroelastic Vibrations," *Aerospace*, Vol. 5, No. 3, 2018, p. 86. https://doi.org/10.3390/aerospace5030086.

[525] Barzgaran, B., Quenzer, J. D., Zongolowicz, A., Hinson, K. A., Mesbahi, M., Morgansen, K., and Livne, E., "Low-cost Wind Tunnel Studies of Gust Alleviation Control Techniques," *18th International Forum on Aeroelasticity and Structural Dynamics*, International Forum on Aeroelasticity and Structural Dynamics (IFASD), 2019, p. 008. URL https://www.asdjournal.org/public/Proceedings/IFASD_2019/IFASD-2019-008.pdf.

[526] Barzgaran, B., Quenzer, Mesbahi, M., Morgansen, K., and Livne, E., "Real-time Model Predictive Control for Gust Load Alleviation on an Aeroelastic Wind Tunnel Test Article," *SciTech 2021 Forum*, AIAA, 2021, p. 0500. https://doi.org/10.2514/6.2021-0500.

[527] Hamada, Y., Saitoh, K., and Kobiki, N., "Gust Alleviation Control using Prior Gust Information: Wind Tunnel Test Results," *IFAC-PapersOnLine*, Vol. 52, No. 12, 2019, pp. 128–133. https://doi.org/10.1016/j.ifacol.2019.11.125.

[528] Hu, Y., Dai, Y., Wu, Y., and Yang, C., "Time-Domain Feedforward Control for Gust Response Alleviation Based on Seamless Morphing Wing," *AIAA Journal*, Vol. 60, No. 10, 2022, pp. 5707–5722. https://doi.org/10.2514/1.J061763.

[529] Hamada, Y., "Flight Test Results of Disturbance Attenuation using Preview Feedforward Compensation," *IFAC-PapersOnLine*, Vol. 50, No. 1, 2017, pp. 14188–14193. https://doi.org/10.1016/j.ifacol.2017.08.2086.

[530] Roger, K. L., Hodges, G. E., and Felt, L., "Active Flutter Suppression - a Flight Test Demonstration," *Journal of Aircraft*, Vol. 12, No. 6, 1975, pp. 551–556. https://doi.org/10.2514/3.59833.

[531] Redd, L., Gilman Jr, J., Cooley, D., and Sevart, F., "Wind-Tunnel Investigation of a B-52 Model Flutter Suppression System," *Journal of Aircraft*, Vol. 11, No. 11, 1974, pp. 659–663. https://doi.org/10.2514/3.60401.

[532] Sensburg, O., Honlinger, H., Noll, T., and Huttsell, L., "Active Flutter Suppression on an F-4F Aircraft," *Journal of Aircraft*, Vol. 19, 1982, pp. 354–359. https://doi.org/10.2514/3.57404.

[533] Roizner, F., Raveh, D., and Karpel, M., "Safe Flutter Tests Using Parametric Flutter Margins," *Journal of Aircraft*, Vol. 56, 2018, pp. 228–238. https://doi.org/10.2514/1.C035045.

[534] Heidersbach, R., Seth, D., McCrink, M., and Karpel, M., "Safe Flutter Flight Testing of an Unmanned Aerial Vehicle Utilizing Parametric Flutter Margin," *SciTech 2023 Forum*, AIAA, 2023, p. 2071. https://doi.org/10.2514/6.2023-2071.

[535] Tischler, M. B., Berger, T., Ivler, C. M., Mansur, M. H., Cheung, K. K., and Soong, J. Y., *Practical Methods for Aircraft and Rotorcraft Flight Control Design: An Optimization-Based Approach*, AIAA, 2017. https://doi.org/10.2514/4.104435.

[536] Theis, J., Pfifer, H., and Seiler, P. J., "Robust Control Design for Active Flutter Suppression," *Atmospheric Flight Mechanics Conference*, AIAA, 2016, p. 1751. https://doi.org/10.2514/6.2016-1751.

[537] Kotikalpudi, A., Danowsky, B. P., Schmidt, D., Theis, J., and Seiler, P., "Flutter Suppression Control Design for a Small, Flexible Flying-wing Aircraft," *2018 Multidisciplinary Analysis and Optimization Conference*, AIAA, 2018, p. 3426. https://doi.org/10.2514/6.2018-3426.

[538] Theis, J., Pfifer, H., and Seiler, P., "Robust Modal Damping Control for Active Flutter Suppression," *Journal of Guidance, Control, and Dynamics*, Vol. 43, No. 6, 2020, pp. 1056–1068. https://doi.org/10.2514/1.G004846.

[539] Bennett, R. M., Eckstrom, C. V., Rivera Jr, J. A., Dansberry, B. E., Farmer, M. G., and Durham, M. H., "The Benchmark Aeroelastic Models Program: Description and Highlights of Initial Results," Tech. Rep. TM-104180, NASA, 1991. URL https://ntrs.nasa.gov/citations/19920005831.

[540] Durham, M., Keller, D., Benett, R., and Wieseman, C., "A Status Report on a Model for Benchmark Active Controls Testing," *32nd Structures, Structural Dynamics, and Materials Conference*, AIAA, 1991, p. 1011.

[541] Waszak, M., "Modeling the Benchmark Active Control Technology Wind-tunnel Model for Application to Flutter Suppression," *21st Atmospheric Flight Mechanics Conference*, AIAA, 1996, p. 3437. https://doi.org/10.2514/6.1996-3437.

[542] Mukhopadhyay, V., "Transonic Flutter Suppression Control Law Design Using Classical and Optimal Techniques with Wind Tunnel Results," *40th Structures, Structural Dynamics, and Materials Conference and Exhibit*, AIAA, 1999, p. 1396. https://doi.org/10.2514/6.1999-1396.

[543] Mukhopadhyay, V., "Transonic Flutter Suppression Control Law Design and Wind-tunnel Test Results," *Journal of Guidance, Control, and Dynamics*, Vol. 23, No. 5, 2000, pp. 930–937. https://doi.org/10.2514/2.4635.

[544] Scott, R. C., and Pado, L. E., "Active Control of Wind-tunnel Model Aeroelastic Response Using Neural Networks," *Journal of Guidance, Control, and Dynamics*, Vol. 23, No. 6, 2000, pp. 1100–1108. https://doi.org/10.2514/2.4661.

[545] Haley, P., and Soloway, D., "Generalized Predictive Control for Active Flutter Suppression," *Journal of Guidance, Control, and Dynamics*, Vol. 24, No. 1, 2001, pp. 154–159. https://doi.org/10.2514/2.4696.

[546] Waszak, M. R., "Robust Multivariable Flutter Suppression for Benchmark Active Control Technology Wind-tunnel Model," *Journal of Guidance, Control, and Dynamics*, Vol. 24, No. 1, 2001, pp. 147–153. https://doi.org/10.2514/2.4694.

[547] Heeg, J., "Overview and lessons learned from the Aeroelastic Prediction Workshop," *54th AIAA/ASME/ASCE/AHS/ASC Structures, Structural Dynamics, and Materials Conference*, AIAA, 2013, p. 1798. URL https://c3.ndc.nasa.gov/dashlink/static/media/dataset/S1A-paper.pdf.

[548] Vipperman, J. S., Clark, R. L., Conner, M., and Dowell, E. H., "Experimental Active Control of a Typical Section Using a Trailing-edge Flap," *Journal of Aircraft*, Vol. 35, No. 2, 1998, pp. 224–229. https://doi.org/10.2514/2.2312.

[549] Vipperman, J. S., Barker, J. M., Clark, R. L., and Balas, G. J., "Comparison of μ-and H-Synthesis Controllers 2 on an Experimental Typical Section," *Journal of Guidance, Control, and Dynamics*, Vol. 22, No. 2, 1999, pp. 278–285. https://doi.org/10.2514/2.4375.

[550] McEver, M. A., Ardelean, E. V., Cole, D. G., and Clark, R. L., "Active Control and Closed-loop Identification of Flutter Instability in Typical Section Airfoil," *Journal of Guidance, Control, and Dynamics*, Vol. 30, No. 3, 2007, pp. 733–740. https://doi.org/10.2514/1.26335.

[551] Shao, K., Wu, Z., Yang, C., Chen, L., and Lv, B., "Design of an Adaptive Gust Response Alleviation Control System: Simulations and Experiments," *Journal of Aircraft*, Vol. 47, No. 3, 2010, pp. 1022–1029. https://doi.org/10.2514/1.46689.

[552] Huang, R., Qian, W., Zhao, Y., and Hu, H., "Flutter Analysis: Using Piecewise Quadratic Interpolation with Mode Tracking and Wind-tunnel Tests," *Journal of aircraft*, Vol. 47, No. 4, 2010, pp. 1447–1451. https://doi.org/10.2514/1.47687.

[553] Huang, R., Hu, H., and Zhao, Y., "Single-input/single-output Adaptive Flutter Suppression of a Three-dimensional Aeroelastic System," *Journal of Guidance, Control, and Dynamics*, Vol. 35, No. 2, 2012, pp. 659–665. https://doi.org/10.2514/1.55746.

[554] Qian, W., Huang, R., Hu, H., and Zhao, Y., "New Method of Modeling Uncertainty for Robust Flutter Suppression," *Journal of Aircraft*, Vol. 50, No. 3, 2013, pp. 994–999. https://doi.org/10.2514/1.C031987.

[555] Qian, W., Huang, R., Hu, H., and Yonghui, Z., "Active Flutter Suppression of a Multiple-actuated-wing Wind Tunnel Model," *Chinese Journal of Aeronautics*, Vol. 27, No. 6, 2014, pp. 1451–1460. https://doi.org/10.1016/j.cja.2014.10.011.

[556] Huang, R., Zhao, Y., and Hu, H., "Wind-tunnel Tests for Active Flutter Control and Closed-loop Flutter Identification," *AIAA Journal*, Vol. 54, No. 7, 2016, pp. 2089–2099. https://doi.org/10.2514/1.J054649.

[557] Yang, Z., Huang, R., Zhao, Y., and Hu, H., "Design of an Active Disturbance Rejection Control for Transonic Flutter Suppression," *Journal of Guidance, Control, and Dynamics*, Vol. 40, No. 11, 2017, pp. 2905–2916. https://doi.org/10.2514/1.G002690.

[558] Qian, W., "Robust Flutter Suppression and Wind-tunnel Tests of a Three-dimensional Wing," *Journal of Aerospace Engineering*, Vol. 31, No. 6, 2018, p. 04018099. https://doi.org/10.1061/(ASCE)AS.1943-5525.0000925.

[559] Dillinger, J., Mai, H., Krüger, W. R., Schmidt, T. G., and Stalla, J. F., "Design, Manufacturing and Identification of an Actively Controlled Flexible Wing for Subsonic Wind Tunnel Testing," *International Forum on Aeroelasticity and Structural Dynamics 2024*, 2024, p. 121. URL https://conf.ifasd2024.nl/proceedings/documents/121.pdf.

[560] Winther, B., Shirley, W., and Heimbaugh, R., "Wind-tunnel Investigation of Active Controls Technology Applied to a Dc-10 Derivative," *Journal of Guidance and Control*, Vol. 4, No. 5, 1981, pp. 536–542. https://doi.org/10.2514/3.56103.

[561] Adams Jr, W., Christhilf, D., Waszak, M., and Design, T., "Evaluation of Three Active Flutter Suppression Controllers," Tech. Rep. TM-4338, NASA, 1992. URL https://ntrs.nasa.gov/citations/19930000882.

[562] Waszak, M. R., and Srinathkumar, S., "Flutter Suppression for the Active Flexible Wing-a Classical Design," *Journal of Aircraft*, Vol. 32, No. 1, 1995, pp. 61–67. https://doi.org/10.2514/3.46684.

[563] Mukhopadhyay, V., "Flutter Suppression Control Law Design and Testing for the Active Flexible Wing," *Journal of Aircraft*, Vol. 32, No. 1, 1995, pp. 45–51. https://doi.org/10.2514/3.46682.

[564] Scott, R., Vetter, T., Penning, K., Coulson, D., and Heeg, J., "Aeroservoelastic Testing of a Sidewall Mounted Free Flying Wind-tunnel Model," *26th AIAA Applied Aerodynamics Conference*, AIAA, 2008, p. 7186. https://doi.org/10.2514/6.2008-7186.

[565] Heaney, P. S., and Quindlen, J. F., "Overview of the Integrated Adaptive Wing Technology Maturation Wind-tunnel Test Objectives," *SciTech 2024 Forum*, AIAA, 2024, p. 2509. https://doi.org/10.2514/6.2024-2509.

[566] Scott, R. C., Bartels, R. E., Funk, C. J., Allen, T. J., Sexton, B. W., Dykman, J. R., and Coulson, D. A., "Aeroservoelastic Test of the Subsonic Ultra-green Aircraft Research Truss-braced Wing Model," *Journal of Guidance, Control, and Dynamics*, Vol. 39, No. 8, 2016, pp. 1820–1833. https://doi.org/10.2514/1.G000265.

[567] Hamada, Y., Saitoh, K., and Kobiki, N., "Gust Alleviation Control using Prior Gust Information: Wind Tunnel Test Results," *IFAC-PapersOnLine*, Vol. 52, No. 12, 2019, pp. 128–133. https://doi.org/10.1016/j.ifacol.2019.11.125.

[568] Takase, R., Fujita, K., Hamada, Y., Tsuchiya, T., Shimomura, T., and Suzuki, S., "Robust C* Control Law Design Augmented with LIDAR-Based Gust Information," *IFAC-PapersOnLine*, Vol. 52, No. 12, 2019, pp. 122–127. https://doi.org/10.1016/j.ifacol.2019.11.119.

[569] Zhou, Y., Wu, Z., and Yang, C., "Gust Alleviation and Wind Tunnel Test by Using Combined Feedforward Control and Feedback Control," *Aerospace*, Vol. 9, No. 4, 2022, p. 225. https://doi.org/10.3390/aerospace9040225.

[570] Sharqi, B., Cesnik, C. E., Joels, T., and Raveh, D. E., "3D-Printed Swept-Wing Wind Tunnel Model Characterization for Aeroelastic Studies," *International Forum on Aeroelasticity and Structural Dynamics*, 2022, p. 079. URL https://www.researchgate.net/publication/378310146_3D-PRINTED_SWEPT-WING_WIND_TUNNEL_MODEL_CHARACTERIZATION_FOR_AEROELASTIC_STUDIES.

[571] Castillo Zuñiga, D. F., Giacobini Souza, A., da Silva, R. G., and Sandoval Góes, L. C., "Response and Operational Modal Analysis from Wind Tunnel Test of the EOLO Flexible

Aircraft," *AIAA Scitech 2021 Forum*, AIAA, 2021, p. 1389. https://doi.org/10.2514/6.2021-1389.

[572] Peloubet Jr, R., Haller, R., and Bolding, R., "F-16 Flutter Suppression System Investigation Feasibility Study and Wind Tunnel Tests," *Journal of Aircraft*, Vol. 19, No. 2, 1982, pp. 169–175. https://doi.org/10.2514/3.57371.

[573] Peloubet Jr, R., Haller, R., and Bolding, R., "Recent Developments in the F-16 Flutter Suppression with Active Control Program," *Journal of Aircraft*, Vol. 21, No. 9, 1984, pp. 716–721. https://doi.org/10.2514/3.45019.

[574] Hwang, C., Johnson, E., and Pi, W., "Recent Development of the YF-17 Active Flutter Suppression System," *Journal of Aircraft*, Vol. 18, No. 7, 1981, pp. 537–545. https://doi.org/10.2514/3.57523.

[575] Johnson, E., Hwang, C., Pi, W., Kesler, D., Joshi, D., and Harvey, C., "Test Demonstration of Digital Control of Wing/store Flutter," *Journal of Guidance, Control, and Dynamics*, Vol. 6, No. 3, 1983, pp. 176–181. https://doi.org/10.2514/3.57523.

[576] Hwang, C., and Pi, W., "Optimal Control Applied to Aircraft Flutter Suppression," *Journal of Guidance, Control, and Dynamics*, Vol. 7, No. 3, 1984, pp. 347–354. https://doi.org/10.2514/3.1986.

[577] Murrow, H., and Eckstrom, C., "Drones for Aerodynamic and Structural Testing (Dast)-a Status Report," *Journal of Aircraft*, Vol. 16, No. 8, 1979, pp. 521–526. https://doi.org/10.2514/3.58558.

[578] Newsom, J. R., and Pototzky, A. S., "Analysis and Flight Data for a Drone Aircraft with Active Flutter Suppression," *Journal of Aircraft*, Vol. 19, No. 11, 1982, pp. 1012–1018. https://doi.org/10.2514/3.44805.

[579] Newsom, J. R., Pototzky, A. S., and Abel, I., "Design of a Flutter Suppression System for an Experimental Drone Aircraft," *Journal of Aircraft*, Vol. 22, No. 5, 1985, pp. 380–386. https://doi.org/10.2514/3.45135.

[580] Nissim, E., "Design of Control Laws for Flutter Suppression Based on the Aerodynamic Energy Concept and Comparisons with Other Design Methods," *30th Structures, Structural Dynamics and Materials Conference*, AIAA, 1990, p. 1212. https://doi.org/10.2514/6.1989-1212.

[581] Nissim, E., "Order Reduction of Linear-quadratic-gaussian-designed Controllers," *Journal of guidance, control, and dynamics*, Vol. 16, No. 6, 1993, pp. 1154–1161. https://doi.org/10.2514/3.21140.

[582] Burnett, E., Atkinson, C., Beranek, J., Sibbitt, B., Holm-Hansen, B., and Nicolai, L., "Ndof Simulation Model for Flight Control Development with Flight Test Correlation," *AIAA Modeling and Simulation Technologies Conference*, AIAA, 2010, p. 7780. https://doi.org/10.2514/6.2010-7780.

[583] Hjartarson, A., Seiler, P. J., Packard, A., and Balas, G. J., "LPV Aeroservoelastic Control Using the Lpvtools Toolbox," *AIAA Atmospheric Flight Mechanics (AFM) Conference*, AIAA, 2013, p. 4742. https://doi.org/10.2514/6.2013-4742.

[584] Ryan, J. J., and Bosworth, J. T., "Current and Future Research in Active Control of Lightweight, Flexible Structures Using the X-56 Aircraft," *52nd Aerospace Sciences Meeting*, AIAA, 2014, p. 0597. https://doi.org/10.2514/6.2014-0597.

[585] Burnett, E., Beranek, J., Holm-Hansen, B., Atkinson, C., and Flick, P., "Design and Flight Test of Active Flutter Suppression on the X-56A Multi-utility Technology Test-bed Aircraft," *The Aeronautical Journal*, Vol. 120, No. 1228, 2016, pp. 893–909. https://doi.org/10.1017/aer.2016.41.

[586] Grauer, J. A., and Boucher, M., "System identification of flexible aircraft: lessons learned from the X-56A Phase 1 flight tests," *SciTech 2020 Forum*, AIAA, 2020, p. 1017. https://doi.org/10.2514/6.2020-1017.

[587] Cesnik, C. E., Senatore, P. J., Su, W., Atkins, E. M., and Shearer, C. M., "X-HALE: a Very Flexible Unmanned Aerial Vehicle for Nonlinear Aeroelastic Tests," *AIAA journal*, Vol. 50, No. 12, 2012, pp. 2820–2833. https://doi.org/10.2514/1.J051392.

[588] Sharqi, B., and Cesnik, C. E., "Ground Vibration Testing on Very Flexible Aircraft," *AIAA Scitech 2020 Forum*, AIAA, 2020, p. 1902. https://doi.org/10.2514/6.2020-1902.

[589] Pfifer, H., and Danowsky, B. P., "System Identification of a Small Flexible Aircraft-invited," *AIAA Atmospheric Flight Mechanics Conference*, AIAA, 2016, p. 1750. https://doi.org/10.2514/6.2016-1750.

[590] Schmidt, D. K., "Matlab-based Flight-dynamics and Flutter Modeling of a Flexible Flying-wing Research Drone," *Journal of Aircraft*, Vol. 53, No. 4, 2016, pp. 1045–1055. https://doi.org/10.2514/1.C033539.

[591] Schmidt, D. K., Zhao, W., and Kapania, R. K., "Flight-dynamics and Flutter Modeling and Analyses of a Flexible Flying-wing Drone-invited," *AIAA Atmospheric Flight Mechanics Conference*, AIAA, 2016, p. 1748. https://doi.org/10.2514/6.2016-1748.

[592] Schmidt, D. K., "Stability Augmentation and Active Flutter Suppression of a Flexible Flying-wing Drone," *Journal of Guidance, Control, and Dynamics*, Vol. 39, No. 3, 2016, pp. 409–422. https://doi.org/10.2514/1.G001484.

[593] Schmidt, D. K., Danowsky, B. P., Seiler, P. J., and Kapania, R. K., "Flight-dynamics and Flutter Analysis and Control of an Mdao-designed Flying-wing Research Drone," *SciTech 2019 forum*, AIAA, 2019, p. 1816. https://doi.org/10.2514/6.2019-1816.

[594] Schmidt, D. K., Danowsky, B. P., Kotikalpudi, A., Theis, J., Regan, C. D., Seiler, P. J., and Kapania, R. K., "Modeling, Design, and Flight Testing of Three Flutter Controllers for a Flying-wing Drone," *Journal of Aircraft*, Vol. 57, No. 4, 2020, pp. 615–634. https://doi.org/10.2514/1.C035720.

[595] Consortium, F., et al., "Flutter Free Flight Envelope Expansion for Economical Performance Improvement," , 2015. https://doi.org/10.3030/636307.

[596] Stahl, P., Sendner, F.-M., Hermanutz, A., Rößler, C., and Hornung, M., "Mission and Aircraft Design of FLEXOP Unmanned Flying Demonstrator to Test Flutter Suppression Within Visual Line of Sight," *17th AIAA Aviation Technology, Integration, and Operations Conference*, AIAA, 2017, p. 3766. https://doi.org/10.2514/6.2017-3766.

[597] Luspay, T., Ossmann, D., Wuestenhagen, M., Teubl, D., Baár, T., Pusch, M., Kier, T. M., Waitman, S., Iannelli, A., Marcos, A., et al., "Flight Control Design for a Highly Flexible Flutter Demonstrator," *SciTech 2019 Forum*, AIAA, 2019, p. 1817. https://doi.org/10.2514/6.2019-1817.

[598] Waitman, S., and Marcos, A., "$\mathcal{H}_\infty$ Control Design for Active Flutter Suppression of Flexible-wing Unmanned Aerial Vehicle Demonstrator," *Journal of Guidance, Control, and Dynamics*, Vol. 43, No. 4, 2020, pp. 656–672. https://doi.org/10.2514/1.G004618.

[599] Takarics, B., and Vanek, B., "Robust Control Design for the FLEXOP Demonstrator Aircraft via Tensor Product Models," *Asian Journal of Control*, Vol. 23, No. 3, 2021, pp. 1290–1300. https://doi.org/10.1002/asjc.2547.

[600] Patartics, B., Lipták, G., Luspay, T., Seiler, P., Takarics, B., and Vanek, B., "Application of Structured Robust Synthesis for Flexible Aircraft Flutter Suppression," *IEEE Transactions on Control Systems Technology*, Vol. 30, No. 1, 2021, pp. 311–325. https://doi.org/10.1109/TCST.2021.3066096.

[601] Castillo Zuñiga, D. F., Giacobini Souza, A., and Goes, L. C. S., "Development of an Aeroelastic In-flight Testing System for a Flexible Wing Unmanned Aerial Vehicle Using Acceleration and Strain Sensors," *AIAA Scitech 2019 Forum*, AIAA, 2019, p. 2033. https://doi.org/10.2514/6.2019-2033.

[602] Zou, Q., Mu, X., Li, H., Huang, R., and Hu, H., "Robust Active Suppression for Body-freedom Flutter of a Flying-wing Unmanned Aerial Vehicle," *Journal of the Franklin Institute*, Vol. 358, No. 5, 2021, pp. 2642–2660. https://doi.org//10.1016/j.jfranklin.2021.01.012.

[603] Zou, Q., Huang, R., and Hu, H., "Body-freedom Flutter Suppression for a Flexible Flying-wing Drone via Time-delayed Control," *Journal of Guidance, Control, and Dynamics*, Vol. 45, No. 1, 2022, pp. 28–38. https://doi.org/10.2514/1.G006114.

[604] Zou, Q., Huang, R., Mu, X., Hu, H., Fan, Z., and Liu, H., "Body-freedom Flutter Analysis and Flight Test for a Flying-wing Aircraft Testbed," *Mechanical Systems and Signal Processing*, Vol. 221, 2024, p. 111717. https://doi.org/10.1016/j.ymssp.2024.111717.

[605] Zou, Q., Huang, R., Hu, H., and Liu, H., "Studying Body-Freedom Flutter Mechanism via a Rigid-Elastic Aeroelastic Model of Reduced-Order," *Aerospace Science and Technology*, 2025, p. 110155. https://doi.org/10.1016/j.ast.2025.110155.

[606] Dempster, J. B., and Arnold, J. I., "Flight Test Evaluation of an Advanced Stability Augmentation System for B-52 Aircraft." *Journal of Aircraft*, Vol. 6, No. 4, 1969, pp. 343–348. https://doi.org/10.2514/3.44062.

[607] Hodges, G., and McKenzie, J., "Performance compatibility and flight testing of B-52 CCV systems," *Aircraft Systems and Technology Meeting*, AIAA, 1975, p. 1035. https://doi.org/10.2514/6.1975-1035.

[608] Arnold, J. I., and Murphy, F. B., "B-52 Control Configured Vehicles: Flight Test Results," *Advanced Control Technology and Its Potential for Future Transport, NASA TMX-3409 (1976/8)*, 1976, pp. 75–89. URL https://ntrs.nasa.gov/citations/19760024051.

[609] Triplett, W. E., "A Feasibility Study of Active Wing/store Flutter Control," *Journal of Aircraft*, Vol. 9, No. 6, 1972, pp. 438–444. https://doi.org/10.2514/3.59009.

[610] Triplett, W. E., Kappus, H.-P. F., and Landy, R. J., "Active Flutter Control-An Adaptable Applicationto Wing/Store Flutter," *Journal of Aircraft*, Vol. 10, No. 11, 1973, pp. 669–678. https://doi.org/10.2514/3.60281.

[611] Sensburg, O., Honlinger, H., Noll, T., and Huttsell, L., "Active Flutter Suppression on an F-4F Aircraft," *Journal of Aircraft*, Vol. 19, No. 5, 1982, pp. 354–359. https://doi.org/10.2514/3.57404.

[612] Lind, R., and Brenner, M., "Robust Flutter Margins of an F/A-18 Aircraft from Aeroelastic Flight Data," *Journal of Guidance, Control, and Dynamics*, Vol. 20, No. 3, 1997, pp. 597–604. https://doi.org/10.2514/2.4082.

[613] Gupta, K., Doyle, T., and Hahn, E., "Ae/flutter Simulation and Flight Test Correlation of the F/A-18 Active Aeroelastic Wing (AAW)," *43rd AIAA Aerospace Sciences Meeting and Exhibit*, AIAA, 2005, p. 233. https://doi.org/10.2514/6.2005-233.

[614] Seiler, P., Balas, G., and Packard, A., "Linear Parameter Varying Control for the X-53 Active Aeroelastic Wing," *AIAA Atmospheric Flight Mechanics Conference*, AIAA, 2011, p. 6290. https://doi.org/10.2514/6.2011-6290.

[615] Chipman, R. R., Zislin, A. M., and Waters, C., "Control of Aeroelastic Divergence," *Journal of aircraft*, Vol. 20, No. 12, 1983, pp. 1007–1013. https://doi.org/10.2514/3.48204.

[616] Rimer, M., Chipman, R., and Mercadante, R., "Divergence/flutter Suppression System for a Forward Swept-wing Configuration with Wing-mounted Stores," *Journal of Aircraft*, Vol. 21, No. 8, 1984, pp. 631–638. https://doi.org/10.2514/3.45034.

[617] Peloubet, R. P., "NASA Aeroelasticity Handbook Volume 2: Design Guides Part 2," Tech. Rep. TP—2006-212490, NASA, 2006. URL https://ntrs.nasa.gov/citations/20070008370, edited by, D. D. Liu, D. Sarhaddi, and F. M. Piolenc.

[618] Iovnovich, M., Nahom, T., Presman, M., Avsaid, D., Braier, T., and Raveh, D. E., "Assessment of Advanced Flutter Flight-test Techniques and Flutter Boundary Prediction Methods," *Journal of Aircraft*, Vol. 55, No. 5, 2018, pp. 1877–1889. https://doi.org/10.2514/1.G002690.

[619] Wykes, J. H., Kelpl, M., and Brosnan, M. J., "Flight Test and Analyses of the B-1 Structural Mode Control System at Supersonic Flight Conditions," Tech. Rep. CR-170405, NASA, 1983. URL https://ntrs.nasa.gov/citations/19840005129.

[620] Borst, R., and Strome, R., "E-6 Flutter Investigation and Experience," *Astrodynamics Conference*, AIAA, 1992, p. 4601. https://doi.org/10.2514/6.1992-4601.

[621] Britt, R. T., Jacobson, S. B., and Arthurs, T. D., "Aeroservoelastic Analysis of the B-2 Bomber," *Journal of Aircraft*, Vol. 37, No. 5, 2000, pp. 745–752. https://doi.org/10.2514/2.2674.

[622] Hamada, Y., Kikuchi, R., and Inokuchi, H., "LIDAR-based Gust Alleviation Control System: Obtained Results and Flight Demonstration Plan," *IFAC-PapersOnLine*, Vol. 53, No. 2, 2020, pp. 14839–14844. https://doi.org/10.1016/j.ifacol.2020.12.1928.

[623] Miyazawa, Y., and Dowell, E., "Robust Control System Design with Multiple Model Approach and Its Application to Active Flutter Control," *Guidance, Navigation and Control Conference*, AIAA, 1989, p. 3578. https://doi.org/10.2514/6.1989-3578.

[624] Xiong, G., and Yang, C., "Synthesis on Flutter Suppression Control Law for Active Aeroelastic Wing," *19th AIAA Applied Aerodynamics Conference*, AIAA, 2001, p. 1463. https://doi.org/10.2514/6.2001-1463.

[625] Danowsky, B. P., Thompson, P., Lee, D.-C., and Brenner, M. J., "Modal Isolation and Damping for Adaptive Aeroservoelastic Suppression," *AIAA Atmospheric Flight Mechanics (AFM) Conference*, AIAA, 2013, p. 4743. https://doi.org/10.2514/6.2013-4743.

[626] Micheli, B., "Active Flutter Suppression: Quantification of Performance Loss Due to Actuator Saturation," *Journal of Guidance, Control, and Dynamics*, Vol. 47, No. 11, 2024, pp. 2333–2350. https://doi.org/10.2514/1.G008146.

[627] Faïsse, E., Vernay, R., Vetrano, F., Alazard, D., and Morlier, J., "Adding Control in Multidisciplinary Design Optimization of a Wing for Active Flutter Suppression," *SciTech 2021 Forum*, AIAA, 2021, p. 0892. https://doi.org/10.2514/6.2021-0892.

[628] Faïsse, E., Vernay, R., Vetrano, F., Morlier, J., and Alazard, D., "Aeroservoelastic Wing Sizing Using Integrated Structural and Control (Co-design) Optimization," *SciTech 2022 Forum*, AIAA, 2022, p. 2243. https://doi.org/10.2514/6.2022-2243.

[629] Fournier, H., Vernay, R., Massioni, P., Pham, M. T., and Bako, L., "Active Flutter Suppression $\mathcal{H}_\infty$ Synthesis using Multiple Models with Imposed Aeroelastic Poles," *SciTech 2023 Forum*, AIAA, 2023, p. 0686. https://doi.org/10.2514/6.2023-0686.

[630] de Souza, A. D. R., Poussot-Vassal, C., Vuillemin, P., and Zucco, J. T., "Aircraft Flutter Suppression: from a Parametric Model to Robust Control," *2023 European Control Conference (ECC)*, IEEE, 2023, pp. 1–6. https://doi.org/10.23919/ECC57647.2023.10178141.

[631] Karpel, M., Moulin, B., and Idan, M., "Robust Aeroservoelastic Design with Structural Variations and Modeling Uncertainties," *Journal of Aircraft*, Vol. 40, No. 5, 2003, pp. 946–954. https://doi.org/10.2514/2.6871.

[632] Moulin, B., "Robust Controller Design for Active Flutter Suppression," *AIAA Guidance, Navigation, and Control Conference and Exhibit*, AIAA, 2004, p. 5115. https://doi.org/10.2514/6.2004-5115.

[633] Xiang, J., Yan, Y., and Li, D., "Recent Advance in Nonlinear Aeroelastic Analysis and Control of the Aircraft," *Chinese journal of aeronautics*, Vol. 27, No. 1, 2014, pp. 12–22. https://doi.org/10.1016/j.cja.2013.12.009.

[634] Wu, Z., and Cooper, J. E., "Active Flutter Suppression Combining the Receptance Method and Flutter Margin," *57th AIAA/ASCE/AHS/ASC Structures, Structural Dynamics, and Materials Conference*, AIAA, 2016, p. 1227. https://doi.org/10.2514/6.2016-1227.

[635] Waitz, S., "Active Flutter Suppression of a Highly Flexible Swept Wing Through Multiple Flap Control," *19th International Forum on Aeroelasticity and Structural Dynamics 2022*, AIAA, 2022, p. 72. URL https://elib.dlr.de/188295/1/IFASD-2022-072.pdf.

[636] Richards, R., Islam, S. A., and Bernstein, D. S., "Predictive Cost Adaptive Control of the BACT Flutter Model," *SciTech 2024 Forum*, AIAA, 2024, p. 1731. https://doi.org/10.2514/6.2024-1731.

[637] Ting, K.-Y., Berg, J., Mesbahi, M., and Livne, E., "Aeroservoelastic Wind Tunnel Evaluation of H∞ Active Flutter Suppression," *AIAA SCITECH 2026 Forum*, AIAA, 2026, p. 1058. https://doi.org/10.2514/6.2026-1058.

[638] Williams, O., Samuell, M., Sarwas, E. S., Robbins, M., and Ferrante, A., "Experimental Study of a CFD Validation Test Case for Turbulent Separated Flows," *SciTech 2020 Forum*, 2020, p. 0092. https://doi.org/10.2514/6.2020-0092.

[639] Chaparro, D., Fujiwara, G. E., Ting, E., and Nguyen, N. T., "Aerodynamic Modeling of Transonic Aircraft Using Vortex Lattice Coupled with Transonic Small Disturbance for Conceptual Design," *34th AIAA Applied Aerodynamics Conference*, AIAA, 2016, p. 3418. https://doi.org/10.2514/6.2016-3418.

[640] Balas, G. J., Doyle, J. C., Glover, K., Packard, A., and Smith, R., *μ-Analysis and Synthesis Toolbox*, 1st ed., MUSYN Inc. and The MathWorks, Natick MA, 1993. URL https://vismod.media.mit.edu/pub/clarkson/boring/Doc%20CD/help/pdf_doc/mutools/mu.pdf.

[641] Balas, G., Chiang, R., Packard, A., and Safonov, M., *Robust Control Toolbox User's Guide*, 1st ed., The MathWorks, Inc., Natick MA, 2005.

[642] Balas, G., Chiang, R., Packard, A., and Safonov, M., *Robust Control Toolbox User's Guide 2020a*, 30th ed., The MathWorks, Inc., Natick MA, 2020, Chaps. 2,7. URL https://www.mathworks.com/help/robust/.

[643] Doyle, J., Glover, K., Khargonekar, P., and Francis, B., "State-space Solutions to Standard H_2 and H_∞ Control Problems," *1988 American Control Conference*, IEEE, 1988, pp. 1691–1696. https://doi.org/10.1109/9.29425.

[644] Skogestad, S. and Postlethewaite, I., *Multivariable Feedback Control: Analysis and Design*, 2nd ed., John Wiley & Sons, 2007, Chaps. 9,10. https://doi.org/10.5555/1121635.

[645] McLean, D., *Automatic Flight Control Systems*, Prentice Hall, 1990. https://doi.org/10.1177/002029400303600602.

[646] Schmidt, D. K., *Modern Flight Dynamics*, McGraw-Hill, 2012.

[647] Baldelli, D., Chen, P.-C., and Panza, J., "Unified Aeroelastic and Flight Dynamic Formulation via Rational Function Approximations," *Journal of Aircraft*, Vol. 43, No. 3, 2006, pp. 763–772. https://doi.org/10.2514/1.16620.

[648] Lind, R., and Brenner, M., *Robust Aeroservoelastic Stability Analysis*, Springer, 1999. https://doi.org/10.1007/978-1-4471-0849-8.

[649] Quenzer, J. D., Barzgaran, B., Mesbahi, M., and Morgansen, K., "The Generic Wide Body Aircraft Model," *2018 Guidance, Navigation, and Control Conference*, AIAA, 2018, p. 0877. https://doi.org/10.2514/6.2018-0877.

[650] Gangsaas, D., Ly, U., and Norman, D.,, "Practical Gust load Alleviation and Flutter Suppression Control Laws Based on a LQG Methodology," *19th Aerospace Sciences Meeting*, AIAA, 1981, p. 21. https://doi.org/10.2514/6.1981-21.

[651] Karpel, M., Moulin, B., and Chen, P., "Dynamic Response of Aeroservoelastic Systems to Gust Excitation," *Journal of Aircraft*, Vol. 42, No. 5, 2005, pp. 1264–1272. https://doi.org/10.2514/1.6678.

[652] Etkin, B., Hughes, P., and Zhu, S., "Equivalent Deterministic Inputs for Random Processes," *Journal of Guidance, Control, and Dynamics*, Vol. 7, No. 4, 1984, pp. 477–482. https://doi.org/10.2514/3.19881.

[653] Takaba, K., "A Tutorial on Preview Control Systems," *SICE 2003 Annual Conference*, Vol. 2, IEEE, 2003, pp. 1388–1393. URL https://ieeexplore.ieee.org/document/1324171.

[654] Gahinet, P. and Apkarian, P., "A Linear Matrix Inequality Approach to H_∞ Control," *International journal of robust and nonlinear control*, Vol. 4, No. 4, 1994, pp. 421–448. https://doi.org/10.1002/rnc.4590040403.

[655] Apkarian, P. and Noll, D., "Nonsmooth H_∞ Synthesis," *Transactions on Automatic Control*, Vol. 51, No. 2, 2006, pp. 382–382. https://doi.org/10.1109/TAC.2005.860290.

[656] Rabiner, L., Schafer, R. W., and Rader, C., "The Chirp Z-transform Algorithm," *IEEE transactions on audio and electroacoustics*, Vol. 17, No. 2, 1969, pp. 86–92. https://doi.org/10.1109/TAU.1969.1162034.

[657] Rabiner, L. R., Gold, B., and Yuen, C. K., "Theory and Application of Digital Signal Processing," *IEEE Transactions on Systems, Man, and Cybernetics*, Vol. 8, No. 2, 1978, pp. 146–146. https://doi.org/10.1109/TSMC.1978.4309918.